COMPUTATIONAL DESIGN, SYNTHESIS AND OPTOELECTRONIC CHARACTERISATION OF THERMALLY ACTIVATED DELAYED FLUORESCENT MATERIALS : DONOR-ACCEPTOR AND MULTI-RESONANCE DESIGNS

David Luke Starkey Hall

A Thesis Submitted for the Degree of PhD
at the
University of St Andrews

2022

Candidate's declaration

I, David Hall, do hereby certify that this thesis, submitted for the degree of PhD, which is approximately 77,000 words in length, has been written by me, and that it is the record of work carried out by me, or principally by myself in collaboration with others as acknowledged, and that it has not been submitted in any previous application for any degree. I confirm that any appendices included in my thesis contain only material permitted by the 'Assessment of Postgraduate Research Students' policy.

I was admitted as a research student at the University of St Andrews in September 2016.

I received funding from an organisation or institution and have acknowledged the funder(s) in the full text of my thesis.

Date 13/10/2021 Signature of candidate

Supervisor's declaration

I hereby certify that the candidate has fulfilled the conditions of the Resolution and Regulations appropriate for the degree of PhD in the University of St Andrews and that the candidate is qualified to submit this thesis in application for that degree. I confirm that any appendices included in the thesis contain only material permitted by the 'Assessment of Postgraduate Research Students' policy.

Date 13/10/2021 Signature of supervisor

Date 13/10/2021 Signature of supervisor

Permission for publication

In submitting this thesis to the University of St Andrews we understand that we are giving permission for it to be made available for use in accordance with the regulations of the University Library for the time being in force, subject to any copyright vested in the work not being affected thereby. We also understand, unless exempt by an award of an embargo as requested below, that the title and the abstract will be published, and that a copy of the work may be made and supplied to any bona fide library or research worker, that this thesis will be electronically accessible for personal or research use and that the library has the right to migrate this thesis into new electronic forms as required to ensure continued access to the thesis.

I, David Hall, confirm that my thesis does not contain any third-party material that requires copyright clearance.

The following is an agreed request by candidate and supervisor regarding the publication of this thesis:

Printed copy

Embargo on part (embargo data and thesis but not title) of print copy for a period of 1 year on the following ground(s):

- Publication would preclude future publication

Supporting statement for printed embargo request

Not all the material in this thesis has been published at the current stage.

Electronic copy

Embargo on all of electronic copy for a period of 1 year on the following ground(s):

- Publication would preclude future publication

Supporting statement for electronic embargo request

Not all the material in this thesis has been published at the current stage.

Title and Abstract

- I agree to the title and abstract being published.

Date 13/10/2021 Signature of candidate

Date 13/10/2021 Signature of supervisor

Date 13/10/2021 Signature of supervisor

Underpinning Research Data or Digital Outputs

Candidate's declaration

I, David Hall, understand that by declaring that I have original research data or digital outputs, I should make every effort in meeting the University's and research funders' requirements on the deposit and sharing of research data or research digital outputs.

Date 13/10/2021 Signature of candidate

Permission for publication of underpinning research data or digital outputs

We understand that for any original research data or digital outputs which are deposited, we are giving permission for them to be made available for use in accordance with the requirements of the University and research funders, for the time being in force.

We also understand that the title and the description will be published, and that the underpinning research data or digital outputs will be electronically accessible for use in accordance with the license specified at the point of deposit, unless exempt by award of an embargo as requested below.

The following is an agreed request by candidate and supervisor regarding the publication of underpinning research data or digital outputs:

Embargo on all of electronic files for a period of 1 year on the following ground(s):

- Publication would preclude future publication

Supporting statement for embargo request

Not all the material in this thesis has been published at the current stage.

Date 13/10/2021 Signature of candidate

Date 13/10/2021 Signature of supervisor

Date 13/10/2021 Signature of supervisor

Abstract

This thesis concerns the study of organic TADF materials, focussing on donor-acceptor (D-A TADF) and multi-resonance (MR-TADF) emitters. Materials were developed in silico, they were then synthesized, characterized and finally tested in OLED devices.

Chapter 1 introduces the various radiative decay pathways available in electronically excited molecules from photoluminescence and electroluminescence. D-A TADF and MR-TADF emitters are discussed in detail.

Chapter 2 introduces the background behind the computational methods undertaken. These include Hartree Fock, coupled cluster and DFT.

Chapter 3 investigates the impact of donor dendrons in the TADF emitter **2CzPN.** Donor extension improves k_{RISC} but at the expense of increasing non-radiative pathways.

Chapter 4 discloses a new acceptor unit, BImPy, which is coupled to phenoxazine as a donor, with TADF observed. The torsion angle within the acceptor was modulated as a function of *N*-substitution, with 4 emitters studied.

In Chapter 5 a computational investigation of a series of 14 literature D-A TADF emitters is undertaken, with calculated T_1, T_2, S_1, ΔE_{ST}, ΔE_{ST2} and ΔE_{T2T1} along with S_1, T_1 and T_2 excited state natures from DFT compared with SCS-CC2, with M06-2X and CAM-B3LYP performing well.

Chapter 6 presents an accurate method for computational modelling of MR-TADF, SCS-CC2. This method is then used to design two new MR-TADF emitters which were synthesized and their optoelectronic properties evaluated with OLEDs fabricated.

In Chapter 7 the calculated S_1, T_1 and ΔE_{ST} of 35 literature MR-TADF emitters from SCS-CC2 and TD(A)-DFT are compared with experimental values, with SCS-CC2 performing well. Using SCS-CC2 the properties of MR-TADF emitters are discussed and further studies of related INVEST materials and D-A emitters that contain a MR-TADF acceptors are undertaken.

Chapter 8 presents a new class of MR-TADF emitter without acceptor units designed using SCS-CC2. Modest TADF in doped films and high performing hyperfluorescent OLEDs are presented.

Abstract

Cette thèse de doctorat concerne l'étude de matériaux organiques TADF, en particulier, des émetteurs donneur-accepteur (D-A TADF) et multi-résonnant (MR-TADF). Les matériaux ont été développés in silico, caractérisés et finalement testés en dispositifs OLED.

Le chapitre 1 introduit les différents chemins de désactivation radiative disponibles à partir des états excités d'une molécule lorsqu'on considère un mécanisme de photoluminescence ou d'électroluminescence. Les notion d'émetteurs D-A TADF et MR-TADF sont introduites de manière détaillée.

Le chapitre 2 introduit les méthodes computationnelles utilisées dans cette thèse. Celles-ci incluent la méthode Hatree-Fock, la théorie de la fonctionnelle de la densité (DFT) et les méthodes du cluster couplé.

Le chapitre 3 étudie l'impact de l'extension de l'unité donneuse à partir de l'émetteur TADF **2CzPN**. L'extension de l'unité donneuse améliore k_{RISC} mais augmente d'un autre côté la contribution des chemins de désactivation non-radiative.

Le chapitre 4 introduit un nouvel unité acceptrice, BImPy, qui couplée à une phenoxazine comme donneur donne lui à un comportement TADF. L'angle de torsion au niveau de l'accepteur a été modulé grâce à la présence de différents substituants résultant en 4 nouveaux émetteurs.

Le chapitre 5 consiste en une étude computationnelle d'une série de 14 émetteurs D-A TADF extraits de la littérature. Les énergies et les natures des états excités T_1, T_2, S_1 ainsi que les différences d'énergies entre ceux-ci ΔE_{ST}, ΔE_{ST2} and ΔE_{T2T1} ont été calculés au niveau TD-DFT et comparés aux résultats obtenus avec la méthode SCS-CC2. Les fonctionnelles M06-2X et CAM-B3LYP ont été identifiés comme les plus appropriées pour le calcul de cette famille de molécules.

Le chapitre 6 présente une méthode précise pour modéliser les MR-TADF, à savoir la méthode SCS-CC2. Cette méthode est utilisée pour concevoir deux nouveaux émetteurs MR-TADF qui ont été synthétisés, caractérisés et testés dans des dispositifs OLED.

Dans le chapitre 7, les énergies des états S_1, T_1 ainsi que le ΔE_{ST} de 35 émetteurs MR-TADF de la littérature calculés au niveau SCS-CC2 et TD(A)-DFT ont été comparés avec des données expérimentales montrant que les ΔE_{ST} calculés au niveau SCS-CC2 reproduisent très bien l'expérience. En utilisant la méthode SCS-CC2, les propriétés des émetteurs MR-TADF sont discutés et l'étude de composés INVEST et D-A contenant un accepteur MR-TADF a été réalisée.

Le chapitre 8 présente une nouvelle classe d'émetteur MR-TADF sans unité acceptrice conçue sur base de calculs SCS-CC2. Un comportement TADF modeste a été observé dans des films dopés et des OLEDs basées sur le principe d'hyperfluorescence ont été présentées.

Declaration

I fully acknowledge that the work presented is my own. The research has been carried out in the groups of Prof. Eli Zysman-Colman (University of St Andrews) and Prof. Yoann Olivier (University of Mons/University of Namur). The work has been highly interdisciplinary with contributions from collaborators that are listed below.

Chapter 1: I am the primary author of the text.

Chapter 2: I am the primary author of the text.

Chapter 3: Computational studies were undertaken by me. Synthesis was undertaken by me though **Cz-2CzPN** was initially prepared by Dr. Michael Yin Wong (University of St Andrews), subsequent samples were synthesized by me. UV-Vis absorption, electrochemistry and SS photophysics were measured by me. Time-resolved PL decays and Φ_{PL} were measured by Eimantas Duda and Dr. Sergey Bagnich (University of Bayreuth). Single crystal data collection and crystal solving was performed by Dr. Cameron L. Carpenter-Warren and Dr. David B. Cordes (University of St Andrews). I am the primary author of this text. The work in this chapter has been published; *J. Phys. Chem. B*, 2022, **126**, 552.

Chapter 4. Computational studies were undertaken by me. Synthesis was undertaken by me. UV-Vis absorption, electrochemistry and SS photophysics were undertaken by me. Time-resolved PL decays and Φ_{PL} were measured by Eimantas Duda and Dr. Sergey Bagnich (University of Bayreuth). TGA and DSC were measured by Francesco Rodella (University of Bayreuth). Single crystal data collection and crystal solving was performed by Dr. Cameron L. Carpenter-Warren and Dr. David B. Cordes (University of St Andrews). OLED devices were fabricated by Dr. Pachaiyappan Rajamalli (University of St Andrews). I am the primary author of this text. The work in this chapter has been published; *Adv. Optical Mater*., 2021, **9**, 2100846.

Chapter 5. Computational studies were undertaken by me. I am the primary author of this text.

Chapter 6. Computational studies were undertaken by me. Synthesis was undertaken by Dr. Subeesh Suresh. UV-Vis absorption, electrochemistry and SS photophyscis were undertaken by me. Time-resolved PL decays were measured by Eimantas Duda and Dr Sergey Bagnich (University of Bayreuth). Φ_{PL} studies were undertaken by me. Single crystal data collection and crystal solving was performed by Dr David B. Cordes (University of St Andrews). OLED devices were fabricated by Dr Paloma L. dos Santos (University of St Andrews). I am the primary author of this text. The work in this chapter has been published; *Adv. Optical Mater*., 2020, **8**, 1901627.

Chapter 7. Computational studies were undertaken by me, based on initial work from Dr. Anton Pershin (University of Mons). I am the primary author of this text. Publications based on this work are; *Nat. Commun*., 2019, **10**, 597, *J. Am. Chem. Soc*., 2020, **142**, 6588, *Angew. Chem. Int. Ed*., 2020, **59**, 3156, *Mater. Chem. Front*., 2020, **4**, 2018, *Chem. Sci.,* 2022, **13**, 1665 and *J. Mater. Chem. C,* 2022*,* 10.1039/D2TC00198E and submitted for publication in; *J. Chem. Theory. Comput*, 10.33774/chemrxiv-2021-496gn.

Chapter 8. Computational studies were undertaken by me. Synthesis was undertaken by me. UV-Vis absorption, electrochemistry and SS photophysics were undertaken by me. Time-resolved PL decays and Φ_{PL} were undertaken by Eimantas Duda and Dr. Sergey Bagnich (University of Bayreuth) and me. Simulated singlet and triplet emission spectra was prepared by Prof. David Beljonne (University of Mons). Single crystal data collection and crystal solving was performed by Prof. Alex M. Z. Slawin (University of St Andrews). OLED devices were fabricated by Kleitos Stravrou and Dr. Andrew Danos (Durham University). I am the primary author of this text. The work in this chapter has been published; *Mater. Horizons*, 2022, 10.1039/d1mh01383a.

Acknowledgments

I would firstly like to thank my family. To my parents for supporting me throughout my studies. Although I know you would rather I entered a more conventional profession, I hope I have done you proud. Secondly my grandparents, Irene Starkey, Joyce Hall, Hubert Starkey and Roy Hall. Unfortunately, none of you are here to see this but you all gave me the opportunities to be here, and I will always be grateful. To my friends back home and from Durham you have all been wonderful, especially you Aran. Our constant communication and trips together have kept me going throughout.

I would like to thank my Secondary school chemistry teach Mr Gibson who taught me to love chemistry, I am not sure where you are, but you were an inspiration. Next, I must thank Prof. Martin Bryce, my master's supervisor at Durham University. Your third-year course in organic electronics introduced me to this field and is why I am here today.

Thanks to Prof. Eli Zysman-Colman for offering me the position and continued guidance and support, your continued positivity and enthusiasm is infectious. Although I actively avoided computational chemistry throughout my undergraduate, Prof. Yoann Olivier introduced me to it, and encouraged me to embrace it. You have always been so kind and everything I know in this field is due to you, merci. This was further assisted by fruitful discussion with Prof. Juan Carlos Sancho-Garcia and Prof. David Beljonne. Throughout this work I have collaborated with many people. Thanks to Prof. Anna Köhler, Eimantas Duda and Dr Sergey Bagnich, from the University of Bayreuth, for working alongside me over many projects. It has been a very rewarding collaboration. Thanks to Prof. Andy Monkman, Kleitos Stavrou and Dr. Andrew Danos from Durham University. Thanks to the X-ray team in St Andrews, Dr Cameron L. Carpenter-Warren, Dr David B. Cordes and Prof. Alex M. Z. Slawin for producing structures on often questionable samples. Half of my time has been spent using computational resources, thank you Sébastien Kozlowskyj for all your help while using the servers. Dr Anton Pershin introduced me to MR-TADF modelling, which has formed a major part of my PhD.

Thanks to both groups in St Andrews and Mons. Particularly to Claus, Diego, Laura and Adam who brought so much fun at the start of my PhD. Adrian, you were my adoptive MChem student in my

first year, we had so much joy and I hope I helped you throughout your work. Nidhi, you worked alongside me for many years, and taught me so much about physics and we formed an excellent team, and of course the co-founder of wine Fridays. We have had quite the dramatic time with fires, fights and of course a car crash but it was a good journey! Dongyang and Jiyu, we have undertaken this journey together, it has been wonderful getting to know you both, good luck with the next steps and I hope to see you in China for some karaoke soon. Sam, we have been friends since day one and housemates for a long time. I know I often drove you crazy especially during lockdowns, but we had a great time. My highlight was our Peep Show movies list, especially our 'All the Blues' evening. Dr. Subeesh Madayand Suresh, I will always be in awe of your synthetic skills and kindness, you are what every postdoc should aspire to, thank you for all your help. Dr. Pachaiyappan Rajamalli you were here at the start and were a truly wonderful collaborator. In recent years new PhD members have joined, and although I must thank you all for collaborations and help, the fun I have had with Etty, Tim and Oil deserves a special mention, you have all kept me smiling. In Mons, to all the wonderful people who made me feel welcome, thanks for showing me the sights of Belgium and the many beers. Finally, a selection of visiting German students who have passed through the doors of St Andrews deserve particular mention, initially to Eduard and Fabian. The final student I crossed paths with for one week initially and she has since returned to St Andrews and after some initial confusing interactions in the lab has become my partner. These have been the toughest months of my PhD, but you have kept me sane, thank you Lea. I should have finished in October 2020, but the fire and the pandemic pushed this back one year, and although most people would resent that, I cannot as it allowed me to meet you properly. I am excited for what our future holds, thank you for everything.

This PhD has been a roller-coaster of extreme highs and extreme lows. But the people I have met along the way, masters, PhDs and postdocs alike, have been the highlights of my journey. Good luck to all of you and I hope we cross paths again soon. Don't be a stranger.

The end of this work is a bittersweet moment for me as I am not able to share it with my Nan. I am sorry you missed reading this by a few days, although we both know you wouldn't have found it that interesting. This work is for you, thank you for your support and love throughout my journey.

Funding

This work was supported by Leverhulme Trust (RPG-2016-047).

Computational resources have been provided by the Consortium des Équipements de Calcul Intensif (CÉCI), funded by the Fonds de la Recherche Scientifiques de Belgique (F.R.S.-FNRS) under Grant No. 2.5020.11, as well as the Tier-1 supercomputer of the Fédération Wallonie-Bruxelles, infrastructure funded by the Walloon Region under the grant agreement n1117545.

Research Data access statement

Research data underpinning this thesis are available at:

https://doi.org/10.17630/24d985e0-e808-413d-8877-d7b4204a6f6a

List of Abbreviations

Abbreviations	Expansion
2-MeTHF	2-methyltetrahydrofuran
A	Acceptor
Abs	Absorption
ACQ	Aggregation-caused quenching
AO	Atomic orbital
a.u.	Arbitrary units
BCPO	Bis-4-(N-carbazolyl)phenyl)phenylphosphine oxide
CBP	4,4'-Bis(carbazol-9-yl)biphenyl
CC2	Second order approximate couple cluster
CCSD	Coupled cluster single double
CHex	Cyclohexane
CIE	Commision Internationale de L'Éclairage
CT	Charge transfer
CT-LE	Mixed charge transfer-locally excited
CV	Cyclic voltammetry
Cz	Carbazole
D	Donor
DCM	Dichloromethane
DET	Dexter energy transfer
DFl	Delayed fluorescence
DFT	Density functional theory
DMA	Dimethylacetamide
DMAC	9,9-Dimethyl-9,10-dihydroacridine
DMF	Dimethylformamide

DPA	Diphenylamine
DPEPO	bis[2-(diphenylphosphino)phenyl]ether oxide
DPV	Differential pulse voltammetry
DSC	Differential scanning calorimetry
e^-	Electron
EBL	Electron blocking layer
EML	Emitter layer
E^{ox}	Anodic peak potential
E^{red}	Cathodic peak potential
EQE	External quantum efficiency
EQE_{100}	External quantum efficiency at 100 cd m^{-2}
EQE_{1000}	External quantum efficiency at 1,000 cd m^{-2}
ETL	Electron transporting layer
EtOAc	Ethyl acetate
f	Oscillator Strength
FC	Franck Condon
Fc/Fc^+	Ferrocene/Ferrocenium couple
Fl	Fluorescence
FRET	Förster resonant energy transfer
FWHM	Full width at half maxima
h^+	Hole
HAT-CN	1,4,5,8,9,11-hexaazatriphenylenehexacarbonitrile
HBL	Hole blocking layer
Hex	*n*-Hexane
HF	Hartree Fock
HLCT	Hybrid local charge transfer
HOMO	Highest occupied molecular orbital

HRMS	High resolution mass spectrometry
HTL	Hole transporting layer
IC	Internal conversion
INVEST	Inverted singlet-triplet energy gap
IRF	Instrument response function
IQE	Internal quantum efficiency
ISC	Intersystem crossing
ITO	Indium tin oxide
k_{nr}	Non-radiative rate constant
k_{nr}^{S}	Singlet Non-radiative rate constant
k_{nr}^{T}	Triplet Non-radiative rate constant
k_{ISC}	Intersystem crossing rate constant
k_{RISC}	Reverse Intersystem crossing rate constant
k_{r}^{S}	Fluorescence Radiative rate constant
k_{r}^{T}	Phosphorescence Radiative rate constant
LE	Locally excited
Lum_{max}	Maximum luminance
LUMO	Lowest unoccupied molecular orbital
MAD	Mean average deviation
mCBP	3,3'-di(9H-carbazol-9-yl)bi-phenyl
mCP	1,3-bis(N-carbazolyl)benzene
MeCN	Acetonitrile
MO	Molecular orbital
$[n\mathrm{Bu}_4\mathrm{N}]\mathrm{PF}_6$	Tetrabutylammonium hexafluorophosphate
NMR	Nuclear magnetic resonance
NRD	Non-radiative decay
OLED	Organic light-emitting diode

PFl	Prompt fluorescence
PhCzBCz	9-(2-(9-phenyl-9H-carbazol-3-yl)phenyl)-9H-3,9'-bicarbazole)
PhMe	Toluene
Phos	Phosphorescence
PL	Photoluminescence
PMMA	Polymethyl methacrylate
PhOLED	Phosphorescent organic light emitting diode
PPCz	3,6-bis(diphenylphosphinyl)-9-phenyl-carbazole
PTZ	Phenothiazine
PXZ	Phenoxazine
r^2	Linear correlation coefficient
RIC	Reverse internal conversion
RISC	Reverse intersystem crossing
RMSD	Root mean square deviation
RO_{100}	Roll-off at 100 cd m^{-2}
RTP	Room temperature phosphorescence
S_0	Singlet ground state
S_1	Lowest singlet excited state
S_2	Second lowest singlet excited state
S_3	Third lowest singlet excited state
SCE	Saturated calomel electrode
SCF	Self-consistent field
SCS	Spin component scaled
S_{n+1}	Higher lying singlet states
SOC	Spin orbit coupling
SPA	Singlet exciton-polaron annihilation
SRCT	Short range charge transfer

STA	Singlet triplet annihilation
T_1	Lowest triplet excited state
T_2	Second Lowest triplet excited state
T_3	Third Lowest triplet excited state
TADF	Thermally activated delayed fluorescence
TAPC	4,4′-cyclohexylidenebis[N,N-bis(4-methylphenyl)benzenamine]
TCTA	Tris(4-carbazoyl-9-ylphenyl)amine
T_d	Decomposition temperature
TDA-DFT	Tamm-Dancoff approximation
TD-DFT	Time dependent density functional theory
T_g	Glass temperature
TGA	Thermogravimetric analysis
THF	Tetrahydrofuran
T_m	Melting temperature
TmPyPB	1,3,5-tri(m-pyrid-3-yl-phenyl)benzene
T_{n+1}	Higher lying triplet states
TPA	Triplet polaron annihilation
TSPO1	Diphenyl[4-(triphenylsilyl)phenyl]phosphine oxide
TTA	Triplet triplet annihilation
V_{on}	Turn on voltage
wt%	Weight percent
$\Delta E_{H\text{-}L}$	Energy gap between HOMO and LUMO
ΔE_{ST}	Energy difference between lowest singlet and triplet excited state
ΔE_{ST2}	Energy difference between lowest singlet and second lowest triplet excited state
ΔE_{T2T1}	Energy difference between second lowest triplet and lowest triplet and excited state

ε	Molar extinction coefficient
Φ_{DF}	Delayed fluorescence quantum yield
Φ_{PF}	Prompt fluorescence quantum yield
Φ_{PL}	Photoluminescence quantum yield
λ_{PL}	Photoluminescence emission maximum
λ_{abs}	Absorption maximum
λ_{exc}	Excitation wavelength
λ_{EL}	Electroluminescence emission maximum
μ_{fi}	Transition dipole moment
σ	Standard deviation
τ_d	Delayed fluorescence lifetime
τ_p	Prompt fluorescence lifetime
τ_{ph}	Phosphorescence lifetime

Table of Contents

Motivation

Since the early work out of Kodak demonstrating the first organic light emitting diode (OLED) operating at low voltage,[1] there has been a surge of interest in the field. OLEDs are a mature technology and are now present in most new smartphones. They are used within display applications and offer attractive alternatives to commercially well-established liquid crystal displays (LCD) and inorganic light emitting diodes (LEDs). Compared to LCD systems they offer higher efficiencies owing to their self-luminescent nature, this mitigates the need for a backlight. Further it ensures that power consumption of the device is directly proportional to operation voltage of the system.[2] Compared to LEDs they offer the potential for extremely thin and flexible display applications. Different generations of OLEDs have emerged since the original work by Tang and Van-Syke,[1] characterised by their different mechanisms of light generation. Each of these will be covered in detail, but to summarise they are termed, fluorescence, phosphorescence, triplet-triplet annihilation, hot exciton and thermally activated delayed fluorescence (TADF). The latter is the focus of this work, it was only recognized as an exploitable light generation mechanism in OLEDs in 2007.[3] Early examples centred on copper complexes,[4] and organic tin porphyrin complexes,[5] albeit with very low efficiencies for the latter. External quantum efficiencies (EQE) surpassing 5% in organic emitters were reported in 2011 with the emitter an example of a donor-acceptor (D-A) compound,[6] the most popular strategy for TADF materials design. Although initial efficiencies reported were low (EQE_{max} of 5.3%), work spearheaded by the group of Adachi demonstrated that extremely high efficiencies were possible. Their seminal report in 2012 showed an OLEDs with EQE_{max} of 19.0%.[7] They also introduced design principles to achieve TADF, centred on highest occupied molecular orbital (HOMO) and lowest unoccupied molecular orbital (LUMO) decoupling by bonding electron rich and electron poor moieties together but in a highly twisted architecture. This simple design caused an explosion in the field of organic electronics, with well over 1,000 TADF emitters in the literature.

Computational chemistry has been used to push design of materials, particularly time dependent density functional theory (TD-DFT). These methods allowed accurate and fast modelling of the excited state properties of compounds, which has guided materials development. The first half of this thesis

centres around the design, and probing computational methods to improve modelling, of D-A TADF emitters. New emitters are presented in Chapters 3 and 4, while calculated excited state properties of literature emitters are studied in detail in Chapter 5. Broad emission is apparent in D-A TADF emitters, this is considered detrimental to the colour purity and therefore the performance of OLEDs. For commercial applications high efficiency, good stability and pure colours are required, with D-A TADF systems often not satisfying this final criterion. In 2016, a new design that resulted in TADF and narrowband emission was reported by the group of Hatakeyama.[8] Their design revolved around an alternative strategy to separate HOMO and LUMO orbitals by producing a complementary pattern of the electron density distribution in the ground and excited states based on the presence of electron donating and withdrawing groups embedded within a nanographene fragment, termed multi-resonant TADF (MR-TADF). Unlike D-A systems, there are only a small number of MR-TADF emitters (ca. 100), representing a narrowly defined range of structures.[9] This has been in part driven by poor computational prediction of their excited state, hampering design, with TD-DFT performing poorly. We identified a method to accurately predict the excited state properties of this class of materials and assist in their design, using coupled cluster. This approach is used in the latter half of this thesis to design two new subclasses of MR-TADF emitters in Chapters 6 and 8. In Chapter 7 this approach is undertaken studying a selection of literature emitters. The broad aim of this thesis was to develop and use computational methods to assist in the development of D-A and MR-TADF emitters.

Chapter 1: Introduction and fundamental principles

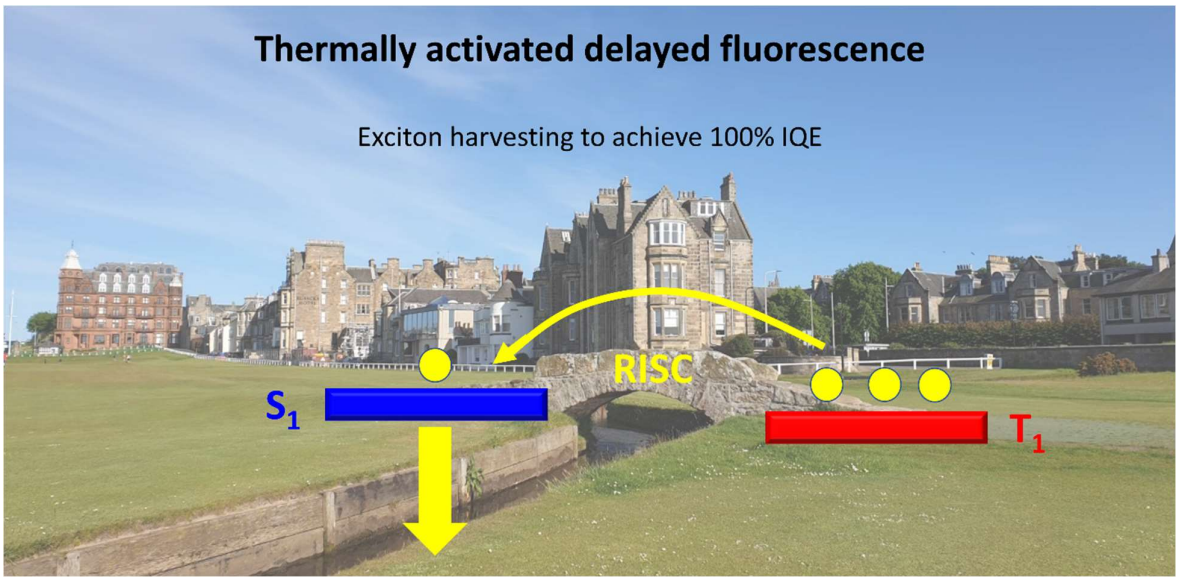

1.1 Excited states

1.1.1 Assignment of states

Throughout this work there are two main electronic excited states of interest, termed singlet and triplet, which are related to the total spin of a system (*vide infra*.). Electrons are fermions with a spin of ½, whose projection along the quantization axis m_s can either be positive or negative providing two eigenstates identified with the two quantum numbers s and m_s,[10] producing the two spin wavefunctions termed α and β (see Figure **1.1**). α is characterized by s = ½ and m_s = ½ while in β, s = ½ and m_s = -½. Interactions of two electrons (denoted as 1 and 2 in equations 1.1 – 1.4) will produce four new eigenstates, calculated as a linear combination of α and β spin wavefunctions, summarized in Figure **1.1**[11];

$$\alpha_1\alpha_2;\ S = 1,\ m_s = 1 \quad (1.1)$$

$$\frac{1}{\sqrt{2}}\{\alpha_1\beta_2 + \alpha_2\beta_1\};\ S = 1,\ m_s = 0 \quad (1.2)$$

$$\beta_1\beta_2;\ S = 1,\ m_s = -1 \quad (1.3)$$

$$\frac{1}{\sqrt{2}}\{\alpha_1\beta_2 - \alpha_2\beta_1\};\ S = 0,\ m_s = 1 \quad (1.4)$$

In equations 1.1, 1.2 and 1.3 each have spin of 1, with three m_s states possible while equation 1.4 has S = 0 and only one m_s term. When considering the total spin quantum number (S) we can assign the excited state as singlet or triplet calculated as:[10]

$$S = 2s + 1 \quad (1.5)$$

Where a singlet state has S = 1 and triplet has S = 3. From the previous eigenstates we can visualise them as vector quantities with three triplet states and one singlet, Figure **1.1**.

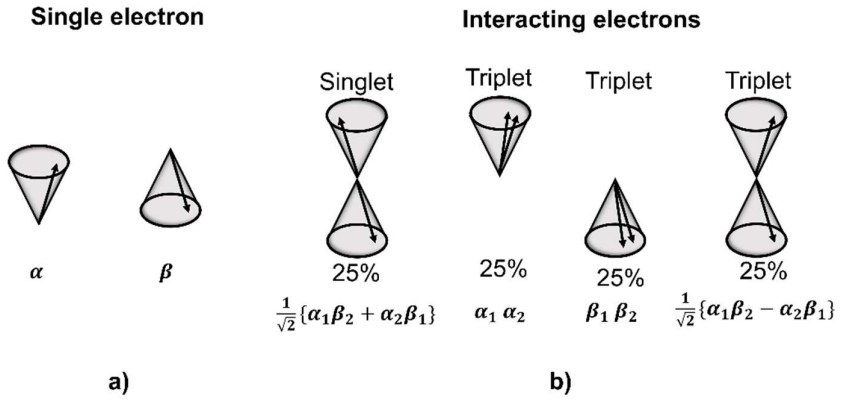

Figure **1.1**. Visualisation of spin wavefunctions in **a**) single electrons and **b**) singlet and triplet states, reproduced from ref.[11]

In the ground state, most molecules have closed-shell electronic structure which is called S_0. From this ground state configuration, promotion of an electron from an occupied orbital to an unoccupied orbital is known as an excitation or an excited state.[11] In most molecular systems, the lowest energy triplet excited state (T_1) is lower in energy than the corresponding lowest energy singlet state (S_1). This is understood in terms of the reduced exchange energy, and reduced Coulomb correlation energy in the triplet state in line with Hund's rules.[10] Examples do exist which claim a violation of Hund's rule[12, 13] and will be presented in more detail in Chapter 7.

1.1.2 Nature of Excited states

The nature of the excited states is determined by the reorganization of the electron density when going from the ground (ϕ_i) to the excited state (ϕ_f). In this thesis most of the transitions discussed occur intramolecularly. The first type of excited state to be considered is a locally excited (LE) state. Here, the molecular orbitals (MOs) involved are the same orbital type (*vide infra*.) and localised on the same part of the molecule with minimal electronic reorganisation, Figure **1.2a,** resulting in an excited state with a similar electrical dipole as the ground state. The second type presented corresponds to a mixed charge transfer-locally excited (CT-LE) state or hybrid local charge transfer (HLCT) state, where there is moderate reorganisation of the electron density upon excitation (Figure **1.2b**). Finally, where transitions occur from two different sites of a molecule resulting in a large excited state dipole and large

electronic density reorganisation, these are known as charge transfer (CT) states (Figure **1.2c**).[14] Transitions can also be described in terms of the orbitals involved in the transition. These can be for instance π – π* or n – π*, where * indicates an antibonding orbital. Here π implies a bonding orbital of π symmetry and n is a non-bonding orbital from a lone pair.

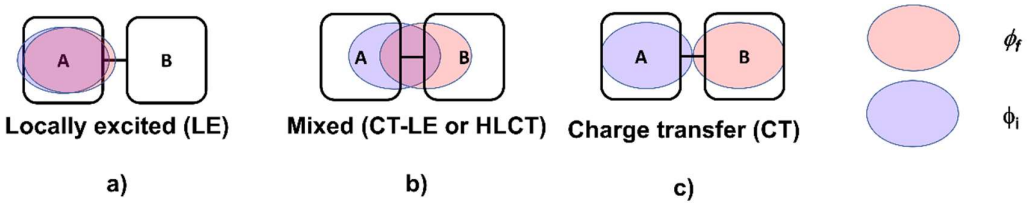

Figure **1.2**. Different excited state configurations based on MO overlap between initial (blue) and final (red) molecular orbitals, in a hypothetical molecule with two different moieties A and B connected covalently to each other.

1.1.3 Excited state transition probability

In organic materials, an excitation occurs according to some selection rules. The first and most important in this work is known as the spin selection rule and relates to the change of spin multiplicity (ΔS) between the ground and excited state:

$$\Delta S = 0 \quad (1.6)$$

This means that there must be no change in spin between the ground and excited state. For closed-shell molecules, the ground state is a singlet S_0. One can expect $S_0 - S_1$ to be allowed, but $S_0 - T_1$ to be forbidden. Exceptions to this rule do exists and are discussed in detail later. The next rule considers the orbital angular momentum, and states that there must be a conservation of orbital angular momentum between the two states of interest.[10] If these selection rules are obeyed then a transition is allowed. The probability of a transition is related to the transition dipole moment, μ_{fi} and is computed on the basis of the initial and final wavefunctions (Ψ_i and Ψ_f^*):[10]

$$\mu_{fi} = \int \Psi_i \hat{\mu} \Psi_f^* d\tau \quad (1.7)$$

If this value is non-zero then a transition is considered allowed, while a value of zero implies that the transition is forbidden. The transition probability is described in terms of the oscillator strength (f) and relates to μ_{fi}:

$$f \propto {\mu_{fi}}^2 \quad (1.8)$$

If $f = 0$ then the transition is forbidden.

1.2 Photophysics

1.2.1 Absorption

Materials can undergo excitation upon absorption of a photon, this is known as photoexcitation. Depending on the energy of the photon, electrons can be excited into rotational, vibrational or electronic levels.[15] The latter is the most relevant in this work. If the energy of excitation is sufficient, the molecule can become electronically excited with promotion of an electron from an occupied MO to an unoccupied MO, this is usually based on a highest occupied molecular orbital (HOMO) to the lowest unoccupied molecular orbital (LUMO) transition, but alternatives are possible. Excitation of an electron following absorption occurs at around 10^{-15} seconds.[16] We make the assumption that on the timescale of the transition, nuclei of a molecule are fixed which is known as the Franck-Condon principle.[17] This excited state of a fixed geometry is known as the Franck Condon (FC) state, with excitation occurring between the ground state and this FC state, highlighted by the absorptions in Figure **1.3**.

How likely this occurs is related to the oscillator strength (equation 1.8).[10] For an allowed transition, the greater the overlap between wavefunctions, the larger the oscillator strength and hence the more probable the transition. In Figure **1.3** the transitions have been highlighted to two different FC states, one with similar geometry to the ground state structure (Figure **1.3a**) and one where there are changes in geometry in the excited state (Figure **1.3b)**. In Figure **1.3a** $v = 0 \rightarrow v' = 0$ is the main transition, with large wavefunction overlap, while in Figure **1.3b** the $v = 0 \rightarrow v' = 2$ transition dominates.

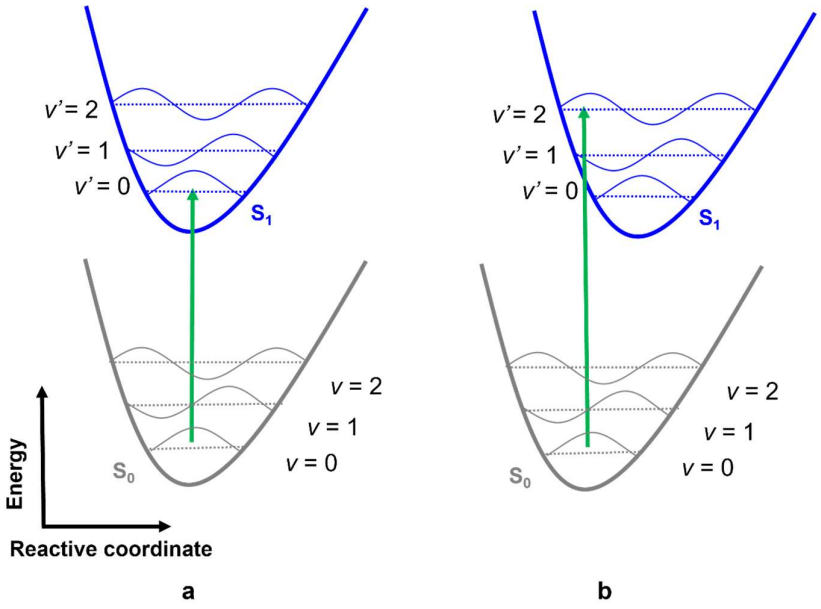

Figure **1.3**. Potential energy diagrams when **a)** ground and FC state are similar geometries, **b)** when ground and FC state have different geometries, where the green line indicates excitation.

Experimentally the degree of absorption can be expressed by the Beer-Lambert Law:

$$Abs = log\frac{I_0}{I_t} = c \times l \times \varepsilon \quad (1.19)$$

Where Abs is absorbance, I_0 is intensity of incident light, I_t is intensity of transmitted light, c is concentration, l is path length and ε is molar extinction coefficient. The value ε, with units M^{-1} cm^{-1} is the primary indicator of how strongly a substance absorbs light at a given wavelength.[18] ε and *f* can be related directly:[19]

$$f = \frac{4.32 \times 10^{-9}}{n} \int \varepsilon(v) dv \quad (1.20)$$

Where *n* is the refractive index and *v* the wavenumber. From here it is clear that ε quantifies the likelihood of a transition occurring, with larger ε suggesting more probable electronic transition.

1.2.2 Jablonski Diagram

In Figure **1.3** the states and transitions are presented considering a potential energy diagram, related to electronic excited states, and vibrations sublevels (*v*) denoted as oscillating waves. An

alternate and simplified way to visualise states and transitions is in the form of the Jablonski diagram (Figure **1.4**).[16] Vertical lines represent transitions between states of the same electronic spin, while horizontal lines are between different electronic spins.[15] The use of Jablonski diagrams will highlight the excited state properties of materials throughout this thesis.

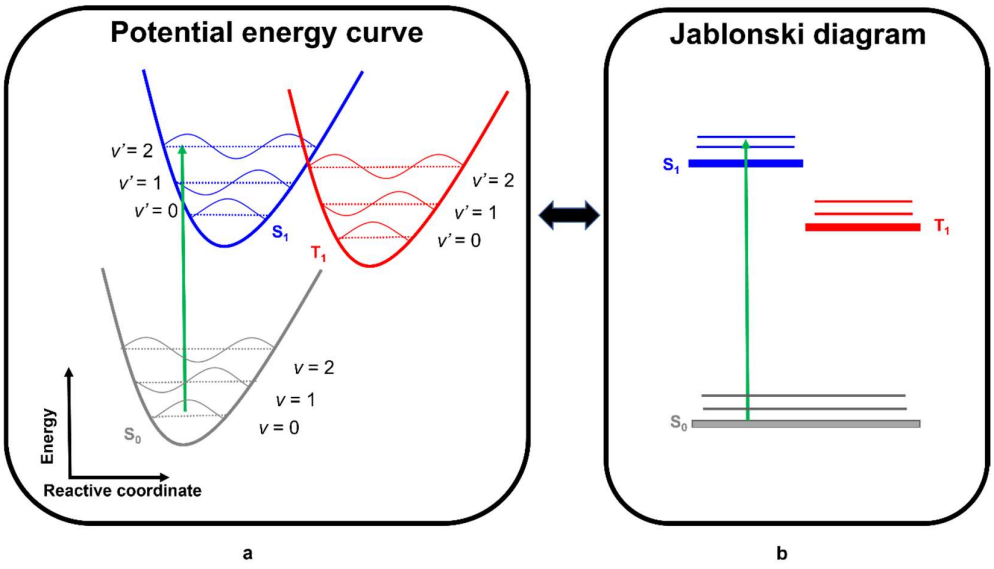

Figure **1.4**. Two main methods to visualise excited state transitions, where **a)** is a potential energy curve and **b)** is a Jablonski diagram, each shows a $v = 0 \rightarrow v' = 2$ transition.

1.2.3 Internal conversion

Internal conversion (IC) is a non-radiative process between different electronic excited state levels of the same spin, indicated by a vertical dotted arrow (Figure **1.5**). Upon optical excitation from the S_0, rapid IC is observed on the order of 10^{-12} s leading to relaxation from higher lying singlets states to S_1. Vibrational relaxation occurs to ensure $v' = 0$ level of S_1 is occupied, with excess vibronic energy dissipated to the surroundings.[10] Emission can then potentially take place from S_1 if the transition is allowed in line with Kasha's rule, with emission occurring preferentially from the lowest energetic excited state.[16] A similar process can also take place once T_n is populated and relaxation down to T_1 is observed. The efficiency of IC is dependent on the energy difference between the states (see section 1.2.5).[20]

1.2.4 Fluorescence

Following IC and vibrational relaxation to $v' = 0$ vibrational level of the S_1 excited state, radiative relaxation in the form of fluorescence can occur, with the excited state relaxing to the ground electronic state, generating light (Figure **1.5**). Adhering to Kasha's rule, as fluorescence occurs from the lowest electronic excited state, the emission spectrum should be independent of excitation energy,[21] with higher lying excited states relaxing first to S_1. Examples of violations of Kasha's rule such as with azulene do exist where emission does not occur from the S_1 state, but these are rare.[20] The relative time scale of fluorescence typically is around $10^{-8} – 10^{-9}$ s.[20]

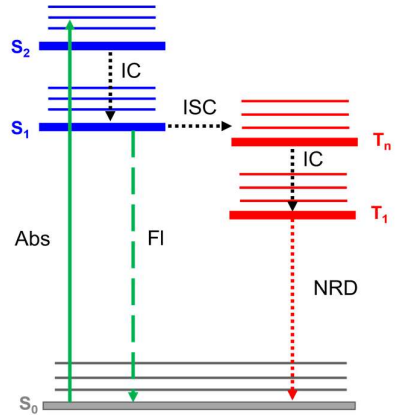

Figure **1.5**. Jablonski diagram of fluorescence, where Abs, Fl, NRD, IC and ISC are absorption, fluorescence, non-radiative decay, internal conversion and intersystem crossing respectively.

In a similar fashion to absorption, fluorescence will occur between vibronic levels of greatest wavefunctional overlap. It is possible to observe this vibronic progression in the emission spectrum. The absorption and emission spectra typically present as mirror images of each other, highlighted well in anthracene (Figure **1.6**). This is due to the ground and excited geometries and the vibronic progression both being similar.[16]

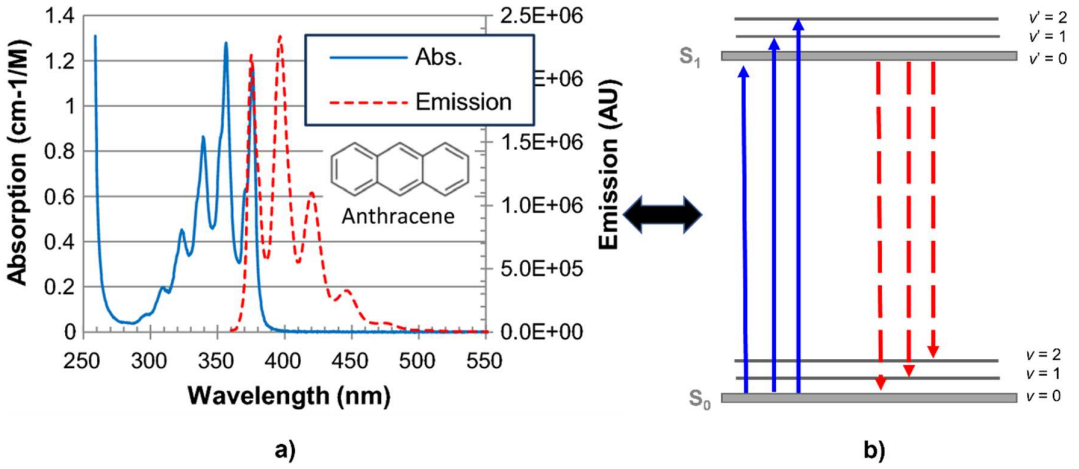

Figure **1.6**. Photophysics of anthracene, where **a)** is the overlapped absorption (blue lines) and emission (red dashed lines) obtained in benzene, obtained with permission,[22] and **b)** is the Jablonski diagram highlighting the vibronic transitions observed in **a)**.

The energetic difference between the absorption and emission peak maxima is known as the Stokes shift.[16] In most molecular systems, emission is red shifted (bathochromic shift) compared to absorption, owing to the relaxation to the v' = 0 vibrational level of S_1, which is energetically lower than the other vibrational levels that are populated during the absorption process. Furthermore, S_1 may be stabilized prior to fluorescence, *via* interactions with its environment. This is observed in solvents, where fast solvent reorganisation (10^{-10} – 10^{-11} s) can occur, with the solvent dipoles interacting with the electrical dipole of the excited molecule, reducing the S_1 energy (Figure **1.7a**). If S_1 has a larger dipole moment than the corresponding ground state, the S_1 state is lowered in energy, narrowing the energy gap between S_1 and S_0.[23] The larger the dipole of S_1 the greater the extent of solvent stabilisation. The magnitude of solvent effects is also governed by its dielectric constant with more polar solvents stabilizing S_1 more, highlighted in Figure **1.7b** moving from hexane (Hex) to the more polar acetonitrile (MeCN). This is known as positive solvatochromism, which appears to be very large when an excited state has a large-excited dipole, for example when CT excited states are involved. The extent of these effects is less for LE systems,[24] which exhibit a smaller difference in electrical dipole between S_0 and S_1. The magnitude of solvatochromism is often used to discriminate whether the nature of the excited state is LE or CT. Negative solvatochromism, which is a blue shift (hypsochromic shift) with increasing

solvent polarity is possible.[23] This occurs when the electrical dipole of the ground state is larger compared to the one of the excited state resulting in an increasing in the energy gap when moving from an apolar to a polar solvent. This is often observed in n-π* excited states.[23] In frozen solvents, this stabilisation is much weaker.[16]

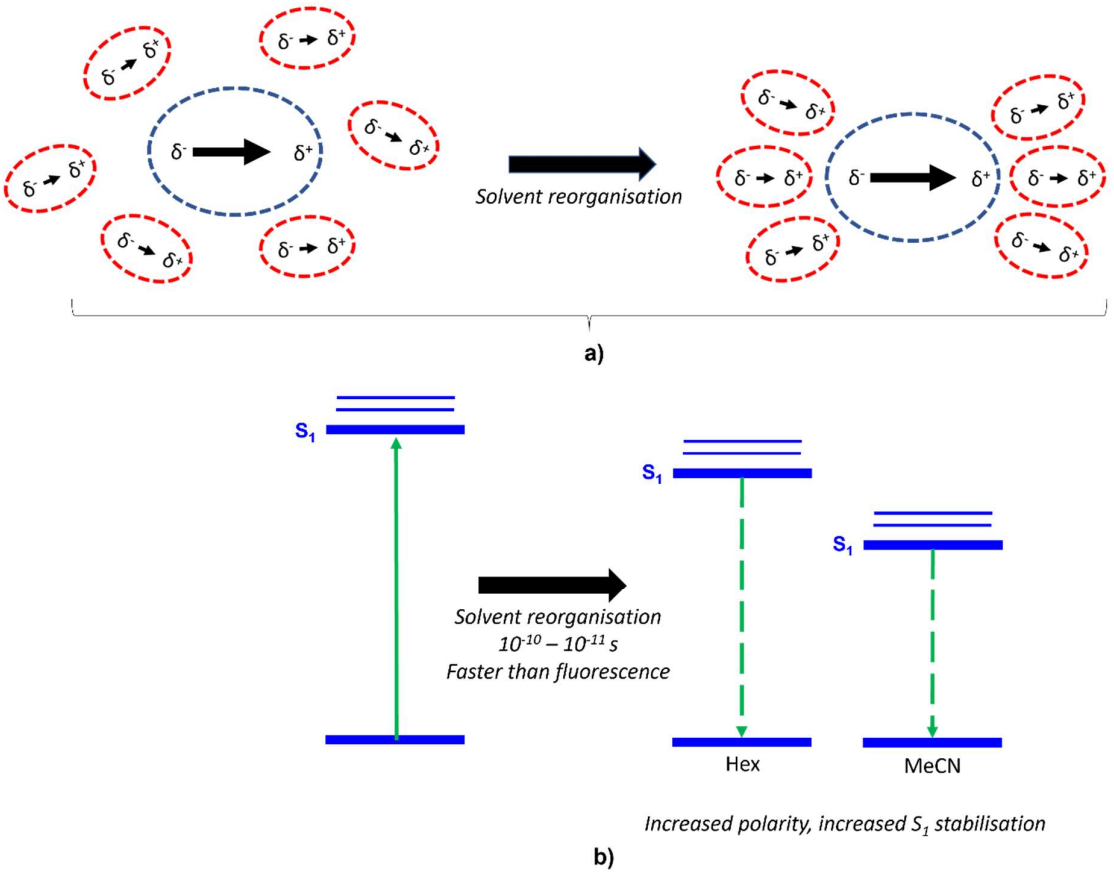

Figure **1.7**. Visualisation of solvent effects in the excited state, **a)** changing arrangement of solvent (red ovals) dipoles following absorption and subsequent relaxation of solute molecule (blue oval), **b)** Jablonski diagram of positive solvatochromism.

Important quantities derived from fluorescence are its photoluminescence quantum yield (Φ_{PL}) and fluorescence lifetime (τ_p), with the former quantifying how efficient radiative decay is and the second indicating the time it takes for the excited state to disappear radiatively, *i.e.* how long the S_1 state exists for.[16] The magnitude of Φ_{PL} is related to its radiative rate, k_r and its non-radiative rate, k_{nr}:

$$\Phi_{PL} = \frac{Emitted\ photons}{Absorbed\ photons} = \frac{k_r}{k_r + k_{nr}} \quad (1.10)$$

k_r describes how fast a material radiatively decays and is related to the wavefunction overlap between the excited and ground state. If the overlap is poor k_r will be inefficient and non-radiative decay can occur competitively. Such processes could be collision interactions with external molecules such as solvents, or oxygen. Another non-radiative pathway is intersystem crossing (ISC), where the electron in S_1 migrates to T_1. If the value of Φ_{PL}, were unity, it would indicate no competing non-radiative decay processes are present. To maximise Φ_{PL}, k_r must be high, and k_{nr} low.

1.2.5 Intersystem Crossing

ISC is radiationless process where communication between S_n and T_n occurs, highlighted on the Jablonski diagram as horizontal lines (Figure **1.5**). It occurs at a time scale of around 10^{-6} – 10^{-8} s in many organic systems, increasing to as high as 10^{-12} s for some iridium complexes, where it outcompetes k_r from the singlet state.[20] Based on the spin selection rule this is a formally spin forbidden process; however, it can occur if spin mixing occurs between the singlet and the triplet states involved in the ISC process. Spin mixing can arise from either spin orbit coupling (SOC) or hyperfine interaction (HFI). The HFI is generally assumed to be much smaller (~ μeV) than SOC (< 0.1 meV) in single molecules.[25] SOC involves the interactions of spin angular momentum and orbital angular momentum, allowing spin selection rule (equation 1.6) to be relaxed.[11] The extent of SOC relates firstly to El Sayed's rules.[26] This states that ISC is only possible when spin inversion is accompanied by a change in angular momentum, as this ensures total angular momentum is conserved.[27] In the original paper, this was exemplified by transitions such as $^1\pi\pi^* \rightarrow {}^3\pi\pi^*$ and $^1n\pi^*$ - $^3n\pi^*$ having negligible SOC while $^1\pi\pi^* \rightarrow {}^3n\pi^*$ and $^1n\pi^* \rightarrow {}^3\pi\pi^*$ have much larger SOC. In the latter two, there is a change in orbital type that accompanies the change in spin. This concept can be expanded further to encompass El Sayed-allowed transitions between CT and LE states, where $^1CT \rightarrow {}^3CT$ would be formally forbidden, assuming the transition to these excited states involve the same orbitals, while $^1CT \rightarrow {}^3LE$ is allowed. A further manner to increase SOC is in the form of the heavy atom effect, with SOC scaling to Z^4, with Z the atomic charge of an atom involved in the transition.[11] It is often observed in transition metal complexes where use of heavy Iridium and Platinum ensures large SOC and efficient ISC. Inclusion of heavy atoms such as bromine has also been a popular method to enhance ISC. The rate of ISC is also related to Franck-Condon

weighted density of states. This states that k_{ISC} is related to the degree of vibrational overlap between T_1 and S_1 wavefunctions. If the two states have similar geometries, the probability of spin conversion is exponentially dependent on the energy gap between the two states.[27] This is known as the weak electron-phonon coupling limit (Figure **1.8a**). Alternatively, when the states have different geometries ISC occurs through a conical intersection of the potential energy surface (PES). In this scenario, known as the strong electron-phonon coupling limit, ISC is dependent on both the energy gap between the two states and the reorganisation energy to go from S_1 to T_1 (Figure **1.8b**).

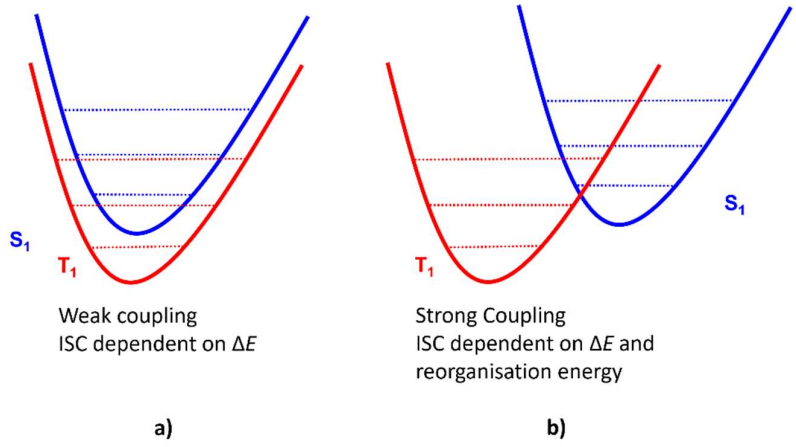

Figure **1.8**. S_1 to T_1 PES in **a**) the weak and **b**) strong electron-phonon coupling.

The two routes reported above only involve the direct conversion from S_1 to T_1. However, in ISC the Born-Oppenheimer approximation is no longer strictly true and electronic and nuclear degrees of freedom should be considered with SOC now also a function of the nuclear coordinates.[27] The direct conversion from S_1 to T_1 might not be the most likely spin conversion path because of too weak SOC, so that ISC could take place from S_1 to a higher-lying triplet state, where IC can take place populating T_1. This mechanism is quoted as spin-vibronic coupling.[20] This has been invoked in porphyrin compounds, where S_1 and T_1 have π-π^* character, while higher lying states have σ-π^* contributions. Inclusion of these states ensures significant SOC based on El Sayed's rules with ISC possible.[27] It has also been invoked for efficient ISC in carbonyl compounds, with inclusion of n-π^* character via vibronic interactions ensuring increased SOC.[20]

1.2.6 Phosphorescence

Similarly to ISC, phosphorescence, which is emission from a triplet state (Figure **1.9**), is a spin-forbidden process. Phosphorescence is achieved by ensuring SOC is significant and is also dependent on the energy gap between T_1 and S_0.[15] Increased SOC can again be achieved *via* the heavy atom effect, often by incorporation of transition metal centres. Phosphorescent emitters without transitions metals do exists, coined room temperature phosphorescence (RTP) materials here. Phosphorescence is possible in these compounds owing to the use of heavy atoms such as halogens[28] or sulfur[29] which increase SOC *via* the heavy atom effect, further the systems are extremely rigid, which minimise non-radiative decay losses.[30] Large singlet triplet energy gap (ΔE_{ST}) is often desirable to prevent unwanted reverse intersystem crossing (RISC, *vide infra*). Owing to the different extents of SOC in the systems varying phosphorescence lifetimes are observed, being $10^3 - 10^6$ s^{-1} for transition metal complexes, increasing to $10^1 - 10^{-2}$ s^{-1} for purely organic systems.[11] In frozen media phosphorescence is often enhanced, with non-radiative pathways suppressed.[15]

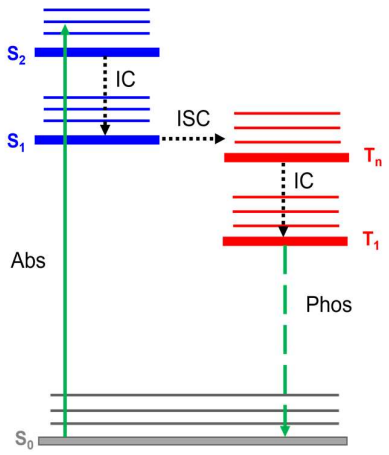

Figure **1.9**. Jablonski diagram of phosphorescence, where ISC and Phos are intersystem crossing and phosphorescence respectively.

1.2.7 Triplet-Triplet Annihilation

The Triplet-Triplet annihilation (TTA) mechanism was first proposed in 1963 in pyrene,[31] hence the early name of p-type fluorescence. TTA had been observed prior to this, with reports of dual

emission reported in anthracene, perylene, phenanthrene and pyrene which were subsequently assigned to TTA. Following initial excitation from S_n, T_1 is populated following ISC. When the lifetime of the T_1 state is sufficiently long then bimolecular interactions can occur,[32] wherein their collision can induce a state change *via* Dexter energy transfer (DET, *vide infra*). The interactions produce a variety of excited state species including triplet, quintet and singlet,[33] with the latter able to radiatively relax. We now consider the latter term, with a bimolecular interaction of T_1 states producing two singlet states, one twice the energy of T_1 and the other S_0. The excited singlet state will undergo radiative decay, at a longer lifetime than any initial prompt fluorescence (Figure **1.10**). As the mechanism is bimolecular in nature then there will be a quadratic dependence on the rate of TTA with increasing power and concentration. Where increased power increases the number of available T_1 states and hence likelihood of TTA.[34 35]

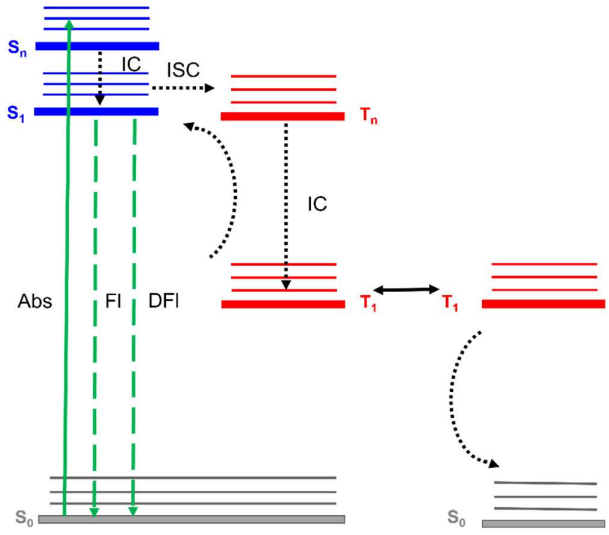

Figure **1.10.** Jablonski diagram of radiative TTA, where collision of T_1 states between two molecules produces one singlet excited state and one singlet ground state. Where DFl, is delayed fluorescence.

1.2.8 Thermally activated delayed fluorescence

Thermally activated delayed fluorescence (TADF) has been known for decades, originally described as E-type fluorescence[36] from the study of **Eosin Y** (*vide infra*), and is the focus of this thesis. Early reports using fluorescein showed TADF[37, 38] but it was not explicitly described as TADF in these

examples.[39] Following initial excitation, fast emission in the form of prompt fluorescence is observed. ISC in compounds that are TADF is competitive with radiative decay and so there is also a population of T_1. These T_1 states can undergo the reverse mechanism to ISC (RISC), where T_1 is converted to S_1 (Figure **1.11**). The criteria for RISC mirror those for ISC. These are discussed in detail later in section 1.5.2. As T_1 is lower in energy than S_1, RISC is by definition an endothermic process. The conversion of S_1 to T_1 and vice versa can occur over many cycles until radiative decay takes place, or excited energy is lost to the surroundings.[40] Delayed fluorescence occurs at times scales of 10^{-7} – 10^{-3} s. This delayed fluorescence occurs from the same excited state as the prompt fluorescence. As it is an endothermic process it can be thermally activated at higher temperatures. This is a key parameter used to distinguish between TTA and TADF as both are delayed fluorescence processes.

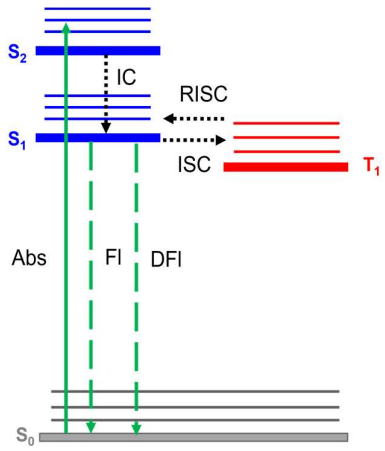

Figure **1.11**. Jablonski diagram of TADF, where RISC is reverse intersystem crossing.

Beyond fluorescein and **Eosin-Y**, other examples have been studied throughout the years (Figure **1.12**), with TADF reported for C_{60}[41] and also C_{70}.[42] It was first noted in C_{70}, where an improved Φ_{PL} from < 1% to 8% was observed when solutions were degassed and the temperature increased, thereby confirming TADF. A ΔE_{ST} of 0.27 eV was determined in paraffin oil. In C_{60} in USP light oil, there is an almost 1:1 ratio of prompt vs delayed fluorescence found. This is a lower ratio than observed in C_{70}, which was attributed to the higher ΔE_{ST} of 0.36 eV measured for C_{60}.[40] The smaller ΔE_{ST} in C_{70} was assigned to its larger molecular size that results in a reduced electron repulsion of S_1.[43] Benzophenone (Figure **1.12**) and several derivatives were reported to undergo a delayed fluorescence

mechanism,[44] which was found to be temperature dependent. For benzophenone the ratio of delayed fluorescence compared to phosphorescence in benzene was 0.10 at 298 K but increased to 0.21 at 329 K showing a clear temperature dependence. TADF in benzophenone is possible due to the sufficiently small ΔE_{ST} of 0.21 eV. TADF has been reported for thiones like thioxanthone, where again prompt fluorescence, phosphorescence and TADF were all observed in solution.[45] A range of thiones (**PT**, **BPT**, **XT** and **TMIT**) have been studied and examples are shown in Figure **1.12**.

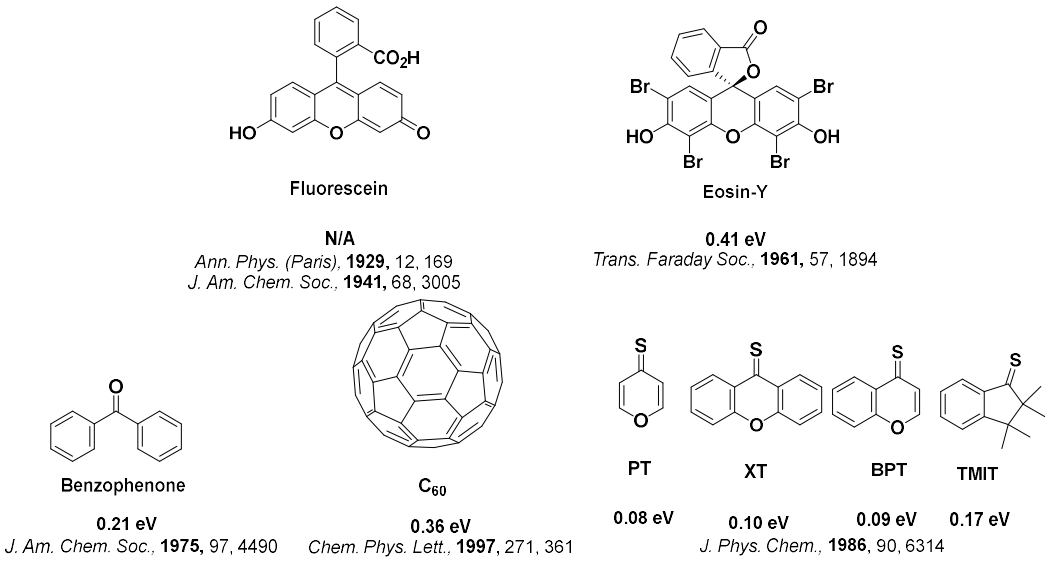

Figure **1.12**. Structures of early reported TADF emitters and their reported ΔE_{ST} values.

1.2.9 Energy and electron Transfer

The next excited state phenomenon that must be considered is energy transfer between species, Förster resonance energy transfer (FRET) and DET.[46] FRET involves transfer of energy between two molecules (termed donor, D, and acceptor, A). There is a dipole-coupled energy transfer where the dipoles of the two systems interact, ensuring D is no longer excited while A is now excited. From here A is able to radiatively decay (**Figure 1.13**).[47] The FRET efficiency is dependent on the overlap of emission of D and absorption of A. Its rate is expressed as:[48]

$$k_{FRET} = \frac{9000\ln(10)k^2}{128n^4N_A\tau_r^0(D)(R_{DA})^6}J \quad (1.11)$$

Here k is the orientation parameter, n is the refractive index, $\tau_r^0(D)$ is the lifetime of the donor species, R_{DA} is the distance between D and A and J is the overlap integral between the emission of the D and the absorption of the A.

DET is an alternative energy transfer process, involving a double electron exchange interaction, the result of direct electronic communication between the two species.[49] An excited electron is transferred from the orbital of D to A, while an electron of A is transferred to D, with A now excited and able to radiatively decay and D in the ground state (Figure **1.13**). It requires overlap of the interacting orbitals, hence occurs at short distances, with its rate expressed as:

$$k_{DET} = KJe^{-2R_{DA}/L} \quad (1.12)$$

Where K is a specific experimental parameter related to D and A orbital overlap, J is the overlap integral, R_{DA} is the distance between D and A and L relates to the van der Waals radii of D and A. When comparing FRET and DET the changing expression for R_{DA} is key, with FRET a longer-range process compared to DET.

Finally, we must consider electron transfer. This involves the transfer of an electron between two species and is responsible for charge hopping in organic light emitting diodes (OLEDs) (*vide infra*.). Again, it is described in terms of D and A components. In charge hopping, D is reduced (radical anion) and A is neutral. Upon electron transfer, A is now reduced and D oxidised, so D is now neutral (**Figure 1.13**). In order for electron transfer to occur, it must be thermodynamically allowed (i.e. $\Delta G^0 < 0$) and this can be assessed based on Marcus theory.[50] [51]

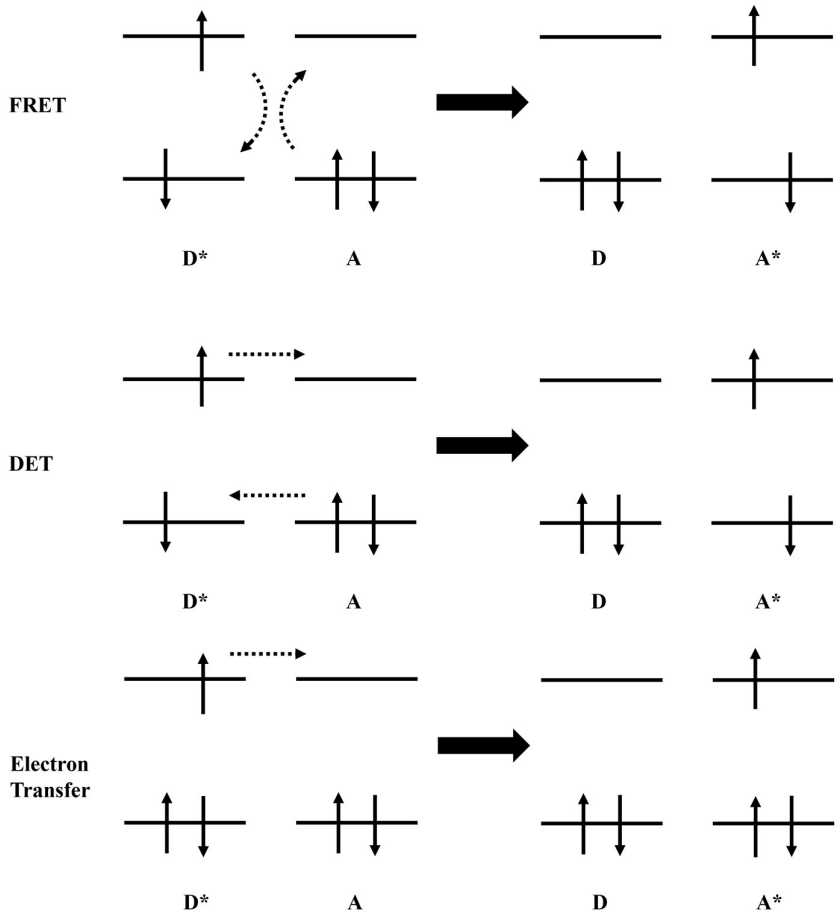

Figure **1.13**. FRET, DET and electron transfer between two molecules D and A.

1.3 Electroluminescence

1.3.1 Mechanism

Electroluminescence is the generation of light upon application of an electronic current. Charges are injected into the material from the anode and cathode. The material is then oxidized or reduced, respectively, forming radical cations (holes, h^+) and radical anions (electrons, e^-) (Figure **1.14**). Charge hopping then occurs with the holes and electrons, allowing migration through the device stack, the mechanism here is electron transfer (*vide supra*). The recombination of a hole and an electron occurs due to Coulombic interactions producing an exciton, which is an electron-hole pair that is then capable of radiatively decaying to generate light.[52, 53] As both the hole and electron are fermions, there are four possible recombination's (see section 1.1 for more detail), netting one exciton with singlet multiplicity

and three excitons with triplet multiplicity (Figure **1.14**).[11] Exciton formation is described according to Langevin theory, where the probability of formation increases with greater density of holes and electrons and with increased charge mobility.[54] [55] Unlike photoluminescence where photoexcitation results the initial formation of singlets, electroluminescence provides a mechanism for direct population of triplets. Conventional pathways such as IC, ISC, fluorescence, phosphorescence, TTA and TADF can all subsequently occur.

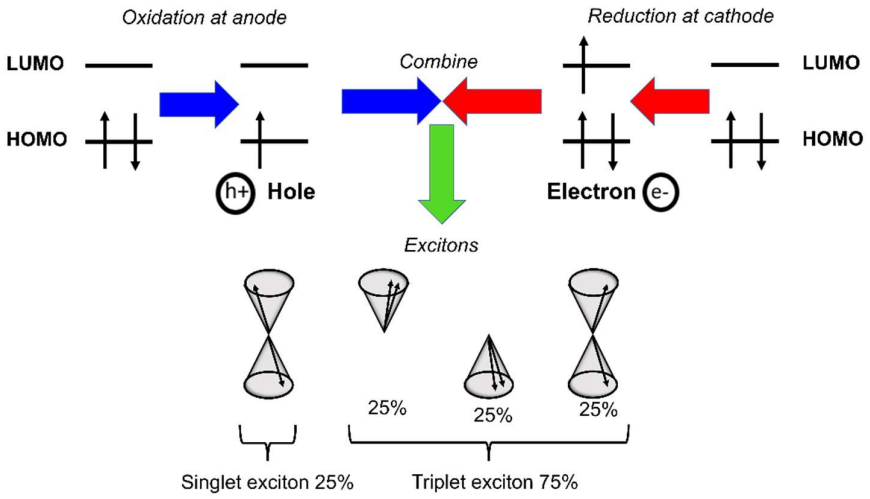

Figure **1.14**. Simplified mechanism for exciton generation.

The first reported example of electroluminescence in a purely organic system was in 1963, when it was observed in an anthracene single crystal.[56] Fluorescence associated with anthracene was observed when a driving force of 400 V was applied. Although this was an important breakthrough in electroluminescence, the very high voltage required meant it had no commercial use. The large driving voltage was needed due to the thickness of the anthracene crystal. It was proposed that by using organic films, which are thinner than crystals, better power efficiency could be obtained. When the anthracene was vacuum-deposited, forming an organic film, a driving voltage of only 12 V was needed to produce the observed fluorescence, as documented by Vincent *et al*.[57]

1.3.2 Organic light-emitting diodes

The vision of an OLED functioning at low bias was realised in 1987 by Tang and Vanslyke.[1] The OLED was a two layer device sandwiched between a cathode and anode, where **Alq_3** was used as the emitter and a diamine, 4,4′-cyclohexylidenebis[N,N-bis(4-methylphenyl)benzenamine] (TAPC), was used to assist hole transport. Although its EQE_{max} was only reported as 1% in this initial work, it did spark a new era of research. An operating voltage of <10 V was a remarkable improvement compared to the original anthracene example. The stark improvement in performance of the device was due to the use of a bilayer device architecture and thin organic films for each layer. The thin organic films ensured much improved charge mobility. The charges migrate through the multilayer stack of organic semiconductor materials by a charge hopping electron transfer mechanism.[58] This energy transfer occurs at the interface between layers, and requires an energy input to overcome the activation energy barrier between the two layers. This migration continues until the holes and electrons meet forming excitons, with this ideally occurring within the emitting layer (EML) where the emitter materials are located. They recombine on these molecules to form the exciton (Figure **1.15**).[53] The layers themselves are transparent, and in combination with a transparent electrode, usually the indium tin oxide (ITO) anode, light can leave the device.[59] The mechanism by which these excitons decay results in different maximum internal quantum efficiencies (IQEs).

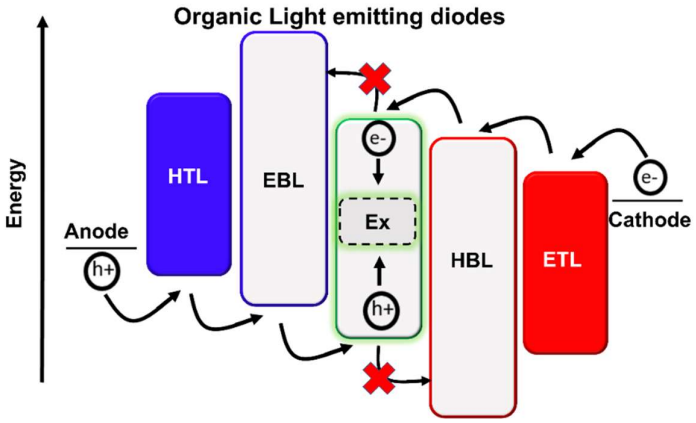

Figure **1.15**. Simplified energy diagram of an OLED stack, with hopping mechanism identified, where HTL, EBL, HBL and ETL are hole transporting layer, electron blocking layer, hole blocking layer and electron transport layer respectively.

The main purpose of a multilayer device is to ensure efficient hole-electron recombination within the EML.[52] Various materials, like hole blocking layers (HBL) and electron blocking layers (EBL), can be added to ensure charge recombination occurs within the EML of the device. Deep HOMO and LUMO of the HBL and EBL respectively prevent transportation of charges beyond the EML (Figure **1.15**, highlighted by red crosses), as the charge hopping is now energetically unfavourable. Hole transporting layers (HTL) and electron transporting layers (ETL) facilitate efficient charge transport from the electrodes to the emissive layer, with careful alignment of their HOMO and LUMO levels respectively ensuring electron transfer is energetically favourable.[53] HTL materials are electron rich systems. ETL materials are electron poor systems.[60] Injection layers assist injection of charge into the respective layers from the anode or cathode and have energy levels closely aligned with those of the work functions of the electrodes. A simplified energy diagram of an OLED stack can be seen in Figure **1.15**, and representative materials can be seen in Figure **1.16**.

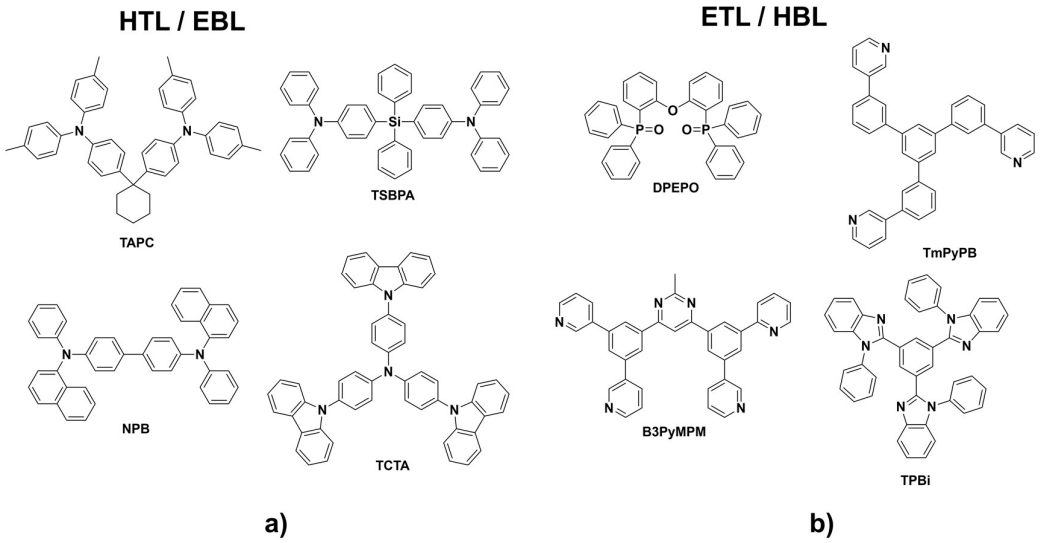

Figure **1.16**. OLED transport and blocking materials where **a**) is a selection of HTL and EBL materials and **b**) selection of ETL and HBL materials.

1.3.3 OLED efficiency

The efficiency of an OLED, the ratio of injected charges to photons leaving the device, is quantified in terms of its external quantum efficiency (EQE).[61, 62] This efficiency is dependent on factors both intrinsic and extrinsic to the nature of the emitter:

$$EQE = \gamma \times \Phi_{PL} \times \Phi_r \times \Phi_{out} \quad (1.13)$$

The first term, γ, is the hole-electron recombination factor, which is assumed to be unity. γ relates to the likelihood of the holes and electrons recombining to form excitons.[63] The second term, Φ_{PL}, describes the fraction of excitons that will decay radiatively to generate light.[64] Molecular design is key to optimizing this parameter as the radiative decay rate must be enhanced, for instance by ensuring strong wavefunction overlap between the ground and excited states, while non-radiative decay must be suppressed, by for instance reducing, aggregation caused quenching (ACQ).[49] Although it is usually described as a photophysical phenomenon, the radiative decay pathways should be identical for electroluminescence and hence comparisons between them can be made.[62, 64] The third term, Φ_r, is the number of emissive excitons generated per hole-electron recombination. This efficiency is related to one of the exciton harvesting mechanisms outlined below. The product of these three terms is the IQE.[65] The fourth term, Φ_{out}, is the light outcoupling efficiency, and describes the fraction of light that can escape the device. This is linked to both the optics of the device and to the orientation of the transition dipole moment of the emitter molecules.[65, 66, 67] For isotropic emitters, Φ_{out} is no greater than 0.3,[65] assuming no use of external outcoupling sheets. Modulating the emitter design to enhance the light-outcoupling efficiency remains a challenge.[65, 67]

1.3.4 OLED stability

The maximum EQE (EQE_{max}) values are often reported at extremely low brightness, so are not particularly relevant metrics. A practical brightness is described as around 100 cd m^{-2} or larger depending on the application in question, with EQE reported at these values generally more useful with EQE at 100 cd m^{-2} and 1,000 cd m^{-2} often quoted named EQE_{100} and EQE_{1000} respectively.[68] Efficiency roll-off is defined as the decrease in efficiency with increasing current density or luminance, and is a

key indirect parameter when assessing device stability.[69] Roll-off at 100 cd m^{-2} (RO_{100}) can be calculated as follows:

$$RO_{100} = \frac{EQE_{max} - EQE_{100}}{EQE_{max}} \quad (1.14)$$

Another metric to quantify device stability is operational lifetime (LT_n), which is the time in hours taken for the luminance to decrease by a certain percentage (subscript n) at a fixed operational voltage.[70, 71] The luminance and percentage can vary and there is no universal set of values. Device stability is linked to triplet excitons, which can undergo undesired interactions with other excitons or with polarons (hole and electrons).[69] These exciton interaction pathways include TTA and singlet triplet annihilation (STA). The next class involve interactions between polarons and excitons, these are singlet polaron annihilation (SPA) and triplet polaron annihilation (TPA). Interactions of excitons or polarons produce higher energy species, which are capable of catalysing the photochemical degradation of the materials involved,[72] decreasing the OLED stability; this has been studied by mass spectrometry.[73] With increased exciton concentration these pathways become increasingly likely. The long lifetime of the triplet excitons is the key problem as this increases the probability that these bimolecular interactions can occur.[73]

1.3.5 OLED colours

In OLEDs there are 4 colours that are important: blue, green and red for display applications and white for lighting. One of the ways to characterise these colours is using the Commission International de l'Éclairage (CIE) 1931 diagram, where colours are reported as points on the diagram corresponding to human colour vision, i.e., which colours can be perceived by the human eye (Figure **1.17**).[74] Colours can be defined according to the standard red blue green (sRBG), which assigns red, blue and green as (0.64, 0.33), (0.15, 0.06) and (0.30, 0.60), respectively,[75] with all observable colour points contained within a triangle of the connecting points (Figure **1.17**, circles and solid white line). The current industry standard for ultra HD-TVs is based on BT.2020, and these colours are now defined as (0.13, 0.05), (0.17, 0.80) and (0.71, 0.29) for blue, green and red, respectively (Figure **1.17**, squares and dotted black line).[76] Within these triangles mixing of the various points can display all the colours

corresponding to the points inside. In terms of white light there are often two values quoted. The first is considered pure white at (0.33, 0.33) while the second is referred to as warm white at (0.45, 0.41).[77] Warm white is the colour associated with incandescent light and the most comfortable for human eyes. The position of an emitters coordinates is dependent on its emission maximum and the width of emission, often quoted as the emission width at half the emission maxima (FWHM).

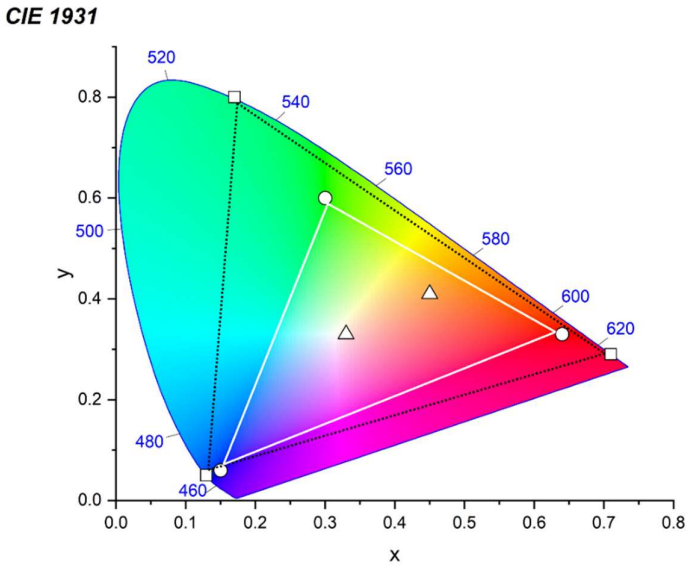

Figure **1.17**. CIE diagram where sRBG colour points are highlighted as circles (connected by solid white lines), BT.2020 as squares (connected by dotted black line) and white coordinates as triangles.

In the primary colours, blue, green and red, the key to colour tuning relates to the S_1 energy of species (or T_1 for phosphorescence). The lower the excited state energy the redder emission. Currently in the TADF literature there is are many more examples blue and green emitters compared to red.[78] One reason for this is that high performance and efficient blue emitters are still sought after in industry.[68, 70] Blue OLEDs suffer from efficiency and stability issues, which is in part a result of there being very few suitable high triplet energy hosts available. Hosts are used in OLEDs to prevent emitters from aggregating together, which is detrimental to performance. An ideal host has a wider bandgap and higher T_1 than the emitter along with ambipolar character to aid in charge transport through the EML[79]. Achieving all these is problematic for blue emitters.

1.4 Exciton Harvesting in OLEDs

There are five main exciton harvesting mechanisms that control IQE, that have been explored in OLEDs. The simplified Jablonski diagrams of each are shown in Figure **1.18**-**1.23**. These are summarized briefly below.

1.4.1 Fluorescence

OLEDs that use fluorescent emitters can only reach a maximum IQE of 25%,[1] as only singlet excitons are emissive, while radiative decay of the triplet is formally spin-forbidden (Figure **1.18**).[11] Triplet excitons decay to the ground state non-radiatively. This was the first class of OLEDs developed, using either small molecule fluorophores such as the archetypal **Alq_3,** where the authors obtained an EQE_{max} of ~1%, [1] or conjugated polymers such as **PPV,** where they obtained an EQE_{max} of ~0.05% (Figure **1.18**).[80] Without inclusion of outcoupling effects, the maximum EQE at this stage was limited to 5%. Despite the limited efficiencies interest around these materials still exist.[81]

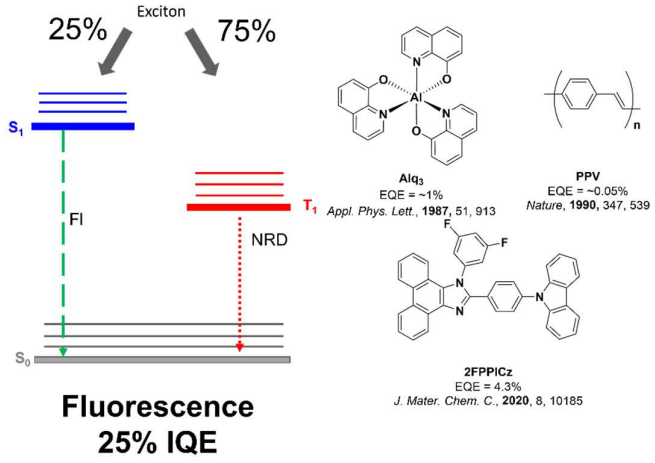

Figure **1.18**. Jablonski diagram of fluorescence from electroluminescence along with structures and associated EQE_{max} values reported in the original literature.

1.4.2 Phosphorescence

A first solution to circumvent the non-radiative loss of triplet excited states relied the introduction of heavy metals centres within the emitter layer. Baldo *et al.*[82] used a platinum complex **PtOEP** alongside an **Alq_3** host (Figure **1.19**) to provide an avenue for enhancing SOC that led to

increase of both the ISC and phosphorescent rates.[83] The much faster ISC resulted in complete conversion of the 25% S_1 states into T_1, while the increased phosphorescent rate turned on the radiative decay of the T_1 state. The IQE_{max} for phosphorescent OLEDs (PhOLEDs) is 100%.[84] State-of-the-art phosphorescent OLEDs employ organometallic emitters containing primarily 5d transition metals such as iridium with EQE_{max} reaching 30% in many examples (Figure **1.19**).[85] [86, 87] Intense research into PhOLEDs has led to devices covering the full visible range and the commercialisation of red and green emitters for PhOLEDS. The very low natural abundance of these noble metals,[88] stability of blue emitters,[89] environmental concerns[90] and the patent stronghold afforded by one company (Universal Display Corporation) are all detracting features that have driven the search for alternative classes of emitter materials. RTP (*i.e.* phosphorescence without transition metals) have also been used in OLEDs, however, their performance remains poor owing to long excited state lifetimes with lower phosphorescent rates, with 4% the current top for **SiAz** (Figure **1.19**).[28, 91] [92]

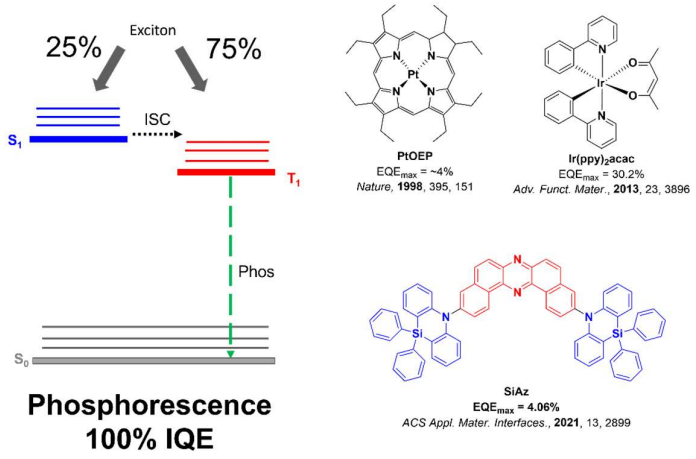

Figure **1.19**. Jablonski diagram of phosphorescence from electroluminescence along with structures and associated EQE_{max} values.

1.4.3 Triplet-Triplet Annihilation

TTA is another mechanism that overcomes the IQE_{max} of 25% for fluorescent compounds.[93] Mentioned previously as a detrimental decay pathway[94] it has actually been utilized as an exciton harvesting pathway.[33] Bimolecular annihilation of two triplet excitons can potentially generate excitons of different spin multiplicities including triplet, quintet and singlet with the latter able to decay

radiatively. Thermodynamically speaking TTA is expected to take place in a given material once twice the energy of the T_1 state exceeds the S_1. The maximum IQE, is 62.5%, corresponding to the contributions from the 25% of directly formed singlet excitons and half of the 75% of the directly formed triplet excitons (37.5%) as two triplet excitons are required to form one singlet exciton (Figure **1.20**).[93] The probability that TTA occurs is a function of the concentration of triplet excitons, which is dependent on the concentration of emitters, the lifetime of the triplet exciton and the current density in an OLED device. It has been successfully exploited in blue OLEDs, and is the primary mechanism exploited in commercial blue OLEDs.[35] Owing to their low lying triplets, anthracene and pyrene are very popular components in TTA based emitters.

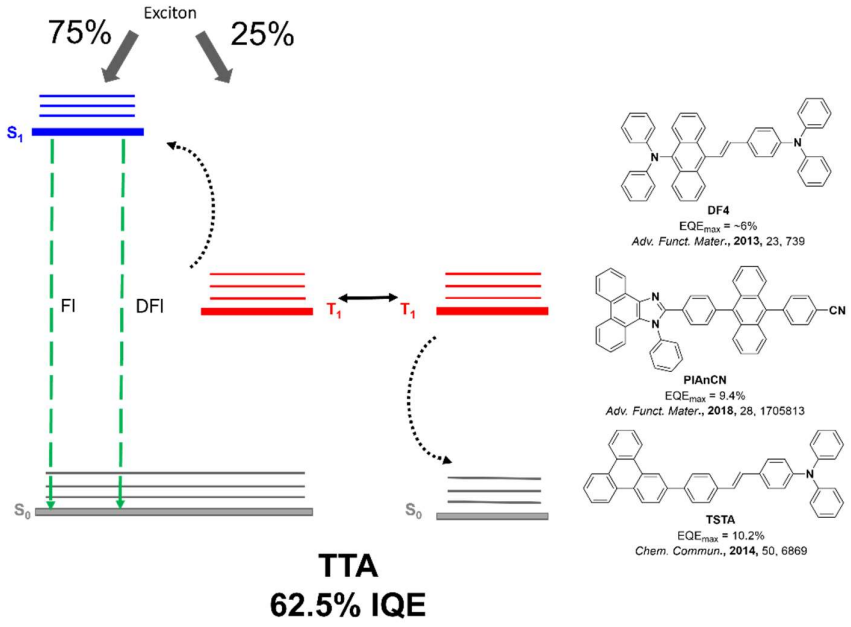

Figure **1.20**. Jablonski diagram of TTA from electroluminescence along with structures and associated EQE_{max} values.

1.4.4 Hot exciton

Perhaps the least explored exciton harvesting mechanism involves hot excitons.[95, 96] This process involves conversion of higher energy triplet excitons (T_n) such as T_2, into singlet excitons *via* RISC (Figure **1.21**).[97] This is only possible when T_n and S_1 are nearly isoenergetic. The maximum Φ_r is 100%;[96] however, as IC from T_n to T_1 competes with RISC the actual Φ_r is generally much lower. It is

usually key that T_n and T_1 have a large energy difference, which contributes to decreasing the rate of IC between the two (*vide supra*).[96, 98] Alternatively, the route could occur via T_n and S_n with IC from S_n to S_1 followed by radiative decay.[99] [100] Only a relatively small number of organic emitters have been reported to emit via a hot exciton mechanism and there has generally been a paucity of direct evidence provided to support that this is the operational exciton harvesting mechanism. Computational approaches have instead been used to corroborate its presence, able to predict the levels of higher lying singlet or triplet states.[97] Unlike the other mechanisms reported, photophysically it has not been probed in great detail, with the primary characteristics a large ΔE_{ST} (ruling out TADF), linear power dependence (ruling out TTA), EQE_{max} surpassing 5% (ruling out fluorescence) and no favourable orientation.[97, 101] Recently, transient Electron paramagnetic resonance was used with **DPAAnCN** (Figure **1.21**),[97] with two contrasting profiles observed highlighting two triplet states of contrasting nature, a key component of the hot-exciton mechanism. The energetics were still determined computationally.

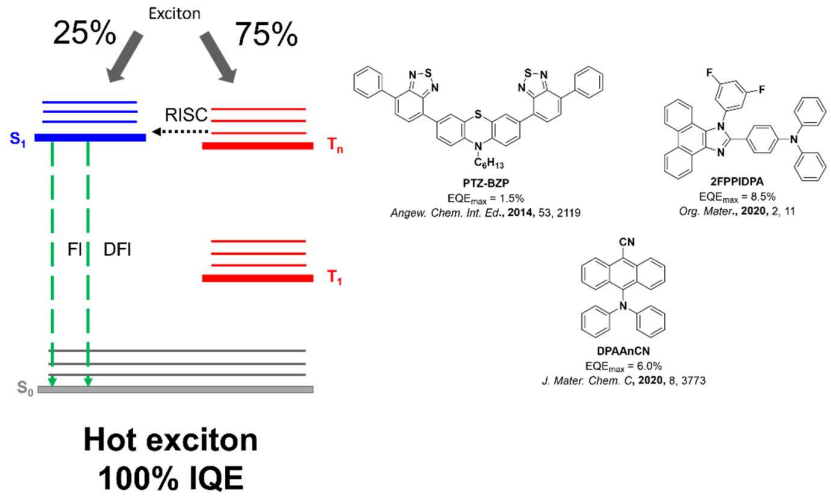

Figure **1.21**. Jablonski diagram of hot exciton from electroluminescence along with structures and associated EQE_{max} values.

1.4.5 Thermally activated delayed fluorescence

TADF is an exciton harvesting mechanism that converts triplet excitons to singlet excitons by RISC (Figure **1.22**). It was first exploited as an exciton harvesting mechanism in OLEDs only in 2007

with a copper complex**, [Cu(μ-I)dppb]$_2$**, employed as the emitter, where the OLEDs showed an EQE$_{max}$ of 4.8% (Figure **1.22**).[3] EQEs surpassing 5%, the threshold commonly accepted for the recruitment of triplet excitons to generate light, were first reported in 2010, again using a copper complex, **{Cu(PNP-^{t}Bu)}$_2$**, with EQE$_{max}$ 16.1% (Figure **1.22**).[4] Diverting from copper, in 2009 a tin porphyrin complex, **SnF$_2$-OEP** (Figure **1.22**), was reported as an emitter in OLEDs; however, the efficiencies were low and the contribution of TADF to emission was minimal.[5] The first Donor-Acceptor (D-A) TADF emitters used in OLEDs were reported in 2011 where the devices showed an EQE$_{max}$ of 5.3% for the D-A emitter **PIC-TRZ** (Figure **1.22**). Exceptional efficiencies, well above the theoretical maximum for fluorescent OLEDs, were first reported in 2012 where devices with an EQE$_{max}$ of 19.3% were realised with **4CzIPN** as the emitter (*vide infra*).[7] Efficiencies surpassing EQE$_{max}$ of 20% have been reported for devices of all colours utilizing the TADF mechanism,[78] with examples nearing 40% now emerging.[102, 103] However, issues with device stability still exist as triplet quenching pathways remain owing to the relatively long excited state lifetime of the emitters. Methods to increase RISC rate are therefore important, reducing the likelihood of triplet quenching and improving device roll-off.[104]

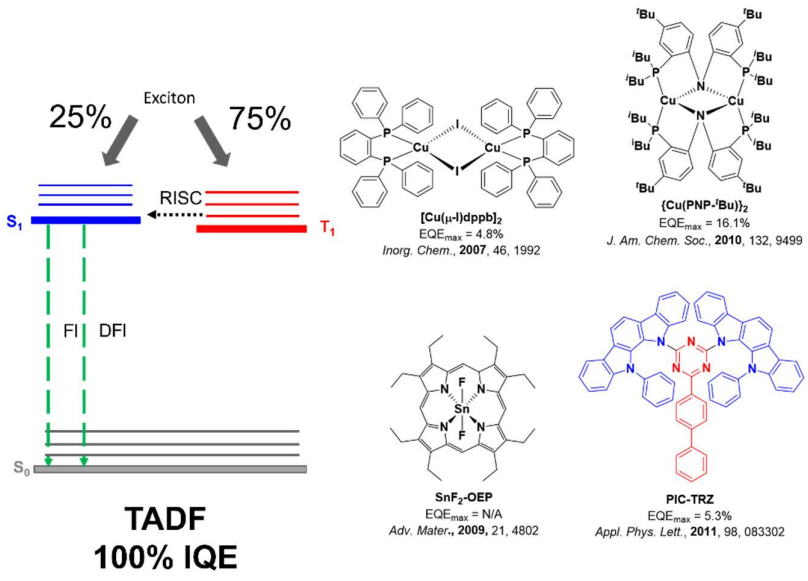

Figure **1.22**. Jablonski diagram of TADF from electroluminescence along with early emitters and associated EQE$_{max}$ values.

1.5 TADF Mechanism

As the field has evolved, the spectroscopic understanding of TADF and its mechanism along with the techniques to measure have matured. Although the OLEDs themselves involve electroluminescence, the most common strategies to probe TADF involve photoluminescence studies. This provides a fundamental understanding of the photophysics within the emissive layer.

1.5.1 Delayed fluorescence

As delayed fluorescence in TADF implies a $T_1 - S_1$ conversion, it does not occur on the same time scale as the prompt fluorescence (Figure **1.23a**). Owing to this, fluorescence at two different lifetimes can be observed (Figure **1.23**).[105] The time-resolved emission of TADF compounds can be measured using single photon counting, integration of spectra at different time gating[106] and streak camera analysis. These lifetime measurements are usually exponentially fitted with biexponential delay expected corresponding to prompt and delayed fluorescence, with prompt and delayed lifetimes (τ_p and τ_d) with the former occurring at $10^{-9} - 10^{-7}$ s and the later $10^{-7} - 10^{-2}$ and are extracted as follows:[39]

$$I = A_{PF} \exp\left(-\frac{t}{\tau_p}\right) + A_{DF} \exp\left(-\frac{t}{\tau_d}\right) \quad (1.15)$$

As $T_1 - S_1$ conversion is an endothermic process, increasing contributions from the delayed fluorescence will be observed with increasing temperature, as the energetic barrier for conversion is overcome.[107] These often involve a change in the intensity of the delayed component with temperature. When the temperature is sufficiently low there will be too little energy for RISC to occur and no delayed fluorescence will be observed. As triplets are used in the TADF mechanisms, techniques probing their inclusion are important. This is often observed with introduction of oxygen where its ground state triplet state can quench the triplet state of the excited TADF compound.[39] This results in a decrease in Φ_{PL}.[108] However, it is important to recognize that oxygen can also quench singlet excited states, hence it is not the ideal method to probe triplet inclusion.[109] One key spectroscopic technique for confirming TADF is a power dependence study. This probes the changing emission intensity with variance in laser power. An expected linear dependence provides strong evidence that the emission is from a monomolecular

process, in line with TADF. A quadratic dependence would suggest a bimolecular emission process such as for TTA.

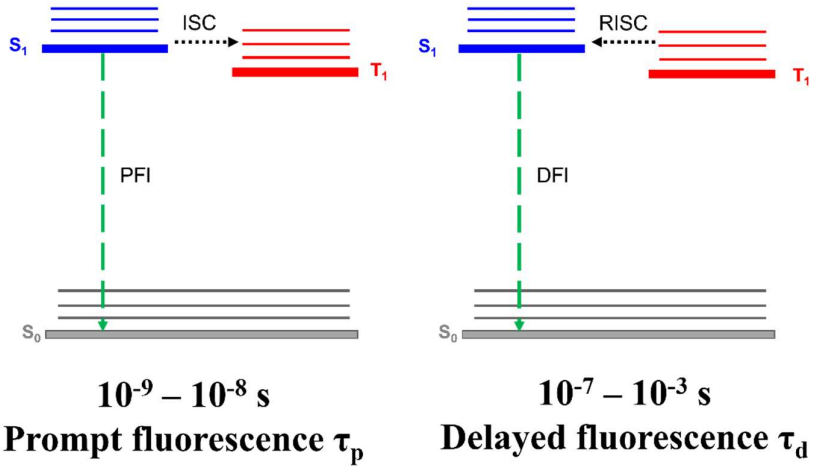

Figure **1.23**. Jablonski diagrams of prompt and delayed fluorescence.

1.5.2 Reverse intersystem crossing

The degree and efficiency of TADF relates to how efficient is triplet to singlet conversion, so is related to the rate of RISC (k_{RISC}). [110] RISC undergoes the reverse mechansim to ISC, with triplets converted to singlets, and is achieved by the same methods (see section 1.2.5). The intersystem and reverse intersystem crossing rates, k_{ISC} and k_{RISC}, describe the rate of interconversion between singlet and triplet excitons, respectively. It is possible to extract these rates from time time-resolved PL decays. The percentage components for prompt and delayed fluorescence are PF and DF and related to the area of the prompt/delayed fluorescence (A_{PF} and A_{DF}) and lifetimes, τ_p and τ_d calculated as:[39]

$$PF = \frac{A_{PF} \times \tau_{PF}}{(A_{PF} \times \tau_{PF}) + (A_{DF} \times \tau_{DF})} \quad (1.16) \qquad DF = \frac{A_{DF} \times \tau_{DF}}{(A_{DF} \times \tau_{DF}) + (A_{PF} \times \tau_{PF})} \quad (1.17)$$

These can be converted to the prompt and delayed quantum yields (Φ_p and Φ_d, respectively) in relation to the overall quantum yield:

$$\Phi_p = PF \times \Phi_{PL} \quad (1.18) \qquad \Phi_d = DF \times \Phi_{PL} \quad (1.19)$$

Rate constants were calculated according to method described by Masui *et al*,[111] where k_p and k_d are the prompt and delayed fluorescence rates, and k_{ISC} and k_{RISC} are the intersystem and reverse intersystem crossing rates calculated by:

$$k_p = 1 / \tau_p \quad (1.20)$$

$$k_d = 1 / \tau_d \quad (1.21)$$

$$k_{ISC} = k_r \times (1 - \Phi_p) \quad (1.22)$$

$$k_{RISC} = \frac{k_p \times k_d}{k_{ISC}} \left(\frac{\Phi_d}{\Phi_p} \right) \quad (1.23)$$

$$k_{nr} = k_d - \Phi_p \, k_{RISC} \quad (1.24)$$

In these equations several assumptions are made, firstly that k_{ISC} and k_r^S are much larger than k_{RISC} and k_{nr}^T. Secondly, that k_{nr}^S and k_r^T are 0. Finally, prompt emission should be independent of temperature. Although widely accepted as too simple an approximation,[39, 109] these are likely the most appropriate for the emitters in this work. k_{RISC} can only occur if state mixing between triplet and singlet states is possible. First and second order perturbation theory of states provide the avenues to state mixing.

1.5.2.1 First order

To a first approximation, first order mixing can be considered as that which occurs directly between S_1 and T_1. The extent of state mixing between S_1 and T_1 can be quantified in relation to the first order mixing coefficient, λ:[7]

$$\lambda \approx \frac{SOC_{S1-T1}}{\Delta E_{ST}} \quad (1.25)$$

λ is directly proportional to the magnitude of SOC, and inversely proportional to the energy difference between the singlet and triplet states, ΔE_{ST}. SOC magnitude is essentially controlled by the presence of heavy atom as well as El Sayed's rules (see section 1.2.5) However, the majority of TADF emitters contain lowest energy singlet and triplet excited states that are both CT in nature (*vide infra*), and hence often SOC between these states remains very small.[24] As most TADF emitters are composed

of light elements, the influence of the heavy atom effect in SOC is minimal. The next component is based on reduction of ΔE_{ST}. The threshold value of ΔE_{ST} where we observe non-negligible RISC is often presented as <0.2 eV.[110] When considering that both T_1 and S_1 originates from a HOMO to LUMO transition [5] one can write the energy of the those states E_T and E_S, respectively as well as ΔE_{ST} within the frame of Hartree-Fock (HF) theory:

$$E_S = E + J + K \quad (1.26)$$

$$E_T = E + J - K \quad (1.27)$$

$$\Delta E_{ST} = E_S - E_T = (E + J + K) - (E + J - K) = 2K \quad (1.28)$$

$$K = \iint \Phi_L(1)\Phi_H(2)\left(\frac{e^2}{r_1 - r_2}\right)\Phi_L(2)\Phi_H(1)\, dr_1\, dr_2 \quad (1.29)$$

Where J is linked to the mean field Coulombic interactions and the K is the exchange interaction energy. Equations 1.28 and 1.29 highlight that minimizing K will lead to a minimized ΔE_{ST}. The exchange energy is itself governed by the degree of orbital overlap involved in the transition to S_1/T_1 from S_0, which in this case, we hypothesized to be dominated by a HOMO to LUMO transition (equation 1.29). ϕ_H and ϕ_L are the spatial part of the wavefunctions of the HOMO and LUMO, e is the electronic charge and r_1 and r_2 indicate position vectors of electron 1 and electron 2, respectively.[110] Based on equation 1.29, it is clear the simplest way to reduce ΔE_{ST} is to minimize overlap between HOMO and LUMO density. This is the primary design criteria for TADF materials.

A consequence of segregating the HOMO and LUMO orbitals on different parts of the molecule results in a decrease of the radiative rate constant, k_r,[7] owing to reduced wavefunction overlap. A careful balance between small ΔE_{ST} and reasonable k_r is key to obtain emitters with high IQEs.[112] The value of ΔE_{ST} can be obtained spectroscopically. As k_{RISC} is a temperature dependent process it can be extracted from an Arrhenius analysis:

$$k_{RISC} \propto \exp\left(-\frac{\Delta E_a}{k_B T}\right) \quad (1.30)$$

Where ΔE_a is the activation energy, k_B is the Boltzmann constant and T is temperature. If RISC were directly dependent on ΔE_{ST}, a direct correlation between E_a and ΔE_{ST} would be observed.[113] A trend of smaller ΔE_{ST} producing fastest RISC is observed; however, the relationship isn't always linear, with emitters with relatively large ΔE_{ST} and fast k_{RISC} widespread.[114] Therefore TADF efficiency may not only be explained just in terms of the first order mixing of states. Spin-vibronic coupling of states may also be important, which implies second order mixing.

1.5.2.2 Second order

RISC may proceed not simply directly from T_1 to S_1 but may involve other excited states, which can be accessed due to spin-vibrational coupling. In this second order picture, the Born Oppenheimer approximation is broken,[25] and electronic and vibrational degrees of freedom have to be considered. As a consequence, up conversion from T_1 to S_1 occurs through higher lying triplet states (T_{1+n}) that are accessible thanks to strong vibrational coupling between T_1 and T_{1+n}. This is often described as reverse internal conversion (RIC) between the T_1 and higher lying T_{1+n}. If one of these higher-lying triplet states is of a different electronic nature than that of S_1 then SOC will be significantly enhanced and RISC can then proceed (Figure **1.24**).[24] The vibrational coupling between T_1 and T_{1+n} states is maximized when T_1 and T_{1+n} states are close in energy allowing efficient RIC to occur.[24, 115] Additionally, a negative ^{3}LE/^{1}CT gap accelerates RISC between the two states.[113]

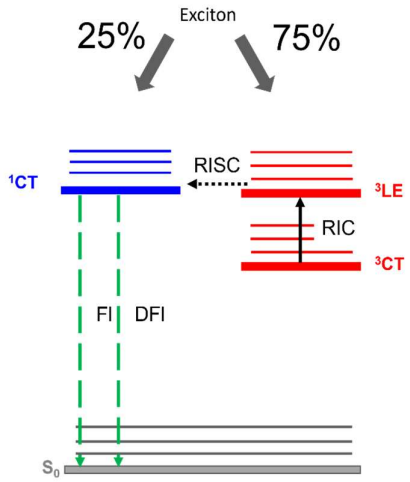

Figure **1.24**. Jablonski diagram of TADF via intermediate ^{3}LE triplet state.

1.5.3 Examples of modulating second-order state mixing

Noda *et al.*[115] reported a series of structurally related emitters for which k_{RISC} correlates very well with the evolution of the ^{3}CT and ^{3}LE energy gaps (ΔE_{TT}) among a series of compounds. Based on the parent emitter **5CzBN**, the energy difference between ^{3}CT and ^{3}LE is 0.32 eV, ΔE_{ST} = 0.17 eV and the corresponding k_{RISC} is 2.2 × 10^5 s^{-1}. Replacement of two of the carbazoles for phenyl-substituted carbazoles introduced ^{3}LE states closer to ^{3}CT, reducing the gap to 0.16 eV for **3Cz2DPhCzBN**, which translated into enhanced k_{RISC} of 7.2 × 10^5 s^{-1} (Figure **1.25**), with a similar ΔE_{ST} similar of 0.15 eV. The activation energy of **5CzBN** and **3Cz2DPhCzBN** were smaller than the ΔE_{ST}, calculated to be 0.13 eV and 0.06 eV thanks to the role of intermediate triplet states. This translated to an improved device lifetime, where the LT_{97} was 3 hours for **5CzBN**, increasing to 110 hours for **3Cz2DPhCzBN**.

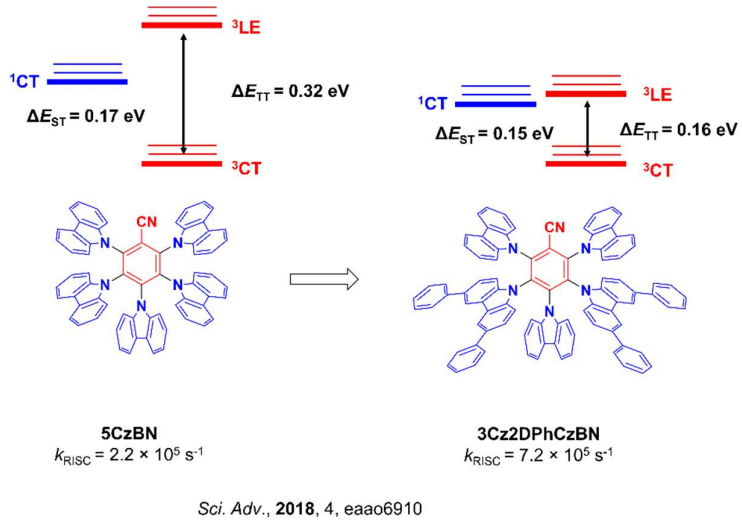

Figure **1.25**. Tailoring of ^{3}CT ^{3}LE levels for improved k_{RISC}.

Altering the polarity of the medium will also affect k_{RISC} as shown by Etherington *et al.*[24] Owing to their larger electrical dipoles, CT states are more stabilized than LE states in polar media. Fine tuning of CT alignment with the LE levels was observed in **DPTZ-DBTO2**, where the fastest k_{RISC} was observed when ^{1}CT – ^{3}LE and ^{3}CT – ^{3}LE each possessed the smallest energy gap; two other scenarios were presented where CT and LE states were energetically very different, producing slow k_{RISC} (Figure **1.26**).[24, 116]

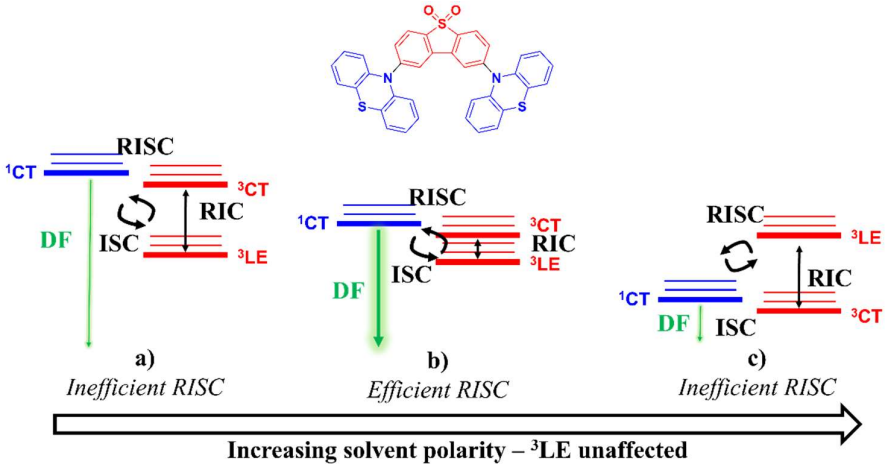

Figure **1.26.** Change in CT and LE excited states energy levels of **DPTZ-DBTO2** when varying the polarity of the medium, where **a**) shows weak k_{RISC}, **b**) the highest performing k_{RISC} and **c**) weak $k_{RISC.}$

The conformational flexibility inherent in the emitter can also affect RISC rates, with extremely rigid systems having slow k_{RISC}.[30, 117] The rigid emitters hinder the necessary vibrations required for RIC between triplet states, ultimately hampering RISC as spin-vibronic coupling is weak. This was highlighted in work by Ward *et al.*[30] where bulky substituents were added to phenothiazine (PTZ) on the parent emitter, **DPTZ-DBTO2**. Clear TADF was observed for the parent in doped films; however, upon addition of isopropyl groups at the 1 position, **DPTZ-^{i}Pr-2DBTO2** (originally **3** in the literature, Figure **1.27a**) TADF was no longer visible, and instead RTP was the dominant mechanism. Hempe *et al.*[117] undertook a similar study where bulky substituents were added at different positions (Figure **1.27b**). Despite similar ΔE_{ST} of 0.19 eV and 0.20 eV for **1a** and **1b**, addition of the bulky adamantyl groups produced a decreased k_{RISC} from 5.4×10^5 s^{-1} to 2.9×10^5 s^{-1} in *ortho*-dichlorobenzene, which was attributed to the increased steric bulk reducing vibronic modes that facilitate RISC (Figure **1.27b**). The explicit design of materials that aims to maximize spin-vibronic coupling is in its infancy; however, clear rules are already apparent where 1) the emitter should not be too rigid, 2) functionalities should be incorporated to introduce ^{3}LE states near ^{1}CT leading to small ^{1}CT-^{3}LE and small ^{3}LE-^{3}CT.

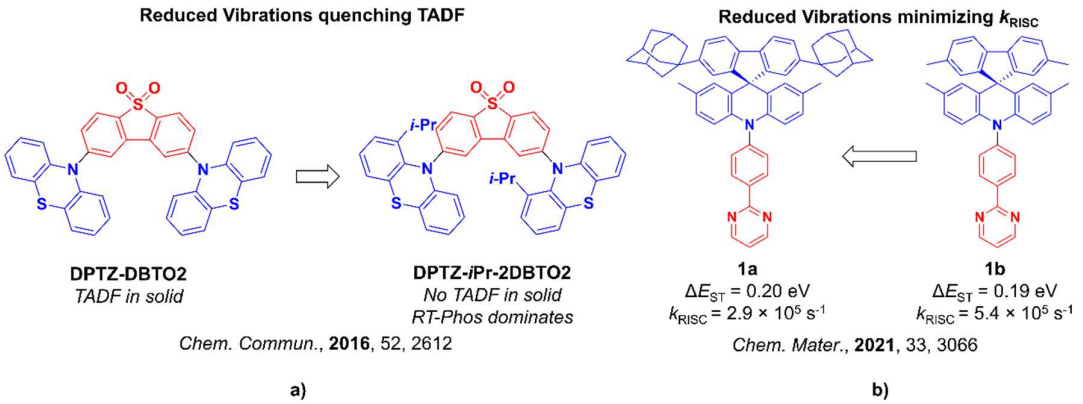

Figure **1.27.** Change in TADF properties when varying the emitters rigidity, where **a**) highlights the shutdown of TADF properties by adding ^{i}Pr subsitution and **b**) where k_{RISC} was reduced upon adamantyl subsitution.

1.6 TADF emitter design

1.6.1 Donor-acceptor systems

The most popular TADF emitter design is based on a D-A architecture in which these two moieties are in poor electronic communication with each other.[110, 112] Here, the HOMO is localized on the donor and the LUMO on the acceptor, ensuring a small exchange energy and hence a small ΔE_{ST} according to equation 1.29 (Figure **1.28**). The stronger the donor and acceptor motifs, the more localized the electron density will be on the HOMO and LUMO, respectively, leading to smaller ΔE_{ST} (Figure **1.28**). The relative conformation of the donor and acceptor groups also controls the spatial separation of the frontier orbitals, with more twisted conformations leading to reduced conjugation and hence smaller ΔE_{ST}. From a molecular design standpoint, this can be achieved through (1) the use of substituents close to the D-A bond such as addition of methyl groups[118] or (2) the inclusions of multiple donor or acceptor groups which force large torsion to mitigate steric congestion, with twisted geometries providing less interaction between groups.[7] 9,9-Dimethyl-9,10-dihydroacridine (DMAC), phenoxazine (PXZ) and phenothiazine (PTZ) achieve this prior to substitution owing to their bulky nature.[118] Achieving TADF using D-A design is the cornerstone of Chapters 3 – 5, where new materials have been presented along with an improved mechanistic understanding informed by in silico modelling studies. The molecules

which have been modelled in Chapters 5 and 7 are discussed here along with other representative compounds.

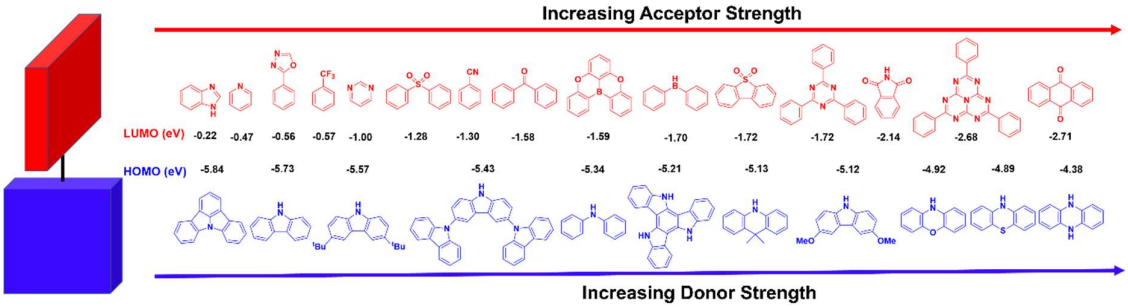

Figure **1.28.** Donor acceptor TADF emitter design, with examples of widely used Donors and acceptors and their respective HOMO and LUMO values calculated in the gas phase using PBE0/6-31G(d,p). The HOMO-LUMO values of the D-A compounds are not shown.

Although thousands of donor-acceptor TADF emitters have been reported, they are ultimately composed of a relatively limited number of units, some of which are summarised in Figure **1.29**.[119] Colour tuning in D-A systems is possible by altering the nature of the donor and acceptor groups, which affects both the band gap, ΔE, and the energy of the excited states. Increasing donor strength destabilizes the HOMO, while increased acceptor strength stabilizes the LUMO, both of which decrease the energy of the excited states (Figure **1.28**). Exceptional efficiencies of D-A systems have been achieved able to match established phosphorescent examples. A summary of the key D-A TADF milestones can be found in Figure **1.29**.

The first D-A TADF OLED reported in 2011 is composed of a triazine acceptor linked to carbazole (Cz) donor units, **PIC-TRZ** (Figure **1.22** and Figure **1.29**).[6] The small ΔE_{ST} of 0.11 eV in 6 weight percent (wt%) (1,3-bis(N-carbazolyl)benzene (mCP) films ensured TADF would be feasible at room temperature, the τ_d is ~230 μs. The devices showed low efficiencies, with an EQE_{max} of 5.3%, which was assigned to the low Φ_{PL} of the material (34%) and inefficient RISC.

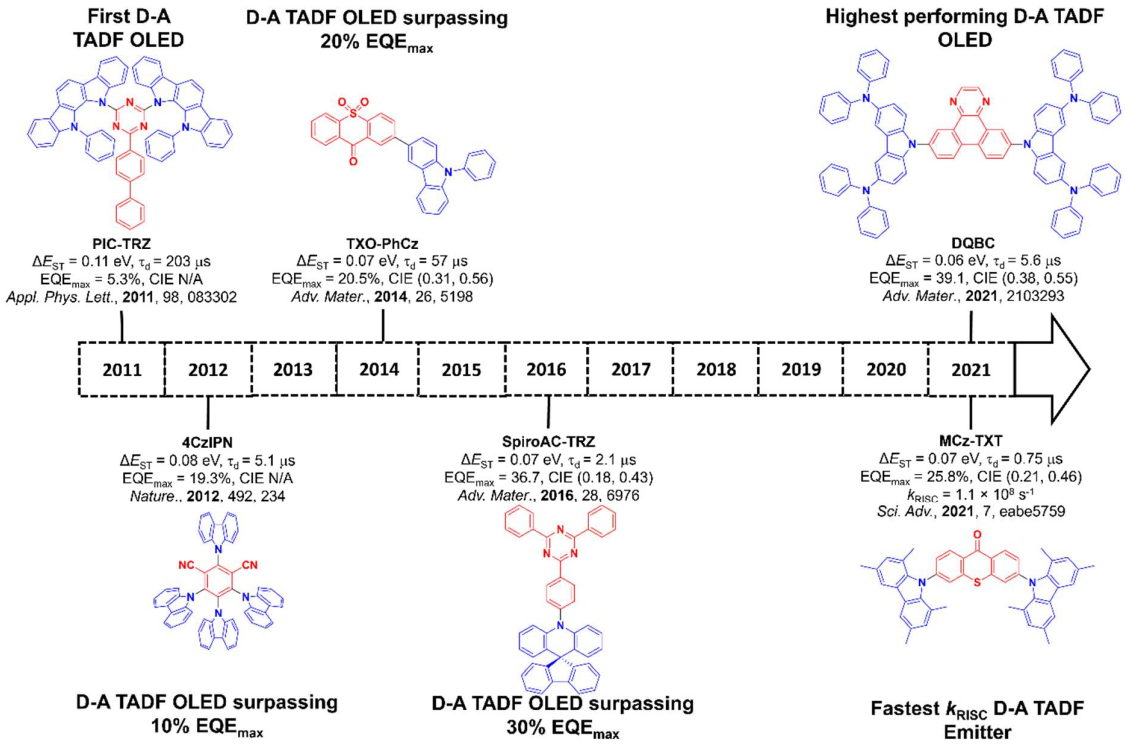

Figure **1.29**. Timeline, structures, properties and device data of key milestones in D-A TADF emitter development.

Subsequent work by the same group[7] used carbazole donors linked to phthalonitrile acceptors. The position and number of the donors about the acceptor produced efficient devices covering the full spectral range with impressive EQE$_{max}$ of 19.3%, 11.2% and 8.0% reported for the devices with **4CzIPN**, **4CzTPNPh** and **2CzPN** at λ_{PL} of 509 nm, 583 nm and 477 nm, respectively (Figure **1.30**). For **2CzPN**, changing the device stack produced devices with improved efficiencies where the EQE$_{max}$ improved to 14.0%.[120] Replacement of the nitriles in **2CzPN** with oxadiazoles resulted in a blue shift of the emission with the CIE coordinates moving from (0.16, 0.30) in the **2CzPN** device to (0.15, 0.11) with **2CzdOXD4MeOPh** (Figure **1.30**). The weaker acceptor resulted in less efficient TADF characteristics, with ΔE_{ST} increasing from 0.09 eV in **2CzPN** to 0.46 eV in **2CzdOXD4MeOPh** in 6 wt% and 10 wt% mCP films respectively, corresponding to lower EQE$_{max}$ of 6.6%. **3CzFCN**[121] is structurally very similar to **4CzIPN** but crucially incorporates fluorine atoms as acceptors (Figure **1.30**). Although frequently used as electronic modulators of phosphorescent compounds, it has been

underexplored in TADF emitters. Blue emission with λ_{PL} = 443 nm, Φ_{PL} = 74% and ΔE_{ST} of 0.06 eV were achieved in 10 wt% CzSi (9-(4-tert-butylphenyl)-3,6-bis(triphenylsilyl)-9H-carbazole) films. In this example, blue solution-processed devices showed EQE_{max} of 17.8% at CIE (0.16, 0.19). Other derivatives of nitrile series were developed, where the OLEDs showed improved EQE_{max} in part due to the careful control of ^{3}LE and ^{3}CT levels. Two emitters, **4CzBN** and **5CzBN** displayed efficient k_{RISC} of 1.8 × 10^5 s^{-1} and 2.4 × 10^5 s^{-1}, respectively, much faster than that of **2CzPN** at 0.06 × 10^5 s^{-1} (Figure **1.30**). Other derivatives, **2CzBN**, **o-3CzBN** and **m-3CzBN** (Figure **1.30**), did not show TADF owing to poor alignment of the LE states, despite similar ΔE_{ST} to **4CzBN** and **5CzBN** (ΔE_{ST} 0.17 – 0.24 eV in Toluene, PhMe). OLEDs of **4CzBN** and **5CzBN** displayed high EQE_{max} of 20% and 24%, respectively.

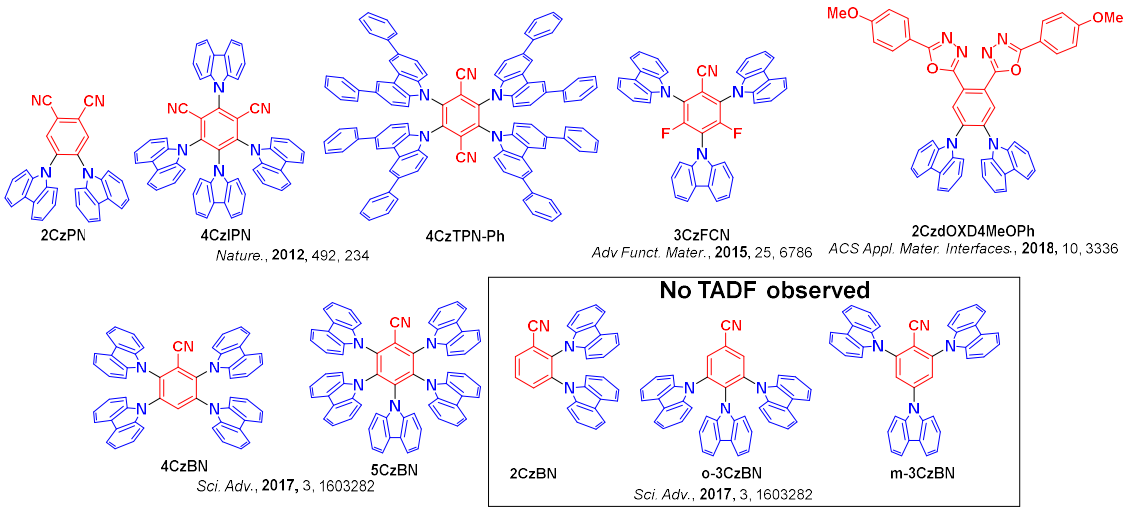

Figure **1.30**. Structures of discussed TADF emitters containing nitrile acceptors (and derivatives).

In 2014, Wang *et al.*[122] presented the first TADF OLED with an EQE_{max} surpassing 20% using the emitter **TXO-PhCz** (Figure **1.29** and **1.31**). In doped films, high Φ_{PL} of 90%, small ΔE_{ST} of 0.07 eV and a τ_d of 52 μs were reported. The OLED showed an EQE_{max} of 21.5% at CIE (0.31, 0.56). The material also displayed AIE properties. Another sulfone-based derivative, **DMAC-DPS**,[123] is an example of a deep blue emitter (Figure **1.31**). Its properties are λ_{PL} at 464 nm and a small ΔE_{ST} of 0.08 eV and a very short τ_d of 3.1 μs in 10 wt% mCP films. Its desirable combination of high Φ_{PL} and short τ_d has since led to it being used as an assistant dopant in Hyperfluorescence-OLEDs (see section 1.7 and Chapter 8). An alternative acceptor, namely dibenzothiophene-S,S-dioxide, has been extensively

studied by Monkman and co-workers when coupled to PTZ, **PTZ-DBTO2** (Figure **1.31**).[25, 124] Green emission with λ_{PL} = 584 nm and very small ΔE_{ST} of 0.02 eV in 10 wt% Zeonex films was reported for this compound.[124] Devices showed EQE_{max} of 22.0%. An alternative design based on this acceptor was introduced by the same group in combination with a central trizatruxene donor, **TAT-3DBTO2** (Figure **1.31**).[125] The Φ_{PL} is unity and there is an extremely small ΔE_{ST} of 0.03 eV in 10 wt% Bis-4-(N-carbazolyl)phenyl)phenylphosphine oxide (BCPO) films. The excellent TADF properties translated to devices with 30.9% EQE_{max} at CIE (0.26, 0.46), with RO_{100} of 6%.

A ketone acceptor with DMAC donor, **ACRXTN** (Figure **1.31**), showed moderately efficient devices with EQE_{max} of 12.1%.[104] However, the authors showed excellent efficiency roll-off with EQE at 1,000 cd m^{-2} of 11.0%, which was attributed to its efficient k_{RISC}. Subsequent computational work has since highlighted that the efficient RISC is triggered by energetic alignment between ^{3}LE, ^{3}CT and ^{1}CT states .[126] A similar derivative was recently reported by Aizawa *et al.*,[127] where the bridging oxygen was replaced with sulfur and tetramethyl-carbazole was used as the donor, **MCz-TXT** (Figure **1.31**). This compound shows extremely efficient k_{RISC} at 1.1×10^8 s^{-1}, the highest reported k_{RISC} rate to date. This was achieved owing to strong SOC between S_1 and T_1, in part due to the inclusion of the heavier sulfur, along with a close lying LE state. Efficient triplet harvesting was observed in devices with EQE_{max} = 25.8% at CIE (0.21, 0.46), the device showed an impressive EQE of 21.6% even at 10,000 cd m^{-2}. A benzophenone acceptor was used alongside extended carbazole donors in **CC2BP** (Figure **1.31**).[128] This emitter has λ_{PL} = 475 nm, and a long τ_d of 460 μs owing to its moderate ΔE_{ST} of 0.14 eV in 6 wt% bis[2-(diphenylphosphino)phenyl]ether oxide (DPEPO) films. Despite the long τ_d, good devices with EQE_{max} of 14.3% were reported at CIE (0.17, 0.27). A diketone acceptor, itself a MR-TADF emitter (*vide infra*), was used in combination with DMAC donors, **QAO-DAc** (Figure **1.31**).[129] The D-A-D emitter showed a λ_{PL} = 548 nm, Φ_{PL} = 90%, τ_d = 7.8 μs and ΔE_{ST} = 0.03 eV, which showed a red shifted, though broadened emission but with enhanced TADF efficiency compared to the acceptor only (i.e., **DiKTa**/**QAO**, *vide infra*.). High efficiency devices were reported with EQE_{max} 23.9% and EQE_{1000} 20.3% at CIE (0.41, 0.56).

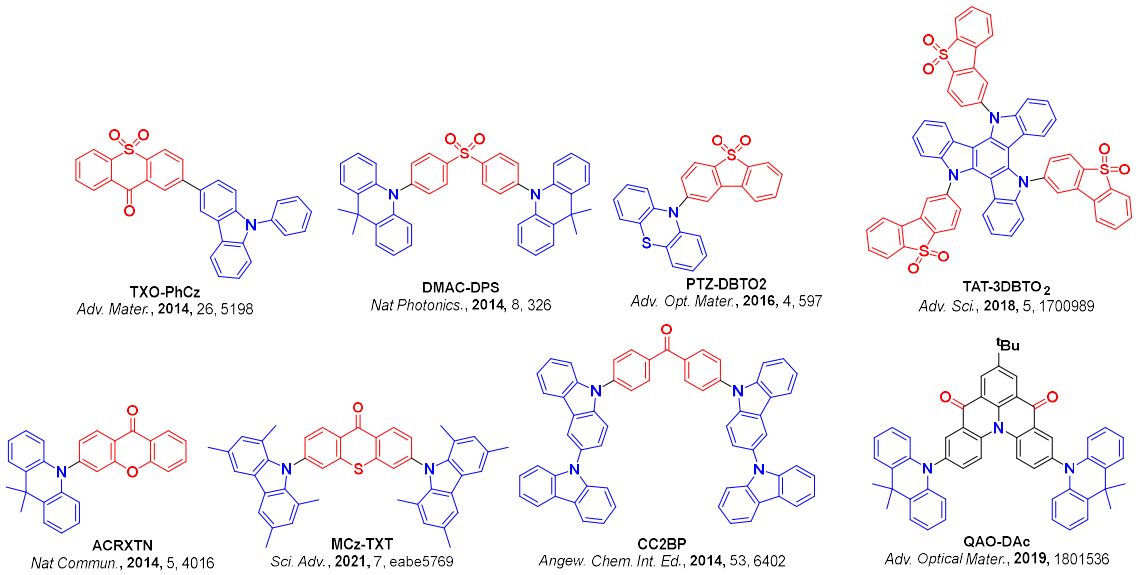

Figure **1.31**. Structures of discussed TADF emitters composed of sulfur and ketone acceptor functionalities.

The device with **DACT-II** (Figure **1.32**), a compound containing an extended donor coupled to a triazine acceptor,[130] showed very high EQE_{max} of 29.6%, which improved to 41.5% with an outcoupling sheet, representing one of the best performing devices to date. The small ΔE_{ST} of 0.01 eV in 9 wt% CBP (4,4'-Bis(carbazol-9-yl)biphenyl) and high Φ_{PL} of unity were proposed as the main factors for the efficient devices. Further, preferential horizontal orientation of the emitter in doped films was recorded, resulting in a strong light outcoupling efficiency. A related emitter where the donor was replaced with a silicon containing analogue of DPAC, **DTPDDA** (Figure **1.32**),[131] showed deep blue emission with λ_{PL} of 444 nm, Φ_{PL} of 74% and ΔE_{ST} of 0.14 eV in 16 wt% mCP:Diphenyl[4-(triphenylsilyl)phenyl]phosphine oxide (TSPO1) films. Two delayed lifetimes were observed at 2.3 µs and 25.4 µs. Blue devices with an EQE_{max} of 22.3% were reported at CIE (0.15, 0.20), with large roll-off with EQE_{1000} of 10.7%. A spiro acridine analogue (**SpiroAc-TRZ,** Figure **1.32**) was reported by Lin *et al.*[132] This compound showed Φ_{PL} of unity in 12 wt% mCPCN films, with low ΔE_{ST} of 0.07 eV, and strong horizontal orientation of the emitter. These features led directly to devices that showed impressive EQE_{max} of 36.7%, linked to a high outcoupling efficiency of 38.3%, greater than the 30% observed in isotropic emitters. This was the first example of a TADF OLED with EQE_{max} surpassing

30%, a major milestone in their development. Efficient TADF performance was reported recently by Cui *et al.*,[72] when multiple donors were linked to a triazine acceptor, **5Cz-TRZ** (Figure **1.32**). Efficient k_{RISC} of 1.5 × 10^7 s^{-1} was observed as T_1 contained significant LE contribution, ensuring large SOC between S_1 and T_1 while the compound also has a small ΔE_{ST} of 0.03 eV. Efficient TADF in **5Cz-TRZ** translated to excellent device performances, with EQE_{max} 29.3% at 486 nm, with RO_{1000} a mere 2.4% owing to its excellent triplet harvesting. Using an alternative nitrogen heterocycle, with identical donors to **DACT-II,** Chen *et al*,[103] presented a highly orientated emitter, **DQBC** (Figure **1.32**). In doped 9-(3-(9H-carbazol-9-yl)phenyl)-9H-3,9′-bicarbazole (mCPBC) films, high Φ_{PL} of 95%, short τ_d of 5.6 μs and small ΔE_{ST} of 0.06 eV were reported. These along with its high orientation corresponded to excellent EQE_{max} of 39.1%, the highest performing emitter to date. An impressive EQE_{100} of 36.1% was reported, decreasing to 29.1% at 1,000 cd m^{-2}.

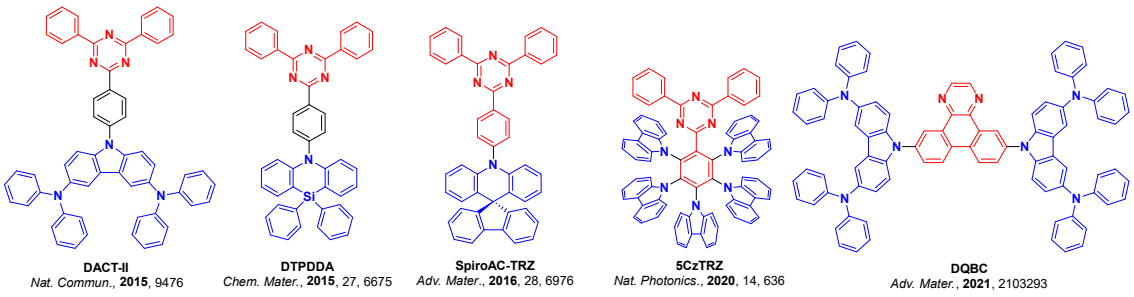

Figure **1.32**. Structures of discussed emitters composed of nitrogen heterocycle acceptors.

A strongly orientated material, **CzDBNA** (Figure **1.33**), was reported by Wu *et al.*,[133] that showed a ΔE_{ST} = 0.03 eV, τ_d = 3.2 μs and Φ_{PL} = 100% in 10 wt% CBP films. The nearly horizontally orientated TDM ensured high outcoupling efficiency. The devices are some of the highest performing TADF OLEDs to date with EQE_{max} = 37.8% at CIE (0.31, 0.61), while EQE at 5,000 cd m^{-2} remained high at 34.1%. Further, long operational device lifetimes were reported with LT_{50} of 315 hours. Although orientation is clearly a useful strategy to achieve high performing OLEDs, design of materials which undergo preferential orientation is poorly understood.[134] Two extremely efficient emitters were reported using boron emitters, **TDBA-Ac** and **TDBA-DI** (Figure **1.33**).[102] The acceptor is quite popular and is based on **DOBNA**, which has been reported as an MR-TADF emitter on its own (*vide infra*.).

Both showed efficient blue emission, with λ_{PL} = 458 and 456 nm in dilute toluene, Φ_{PL} = 93% and 99%, ΔE_{ST} = 0.06 eV and 0.05 eV and short τ_d of 1.8 μs for both in 20 wt% DBFPO films. Extremely efficient devices were reported with EQE_{max} of 25.7% and 38.2% at CIE (0.14, 0.15) and (0.15, 0.28), with the latter one of the highest performing D-A emitters to date, facilitated by its highly horizontally orientated configuration in films. High EQE_{1000} of 18.9% and 34.3% were reported owing to their fast k_{RISC} values of 0.99 and 1.1×10^6 s^{-1}, respectively. A similar acceptor was used alongside an extended donor, **M3CzB** (Figure **1.33**).[135] this compound showed blue emission at 445 nm, and despite a moderate ΔE_{ST} of 0.14 eV, a relatively short τ_d of 7.8 μs was reported. The OLEDs showed an EQE_{max} 30.7%, with moderate roll-off where EQE_{1000} = 21.6%. A series of D-A-D emitters were reported by Meng *et al*,[136] using the same acceptor and with DMAC donors at different positions, ***m*-AC-DBNA**, ***p*-AC-DBNA** and ***m*'-AC-DBNA** (Figure **1.33**). Similar photphysical properties were reported for all three compounds, with λ_{PL} = 492 – 498 nm, Φ_{PL} = 87 – 96%, τ_d = 1.5 – 7.8 μs and ΔE_{ST} = 0.01 – 0.03 eV. However, the OLEDs showed varying performances with EQE_{max} 14.1% for ***m*'-AC-DBNA**, 17.1% for ***m*-AC-DBNA** and 20.5% for ***p*-AC-DBNA**. Introduction of methyl groups about the carbazole donor ensured large D-A torsion in **TMCz-BO** and **TMCz-3P** (Figure **1.33**). This translated into these compounds showing ΔE_{ST} of 0.02 eV and 0.13 eV and modest τ_d of 0.8 μs and 14.5 μs, respectively. High EQE_{max} of 20.7% and 20.4% were obtained at CIE (0.14, 0.18) and (0.14, 0.26). The shorter τ_d in **TMCz-BO** translated into the device showing an improved roll-off with EQE_{1000} of 17.4% and 12.8%, respectively.[137] A simple D-A structure, **2e** (renamed **PXZ-DOBNA** here, Figure **1.33**)[138] showed sky blue emission with λ_{PL} = 492 nm, Φ_{PL} = 92%, τ_d = 2.7 μs and ΔE_{ST} of 0.08 eV in 1 wt% Polymethyl methacrylate (PMMA). Devices showed modest EQE_{max} of 15.5% but good efficiency roll-off as EQE_{1000} was maintained at ~14.8%. This group of emitters contain an MR-TADF acceptor but have D-A properties and are discussed in more detail in Chapter 7. Mumata *et al*. presented a blue emitter, **ACRPOB** (Figure **1.33**),[139] with λ_{PL} 475 nm and Φ_{PL} 80% in PhMe and a short τ_d of 1.6 μs due to its ΔE_{ST} of 0.10 eV was reported. Devices showed an EQE_{max} of 21.7% at CIE (0.16, 0.29), and the EQE_{1000} remained around 20%. A boron-containing emitter was reported by Kitamoto *et al.*, **PXZ-PXB** (Figure **1.33**).[140] In PhMe the λ_{PL} is 482 nm, and a ΔE_{ST} 0.03 eV resulted in a short τ_d of 1.9 μs. Efficient TADF properties and

high Φ_{PL} of unity in 6 wt% DPEPO translated to high performance devices with EQE_{max} 22.1%. These latter two are discussed again in Chapter 5, where they have been modelled.

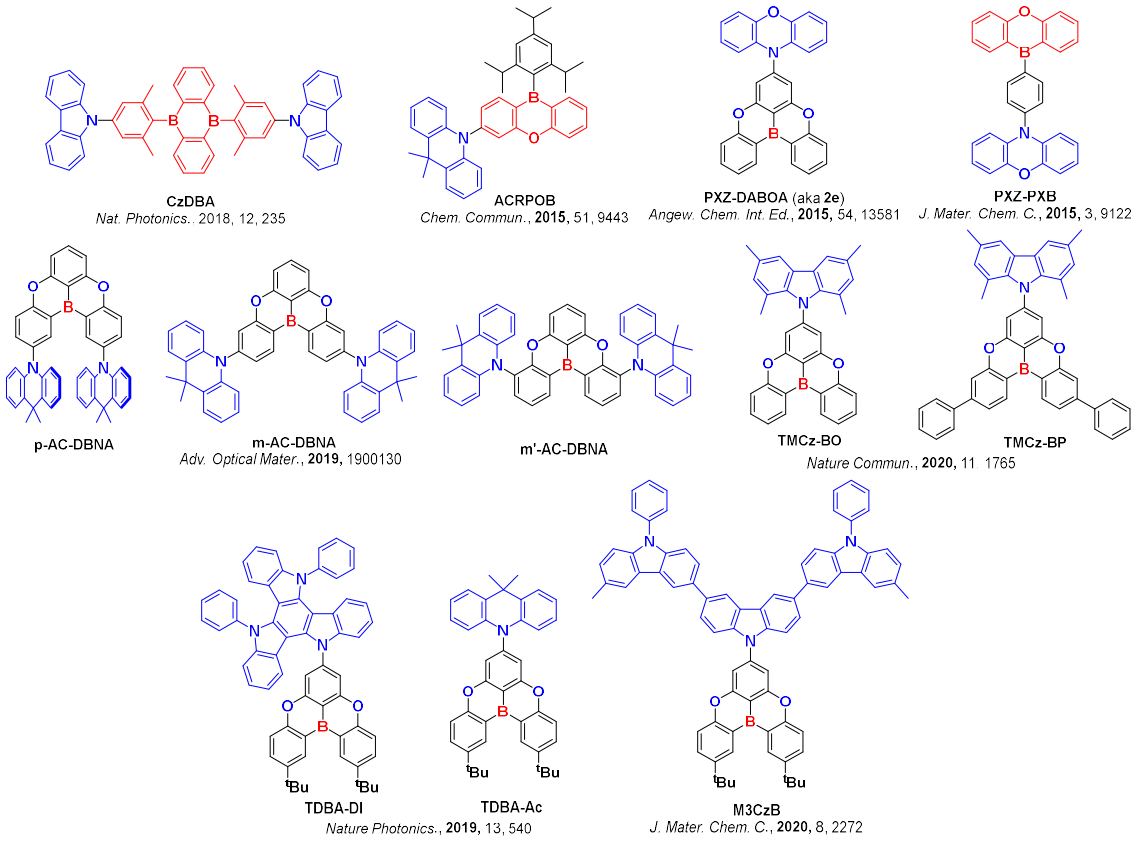

Figure **1.33**. Structures of discussed emitters with boron containing acceptors

An alternative strategy to separate HOMO and LUMO orbitals employs spiro conjugation (Figure **1.34**). This strategy uses the non-conjugated spiro unit to completely decouple HOMO and LUMO densities. It was used by Nasu *et al.*[141] in the form of **ACRSA** (Figure **1.34**), where the HOMO is situated on the acridan donor and the LUMO on the xanthone. The well separated HOMO and LUMO produced a small ΔE_{ST} of 0.06 eV and short τ_d of 5.3 μs in 20 wt% 2,8-Bis(diphenylphosphoryl)dibenzo[b,d]furan (PPF). Devices showed moderate EQE_{max} of 16.5% at electroluminescence emission maximum (λ_{EL}) of 494 nm. This emitter has been subsequently investigated in Chapter 5. An alternative spiro design utilized cyano acceptor units,[142] with HOMO situated on the acridan donor and LUMO on the cyano half, **ACRFLCN** (Figure **1.34**). Small ΔE_{ST} of 0.01 eV and modest Φ_{PL} of 67% were reported. τ_d was long, at 3.9 ms, despite the small ΔE_{ST}, no reason

was provided. Devices were fabricated with impressive EQE_{max} of 10.1% despite its long lifetime. Using the same acceptor unit, coupled to diphenylamine donors, Nakagawa *et al* presented **Spiro-CN** (Figure **1.34**).[143] This was the first reported TADF emitter containing a spiro unit. Small ΔE_{ST} and promising τ_d of 0.06 eV and 14 μs respectively were reported, however the Φ_{PL} was low, only 27%. The low Φ_{PL} reflected in poorly performing devices with EQE_{max} of 4.4%. al λ_{EL} of 550 nm. Using diphenylamine units again, an alternative design with dipyridine acceptor was presented, **DPAA-AF** (Figure **1.34**).[144] Largely decoupled HOMO and LUMO components produced small ΔE_{ST} of 0.02 eV, with short τ_d of 4.3 μs. In 6 wt% mCP films, promising Φ_{PL} was presented being 70%. Sky blue devices were prepared (λ_{EL} = 499 nm) with EQE_{max} of 9.6%. Recently, we reported three high performing SFX-based spiro-conjugated emitters with diphenylamine donors again,[145] **SFX-PO-DPA**, **SFX-PO-DPA-Me** and **SFX-PO-DPA-OMe** (Figure **1.34**). Despite the well separated HOMO-LUMO densities and reported low oscillator strength, high Φ_{PL} were measured at 50%, 70% and 58%, respectively, in doped mCP films. Each emitter showed small ΔE_{ST} of 0.01 – 0.05 eV and k_{RISC} of 2.3 – 2.6 × 10^5 s^{-1}. Devices showed EQE_{max} of 11.0%, 23.0% and 16.0%, respectively, while the EQE_{100} remained high at 9.0%, 19.0% and 14.0%. These emitters were studied computationally to ascertain why Φ_{PL} is high despite the decreased oscillator strength. k_r was calculated experimentally and theoretically with the latter two orders of magnitude smaller. The vibrational modes in this molecule were modelled, with distortions around the sp^3 carbon allowing sufficient overlap for significant k_r, which matches experimental values. In spiro emitters, light emission is vibrationally-assisted leading to non-negligible k_r.

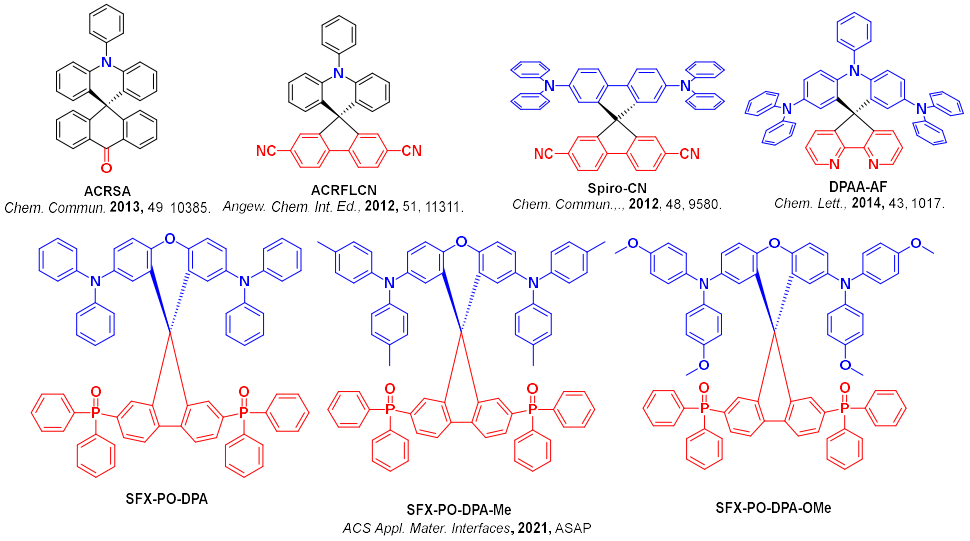

Figure **1.34**. Structures of TADF emitters which contain spiro units.

1.6.2 MR-TADF

So far, the primary strategy to separate HOMO and LUMO density has relied on spatial separation using a twisted conformation between donors and acceptors. Although all visible colours have been reported in D-A TADF emitters, in most the emission is broad.[146] This is characteristic of emission occurring from CT states where there is frequently a large reorganisation between ground and excited states.[147] Broad emission spectra are detrimental for colour purity,[148] which is desirable in OLEDs.[146] The broadness of the emission is quantified using the FWHM. The impact of emission broadness on colour purity can be observed in Figure **1.35**, where two emission spectra of the same emission maximum (460 nm) have been simulated, one with a FWHM of 20 nm and the other, 100 nm, corresponding to CIE coordinates of (0.14, 0.03) and (0.15, 0.17) respectively. The narrower simulated spectrum is much closer to the desired CIE value for blue for BT.2020, quoted as (0.13, 0.05) which is the current standard for ultra HD-TVs (see section 1.3.5 for more detail).[76]

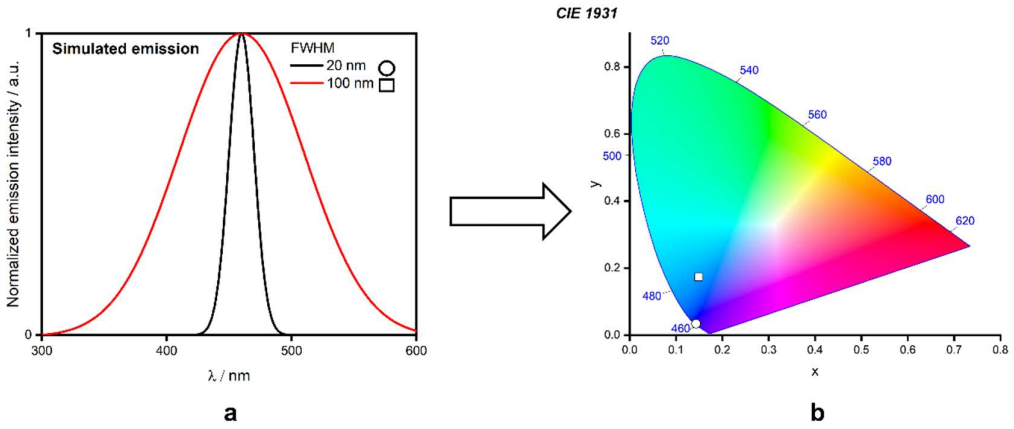

Figure **1.35**. Simulated emission spectra (**a**) with FWHM 100 nm (red) and 20 nm (black) and (**b**) their corresponding CIE plots, where circle indicates 20 nm and square 100 nm.

In 2016 a new strategy was introduced by Hatakeyama *et al.*, based on p- and n-doped nanographene fragments.[8] Exploiting complementary resonance effects, the electron density distribution of the HOMO and LUMO orbitals are localized on neighbouring atoms in the heteroacene, ensuring a sufficiently small ΔE_{ST} to turn on TADF (Figure **1.36**).[9] MR-TADF emitters possess a rigid structure and thus there is little geometry reorganization from the ground to the excited state, resulting in small Stokes shifts and narrowband emission (i.e., small FWHM).[149] The emissive excited state possesses short-range charge transfer (SRCT) character, reflected in a small degree of positive solvatochromism observed in the PL spectra and assisting narrow emission.[149]

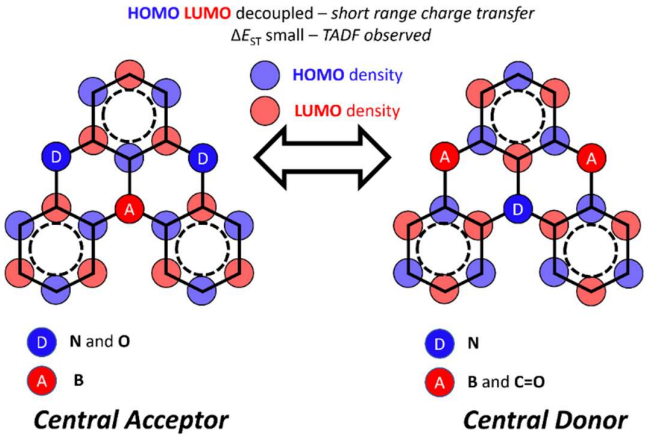

Figure **1.36**. Simplified HOMO LUMO picture of the two central MR-TADF cores.

Thus far, the structural diversity MR-TADF emitters remains small as are the number of examples; however, since being first employed as emitters in OLEDs, examples of devices across the visible spectrum and examples showing efficiencies surpassing 30% have emerged.[150 151, 152] A timeline of key MR-TADF OLED developments is shown in Figure **1.37** with the different structural classes and high performing blue, green and red emitters showcased. The study of MR-TADF emitters is the core of the studies in Chapters 6 – 8. Here examples which have been modelled in Chapter 7 are presented along with other representative examples.

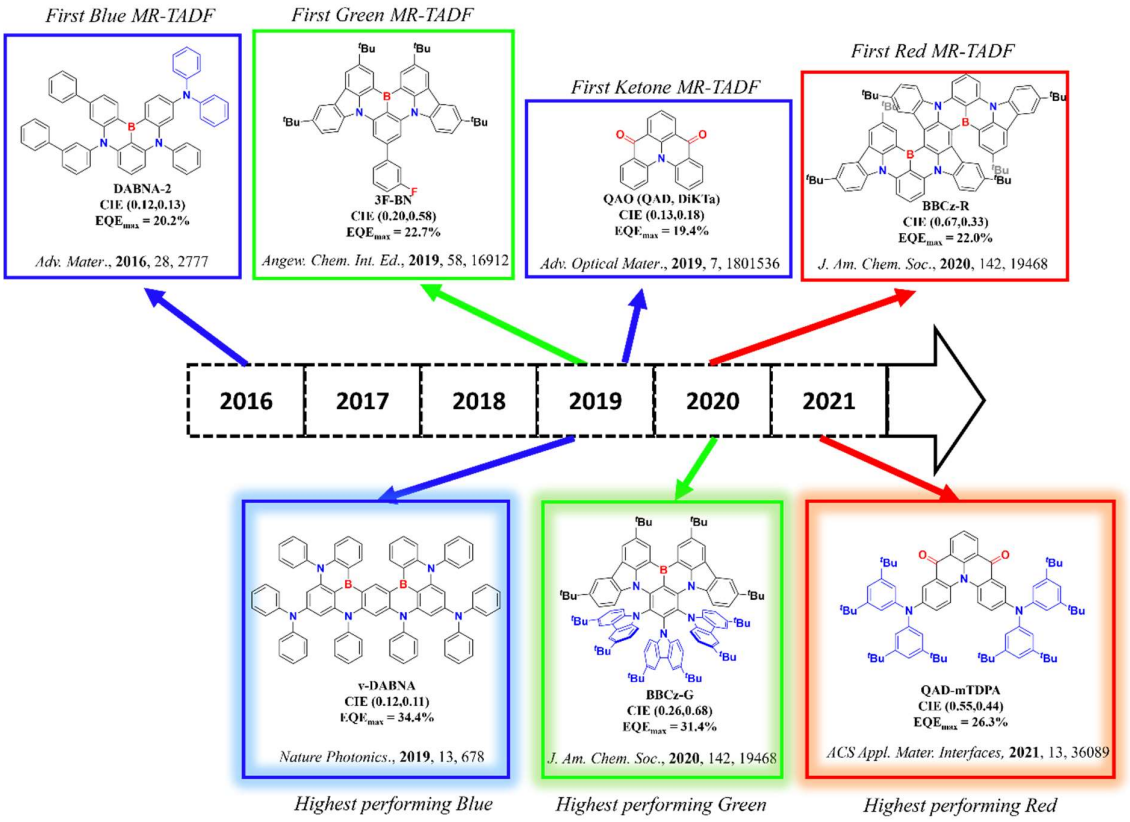

Figure **1.37**. Timeline of key milestones in MR-TADF OLEDs.

The most common design incorporates a central boron as the acceptor with oxygen or nitrogen groups acting as the donors. The first examples of MR-TADF emitters reported by Hirai *et al.*[138] possess this motif as exemplified by compound **2** (later called **DOBNA**, Figure **1.38**).[153] Measurements in solution showed a small ΔE_{ST} of 0.15 eV in EtOH; however, no time-resolved PL was collected. The photophysics of this compound was revisited recently,[153] and the authors reported solid-state data in 1

wt% PMMA with a ΔE_{ST} of 0.18 eV, a λ_{PL} of 398 nm with a τ_d of 66 μs. No devices were fabricated in either report. The same group subsequently reported two emitters, **DABNA-1** and **DABNA-2** (Figure **1.38**), where the oxygen donor atoms where replaced by nitrogen atoms as the donating species.[8] Excellent Φ_{PL} values in 1 wt% 3,3'-di(9H-carbazol-9-yl)bi-phenyl (mCBP) of 88% and 90% were achieved for **DABNA-1** and **DABNA-2**, respectively, with λ_{PL} red-shifted compared to **DOBNA** at 460 nm for **DABNA-1** and 469 nm for **DABNA-2**. Modest ΔE_{ST} of 0.18 eV and 0.14 V along with lifetimes of 94 μs and 65 μs were reported for **DABNA-1** and **DABNA-2**, respectively. Vacuum-deposited OLEDs with **DABNA-1** and **DABNA-2** as the emitter showed EQE_{max} of 13.5% and 20.2%, respectively. The most attractive feature of these emitters is their narrow FWHM that ensures pure blue emission with CIE coordinates of (0.13, 0.09) and (0.12, 0.13) for the devices with **DABNA-1** and **DABNA-2**, respectively. This report documents the first examples of MR-TADF emitters employed in devices; however, despite the promising EQE_{max} values, the devices suffered from severe efficiency roll-off with EQE_{100} of ~6.3% and ~13.3%, and the EQEs at a luminance of 1,000 cd m^{-2} were not reported. A D_3-symmetric derivative of **DABNA-1**, **TABNA** (named **2** in the original report, Figure **1.38**)[154] showed moderate Φ_{PL} in 1 wt% PMMA of 54% and a comparable ΔE_{ST} of 0.21 eV. A narrow FWHM of 28 nm at λ_{PL} = 399 nm was observed; however, no devices were reported. ***t*DABNA**, a *tert*-butyl decorated analogue of **DABNA-1** was reported by Han *et al* (Figure **1.38**).[155] This compound was used as both an emitter in an OLED and as the terminal emitter component of a Hyperfluorescence-OLED with **DMAC-DPS** employed as the triplet harvester (see chapter 8 for more details). In 5 wt% DPEPO films, the Φ_{PL} is 85% with ΔE_{ST} of 0.17 eV, which resulted in long delayed lifetimes of 83 μs. The EQE_{max} of the device was 25.1%, but with large roll-off where the EQE_{100} was 6.0%.

In 2018, Matsui *et al.* introduced a slightly extended design strategy,[156] wherein they altered the number of boron atoms in the three emitters, **B2**, **B3** and **B4** (Figure **1.38**). Moderate Φ_{PL} values of 53%, 33%, 57% and ΔE_{ST} of 0.19 eV, 0.15 eV, 0.15 eV, respectively, were reported in 1 wt% PMMA doped films. All three compounds show blue emission with λ_{PL} = 455 nm, 441 nm and 450 nm, and FWHM of 32 nm, 34 nm and 38 nm, respectively, for **B2**, **B3** and **B4**. Only **B2** was used as an emitter in a device, performing similarly to the device with **DABNA-2** with an EQE_{max} of 18.3% and EQE_{100}

of 12.6% compared to 20.2% and 12.4%, respectively, for the OLED with **DABNA-2**. A linearly extended emitter, ***ν*-DABNA** (Figure **1.38**),[150] was introduced by Kondo *et al.* and the OLEDs showed excellent performance with an EQE_{max} of 34.4% at CIE (0.12, 0.11), representing the most efficient blue TADF emitter to date. A minimal efficiency roll-off was reported with EQE at 1,000 cd m^{-2} of 26.1% owing to the efficient k_{RISC} of 2.0×10^5 s^{-1}. Although k_{RISC} is low compared to D-A counterparts, this is one of the highest values reported for MR-TADF emitters (*vide infra*.). This is likely due to the small ΔE_{ST} of 0.02 eV, which is significantly smaller than those of most MR-TADF emitters, where the ΔE_{ST} is typically above 0.10 eV. There is no explanation provided for why this compound shows such a small ΔE_{ST}.

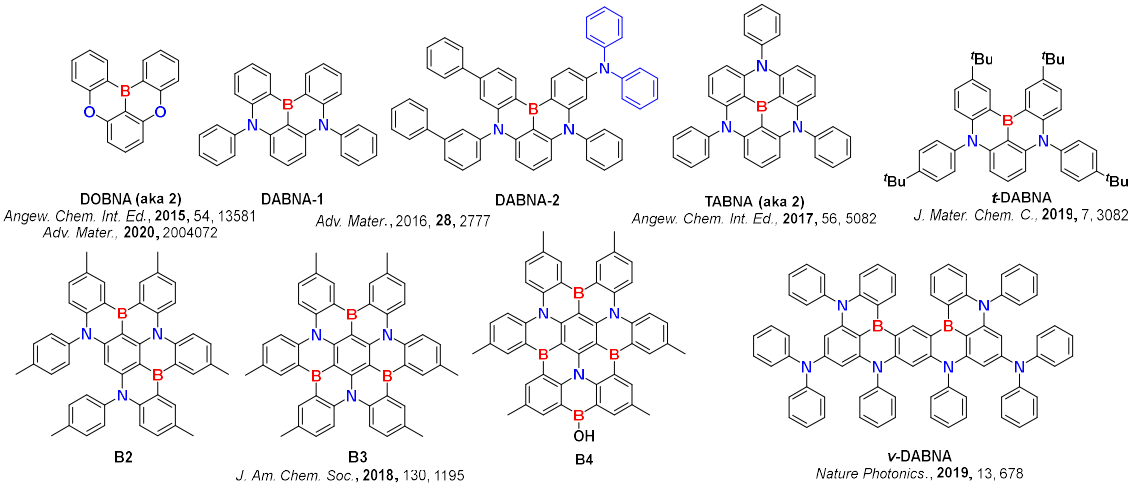

Figure **1.38**. Structures of discussed BN(O) MR-TADF emitters

A new design series has recently emerged based on the original **DABNA-1**, however, the diphenyl amine fragments were replaced with di-*tert*-butylcarbazole (Figure **1.39**). The parent, **DtBuCzB**,[157] displays sky blue emission with λ_{PL} of 493 nm, Φ_{PL} = 88%, a τ_d of 69 μs and ΔE_{ST} of 0.13 eV in 1 wt% mCBP films. Compared to **DABNA-1** there is a red shift in the emission and a slightly reduced ΔE_{ST} (λ_{PL} = 460 nm and ΔE_{ST} = 0.18 eV for **DABNA-1** in 1 wt% mCBP) owing to and increased conjugation afforded by the fused structure.[158] Devices with EQE_{max} 21.6% at CIE (0.10,0.42) were reported. It has been subsequently reported under the name **BBCz-SB**,[151] wherein an improved EQE_{max} of 27.8% was reported. Jiang *et al.*[159] reported the analogue, **BN-DMAC**, where there is the

incorporation of bridging DMAC groups (Figure **1.39**). This compound shows sky blue emission with λ_{PL} of 485 in PhMe and a ΔE_{ST} of 0.14 eV. Attractive photophysical properties were reported in 1 wt% mCBP with Φ_{PL} of 63% and τ_d of 13.9 μs. The OLEDs showed an EQE_{max} of 21.1% at CIE (0.14, 0.54). The roll-off was moderate, with an EQE_{1000} of 12.5%. The phenoxazine- and phenothiazine-containing analogues were recently reported by Hua *et al*.,[160] **PXZBN** and **PTZBN** (Figure **1.39**). Both emit in the green region with λ_{PL} of 515 and 519 nm, and Φ_{PL} of 84% and 80%, respectively in 1 wt% mCBP:PO-TCTA films. In PhMe both compounds showed similar ΔE_{ST} of 0.19 eV and 0.15 eV, but the incorporation of the sulfur decreased the delay time in films from 25.3 μs to 16.1 μs and improved k_{RISC} from 0.56×10^5 s^{-1} to 1.17×10^5 s^{-1} due to the heavy atom effect from sulfur increasing SOC. Improved k_{RISC} translated into improved device performance with EQE_{max} of 17.1% and 25.5% for **PXZBN** and **PTZBN**, respectively. The roll-off is attenuated too where the device with **PTZBN** showed an EQE_{1000} of 17.2% compared to 7.4%, which represents a roll-off of 33% and 58%.

Substitution of **D*t*BuCzB** has proved a popular strategy to modulate the photophysics of this class of MR-TADF emitters. Zhang *et al*.[161] reported the first examples of green MR-TADF OLEDs with λ_{EL} of 501 nm, 498 nm and 493 nm for the devices with **BN-2F**, **BN-3F** and **BN-4F**, respectively (Figure **1.39**). The electron withdrawing fluorine-substituted phenyl groups stabilize the LUMO compared to the parent compound. ΔE_{ST} of 0.16 eV, 0.08 eV and 0.11 eV and τ_d of 25.9 μs 16.7 μs and 19.0 μs were observed, along with high Φ_{PL} of 88.7%, 83.4% and 91.4% for **BN-2F**, **BN-3F** and **BN-4F** respectively. Green hyperfluorescent (*vide infra*.) devices with EQE_{max} of 22.0%, 22.7% and 20.9% were fabricated at CIE coordinates (0.16, 0.60), (0.20, 0.58) and (0.12, 0.48) for the devices with **BN-2F**, **BN-3F** and **BN-4F**, respectively. Xu *et al*.,[162] reported the use of stronger acceptors added *para* to boron. The acceptors used were triazine, phenyltriazine, pyrimidine and cyano pyrimidine, in emitters **D*t*CzB-DPTRZ**, **D*t*CzB-TPTTRZ**, **D*t*CzB-PPm** and **D*t*CzB-CNPm**, respectively (Figure **1.39**). Each of these compounds also has a lower-lying LUMO than the parent due to stabilisation from these withdrawing groups (Figure **1.38**), thus decreasing the band gap and red shifting the emission to λ_{PL} of 521, 501, 499 and 515 nm, respectively, in PhMe compared to **D*t*BuCzB** (λ_{PL} = 481 nm in PhMe).[157] ΔE_{ST} of 0.17 eV, 0.11 eV, 0.08 eV 0.12 eV were recorded in PhMe glass,[162] along with high Φ_{PL} in 3

wt% 9-(2-(9-phenyl-9H-carbazol-3-yl)phenyl)-9H-3,9'-bicarbazole) (PhCzBCz) films of 87%, 95%, 94% and 87% for **D*t*CzB-DPTRZ**, **D*t*CzB-TPTTRZ**, **D*t*CzB-PPm** and **D*t*CzB-CNPm**, respectively. The OLEDs showed EQE_{max} of 24.6%, 29.8%, 28.6% and 25.0%, at CIE (0.33, 0.63), (0.18, 0.67), (0.16, 0.66) and (0.35, 0.63) for the devices with **D*t*CzB-DPTRZ**, **D*t*CzB-TPTTRZ**, **D*t*CzB-PPm** and **D*t*CzB-CNPm**, respectively. Contrasting device performances were noted with extremely high roll-off of 70% and 42% at 100 cd m^{-2} for **DtCzB-DPTRZ** and **DtCzB-CN-Pm** compared to 11% and 15% for **D*t*CzB-TPTTRZ** and **D*t*CzB-PPM**. This was attributed to more efficient k_{RISC} for the latter two, which are an order of magnitude higher (10^4 s^{-1} compared to 10^3 s^{-1}).

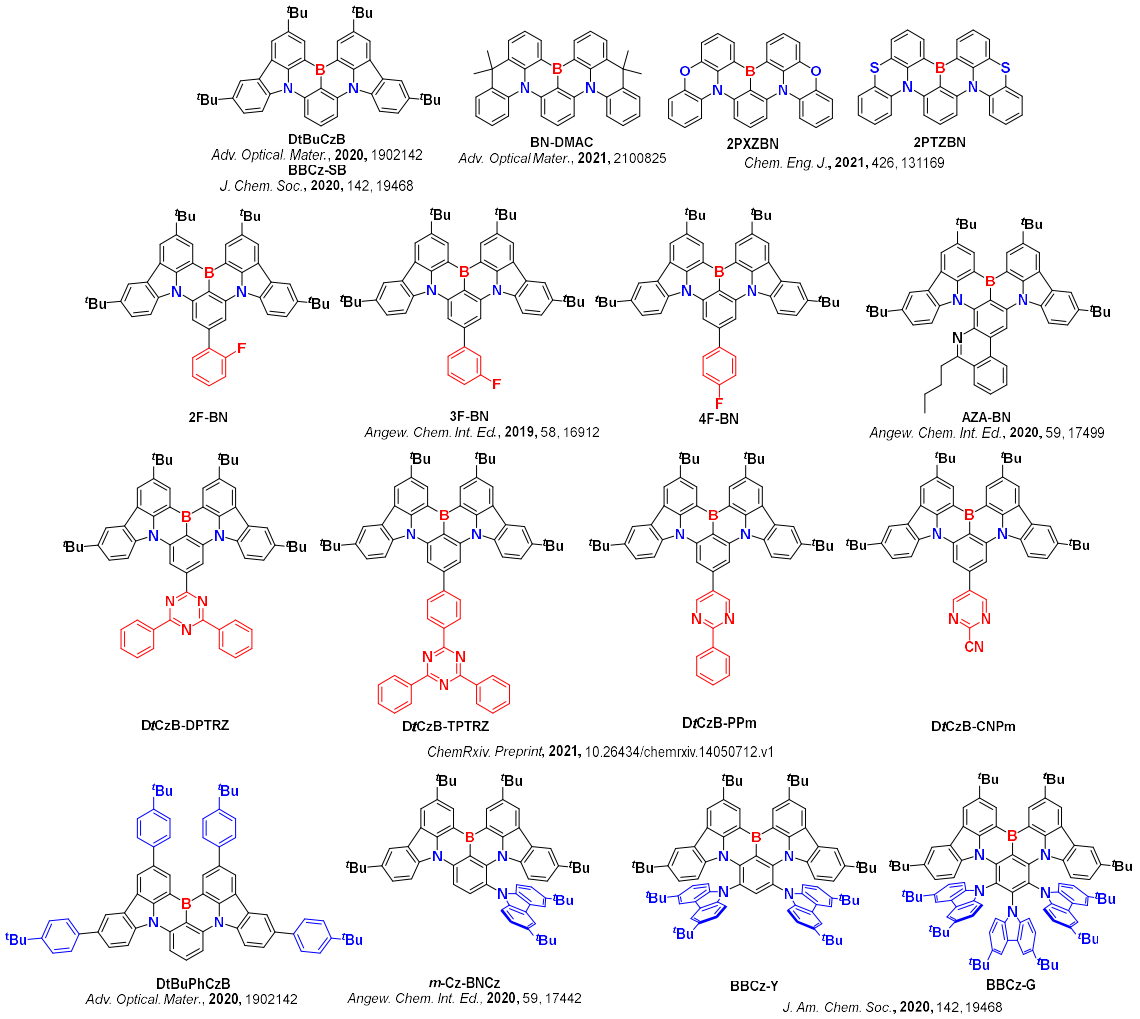

Figure **1.39**. Structures of discussed BN MR-TADF emitters containing carbazole.

Increased conjugation from *tert*-butyl (*t*Bu) Phenyl groups, **D*t*BuPhCzB**,[157] red shifted emission to λ_{PL} 508 nm in 1 wt% mCBP (compared to 493 nm in 1 wt% mCBP for **D*t*BuCzB**), and had minimal impact on ΔE_{ST} and τ_d, each measured as 0.10 eV and 61 μs compared to 0.13 eV and 69 μs reported for **D*t*BuCzB** (Figure **1.39**). Green devices with EQE_{max} of 23.4% at CIE (0.15,0.61) were presented. Addition of donating substituents on this core unit has also been investigated. A *tert*-butyl carbazole unit coupled *meta* to the boron, ***m*-Cz-BNCz** (Figure **1.39**),[152] produced a red shifted emission compared to the parent, with λ_{PL} of 528 nm in 10 wt% PhCzBCz (compared to 481 nm for **D*t*BuCzB**). This occurs as the electron donating *tert*-butyl carbazole destabilises the HOMO, which is located *meta* to the boron atom (Figure **1.40**). Addition of the *t*Bu-carbazole produces a smaller ΔE_{ST} of 0.08 eV in PhMe glass and a remarkably fast τ_d of 0.86 μs in 10 wt% PhCzBCz. However, with the groups added to the core a broadening of emission spectra is observed with a FWHM in toluene of 38 nm compared to 22 nm for **D*t*BuCzB**,[157] likely due to increased conformational flexibility between carbazole and the core. Efficient devices with EQE_{max} of 31.4% at CIE (0.26, 0.68) were observed, the EQE_{100} remained high at 29%. Building from this example, two derivatives where the number of carbazoles increased to 2 and 3 were reported in the form of **BBCz-Y** and **BBCz-G** (Figure **1.39**). In the former the second *meta* position is occupied, while in the latter both *meta* and the *para* positions are occupied. Compared to ***m*-Cz-BNCz**, a red shifted emission is observed for **BBCz-Y** in toluene, moving from 519 nm to 549 nm, while it is largely unaffected in **BBCz-G** at 517 nm. For **BBCz-Y**, the second donating *t*BuCz destabilized the HOMO further. In **BBCz-G** a combination of increased HOMO (from *meta* substitution) and increased LUMO (from *para* substitution) ensures a blue shifted emission compared to **BBCz-Y**, similar to that for ***m*-CZBNCz** (Figure **1.40**). Both compounds possess identical ΔE_{ST} of 0.14 eV and similar τ_d of 13 μs and 11 μs, respectively, in 2 wt% mCBP. Efficient OLEDs with EQE_{max} 29.3% and 31.8% at CIE of (0.37, 0.61) and (0.26, 0.68) were fabricated for the devices with **BBCz-Y** and **BBCz-G**, respectively. This was maintained at 100 cd m^{-2}, with EQE of ~25.8% and ~29.5% for **BBCz-Y** and **BBCz-G**, with the latter the highest performing green MR-TADF emitter to date.

A fused conjugated derivative was synthesised, **AZA-BN** by Zhang *et al.* (Figure **1.39**).[163] This resulted in a red shifted emission at λ_{PL} of 522 nm in PhMe compared to **DtBuCzB** (λ_{PL} = 481 nm in

PhMe).[157] Density functional theory (DFT) results confirmed that there is greater conjugation in this compound, resulting in a smaller band gap.[163] The compound shows a ΔE_{ST} of 0.18 eV and a near unity Φ_{PL} of 99.7% in PhMe. In 4 wt% mCBP films, a Φ_{PL} of 94% and a long τ_d of 160 μs were recorded. The OLEDs showed an EQE_{max} of 25.7% at CIE (0.28 ,0.69), but the roll-off was high with the EQE_{1000} dropping to 9%. The roll-off could be mitigated by moving to a Hyperfluorescence-OLED using $Ir(ppy)_3$ as an assistant dopant. The EQE_{1000} in the Hyperfluorescence-OLEDs was 19.1%.

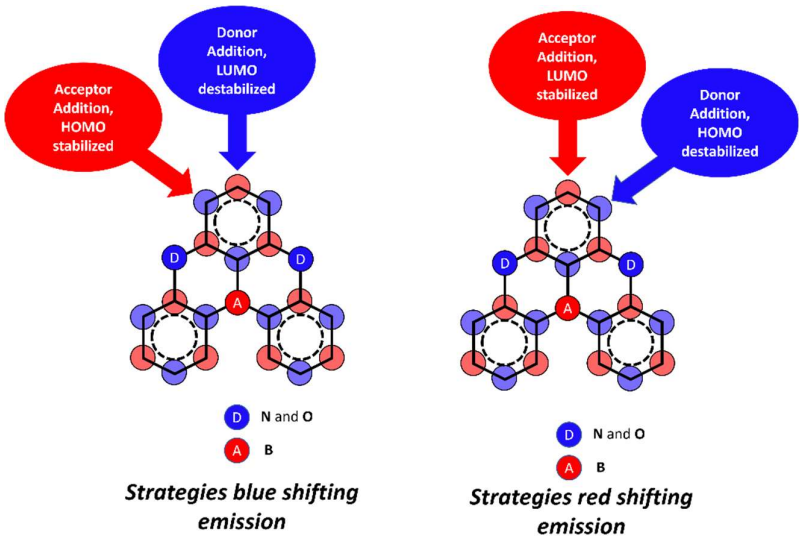

Figure **1.40.** Strategies to colour tune MR-TADF emitters using donor and acceptor substituents, where blue balls are HOMO density and red balls are LUMO density

Recently, several red emitters have been reported that rely on the nitrogen and boron atoms being *para* with respect to each other.[151, 164] **BBCz-DB** and **BBCz-R** (Figure **1.41**),[151] show deeply contrasting colours of 471 nm and 619 nm in 2 wt% mCBP, respectively. This can be explained owing to the position of the donating and withdrawing atoms. The results are analogous to the previously discussed donor and acceptor substitution patterns (Figure **1.40**) but maintained in a rigid framework here ensuring the narrow emission is observed. The two emitters displayed similar TADF properties with ΔE_{ST} of 0.15 eV and 0.19 eV in PhMe glass and τ_d of 35 and 53 μs in 2 wt% mCBP, respectively. It appears that the atomic positions of the donating and accepting atoms influenced only the colour and not the TADF properties. Devices with **BBCz-SB** and **BBCz-R** showed CIE of (0.12, 0.18) and (0.67,

0.33) and EQE_{max} of 29.3% and 22.0%, respectively, the latter is the first reported red MR-TADF OLED. Severe efficiency roll-off was observed for **BBCz-R** where the EQE_{1000} could not be measured, while it was 5.5% for **BBCz-DB**. The same approach to red shift emission with the inclusion of donating/accepting groups *para* to each other was recently employed by Zhang *et al.*[165] Here the generation of partial bonding/antibonding character was attributed by the authors to explain the decreasing energy gap. Two emitters **R-BN** and **R-TBN** (Figure **1.41**) with λ_{PL} of 672 and 698 nm, respectively, and Φ_{PL} of unity for both in 3 wt% CBP were presented. The ΔE_{ST} values were measured to be 0.18 eV and 0.16 eV, respectively, in PhMe glass, leading to very long τ_d of 310 and 710 μs in 3 wt% CBP films. Conventional OLED devices were not presented but these compounds were rather used as terminal emitters in Hyperfluorescence-OLEDs alongside an assistant dopant $Ir(mphmq)_2tmd$. The devices showed near infra red (NIR) emission, with CIE (0.72, 0.28) for both devices and EQE_{max} of 28.4 and 28.1% for **R-BN** and **R-TBN**, respectively. This is the highest performing NIR Hyperfluorescence-OLED to date; notably, no discussion of roll off was included.

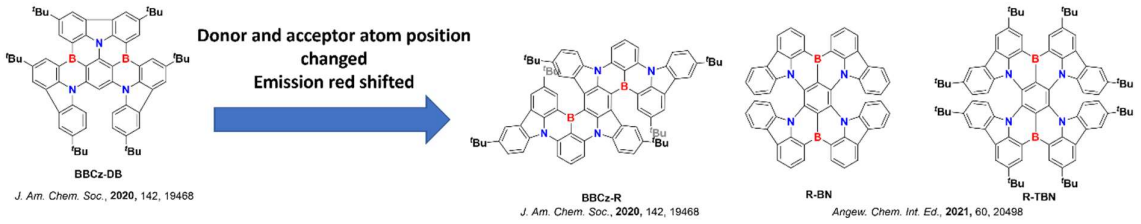

Figure **1.41**. Strategies to red shift MR-TADF emitters and discussed structures.

The design strategy where there is a central nitrogen has also been explored (Figure **1.42**), reported initially by Oda *et al.*;[166] these emitters are discussed in more detail in Chapter 6. Ikeda *et al.*[153] presented a central donor MR-TADF emitter also containing oxygen donors which was used in conjunction with boron acceptors, in a linearly extended pattern, generating a green emitter (λ_{PL} = 506 nm) **OAB-ABP-1** (Figure **1.42**).[153] In 1 wt% DOBNA-OAr films this compound displayed ΔE_{ST} of 0.12 eV, τ_d of 32 μs and Φ_{PL} of 90%. Solution-processed green devices showed an EQE_{max} of 21.8% at CIE (0.12,0.63). The OLEDs showed excellent efficiency roll-off, with the EQE remaining 17.4% at 1,000 cd m^{-2}. The devices showed a lifetime of 11 hours (LT_{50}) at a luminance of 300 cd m^{-2}. Nagata *et al*,[167] reported an inverted **DABNA-1** structure, which also incorporated fused sulfur-containing rings, **BSBS-**

N1 (Figure **1.42**). Compared to previously reported MR-TADF emitters the k_{RISC} is fast at 1.9×10^6 s^{-1}. Fast k_{RISC} was attributed to the incorporation of heavier sulfur atoms, which increased the SOC within the system via the heavy atom effect, translating to increased state mixing and efficient TADF. In 2 wt% mCBP doped films the λ_{PL} is 478 nm, ΔE_{ST} = 0.14 eV, Φ_{PL} = 89% and the τ_d = 5.6 μs. OLEDs showed an EQE_{max} of 21.0% at CIE (0.11, 0.22), and despite the fast k_{RISC}, large roll-off was observed, with EQE_{100} ~16.3%.

There are now a number of MR-TADF emitters where boron atoms are replaced with ketone acceptors (Figure **1.42**). Coincidentally reported by Yuan *et al.* [129] to our own work, the early examples are discussed in Chapter 6. Since this first report other analogues have been reported, that incorporate embedding a DMAC, PXZ or PTZ groups within the MR-TADF scaffold,[168] producing the emitters **DQAO**, **OQAO** and **SQAO** (Figure **1.42**). The introduction of O and S atoms resulted in a substantial red shift in the emission, with λ_{PL} in PhMe of 465, 520 and 552 nm, respectively, and this was coupled with a slight broadening of the emission spectrum, with FWHM of 33 nm, 36 nm and 54 nm, respectively. **SQAO** also shows a more pronounced positive solvatochromism, suggesting that the excited state here contains more CT character than the other two. The three compounds show similar ΔE_{ST} of 0.19 eV, 0.16 eV and 0.16 eV, respectively, while τ_d are 111 μs, 205 μs and 78 μs; the latter is likely shorter due to increased SOC from the heavier sulfur, but this was not explicitly mentioned by the authors. The devices show EQE_{max} of 15.2%, 20.3% and 17.8% for the OLEDs with **DQAO**, **OQAO** and **SQAO**, respectively, at CIE (0.12, 0.18), (0.32, 0.65) and (0.47, 0.52); the efficiencies decreased to 8.5%, 15.1% and 13.6% at 100 cd m^{-2}. Yasuda *et al.* reported a family of linearly extended emitters, **QA-1**, **QA-2** and **QA-3** (Figure **1.42**).[169] Each displayed TADF characteristics in 3 wt% 3,6-bis(diphenylphosphinyl)-9-phenyl-carbazole (PPCz) doped films, with ΔE_{ST} of 0.29 eV, 0.19 eV and 0.19 eV, respectively, and τ_d of 655 μs, 48 μs and 307 μs. The long τ_d for **QA-1** can be rationalized by its much larger ΔE_{ST}, while the differences in delayed lifetimes between **QA-2** and **QA-3** were attributed to the presence of intermediate triplet states in **QA-2** that contribute to an enhanced k_{RISC} via spin vibronic coupling. Similar λ_{PL} at 457 nm and 465 nm were observed for **QA-1** and **QA-2**, respectively, while replacing two of the carbonyl groups with oxygen atoms produced a red shifted

emission with λ_{PL} at 523 nm. Devices with **QA-1**, **QA-2** and **QA-3** showed EQE_{max} at 17.1%, 19.0% and 16.6%, respectively, at CIE of (0.14, 0.12), (0.13, 0.14) and (0.26, 0.62). The extremely long τ_d for **QA-1** contributed to significant efficiency roll-off, with a RO_{100} of 93%, attributed to TTA and STA quenching pathways. The RO_{100} were smaller for both **QA-2** and **QA-3** devices at 42% and 40%, respectively.

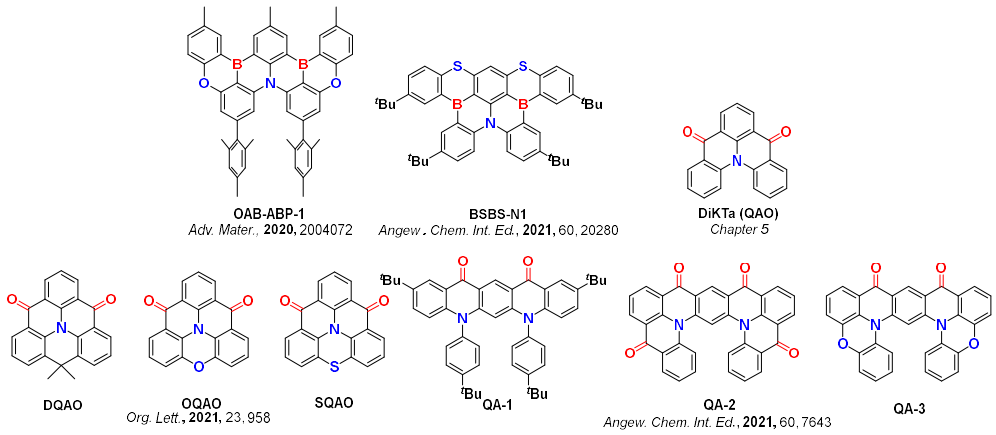

Figure **1.42**. Structures of discussed MR-TADF emitters with central nitrogen

Nearly 100 MR-TADF OLEDs now exist, covering the full spectral range, however the majority suffer from severe efficiency roll-off. Early examples did not reach brightnesses above 1,000 cd m^{-2}, while more recent studies still highlight low efficiencies at this practical brightness. This can be attributed to the inefficient k_{RISC} observed in most MR-TADF emitters, that is substantially slower than the highest performing D-A systems. Figure **1.43** shows the reported k_{RISC} values of all MR-TADF emitters that were available with varying ΔE_{ST}, compared to the highest performing D-A emitters. A modest trend in increasing k_{RISC} with decreasing ΔE_{ST} is apparent, however, similarly to D-A emitters it is not perfectly linear.[114] Strategies to improve k_{RISC} in MR-TADF emitters are limited, with incorporation of sulfur in **BSBS-N1** (Figure **1.42**), **PTZ-BN** (Figure **1.39**) and **SQAO** (Figure **1.42**) attributed to increase SOC. Comparisons between the oxygen, **PXZ-BN**, and sulfur, **PTZ-BN**, derivatives did indeed show an improved k_{RISC}, while shorter τ_d was apparent for **SQAO** compared to **OQAO**. Much like D-A systems, introduction of intermediate triplet states was used as a rationale for increased k_{RISC} between **QA-2** and **QA-3** (Figure **1.42**), with the former having several intermediate

states, leading to improved device performance. The position of higher lying triplet states (T_{n+1}) has not been studied in great detail for MR-TADF emitters.

One trend that is notable is the higher k_{RISC} values upon incorporation of a carbazole substitution (Figure **1.43**, blue squares), with ***m*-CzBNCz** showing one of the fastest k_{RISC}. Improvements were seen moving from **BBCz-SB** (no donors), **BBCz-Y** (2 donors) and **BBCz-G** (3 donors), Figure **1.39** for structures, with k_{RISC} of 1.4, 10 and 18 × 10^4 s^{-1} respectively in PhMe solution. There is no noticible trend observed when acceptors are used, and $\underline{k}_{RISC}$ is generally slower (Figure **1.43**, red squares). Further work is needed to elucidate the link between structure and k_{RISC} in MR-TADF emitters, and to thus enhance it.

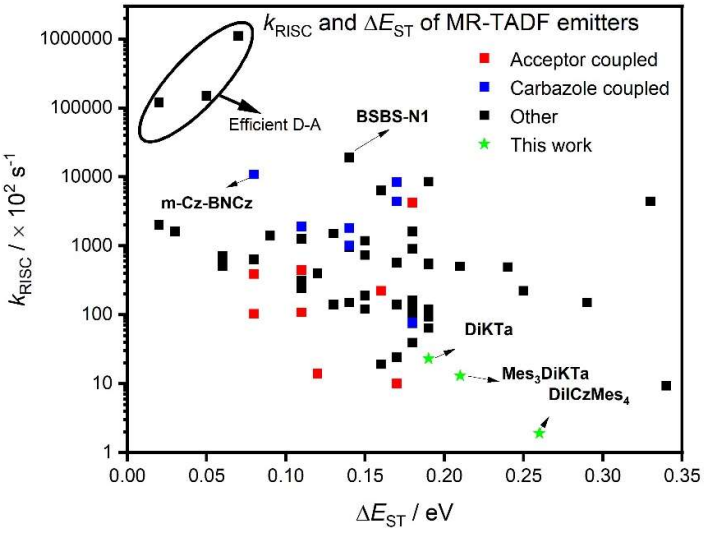

Figure **1.43**. Changing k_{RISC} with varying ΔE_{ST} of literature MR-TADF emitters, where emitters presented in Chapter 6 and 8 have been highlighted as green stars.

1.7 TADF and hyperfluorescence

In several of the MR-TADF examples discussed there is a large efficiency roll-off, owing in part to inefficient k_{RISC}. This can be mitigated by using a Hyperfluorescence-OLED architecture.[155, 163] Hyperfluorescence is based on the presence of at least two photoactive species, one responsible for exciton harvesting (termed the assistant dopant) and one responsible for the narrowband emission (termed the terminal emitter). MR-TADF compounds, fluorescent[170] and phosphorescent[171 172] emitters

have been employed the terminal emitters while TADF or phosphorescent compounds act as the assistant dopant. Hyperfluorscence relies on FRET between the assistant dopant and the terminal emitter (Figure **1.44**). The use of MR-TADF terminal emitters has been explored in more detail in Chapter 8. For efficient FRET, overlap between emission of the assistant dopant and the absorption of the emitter is required.[170] It is key to ensure that competing pathways such as DET from the triplet state of the assistant dopant, or direct recombination on the emissive dopant are prevented, which results in lower efficiency. This can be achieved using very low doping of the emitter. In most reported examples, the doping of the terminal emitter is ≤1 wt%, with a larger concentration in TADF assistant dopant present (ca. 20 wt%) to ensure efficient harvesting.

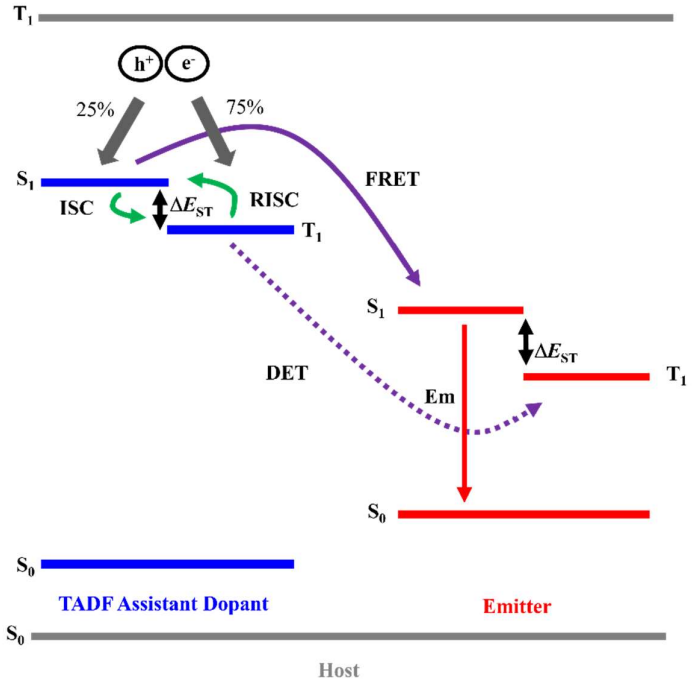

Figure **1.44**. Simplified Hyperfluorescence-OLED mechanism, where purple arrows highlight the different potential energy transfer pathways.

The first example using TADF triplet harvesters in Hyperfluorescence-OLEDs was by Nakanotani *et al.*[170] A series of different TADF emitters and different fluorescent emitters were presented covering the full-visible range. Four different TADF assistant dopants, **ACRSA**, **ACRXTN**, **PXZ-TRZ** and **Tri-PXZ-TRZ** were used alongside fluorescent terminal emitters, **TBPe**, **TTPA**,

TBRb and **DBP**, respectively (Figure **1.45**). The TADF emitters were selected to ensure good overlap with the absorption spectra of each fluorescent component, ensuring efficient FRET. The TADF assistant dopant was doped at between 20 wt% - 50 wt%, while the terminal emitter was doped at 1 wt% for each, to ensure exciton formation occurred preferentially on the assistant dopant. The EQE_{max} are 8.7%, 11.7%, 17.2% and 10.9% at CIE (0.17, 0.30), (0.29, 0.59), (0.45, 0.53) and (0.61, 0.39) for the devices with **ACRSA**:**TBPe**, **ACRXTN**:**TTPA**, **PXZ-TRZ**:**TBRb** and **Tri-PXZ-TRZ**:**DBP**, respectively. Devices of the fluorescent only emitters showed EQE_{max} < 5%. Strategies to minimise DET have been investigated, as this is the primary quenching pathway in Hyperfluorescence-OLEDs. Two TADF emitters were investigated by Yoon *et al.*,[173] **TCNTruX** and **tTCNTrux** (Figure **1.45**). Each had similar k_{RISC} of 1.48 and 1.36 × 10^6 s^{-1}, respectively. Introduction of ^{t}Bu groups helped mitigated DET when used in Hyperfluorescence-OLEDs with **DBP** as the terminal emitter. Reduction of DET improved the LT_{90} at 1,000 cd m^{-2} from 599 hours to 919 hours for the Hyperfluorescence-OLEDs using **TCNTruX** and **tTCNTrux**, respectively.

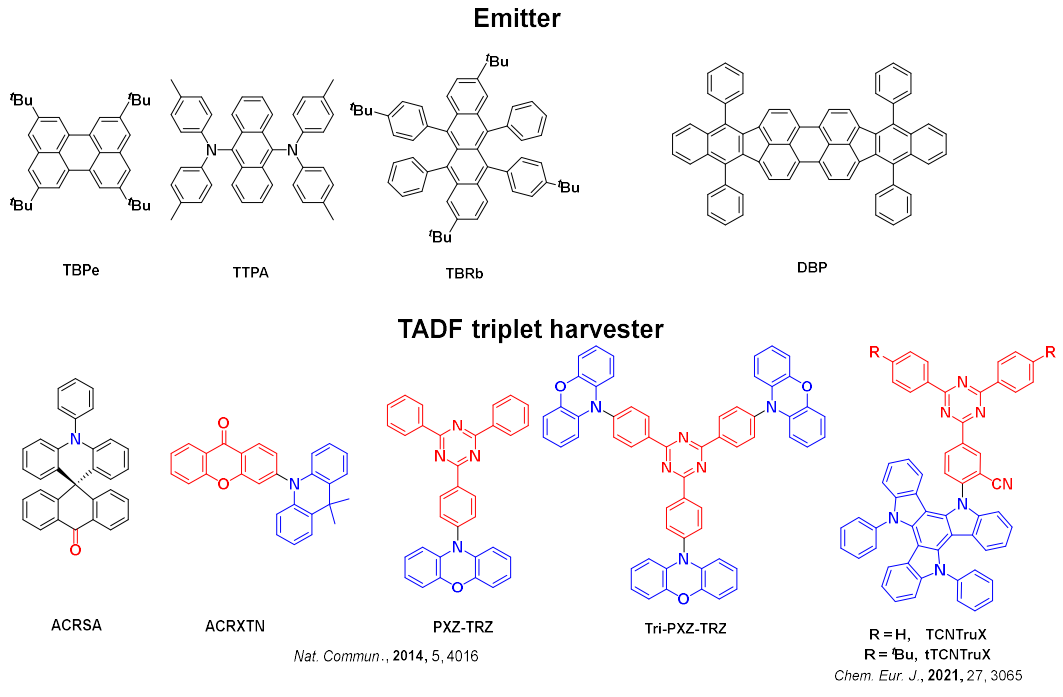

Figure **1.45**. Structures of discussed emitters and TADF triplet harvesters used in Hyperfluorescence-OLEDs

1.8 Computational investigation of TADF materials

Computational chemistry has been used frequently in the literature to design new TADF materials. The nature and energies of the excited states of compounds can be predicted quickly and with high accuracy to design new target materials.[174] The community has also employed calculations to further the mechanistic understanding of TADF materials. A selection of computational approaches undertaken is discussed in the following sections.

1.8.1 Predicting ΔE_{ST}

Although the mechanism behind TADF is more complex than direct RISC from T_1 to S_1, these are still the primary states of interest when modelling new materials. Emitters with calculated small ΔE_{ST} can be considered as promising targets. The S_1 and T_1 states can be modelled computationally using a range of techniques. The most frequently used by the community are DFT methods (*vide infra*), with time-dependent approaches undertaken to compute excited states and thus ΔE_{ST}. In this thesis coupled cluster methods are also used, and these approaches are discussed in more detail in Chapter 2.

Vertical excitation calculations based on the optimized ground-state geometry are the most frequently undertaken in the literature and the vertical ΔE_{ST} is computed from the difference in vertical excitation energies of S_1 and T_1 (Figure **1.46**). These calculations essentially mimic an absorption process and are often wrongly used to interpret the emission properties of TADF materials. When investigating emission properties, it is recommended to proceed with the excited states optimization. However, this is a more computationally costly approach as excited states of interest being reoptimized separately and it is less frequently done. Still, in this case, the excitation energy corresponds to the difference in energy between the optimized ground and excited state i.e. the adiabatic excitation energy (Figure **1.46**).[175] The adiabatic ΔE_{ST} is determined from the difference in energy between the adiabatic S_1 and T_1 excitation energies (Figure **1.46**). Calculations predict the likelihood of the transition based on the oscillator strength, *f*, which, as mentioned before, is proportional to the transition dipole moment (see section 1.1.3). In this thesis, we calculated primarily vertical ΔE_{ST}, and although the adiabatic ΔE_{ST} is more closely related to the measured ΔE_{ST}, work has highlighted that vertical ΔE_{ST} and adiabatic ΔE_{ST}

actually provide similar results when both S_1 and T_1 have the same nature which in TADF D-A compounds usually refers to largely CT states.[175] Excellent agreement has been consistently reported in the literature when groups compare calculated and experimental ΔE_{ST}, particularly for these systems. However, as discussed in detail in Chapters 6 - 8, DFT methods are inappropriate for the accurate prediction of ΔE_{ST} for MR-TADF emitters.

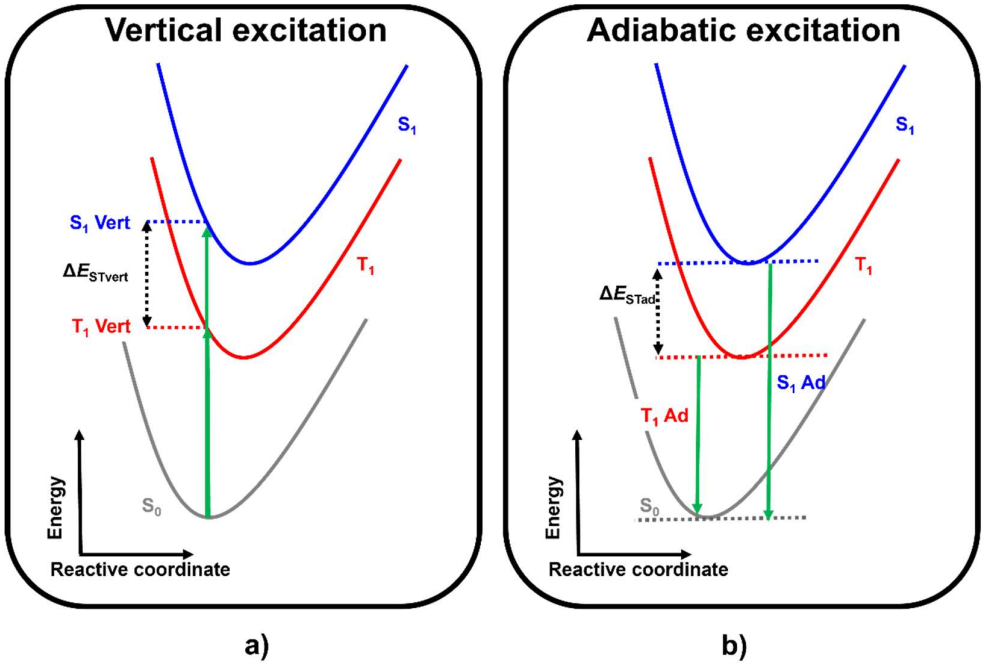

Figure **1.46**. Simplified representation of the calculations of **a**) vertical and **b**) adiabatic ΔE_{ST}.

1.8.2 Benchmarking ΔE_{ST}

In DFT a number of functionals exist characterized by their exchange-correlation potential. In addition to and the choice of a basis set the number of approaches available becomes very large. In the computational chemistry literature, a large portion of the community tries to identify the most accurate methodologies to investigate a group of known compounds. These benchmark studies involve the comparison between some calculated property (y_i) with a given level of theory and the corresponding experimental or higher accuracy method property (y_j). The difference between the two is key, and is described as x. The mean average deviation (MAD, 1.31), root mean square deviation (RMSD, 1.32) and standard deviation, (σ, 1.33) are used allowing us to determine the most appropriate methodology

on a quantitative ground and need to be minimized to testify from the high accuracy of the selected method(s):

$$\mathrm{MAD} = \frac{1}{n}\sum_{i=1}^{n}|x_i| \quad (1.31)$$

$$\mathrm{RMSD} = \sqrt{\frac{1}{n}\sum_{i=1}^{n}|x_i|^2} \quad (1.32)$$

$$\sigma = \sqrt{(\frac{1}{n}\sum_{i=1}^{n}|x_i|^2) - (\frac{1}{n}\sum_{i=1}^{n}|x|)^2} \quad (1.33)$$

$$x = \left|y_i - y_j\right| \quad (1.34)$$

These metrics are used in Chapters 5 and 7.

1.8.3 Higher lying states

The role of higher lying triplet states is becoming prominent in understanding efficient k_{RISC} observed in some materials. Spectroscopically this is difficult to observe often being coined as a 'dark state', with radiative relaxation from the lowest energy excited state. Therefore, in many of the examples reported previously, the role of intermediate triplet states has been inferred from calculations, this is discussed in more detail in Chapter 5.[125] This same approach is often used to decipher the Hot Exciton mentioned previously, with close alignment of a higher lying T_{n+1} and S_1 or S_2 prompting its assignment.[97]

1.8.4 Spin-orbit coupling

In TADF materials, there is up to now a consensus that RISC is driven by SOC between a singlet and triplet state. In recent years, there has been a greater focus to explicitly calculate SOC. Based on calculations on **2CzPN** and **4CzIPN** (Figure **1.47**), it was shown that the increase of SOC between S_1 and T_1 occurs at the expense of an increase of ΔE_{ST}. In line with El-Sayed's rule, the SOC between S_1 and T_1 in these compounds increases as the nature of S_1 and T_1 become more distinct, and is strictly zero when S_1 and T_1 are pure CT.[176] The mixed CT-LE nature of S_1 and T_1 of **2CzPN** and **4CzIPN** is prompted by the fluctuations of the torsion angle between the D and the A which impacts the D-A

electronic interaction. Samanta *et al*. performed calculations of RISC rates using a Marcus-type of rate expression indicated a careful balance between ΔE_{ST} and SOC, this was performed on 15 D-A TADF emitters.[177] When ΔE_{ST} is very large, RISC is slow whatever the value of SOC since ΔE_{ST} appears in the exponential factor of the Marcus rate expression, but as ΔE_{ST} decreases the contribution of SOC to boost k_{RISC} becomes more prominent.

1.8.5 Conformational and vibronic effects

It is important to note that the approaches mentioned so far primarily involve single molecules in either their ground or their excited state geometry. In emitters this is clearly not the whole picture, with a variety of potential conformations available. Intramolecular molecular vibrational modes are also expected to modulate in time the geometries of the D-A TADF emitters due to their conformational flexibility. In 2017, Olivier *et al*.[178] identified the critical role at room temperature of torsion vibrational modes in D-A and linear D-A-D emitters around the donor-acceptor single bond on both the energy of the S_1-T_1 excited states and so $\Delta E_{ST,}$ as well as on boosting the oscillator strength. At the different available torsions, it is observed that the nature of S_1, T_1 excited states evolve and that for more planar geometries both *f* and ΔE_{ST} increase. This rather simple approach helped explain why a TADF emitter with seemingly negligible oscillator strength based on the ground and the S_1 excited often has a large Φ_{PL}, further they highlighted the superior TADF properties predicted in D-A-D systems compared to D-A due to the larger conformational space available, with lower ΔE_{ST} and similar *f* apparent in D-A-D compared to D-A considering the average across all torsions. The role of vibrations within a molecule to RISC mechanism is becoming ever more important. In 2016, Marian *et al.* reported a study that illustrated the importance of intramolecular vibrations in governing the RISC rate in **ACRXTN** (Figure **1.47**).[126] In this compound they occurred along the C=O bond, helping to align ^{3}CT and ^{3}LE close to S_1. A similar approach was used by Gibson *et al.* to understand the RISC mechanism occurring in **PTZ-DBTO2** (Figure **1.47**).[25]

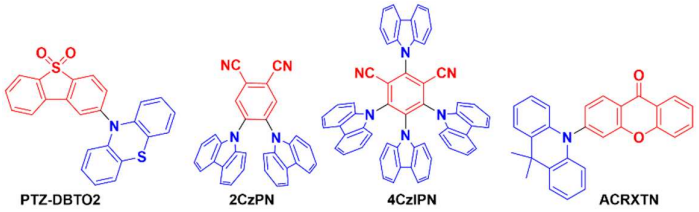

Figure **1.47**. Structures of computationally modelled compounds discussed

1.9 Perspective

This chapter has highlighted how TADF compares to other forms of exciton harvesting. The main principles involved in the mechanism have been presented, and there are many very promising materials. Two classes have been discussed in detail, namely D-A TADF and MR-TADF, although other routes to achieve TADF exist. Both show great potential, but this overview clearly shows that there is room for further development of each to optimise materials design. Finally, computational chemistry, and specifically its role in TADF emitter design and understanding has been presented.

Chapter 2: Quantum Chemistry methods

This chapter focuses on the fundamental background behind the methodologies used in this thesis, namely DFT and Time-Dependent DFT (TD-DFT) for ground state and excited states properties respectively applied mainly to D-A TADF emitters, as well Coupled Cluster (CC) methods employed mostly for MR-TADF emitters.

2.1 Schrödinger equation

The resolution of the Schrödinger equation allows us to access to the electronic properties of atoms and molecules from first principles. Generally, the phenomena studied in quantum-chemistry are stationary so that the potential does not depend on the time parameter but only on the position of the particles. The Schrödinger equation then reduces to the well-known time-independent equation written for a molecular system:[179]

$$\hat{H}\Psi = E\Psi \quad (2.1)$$

Here $\hat{H}$ is the molecular Hamiltonian operator, E is the total energy of the system and Ψ is the wavefunction of the system which yields a probability density. $\hat{H}$ is the sum of two terms: the kinetic energy (T) and the potential energy (V) terms:

$$\hat{H} = -\sum_{i=1}^{N} \frac{\hbar^2}{2m_i} \nabla_i^2 + \sum_{i=1}^{N-1} \sum_{j>i}^{N} \frac{q_i q_j}{rij} \quad (2.2)$$

Where the first half is kinetic energy of all particles, nuclei and electrons of the system (N) where ∇ is the Laplacian operator corresponding to coordinates of the particles of the system:

$$\nabla^2 = \left(\frac{\partial^2}{\partial x_i^2} + \frac{\partial^2}{\partial y_i^2} + \frac{\partial^2}{\partial z_i^2} \right) \quad (2.3)$$

and the second half corresponds to the Coulombic interactions between the different particles within the system, considering both attractive (between electrons and nuclei) and repulsive forces (between electrons or nuclei). Analytical expression of the eigen functions and energies of the time-independent Schrödinger cannot be obtained for N interacting particles. $\hat{H}$ can be simplified by

assuming that nuclei are much heavier than electrons, and thus moving much slower than electrons. This is known as the Born – Oppenheimer approximation. Therefore, the time-independent Schrödinger equation is split into an electronic part solved for a fixed configuration of the nuclei and a nuclear equation. The wavefunction Ψ of the molecular system is thus rewritten as a product of an electronic and a nuclei wavefunction. Within the Born – Oppenheimer approximation with stationary nuclei, the electronic Hamiltonian is written:

$$\hat{H}_{elec} = \hat{T}_{elec} + V_{elec} + V_{nucl-elec} \quad (2.4)$$

Where $\hat{T}_{elec}$ is the kinetic energy term for electrons, V_{elec} is the electron-electron repulsion term and $V_{nuc-elec}$ is the nuclear-electron attraction term. From the resolution of electronic Shrödinger equation, the total electronic energy E_{elec} and the electronic wavefunction Ψ_{elec} are computed for electrons moving in a field of fixed nuclei:

$$\hat{H}_{elec}\Psi_{elec} = E_{elec}\Psi_{elec} \quad (2.5)$$

2.2 Hartree-Fock

The Hartree-Fock (HF) method is one of the pioneering quantum chemical method that allow one to obtain the electronic energy of a system of *N* interacting electrons under the assumption that every electron is moving in the mean field created by the *N*-1 other electrons. A first guess for the electronic wavefunction is obtained as a product of one-electron wavefunctions (ϕ_i):

$$\Psi_{elec} = \phi_1\phi_2\phi_3 \ldots . \phi_N \quad (2.6)$$

In this equation, it is assumed that electrons are independent of each other, with the total probability density calculated from multiplication of the individual contributions. However, this equation neglects the anti-symmetry of the wavefunction, which is fundamental when considering fermions such as electrons. This can be solved when the wavefunction is instead written as a Slater determinant (for *N* electron system):

$$\Psi = \frac{1}{\sqrt{N!}} \begin{vmatrix} \phi_1(r_1) & \phi_2(r_1) & \cdots & \phi_N(r_1) \\ \phi_1(r_2) & \phi_2(r_2) & \cdots & \phi_N(r_2) \\ \cdots & \cdots & \cdots & \cdots \\ \phi_1(r_N) & \phi_2(r_N) & \cdots & \phi_N(r_N) \end{vmatrix} \quad (2.7)$$

The energy of the system is defined as:

$$E = \langle \Psi | \hat{H} | \Psi \rangle \quad (2.8)$$

The HF method and all methods presented in this chapter are based on the variational principle. In short, it says that the energy of the system (E_x) computed on trial wavefunction Ψ_x will always be greater than (or equal) to the true energy of the system (E_0) computed based on the true wavefunction of the system Ψ_0:

$$E_0 = \langle \Psi_0 | \hat{H} | \Psi_0 \rangle \leq E_x = \langle \Psi_x | \hat{H} | \Psi_x \rangle \quad (2.9)$$

The HF equations are derived from this principle and correspond to a set of *N* one-electron equations:

$$\hat{F}_i \phi_i = \epsilon_i \phi_i \quad (2.10)$$

where ϵ_i is the energy of orbital ϕ_i and $\hat{F}_i$ is the Fock operator defined as:

$$\hat{F}_i = \hat{h}_i + \sum_J^N (\hat{J}_j - \hat{K}_j) \quad (2.11)$$

Where $\hat{h}_i$ includes the kinetic electron term and nuclei-electron attraction term, while $\hat{J}_j$ is the coulomb operator, describing the repulsion between electron *i* and the potential created by the other electrons. It is a mean field term and does not involve explicit interaction with individual electrons. $\hat{K}_j$ is the exchange operator describing the repulsive interactions between two electrons of the same spin. These equations are solved as a self-consistent field (SCF) from a given set of orbitals that is defined initially. After each SCF cycle, a new set of orbitals, wavefunction and energies are obtained and reinjected into the HF equations until a predefined convergence criterion is satisfied. From these values the total HF energy can be obtained using the following equation:

$$E_{HF} = \sum_{i=1}^{N} h_i + \frac{1}{2}\sum_{i=1}^{N}\sum_{j=1}^{N}\left(J_{ij} - K_{ij}\right) \quad (2.12)$$

Here ½ is applied before the electron repulsion to correct for double counting of electron repulsion terms. For molecular systems, solving HF equations is usually carried out considering the linear combination of atomic orbitals (LCAO) approximation. This assumes that molecular orbitals (MOs, ϕ_i) are expressed as a linear combination of atomic orbitals (AOs):

$$\phi_i = \sum_{\mu=1}^{M} c_{\mu i}\chi_\mu \quad (2.13)$$

Where $c_{\mu i}$ is the expansion coefficient and χ_μ is the AO, with M the total number of AOs. The AOs are often described as a sum of the basis set functions, such as Gaussians (*vide infra*). Solving HF equations consists of finding the coefficients $c_{\mu i}$ minimizing the HF energy, with a pre-defined basis set used to describe AOs (*vide infra*.). MOs are filled according to the Aufbau principle (orbitals are filled with electrons from the lowest energy orbital), yielding occupied and virtual MOs. As mentioned previously the HF solution is higher in energy than the exact energy, with the difference between the two known as the (Coulomb) correlation energy:

$$E_C = E_0 - E_{HF} \quad (2.14)$$

This is essentially the amount of error which has been introduced by solving HF equations. This is primarily the result of a lack of electron correlation and is quite substantial in some situations such as molecular dissociation.

2.3 Coupled cluster

CC methods have been developed in the 1950's aiming at introducing electron correlation. Building from the ground state HF wavefunction, the CC wavefunction Ψ_{CC} is written as an exponential ansatz:

$$\Psi_{CC} = \exp(\hat{T})\Psi_{HF} \quad (2.15)$$

$\hat{T}$ is known as the cluster operator, with the coupled cluster energy E_{CC} calculated as:

$$E_{CC} = \langle \Psi_{HF} | \exp(-\hat{T}) \hat{H} \exp(\hat{T}) | \Psi_{HF} \rangle \quad (2.16)$$

The cluster operator is unique and obtained as a sum of operators associated with single ($\hat{T}_1$), double ($\hat{T}_2$) triple ($\hat{T}_3$) … excitations. $\hat{T}_1$ and $\hat{T}_2$ operators are defined as:

$$\hat{T}_1 = \sum_{ia} t_a^i \, \hat{a}_a^+ \, \hat{a}_i \quad (2.17)$$

$$\hat{T}_2 = \frac{1}{4} \sum_{ijab} t_{ab}^{ij} \, \hat{a}_a^+ \, \hat{a}_b^+ \, \hat{a}_i \, \hat{a}_j \quad (2.18)$$

Where *t* is the amplitude, *ij* and *ab* are occupied and unoccupied orbitals respectively, and $\hat{a}_i$ and $\hat{a}_a^+$ are the corresponding creation and annhilation operators, respectively. Increasing the number of cluster operators in the summation improves the accuracy of the calculation. Coupled cluster single (CCS), coupled cluster single double (CCSD), coupled cluster single double triple (CCSDT) methods include contributions to the cluster operator up to the first, second and third order, respectively:

$$\Psi_{CCS} = \exp(\hat{T}_1) \Psi_{HF} \quad (2.19)$$

$$\Psi_{CCSD} = \exp(\hat{T}_1 + \hat{T}_2) \, \Psi_{HF} \quad (2.20)$$

$$\Psi_{CCSDT} = \exp(\hat{T}_1 + \hat{T}_2 + \hat{T}_3) \, \Psi_{HF} \quad (2.21)$$

The exponential operator is computed through a Taylor expansion. In the CCSD case, this expansion becomes:

$$\exp(\hat{T}_1 + \hat{T}_2) = 1 + (\hat{T}_1 + \hat{T}_2) + \frac{1}{2!}(\hat{T}_1 + \hat{T}_2)^2 + \frac{1}{3!}(\hat{T}_1 + \hat{T}_2)^3 + \cdots$$

$$= 1 + \hat{T}_1 + \hat{T}_2 + \frac{1}{2}\hat{T}_1^{\,2} + \hat{T}_1\hat{T}_2 + \frac{1}{6}\hat{T}_1^{\,3} + \frac{1}{2}\hat{T}_2^{\,2} + \frac{1}{2}\hat{T}_2^{\,2}\hat{T}_1 + \cdots + \quad (2.22)$$

Considering the full equation 2.22, one can observe single excitation ($\hat{T}_1$), double excitation ($\hat{T}_2$ and $\frac{1}{2}\hat{T}_1^{\,2}$), triple excitation ($\hat{T}_1\hat{T}_2$ and $\frac{1}{6}\hat{T}_1^{\,3}$) and quadruple excitation ($\frac{1}{2}\hat{T}_2^{\,2}$ and $\frac{1}{2}\hat{T}_2^{\,2}\hat{T}_1$) contributions. For CCSD the energy from the Taylor expansion is correct through to the third order expansion.[180] Including higher-order excitations comes at an increased computational cost (*vide infra*.). The overall energy of the system for CCSD is produced as follows;[180]

$$E_{CC} = \langle \Psi_{HF} | \hat{H} \exp(\hat{T}_1 + \hat{T}_2) | \Psi_{HF} \rangle \quad (2.23)$$

The amplitudes t_a^i and t_{ab}^{ij} are calculated from a group of non-linear equations formulated as:

$$\langle \mu_i | \exp(-\hat{T}_1 - \hat{T}_2) \hat{H} \exp(\hat{T}_1 + \hat{T}_2) | \Psi_{HF} \rangle = 0 \quad (2.24)$$

Where μ_i (i = 1 or 2 for CCSD), are singly and doubly excited Slater determinants. All the cluster amplitudes are obtained iteratively[181] with the singly and doubly excited states amplitudes obtained through the following equations:

$$\langle \mu_1 | \hat{H} + [\hat{H}, \hat{T}_2] | \Psi_{HF} \rangle = 0 \quad (2.25)$$

$$\langle \mu_2 \left| \hat{H} + [\hat{H}, \hat{T}_2] + \frac{1}{2} \left[[\hat{H}, \hat{T}_2], \hat{T}_2 \right] \right| \Psi_{HF} \rangle = 0 \quad (2.26)$$

The second order approximate couple cluster (CC2) is an approximation of CCSD,[180] where the energy calculated from the cluster operator is limited to the second order:

$$\exp(\hat{T}_1 + \hat{T}_2) \approx 1 + (\hat{T}_1 + \hat{T}_2) \quad (2.27)$$

In CC2, the $\hat{H}$ can be partitioned into a Fock operator ($\hat{F}$) and fluctuation operator ($\hat{U}$), which represents the electronic correlation:

$$\hat{H} = \hat{F} + \hat{U} \quad (2.28)$$

In CC2, the singly excited amplitudes are identical to the CCSD ones. However, the doubly excited amplitudes are obtained as:

$$\langle \mu_2 | \hat{H} + [\hat{F}, \hat{T}_2] | \Psi_{HF} \rangle = 0 \quad (2.29)$$

This reduces the computational cost compared to CCSD. The series of coupled cluster techniques approaches the Full Configuration Interaction limit when including higher order cluster operators, however this is at the expense of increasing cost. The computational cost evolves with N the number of basis set functions. CCSD computational time evolves as N^6. Moving to CC2 results in a decrease of one order of magnitude of the computational cost. CC3 and CCSDT have even higher cost:[180]

$$HF\ (N^4) \approx CCS(N^4) < CC2\ (N^5) < CCSD\ (N^6) < CC3\ (N^7) < CCSDT\ (N^8)$$

When using the TURBOMOLE package, the resolution of the identity approximation (RI) is applied during each CC2 calculation, and is the method presented in this thesis.[182] This is a further approximation applied to coupled cluster methods which reduces computational cost, not the overall scaling of the method which remains N^5 but its prefactor.[183] Typically, the 4-center two-electron integrals are replaced by three-electron and two-electron integrals computed on an auxiliary basis reducing the computational cost.[184] A further approximation has been applied with some success, known as Spin Component Scaled approximation (SCS). Here, the scaling factors for same-spin (SS, E_{SS}) and opposite spin (OS, E_{OS}) contributions to the correlation energy (E_C) are considered as differnt, when considering same spin or opposite spin.[185] The scaling factors are 1.20 for OS and 0.33 for SS when using SCS. The scaling factors act as extra correlation effects for the calculations. This average effect is included and has highlighted improvements in calculations, particularly considering excited states.[186] The performance of SCS-CC2 has been compared to CC3 in terms of accuracy, with the scaling factors mimicking higher order excitations.[181] SCS-CC2 is the CC method employed in this thesis.

2.4 Linear Response coupled cluster

In linear response theory, one expects that a system submitted to a perturbation of weak amplitude responds linearly to this perturbation. For instance, in the case of optical excitations in molecular systems, the molecular system is perturbed by a weak amplitude electromagnetic field which is expected to affect weakly the energy of the molecules. When applied to CC2, this allows calculation of excited states accounting for accurate electron correlation effects.[180] In CC2 equation, perturbations are introduced, in the form of a one electron perturbation $\widehat{V^t}$. With equation 2.28 now rewritten as:

$$\widehat{H} = \widehat{F} + \widehat{U} + \widehat{V^t} \quad (2.30)$$

Here the first two terms, $\widehat{F}$ and $\widehat{U}$ represent the unperturbed Hamiltonian $\widehat{H}_0$. The time-dependent cluster amplitudes are written as:

$$\langle \mu_1 \left| \widehat{H}(t) + [\widehat{H}(t), \hat{T}_2(t)] \right| \Psi_{HF} \rangle = \frac{i\partial t_{\mu 1}(t)}{\partial t} \quad (2.31)$$

$$\langle \mu_2 \left| \widehat{H}(t) + \left[\hat{F} + \widehat{V^t}(t), \hat{T}_2(t) \right] \right| \Psi_{HF} \rangle = \frac{i\partial t_{\mu 2}(t)}{\partial t} \quad (2.32)$$

Numerous studies have been undertaken, with CC2 allowing excited state calculations of large molecules (up to 100 atoms).[181]

2.5 Density Functional Theory

Compared to HF and CC which are based on the wavefunction, DFT calculates the electronic energy of the molecule based on electronic density $\rho(r)$.[179] The link between the wavefunction and $\rho(r)$ is obtained by the following relation:

$$\rho(r) = N \int \dots \int |\Psi(x_1, x_2, \dots, x_N)|^2 \, dx_2 \dots \, dx_N \quad (2.33)$$

DFT is established based on the two Hohenberg and Kohn theorems. The first Hohenberg-Kohn theorem states that for any given $\rho_0(r)$ characterizing the ground state it is possible to calculate the total energy of the ground state as long as the external potential (V_{ex}) is determined. The second Hohenberg-Kohn theorem states that for any given density, ρ, that is different than the ground state density, the calculation of the total energy of a system results in a higher energy than that of the energy computed for the true ground state density ρ_0:[179]

$$E[\rho] \geq E_0[\rho_0] \quad (2.34)$$

This is essentially a reformulation of the variation principle used in HF (*vide supra*.) in terms of the electronic density. The ground state electronic energy dependent on ρ_0 can be rewritten:

$$E_0[\rho_0] = T[\rho_0] + E_{ee}[\rho_0] + E_{Ne}[\rho_0] \quad (2.35)$$

Where $T[\rho_0]$ is the electron kinetic energy, $E_{ee}[\rho_0]$ is the electron-electron repulsion term and $E_{Ne}[\rho_0]$ the electron-nuclei attraction. The latter is written as:

$$E_{Ne}[\rho_0] = \int \rho_0(r) \, V_{ex}(r) \, dr \quad (2.36)$$

The first two terms of $E_0[\rho_0]$, namely $T[\rho_0]$ and $E_{ee}[\rho_0]$ can be considered universal, independent of the system, defined as the Hohenberg and Kohn functional, $F_{HK}[\rho_0]$:

$$F_{HK}[\rho_0] = T[\rho_0] + E_{ee}[\rho_0] \quad (2.37)$$

$E_{ee}[\rho_0]$ can be separated into two terms, a coulomb term ($J[\rho_0]$) which is a two-body purely classical term and a non-classical term ($E_{ncl}[\rho_0]$):

$$E_{ee}[\rho_0] = \mathrm{J}[\rho_0] + E_{ncl}[\rho_0] = \frac{1}{2} \int\int \frac{\rho_0(r_1)\,\rho_0(r_2)}{r_{12}}\, \mathrm{d}r_1\, \mathrm{d}r_2 + E_{ncl}[\rho_0] \quad (2.38)$$

The $E_{ncl}[\rho_0]$ contribution includes self-interaction error, exchange correlation and Coulomb correlation. The kinetic energy term calculation $T[\rho_0]$ has to be computed in a system of interacting electrons which is not feasible. To circumvent this issue, Kohn and Sham introduced a fictitious system of non-interacting electrons. In this system, the total energy of the system $E_S[\rho_0]$ is written as a sum of the kinetic energy of non-interacting electrons T_S and a local effective (fictitious) external potential $V_{eff}(r)$:

$$V_{eff}[\rho_0(r)] = \sum_i V_S^i\,[\rho_0(r)] \quad (2.39)$$

Where V_S^i is the one-electron operator associated with the external potential. The introduction of a non-interacting system implies that the Schrödinger equation can be rewritten in a set of *N* one-electron Kohn-Sham equations:

$$f_i^{KS}\phi_i = \varepsilon_i\phi_i \quad (2.40)$$

With ϕ_i the Kohn-Sham orbitals and f_i^{KS} the Kohn-Sham operator associated with electron *i,* defined as:

$$f_i^{KS} = -\frac{1}{2}\Delta + V_S^i \quad (2.41)$$

The total wavefunction of the non-interacting system is expressed as a Slater determinant ψ_S written in terms of the ϕ_i (equation 2.7). The kinetic energy of the interacting $T[\rho_0]$ in the interacting system is written in terms of the kinetic energy in the non-interacting one as:

$$T[\rho_0] = T_S[\rho_0] + T_c[\rho_0] \quad (2.43)$$

The differences between $T[\rho_0]$ and $T_S[\rho_0]$ provide $T_c[\rho_0]$ where contributions to the kinetic energy that include correlation in the electron motions is provided. $F_{HK}[\rho_0]$ is now rewritten as:

$$F_{HK}[\rho_0] = T_S[\rho_0] + T_c[\rho_0] + \mathrm{J}[\rho_0] + E_{ncl}[\rho_0] \quad (2.44)$$

In this equation, $T_c[\rho(r)]$ and $E_{ncl}[\rho_0]$ are unknowns and are combined, under the exchange correlation energy $E_{XC}[\rho_0]$:

$$F_{HK}[\rho_0] = T_s[\rho(r)] + \mathrm{J}[\rho(r)] + E_{XC}[\rho(r)] \quad (2.45)$$

Kohn and Sham imposed that the density in the interacting and non-interacting systems are identical and equal to ρ_0. In virtue of the first Hohenberg and Kohn theorem, this means that there exists a link between the external potential V_{ext} in the interacting system and the potential in the non-interacting system V_S. By applying the second Hohenberg and Kohn theorem (*i.e.* the variational principle) on both system $\frac{\partial E_0[\rho_0]}{\partial \rho_0} = \frac{\partial E_S[\rho_0]}{\partial \rho_0} = 0$, V_S becomes:

$$V_S(r) = \int \frac{\rho(r_2)}{r_{12}}\, dr_2 + V_{XC} - \sum_A^M \frac{Z_A}{r_{1A}} \quad (2.46)$$

V_{XC}, the exchange-correlation potential is obtained as the derivative of E_{XC} with respect to ρ:

$$V_{XC} = \frac{\delta E_{XC}}{\delta \rho} \quad (2.47)$$

Similarly, as in HF theory, the Kohn-Sham equations for a molecular system are solved using the LCAO approximation (see equation 2.13). The coefficients are obtained through a SCF procedure. The development in the DFT field aims at finding expressions of V_{XC} such that DFT calculations based on the V_{XC} are able to reproduce experimental data or calculations obtained for instance with wavefunction-based methods.[179]

2.5.1 Local Density Approximation

Local density approximation (LDA) is the simplest approximation to obtain the expression of E_{XC}. This is based on the idea of a uniform electron gas, where the exchange correlation potential V_{XC}^{LDA}

computed within LDA depends on the local electron density only, with each electron experiencing the same local effects:

$$E_{XC}^{LDA}[\rho] = \int \rho(r) V_{XC}^{LDA}[\rho(r)]\, dr \quad (2.48)$$

This uniform electron gas is rather simplistic and for instance does not apply to molecular systems.

2.5.2 Generalized Gradient Approximation

In Generalized gradient approximation (GGA) the exchange correlation potential does not only depend on the local density but also on the gradient of it, $\nabla\rho(r)$:

$$E_{XC}^{GGA}[\rho] = \int f[\rho(r)\nabla\rho(r)]\, dr \quad (2.49)$$

Where *f* is a functional which must be introduced. This term alleviates the previous assumption of homogeneity of the electrons. Various forms of f exist in the literature.[187] They can be derived from first principles or can be calibrated with respect to experimental data.

2.5.3 *Meta*-Generalized Gradient Approximation

GGA have been further improved with *meta*-generalized gradient approximation (m-GGA) functionals, where in addition to the gradient, the second derivative of the density is included in the exchange-correlation functional. Nowadays, a m-GGA functional is referred more typically to one functional that includes a dependence on the reference kinetic energy density $\tau(r)$:

$$E_{XC}^{mGGA}[\rho] = \int f[\rho(r)\nabla\rho(r)\tau(r)]\, dr \quad (2.50)$$

$\tau(r)$ can be expressed as;

$$\tau(r) = \frac{1}{2}|\nabla\phi_i(r)|^2 \quad (2.51)$$

2.5.4 Hybrid functionals – B3LYP, PBE0 and M062X

This is an alternative strategy to improve the description of E_{XC} and in particular to cure the problem of the electron-electron self-interaction. The strategy consists of introducing an amount of HF exchange, *K*, so that the exchange-correlation is rewritten as:

$$E_{XC} = aK + (1-a)E_X{}^{DFT} + E_C{}^{DFT} \quad (2.52)$$

Where the $E_X{}^{DFT}$ is the exchange energy obtained at the DFT level (LDA, GGA, mGGA) and $E_C{}^{DFT}$ is the correlation energy obtained at the DFT level (again LDA or GGA or a mix of both). Popular hybrid functionals such as B3LYP[188] and PBE0[189] contain a fixed amount of exact exchange, 20% and 25% respectively in addition to exchange included at the DFT level. PBE0 is solved as:

$$E_{XC}{}^{PBE0} = \frac{1}{4}E_X{}^{HF} + \frac{3}{4}E_X{}^{PBE} + E_C{}^{PBE} \quad (2.53)$$

Where PBE is a GGA functional and $E_X{}^{PBE}$ and $E_C{}^{PBE}$ are the PBE exchange and correlation energies. In M06-2X, exact exchange is included up to 54% together with mGGA exchange and Coulomb correlation.[190] These three functionals are the three hybrid functionals used in this thesis.

2.5.5 Range separated functionals – CAM-B3LYP, LC-ωPBE and LC-ωHPBE

Range-separated functionals are a branch of hybrid functionals, however the exact exchange varies depending on whether electron-electron interaction is considered to be long range or short range.[191] The former dominated by HF exchange contribution and the latter mainly by DFT-like exchange. Formally speaking, the interelectron Coulomb potential can be expressed as:

$$\frac{1}{r_{12}} = \frac{1-[\alpha+\beta\mathrm{erf}(\omega r_{12})]}{r_{12}} + \frac{\alpha+\beta\mathrm{erf}(\omega r_{12})}{r_{12}} \quad (2.54)$$

Where erf is the error function implemented to connect the short- and long-range components. The first term accounts for the short-range electron-electron interaction and the second term describes long-range electron-electron interaction. The value of the range separation parameter ω varies from functional to functional and defines the interelectronic distance (r_{12}) where electron-electron interaction switch from short- to long-range. The default value of the range separation parameter ω is fixed to 0.400 $Bohr^{-1}$ and 0.330 $Bohr^{-1}$ for LC-ωPBE[192] and CAM-B3LYP[193] functionals, respectively. α describes the magnitude of the HF like exchange incorporated in the short-range interaction while α + β describes the amount of HF like exchange in the long-range interaction. For LC-ωPBE α = 0.0 and α + β = 1.0, with short range interactions described purely using DFT and long-range electron-electron interactions described only considering HF-exchange.[192] Here the DFT term is derived from GGA based functional

PBE. The LC-ωHPBE includes PBE1 exchange instead of PBE exchange.[194] In CAM-B3LYP, $\alpha = 0.19$ and $\alpha + \beta = 0.65$, with short- range and long range both incorporating some exact exchange.[193] This occurs as the DFT exchange part at short distances and the correlation part are taken from the hybrid functional B3LYP (*vide supra*.). Range separated functionals were employed to account for poor description of long range charge transfer effects, with conventional DFT approaches having the tendency to underestimate certain characteristics, such as ionization potentials and excitations.[191]

2.5.6 Tuned range separated functional – LC-ω*PBE and LC-ω*HPBE

In the previously discussed range separated functionals, the short- and long-range contribution of HF and DFT is fixed, along with the range separation parameter ω. Work has highlighted that the value of ω varies greatly on the system in question and the optimal value can be tuned to minimize the error J^2:[175]

$$J^2 = \sum_{i=0}^{1}[\varepsilon_H(N+i) + IP(N+i)]^2 \quad (2.55)$$

Where $\varepsilon_H(N+i)$ and $IP(N+i)$ are the HOMO energy and the ionization potential of a N-electron system (*i.e.* the ground state) and *N*+1-electron system (*i.e.* the radical anion). The vertical electron affinity is assumed to be equivalent to the ionization potential of *N*+1-electron system. In the past, it was shown in numerous publications that the optimally tuned functionals indeed improve the description of different molecular properties such as ionisation potentials and optical gaps, and CT and Rydberg transition energies.[195] In this thesis it has been implemented for the range separate functionals LC-ωPBE and LC-ωHPBE, with tuning indicated as LC-ω*PBE and LC-ω*HPBE. This parameter was optimized for each structure.

2.6 Time dependent density functional theory

Similarly, as in excited calculations with CC2, time dependent density functional theory (TD-DFT) formalism is based on linear response formalism. Runge-Gross theorem is the basis of the TD-DFT theory and is the equivalent of the first Hohenberg and Kohn theorem. It states that there exists a one to one relation between the time-dependent external potential V_{ext} and the time dependent density $\rho(r,t)$.[174] The van Leeuwen theorem, like the Kohn-Sham formalism in ground state DFT theory,

introduced a fictitious non-interacting system ($V_{eff}\ (r,t)$), with a time-dependent external potential $V_{ext}(r,t)$, with a time-dependent density $\rho_S(r,t)$ identical to the time-dependent density $\rho(r,t)$ of the interacting system. From this knowledge the time dependent Kohn Sham equation can be formulated[196];

$$\left[-\frac{1}{2}\sum_i^N \nabla^2 + V_{eff}\ (r,t)\right]\phi_i(r,t) = i\frac{\delta}{\delta t}\phi_i(r,t) \quad (2.56)$$

Where $\phi_i(r,t)$ are the time-dependent Kohn-Sham orbitals, $V_{eff}\ (r,t)$ is split in the same manner as in ground state DFT:

$$V_{eff}\ (r,t) = V_{ext}(r,t) + V_{Hartree}(r,t) + V_{XC}(r,t) \quad (2.57)$$

Density can be calculated from the time dependent Kohn-Sham orbitals;

$$\rho(r,t) = \sum_i^N \left|\phi_i(r,t)\right|^2 \quad (2.58)$$

An important approximation is implemented known as the adiabatic approximation.[197] This states that the time-dependent V_{XC} is replaced by a time independent one equivalent to the ground state one:

$$V_{XC}(r,t) = V_{XC}(r)|_{\rho_0(r)=\rho(r,t)} \quad (2.59)$$

With the assumption that changes in density are slow, with electron density remaining in its eigenstate upon being perturbed.[174]

The application of linear response theory as an alternative to a direct resolution of the time dependent Kohn-Sham equations allows us to access to the excited states energies and eigenstates. In this framework, one can obtain the linear electron density response $\rho^{(1)}(r,t)$, expressed as:[196]

$$\rho^{(1)}(r,t) = \iint d^3r'dt'\chi(r,t,r',t')\,V_{eff}^{(1)}(r',t') \quad (2.60)$$

where $V_{eff}^{(1)}(r',t')$ is the first-order perturbed effective potential and $\chi(r,t,r',t')$ is the first-order response function.

Using a Fourier transform we move from the time-domain to the frequency domain so that the linear electron density response is written as:[197]

$$\rho^{(1)}(r,\omega) = \int d^3r'dt'\chi(\omega,r,r')\, V_{eff}^{(1)}(r',\omega) \quad (2.61)$$

$\chi(\omega,r,r')$ is expressed as[196]:

$$\chi(\omega,r,r') = \sum_{i,a}\left(\frac{\phi_i{*}(r)\,\phi_a(r)\,\phi_i(r')\phi_a{*}(r\prime)}{\omega-(\varepsilon_a-\varepsilon_i)} - \frac{\phi_i(r)\,\phi_a{*}(r)\,\phi_i{*}(r')\phi_a(r\prime)}{\omega+(\varepsilon_a-\varepsilon_i)}\right) \quad (2.62)$$

Where i and a correspond to occupied and unoccupied energy levels, and ε_a and ε_i their respective energies. The poles of the response function correspond to the excitation energies. To find them, the problem can be rewritten in a matrix form, known as TD-DFT equation:[174]

$$\begin{bmatrix} A & B \\ B* & A* \end{bmatrix}\begin{bmatrix} \mathrm{X} \\ \mathrm{Y} \end{bmatrix} = \omega\begin{bmatrix} 1 & 0 \\ 0 & -1 \end{bmatrix}\begin{bmatrix} \mathrm{X} \\ \mathrm{Y} \end{bmatrix} \quad (2.63)$$

With ω the excitation energy calculated, X excitation and Y deexcitation amplitudes. Solving this non-Hermitian eigenvalue problem produces the excited state values. Here A and B are:

$$A_{ia,jb} = \delta_{ij}\delta_{ab}(\epsilon_a - \varepsilon_i) + (ia|jb) + (ia|f_{xc}|jb) \quad (2.65)$$

$$B_{ia,jb} = (ia|bj) + (ia|f_{xc}|bj) \quad (2.66)$$

Where f_{xc} is the exchange-correlation kernel obtained as:

$$f_{xc}(r,t,r',t') = \left.\frac{\delta V_{xc}[\rho](r,t)}{\delta\rho(r',t')}\right|_{\rho=\rho_0} \quad (2.67)$$

The Tamm Dancoff approximation (TDA) is an approximation of the TD-DFT equation where the B matrix is set to 0. The TD-DFT equations reduce to:

$$AX = \omega A \quad (2.68)$$

For excited states exhibiting a large degree of charge transfer, the B matrix elements tend towards 0.[174] Application of TDA appears as a method to solve the triplet instability issue which leads to an overstabilization of the triplet state predicted at the TD-DFT level.[198]

2.7 Basis sets

The basis sets define a set of mathematical functions, usually Gaussian type functions that within the LCAO approximation are each AO.[199] Often, polarisation functions are added on top of core and valence orbitals which allows the electron cloud to further accommodate the change of electron density in the neighbourhood of one atomic site due the presence of other electrons. In this thesis, we used mainly two families of basis set: The Dunning and the Pople basis sets. The first considered Correlation consistent basis sets (also known as Dunning basis set) have been used in this thesis for CC calculations.[200] These basis sets have been designed for converging Post-Hatree-Fock methods systematically to the complete basis set limit. In particular, we consistently used the cc-pVDZ basis set where cc stands for correlation-consistent, p means that the basis set contains polarisation functions (d,f,g, etc…) which depends on the atom type, V stands for valence which means that only valence orbitals are included and DZ means double zeta which involves that the valence orbitals are described by two independent sets of orbitals to allow some flexibility in the orbitals wavefunction. For a carbon atom, which contains 1s core orbital, 2s and 1p valence orbitals, considering the cc-pVDZ results in 14 basis set functions, namely 3 for the 3s, 6 for the 2p and 5 for the d orbitals. Often, the cc-PVDZ basis set is described by the contraction, 3s2p1d. Increasing the size of the basis set to cc-pVTZ results in the in the 4s3p2d1f contraction. Increasing the size of the basis set increases the accuracy of the calculations at the expense of an increasing cost. The next class of basis set considered is Pople type basis sets, with 6-31G(d,p) being used with DFT.[201] This basis set includes 6 gaussian type orbitals (GTOs) for the core electrons, a split valence set of 3 plus 1 GTOs as well as and one p and d GTO polarization function for the hydrogen and heavy atoms (heavier than hydrogens), respectively. The Pople type basis sets are the most commonly used in the community for DFT modelling of TADF emitters.

2.8 Visualising the excited state

2.8.1 Molecular Orbital Picture

In excited state calculations, electronic transition to excited states are represented by a set of one-electron transitions. These one-electron transitions involve the promotion from one MO in the

valence to one MO in the conduction band. If the transition occurring is predominately HOMO-LUMO the analysis of the electronic transition is straightforward.[202] However, when multiple one-electron transition contribute to a given excited states transition, the analysis of the nature of the excited states becomes more complex and a more compact representation of these excited states is required.

2.8.2 Difference density

The difference density matrix ($\Delta\rho$) is straightforwardly generated from the difference in electronic density matrices between the excited state (ρ_{ex}) and ground state (ρ_0):[174, 203]

$$\Delta\rho = \rho_{ex} - \rho_0 \quad (2.69)$$

The difference density highlights the change in electron density pattern between the ground and excited state. The negative and the positive signs taken by $\Delta\rho$ represent a decrease and an increase in electron density when going from the ground to the excited state, respectively.

2.8.3 Attachment detachment

From the calculated $\Delta\rho$, it is possible to obtain the attachment (*A*) and detachment (*D)* densities which corresponds to electronic density that has been created in the excited state (corresponding to the electron or particle density) and that has been depleted from the ground state (corresponding to the hole density), respectively. The diagonalization of $\Delta\rho$ yields the δ matrix which contains the eigenvalues of $\Delta\rho$, *i.e.* the occupation number matrix:[174]

$$U^{\dagger}\Delta\rho U = \delta \quad (2.70)$$

Where U is a transformation matrix containing all the eigenvectors of $\Delta\rho$. The value δ can be split into two separate matrices, the first considering only negative eigenvalues associated with the detachment density matrix, D and only positive eigenvalues associated with the attachment density matrix, A)[174, 203] The D and A matrices are obtained as:

$$U^{\dagger}dU = D \quad (2.71)$$

$$U^{\dagger}aU = A \quad (2.72)$$

In a neutral system there is no net electron gain. The sum of all individual eigenvalues (both positive and negative) numbers equal to 0. The difference density $\Delta\rho$ can be directly obtained from the attachment and detachment densities:

$$\Delta\rho = \mathrm{A} - \mathrm{D} \quad (2.73)$$

2.9 Charge Transfer descriptors

CT descriptors have been developed to determine the nature of the excited states. Typically, they allow us to determine if an excited state is CT, LE or a mix of the two. Here below, CT descriptors based on the difference density and attachment-detachment are presented.

2.9.1 Distance of charge transferred

Distance of charge transferred (D_{CT}) relates to the distance between the barycentre's of $\rho_+(r)$ and $\rho_-(r)$ densities. $\rho_+(r)$ and $\rho_-(r)$ densities include the areas of increasing and decreasing difference density, respectively. The centres of these charges are known as the barycentre's, with one corresponding to increased and one decreased density ($R_+$and R_- respectively) and are defined as:

$$R_+ = \frac{\int r\rho_+(r)dr}{\int \rho_+(r)dr} = (x_+, y_+, z_+) \quad (2.74)$$

$$R_- = \frac{\int r\rho_-(r)dr}{\int \rho_-(r)dr} = (x_-, y_-, z_-) \quad (2.75)$$

D_{CT} the distance between R_+ and R_- is calculated according to:.[204, 205]

$$D_{CT} = R_+ - R_- \quad (2.76)$$

The larger D_{CT}, the greater the extent of CT. However, symmetric systems can yield vanishing D_{CT} because of the overlapping barycentres.[204 202] CT states are quoted as having $D_{CT} > 1.6$ Å and LE states of $D_{CT} < 1.6$ Å.[202]

2.9.2 Charge transferred

The charge transferred (q_{CT}) is computed by integrating ρ_+ (or ρ_-) over the molecular volume. It quantifies the distribution of the charge transferred up electronic excitation. The larger the number, the greater the extent of electronic rearrangement, with values ranging from 0 to 1 corresponding to LE and CT states, respectively.[205]

2.9.3 Overlap between the increase and decrease of difference density contributions

S_{+-} is the overlap between areas of increased and decreased electron density. In practice, C_+ and C_- are defined as the centroids of charges associated with positive and negative density regions for a given electronic transition, respectively and are written as:

$$C_+(r) = A_+ e\left(-\frac{(x-x_+)^2}{2\sigma^2{}_{+x}} - \frac{(y-y_+)^2}{2\sigma^2{}_{+y}} - \frac{(z-z_+)^2}{2\sigma^2{}_{+z}}\right) \quad (2.77)$$

$$C_-(r) = A_- e\left(-\frac{(x-x_-)^2}{2\sigma^2{}_{-x}} - \frac{(y-y_-)^2}{2\sigma^2{}_{-y}} - \frac{(z-z_-)^2}{2\sigma^2{}_{-z}}\right) \quad (2.78)$$

Where A_+ and A_- are the normalization factors chosen to impose the integrated charge on the centroid to be equal to the corresponding density change integrated in the whole space. The overlap between these two points C_+ and C_- provides S_{+-}. A value equal to 1 indicates C_+ and C_- sit completely on each other, while a value of 0 indicates they are completely disconnected, corresponding to LE and CT electronic transitions respectively.

2.9.4 Overlap between A and D

This dimensionless quantity is presented as ϕ_S and is computed as the overlap between the attachment and detachment densities:[206, 207]

$$\phi_S = \frac{1}{\theta}\int dr \sqrt{\rho_{\mathrm{D}}(r)\,\rho_A(r)} \quad (2.79)$$

$$\theta = \frac{1}{2}\left[\int dr \sum_{\tau=A,D} \rho_\tau(r)\right] \quad (2.80)$$

Where ρ_{D} and ρ_A are the attachement and detachment densities, respectively; and θ a normalization factor. The ϕ_S index takes values ranging from 0 to 1, depending on the charge-transfer character of the electronic transition. The lowest bound value appears when there is strictly no overlap between detachment and attachment densities and corresponds to a pure CT (ionic) excitation. The upper bound appears when there is one-to-one overlap of the detachment and attachment densities and corresponds to pure LE excitation.

Chapter 3: Impact of donor extension on a known TADF emitter

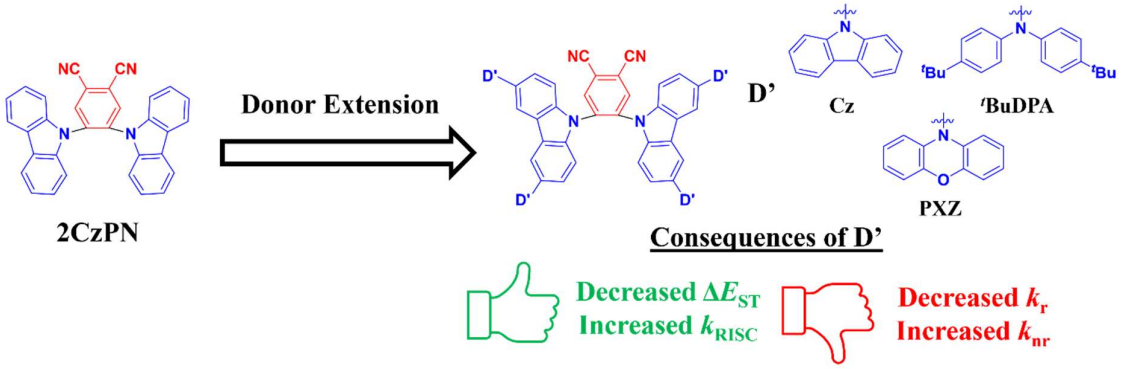

3.1 Introduction

The introduction showcased how reduction in the overlap integral led directly to lower ΔE_{ST} in twisted D-A systems. The introduction also highlighted that this poor overlap of the HOMO and LUMO has an unwanted side effect in the loss of k_r, as the ground and excited state wavefunctions have a small overlap, leading to a small transition dipole moment. For materials design this is paradoxical, as triplet harvesting becomes more efficient at the expense of Φ_{PL}. Strategies that can optimize both would be highly desired. An alternative strategy to separate the HOMO and LUMO has been the use of extended donors.[208] Here, hole density is spread over a donor unit of larger conjugation, allowing reasonable overlap between the donor and acceptor, but with overall sufficient decoupling for a small ΔE_{ST}. Examples have emerged where comparisons are made with a twisted D-A systems and the extended donor, where both produce similar performing TADF emitters (Figure **3.1**).[208, 209] Examples also exist where donor extension has essentially 'turned on' TADF (Figure **3.2**).[208, 210, 211]

Extended donors have been presented in the literature previously, where sufficiently small ΔE_{ST} could be achieved even with small torsion angles between the donor and acceptor. One series was showcased where comparisons between a PXZ donor (**PXZ-Mes$_3$B**),[209] and an extended carbazole donor, where extension was achieved with one or two diphenylamine (DPA) units (**DAC-Mes$_3$B** and **2DAC-Mes$_3$B** for mono and di coupled respectively) [Figure **3.1**]. **PXZ-Mes$_3$B** had an extremely twisted structure owing to its bulky nature forcing a nearly orthogonal conformation (87.3° D-A calculated torsion). The D-A twist was less for carbazole derivatives (53.0° and 51.5° calculated for **DAC-Mes$_3$B** and **2DAC-Mes$_3$B**). ΔE_{ST} was 0.07 eV and Φ_{PL} was 92% for **PXZ-Mes$_3$B**, and despite the small torsion, reasonable ΔE_{ST} of 0.06 eV for each extended was reported in 16 wt% DPEPO with impressive Φ_{PL} of 87% and 100% for **DAC-Mes3B** and **2DAC-Mes3B**, respectively. Devices of the **PXZ-Mes$_3$B** were the highest performing with EQE_{max} of 22.8%, decreasing to 21.6% and 14.0% for **2DAC-Mes$_3$B** and **DAC-Mes$_3$B**. A similar design comparing a PXZ donor (**PXZQ**) and Cz-DPA type donor (**DACQ**) was presented (Figure **3.1**),[208] where the calculated torsion was smaller for **DACQ** (50.0°) compared to **PXZQ** (77.9°). In this example the Φ_{PL} was similar being 84% and 86% for **DACQ** and **PXZQ**, respectively, with improved ΔE_{ST} in **DACQ** of 0.08 eV compared to 0.19 eV for **PXZQ** in

6 wt% DPEPO. The device with **DACQ** showed superior EQE_{max} of 12.8%, while the device with **PXZQ** showed only 10.4%. Another derivative with just carbazole, **CzQ,** was calculated to have a large ΔE_{ST} of 0.77 eV, and hence was not pursued further.

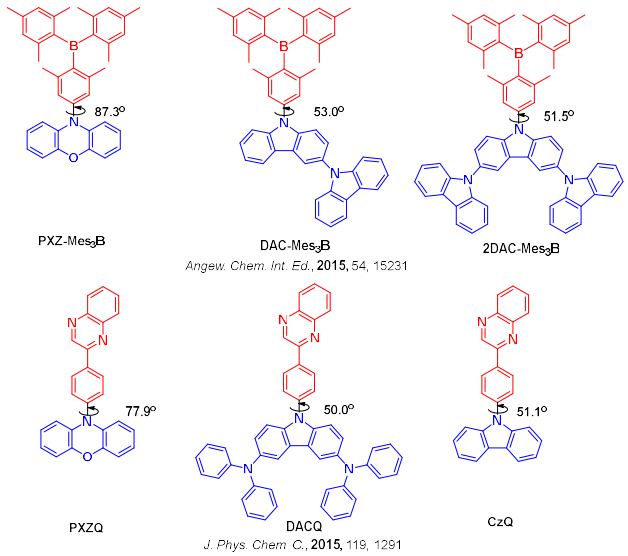

Figure **3.1**. Structures and properties of previous emitters comparing donor extension with conventional D-A TADF emitters, with the calculated D-A torsion highlighted.

Lee *et al.*,[211] presented emitters **CzTA** and **CC2TA** (Figure **3.2**), where the calculated ΔE_{ST} at TD-B3LYP/6-31G(d,p) level, decreased from 0.35 eV to 0.06 eV with the inclusion of donor dendrons in **CC2TA**. When used in 6 wt% DPEPO films reasonable Φ_{PL} of 62% were reported and devices showed an EQE_{max} of 11%. A simple D-A system was investigated[210] where no TADF was observed in either **DCN1** or **DCN2** (Figure **3.2**). These two compounds have calculated ΔE_{ST} of 0.55 eV and 0.61 eV, respectively. Devices with **DCN1** and **DCN2** showed low EQE_{max} of <1.0% and 5.1%, respectively. When additional carbazole substituents were added (**DCN3**), the EQE_{max} improved to 13.3%, this was due to the smaller calculated ΔE_{ST} of 0.13 eV and the corresponding short τ_d of 3.3 μs in PhMe. Extended donors have been frequently used in dendrimer systems.[212] However the focus in this chapter is to link the structure of the donor dendron to the TADF properties of small molecule emitters.

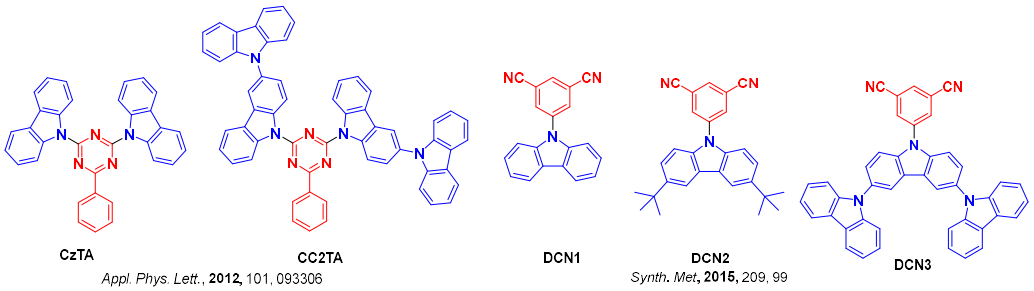

Figure **3.2**. Structures and properties of previous emitters where donor extension has 'turned on' TADF emission.

3.2 Motivation and Chapter outline

In this work we performed a systematic study on derivatives of a known TADF emitter, **2CzPN**.[7] The aim was to assess if a donor extension strategy can lead to improved TADF emitter performance. **2CzPN** was first reported in Adachi and co-worker's ground breaking paper in 2012.[7] This compound is discussed in detail in Chapter 1. They reported large ΔE_{ST} of 0.21 eV in PhMe and long τ_d of 273 μs in 10 wt% mCP films. We designed, synthesised and investigated a series of D'-D-A emitters based on **2CzPN**. The peripheral donors used were carbazole (Cz), diphenylamine (DPA), *tert*butyldiphenylamine (^{t}BuDPA) and phenoxazine (PXZ) (Figure **3.3**), each of which was attached to the central carbazole at the 3 and 6 positions, with the changing photophysical properties key.

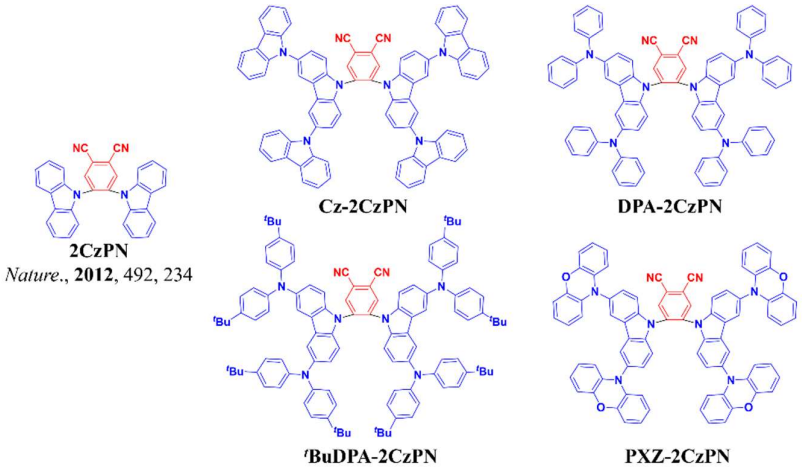

Figure **3.3**. Parent emitter (**2CzPN**) and emitters synthesised in this chapter.

3.3 Results and Discussion

3.3.1 Computations

Calculations were performed on the parent (**2CzPN**) and our 3 target materials with Cz donor (**Cz-2CzPN**), DPA (**DPA-2CzPN**) and PXZ (**PXZ-2CzPN**), with a fourth derivative using *tert*-butyldiphenylamine (**^{t}BuDPA-2CzPN**) also presented, owing to poor solubility of **DPA-2CzPN** (*vide infra*.). Overstabilisation of CT states that often occurs when using low HF-containing DFT functionals PBE0 and B3LYP (25% and 20%, respectively) has been previously outlined.[175] We thus decided to use the higher HF-containing functional M06-2X (54%).[213] Further, studies have indicated that use of TDA-DFT in lieu of conventional TD-DFT improved the prediction of the energy of the triplet states, hence TDA-DFT was used for vertical excitation calculations.[198] Ground state DFT calculations showed a changing HOMO value with the addition of peripheral donors, with the HOMO moving from -7.1 eV, -6.6 eV, -6.2 eV, -6.1 eV and -6.0 eV for **2CzPN**, **Cz-2CzPN**, **^{t}BuDPA-2CzPN**, **DPA-2CzPN** and **PXZ-2CzPN**. For **2CzPN**, HOMO density is centred on Cz units, with large contribution into the phthalonitrile ring. For **Cz-2CzPN**, **DPA-2CzPN** and **^{t}BuDPA-2CzPN**, it is positioned on both the peripheral donors and the inner carbazole substituent, spreading across the whole extended donor unit. For **PXZ-2CzPN** the HOMO density is primarily situated on the peripheral PXZ unit, with minimal contribution on the inner Cz (Figure **3.4**). LUMO density in each case was located predominately on the phthalonitrile unit, with a mild contribution to the carbazole unit in each. Two groupings of LUMO value were obtained, **2CzPN**, **DPA-2CzPN** and **^{t}BuDPA-2CzPN** had similar values of -1.62 eV, -1.66 eV and -1.72 eV, respectively. Lower values were obtained for **Cz-2CzPN** and **PXZ-2CzPN** at -2.06 eV and -2.12 eV. A smaller D-A torsion angle of 53.8 – 55.1° was calculated for **2CzPN**, **DPA-2CzPN** and **^{t}BuDPA-2CzPN**, increasing to 61.2 – 72.9° for **Cz-2CzPN** and **PXZ-2CzPN**. The smaller torsion ensured an increased contribution of electron density to the phthalonitrile acceptor, in turn destabilizing the LUMO, with the effect minimized at larger torsion. This phenomenon is also reflected in the experimental electrochemistry (*vide infra*.).

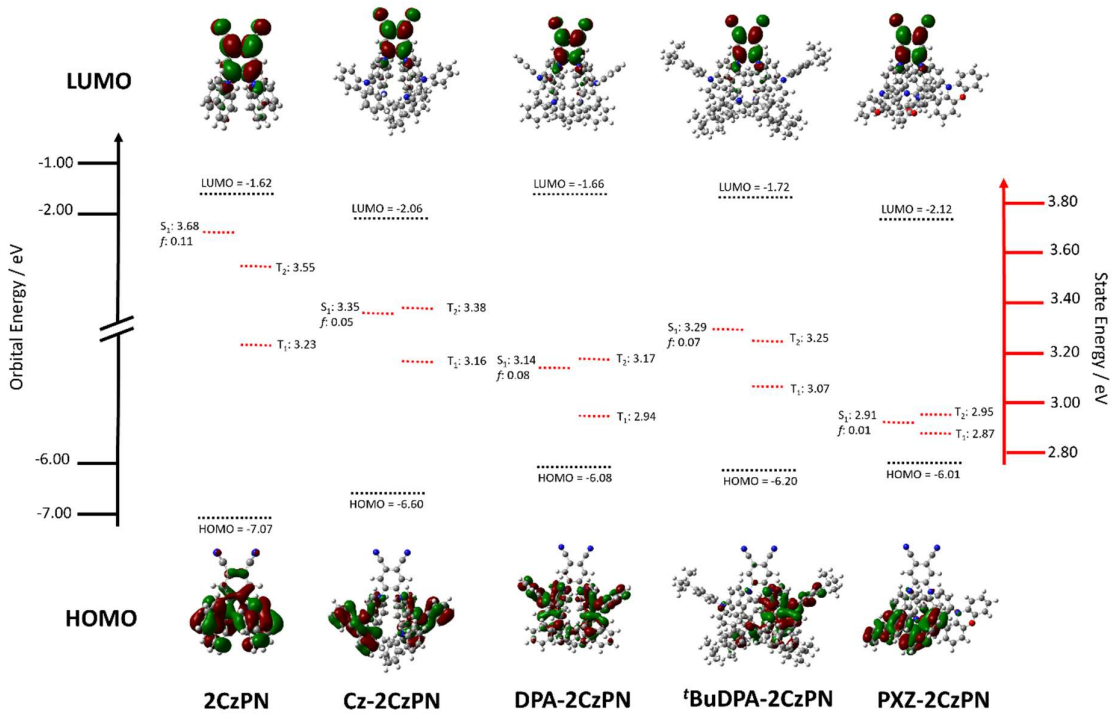

Figure **3.4**. Calculated optoelectronic data for **2CzPN**, **Cz-2CzPN**, **DPA-2CzPN**, **^{t}BuDPA-2CzPN** and **PXZ-2CzPN**, where black is the orbital energies and red is the excited state energies, and HOMO LUMO orbitals.

The attachment detachment density figures were generated for each compound, which mimic hole and electron densities, and the degree of overlap between the two (ϕ_s) was also computed.[202] In each emitter the electron density was situated upon the phthalonitrile acceptor for S_1, T_1 and T_2 (Figure **3.5**). For **2CzPN**, hole density was mainly localized on the carbazole donor with some delocalisation upon the phthalonitrile unit, resulting in a large degree of overlap with ϕ_S corresponding to 0.74 and 0.51 for T_1 and S_1 respectively. Extension of the donor units essentially moved hole density away from the phthalonitrile unit decreasing overlap, with S_1 ϕ_S values dropping to 0.19 – 0.41. With reduced overlap, a decreasing ΔE_{ST} is apparent, but at the expense of decreasing oscillator strength and red shifted emission (Figure **3.5**, Table **3.1**). Calculated ΔE_{ST} decreased from 0.45 eV in **2CzPN** to 0.04 eV in **PXZ-2CzPN**, which had the greatest degree of hole electron wavefunction decoupling, with a large portion of hole density on the peripheral PXZ unit. For **^{t}BuDPA-2CzPN** and **2CzPN** the T_2 state sits between S_1 and T_1, while for the other compounds it is slightly higher in energy than S_1. In each case

the T_2 is similar to T_1, predominately of mixed CT-LE character, unlike many other higher performing emitters where this state usually is assigned as LE.[24, 214] Despite not being purely LE, it is expected the different orbital type of T_2 compared to S_1 should contribute to the RISC mechanism.

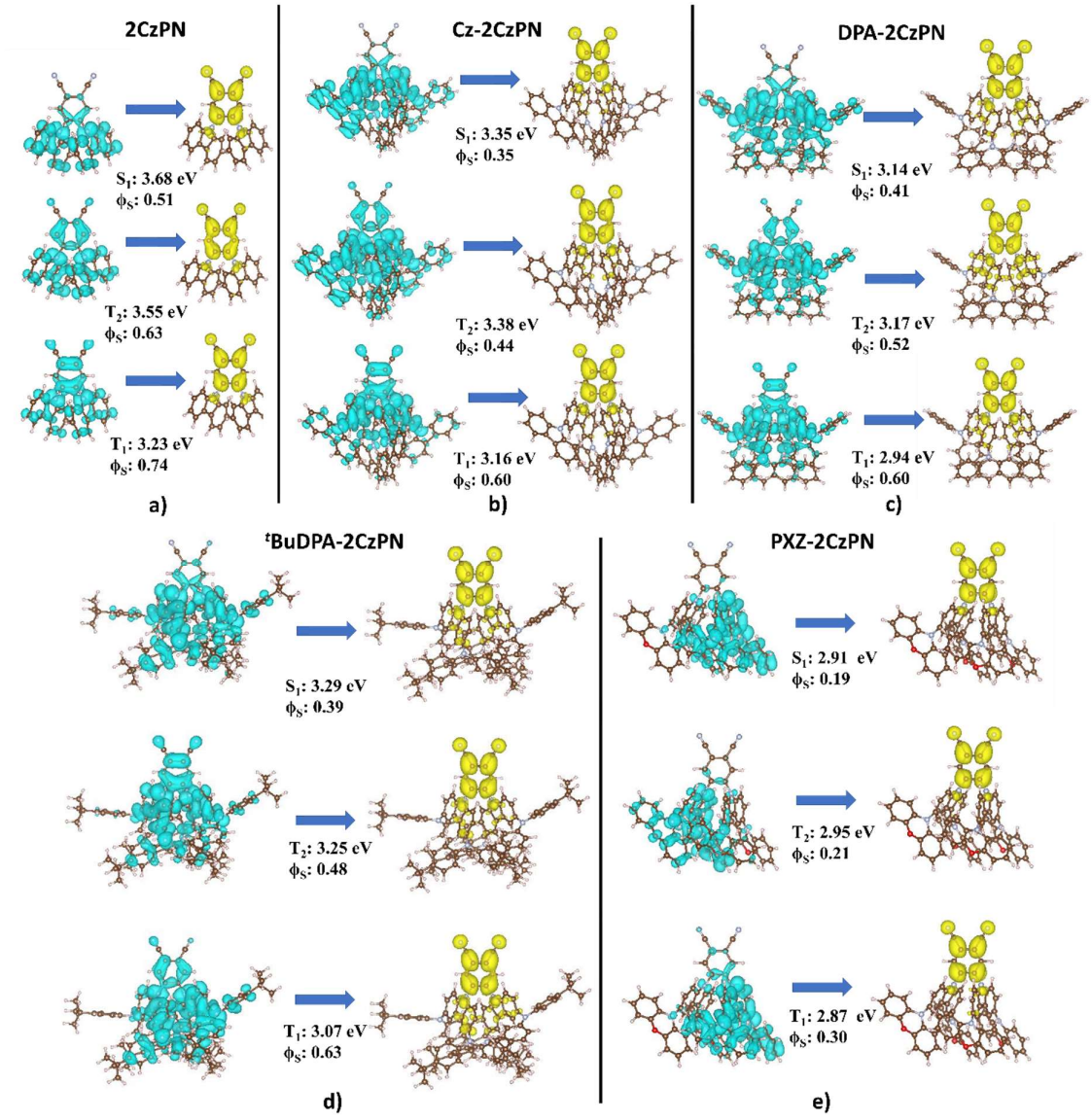

Figure **3.5**. Hole (blue) and electron (yellow) plots of T_1, T_2 and S_1 of each emitter and the calculated overlap between the two (ϕ_s), where the arrow indicates the movement of electronic density between the ground and excited state.

Table **3.1.** Vertical excited state properties of each emitter in their lowest energy ground state conformation

Compound	S_1 (ϕ_S) (eV)	*f*	T_1 (ϕ_S) (eV)	T_2 (ϕ_S) (eV)	ΔE_{ST} (eV)
2CzPN	3.68 (0.51)	0.11	3.23 (0.74)	3.55 (0.63)	0.45
Cz-2CzPN	3.35 (0.35)	0.05	3.16 (0.60)	3.38 (0.44)	0.19
DPA-2CzPN	3.14 (0.41)	0.08	2.94 (0.60)	3.17 (0.52)	0.20
^{t}BuDPA-2CzPN	3.29 (0.39)	0.07	3.07 (0.63)	3.25 (0.48)	0.22
PXZ-2CzPN	2.91 (0.19)	0.01	2.87 (0.30)	2.95 (0.21)	0.04

Calculated at TDA–M06-2X/6-31G(d,p) level, where ϕ_S is an indication of overlap, with a value of 1 = LE nature and a value of 0 = CT. *f* = oscillator strength

3.3.2 Synthesis and crystal structures

Synthesis of the emitters is outlined in (Figure **3.6**). Iodination of Cz occurs in high yield (92%), followed by subsequent protection of the NH with *tert*-butyldimethylsilylchloride producing intermediate **1** (69%). An Ullmann coupling reaction was undertaken to stitch carbazole to the 3,6-positions of intermediate **2** with CuI (83%), while a Buchwald-Hartwig coupling using $Pd(OAc)_2$ was required for ^{t}BuDPA, DPA and PXZ (80%, 86% and 82% respectively) as the Ullmann reaction conditions did not work. Cleavage of the protecting group using TBAF produced the extended donors in near quantitative yields (89 – 95%). An S_{NAr} reaction was undertaken with 4,5-difluorophthalonitrile and NaH to produce the target materials in reasonable yields of between 65% and 85%.

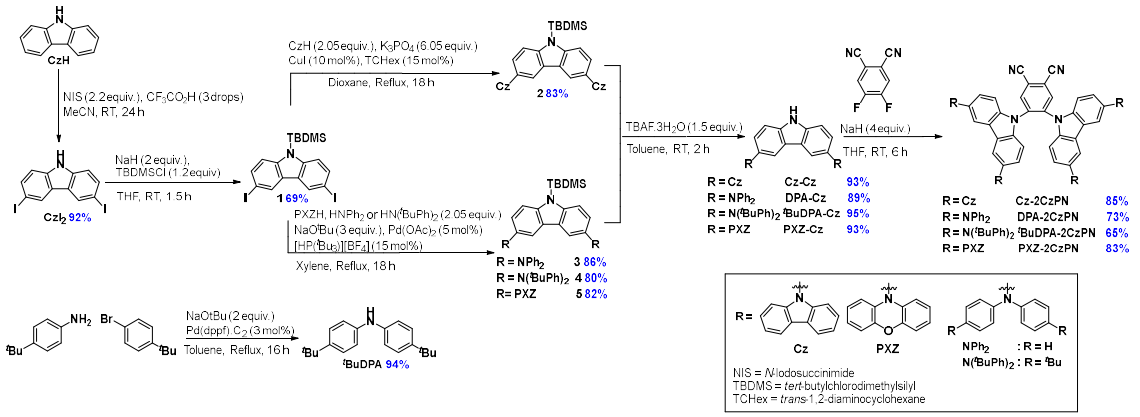

Figure **3.6**. Synthesis of extended donor targets.

Single crystals of **Cz-2CzPN**, **DPA-2CzPN** and **PXZ-2CzPN** were each obtained from a saturated solution of PhMe from either slow evaporation of PhMe or layering with hexane. Two structures of **PXZ-2CzPN** showing different solvation, and slightly different conformations were obtained, designated **PXZ-2CzPN(A)** and **PXZ-2CzPN(B)** (Figure **3.7**). Owing to the insolubility of **DPA-2CzPN**, **^{t}BuDPA-2CzPN** was also synthesised, with DFT suggesting minimal impact on the photophysics while addressing the issues of solubility (Table **3.1**). No further photophysical analysis was undertaken for **DPA-2CzPN** owing to its insolubility but we discuss its crystal structure as crystals of **^{t}BuDPA-2CzPN** were not obtained, and the conformations are calculated to be similar (Table **3.2**). The primary torsions of interest are between the donor and acceptor (D-A) and the inner donor and peripheral donor (D-D'), (Table **3.2** and Figure **3.8**). Both **2CzPN** and **DPA-2CzPN** have similar D-A torsions of 49.3 – 59.8° and 54.5 – 59.1°, respectively, which is in agreement with the calculations (53.8° for **2CzPN** and 54.7° for **DPA-2CzPN**). **^{t}BuDPA-2CzPN** has similar calculated values of 55.1 – 56.3°. The D-A torsion increased for **Cz-2CzPN** to 61.5 – 63.1° and is in agreement with the calculated values of 61.2 and 61.4°, with the larger size and inflexibility of carbazole peripheral substituent the cause. Two distinct D-A angles were obtained for the two conformers with D-A 49.4° - 57.3° in **PXZ-2CzPN(A)** and 60.0° – 65.0° in **PXZ-2CzPN(B)**, with different packing regimes key.

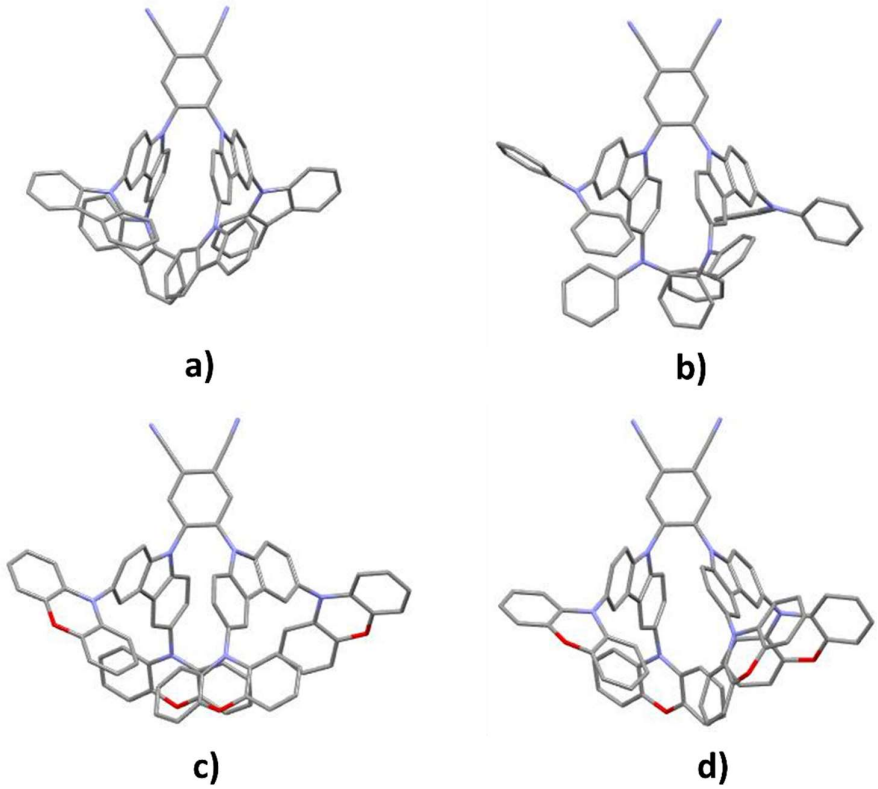

Figure **3.7**. Crystal structures of **a**) **Cz-2CzPN**, **b**) **DPA-2CzPN**, **c**) **PXZ-2CzPN(A)**, **d**) **PXZ-2CzPN(B)**.

The D-D' torsion of the two **PXZ-2CzPN** crystal structures are similar at 74.0 – 78.6° for **PXZ-2CzPN(A)** and 70.6 – 79.2° for **PXZ-2CzPN(B)**, matching DFT calculated geometries reasonably well (55.6 – 68.2°, Table **3.2**). The large torsion here will minimize conjugation between the peripheral PXZ and carbazole. The near orthogonal angles have been previously reported for PXZ coupled to acceptors.[209] Each PXZ is puckered, which has been observed previously in structurally similar phenothiazine donors.[215] The inflexibility of Cz units resulted in large D-D' torsions of between 59.0° and 78.5° in **Cz-2CzPN**, which again are slightly larger than the calculated 48.8° and 65.8°. **DPA-2CzPN** had the smallest torsion of 44.3 – 65.8°, which would ensure a greater degree of conjugation between the donor units, which ensured stronger donor strength (*vide infra*). Calculated D-D' torsion are larger for **^{t}BuDPA-2CzPN** between 55.7 and 80.9°.

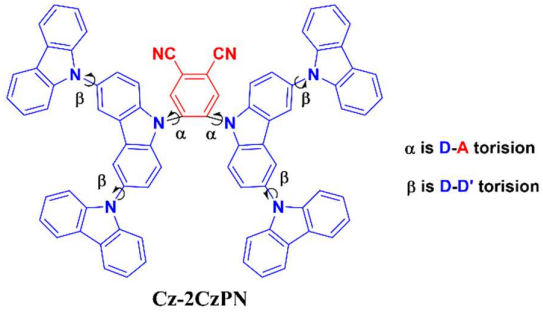

Figure **3.8**. Highlighted investigated torsions in **Cz-2CzPN.**

Table **3.2**. Average torsions from crystal structure and DFT of the functional groups.

Compound	D-A Torsion / ° [a]	D-D' Torsion / ° [a]	D-A Torsion / ° [b]	D-D' Torsion / ° [b]
2CzPN[120]	49.3, 59.8	N/A	53.8	N/A
Cz-2CzPN	61.5, 63.1	59.0-78.5	61.2, 61.4	48.8 – 65.8
DPA-2CzPN	54.5, 59.1	44.3–65.8	54.7	46.1 – 50.4
^{t}BuDPA-2CzPN	-	-	55.1, 56.3	55.7 – 80.9
PXZ-2CzPN	49.4, 57.3[c]	74.0-78.6[c]	69.8 – 72.9	55.6 – 68.2
	60.0, 65.0[d]	70.6–79.2[d]		

[a] Average from crystal structure, [b] Average from Ground state DFT at M06-2X/6-31 g(d,p), [c]**PXZ-2CzPN(A)** [d]**PXZ-2CzPN(B)**.

3.3.3 Electrochemical properties

The electrochemical properties of the emitters, individual donor units and extended donor units were investigated using cyclic voltammetry (CV) and differential pulse voltammetry (DPV) in degassed dichloromethane (DCM) solutions at 298 K. The ferrocene/ferrocenium (Fc/Fc^+) couple was used as the internal standard and the data referenced with respect to a Saturated calomel electrode (SCE), with the data summarized in Tables **3.3** and **3.4**.[216]

The electrochemical behaviour of the individual donor units was investigated (Figure **3.9**). The oxidation of carbazole is irreversible, degrading upon successive scans via a putative electropolymerisation occurring at the 3 and 6 positions (Figure **3.10**), which has been previously reported.[217] The oxidation potential (E^{ox}) from DPV is 1.15 V, matching that previously reported (E^{ox} = 1.16 V in MeCN).[218] Both ^{t}BuDPA and PXZ have quasi-reversible oxidation waves centred at 0.84 V and 0.66 V, respectively, indicating the greater donor strength of PXZ. A cathodic shift is observed for

Cz-Cz compared to Cz (moving from 1.15 V to 1.08 V) in agreement with a similar derivative (where the NH of Cz-Cz was substituted with N-C_6H_{13}, producing E^{ox} of 1.08 V).[217, 219] Only a single oxidation wave is observed suggesting the radical cation is delocalised over the whole Cz-Cz molecule, instead of the separate Cz units. Much like Cz, it is electrochemically unstable, with a second oxidation wave appearing after several scans, assigned again to polymerisation (Figure **3.10b).** Two reversible oxidation waves were observed for ^{t}BuDPA-Cz, assigned to be from Cz and ^{t}BuDPA. Both are cathodically shifted from Cz (1.16 V) and ^{t}BuDPA (0.84 V), with the first E^{ox} wave at 0.49 V (Figure **3.9**). Donor polymerisation is prevented by substituting the 3 and 6 position of carbazole with ^{t}BuDPA. In PXZ-Cz a single quasi-reversible oxidation is observed at 0.71 V, assigned to PXZ, being similar to PXZ only (0.66 V). Although PXZ is the stronger individual donor, the ability of ^{t}BuDPA to conjugate to carbazole ensures ^{t}BuDPA-Cz is the stronger extended donor, reflected in the most cathodically shifted E^{ox} value (Table **3.3**).

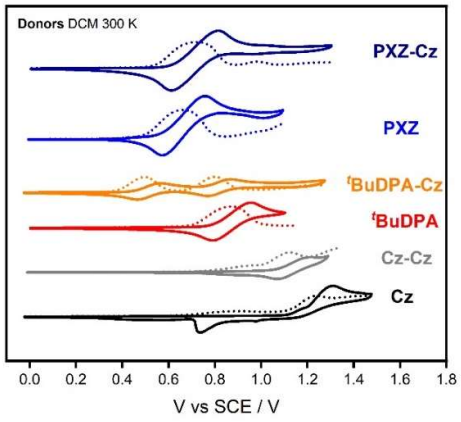

Figure **3.9**. Stacked CV (solid line) and DPV (dotted line) in DCM at 0.05 V s^{-1} scans rate.

Table **3.3**. Electrochemical oxidation data of various donor units.

Compound	**E^{ox} [a] / V [a]**	**HOMO / eV [b]**
Cz	1.15	-5.48
***t*BuDPA**	0.84	-5.18
PXZ	0.66	-5.00
Cz-Cz	1.08	-5.42
***t*BuDPA-Cz**	0.49	-4.83
PXZ-Cz	0.71	-5.06

[a] Reported versus SCE in degassed DCM with 0.1 M Tetrabutylammonium hexafluorophosphate ([nBu$_4$N] PF_6) as the supporting electrolyte and Fc/Fc^+ as the internal reference (0.46 V vs. SCE)[216] calculated from DPV maxima. [b.] The HOMO energies were determined using the relation $E_{HOMO} = -(E^{ox} + 4.8)$ eV.[220]

The electrochemistry of the emitters was next investigated. The CV of **2CzPN** displays an irreversible oxidation wave, with E^{ox} 1.54 V. The HOMO of -5.87 eV agrees with that previously reported (-5.88 eV).[120] The extended derivative, **Cz-2CzPN** also displayed an irreversible oxidation wave, which is cathodically shifted at E^{ox} = 1.28 V owing to the stronger donating ability of Cz-Cz. In both these emitters the material is electrochemically unstable upon oxidation with new peaks appearing after several scans (Figure **3.10c** and **d**).

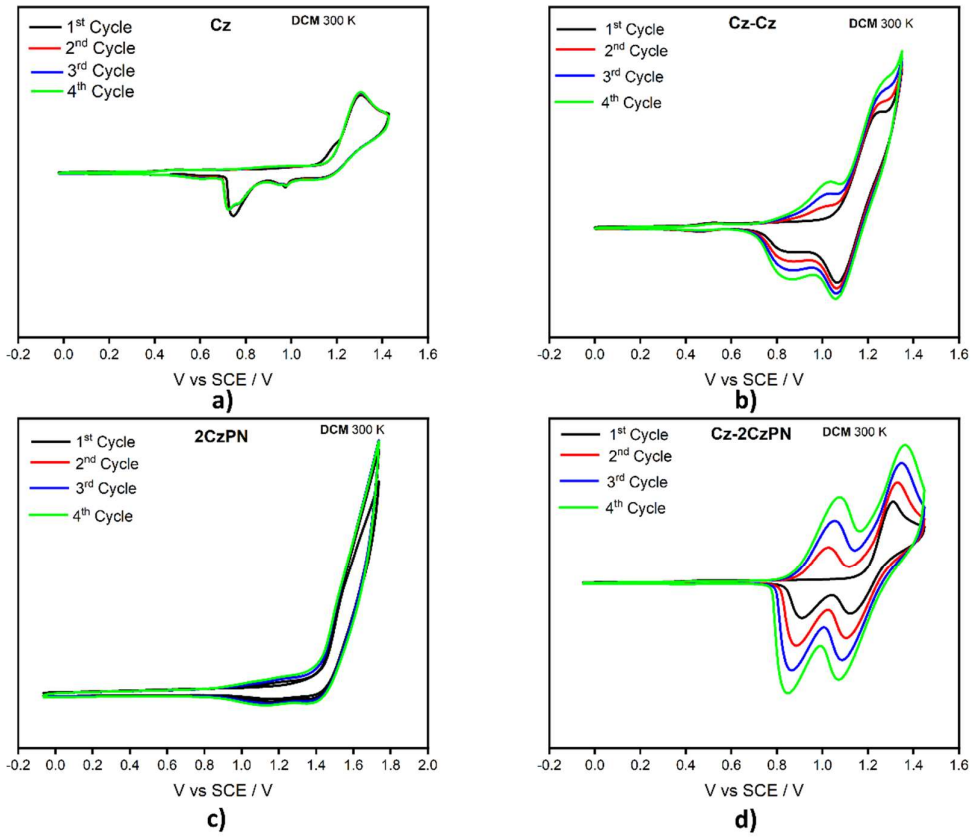

Figure **3.10**. Reversibility of the oxidation wave of carbazole containing compounds tested over several cycles at 0.05 V s^{-1}, where **a)** is Cz, **b)** is Cz-Cz, **c)** is **2CzPN** and **d)** is **Cz-2CzPN**.

Similarly to **^{t}BuDPA-Cz**, two reversible oxidation waves were reported for **^{t}BuDPA-2CzPN**, with the first catholically shifted at 0.72 V compared to **Cz-2CzPN**, in line with the stronger donating ability of **^{t}BuDPA-Cz**. The E^{ox} of **^{t}BuDPA-2CzPN** is anodically shifted compared to **^{t}BuDPA-Cz** on its own, owing to conjugation with the electron-accepting phthalonitrile unit. Reversible oxidation of **PXZ-2CzPN** is centred almost exclusively on PXZ, with an E^{ox} of 0.80 V, which is slightly anodically shifted compared to **PXZ-Cz** (E^{ox} = 0.71 V). This is corroborated by DFT calculations wherein the HOMO is centred on the PXZ unit (Figure **3.4**). The increasing donor strength is reflected in the oxidation potentials with E^{ox} of 1.54 V, 1.28 V, 0.80 V 0.72 V for **2CzPN**, **Cz-2CzPN**, **PXZ-2CzPN** and **^{t}BuDPA-2CzPN**, respectively. The donor strength is an interplay between conjugation between peripheral donors and the central carbazole and the nature of the peripheral donors.

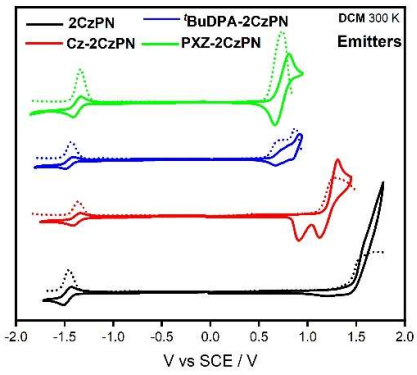

Figure **3.11.** CV (solid lines) and DPV (dotted lines) of **2CzPN** (black), **Cz-2CzPN** (red), **ᵗBuDPA-2CzPN** (blue) and **PXZ-2CzPN** (green). obtained in DCM at 300 K at 0.05 V s^{-1} scan rate.

Reversible reduction waves are apparent for all four emitters, which are centred on the phthalonitrile acceptor unit. Two different groupings of reduction potentials (E^{red}) could be assigned. For **2CzPN** and **ᵗBuDPA-2CzPN**, E^{red} are similar at -1.46 V and -1.43 V, respectively, and these are anodically shifted compared to **Cz-2CzPN** and **PXZ-2CzPN**, with E^{red} of -1.36 V and -1.30 V, respectively. Overall, there is good agreement between the experimentally determined trends and calculated HOMO/LUMO trends across the series, with the two groupings of LUMO levels apparent, the result of differing D-A torsion (*vide supra*.) (Table **3.4**).

Table **3.4.** Electrochemical data of the emitters

Compound	Electrochemistry					DFT		
	E^{ox} [a] (V)	E^{red} [a] (V)	HOMO [b] (eV)	LUMO [b] (eV)	ΔE_{H-L} [c] (eV)	HOMO[d] (eV)	LUMO[d] (eV)	ΔE_{H-L}[d] (eV)
2CzPN	1.54	-1.46	-5.87	-2.88	2.7	-7.07	-1.62	5.45
Cz-2CzPN	1.28	-1.36	-5.62	-2.98	2.6	-6.60	-2.06	4.54
***t*BuDPA-2CzPN**	0.72	-1.43	-5.0	-2.9	2.1	-6.20	-1.72	4.48
PXZ-2CzPN	0.80	-1.30	-5.1	-3.0	2.1	-6.01	-2.12	3.89

[a] Reported versus SCE in degassed DCM with 0.1 M [nBu$_4$N]PF$_6$ as the supporting electrolyte and Fc/Fc$^+$ as the internal reference (0.46 V vs. SCE)[216] calculated from the peak maximum measured by DPV. [b.] The HOMO and LUMO energies were determined using the relation $E_{HOMO/LUMO} = -(E^{ox} / E^{red} + 4.8)$ eV[220]. [c.] $E_{H-L} = |E_{HOMO}-E_{LUMO}|$, [d] The HOMO and LUMO values were determined from M06-2X/6-31G(d,p) ground state structure.

3.3.4 Solution-state photophysical properties

UV-vis absorption data (Table **3.5** and Figure **3.12a**) and absorptivity of each donor and extended donor were reported in toluene at 300 K. Extension of the donors produced a significant increase in molar absorptivity of all reported bands, in line with increased conjugation within these species, which would ensure stronger wavefunctional overlap between the ground and excited states. For **Cz-Cz** and **PXZ-Cz** a sharp peak matching that of **Cz** is observed at around 293 – 296 nm.

Table **3.5**. UV data for individual donors and extended donors in PhMe at 300 K.

Compound	λ (ε) / nm (x 10^3 M^{-1} cm^{-1})
Cz	335 (3), 321 (4), 310 (3), 293 (17) 287 (12)
***t*BuDPA**	289 (9)
PXZ	318 (7), 283 (3)
Cz-Cz	342 (12), 329 (12), 315 (12), 294 (44), 286 (40)
***t*BuDPA-Cz**	395 (2), 361 (8), 304 (51)
PXZ-Cz	347 (9), 319 (20), 296 (24)

UV-vis absorption spectra of the emitters in PhMe show broad, low intensity, low energy bands, which are red shifted from **2CzPN**, **Cz-2CzPN**, **PXZ-2CzPN** and **^{t}BuDPA-2CzPN**, broadly in line with DFT calculated S_1 levels (Table **3.1**). Good agreement was observed between molar absorptivity and the calculated oscillator strength, with **2CzPN** ε = 13 × 10^3 M^{-1} cm^{-1} (*f* = 0.11), **^{t}BuDPA-2CzPN** ε = 13 × 10^3 M^{-1} cm^{-1} (*f* = 0.07), **Cz-2CzPN** ε = 10 × 10^3 M^{-1} cm^{-1} (*f* = 0.05) and **PXZ-2CzPN** ε = 1 × 10^3 M^{-1} cm^{-1} (*f* = 0.01). The changes in oscillator strength and ε are directly related to the degree of CT character of each S_1 excited state, with a decreasing ϕ_s value across the series (0.51, 0.39, 0.35 and 0.11). Note that an increased CT character produces a decrease of both oscillator strength and ϕ_S. The decrease in oscillator strength (0.11 to 0.07) from **2CzPN** to **^{t}BuDPA-2CzPN,** which is not observed experimentally (ε = 13 × 10^3 M^{-1} cm^{-1} for both), is due to the influence of a nearby higher singlet states contributing to ε in **^{t}BuDPA-2CzPN**, which is observed in the simulated absorption spectra where they have peaks of identical intensity (Figure **3.12c**).

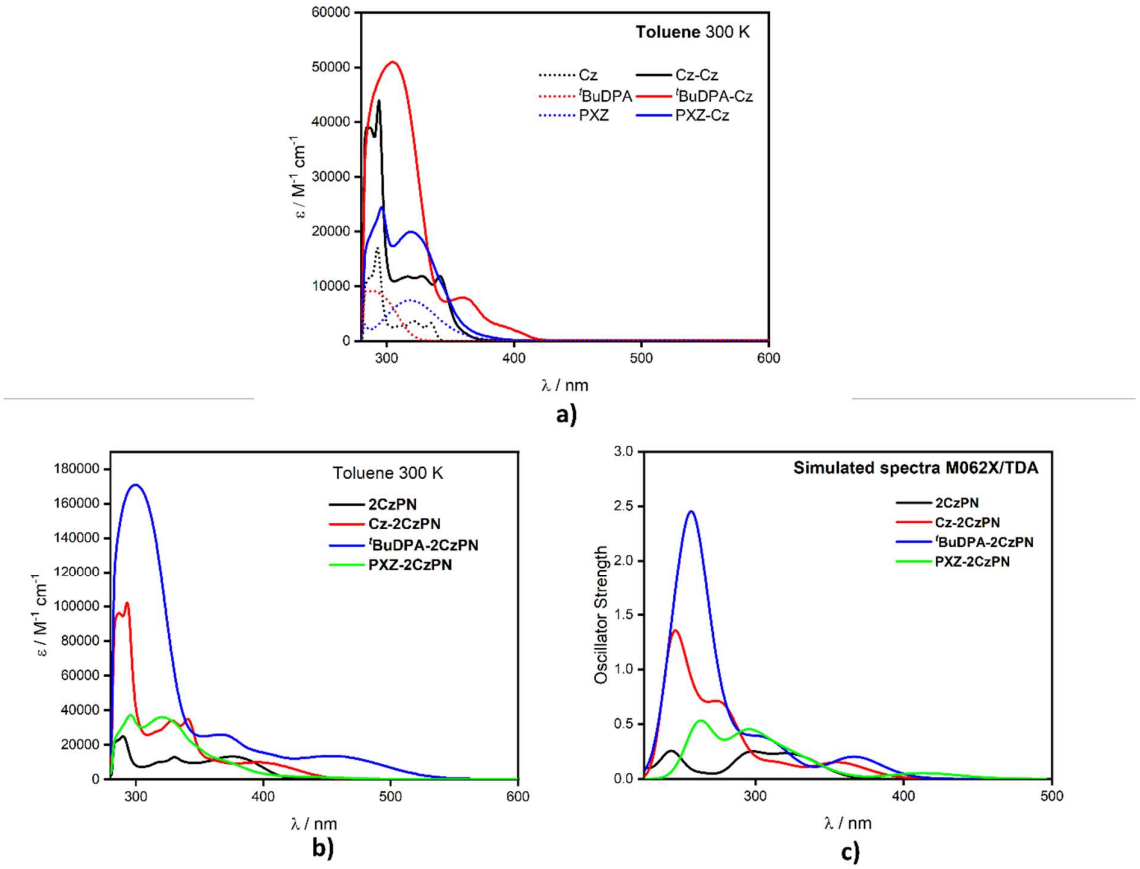

Figure **3.12**. Absorption spectra of **a)** donor fragments in PhMe, **b) 2CzPN**, **Cz-2CzPN**, **^{t}BuDPA-2CzPN** and **PXZ-2CzPN** in PhMe and **c)** simulated spectra of **2CzPN**, **Cz-2CzPN**, **^{t}BuDPA-2CzPN** and **PXZ-2CzPN**, calculated at TDA-M06-2X/6-31G(d,p).

Following initial publication,[221] further analysis was undertaken on the assignment of the bands of the absorption spectra. TDA-M06-2X/6-31G(d,p) based on vertical transitions to the first 50 singlet excited states were performed for each emitter to simulate the absorption spectra (Figure **3.12c**). From here, the important transitions are plotted, which permits deduction of the nature of each absorption band (Figure **3.13**). Excellent agreement exists between the measured and simulated spectra (Figure **3.12b** and **c**).

For **2CzPN** a low energy transition at 381 nm was assigned to the S_1 transition with CT-LE character owing to large hole electron overlap on the phthalonitrile. A higher energy band at 331 nm

was assigned to a similar transition, to that of 381 nm, with identical ε values measured at 13×10^3 M^{-1} cm^{-1}. A higher intensity lower energy band at 290 nm was predicted to be an CT-LE transition with hole-electron overlap situated predominately on the carbazole moiety. In **Cz-2CzPN** a low energy low intensity band at 404 nm was assigned to CT absorption between the extended donor and phthalonitrile unit. Two higher energy bands of greater intensity (at 342 nm and 327 nm) were assigned to transitions from the peripheral carbazoles to the inner carbazole, with some electron density extended onto the phthalonitrile, assigned to a CT-LE transition (Figure **3.12**). A higher energy higher intensity peak at 293 nm was assigned to a LE transition on the extended carbazole unit (Figure **3.13b**). For **^{t}BuDPA-2CzPN**, the low energy band was assigned to a CT transition between the extended donor unit and phthalonitrile. A higher intensity peak at 371 nm between the inner carbazole and phthalonitrile was assigned CT-LE as there is a large overlap between the hole and electron density on the carbazole units. The extremely high intensity transition at 300 nm was assigned to a collection of LE transitions covering the whole ^{t}BuDPA-Cz unit (Figure **3.13c**). For **PXZ-2CzPN** the S_1 state is not clearly observed in the experimental absorption spectra (Figure **3.12b**) owing to its low oscillator strength (0.01). A shoulder peak is observed at 374 nm, assigned to several CT transitions between carbazole to phthalonitrile. A higher intensity higher energy band at 321 nm was assigned to a CT-LE state involving movement of charge from PXZ to Cz (Figure **3.13**). A higher energy band at 296 nm was assigned to be a transition to a LE state as the hole and electron density covers the whole PXZ-Cz unit (Figure **3.13**). The highest intensity band in **Cz-2CzPN**, **^{t}BuDPA-2CzPN** and **PXZ-2CzPN** is similarly assigned to a LE state across the entire extended donor unit, where the largest degree of conjugation exists for the ^{t}BuDPA units that ensure that **^{t}BuDPA-2CzPN** shows the largest ε for this transition.

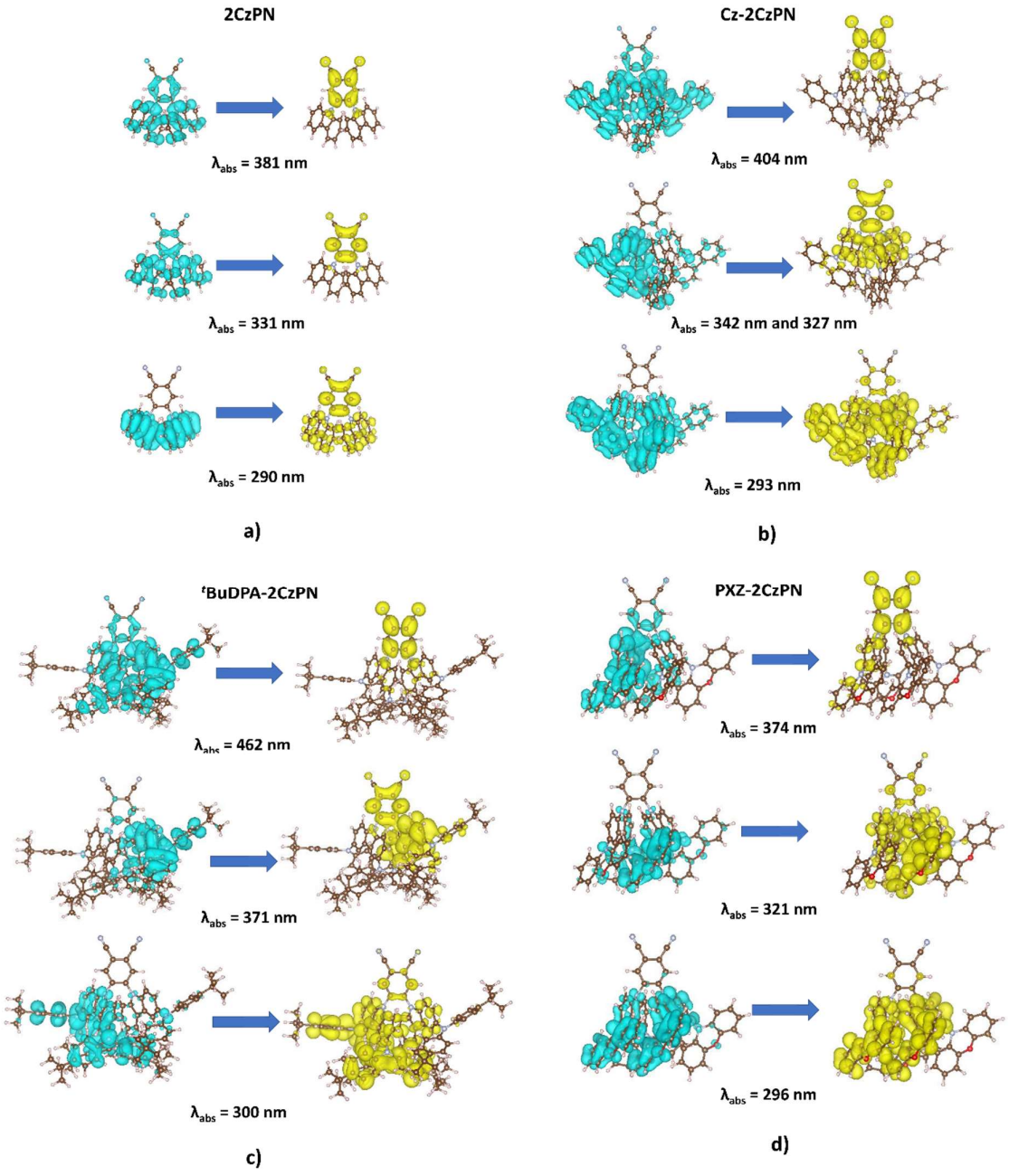

Figure **3.13**. Transitions of major absorption peaks determined from simulated absorption spectra, for **a) 2CzPN**, **b) Cz-2CzPN**, **c) ^{t}BuDPA-2CzPN** and **d) PXZ-2CzPN**, where the arrow indicates the movement of charge, where blue indicates hole density and yellow electron density.

Broad and unstructured emission spectra recorded in PhMe are characteristic of emission from a CT state. With addition of donor units, a red shifted emission is apparent, ranging from 484 nm in **2CzPN** to 667 nm in **PXZ-2CzPN** (Figure **3.15a**), in line with the trend in S_1 energies predicted by

DFT. ΔE_{ST} was determined for each emitter in PhMe, calculated from the difference between the onset of the SS emission and the phosphorescence spectra at 77 K (5 K for **^{t}BuDPA-2CzPN**), which can be translated to fluorescence and phosphorescence spectra respectively (Figure **3.14**). Blue shifted emission is observed at lower temperature owing to freezing of the solvation shell (Figure **3.14**).[16] Addition of the extended donor units produced a significantly smaller ΔE_{ST}, with **2CzPN** being 0.30 eV, **Cz-2CzPN** 0.16 eV and **^{t}BuDPA-2CzPN** and **PXZ-2CzPN** both 0.01 eV. The values obtained are somewhat smaller than those calculated. This is because in solution, the S_1 state is stabilized, and this is not captured in the DFT calculations.

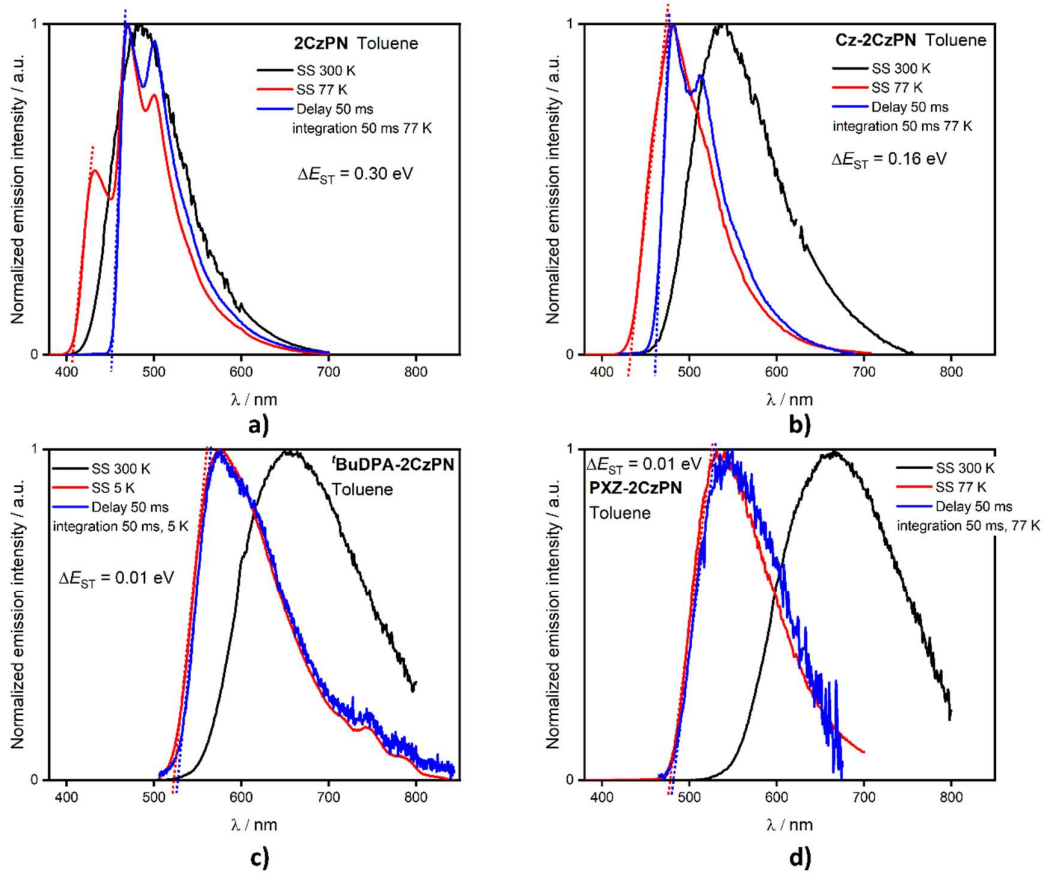

Figure **3.14**. SS emission spectra of **2CzPN** (**a**), **Cz-2CzPN** (**b**), **^{t}BuDPA-2CzPN** (**c**) and **PXZ-2CzPN** (**d**) each emitter in toluene at 300 K and 77 K (5 K for **c**) and gated emission spectra at 77 K (5 K for **c**), where dotted lines present the onset for ΔE_{ST} calculation. Where SS is steady state.

Time-resolved PL decays decays are reported for each emitter (Figure **3.15b**), and show prompt and delayed components, with the former in the ns regime and the latter in the μs regime (Table **3.6**). An initial increase in τ_P was observed from **2CzPN** to **Cz-2CzPN** (27 ns and 42 ns). A significant decrease to 2 ns is apparent for **^{t}BuDPA-2CzPN**, rising again to 23 ns for **PXZ-2CzPN**. Extension of the donor units decreased the lifetime of the delayed component, reported as 6.0 μs, 4.5 μs, 1.2 μs and 2.8 μs for **2CzPN**, **Cz-2CzPN**, **^{t}BuDPA-2CzPN** and **PXZ-2CzPN**, respectively. Φ_{PL} was recorded for each being 38%, 63% 2% and 3% for **2CzPN**, **Cz-2CzPN**, **^{t}BuDPA-2CzPN** and **PXZ-2CzPN,** with only **Cz-2CzPN** having significant contribution from the delayed component, 19%, while the other emitters ranged between 0.02% and 0.04%. The low Φ_{DF} was assigned to collision quenching with the solvent depleting triplet states, with the triplet of **Cz-2CzPN** somewhat shielded by the donor dendrons compared to the other emitters. This was highlighted by DFT calculations where T_1 electron density is predominately centred on the inner carbazole, while all the other emitters have significant density on the peripheral donors (Figure **3.5**). Rates were calculated for each emitter (Table **3.7**), with k_r and k_{nr} probed. Values of k_r were 1.4, 1.1 1.0 and 0.1 × 10^7 s^{-1} for **2CzPN**, **Cz-2CzPN**, **^{t}BuDPA-2CzPN** and **PXZ-2CzPN**, respectively. From these values it is clear that with the presence of the donor dendrons there is a slower k_r. This decrease in k_r is substantial for **PXZ-2CzPN**, being an order of magnitude lower than the others, attributed to the largely decoupled hole and electron wavefunctions, ensuring radiative transitions are less favourable than in the other emitters. This was corroborated with the low calculated oscillator strength (0.01), small ϕ_s (0.19) and low measure ε (1 × 10^3 M^{-1} cm^{-1}) all of which explain the low Φ_{PL} of this emitter (3%). The k_{nr} was calculated to be 1.7, 1.5, 8.3 and 3.6 × 10^5 s^{-1} for **2CzPN**, **Cz-2CzPN**, **^{t}BuDPA-2CzPN** and **PXZ-2CzPN**, respectively. For **^{t}BuDPA-2CzPN** it is much higher and explains the smaller Φ_{PL} compared to **2CzPN** and **Cz-2CzPN** (3% compared to 38% and 63%). The larger k_{nr} is due to the floppy nature of the DPA groups ensuring vibronic loss pathways are significant, further its red shifted emission opens the potential for further losses resulting from the energy gap law.[222] The incorporation of donor dendrons results in an increased k_{nr} for each compound reported. k_{RISC} was calculated for each using the method described in Chapter 1. The k_{RISC} increased from 0.3, 7.5, 8.6 and 171 × 10^3 s^{-1} for **2CzPN**, **PXZ-2CzPN**, **^{t}BuDPA-2CzPN** and **Cz-2CzPN**, respectively. The slower values for the first three are due to quenching of their triplet excited states

(*vide supra*), and must be considered with caution as k_{nr} competes with k_{RISC}. Despite the smaller ΔE_{ST} faster τ_d and k_{RISC} compared to **2CzPN**, in solution the presence of the donor dendrons in **^{t}BuDPA-2CzPN** and **PXZ-2CzPN** is detrimental to the emission properties. At this stage, **Cz-2CzPN** is still promising with an improved Φ_{PL} and k_{RISC} compared to **2CzPN**, with both k_r and k_{nr} minimally affected by the extension.

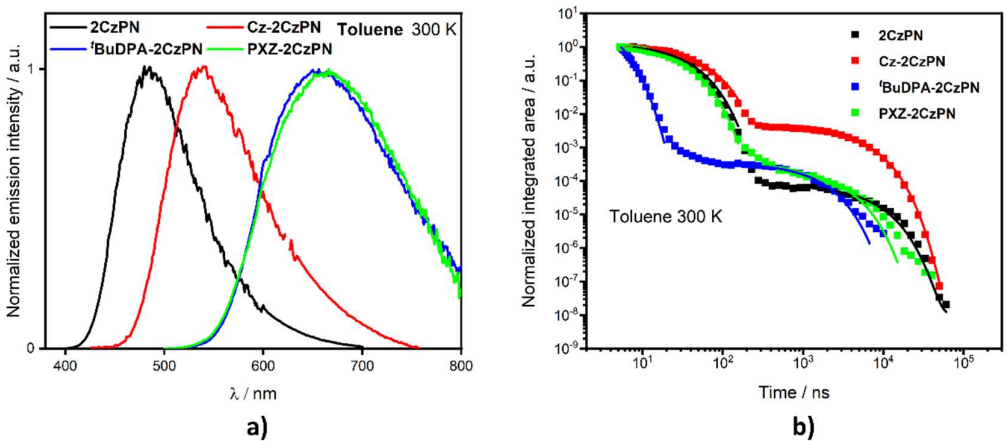

Figure **3.15**. Photophysical data of **2CzPN**, **Cz-2CzPN**, **^{t}BuDPA-2CzPN** and **PXZ-2CzPN** in toluene where **a)** is emission of emitter species, excited at maximum absorption band, **b)** is the time-resolved PL decays of each emitter, excitation wavelength (λ_{exc}) = 355 nm.

Table **3.6**. Photophysical properties of the emitters in dilute PhMe.

Compound	λ_{abs} (ε) / nm ($\times 10^3$ M^{-1} cm^{-1})[a]	λ_{PL} / nm [b]	Φ_{PL}[c] (Φ_{DF}[d]) / %	S_1 / eV [e]	T_1 / eV [f]	ΔE_{ST} / eV	τ_{pf} / ns [g]	τ_{df} / µs [g]
2CzPN	381 (13), 331 (13), 316 (10), 290 (25)	484	38 (0.04)	3.03	2.73	0.30	27	6.0
Cz-2CzPN	404 (10), 342 (35), 327 (35), 318 (28), 293 (102), 288 (96)	538	63 (19)	2.85	2.69	0.16	42	4.5
^{t}BuDPA-2CzPN	462 (13), 401 (15), 371 (26), 300 (171)	659	2 (0.02)	2.37 [h]	2.36 [i]	0.01	2	1.2
PXZ-2CzPN	457 (1), 374 (10), 321 (36), 296 (37)	667	3 (0.06)	2.57	2.56	0.01	23	2.8

[a] Obtained at 300 K, [b] Excited at maximum absorption band at 300 K [c] λ_{exc} = 355 nm calculated in an integrating sphere, [d] Delayed emission yield, from area under time-resolved PL decays, [e] Excited at maximum absorption band at 77 K, calculated from onset of steady state, [f] Excited at maximum absorption band at 77 K, calculated from the onset of gated emission, with 50 ms delay and 50 ms integration time, [g] λ_{exc} = 355 nm, calculated from mono-exponential fitting, [h] Excited at maximum absorption band at 5 K, calculated from onset of steady state, [i] Excited at maximum absorption band at 5 K, calculated from the onset of gated emission, with 50 ms delay and 50 ms integration time.

Table **3.7**. Kinetic properties in PhMe, calculated according to ref.[111]

Compound	k_r / $\times 10^7$ s^{-1}	k_{nr} / $\times 10^5$ s^{-1}	k_{ISC} / $\times 10^7$ s^{-1}	k_{RISC} / $\times 10^3$ s^{-1}
2CzPN	2.01	1.67	2.30	0.28
Cz-2CzPN	1.05	1.47	1.33	171
^{t}BuDPA-2CzPN	0.99	8.33	49.0	8.59
PXZ-2CzPN	0.13	3.57	4.22	7.51

3.3.5 Solid-state photophysical properties

Next the photophysical properties of the compounds were recorded in doped films, with mCP selected owing to its high triplet (2.9 eV) and wide band gap (3.7 eV).[223] Low temperature spectra were recorded to determine ΔE_{ST} (Figure **3.16**). Similar trends to solution are observed, with ΔE_{ST} of 0.23 eV, 0.13 eV, 0.01 eV and 0.03 eV for **2CzPN**, **Cz-2CzPN**, **^{t}BuDPA-2CzPN** and **PXZ-2CzPN**,

respectively. The absence of solvent reorganisation to stabilize the excited state and the freezing out of the conformation of the emitter ensure that emission at room-temperature and low temperature are similar. The red shifted emission across the series is in line with that observed in solution (Figure **3.18a**).

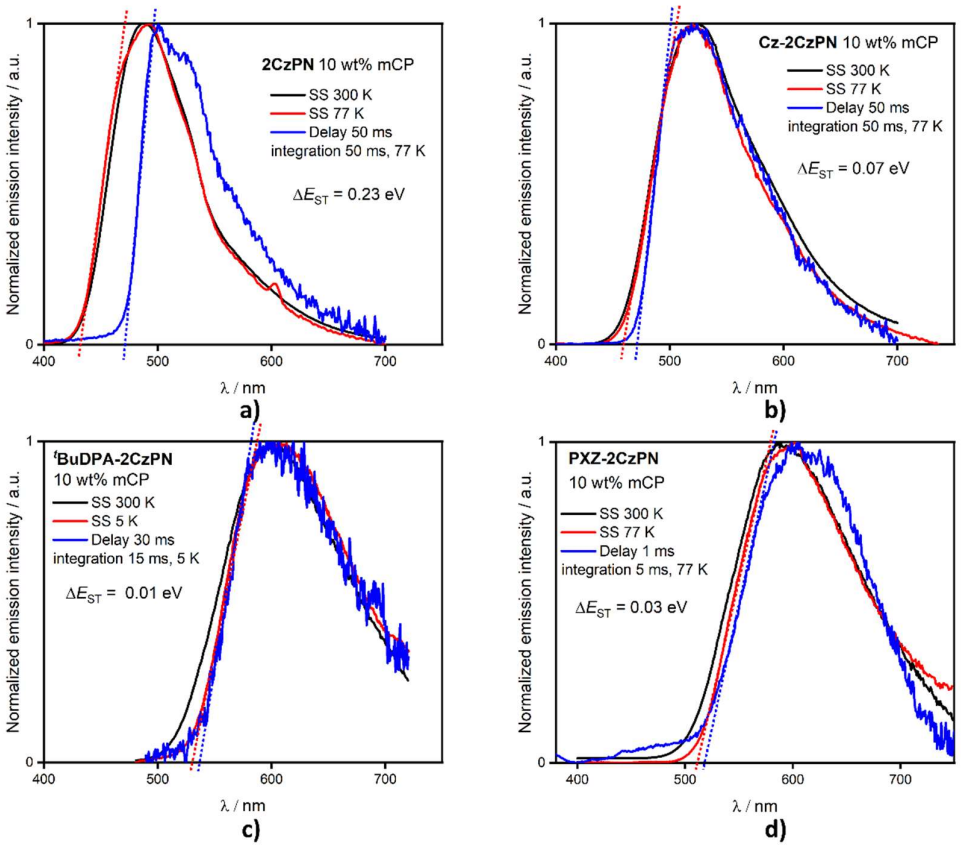

Figure **3.16**. SS emission spectra of each emitter in doped films at 300 K and 77 K (5 K for **c**) and gated emission spectra at 77 K (5 K for **c**), where dotted lines present the onset for ΔE_{ST} calculation, where **a)** is **2CzPN**, **b)** is **Cz-2CzPN**, **c)** is **^{t}BuDPA-2CzPN** and **d)** is **PXZ-2CzPN**.

Time-resolved PL decays were recorded at room-temperature (Figure **3.17**). These show a prompt and delayed component, each of which can be fitted to a mono-exponential decay (Table **3.8**). Similar τ_p were obtained for **2CzPN**, **Cz-2CzPN** and **^{t}BuDPA-2CzPN** of 16 ns, 25 ns and 10 ns, respectively, increasing to 95 ns for **PXZ-2CzPN**. Similarly to solution, a decrease in the delayed lifetime is observed upon donor extension with τ_d of 42.6 µs, 7.0 µs, 2.3 µs and 2.5 µs for **2CzPN**, **Cz-2CzPN**, **^{t}BuDPA-2CzPN** and **PXZ-2CzPN**. An increase in intensity of the delayed component with

increasing temperature evidences the TADF nature for each emitter (Figure **3.17**). Using the temperature dependence, the E_{act} was calculated for **2CzPN**, **Cz-2CzPN** and **^{t}BuDPA-2CzPN**, being 0.08 eV, 0.04 eV and 0.02 eV respectively. For **2CzPN** and **Cz-2CzPN** this was a decrease compared to spectrally determined ΔE_{ST}, calculated to be 0.23 eV and 0.07 eV, highlighting the involvement of higher lying T_{1+n} in the RISC mechanism, which were calculated to be nearby in both of these (Figure **3.4**).

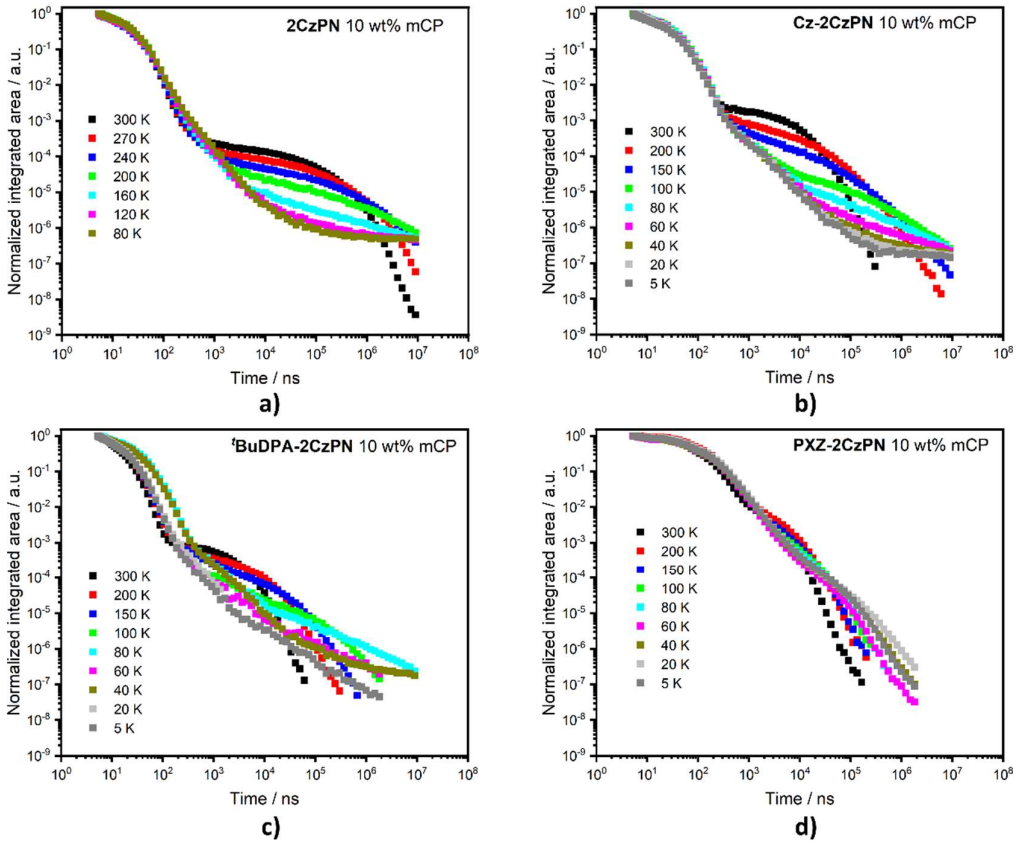

Figure **3.17**. Time-resolved PL decays of each emitter in 10 wt% mCP films at variable temperature, where **a**) is **2CzPN**, **b**) **Cz-2CzPN**, **c**) **^{t}BuDPA-2CzPN** and **d**) **PXZ-2CzPN**, λ_{exc} = 355 nm.

The Φ_{PL} values in the solid state are overall higher than those in solution, attributed to collision quenching in solution, which is not present in films. The Φ_{PL} increased to 93%, 78%, 14% and 23% for **2CzPN**, **Cz-2CzPN**, **^{t}BuDPA-2CzPN** and **PXZ-2CzPN**, respectively compared to solution which were 38%, 63%, 2% and 3%, respectively. Significant contribution to Φ_{PL} from Φ_{DF} was apparent for **2CzPN** and **Cz-2CzPN**, with Φ_{DF} of 47% and 30% respectively. Compared to solution, the Φ_{DF} of **2CzPN** in

film was much higher at 47% compared to 0.04%, owing to loss of collision quenching, which occurred in **2CzPN** in solution. The k_r is 2.9, 1.9, 1.2 and 0.2 × 10^7 s^{-1} for **2CzPN**, **Cz-2CzPN**, **^{t}BuDPA-2CzPN** and **PXZ-2CzPN**, respectively, values that show a similar trend to those in solution. The lower k_r in **PXZ-2CzPN** from decoupled ground and excited state wavefunctions contributes to the small Φ_{PL} of 23% measured for this material. As measured in solution, k_{nr} is greatest for **^{t}BuDPA-2CzPN** at 4.3 × 10^5 s^{-1} compared to 0.03, 0.60 and 3.77 × 10^5 s^{-1} for **2CzPN**, **Cz-2CzPN** and **PXZ-2CzPN**. The high value was again attributed to non-radiative pathways from molecular motion and is responsible for its low Φ_{PL} of 14%. The calculated k_{nr} in the film is slower than in solution for each material since the motion of the emitter is restricted in the film. k_{RISC} was 0.44 to 1.72, 0.69 and 1.26 × 10^5 s^{-1} for **2CzPN**, **Cz-2CzPN**, **^{t}BuDPA-2CzPN** and **PXZ-2CzPN**, respectively; however, the value for the latter two is likely misleading owing to the large k_{nr} (Table **3.9**).[109] Triplet quenching pathways proved to be detrimental to the overall Φ_{PL} for **Cz-2CzPN**, **^{t}BuDPA-2CzPN** and **PXZ-2CzPN**. This is evidenced by analysis of the triplet lifetimes (τ_{ph}) at 5 K, where **^{t}BuDPA-2CzPN** and **PXZ-2CzPN** have triplet lifetimes of 3.5 ms and 0.2 ms compared to 170 ms and 150 ms for **2CzPN** and **Cz-2CzPN**. This highlights that non-radiative decay channels of T_1 are greatest in **^{t}BuDPA-2CzPN** and **PXZ-2CzPN**. When τ_{ph} was recorded at higher temperature (80 K), it decreased to 110 ms and 60 ms for **2CzPN** and **Cz-2CzPN** respectively, with **Cz-2CzPN** undergoing a greater degree of thermally activated triplet quenching, hence its lower Φ_{PL}.

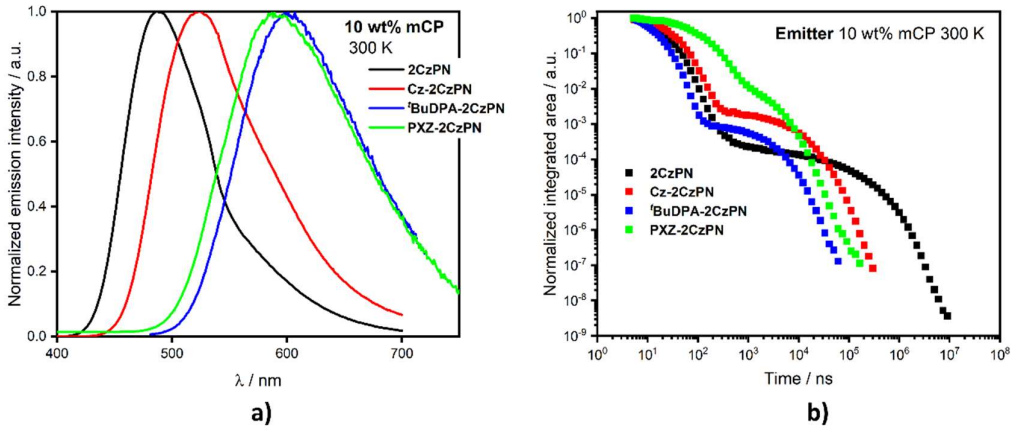

Figure **3.18**. Solid state photophysical data in 10 wt% mCP films at 300 K, where **a**) is emission spectra, λ_{exc} = 300 nm **b**) Time-resolved PL decay data, λ_{exc} = 355 nm.

Table **3.8**. Photophysical data from solid state films, with each doped in 10 wt% mCP.

Compound	λ_{PL} / nm[a]	Φ_{PL} [b] (Φ_{DF}[c]) / %	S_1 / eV [d]	T_1 / eV [e]	ΔE_{ST} / eV	E_{act} / eV	τ_{PF} / ns [f]	τ_{DF} / µs [f]	τ_{ph} / ms [g]
2CzPN	488	93 (47)	2.85	2.62	0.23	0.08	16	42.6	170
Cz-2CzPN	523	78 (30)	2.69	2.62	0.07	0.04	25	7.0	150
^{t}BuDPA-2CzPN	592	14 (1.7)	2.34[h]	2.33[i]	0.01	0.02	10	2.3	3.5
PXZ-2CzPN	603	23 (4.7)	2.40	2.37[j]	0.03	N/A	95	2.5	0.2

[a] Obtained at 300 K, λ_{exc} = 300 nm, [b] λ_{exc} = 355 nm calculated in an integrating sphere, [c] Delayed emission yield, from area under time-resolved PL decays,[d] λ_{exc} = 300 nm at 77 K, calculated from onset of steady state, [e] λ_{exc} = 300 nm at 77 K, calculated from the onset of gated emission, with 50 ms delay and 50 ms integration time, [f] λ_{exc} = 355 nm, calculated from mono-exponential fitting, [g] Phosphorescent lifetime calculated from the mono-exponential fitting at 5 K, λ_{exc} = 355 nm, [h] λ_{exc} = 300 nm at 5 K, calculated from onset of steady state, [i] λ_{exc} = 300 nm at 5 K, calculated from the onset of gated emission, with 30 ms delay and 15 ms integration time, [j] λ_{exc} = 300 nm at 77 K, calculated from the onset of gated emission, with 1 ms delay and 5 ms integration time.

Table **3.9**. Kinetic properties in 10 wt% mCP, calculated according to ref.[111]

Compound	k_r / × 10^7 s^{-1}	k_{nr} / × 10^4 s^{-1}	k_{ISC} / × 10^7 s^{-1}	k_{RISC} / × 10^4 s^{-1}
2CzPN	2.9	0.30	3.38	4.44
Cz-2CzPN	1.9	6.04	2.08	17.2
^{t}BuDPA-2CzPN	1.2	42.6	8.77	6.85
PXZ-2CzPN	0.2	37.7	0.86	12.6

3.4 Conclusions

Here, a series of **2CzPN** derivatives were synthesised containing different donor dendrons, Cz, ^{t}BuDPA and PXZ. Electrochemical analysis of the donors only, revealed unstable electrochemistry for Cz and Cz-Cz, which was mitigated with PXZ and ^{t}BuDPA substitution. Addition of the donor substituents ensured decreased ΔE_{ST} compared to the parent emitter in both solution and film, owing to increased hole and electron wavefunction decoupling, with hole density moved away from the acceptor unit. The k_r and k_{nr} were probed with **PXZ-2CzPN**, having hole and electron densities which are too decoupled. This resulted in k_r being an order of magnitude slower than the other derivatives. The large

degree of available conformations in **^{t}BuDPA-2CzPN** is responsible for the fastest k_{nr} in this material. The slow k_r in **PXZ-2CzPN** and high k_{nr} in **^{t}BuDPA-2CzPN** are evident in the low Φ_{PL} of 14% and 23%, respectively, in 10 wt% mCP. Despite the Φ_{PL} of 78% in 10 wt% mCP and a promising k_{RISC} of 1.72×10^5 s^{-1}, its overall performance was nonetheless worse than that of **2CzPN** (Φ_{PL} of 93%), this due to a thermally activated triplet decay pathway. The use of extended donors results in compounds with smaller ΔE_{ST} and faster k_{RISC}. However, there is also increased k_{nr} and this makes them unattractive materials for OLEDs with this study resulting in poorer performance upon donor substitution than the parent without donor extension. Further study to achieve the paradoxical properties of small ΔE_{ST} and high Φ_{PL} are required and will be discussed again in more detail in Chapters 6 – 8, which focus on MR-TADF emitters.

Chapter 4: Substitution Effects on a New Pyridylbenzimidazole Acceptor for Thermally Activated Delayed Fluorescence and Their Use in Organic Light-Emitting Diodes

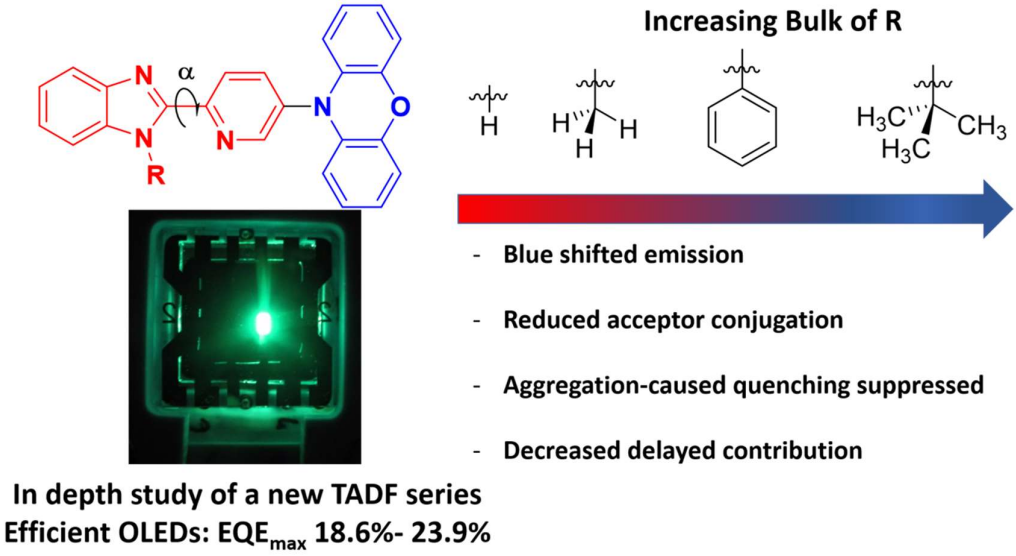

4.1 Introduction

Pyridyl benzimidazoles (BImPy) are composed of two units, both of which have been used as electron accepting units: pyridines (Py) and benzimidazoles (BIm), Figure **4.1**. Derivatives of BImPy have been reported as fluorophores,[224] or as ligands capable of coordinating to metal centres, including copper,[225] ruthenium,[164] iridium,[226] platinum[227] and f block elements such as uranium.[228] Studies of their use in excited state intramolecular proton transfer have been undertaken.[224, 229] Despite the detailed photophysical studies undertaken on BImPy and derivatives, there is only one example wherein it has been used as an emitter in OLEDs without metal centres.[230] The compound was a boron-coordinated adduct (Figure **4.1**), the devices showing blue emission from fluorescence with λ_{EL} = 450 nm.

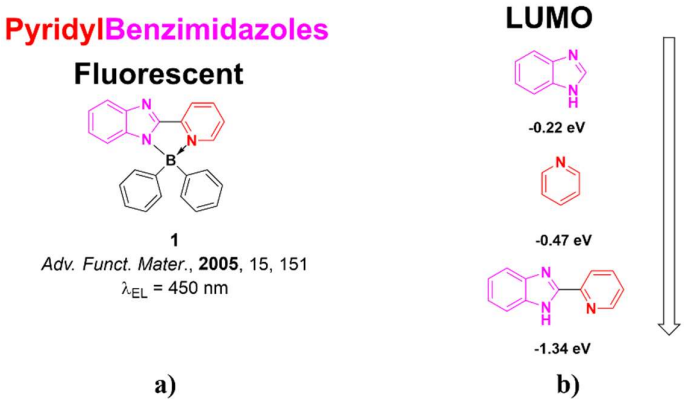

Figure **4.1**. Structure of previously reported BImPy emitter in OLEDs **a**) and changing LUMO characteristics of each component **b**).

Although the TADF properties of BImPy have not been previously reported, there are a number of literature examples of materials showing TADF that contain Py or BIm derivatives. Both Py and BIm are weak acceptors, highlighted in Chapter 1, with computationally calculated LUMO values of -0.47 eV and -0.22 eV, respectively. BImPy is a stronger acceptor as its calculated LUMO is -1.34 eV, due to the increased conjugation present in this species. Py-containing TADF emitters usually place the Py group coupled to other electron withdrawing moieties. The addition of secondary electron-withdrawing moieties include ketone, triazine and cyano groups (*vide infra.*) contribute to further stabilizing the LUMO. Currently only one example exists of pyridine being used as an acceptor on its own, **F1**, with devices with EQE_{max} of 20.6% at λ_{EL} 507 nm (Figure **4.2**). Rajamalli *et al.* reported a high performance

OLED with the emitter **3DPyM-*p*DTC** (Figure **4.2**), which contains pyridine rings within its structure.[231] Using a ketone-Py type of acceptor unit with carbazole donors, an efficient blue emitters was reported with λ_{PL} 477 nm, ΔE_{ST} 0.02, τ_d 10 μs and Φ_{PL} 98% in 7 wt% mCBP. Fabricated devices showed EQE_{max} of 31.9%, the highest of any OLED with a pyridine-containing TADF emitter, and with CIE of (0.14, 0.18) it is one of the most efficient blue TADF OLEDs. Some of the highest performing devices containing D-A TADF emitters with Py-containing acceptors are summarized in Figure **4.2**. BIm and analogues have been used as an acceptor previously; however, owing to its extremely weak accepting abilities, strong donors are required to ensure 1) sufficient HOMO-LUMO decoupling and 2) to produce a band gap in the visible regime. Strong donors used include PTZ and PXZ. A study undertaken by Oshawa *et al*. showcased the importance of strong donors,[232] where moderately efficient TADF was reported for **PXZ-BIP** (Figure **4.2**), with ΔE_{ST} of 0.22 eV, τ_d of 145 μs and EQE_{max} of 20.1%, while the weaker DMAC derivative (**Ac-BIP**) showed ΔE_{ST} of 0.43 eV, τ_d of 281 μs and EQE_{max} 2.6% (ΔE_{ST} and τ_d reported in 10 wt% DPPEO for both emitters).

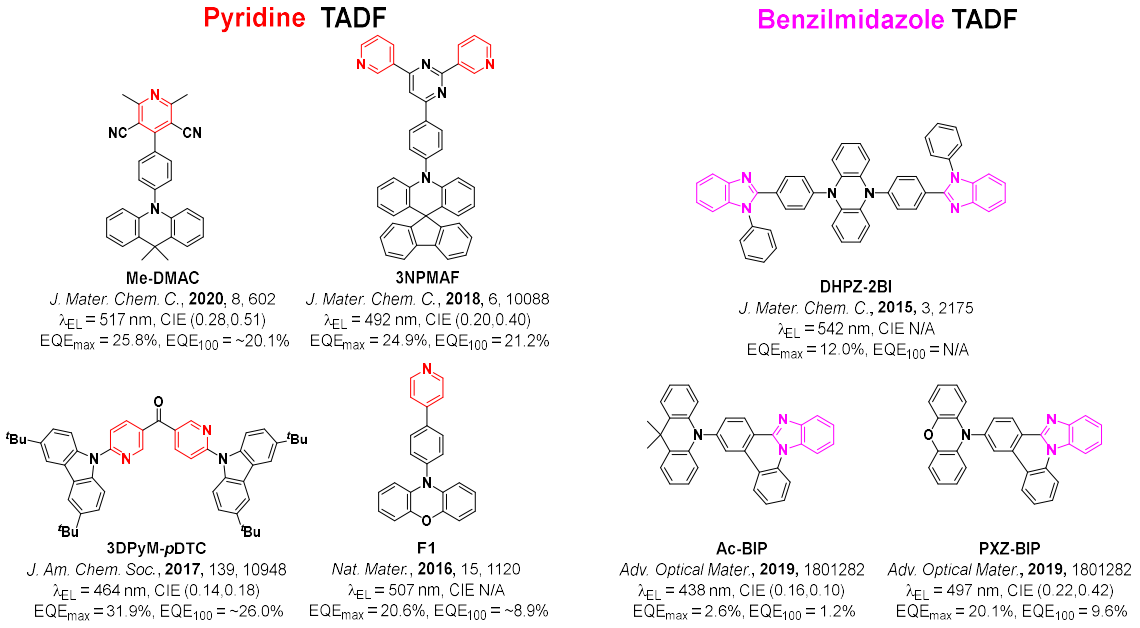

Figure **4.2**. Structures and properties of previous TADF emitters contain Py and BIm acceptor components.

4.2 Motivation and Chapter outline

In Chapter 3 a strategy to improve the performance of TADF emitters in donor-acceptor compounds using donor dendrons was presented. However, in the family of molecules studied, this strategy proved to have a detrimental impact on the photophysical properties of the emitters. In this chapter a new family of acceptors is presented based on the BImPy core and these were coupled to the strong PXZ donor. The structures of the emitters varied as a function of *N*-substitution on the BIm. The parent emitter, **BImPyPXZ**, contains no *N*-substitution, while methyl (**BIm(Me)PyPXZ**), phenyl (**BIm(Ph) PyPXZ**), and *tert*-butyl (**BIm(*t*Bu)PyPXZ**) derivatives generate ever increasing twisted conformation about the C_{BIm}-C_{Py} bond (Figure **4.3**). The increased bulkiness of these groups was introduced to study the impact of modulation of the conformation within the BImPy acceptor on the TADF efficiency. The materials were studied both computationally and experimentally. The electrochemistry and photophysics were investigated, revealing that each emitter shows TADF and that the efficiency can be controlled by the bulkiness of the *N*-substituent. Green-emitting OLEDs were fabricated using **BImPyPXZ**, **BIm(Me)PyPXZ**, and **BIm(Ph)PyPXZ**.

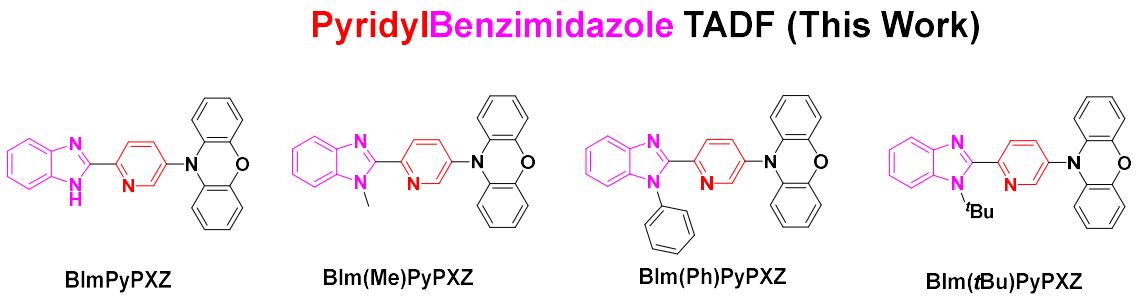

Figure **4.3**. Structures the emitters in this work.

4.3 Results and Discussion

4.3.1 Computations

Starting from BImPy acceptor unit several different donors, Cz, DPA and PXZ were modelled to ascertain a target emitter for TADF applications (Figure **4.4**). Ground state geometry optimization using DFT was performed on each of the emitters using the M06-2X functional in combination with the 6-31G(d,p) basis set. Vertical excitation calculations from the ground state geometry using TDA-

DFT with the same level of theory were also carried out.[198-175] As in Chapter 3, TDA-DFT calculations are preferentially employed with respect to TD-DFT because they address the triplet instability issue.[198] M06-2X was selected over the widely used PBE0 and B3LYP functionals since the latter two tend to over-stabilize CT excited states.[175] Along with excited state energies, the nature of the excited states was probed in terms of the degree of charge-transfer character of the excited calculated state by computing the ϕ_S metric through post-processing of the TDA-DFT calculations.[176] Details surrounding the ϕ_S metric are discussed in detail in Chapter 2. The impact of the donor strength on the TADF properties of the compounds was initially assessed (Figure **4.4**). Calculations suggested that both **BImPyCz** and **BImPyDPA** would act as fluorescent emitters as their ΔE_{ST} are very large at 0.76 eV and 0.83 eV, respectively. On the other hand, **BImPyPXZ**, shows a calculated ΔE_{ST} of 0.05 eV, and hence was the core unit investigated.

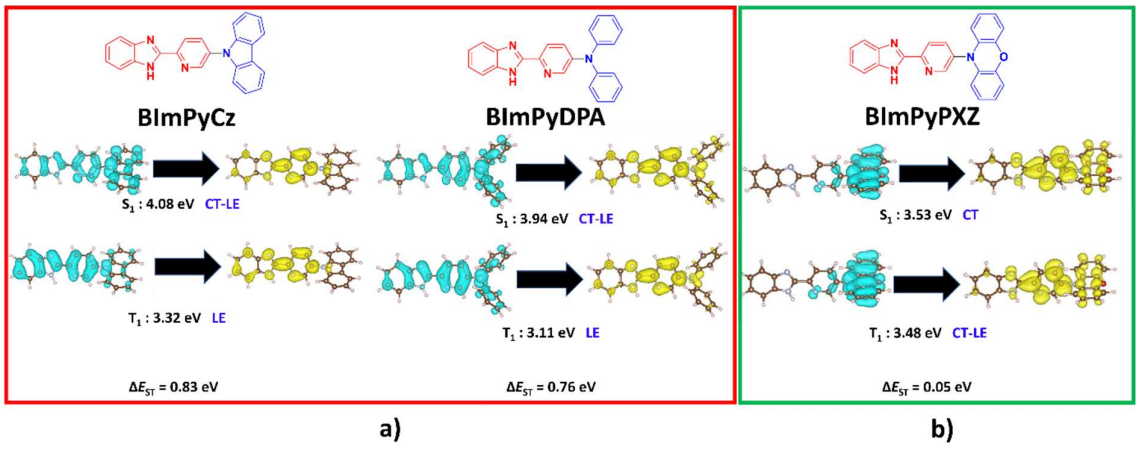

Figure **4.4**. Structures, electron (yellow) and hole (blue) plots of proposed targets. **a**) **BImPyCz** and **BImPyDPA** show large ΔE_{ST}. **b**) **BImPyPXZ** shows a small ΔE_{ST}

The impact of the nature of the *N*-substituent on the optoelectronic and device properties of **BImPyPXZ**-containing emitters was probed. In the ground state, changing the R group alters both the equilibrium torsion angle α and bond length $C_{\gamma'}$-C_{γ} (Table **4.1** and Figure **4.5**). Both **BImPyPXZ** and **BIm(Me)PyPXZ** have a predicted ground state geometry that is planar ($\alpha \sim 0°$) likely stabilized due to a combination of increased conjugation and intramolecular hydrogen bonding.[233] The weakly inductive electron-donating ability of the methyl substituent increases the LUMO energy compared to the parent

BImPyPXZ. A similar observation was reported previously for fluorescent imidazole-based emitters.[234] Owing to the larger size of the Ph and *t*Bu substituents compared to the parent and methylated structures, the torsion angle, α, deviates from the usually favourable α = 0° to 19.5° and 40.8°, respectively, which in turn disrupts conjugation between the BIm and Py heterocycles, increasing the C_{BIm}-C_{Py} bond length slightly (Table **4.1**). A consequence of this conformational change is a predicted increase in the LUMO energy. The destabilization is more pronounced in **BIm(*t*Bu)PyPXZ** as the inductively electron-withdrawing phenyl group in **BIm(Ph)PyPXZ** counteracts the decrease in conjugation due to this bulky substituent.[234] In each example there is very little change in the HOMO level, which is localized on the PXZ. LUMO density is situated in each instance on the BImPy unit (Figure **4.6**). HOMO to LUMO transitions dominate vertical excitations to the S_1 while the T_1 state is a more complex picture involving several different transitions.

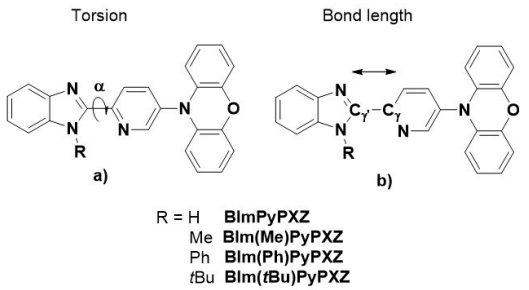

Figure **4.5**. Graphic indicating the investigated **a)** angle for torsion studies and **b)** the investigated bond length.

Table **4.1**. Calculated ground state geometric parameters and energies of HOMO and LUMO of each emitter.

Compound	**Torsion α / °**	**$C_{\gamma'}$-C_{γ} length / Å**	**HOMO / eV**	**LUMO / eV**	**$\Delta E_{H\text{-}L}$ / eV**
BImPyPXZ	0.00	1.47	-6.25	-0.86	5.39
BIm(Me)PyPXZ	0.35	1.47	-6.21	-0.79	5.43
BIm(Ph)PyPXZ	19.5	1.48	-6.20	-0.76	5.45
BIm(*t*Bu)PyPXZ	40.8	1.48	-6.23	-0.60	5.63

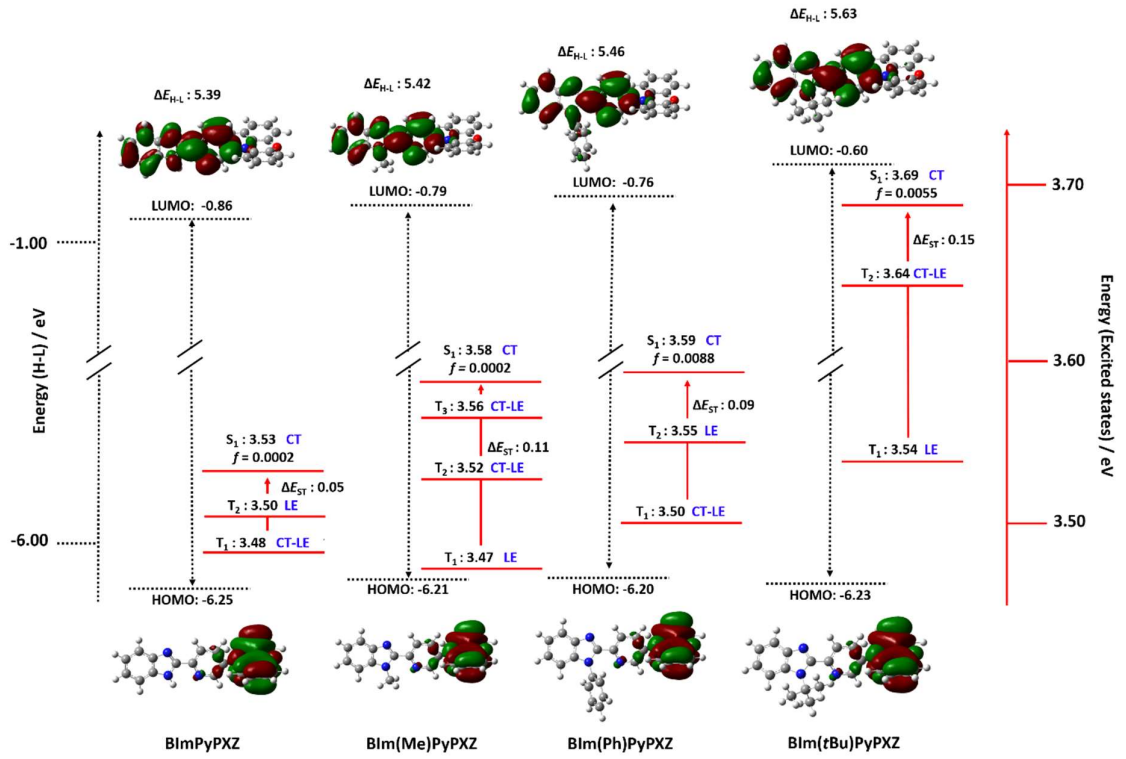

Figure **4.6**. HOMO LUMO plot and values (black) and excited state energies and assigned natures (red) for **BImPyPXZ**, **BIm(Me)PyPXZ**, **BIm(Ph)PyPXZ** and **BIm(*t*Bu)PyPXZ**.

The overall increase in the energy gap between HOMO and LUMO ($\Delta E_{H\text{-}L}$) for **BIm(Me)PyPXZ** compared to **BImPyPXZ** translates also in an increased S_1 energy level from 3.53 eV to 3.58 eV. Similarly, the S_1 energy increases from **BIm(Ph)PyPXZ** (3.59 eV) to **BIm(*t*Bu)PyPXZ** (3.69 eV). Calculated ΔE_{ST} values remain small at 0.05 eV, 0.11 eV, 0.09 eV and 0.15 eV for **BImPyPXZ**, **BIm(Me)PyPXZ**, **BIm(Ph)PyPXZ** and **BIm(*t*Bu)PyPXZ**, respectively. As discussed in Chapter 1, the TADF efficiency is governed not only by the small ΔE_{ST} but also by the magnitude of the SOC between the S_1 and T_1 states where a change in orbital type between the two states required for non-zero SOC, adhering to El Sayed's rules.[24] The excited state nature of each emitter was probed for S_1, T_1, T_2 and T_3 (Figure **4.7**). The S_1 state of each emitter is predominantly CT in nature ($\phi_S < 0.33$). This is a common occurrence for donor-acceptor TADF emitters, and this assignment is supported by their positive solvatochromism (*vide infra.*). The nature of T_1 varies, being CT-LE for **BImPyPXZ** (0.48) and **BIm(Ph)PyPXZ** (0.65), and mostly LE for **BIm(Me)PyPXZ** (0.82) and **BIm(*t*Bu)PyPXZ**

(0.76). Intermediate triplet states were modelled and were close to S_1 (Table **4.2** and Figure **4.7**). The intermediate states are of CT-LE character for **BIm(Me)PyPXZ** (0.67 and 0.57) and **BIm(*t*Bu)PyPXZ** (0.60) and LE for **BImPyPXZ** (0.82) and **BIm(Ph)PyPXZ** (0.81), which is the opposite trend to that observed for the nature of the T_1 state. These intermediate states of differing character to each other and to the S_1 state are expected to facilitate RISC due to spin-vibronic coupling.[24, 235]

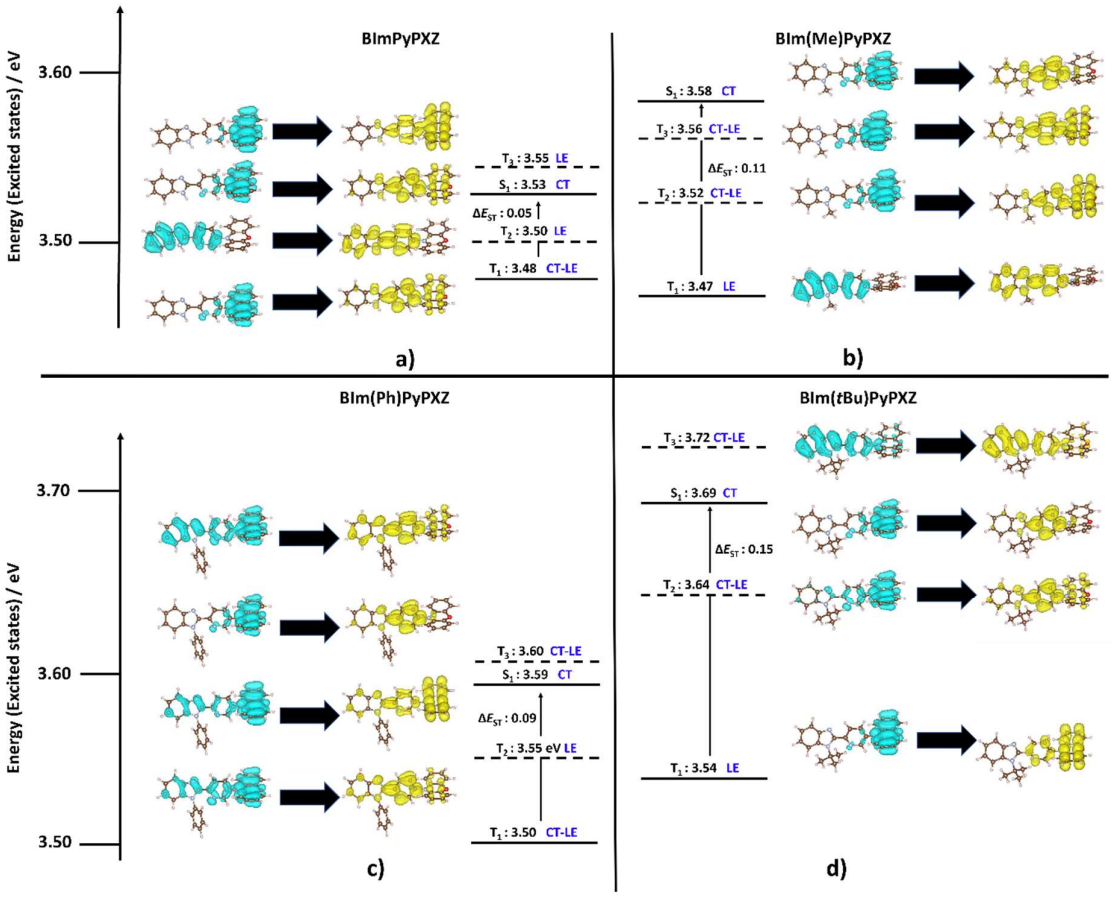

Figure **4.7**. Excited state energies and hole (blue) and electron (yellow) plots for each of the targets and the assigned nature, where CT, LE and CT-LE are charge transfer, locally excited and a combination of the two respectively, with black arrows indicating the transtions to the excited state for S_1, T_1, T_2 and T_3 of **a) BImPyPXZ, b) BIm(Me)PyPXZ, c) BIm(Ph)PyPXZ** and **d) BIm(*t*Bu)PyPXZ**.

Table **4.2**. Excited state properties of each emitter at their lowest energy ground state conformation.

Compound	S_1 (ϕ_S) / eV	*f*	T_1 (ϕ_S) / eV	T_2 (ϕ_S) / eV	T_3 (ϕ_S) / eV	ΔE_{ST} / eV
BImPyPXZ	3.53 (0.24)	0.0002	3.48 (0.48)	3.50 (0.82)	3.55 (0.71)	0.05
BIm(Me)PyPXZ	3.58 (0.24)	0.0002	3.47 (0.82)	3.52 (0.67)	3.56 (0.57)	0.11
BIm(Ph)PyPXZ	3.59 (0.28)	0.0088	3.50 (0.65)	3.55 (0.81)	3.60 (0.73)	0.09
BIm(*t*Bu)PyPXZ	3.69 (0.29)	0.0055	3.54 (0.76)	3.64 (0.60)	3.72 (0.81)	0.15

Where ϕ_S is an indication of overlap calculated, with a value of 1 = LE nature and a value of 0 = CT.

From the four emitters, several different ground state α values are reported (Table **4.1**). This prompted investigations into the accessibility of other angles α (Figure **4.8**), which might be available at room temperature. Previous studies have been undertaken, probing changing excited state properties as a function of torsion angle, with the emphasis usually on D-A torsion.[178, 236] In order to probe the significance of torsion around α the torsion potential about the C_{BIm}-C_{Py} bond was computed (Figure **4.8a**) for each emitter, varying the α dihedral angle in increments of 5°. Each conformer was reoptimized at M06-2X/6-31G(d,p) level in the ground state. Vertical excited state TDA-DFT calculations were then carried out for each ground-state conformer investigating the excited-state properties including ΔE_{ST}, emission energy and the nature of the excited states. Here a Boltzmann population distribution analysis was applied to assess the contribution at room temperature of the different conformers to the photophysical landscape (Figure **4.8**, Table **4.3**). For **BImPyPXZ**, there is a large increase in energy as conjugation is disrupted from the optimized conformation with α = 0°, with a barrier to rotation occurring at 90° at ~12 kcal/mol. There is a second, smaller rotational barrier of ~10 kcal/mol at 180° due to steric interaction between NH and CH hydrogen atoms on the adjacent heterocycles (Figure **4.8b**). The rotational profile for **BIm(Me)PyPXZ** is similar with an energy minimum at α = 0°, although the largest barrier of ~11 kcal/mol occurs at 180° due to steric hindrance between the proton and the methyl group on the Py and BIm units, respectively (Figure **4.8c**). The lowest energy conformer for **BIm(Ph)PyPXZ** occurs at α = 20° and its rotational barrier is the lowest amongst the four compounds, peaking at ~7 kcal/mol at 180° (Figure **4.8d**). Finally, the steric interactions of the *tert*-butyl group in **BIm(*t*Bu)PyPXZ** have more effect on both α, which now is 40°

for the lowest energy conformer, and the barrier to rotation, which is ~14 kcal/mol, centred at 180° (Figure **4.8e**).

The vertical excited states, S_1 and $T_{1\text{-}3}$ were computed along with their respective natures as well as the ΔE_{ST}, varying the torsion angle, α, within the ground state torsion energy potential calculated previously. From here the Boltzmann averaged electronic distribution could be calculated considering accessible conformations. Table **4.3** summarizes the conformational analysis of the Boltzmann-averaged excited state energies based on their population distribution, ϕ_S, ΔE_{ST}, oscillator strength for each emitter. When comparing Table **4.3** and Table **4.2** it is clear that changing α actually has a very minimal impact on these parameters. The standard deviations of each of the excited state energies, ϕ_S values and ΔE_{ST} were also calculated across the range of torsion angles, which are indicated by the values in brackets in Table **4.3**. We note that the standard deviations of the T_1, T_2 and S_1 excited state energies as well as their corresponding ϕ_S are small for all compounds with the exception of **BIm(*t*Bu)PyPXZ**. The excited state energies and their nature is rather insensitive with respect to the α torsion angle.

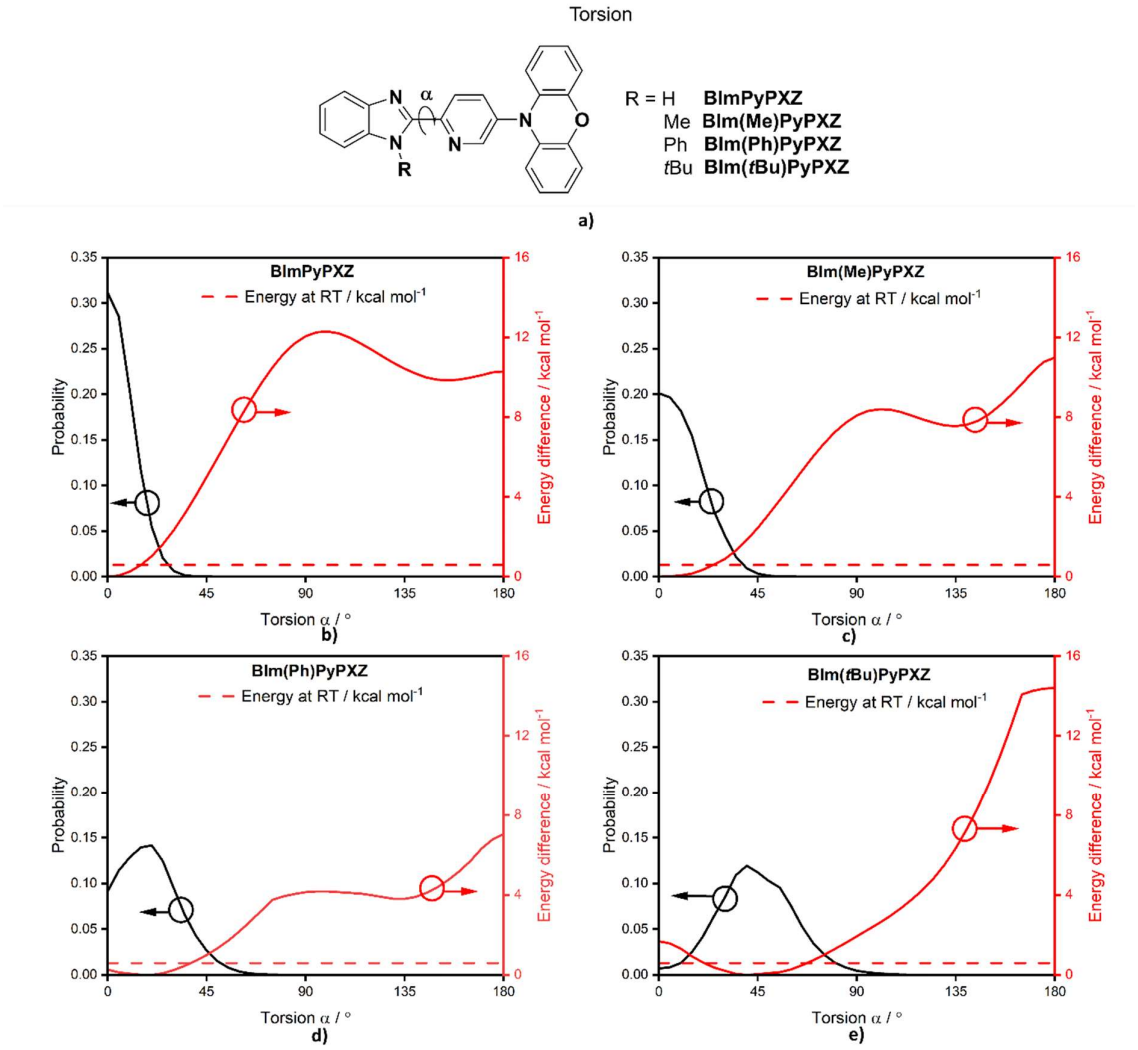

Figure **4.8**. Boltzmann probability distribution (black) and energy difference from lowest energy conformer (red) calculated around torsion α **a)** highlights the angle probed for **b) BImPyPXZ**, **c) BIm(Me)PyPXZ**, **d) BIm(Ph)PyPXZ** and **e) BIm(tBu)PyPXZ**. The dashed horizontal line represents the energy at room temperature.

Table **4.3**. Boltzmann averaged vertical excitation energies and ϕ_S values calculated over a range of conformations with α running from 0° to 180° at 5° intervals. The values in parentheses are the standard deviations on the different parameters computed.

Compound	T_1 / eV	T_2 / eV	T_3 / eV	S_1 / eV	ϕ_S T_1	ϕ_S T_2	ϕ_S T_3	ϕ_S S_1	ΔE_{ST} / eV
BImPyPXZ	3.46	3.52	3.57	3.54	0.58	0.80	0.72	0.26	0.08
	(0.02)	(0.02)	(0.02)	(0.01)	(0.07)	(0.02)	(0.02)	(0.01)	(0.02)
BIm(Me)PyPXZ	3.48	3.54	3.59	3.60	0.75	0.75	0.64	0.27	0.11
	(0.03)	(0.03)	(0.04)	(0.02)	(0.05)	(0.06)	(0.06)	(0.01)	(0.01)
BIm(Ph)PyPXZ	3.48	3.54	3.63	3.59	0.65	0.76	0.76	0.29	0.11
	(0.05)	(0.03)	(0.09)	(0.03)	(0.04)	(0.07)	(0.05)	(0.03)	(0.04)
BIm(tBu)PyPXZ	3.53	3.65	3.81	3.71	0.75	0.59	0.77	0.29	0.19
	(0.03)	(0.08)	(0.15)	(0.07)	(0.03)	(0.14)	(0.10)	(0.01)	(0.06)

4.3.2 Synthesis and crystal structures

Each of the emitters was obtained following a multistep synthesis as documented in Figure **4.9**. 5-Bromo-pyridine-2-carbaldehyde was first protected as its acetal, **6,** in an excellent yield of 95%. Protection is essential for the subsequent cross-coupling step; direct cross-coupling was not possible, which was attributed to metal binding between the oxygen and nitrogen atoms of the substrate. A Buchwald-Hartwig cross-coupling reaction installed the phenoxazine donor onto the pyridine (**7**) in a good yield of 83%. Removal of the acetal under acidic conditions afforded a red-colored compound, **PXZPyCHO**, in near quantitative yields. Functionalized 2-nitroanilines were synthesized via S_{NAr} reactions of 2-fluoronitrobenzene using aniline or *tert*-butylamine in reasonable yields of 49% and 54% respectively. Subsequent reduction afforded the relevant functionalized diaminobenzenes in good yields of 90% and 88%. Following the literature, condensation of these intermediates with **PXZPyCHO** produced **BImPyPXZ**, **BIm(Ph)PyPXZ** and **BIm(*t*Bu)PyPXZ** in yields of between 65% and 94%.[237] The last target compound, **BIm(Me)PyPXZ**, was synthesized via methylation of **BImPyPXZ** using MeI in 96% yield. Purification by temperature-gradient vacuum sublimation of the columned compounds afforded pure **BImPyPXZ**, **BIm(Me)PyPXZ** and **BIm(Ph)PyPXZ**; however, cleavage of

the *N*-*t*Bu bond in **BIm(*t*Bu)PyPXZ** occurred under these conditions, thus preventing its use in vacuum-deposited OLEDs.

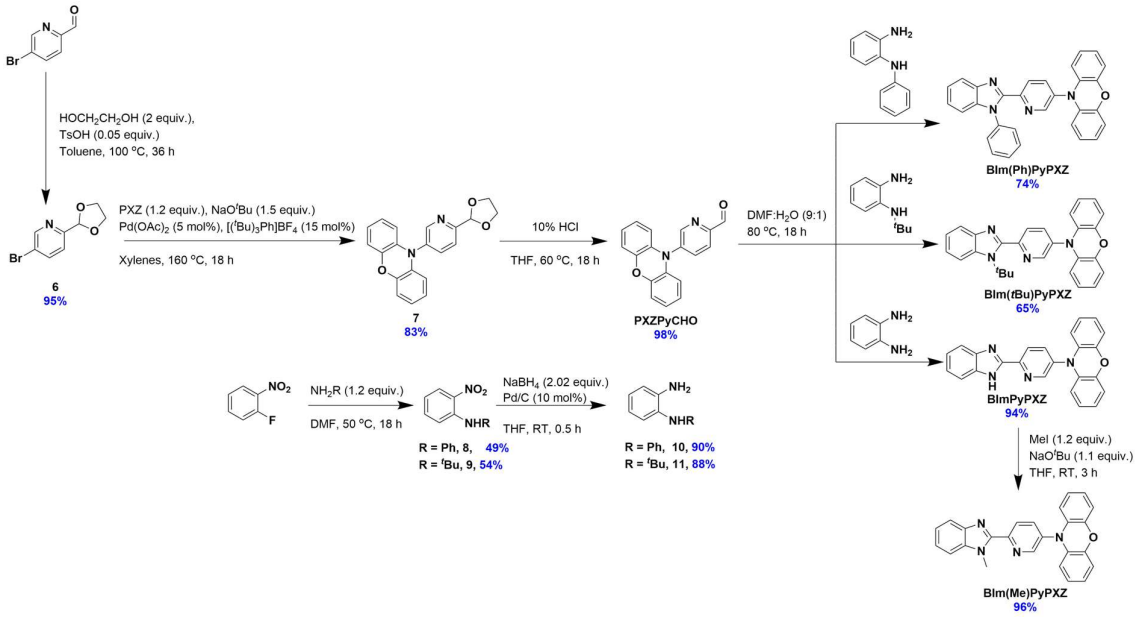

Figure **4.9.** Synthesis of the target emitters.

Crystals suitable for single crystal X-ray diffraction were grown for **BImPyPXZ**, **BIm(Me)PyPXZ**, **BIm(Ph)PyPXZ** and **BIm(*t*Bu)PyPXZ**. Both **BIm(Ph)PyPXZ** and **BImPyPXZ** were grown via slow vapor diffusion of hexane into a saturated solution of toluene, with several different **BImPyPXZ** conformers isolated hence a range of values presented. **BIm(Me)PyPXZ** was grown from a saturated solution of chloroform layered with ethanol. **BIm(*t*Bu)PyPXZ** was grown from a saturated solution of dichloromethane layered with hexane. All the structures displayed similar PXZ-Py torsions, ranging from 60.0 to 89.7°. The large torsion is often observed in TADF emitters with PXZ donors owing bulky PXZ forcing a large twist,[209] which was also observed in **PXZ-2CzPN** (see Chapter 3). Some variation did exist arising from the degree of pucker and how this interacts with the pyramidalization of the PXZ nitrogen.[238] **BIm(Me)PyPXZ** contains a planar PXZ, with π-stacking interactions occurring between co-facial PXZ groups (Figure **4.10a**), resulting in π-stacked chains along the *a*-axes. The structure of **BImPyPXZ** shows PXZ donors with a range of slightly puckered conformations (angles between PXZ phenyl ring planes 5.4 - 12.3°, Figure **4.10b** and **c**). The primary

intermolecular interactions in this compound are hydrogen bonds between imidazole moieties, giving rise to chains along the *b*-axis. In contrast, the PXZ donor in **BIm(Ph)PyPXZ** has a decidedly puckered conformation (angle between PXZ phenyl ring planes 23.0°), similar to that previously observed for phenothiazine donors.[215] In **BIm(*t*Bu)PyPXZ**, two different PXZ conformers were observed in the same structure, one with a planar PXZ (Figure **4.11e** and **f**) and the other adopting an intermediate puckered shape (angle between PXZ phenyl ring planes 16.5°, Figure **4.11**). No π-π interactions are observed between planar PXZ moieties in this compound. There is no consistent trend to suggest that particular solid-state intermolecular interactions drive a tendency for planar vs puckered PXZ groups in **BIm(*t*Bu)PyPXZ**.

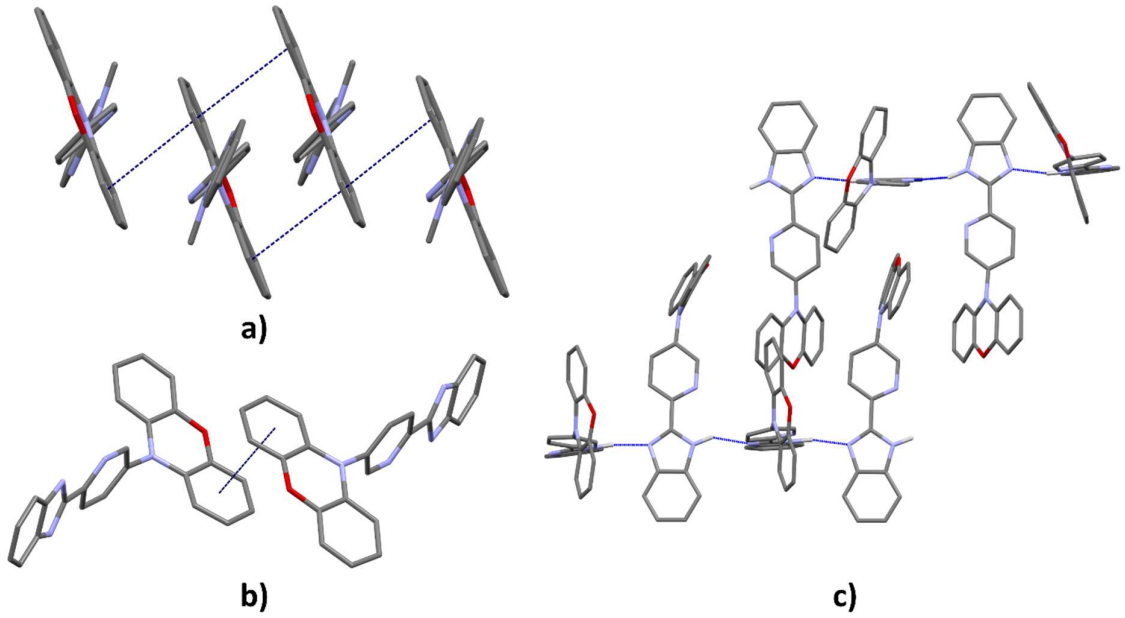

Figure **4.10**. Crystal packing regimes for **a**) **BIm(Me)PyPXZ** three-layered π-stacking motif forming chains along the crystallographic *a*-axis (hydrogens omitted for clarity), **b**) the single π-stacking interaction within the **BImPyPXZ**, with hydrogens omitted for clarity, and **c**) the one-dimensional hydrogen-bonded chains in **BImPyPXZ** along the crystallographic *b*-axis, with hydrogens not involved in hydrogen bonding omitted.

The next angle of importance is α, the torsion between the benzimidazole and the substituted pyridine (Figure **4.11**), which was also probed computationally (Figure **4.8**). This torsion will govern

the conjugation length of the acceptor. The different compounds show three ranges of torsions, broadly corresponding to the steric bulk of the *N*-substituent within the plane of the benzimidazole in line with calculations. These result in near-planar arrangements of the two rings for **BImPyPXZ** and **BIm(Ph)PyPXZ** [torsions of 1.6 - 12.4° and 4.59°, Figure **4.11b** and **d** respectively], an intermediate arrangement for **BIm(Me)PyPXZ** [torsion of 23.9°Figure **4.11c**], and the rings tending towards orthogonality for **BIm(*t*Bu)PyPXZ** (Figure **4.11e** and **f**). In most of the examples in the present study the computed value of α in the lowest energy conformation and the value of α derived from the crystal structure deviate significantly (Δα >15°), likely due to the significant influence of both intra- and intermolecular interactions in the crystal exert on the conformational landscape.

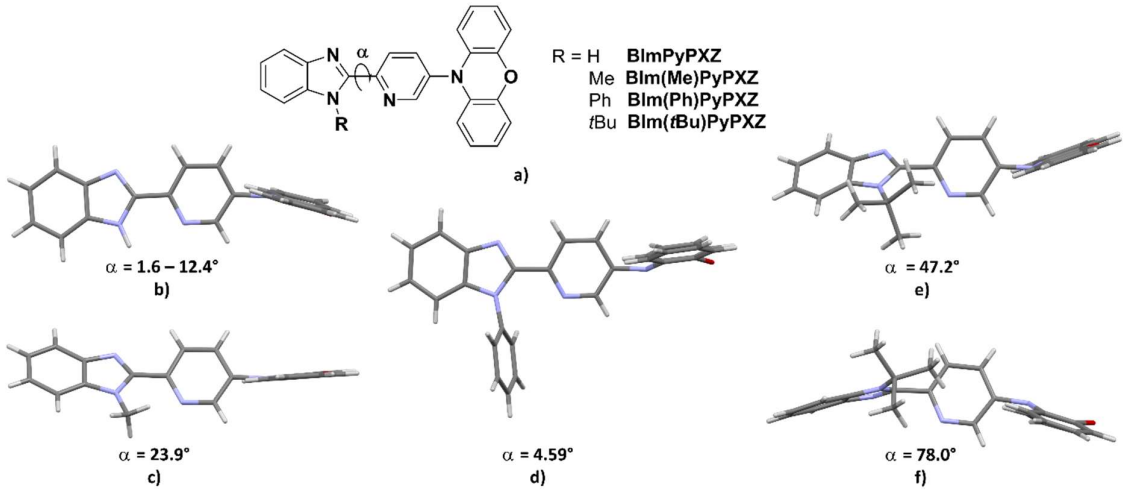

Figure **4.11**. Torsion study of crystals where **a)** highlights angle α, and single crystals of **b) BImPyPXZ**, **c) BIm(Me)PyPXZ**, d) **BIm(Ph)PyPXZ** and the two conformers obtained for **BIm(*t*Bu)PyPXZ** with **e)** planar PXZ and **f)** puckered PXZ, where angle α has been included for each.

Table **4.4**. Summary of structural and calculated lowest energy values of α and barrier to rotation calculated at M06-2X in the gas phase.

Compound	Crystal structure α / °	Lowest energy α / °	Barrier to rotation / kcal/mol
BImPyPXZ	1.6 - 12.4	0	12
BIm(Me)PyPXZ	23.9	0.35	11
BIm(Ph)PyPXZ	4.59	19.5	7
BIm(*t*Bu)PyPXZ	47.2, 78.0	40.8	14

4.3.3 Thermal properties

Thermogravimetric analysis (TGA) and differential scanning calorimetry (DSC) were performed to assess the thermal properties of the four emitters (Figure **4.12** **4.13**, and Table **4.5**). **BImPyPXZ**, **BIm(Me)PyPXZ** and **BIm(Ph)PyPXZ** showed similar TGA behavior with temperatures T_d, of 5% weight loss of 346 °C, 341 °C and 355 °C, respectively, indicative of their high thermal stability. The T_d of 276 °C is significantly lower for **BIm(*t*Bu)PyPXZ** indicating that the benzimidazole with the *tert*-butyl substituent is not thermally stable, which was also apparent during attempted vacuum sublimation.

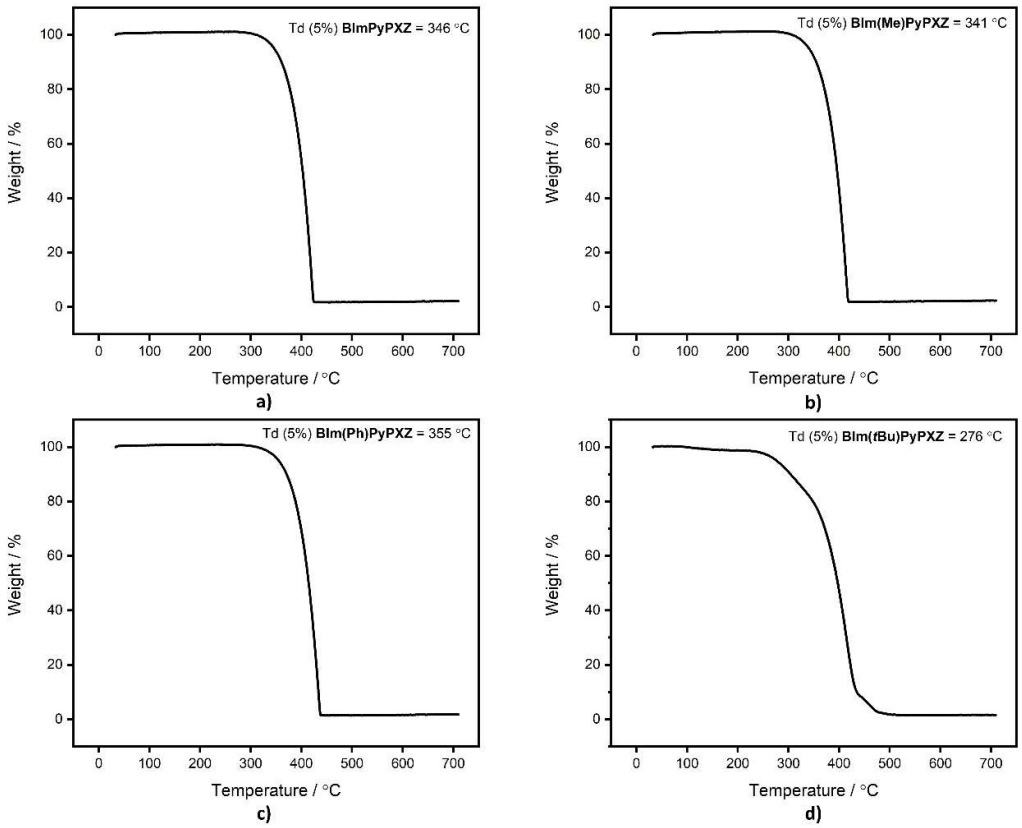

Figure **4.12**. TGA of emitters, where temperature of 5% weight loss is reported. **a**) **BImPyPXZ**, **b**) **BIm(Me)PyPXZ**, **c**) **BIm(Ph)PyPXZ** and **d**) **BIm(tBu)PyPXZ.**

BImPyPXZ shows a glass transition temperature (T_g) of 97 °C in the DSC experiment. The material recrystallizes at about 160 °C and finally melts at 260 °C. **BIm(Me)PyPXZ** exhibits a glass transition at 64 °C. Its melting behavior is rather complex and the occurrence of two melting temperatures (T_m) in the first and second heating cycle in Figure **4.13b** points to the formation of two polymorphs. This is further supported when the material is investigated using different cooling rates with slow and fast temperature ramps as shown in Figure **4.13c**. Here, the melting points of both polymorph 1 at 225 °C and of polymorph 2 at 210 °C become visible. The T_g of **BIm(Ph)PyPXZ** is 73 °C. In the first heating cycle, the material is observed to melt at 162 °C. Upon cooling, no recrystallization occurs and, subsequent heating only a T_g is observed. Due to the thermal instability of **BIm(*t*Bu)PyPXZ** the DSC experiments have to be interpreted with great care. From Figure **4.13e** only a T_g of about 80 °C can be estimated.

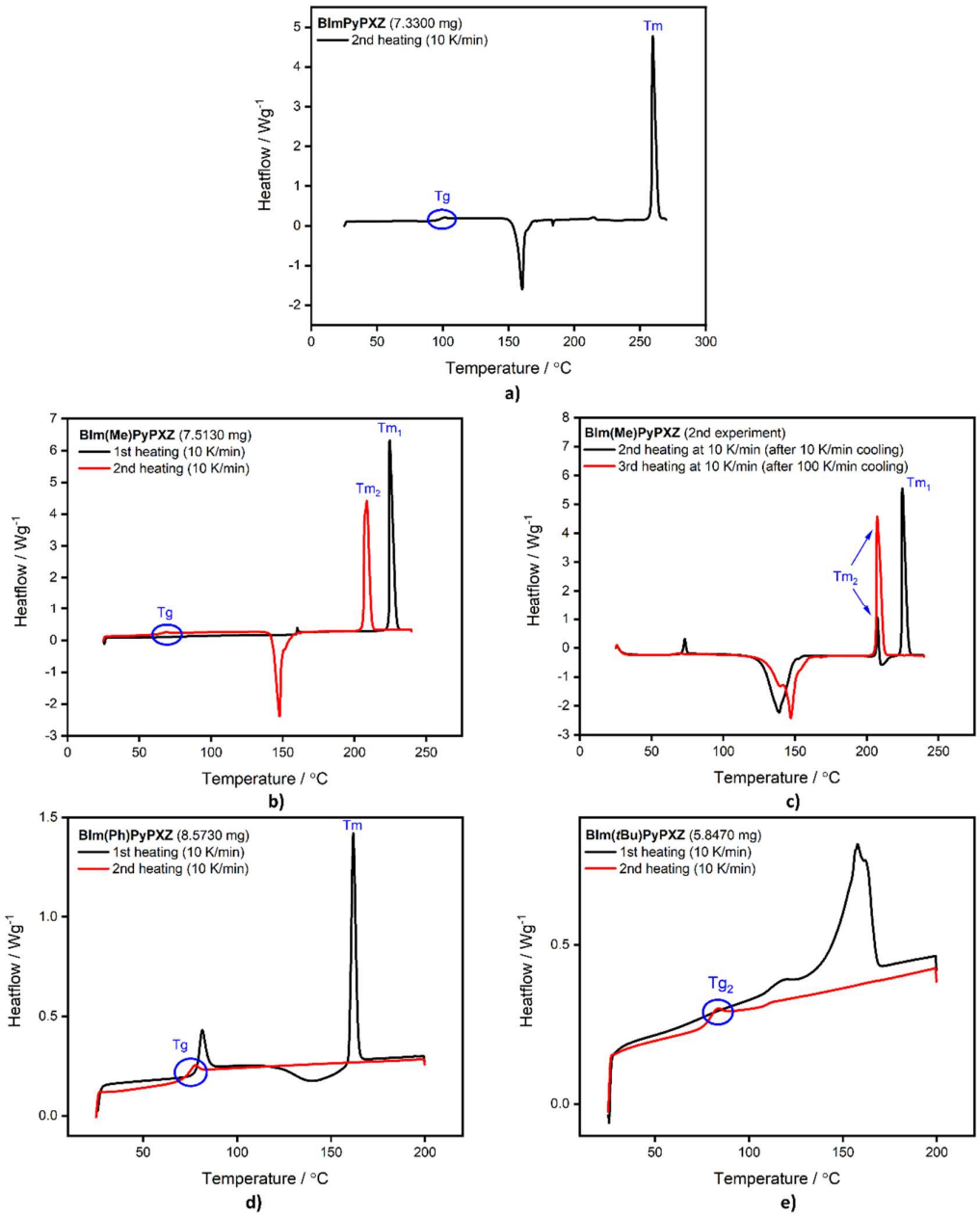

Figure **4.13**. DSC of the emitters with T_g and T_m indicated, only heating scan data is shown. Where **a**) is **BImPyPXZ**, **b**) is **BIm(Me)PyPXZ**, **c**) is **BIm(Me)PyPXZ** showing both a second heating (following a slower cooling of 10 K/min) and a third heating (following a fast cooling of 100 K/min), indicating two different crystallisations occurring, **d**) is **BIm(Ph)PyPXZ** and **e**) is **BIm(tBu)PyPXZ.**

Table **4.5.** Thermal data of powders.

Compound	T_d / °C	T_g / °C	T_m / °C
BImPyPXZ	346	97	260
BIm(Me)PyPXZ	341	64	210, 225
BIm(Ph)PyPXZ	355	73	162
BIm(*t*Bu)PyPXZ	276	ca. 80	

T_d is decomposition temperature accounting for 5% weight loss, T_g is obtained from the second scan, all performed under N_2 atmosphere.

4.3.4 Electrochemical properties

The electrochemical behaviour in MeCN of each emitter was investigated using CV and DPV (Figure **4.14** and Table **4.6**). Each of the emitters displayed nearly identical reversible oxidation waves with values between 0.74 V – 0.76 V, originating from oxidation of the PXZ donor, in line with the values obtained for PXZ on its own (E^{ox} of 0.66 V in DCM), see Chapter 3. There is negligible impact on the oxidation potential from the presence or absence of *N*-substitution on the benzimidazole acceptor, occurring almost exclusively on PXZ. Reduction waves involving the BImPy acceptor are irreversible, with the reduction potentials varying as a function of both the inductive effect of the *N*-substituent and the degree of conjugation present within the BImPy acceptor, ranging from -1.82 V to -2.22 V when conjugation is greatest in **BImPyPXZ** and smallest for **BIm(*t*Bu)PyPXZ**, respectively. The corresponding HOMO/LUMO levels are shown in Table **4.6**. The changing $\Delta E_{H\text{-}L}$ values are in good agreement with DFT (Table **4.2** and Figure **4.6**), with an increase in the gap resulting mainly from destabilization of the LUMOs while the HOMO values remain largely unchanged as these are situated predominately on the PXZ (calculated to be -6.25 eV and -6.20 eV and measured between -5.18 eV and -5.16 eV).

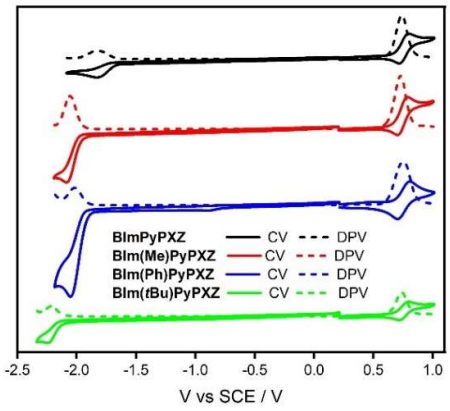

Figure **4.14.** Electrochemical data of **BImPyPXZ**, **BIm(Me)PyPXZ**, **BIm(Ph)PyPXZ** and **BIm(*t*Bu)PyPXZ** where solid lines are CV and dashed lines are DPV, scan rate = 0.05 V s^{-1}.

Table **4.6**. Electrochemical data at 300 K in degassed MeCN.

Compound	E^{ox}_{pa} [a] / V	E^{red}_{pc} [a] / V	HOMO [b] / eV	LUMO [b] / eV	$\Delta E_{H\text{-}L}$ [c] / eV
BImPyPXZ	0.74	-1.82	-5.16	-2.60	2.56
BIm(Me)PyPXZ	0.74	-2.05	-5.16	-2.37	2.79
BIm(Ph)PyPXZ	0.76	-2.02	-5.18	-2.40	2.78
BIm(*t*Bu)PyPXZ	0.74	-2.22	-5.16	-2.20	2.96

[a] In degassed MeCN with 0.1 M [nBu$_4$N]PF$_6$ as the supporting electrolyte and Fc/Fc$^+$ as the internal reference (0.38 V vs. SCE)[227] calculated from the peak maxima of DPV. [b.] The HOMO and LUMO energies were determined using the relation $E_{HOMO/LUMO} = -(E^{ox} / E^{red} + 4.8)$ eV,[220] [c.] $\Delta E_{H\text{-}L} = |E_{HOMO} - E_{LUMO}|$.

4.3.5 Solution-state photophysical properties

The UV-Vis absorption spectra in cyclohexane (CHex), PhMe, DCM and MeCN are shown in Figure **4.15**, which qualitatively agree with the simulated absorption spectra (Figure **4.16**). In PhMe (Table **4.8**), each emitter shows a low energy band around 400 nm, with molar absorptivity values, ε, of 2000 – 3000 M^{-1} cm^{-1} associated with a transition to a mixed ^{1}CT-LE state with a predominant CT character; the hole density is situated on PXZ while the electron density is located on both PXZ and Py rings (Figure **4.16**). This band in each emitter is assigned to a transition to S_3. A second high-intensity (ε of 19,000 – 35,000 M^{-1} cm^{-1}) band at between 300 and 333 nm is assigned to a LE transition with the

hole and electron densities completely localized on the BImPy unit (Figure **4.16**). This band in each emitter is assigned to a transition to S_4. Both of these absorption bands in **BIm(*t*Bu)PyPXZ** are blue-shifted with respect to the other compounds because of its more twisted conformation resulting in a decrease of the conjugation length within the acceptor group. There is also a decrease in the molar absorptivity for **BIm(*t*Bu)PyPXZ** compared to the other emitters, likewise, explained by the increasing bulkiness of the peripherical substituents when comparing **BImPyPXZ** to **BIm(*t*Bu)PyPXZ**, which is related to the more twisted conformation about the C_{BIm}-C_{Py} bond that leads to reduced conjugation and lower oscillator strength.

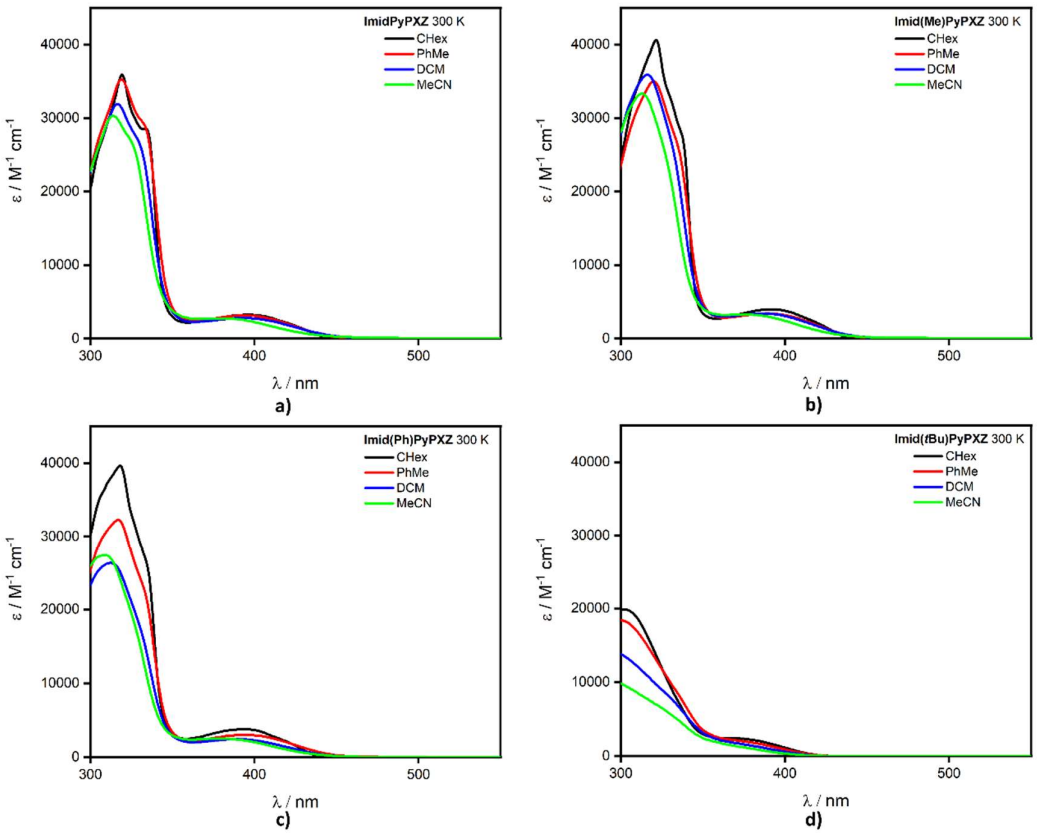

Figure **4.15**. Absorptivity spectra of each emitter in CHex, PhMe, DCM and MeCN. Where **a**) is **BImPyPXZ**, **b**) is **BIm(Me)PyPXZ**, **c**) is **BIm(Ph)PyPXZ** and **d**) is **BIm(*t*Bu)PXZ.**

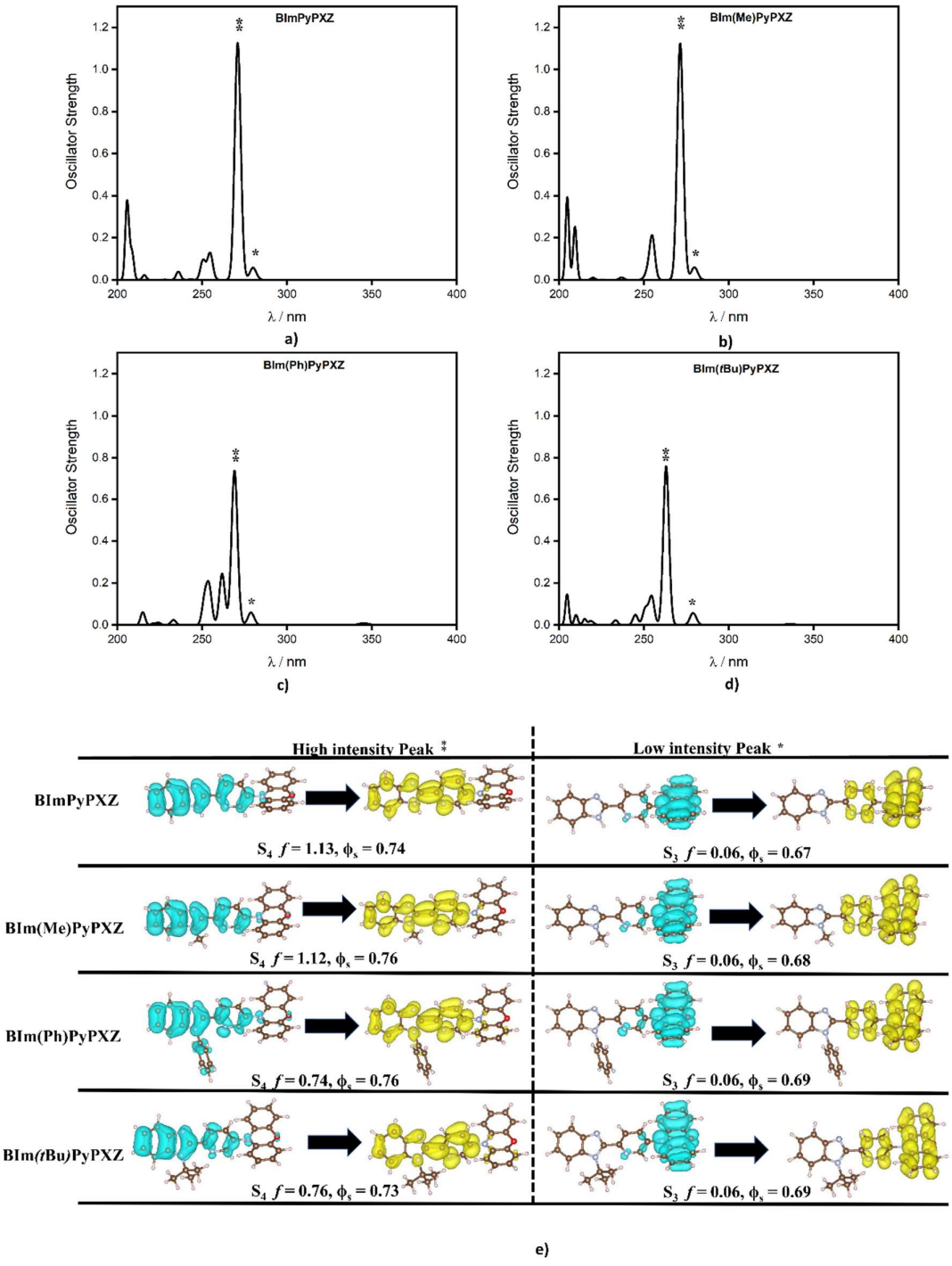

Figure **4.16.** Simulated gas-phase absorption spectra calculated at for the first 15 singlet excited states for **a) BImPyPXZ**, **b) BIm(Me)PyPXZ**, **c) BIm(Ph)PyPXZ** and **d) BIm(*t*Bu)PyPXZ** and **e)** the major transitions of interest, where blue is the electron and yellow is the hole and the arrow highlights the electronic transition.

A modest blue-shift in absorption is observed upon increasing solvent polarity for each emitter (Figure **4.15**). To probe this, solvent state specific calculations using the integral equation formalism variant of the polarizable continuum model (IEFPCM) were performed considering two solvents of significantly different polarity: MeCN and CHex to determine the solvated excited energies. In these calculations, the electronic density of the emitters and the solvent reaction field are relaxed together self-consistently. This requires calculations of the individual $S_{1\text{-}4}$ excited states, with S_3 and S_4 the states of interest here where according to simulated spectra these were the states of interest (Figure **4.16**). The observed hypsochromic shifts of these excited states is corroborated by these calculations (Table **4.7**).

Table **4.7**. S_3 and S_4 excited states calculated with solvent specific calculations

Compound	Solvent	S_3 / eV	S_4 / eV
BImPyPXZ	**CHex**	4.45	4.46
	MeCN	4.58	4.50
BIm(Me)PyPXZ	**CHex**	4.43	4.49
	MeCN	4.59	4.47
BIm(Ph)PyPXZ	**CHex**	4.44	4.53
	MeCN	4.46	4.64
BIm(*t*Bu)PyPXZ	**CHex**	4.44	4.59
	MeCN	4.48	4.83

Calculated with TDA-M06-2X/6-31G(d,p).

The photophysical properties in PhMe are summarised in (Table **4.8**) and the photoluminescence spectra shown in Figure **4.17**. The emission for each compound is broad and unstructured, indicative of an excited state with a dominant CT character. In line with computations, and consistent with the ground state optoelectronic characterization, the bluest emission at λ_{PL} = 497 nm occurs for **BIm(*t*Bu)PyPXZ**. **BImPyPXZ** shows the greenest emission at 513 nm, followed by **BIm(Ph)PyPXZ** at 509 nm and **BIm(Me)PyPXZ** at 501 nm in PhMe (Figure **4.17**). The trends in emission maxima match those calculated in the DFT study, when considering the Boltzmann-averaged population of conformations for each emitter (Table **4.3**). A minimal delayed component was observed

in toluene. The low intensity of the DF in solution was attributed to collisional quenching, minimizing triplet excited states (Figure **4.17b**).

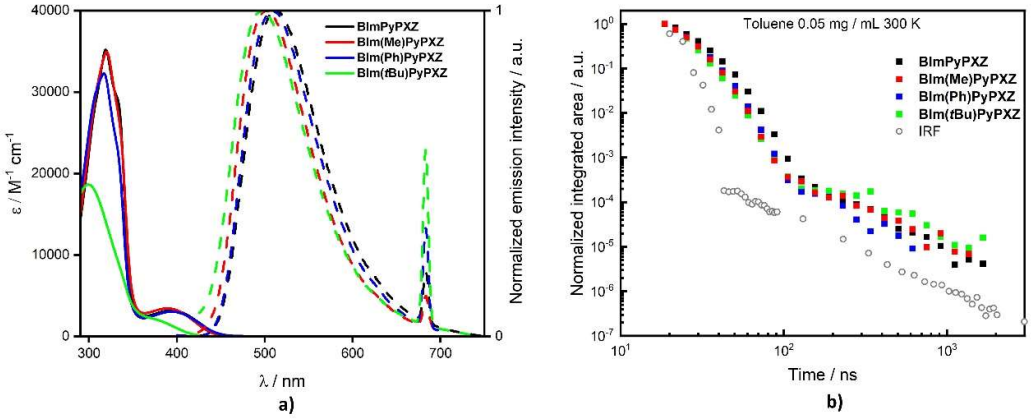

Figure **4.17.** Photophyscial data of **BImPyPXZ**, **BIm(Me)PyPXZ**, **BIm(Ph)PyPXZ** and **BIm(*t*Bu)PyPXZ** in PhMe at 300 K, where **a)** is absorption (solid) and emission (dashed), λ_{exc} = 360 nm and **b)** is lifetime, λ_{exc} = 355 nm.

Positive solvatochromism was observed, corroborating the CT assignment for the emissive excited state (Figure **4.18**). The photoluminescence quantum yields in toluene, Φ_{PL}, range between 25% and 40%. It is speculated that the lowest Φ_{PL} observed for **BIm(*t*Bu)PyPXZ** is associated with a higher non-radiative decay rate towards the ground state, in line with the broader distribution of conformations accessible at room temperature along with its smaller oscillator strength linked to slower radiative decay rates.

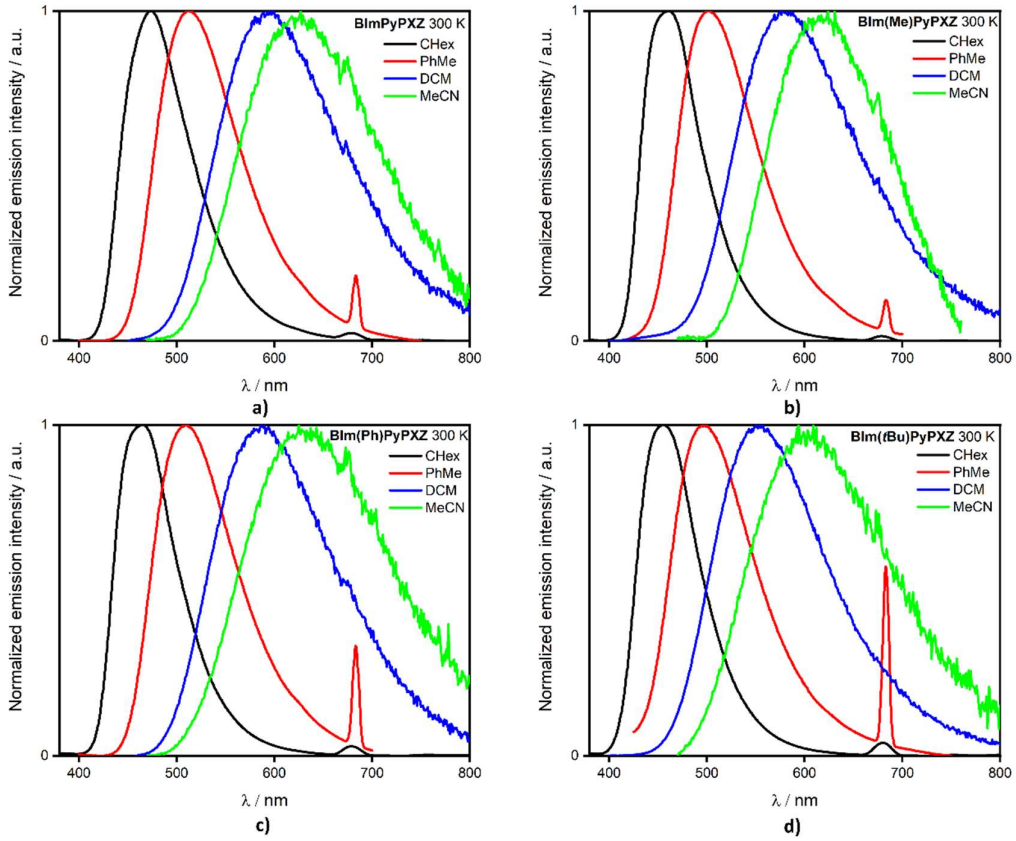

Figure **4.18**. Solvatochromic study of each emitter in CHex, PhMe, DCM and MeCN, where the sharp peak centred around 680 nm is due to the second harmonic oscillator peak. λ_{exc} = 340 nm for CHex and PhMe, 360 nm for DCM and 390 nm for MeCN. Where **a**) is **BImPyPXZ**, **b**) is **BIm(Me)PyPXZ**, **c**) is **BIm(Ph)PyPXZ** and **d**) is **BIm(*t*Bu)PyPXZ.**

The ΔE_{ST} values were determined from the difference in onset energies of the fluorescence and phosphorescence spectra recorded at 77 K (Figure **4.19**). Owing to phosphorescence dominating the SS emission at 77 K, fluorescence at 77 K was inferred by subtracting the gated phosphorescence emission from SS at 77 K. ΔE_{ST} values are larger for **BIm(Me)PyPXZ**, **BIm(Ph)PyPXZ** and **BIm(*t*Bu)PyPXZ**, with values of 0.29 eV, 0.23 eV and 0.33 eV, respectively, while for **BImPyPXZ** ΔE_{ST} is much smaller at 0.12 eV (Figure **4.19** and Table **4.8**). Although the values recorded are larger than those predicted using TDA-DFT, the trends are manifestly the same (Table **4.2**).

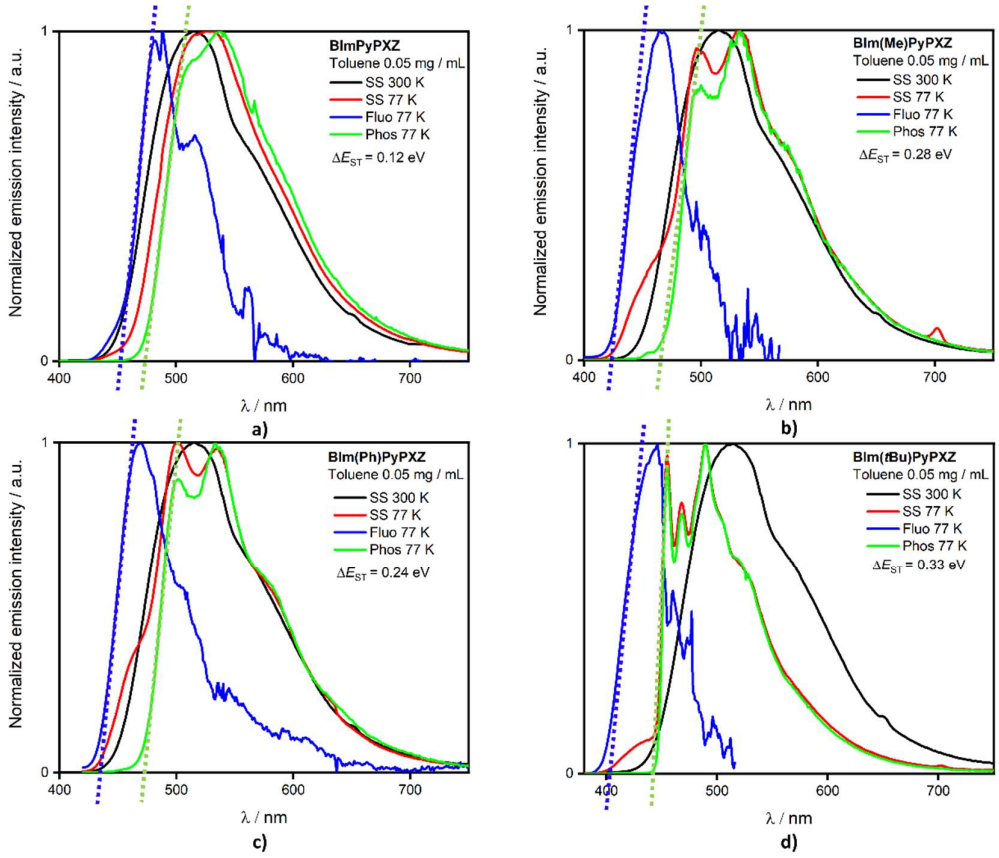

Figure **4.19**. ΔE_{ST} measurements for each emitter in PhMe, where Phos 77 K has gate = 2 ms, window = 10 ms. Fluo 77 K was obtained by subtracting Phos 77 K from SS 77 K as phosphorescence dominated in each case. $\Delta E_{ST} = S_1 - T_1$ where S_1 and T_1 are calculated from the onset of Fluo 77 K and Phos 77 K (dashed lines), respectively, λ_{exc} = 380 nm. Where **a**) is **BImPyPXZ**, **b**) is **BIm(Me)PyPXZ**, **c**) is **BIm(Ph)PyPXZ** and **d**) is **BIm(*t*Bu)PyPXZ.** Where Fluo, Phos and SS are fluorescence, phosphorescence and steady state respectively.

Table **4.8**. Summary of the solution-state optoelectronic properties in PhMe.

Compound	λ_{abs}[a] / nm	λ_{PL}[a] / nm	Φ_{PL}[b] / %	S_1[c] / eV	T_1[d] / eV	ΔE_{ST}[e] / eV
BImPyPXZ	319 (35), 333 (29), 399 (3)	513	31	2.74	2.62	0.12
BIm(Me)PyPXZ	321 (35), 392 (3)	501	36	2.93	2.64	0.29
BIm(Ph)PyPXZ	317 (32), 400 (3)	509	40	2.86	2.63	0.23
BIm(tBu)PyPXZ	300 (19), 384 (2)	497	25	3.11	2.78	0.33

[a] Concentration: 1 - 2 × 10^{-5} M in PhMe, λ_{exc} = 340 nm. [b] Determined via the relative method compared to quinine sulfate as the reference (Φ_{PL} = 54.6% in 1 M H_2SO_4) under N_2, λ_{exc} = 360 nm.[239] [c] Obtained from the onset of the fluorescence spectrum at 77 K, which was determined by subtraction of the phosphorescence spectrum at 77 K from the steady-state PL spectrum at 77 K. [d] Calculated from the onset of the phosphorescence spectra (delay: 2 ms, window: 10 ms integration, λ_{exc} = 380 nm).[e] $\Delta E_{ST} = E(S_1) - E(T_1)$.

4.3.6 Solid-state photophysical properties

With a view to fabricating OLEDs, mCP was selected as a suitable host material owing to its high triplet energy (2.9 eV) and wide HOMO-LUMO gap (HOMO = - 6.1 eV, LUMO = -2.4 eV).[223] For each emitter, a concentration screen was undertaken in order to determine the doping at which maximum Φ_{PL} occurs (Figure **4.20b**). **BImPyPXZ** displayed severe ACQ (possibly arising from its ability to form strong hydrogen bonds, which were observed in the crystal, Figure **4.10c**) with an exponential decrease in Φ_{PL} with increased doping, and so 1 wt% was used in order to maintain a high Φ_{PL}. *N*-substitution mitigated somewhat ACQ and the highest values of Φ_{PL} were obtained at 7 wt% doping concentration for the other three emitters (Figure **4.20**). A modest increase in Φ_{PL} for these is apparent before a decrease at 7 wt%. This increase is attributed to improved energy transfer between host and emitter at higher concentration, being inefficient at the lower concentrations, decreasing Φ_{PL}. Beyond 7 wt% ACQ dominates despite improved efficiency of emitter excitation with a steady Φ_{PL} decrease at increasing concentration. For **ImidPyPXZ** ACQ is the dominant decay pathway even at lower concentrations. The addition of bulky substituents to suppress ACQ is a known strategy.[240] Photoluminescence quantum yields of 58%, 68% and 49% were reported for 7 wt% films of **BIm(Me)PyPXZ**, **BIm(Ph)PyPXZ** and **BIm(*t*Bu)PyPXZ**, respectively, while the Φ_{PL} is 60% for the 1 wt% doped film of **BImPyPXZ**. The trend in emission maxima of the 7 wt% doped films in mCP is

different to that observed in solution with **BIm(Ph)PyPXZ** exhibiting the most red-shifted emission (λ_{PL} = 517 nm), followed by **BImPyPXZ** (λ_{PL} = 513 nm), **BIm(Me)PyPXZ** (λ_{PL} = 508 nm) and **BIm(*t*Bu)PyPXZ** (λ_{PL} = 501 nm), following the trends in conjugation length observed in the crystal structures with **BIm(Ph)PyPXZ** and **BImPyPXZ** being the most conjugated due to the smallest α, followed by **BIm(Me)PyPXZ** and **BIm(*t*Bu)PyPXZ**. (Figure **4.20a**).

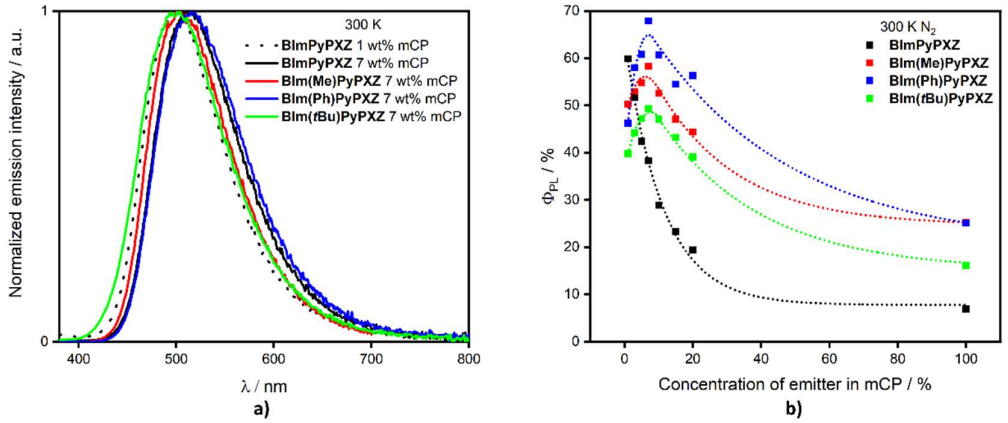

Figure **4.20**. Solid-state photophyical data of the emitters. **a**) PL spectra of spin-coated doped mCP films. λ_{exc} = 340 nm. **b**) Φ_{PL} at varying doping concentration of spin-coated mCP films under N_2. λ_{exc} = 340 nm, where fittings were applied to guide the reader to trends in Φ_{PL}.

The emission lifetime of each emitter was recorded using time-resolved PL. The PL decays at room temperature are displayed in Figure **4.21** and subsequent lifetimes and rates reported in Table **4.9**. In addition to the prompt decay, a delayed decay is visible from about 100 ns, i.e., from 0.1 μs onwards. The delayed decay is not monoexponential as we would expect from TADF behaviour. Rather, its stretched-out nature indicates a superposition of a large number of decay times. It is hypothesised that this reflects the statistical distribution of torsion angles that prevails in a disordered thin film, in line with the large number of torsions identified from DFT torsion screen (Figure **4.8**). There, molecules can be trapped in a kinetically-frozen non-equilibrium geometry as opposed to a solution, where molecules can adopt their preferred equilibrium geometry. Correspondingly, the decay of the DF is not characterized by a single individual decay time, but rather by a mean value, calculated according to

$\tau_{d,avg} = \int I(t) \cdot t\, dt / \int I(t)\, dt$ and listed in Table **4.9**.[16] The introduction of the substituent leads to an average lifetime that is about 2-3 times that of the unsubstituted parent compound **BImPyPXZ**.

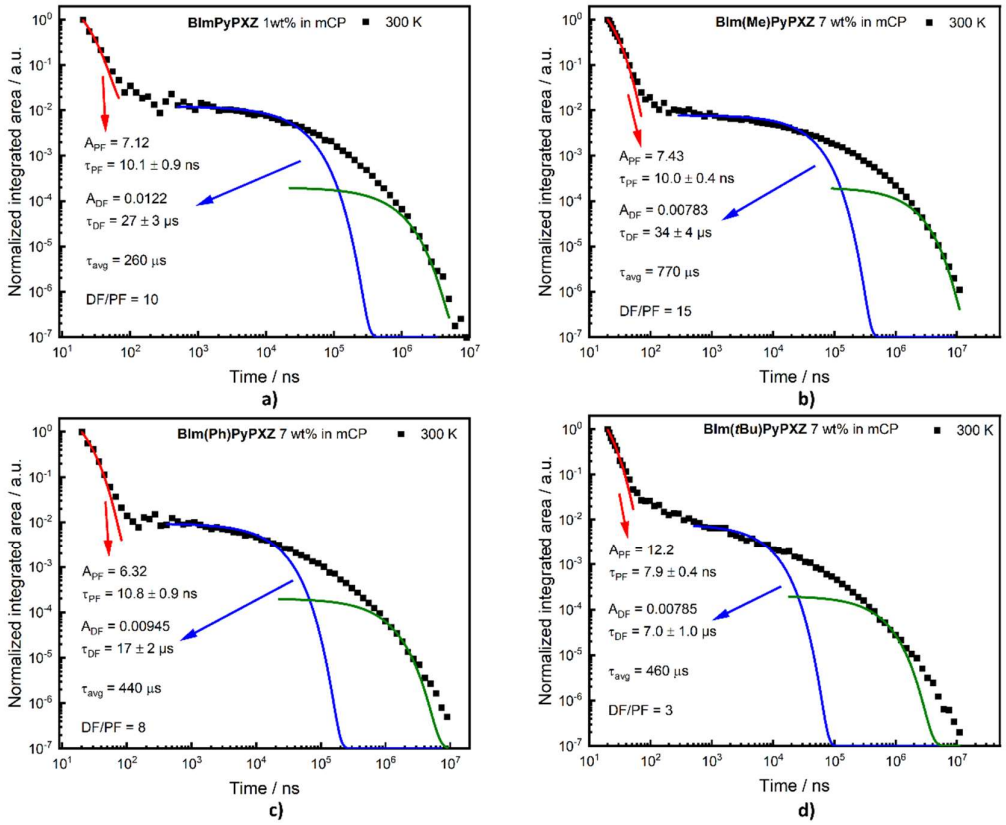

Figure **4.21**. Room temperature PL decay of **a**) **BImPyPXZ**, **b**) **BIm(Me)PyPXZ**, **c**) **BIm(Ph)PyPXZ** and **d**) **BIm(*t*Bu)PyPXZ** in mCP, λ_{exc} = 355 nm. Also shown are the prompt decay (red line), shortest monoexponential fit to the DF that is possible, $I(t) = A_{DF}\, exp\left(-\frac{t}{\tau_{df}}\right)$, as a blue line along with the pertinent fit parameters. The longest possible monoexponential fits with A_{DF}=0.0002 is also given as green line for reference.

The shortest exponential decays in the distribution are indicated by a blue line in Figure **4.21**, and their overall contribution to the DF intensity is listed in Table **4.9**. The value of the longest-lived component would depend on how low intensities one wishes to consider. The decays with an initial intensity fraction of 0.02% have lifetimes around 1 ms and are indicated in by a green line in Figure **4.21** for reference. This distribution of lifetimes reflects a distribution of RISC rates. If RISC rates are

calculated on the basis of the measured lifetimes, then the average DF lifetimes imply average RISC rates in the range of 10^{3-4} s^{-1} for all compounds. The highest RISC rates obtained from the shortest lifetime contributions are around $5\pm1 \times 10^5$ s^{-1} for all compounds. These were calculated according to equations presented by Masui *et al.*[111] (see Chapter 1 for detail). The average k_{RISC} values are 4.02, 2.05, 1.98 and 0.75×10^4 s^{-1} for **BImPyPXZ**, **BIm(Me)PyPXZ**, **BIm(Ph)PyPXZ** and **BIm(*t*Bu)PyPXZ**, with substitution decreasing k_{RISC} . The shortest decays are about 10-60 times shorter than the average decay times and similar for all compounds except **BIm(*t*Bu)PyPXZ**, which is notably shorter at 6 µs. As this compound also has a lower Φ_{PL}, this particular shorter lifetime is mainly due to an increased non-radiative decay due to its higher torsional degree of freedom and reduced oscillator strength (Figure **4.8e**). Superimposed spectra at 10 µs and 1 ms were identical which ruled out possible RTP which may have accounted for the long and variable lifetime at 300 K (Figure **4.22**).

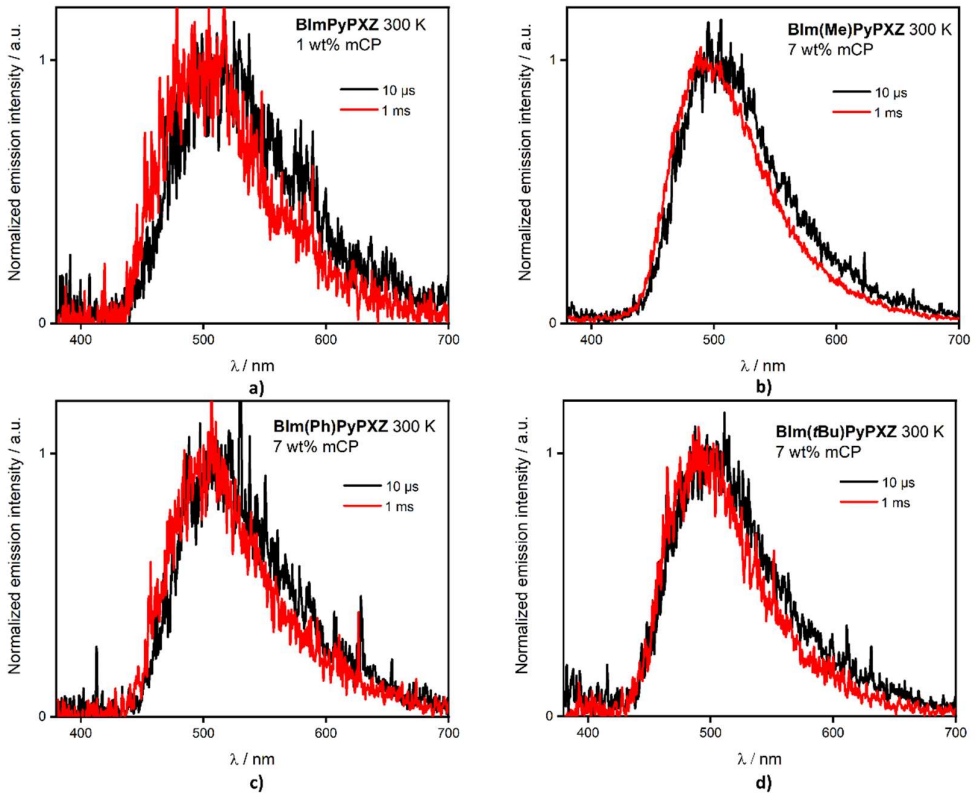

Figure **4.22**. Emission spectra in doped films at 300 K at 10 µs and 1 ms, λ_{exc} = 355 nm, where **a**) is **BImPyPXZ** 1 wt% in mCP, **b**) is **BIm(Me)PyPXZ** 7 wt% in mCP, **c**) is **BIm(Ph)PyPXZ** 7 wt% in mCP and **d**) **BIm(*t*Bu)PyPXZ** in 7 wt% mCP.

The delayed emission is temperature-dependent, showing the expected increase with rising temperature that is indicative of TADF (Figure **4.23**). The ΔE_{ST} values were calculated from the difference in onset energies of the fluorescence and phosphorescence spectra recorded at 77 K (Figure **4.24**) and range between 0.21 eV [for **BIm(Me)PyPXZ**] and 0.32 eV [for **BIm(*t*Bu)PyPXZ**]. The differences in trends for ΔE_{ST} in mCP compared to both PhMe and DFT calculations are likely due to different populations of conformers in each medium.

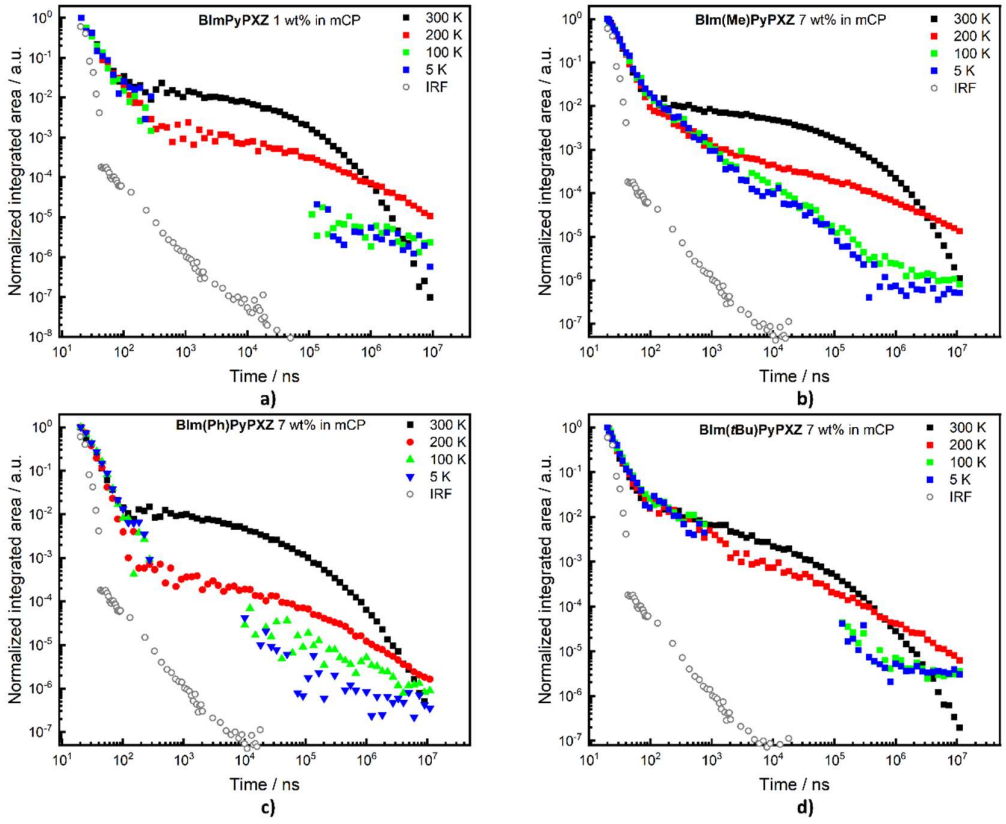

Figure **4.23**. Temperature-dependent time-resolved PL in doped mCP films, λ_{exc} = 355 nm. **a)** 1 wt% **BImPyPXZ** in mCP **b)** 7 wt% **BIm(Me)PyPXZ** in mCP **c)** 7 wt% **BIm(Ph)PyPXZ** in mCP **d)** 7 wt% **BIm(*t*Bu)PyPXZ** in mCP., where IRF is the instrument response function.

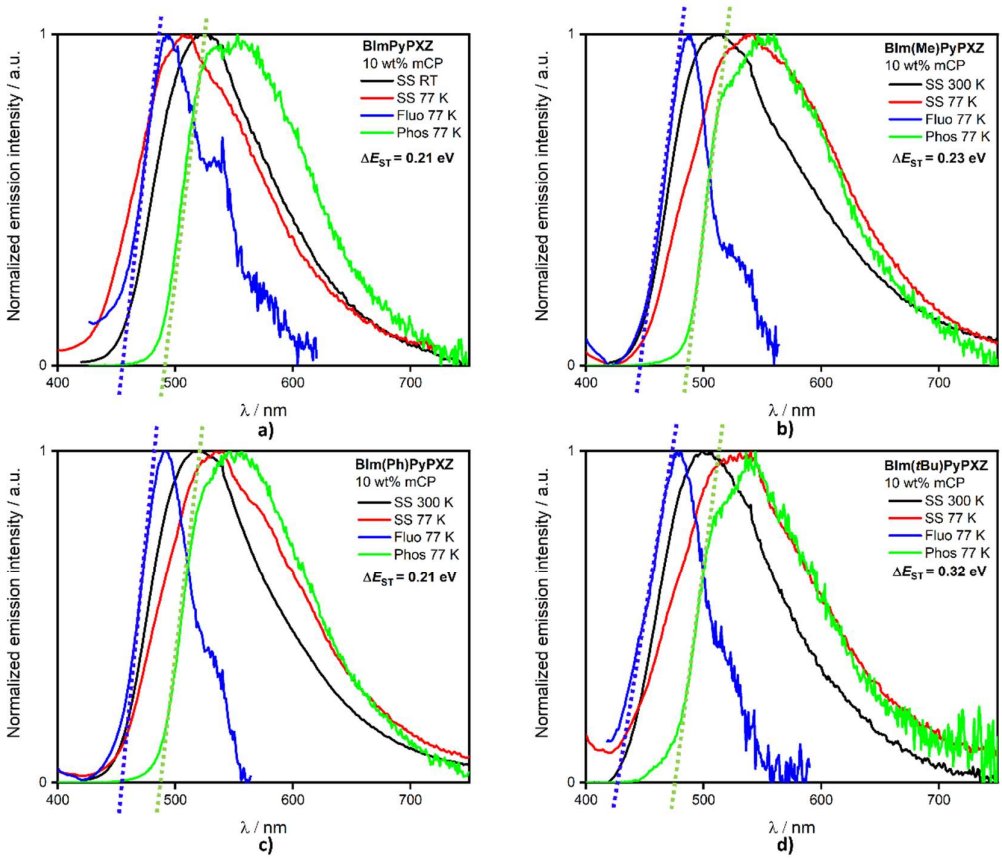

Figure **4.24**. ΔE_{ST} measurements for each emitter in 10 wt% mCP, where Phos 77 K has gate = 2 ms, window = 10 ms. Fluo 77 K was obtained by subtracting Phos 77 K from SS 77 K as phosphorescence dominated in each case. $\Delta E_{ST} = S_1 - T_1$ where S_1 and T_1 are calculated from the onset of Fluo 77 K and Phos 77 K (dashed lines), respectively, $\lambda_{exc} = 380$ nm. Where **a**) is **BImPyPXZ**, **b**) is **BIm(Me)PyPXZ**, **c**) is **BIm(Ph)PyPXZ** and **d**) is **BIm(*t*Bu)PyPXZ**.

Table **4.9**. Summary of the solid-state optoelectronic properties in spin-coated doped films in mCP.

Compound	λ_{PL}[a] / nm	Φ_{PL}[b] (Φ_{DF}) / %	S_1[c] / eV	T_1[c] / eV	ΔE_{ST}[d] / eV	τ_p[e] / ns	$\tau_{d,avg}$[f] / µs	τ_{short}[g] / µs	k_{ISC}[h] / × 10^7 s^{-1}	k_{RISC}[i] / × 10^4 s^{-1}	k_{RISC}[j] / × 10^5 s^{-1}
BImPyPXZ[k]	501 (513[l])	59.3 (53.9)	2.77	2.56	0.21	10.1	260	27 (44%)	9.37	4.02	3.91
BIm(Me)PyPXZ[l]	508	58.3 (54.7)	2.79	2.56	0.23	10.0	770	34 (25%)	9.64	2.05	4.57
BIm(Ph)PyPXZ[l]	517	67.9 (60.4)	2.76	2.55	0.21	10.8	440	17 (30%)	8.56	1.98	5.12
BIm(tBu)PyPXZ[l]	501	49.3 (37.0)	2.95	2.62	0.33	7.9	460	7.0 (21%)	11.1	0.75	4.91

[a] λ_{exc} = 340 nm, [b] determined using an integrating sphere. λ_{exc} = 340 nm, [c] S_1 and T_1 calculated from onset of the fluorescence spectrum at 77 K and the phosphorescence spectrum (delay: 2 ms; window: 10 ms integration) at 77 K, where the fluorescence was inferred by subtracting the phosphorescence spectrum from the steady-state PL spectrum, [d] ΔE_{ST} = E(S_1) – (T_1), [e] Calculated from mono-exponential fitting, [f] Calculated as the average lifetime, according to $\tau_{d,avg} = \int I(t) \cdot t \, dt / \int I(t) \, dt$, [g] monoexponential component of the lifetime distribution, along with its contribution to the overall DF signal in %. [h] Calculated from ref,[111] [i] calculated from ref[111] from average delayed lifetime, [j] calculated from ref[111] from shortest delay [k] 1 wt% emitter in mCP, [l] 7 wt% emitter in mCP.

4.3.7 Device properties

Owing to their promising photophysical behaviour, vacuum-deposited OLEDs were fabricated for **BImPyPXZ**, **BIm(Me)PyPXZ** and **BIm(Ph)PyPXZ**. Due to the instability of the emitter upon sublimation, devices containing **BIm(*t*Bu)PyPXZ** were not prepared. The optimized device stack used was: ITO / TAPC (40 nm) / Tris(4-carbazoyl-9-ylphenyl)amine [TCTA] (10 nm) / Emitter:mCP (30 nm) / DPEPO (5 nm) / 1,3,5-tri(m-pyrid-3-yl-phenyl)benzene [TmPyPb] (50 nm) / LiF (1 nm) / Al, ITO is the anode, TAPC and TCTA act as hole-transporting layers, mCP is the host, DPEPO acts as a hole-blocking layer, TmPyPB is the electron-transporting material, and LiF modifies the work function of the aluminium cathode (Figure **4.25**). Four devices are presented where device **1a** contains 1 wt% **BImPyPXZ**, device **2a** contains 7 wt% **BIm(Me)PyPXZ**, device **3a** contains 7 wt% **BIm(Ph)PyPXZ**

and device **4a** contains 1 wt% **BIm(Me)PyPXZ**, the latter of which was fabricated to assess the impact of doping concentration on the performance of the OLED.

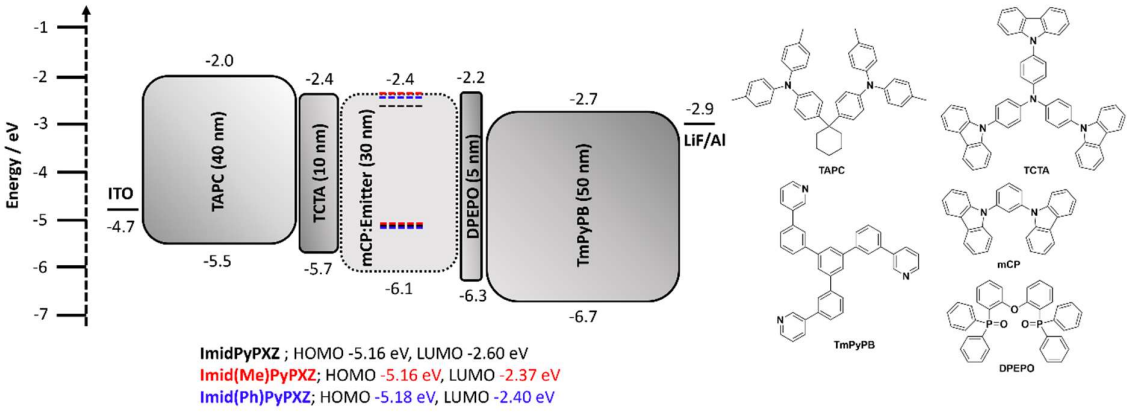

Figure **4.25**. Device architecture including energy levels for devices, and structures of materials used.

The electroluminescence spectra are shown in Figure **4.26a** and the corresponding CIE coordinates plotted in Figure **4.26b** along with device data in Table **4.10**. The λ_{EL}, match well with the corresponding λ_{PL}. Device **3a**, containing **BIm(Ph)PyPXZ**, shows the most red-shifted emission (λ_{EL} 518 nm). Excellent EQE_{max} were reported for the series of 18.6%, 23.9% and 22.2%, respectively, for **BImPyPXZ** (1 wt% mCP), **BIm(Me)PyPXZ** (7 wt% mCP) and **BIm(Ph)PyPXZ** (7 wt% mCP) (Figure **4.26c**). As the previous Φ_{PL}s were recorded with spin-coated films, the Φ_{PL} of vacuum-evaporated films were also measured (1 wt% **BImPyPXZ**, and 7 wt% **BIm(Me)PyPXZ** and **BIm(Ph)PyPXZ** in mCP), with values of 63%, 69% and 62%, respectively. These values are similar to those obtained for spin-coated films, (60%, 58% and 68%, respectively); small differences are likely due to differences in packing in the films as a result of the two processes.[149] Considering these values and assuming 100% charge recombination and a maximum outcoupling efficiency of 30%, the theoretical EQE_{max} for devices **1a**, **2a** and **3a** are ~19%, ~21% and ~19% respectively, indicating 100% exciton utilization efficiency and confirming the operation of TADF in the device. Each of the devices shows moderate efficiency roll-off at 100 cd m^{-2} of 24%, 19% and 13% of the EQE_{max} for devices **1a**, **2a** and **3a**, respectively. There is a more severe efficiency roll-off at 1,000 cd m^{-2}, with EQE_{1000} decreasing to 6.3%,

11.7% and 9.6%, respectively. This is due to the increased number of charge carriers, increasing the likelihood of annihilation pathways, with the long lifetimes of the triplet state exacerbating this issue.

The effect of doping concentration on the device performance was compared (devices **2a** and **4a**) where the emitter, **BIm(Me)PyPXZ**, was doped into the mCP film at 7 wt% and 1 wt%, respectively. There is a slight red-shift apparent upon increased doping that is similar to the effect observed for increased doping on the λ_{PL}, shifting from 501 nm to 511 nm when doping is increased from 1 wt% to 7 wt%. The EQE_{max} increased slightly from 21.4% to 23.9% upon increasing the doping, in line with the Φ_{PL} data (Figure **4.20**). The improved exciton harvesting at higher brightness becomes apparent when considering the maximum luminance (Lum_{max}), which is doubled for devices with 7 wt% doping, nearing 18,000 cd m^{-2}, compared to the devices with the emitter at 1 wt% doping where it was ~8,000 cd m^{-2}. A similar value was achieved for the 1 wt% **BImPyPXZ** (device **1a**), at around 8,000 cd m^{-2}. The device using **BIm(Ph)PyPXZ** showed the greatest Lum_{max}, at more than 21,000 cd m^{-2}. Higher doping provides more emitters for exciton harvesting reducing the impact of quenching pathways.

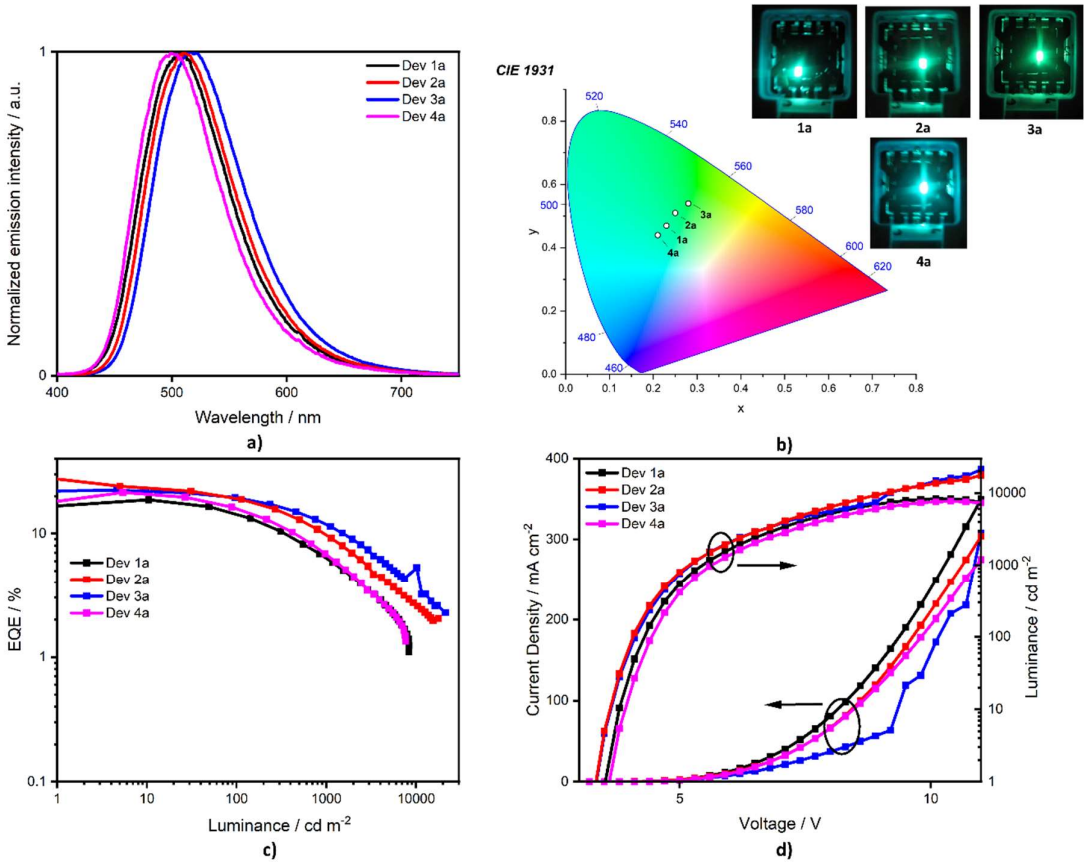

Figure **4.26**. OLED device series **a**. **a**) electroluminescence spectra. **b**) CIE coordinates. **c**) external quantum efficiency versus luminance. **d**) current density/luminance versus voltage.

Table **4.10**. Device properties of the various emitters in vacuum evaporated OLEDs.

Compound (Device)	V_{on} / V	λ_{EL} / nm	EQE_{max}; EQE_{100}; EQE_{1000} / %	Cd_{max} / A	lm_{max} / W	Lum_{max} / cd m^{-2}	CIE (8 V)
BImPyPXZ (1a [a])	3.5	508	18.6; 14.1; 6.3	50	42	8355	0.23,0.47
BIm(Me)PyPXZ (2a [b])	3.3	511	23.9; 19.3; 9.6	68	62	17711	0.25,0.51
BIm(Ph)PyPXZ (3a [b])	3.3	518	22.2; 19.3; 11.7	67	60	21227	0.28,0.54
BIm(Me)PyPXZ (4a [a])	3.6	501	21.4; 15.7; 6.6	54	45	7697	0.21,0.44

[a] 1 wt% emitter in mCP, [b] 7 wt% emitter in mCP.

4.4 Conclusions

A new acceptor unit, pyridylbenzimidazole has been introduced into the donor-acceptor TADF collection, in which varying the *N*-substitution of the benzimidazole modulates both the emission energy and mitigates against ACQ. The bulkier the *N*-substituent, the larger the torsion between the pyridine and benzimidazole rings. This has a direct consequence on ΔE_{ST}, the emission colour and k_{RISC}, with substitution having a negative impact on k_{RISC}. Efficient OLEDs were fabricated, with EQE_{max} surpassing 20% for **BIm(Me)PyPXZ** and **BIm(Ph)PyPXZ**. Functionalised derivatives allowed for high-performance OLEDs to be fabricated at increased doping, resulting in devices showing much higher maximum luminance values compared to the lower doped non-functionalized emitter. These results illustrate a family of high-performance TADF emitters.

Chapter 5: Benchmarking DFT functionals for excited states calculations of Donor Acceptor TADF emitters: Focus on energy differences and nature of the excited states relevant to Reverse Intersystem Crossing

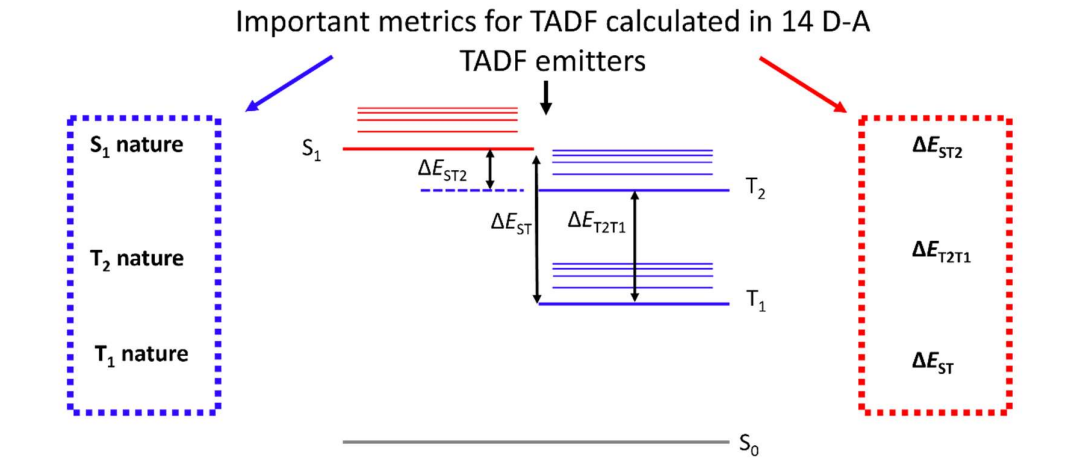

SCS-CC2 vs B3LYP, PBE0, M06-2X, LC-ωPBE, LC-ω*PBE, LC-ω*HPBE & CAM-B3LYP

M06-2X and CAM-B3LYP offer most consistent results!

5.1 Introduction

In Chapter 1 the importance of intermediate triplet states and differing natures of excited states were highlighted as key parameters to facilitate efficient k_{RISC} in D-A TADF emitters.[24, 25] A recap of the proposed mechanism for RISC involving intermediate triplet states is summarised in Figure **5.1**, with a close lying ^{3}LE state required to ensure non-vanishing SOC.

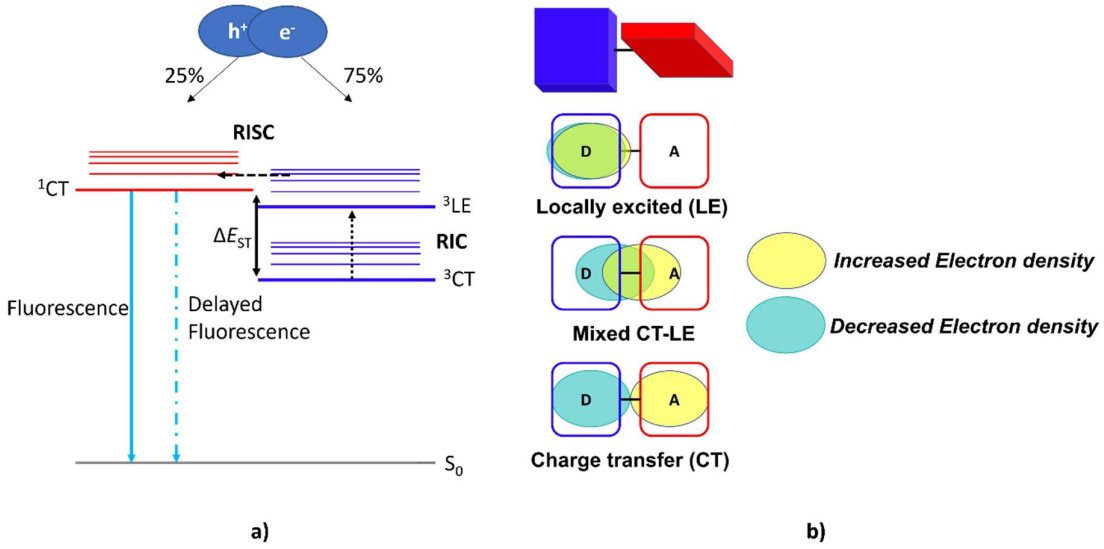

Figure **5.1**. **a**) Simplified Jablonski diagram showing a TADF mechanism involving spin-vibronic coupling to an intermediate triplet state; **b**) simplified picture of the electronic density distribution of different electronic excited states in a D-A molecule.

The energies as well as the nature of the triplet excited states participating in RISC are difficult to assess from spectroscopic measurements and are obtained from computational methods, mainly using TD-DFT. Intermediate triplet states have been invoked to explain fast k_{RISC} of 1.5×10^7 s^{-1} in 10 wt% BCPO films, with the emitter **TAT-3DBTO2** (Figure **5.2**),[125] where computationally around 12 intermediate triplet states were calculated to be within a narrow range of 0.2 eV of T_1. The high density of intermediate triplet excited states is seen as the reason for the high k_{RISC}. Efficient k_{RISC} of 1.1×10^8 s^{-1} in 10 wt% mCBP was reported for **MCz-TXT** (Figure **5.2**),[127] the fastest reported to date. The proposed mechanism inferred from calculations using ω tuned TDA-LC-BLYP involved RISC from a strongly localised T_2 state; RISC from T_1 being inefficient because of the large CT character of this

state and thus a much smaller SOC with S_1. In this compound the inclusion of sulfur also increased the SOC and thus k_{RISC} from the heavy atom effect. Wada *et al.*[241] reported a through space CT emitter, **TpAT-tFFO** (Figure **5.2**), which shows efficient k_{RISC} of 1.2×10^7 s^{-1}. High k_{RISC} was attributed to a close alignment of ^{3}CT, ^{3}LE and ^{1}CT excited states, which were calculated at TD-LC-ω*PBE/6-31G(d) level of theory. High k_{RISC} of 1.5×10^7 s^{-1} was reported for **5Cz-TRZ** by Cui *et al* (Figure **5.2**).[72] The extremely efficient rate here was rationalized in terms of the different natures of S_1 and T_1, confirmed by natural transition orbital calculations, and the small ΔE_{ST} of 0.02 eV. The authors also suggested a second route involving T_2, which was calculated to be 0.24 eV higher than T_1. Furthermore, this T_2 state also showed differing nature compared to S_1, resulting in a large SOC value here between T_2 and S_1. The picture presented in these literature examples largely supports the presence of pure CT and LE states. Recently, using a combination of molecular dynamics (MD) and excited state calculations using TDA-DFT, Olivier *et al.*[176] demonstrated that the nature of the excited states is often more complex, often mixed between CT and LE.

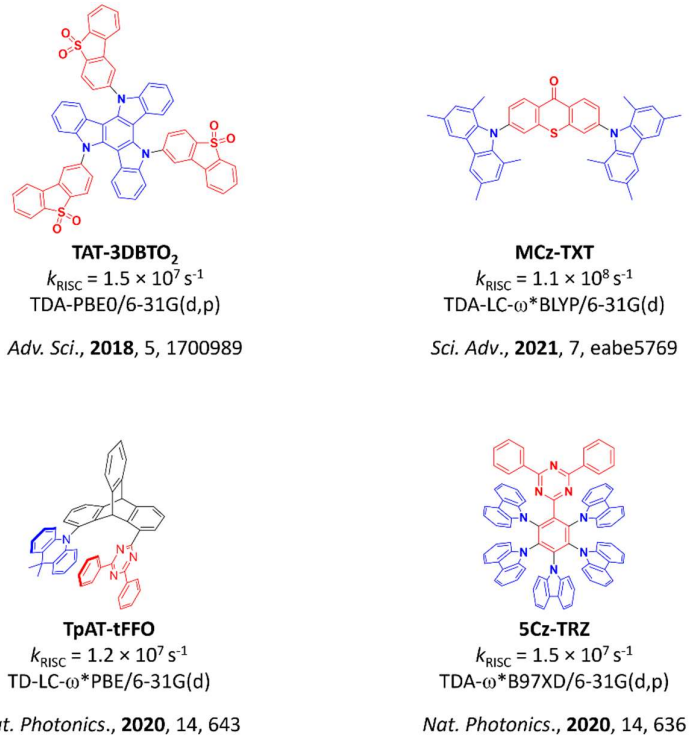

Figure **5.2.** Structures, experimental k_{RISC} values and the DFT method employed to compute the T_1, T_2 and S_1 excited states energies for TADF in these literature-reported emitters.

In each of these examples, different TD-DFT methodologies are employed to determine both the excited state energies and their nature (Figure **5.2**). This is often biasing the interpretation of the experimental data and so the overall picture of the TADF mechanism.[175, 198] Benchmark computational studies, which focused on the comparison of the energies of the excited states (and thus ΔE_{ST}) computed using different DFT functionals are a useful tool to guide functional choice, several have been undertaken on TADF emitters. Based on a set of six compounds, Moral *et al*.[23] showed that the use of TDA-DFT led to a more accurate prediction of ΔE_{ST}, compared to TD-DFT. Using a larger set of seventeen molecules that possess a wide range of experimental ΔE_{ST} values, Sun *et al*.[25] demonstrated that PBE0, M06-2X as well as ω-tuned range-separated functionals such as LC-ωPBE offered excellent agreement between experimental and computed ΔE_{ST}. A recent study by Kunze *et al.*[39] covering twenty-seven TADF emitters across a range of structural classes demonstrated how the use of spin-unrestricted and restricted open-shell Kohn−Sham self-consistent field calculations in combination with a polarizable-continuum can be used to compute with very high accuracy the adiabatic ΔE_{ST} (MAD of 0.025 eV). Each of these previous studies compared experimental ΔE_{ST} with the calculated values, and only considered S_1 and T_1 to evaluate the efficiency of the TADF process. The direct comparison to experiment can be problematic since experimental data are often obtained from a variety of media and parameters are determined in different ways (for example, ΔE_{ST} is often either calculated from the onsets or emission maxima). A recent study by Cardeynaels *et al.*[40] probed the modelling of intermediate triplet state, T_2, of ten D-A emitters by DFT methods and comparing the results to CC2 calculations. This study revealed that M06-2X provided the smallest MAD of 0.13 eV for the absolute energy of T_2. Beyond this one report, the comparison between the energies of higher lying triplet states computed at the TD(A)-DFT and a wavefunction-based methodology has not been undertaken.

5.2 Motivation and Chapter outline

In Chapters 3 and 4, the k_{RISC} mechanism of both series of emitters were highlighted to likely involve close lying triplet states. As mentioned in the previous sections, different computational approaches have been used to characterize the singlet and triplet excited states of TADF emitters; however, previous benchmark studies have mostly focused solely on ΔE_{ST} values until recently. In each

of these the nature of the excited states was not analysed. Here, we undertook a computational study of 14 emitters (Figure **5.3**), of varying structures and TADF properties (ΔE_{ST} of 0.01 eV – 0.22 eV and τ_d of 1.0 μs to 460 μs reported experimentally). Each of the emitters has been discussed in detail in Chapter 1.

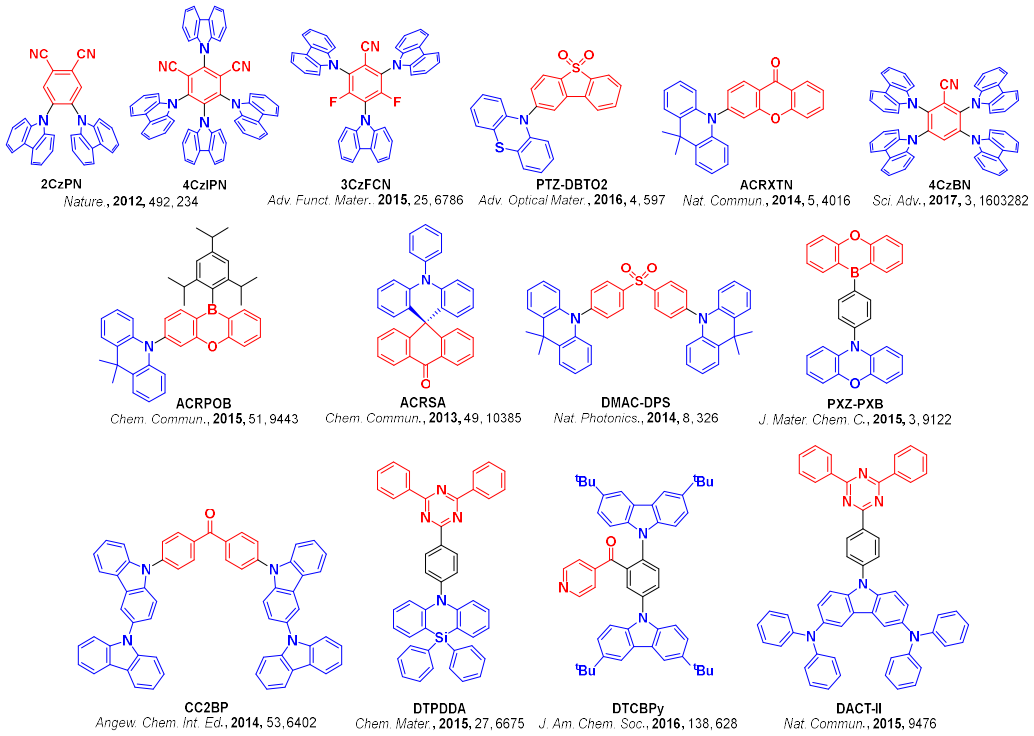

Figure **5.3**. Chemical structures of the TADF emitters in this study.

The S_1, T_1, T_2, ΔE_{ST}, the energy difference between lowest singlet and second lowest triplet excited state (ΔE_{ST2}) and the energy difference between second lowest triplet and lowest triplet and excited state (ΔE_{T2T1}) were computed at the TD-DFT and TDA-DFT levels with popular DFT functionals such as B3LYP, PBE0, M06-2X, LC-ωPBE LC-ω*PBE, LC-ω*HPBE and CAM-B3LYP, and these values cross-compared to those calculated using SCS-CC2, with MAD, RMSD and σ used to highlight the changes between the two approaches. At TD(A)-DFT, the 6-31G(d,p) basis set was used, while the SCS-CC2 calculations used the cc-pVDZ basis set as previous studies have shown its high accuracy despite its modest size.[147] Differentiating the present study from previous ones, the natures of T_1, T_2 and S_1 were compared using CT descriptors such as D_{CT}, q_{CT} and S_{+-}. These descriptors relied on

Δρ as well as ϕ_S (see Chapter 2 for details of these metrics and the computational methodologies employed). Notably, ϕ_S is not accessible from SCS-CC2 calculations and so Δρ was used as the metric comparator between TD(A)-DFT and SCS-CC2 (Figure **5.4**). M06-2X and CAM-B3LYP best reproduced the nature of the excited states that were calculated by SCS-CC2; however, the descriptions of the nature of T_1 and T_2 across the series of compounds are considerably less accurate than that of S_1. Further work in terms of functional development is required to improve the predictive accuracy of the nature of the triplet states.

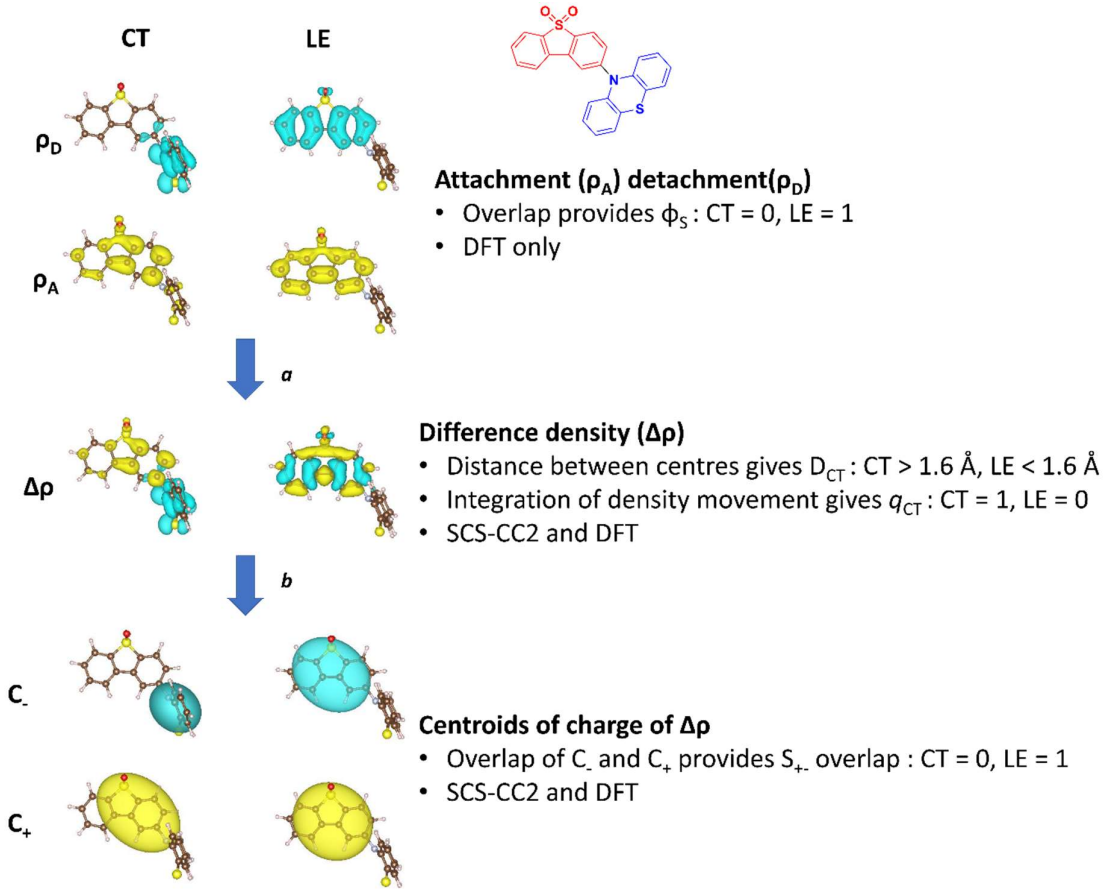

Figure **5.4**. Pictures of the electronic density associated with a given excited state and the corresponding metrics to quantify the degree of CT for a representative donor-acceptor TADF compound, **PTZ-DBTO2** using each CT descriptor. The attachment, detachment, difference density as well as the centroids of charges were all computed at TDA-CAM-B3LYP/6-31G(d,p) level of theory.

5.3 Results and Discussion

5.3.1 Excited-state energies

We started by investigating the energies of S_1, T_1 and T_2 (complete data set available in supporting information). There is an evident and consistent underestimation of the excited states energies for B3LYP and PBE0 with both TD-DFT and TDA-DFT compared to SCS-CC2. This is due to the over stabilisation of CT states, which has been widely reported,[202] and mainly arises from self-interaction errors due to the low content of HF like exchange which is evident in the large MAD values (Table **5.1**) for S_1, T_1 and T_2. For both B3LYP and PBE0 a slightly improved MAD is achieved for both triplet states using TDA-DFT compared with TD-DFT, which is due to an improved triplet character description (*vide infra*.). The S_1 state is predicted with a similar level of accuracy using either TD-DFT or TDA-DFT. Indeed, TD-DFT and TDA-DFT are formally equivalent when the excited states bear a strong CT character, as is usually observed for the S_1 state of D-A TADF materials. A smaller standard deviation is thus reported for both T_1 and T_2 than for S_1 because the exchange interaction tends to increase the LE character (decrease the CT character) of these latter states in comparison to S_1. This is further stressing the systematic overstabilization of excited states energies with strong CT obtained with low HF exchange functionals. The use of M06-2X results in vastly improved excited state energy prediction for T_1, T_2 and S_1, with a reduced MAD for each compound compared to SCS-CC2 (Table **5.1**). This is due to the increased HF like contribution in this functional, which improves the description of CT excited states, with the overstabilisation in observed in B3LYP and PBE0 not reported. Excellent agreement for both T_1 and T_2 is obtained for TDA-DFT calculations using LC-ωPBE without tuning ω, while TD-DFT calculations using the same functional largely underestimate the T_1 energies. This is likely due to the more accurate description of states with significant LE character using this functional while states with significant CT character are not well described. The ω-tuned LC-ω*PBE (LC-ω*HPBE) functionals partially address the issue observed with LC-ωPBE, leading to a decrease in T_1 and T_2 MADs, especially at the TDA-DFT level (see Table **5.1**). The MAD for S_1 is very similar for both LC-ω*PBE and LC-ω*HPBE using either TD-DFT and or TDA-DFT. The use of TDA-CAM-B3LYP results in a closer agreement with SCS-CC2 than with TD-CAM-B3LYP, which essentially

comes from an improved description of LE-dominated triplet states. The S_1 energy is also well predicted with CAM-B3LYP as this functional has been designed to more accurately describe CT states. Based on this analysis, it is clear that TDA-DFT calculations are more accurate than TD-DFT calculations. Both M06-2X and CAM-B3LYP calculations produce the smallest MAD and smallest standard deviation to the SCS-CC2 results. The summary of MAD, RMSD and σ are found in Table **5.1** and Figure **5.6**.

Table **5.1**. MAD, RMSD and σ on the energies of the investigated excited states in comparison to SCS-CC2.

	S_1 / eV			T_1 / eV			T_2 / eV		
	MAD	**RMSD**	**σ**	**MAD**	**RMSD**	**σ**	**MAD**	**RMSD**	**σ**
TD - CAM-B3LYP	0.10	0.12	0.06	0.46	0.46	0.07	0.47	0.50	0.15
TDA - CAM-B3LYP	0.10	0.13	0.08	0.12	0.14	0.08	0.15	0.17	0.08
TD - LC-ωPBE	0.56	0.61	0.25	0.76	0.77	0.09	0.82	0.83	0.16
TDA - LC-ωPBE	0.61	0.67	0.26	0.09	0.11	0.06	0.13	0.17	0.10
TD - LC-ω*PBE	0.45	0.47	0.14	0.52	0.53	0.10	0.56	0.57	0.10
TDA - LC-ω*PBE	0.43	0.46	0.14	0.46	0.48	0.14	0.48	0.49	0.11
TD - LC-ω*HPBE	0.45	0.47	0.13	0.52	0.53	0.10	0.56	0.57	0.10
TDA - LC-ω*HPBE	0.44	0.46	0.14	0.46	0.48	0.14	0.48	0.49	0.11
TD - B3LYP	1.03	1.06	0.24	0.89	0.91	0.18	0.80	0.81	0.14
TDA - B3LYP	1.03	1.06	0.23	0.89	0.90	0.17	0.76	0.78	0.17
TD - PBE0	0.85	0.88	0.21	0.77	0.78	0.12	0.74	0.74	0.11
TDA - PBE0	0.84	0.87	0.21	0.72	0.74	0.15	0.63	0.65	0.13
TD - M06-2X	0.15	0.18	0.10	0.15	0.19	0.12	0.18	0.20	0.08
TDA - M06-2X	0.12	0.14	0.07	0.12	0.16	0.11	0.12	0.14	0.08

5.3.2 Relative energy differences

We now turn to the prediction of the energy differences between excited states (Table **5.2**, Figure **5.6**), values that are relevant when ascertaining k_{RISC}. Despite the large overstabilization of the excited state energies computed with PBE0 and B3LYP at both TD-DFT and TDA-DFT, the MADs for ΔE_{ST} are small (Table **5.2**, Figure **5.6**). This is due to the similar but large MADs computed for T_1 and S_1. However, the MADs for ΔE_{S1T2} and ΔE_{T1T2} and their associated standard deviations are much larger than for the other functionals (Table **5.2**). Specifically, in five examples (**PXZ-PXB**, **PTZ-DB2OT**, **DTPDDA**, **DTCBPy** and **DACT-II**) T_2 is predicted to be higher in energy than S_1 using DFT methods while this is not observed with SCS-CC2 (Figure **5.5**). Each of these five compounds displays S_1 and T_1 states that have large CT character, both of which are stabilized compared to other low-lying excited states (*vide infra*). ΔE_{ST}, ΔE_{S1T2} and ΔE_{T2T1} computed with M06-2X (using either TDA-DFT or TD-DFT) are all very close to those computed with SCS-CC2. The smaller MAD at the TDA-DFT compared to TD-DFT is again ascribed to the former handling better the triplet instability issue.[198]

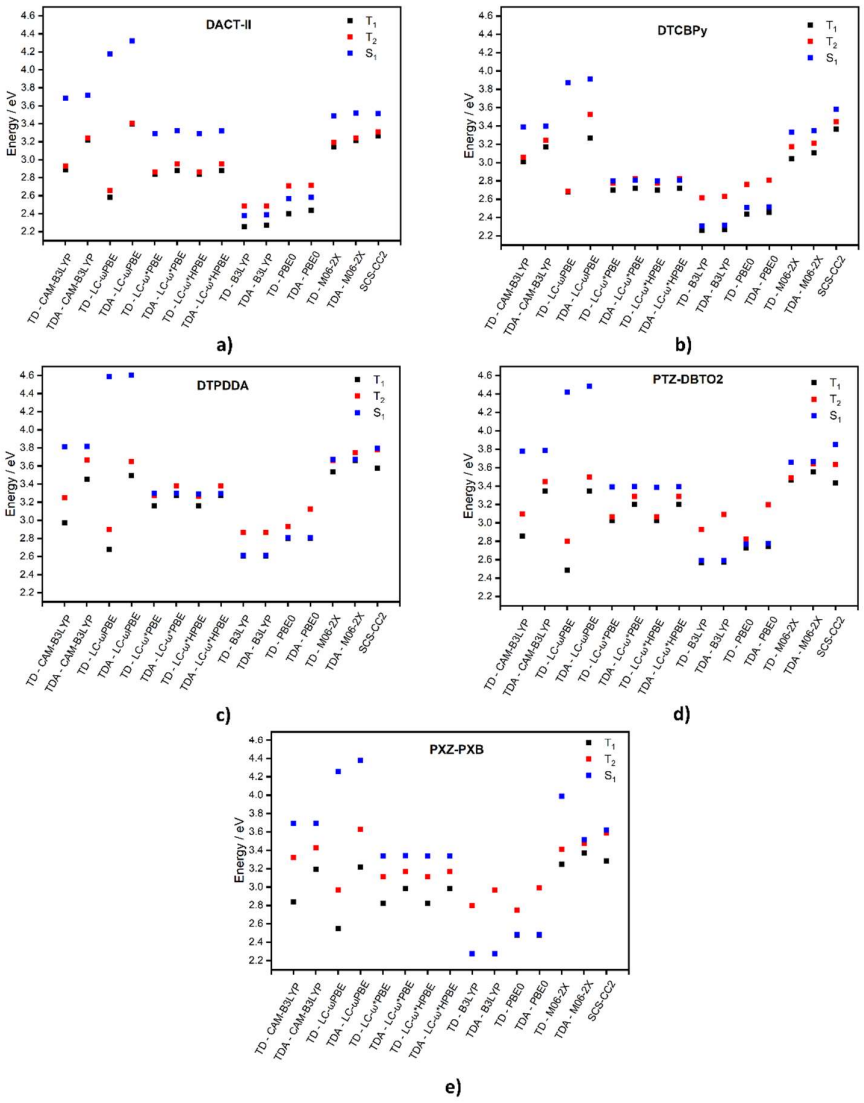

Figure **5.5**. Calculated energies of D-A TADF emitters discussed for TD(A)-DFT and SCS-CC2.

ΔE_{ST} and ΔE_{S1T2} show large MAD values when the functional LC-ωPBE is used at both TDA-DFT and TD-DFT levels, in line with the larger MAD for S_1 energy calculations in comparison to both the MAD of T_1 and T_2 excited states energies (Table **5.1**). For both TDA-DFT and TD-DFT calculations, by tuning ω in the LC-ω*PBE and LC-ω*HPBE functionals, all relative energy differences are now in good agreement with the corresponding ones computed at the SCS-CC2 level (Table **5.2**), owing to a much better handling of CT states that is reflected in the largely stabilized S_1 (Table **5.1**). TDA-CAM-B3LYP calculations for ΔE_{ST}, ΔE_{S1T2} and ΔE_{T2T1} are in good agreement with those using SCS-CC2. In contrast, the MAD values for ΔE_{ST} and ΔE_{S1T2} are much larger using TD-CAM-B3LYP

(Table **5.2**, Figure **5.6**). The similar MAD value for ΔE_{T1T2} at both TD-DFT and TDA-DFT levels suggest that TDA acts similarly on both T_1 and T_2. Overall, this study reveals the importance for the use of TDA-DFT when employing CAM-B3LYP to predict accurately the relative energies of the low-lying excited states.

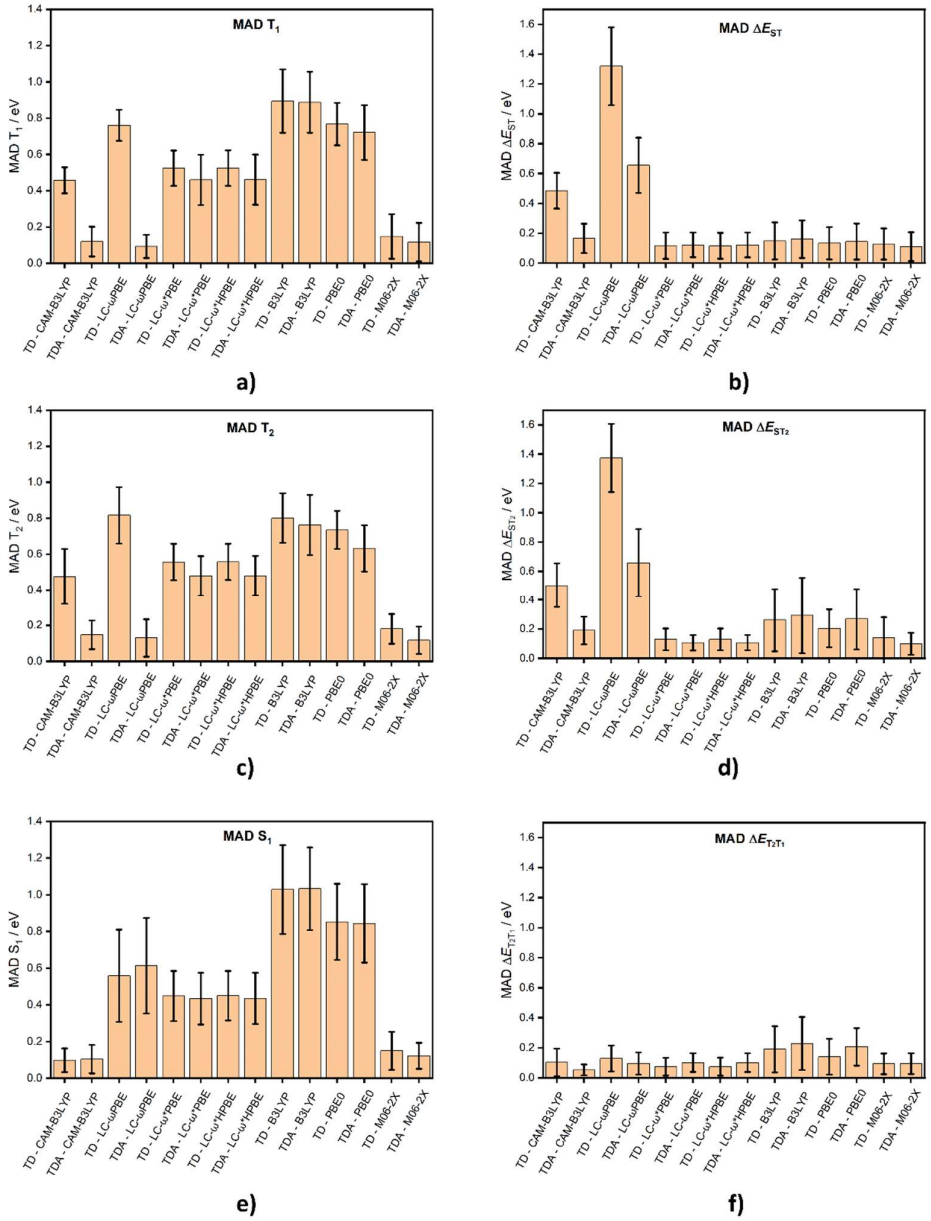

Figure **5.6**. MAD and σ for each functional in comparison to SCS-CC2, where **a)** is T_1, **b)** ΔE_{ST}, **c)** T_2, **d)** ΔE_{ST2}, **e)** S_1, and **f)** ΔE_{T2T1}.

Based on the calculations of both the absolute and relative energies of the excited states, we can conclude that functionals containing a lower HF like exchange content such as PBE0 and B3LYP are not appropriate. M06-2X provides a much better description of the excited state energies. The use of CAM-B3LYP within the TDA-DFT approximation is also an appropriate methodology. LC-ωPBE is also not recommended to be used as it offers a poorly described excited state picture, mainly due to the problematic prediction of the S_1 energy. Tuning of ω improves significantly the prediction of S_1, and both LC-ω*PBE and LC-ω*HPBE perform essentially identically. However, our current investigation tends to show that relying on range-separated functionals for which ω is tuned might not be needed in order to obtain a reliable excited state picture of D-A TADF emitters. Indeed, alternatives such as M06-2X and CAM-B3LYP show comparable accuracies to LC-ω*PBE and LC-ω*HPBE and are thus recommended when evaluating the relative energies between excited states. A full summary of MAD, RMSD and σ is found in Table **5.2** and Figure **5.6**.

Table **5.2**. MAD RMSD and σ of the energy differences between the considered excited states in comparison to SCS-CC2.

	ΔE_{ST} / eV			ΔE_{S1T2} / eV			ΔE_{T2T1} / eV		
	MAD	**RMSD**	**σ**	**MAD**	**RMSD**	**σ**	**MAD**	**RMSD**	**σ**
TD - CAM-B3LYP	0.49	0.50	0.12	0.50	0.52	0.15	0.10	0.14	0.09
TDA - CAM-B3LYP	0.17	0.19	0.10	0.19	0.21	0.09	0.05	0.06	0.04
TD - LC-ωPBE	1.32	1.34	0.26	1.37	1.39	0.23	0.13	0.16	0.09
TDA - LC-ωPBE	0.65	0.68	0.19	0.66	0.70	0.23	0.10	0.12	0.07
TD - LC-ω*PBE	0.12	0.15	0.09	0.13	0.15	0.07	0.07	0.09	0.06
TDA - LC-ω*PBE	0.12	0.15	0.08	0.11	0.12	0.05	0.10	0.12	0.06
TD - LC-ω*HPBE	0.12	0.14	0.09	0.13	0.15	0.07	0.07	0.10	0.06
TDA - LC-ω*HPBE	0.12	0.15	0.08	0.11	0.12	0.05	0.10	0.12	0.06
TD - B3LYP	0.15	0.19	0.12	0.26	0.34	0.21	0.19	0.24	0.15
TDA - B3LYP	0.16	0.20	0.13	0.29	0.39	0.26	0.23	0.29	0.18
TD - PBE0	0.13	0.17	0.11	0.20	0.24	0.13	0.14	0.18	0.12
TDA - PBE0	0.14	0.19	0.12	0.27	0.34	0.21	0.21	0.24	0.13
TD - M06-2X	0.13	0.16	0.10	0.14	0.20	0.14	0.09	0.12	0.07
TDA - M06-2X	0.11	0.15	0.10	0.10	0.12	0.07	0.09	0.12	0.07

5.3.3 Oscillator strength

The oscillator strength was calculated for each singlet state and comparisons made between TD(A)-DFT and SCS-CC2 (Figure **5.7** and Table **5.1**). There were consistent predictions across the series of functionals (MAD < 0.05); however, σ ranged more widely from 0.04 to 0.12. A slight improvement was found when using TD-DFT compared to TDA-DFT. Despite their poorly described excited states, B3LYP, PBE0 and LC-ωPBE provide the smallest MAD and σ. It is not clear why they perform the best for oscillator strength prediction.

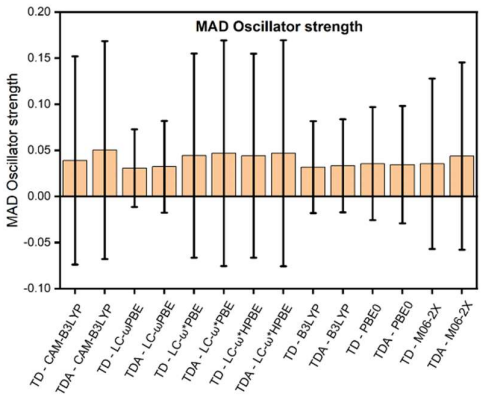

Figure **5.7**. RMSD and MAD for oscillator strength of each functional compared to SCS-CC2, where **a)** is MAD and **b)** is RMSD.

Table **5.3**. MAD, RMSD and σ of DFT calculated oscillator strength related to SCS-CC2.

	CAM-B3LYP		**LC-ωPBE**		**LC-ω*PBE**		**LC-ω*HPBE**		**B3LYP**		**PBE0**		**M06-2X**	
	TD	**TDA**	**TD**	**TDA**	**TD**	**TDA**	**TD**	**TDA**	**TD**	**TDA**	**TD**	**TDA**	**TD**	**TDA**
MAD	0.04	0.05	0.03	0.03	0.04	0.05	0.04	0.05	0.03	0.03	0.04	0.03	0.04	0.04
RMSD	0.12	0.13	0.05	0.06	0.12	0.13	0.12	0.13	0.06	0.06	0.07	0.07	0.10	0.11
σ	0.11	0.12	0.04	0.05	0.11	0.12	0.11	0.12	0.05	0.05	0.06	0.06	0.09	0.10

5.3.4 Nature of Excited states - DFT

Firstly, the nature of the excited states were investigated by computing the ϕ_s index for each emitter at TD(A)-DFT, with a full summary of values available in the supporting information. For most emitters, the S_1 state is predicted to be more CT-like compared to T_1, (lower ϕ_s values) as the exchange interaction increases the spatial confinement of triplet states and thus their LE character. Across all emitters in this study a modest increase in the CT character of the S_1 state is observed when TDA-DFT is used instead of TD-DFT. This is due to the fact that TD-DFT reduces to TDA-DFT when excited states with a large CT character are computed.[198] Interestingly, when tracking the nature of the two lowest triplet excited states, we sometimes observe a state inversion depending on the use of either TD-DFT or TDA-DFT. This is particularly evident for **DTPDDA** (Figure **5.8a**), where LC-ω*PBE, LC-

ω*HPBE and M06-2X at TD-DFT predict a T_1 state with a LE character ($\phi_S > 0.8$), while T_2 remains mainly CT ($\phi_S < 0.4$). However, when TDA-DFT is employed, the T_1 is now a CT state ($\phi_S < 0.4$) with a nature that is very similar to those of T_2 calculated using TD-DFT, while T_2 becomes LE ($\phi_S > 0.8$). These two states are very close in energy to each other (between 0.09 eV and 0.13 eV), with the LE state being pushed above the CT state in TDA-DFT because of its better handling of the triplet instability issue.

The PBE0 and B3LYP functionals display very similar ϕ_S values and tend to predict T_1 and T_2 states to have an increased CT character in comparison to the other functionals. LC-ωPBE appears to be the outlier functional, often resulting in a much larger ϕ_S value. As an example, **PXZ-PXB** has a predicted ϕ_S value for S_1 of > 0.7 while all other DFT functionals predict $\phi_S < 0.3$ (Figure **5.8b**). This is evidence of one of the potential issues encountered with long-range corrected functionals, which tend to destabilize CT states. CAM-B3LYP, LC-ω*PBE, LC-ω*HPBE and M06-2X consistently report very similar ϕ_S values for the S_1 state across the family of emitters in this study, irrespective of whether TD-DFT or TDA-DFT is used. For the triplets, we see a larger spread in T_1 and T_2 ϕ_S values predicted by the CAM-B3LYP, LC-ω*PBE, LC-ω*HPBE and M06-2X functionals compared to S_1.

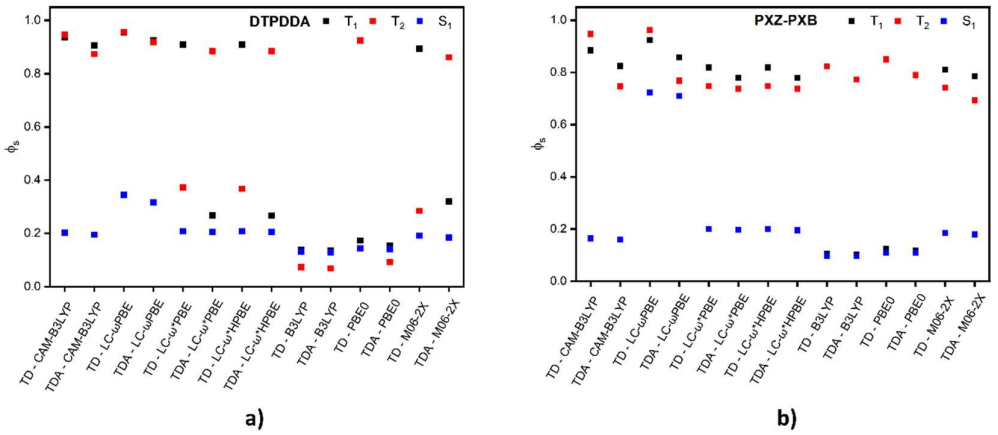

Figure **5.8**. Evolution of ϕ_S values for **a**) **DTPDDA** and **b**) **PXZ-PXB**.

5.3.5 Comparison of the nature of the excited states as predicted using TD(A)-DFT and SCS-CC2

In this section, we embark on a comparison of the nature of the excited states between the different functionals and our reference method SCS-CC2. The nature of the excited state is predicted on the basis of a post-analysis of the difference density. Attachment-detachment formalisms were converted to a difference density picture for all excited states obtained at the TD(A)-DFT level. We compare this picture to the difference density computed at the SCS-CC2 level. From here the MAD, RMSD and σ is obtained for each D_{CT}, q_{CT} and S_{+-} comparing TD(A)-DFT with SCS-CC2.

5.3.5.1 Singlet state

The nature of the S_1 state calculated using DFT and SCS-CC2 methods was compared by computing the q_{CT}, D_{CT} and S_{+-} of S_1 descriptors. While TD(A)-DFT and SCS-CC2 predict a S_1 state with a dominant CT character for essentially all the emitters, one clear outlier exists in terms of **DACT-II**. For this emitter TD(A)-DFT predicts an excited state with largely CT character, while SCS-CC2 predicts that this state contains mainly LE character. Interestingly, the S_2 excited state predicted by TD(A)-DFT is LE-like while SCS-CC2 calculations suggest it is a CT state, which reflects an inversion of S_1 and S_2 (see difference density plots in Figure **5.9**); the energy difference between S_1 and S_2 is small at 0.06 eV using SCS-CC2 while at the TD(A)-DFT, this energy difference is larger, ranging at 0.08 eV to 0.31 eV. Because of this state inversion, the data corresponding to **DACT-II** were removed from the averages on the overall collective data.

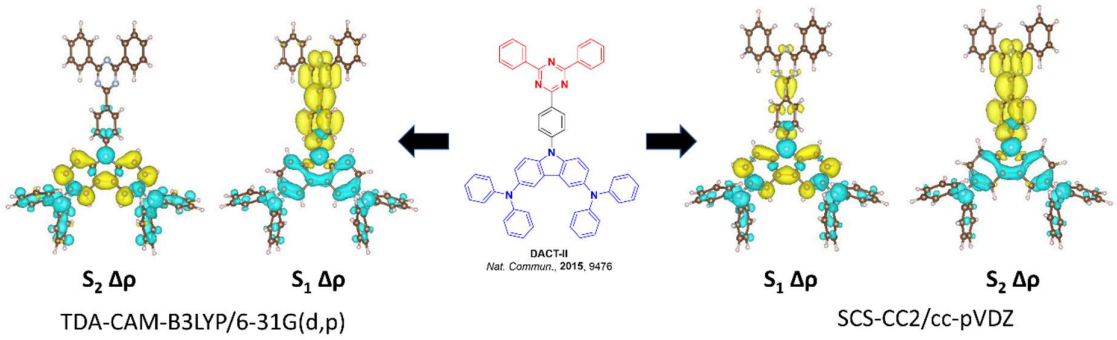

Figure **5.9**. Change in Δρ singlet picture for **DACT-II** between (left) TDA-CAM-B3LYP/6-31G(d,p) and SCS-CC2/cc-pVDZ (right) calculations.

The evaluation of the CT descriptors for the set of compounds confirms the close agreement between CAM-B3LYP and SCS-CC2 for the nature of the S_1 state (Figure **5.10**). The other range-separated functional, LC-ωPBE does not perform as well, with large MAD and σ values for q_{CT}, D_{CT} and S_{+-} (Table **5.4**), which are associated with predicted state inversion in **ACRXTN**, **DTCBPy**, **PTZ-DBTO2** and **PXZ-PXB**, with S_1 predicted to be largely LE (*vide supra*.). When either LC-ω*PBE and LC-ω*HPBE are used, there is close agreement for the description of S_1 and its associated energy with those computed by SCS-CC2. Neither PBE0 nor B3LYP at TD-DFT and TDA-DFT accurately predict the nature of S_1 (Table **5.4**). Their overestimation of the CT character explains the heavily stabilized S_1 energy values reported for the absolute energies and subsequent high MAD (Table **5.1**). Finally, the M06-2X functional provides a similar and equally accurate picture of the nature of S_1 with that of CAM-B3LYP. Based on this analysis, the use of either CAM-B3LYP, M06-2X, LC-ω*PBE or LC-ω*HPBE to obtain accurate predictions of the nature and energy of the S_1 state is encouraged.

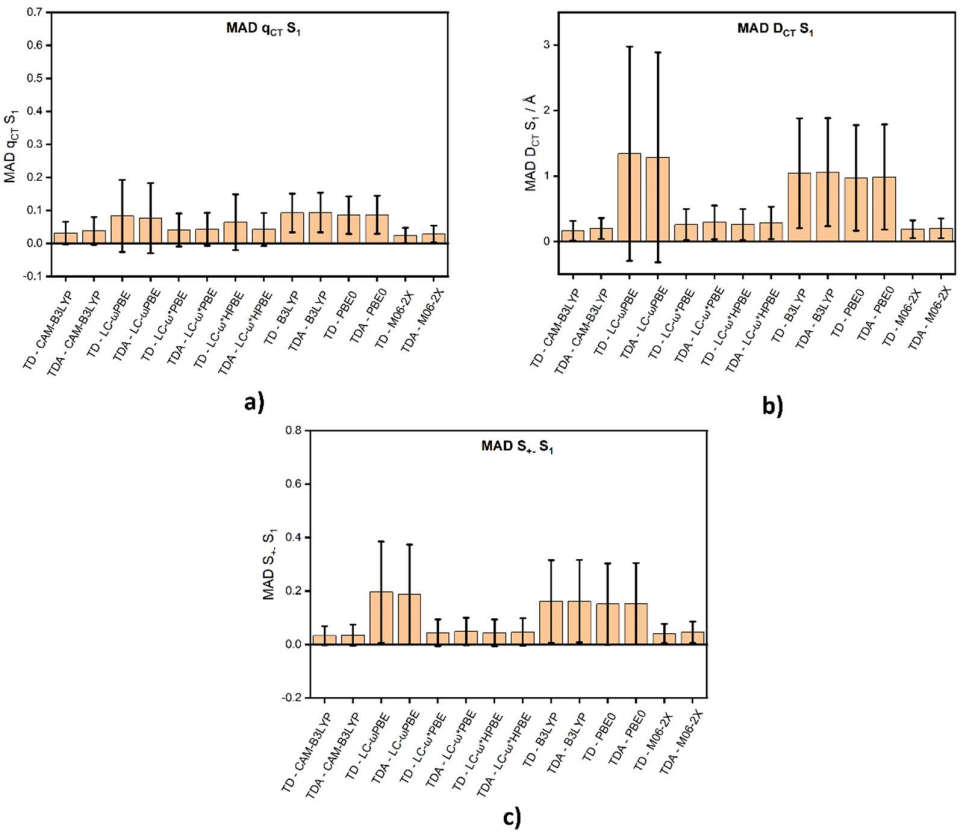

Figure **5.10**. MAD data for the S_1 state nature between TD(A)-DFT and SCS-CC2 calculations, where **a**) is q_{CT}, **b**) is D_{CT} and **c**) is S_{+-}

Table **5.4**. MAD, RMSD and σ data for the S_1 state nature between TD(A)-DFT and SCS-CC2 calculations, where **a**) is q_{CT}, **b**) is D_{CT} and **c**) is S_{+-}

	q_{CT} S_1			D_{CT} S_1 / Å			S_{+-} S_1		
	MAD	**RMSD**	**σ**	**MAD**	**RMSD**	**σ**	**MAD**	**RMSD**	**σ**
TD - CAM-B3LYP	0.03	0.05	0.03	0.17	0.22	0.15	0.03	0.05	0.04
TDA - CAM-B3LYP	0.04	0.06	0.04	0.20	0.26	0.16	0.04	0.05	0.04
TD - LC-ωPBE	0.08	0.14	0.11	1.34	2.12	1.64	0.20	0.27	0.19
TDA - LC-ωPBE	0.08	0.13	0.11	1.29	2.06	1.60	0.19	0.26	0.19
TD - LC-ω*PBE	0.04	0.06	0.05	0.26	0.35	0.24	0.04	0.07	0.05
TDA - LC-ω*PBE	0.04	0.07	0.05	0.29	0.39	0.26	0.05	0.07	0.05
TD - LC-ω*HPBE	0.06	0.11	0.08	0.26	0.35	0.24	0.04	0.07	0.05
TDA - LC-ω*HPBE	0.04	0.07	0.05	0.28	0.38	0.25	0.05	0.07	0.05
TD - B3LYP	0.09	0.11	0.06	1.04	1.34	0.84	0.16	0.22	0.15
TDA - B3LYP	0.09	0.11	0.06	1.06	1.34	0.83	0.16	0.22	0.15
TD - PBE0	0.09	0.10	0.06	0.97	1.26	0.81	0.15	0.21	0.15
TDA - PBE0	0.09	0.10	0.06	0.98	1.27	0.80	0.15	0.22	0.15
TD - M06-2X	0.02	0.03	0.02	0.19	0.23	0.14	0.04	0.05	0.04
TDA - M06-2X	0.03	0.04	0.03	0.20	0.25	0.15	0.05	0.06	0.04

4.2.2 Triplet states

The data associated with the prediction of the triplet state character is next discussed. The nature of T_1 as computed at TDA-CAM-B3LYP is closer to the one predicted with SCS-CC2 than at the TD-CAM-B3LYP level (see CT Table **5.5**). However, the opposite is observed for T_2, wherein the MAD values of the CT descriptors increase when moving from TDA-DFT to TD-DFT (Table **5.6**). Overall, it should be noted that the T_1 and T_2 MAD values are significantly larger than the respective S_1 observations (Figure **5.10**). LC-ωPBE does a poor job in predicting the nature of both T_1 and T_2; still, the use of TDA improved the MAD for each excited state descriptor compared to TD-DFT. Unfortunately, neither the use of LC-ω*PBE nor LC-ω*HPBE produced a more accurate descriptor of the triplet state character (MAD values similar to those of LC-ωPBE) despite there being a significant

improvement in the quality of the energy prediction (*vide supra*.). As for S_1, both B3LYP and PBE0 produce erroneous T_1 and T_2 assignments as the CT character of these states is overestimated, with the largest MAD reported for these compared to all other functionals (Figure **5.11**), using most metrics. Inclusion of greater HF like contribution within M06-2X improves the triplet description, though the discrepancy compared to SCS-CC2 is much larger than that observed for the description of the S_1 state (Figure **5.11**).

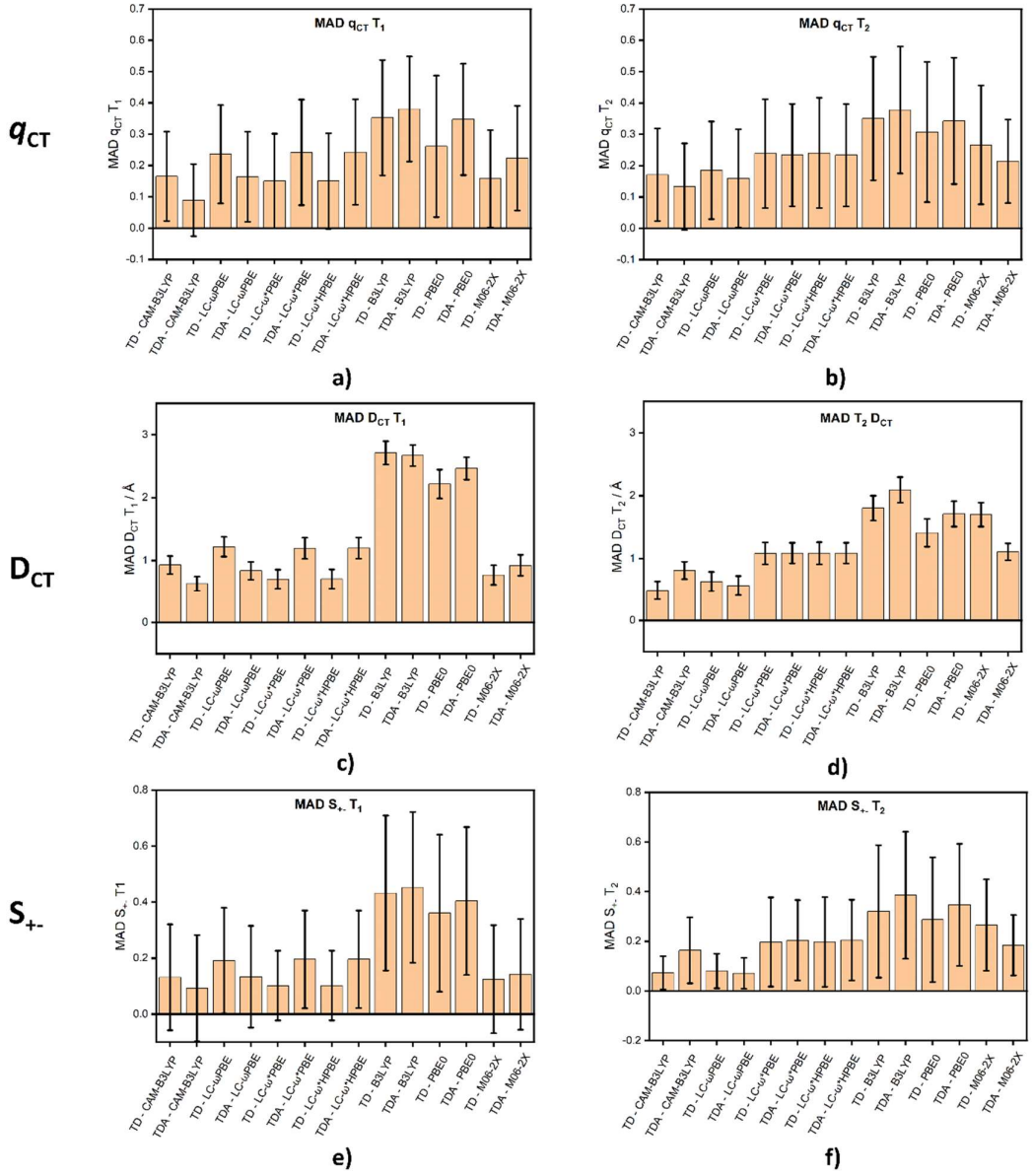

Figure **5.11**. MAD data for the T_1 (left) and the T_2 (right) states nature between TD(A)-DFT and SCS-CC2 calculations, where **a**) and **b**) are q_{CT}, **c**) and **d**) are D_{CT} and **e**) and **f**) are S_{+-}

Table **5.5.** MAD, RMSD and σ data for the T_1 state nature between TD(A)-DFT and SCS-CC2 calculations, where **a**) is q_{CT}, **b**) is D_{CT} and **c**) is S_{+-}

	q_{CT} T_1			D_{CT} T_1 / Å			S_{+-} T_1		
	MAD	**RMSD**	**σ**	**MAD**	**RMSD**	**σ**	**MAD**	**RMSD**	**σ**
TD - CAM-B3LYP	0.17	0.22	0.14	0.93	1.63	0.14	0.13	0.23	0.19
TDA - CAM-B3LYP	0.09	0.15	0.12	0.63	1.29	0.12	0.09	0.21	0.19
TD - LC-ωPBE	0.24	0.28	0.16	1.22	1.83	0.16	0.19	0.27	0.19
TDA - LC-ωPBE	0.16	0.22	0.14	0.84	1.48	0.14	0.13	0.23	0.18
TD - LC-ω*PBE	0.15	0.21	0.15	0.70	1.07	0.15	0.10	0.16	0.12
TDA - LC-ω*PBE	0.24	0.30	0.17	1.19	1.75	0.17	0.20	0.26	0.17
TD - LC-ω*HPBE	0.15	0.21	0.15	0.70	1.07	0.15	0.10	0.16	0.12
TDA - LC-ω*HPBE	0.24	0.30	0.17	1.20	1.75	0.17	0.20	0.26	0.17
TD - B3LYP	0.35	0.40	0.18	2.71	3.45	0.18	0.43	0.51	0.28
TDA - B3LYP	0.38	0.42	0.17	2.67	3.46	0.17	0.45	0.53	0.27
TD - PBE0	0.26	0.35	0.23	2.22	3.17	0.23	0.36	0.46	0.28
TDA - PBE0	0.35	0.39	0.18	2.46	3.27	0.18	0.40	0.48	0.26
TD - M06-2X	0.16	0.22	0.16	0.77	1.35	0.16	0.12	0.23	0.19
TDA - M06-2X	0.22	0.28	0.17	0.92	1.74	0.17	0.14	0.24	0.20

Table **5.6**. MAD, RMSD and σ data for the T_2 state nature between TD(A)-DFT and SCS-CC2 calculations, where **a**) is q_{CT}, **b**) is D_{CT} and **c**) is S_{+-}

	q_{CT} T_2			D_{CT} T_2 / Å			S_{+-} T_2		
	MAD	**RMSD**	**σ**	**MAD**	**RMSD**	**σ**	**MAD**	**RMSD**	**σ**
TD - CAM-B3LYP	0.17	0.14	0.15	0.49	0.65	0.15	0.07	0.10	0.07
TDA - CAM-B3LYP	0.13	0.12	0.14	0.81	1.07	0.14	0.16	0.21	0.13
TD - LC-ωPBE	0.19	0.16	0.16	0.63	0.77	0.16	0.08	0.11	0.07
TDA - LC-ωPBE	0.16	0.14	0.16	0.56	0.73	0.16	0.07	0.09	0.06
TD - LC-ω*PBE	0.24	0.15	0.17	1.08	1.60	0.17	0.20	0.27	0.18
TDA - LC-ω*PBE	0.23	0.17	0.16	1.09	1.45	0.16	0.20	0.26	0.16
TD - LC-ω*HPBE	0.24	0.15	0.18	1.08	1.60	0.18	0.20	0.27	0.18
TDA - LC-ω*HPBE	0.23	0.17	0.16	1.09	1.45	0.16	0.20	0.26	0.16
TD - B3LYP	0.35	0.18	0.20	1.80	2.84	0.20	0.32	0.42	0.27
TDA - B3LYP	0.38	0.17	0.20	2.09	3.04	0.20	0.39	0.46	0.26
TD - PBE0	0.31	0.23	0.22	1.41	1.96	0.22	0.29	0.38	0.25
TDA - PBE0	0.34	0.18	0.20	1.71	2.74	0.20	0.35	0.42	0.25
TD - M06-2X	0.27	0.16	0.19	1.70	2.27	0.19	0.27	0.32	0.18
TDA - M06-2X	0.21	0.17	0.13	1.11	1.56	0.13	0.18	0.22	0.12

5.4 Conclusions

We have compared the results of DFT calculations across a series of commonly used functional to predictions made using SCS-CC2 of (i) vertical excitation energies, (ii) vertical excitation energy differences and (iii) nature of excited states for a series of fourteen TADF emitters. The objective of our study was to determine the best choice of functional for modelling the optoelectronic properties of donor-acceptor TADF compounds.[24, 72, 241] We observed that TDA-DFT calculations provided a more accurate prediction of the vertical excitation energies compared to TD-DFT, as has been previously documented.[198] [175] Both TDA-M06-2X and TDA-CAM-B3LYP calculations provide very good agreement for S_1, T_1 and T_2; TDA-LC-ωPBE calculations produce reasonably accurate T_1 and T_2 energies, but consistently overestimate the S_1 energy. B3LYP, PBE0 and the ω-tuned functionals

consistently underestimate triplet and singlet state energies, resulting in large deviations from the SCS-CC2 calculations. When considering excited state energy gaps, TD(A)-LC-ωPBE produce large deviations in both ΔE_{ST} and ΔE_{ST2}, the result of the much larger MAD for S_1 than for T_1 and T_2. ΔE_{T2T1} is much better reproduced for most functionals in comparison with ΔE_{ST} and ΔE_{ST2}. However, PBE0 and B3LYP show comparable MADs but larger standard deviations when evaluating ΔE_{T2T1} questioning their reliability in predicting this parameter. Of the functionals evaluated, TDA-M06-2X and TDA-CAM-B3LYP offer the most accurate predictions, evidence by their low MAD for ΔE_{ST} ΔE_{ST2} and ΔE_{T2T1}; the MAD values increased for the analogous TD-DFT calculations as here the triplet states are over stabilized.

Finally, the nature of the excited states was investigated, computing the q_{CT}, D_{CT} and S_{+-} CT descriptors for T_1, T_2 and S_1 excited states. Apart from **DACT-II**, the nature of the S_1 state is in good agreement with SCS-CC2 when considering the CAM-B3LYP and the M06-2X functionals for both TD-DFT or TDA-DFT calculations. By contrast, B3LYP and PBE0 perform worse with S_1 states predicted to have a larger CT character. When tuning the range separation parameter, LC-ω*PBE and LC-ω*HPBE perform better compared to the original LC-ωPBE functional and with a similar accuracy as for the CAM-B3LYP and M06-2X functionals. Overall, we found that regardless of the functional the excited state description is not as well reproduced for triplets as it is for singlets, which is reflected in the larger MAD for every CT descriptor. Of the functionals assessed that did not require parameter tuning, both CAM-B3LYP and M06-2X provide the most accurate predictions of the character of the low-lying excited states. Based on these modelled functionals one can infer that the most appropriate functionals of choice are CAM-B3LYP and M06-2X using TDA-DFT to obtain the most accurate modelling for TADF materials, however direct assignment of T_1 and T_2 natures must be done with caution, with problems in characterisation of their nature apparent.

Chapter 6: Improving processability and efficiency of multi-resonant TADF emitters: A design strategy

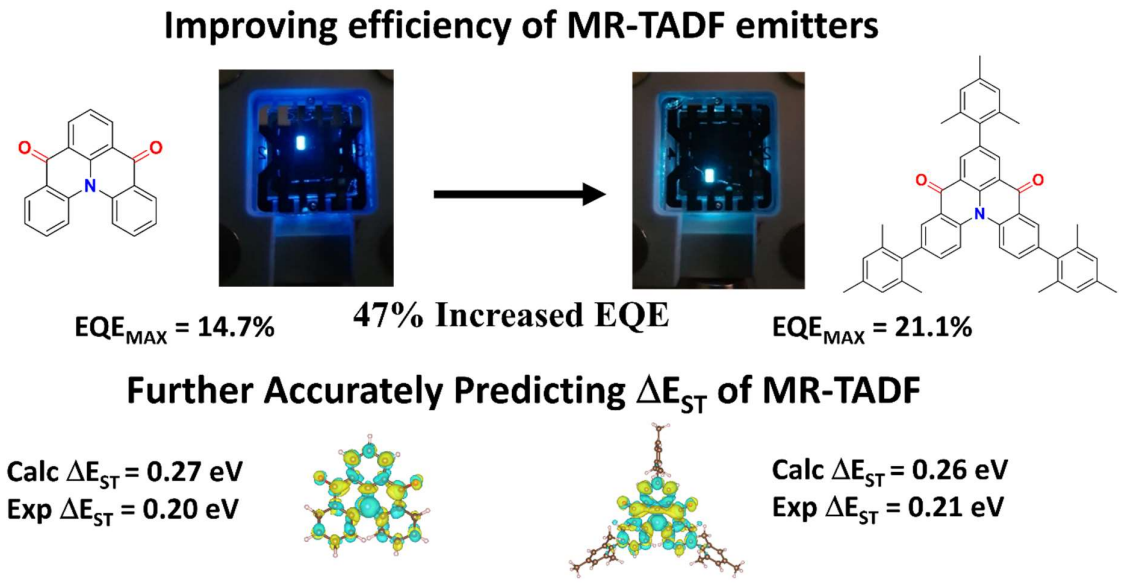

6.1 Introduction

Chapters 3 - 5 have showcased D-A TADF materials with promising TADF properties; however, the synthesised materials all showed broad emission spectra (>80 nm), which for commercial applications is undesirable (see Chapter 1 for details). An alternative class of OLED emitter materials, coined MR-TADF, was introduced by Hatakeyama and co-workers in 2016;[8] an earlier material (**DOBNA**, originally named **2a**[138]) was previously reported by the same group.[138 153] Discussion of the photophysical properties of MR-TADF emitters are presented in Chapter 1. The structures highlighted in Figure **6.1** were reported in the literature while undertaking this work. Unlike D-A materials there were relatively few MR-TADF emitters at the time of the beginning of this project and all of these were composed of a central boron atom, with peripheral donor groups *para* to it thereby ensuring the presence of the complimentary electron density distribution pattern (Figure **6.1**). It should be noted that a high performing deep blue emitter, **TBN-TPA**[242] (Figure **6.1**) which was reported has recently been shown to have a different structural motif, **CzDABNA-NP-TB**.[243]

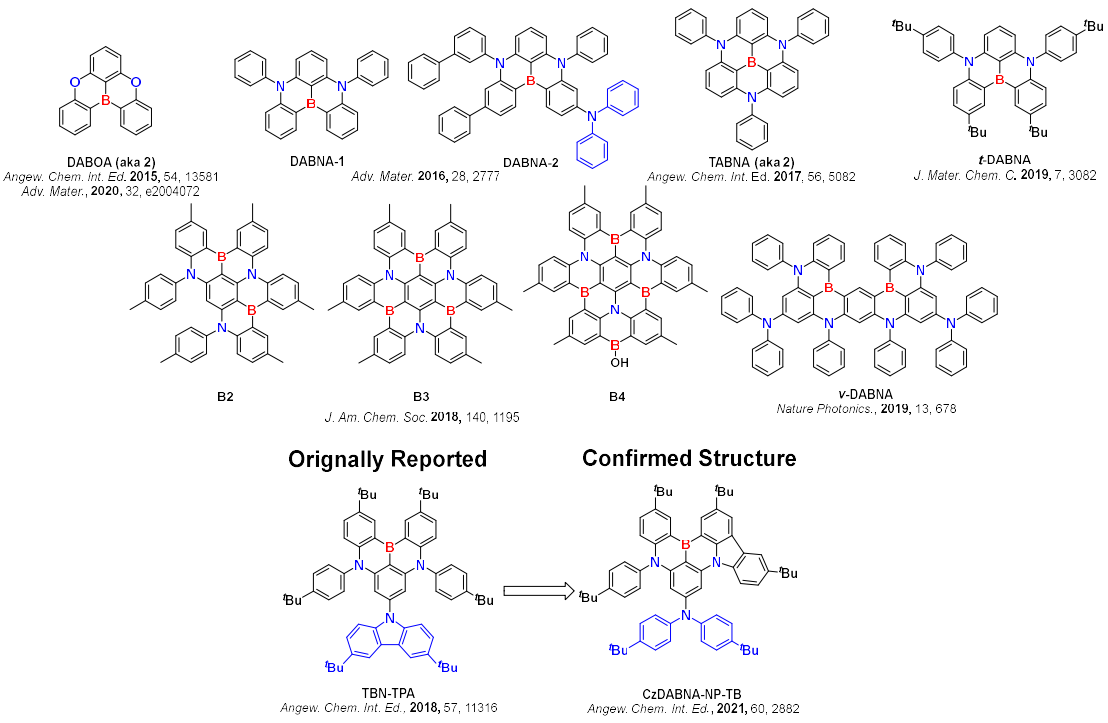

Figure **6.1**. Structures of boron-containing MR-TADF emitters reported while undertaking this work.

The discovery of other motifs that show MR-TADF has largely been hampered by the poor predictive performance of quantum chemical calculations that fail to accurately describe the excited states of this class of materials, unlike for D-A systems where good agreement is observed. Indeed, from the compounds shown in Figure **6.1**, ΔE_{ST} is poorly predicted by the DFT methods employed in their publications. We[147] investigated computationally the TADF properties of two emitters, **DABNA-1** and **TABNA** (Figure **6.1**). In this study, overestimation of ΔE_{ST} was reported when DFT methods were used, in line with the previous computational analysis in the literature, while SCS-CC2 calculations provided excellent agreement to experiment (ΔE_{ST} 0.18 eV and 0.21 eV reported experimentally, in 1 wt% mCBP and PMMA, respectively), with calculated values of 0.15 eV and 0.20 eV, respectively. In this study it was clear that adiabatic ΔE_{ST} and vertical ΔE_{ST} (see Chapter 1 for details) provided similar results. In addition, the use of a smaller basis set of cc-pVDZ compared to def-TZVP also produced similar results.

6.2 Motivation and Chapter outline

Following this work highlighting accurate ΔE_{ST} prediction in MR-TADF materials using SCS-CC2, the aim was to develop a new MR-TADF emitter design. Two emitters were designed, **DiKTa** and **Mes$_3$DiKTa**, with a central nitrogen donor and carbonyl acceptors. **DiKTa** had previously been reported as a fluorescent emitter[244] and during the undertaking of this work one of designed emitters, **DiKTa**, was published and identified as an MR-TADF emitter by two groups (Figure **6.2**).[129, 245]

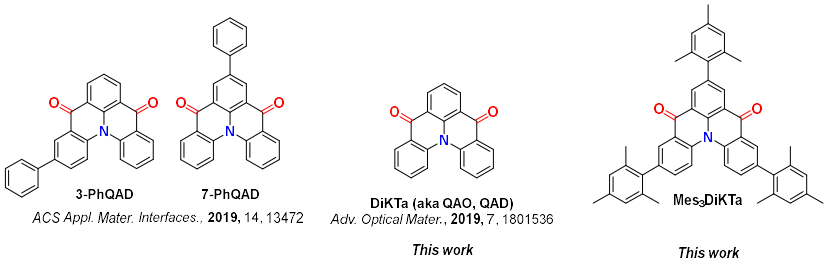

Figure **6.2.** Structures of materials studied in this work and emitters reported while undertaking this work.

The effect of mesityl substitution (**Mes$_3$DiKTa**) compared to the parent (**DiKTa**) is discussed in terms of the solid-state structure, the electrochemistry, photophysics of the compounds as well as the performance of the devices. **Mes$_3$DiKTa** shows improved electrochemical stability and reduced ACQ and no evidence of aggregate emission in doped films. Further, despite moderately decreased k_{RISC}, improved device performance was observed with **Mes$_3$DiKTa** where the EQE_{max} increased compared to the device with **DiKTa** from 14.7% to 21.1%. Good agreement between SCS-CC2 calculated and experimentally observed ΔE_{ST} was observed.

6.3 Results and Discussion

6.3.1 Computations

Based on our previous work,[147] the approach for materials design centred on SCS-CC2/cc-pVDZ calculations, ensuring an affordable yet accurate method. Firstly, the previously studied **DABNA-1** and **TABNA**, and three other MR-TADF materials, **DABNA-2**, **DOBNA** and ***t*DABNA** (Figure **6.1**) were investigated with SCS-CC2 alongside conventional DFT methods, comparing calculated and experimental ΔE_{ST} (Figure **6.3**). TD-DFT and TDA-DFT calculations using the functionals B3LYP, PBE0, CAM-B3LYP, M06-2X, LC-ωPBE and LC-ω*PBE in conjunction with the 6-31G(d,p) basis set were employed using a ground-state optimized geometry and these were cross-compared with SCS-CC2/cc-pVDZ calculations. In line with the previous study, extremely large ΔE_{ST} were predicted for the DFT calculations, values that are much larger than those experimentally determined (solid red line, Figure **6.3**). SCS-CC2/cc-pVDZ calculations provided excellent ΔE_{ST} predictions.

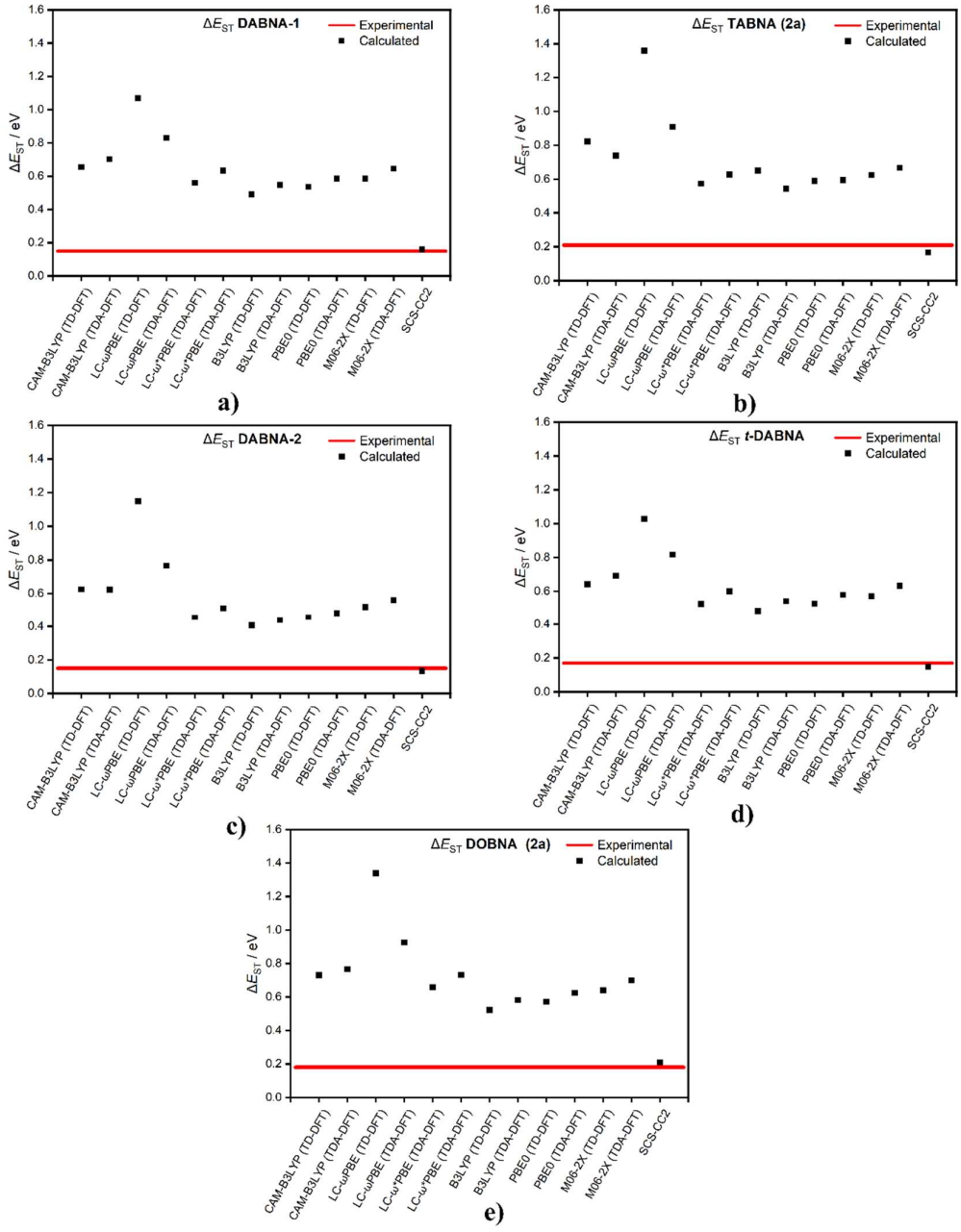

Figure **6.3**. ΔE_{ST} calculated from vertical excitation for a range of DFT functionals and SCS-CC2, compared to experimental ΔE_{ST} (red solid line) for **a**) **DABNA-1**, **b**) **TABNA**, **c**) **DABNA-2**, **d**) ***t*-DABNA** and **e**) **DOBNA**.

In the literature, the SRCT excited state is inferred from the pattern of the HOMO and LUMO pictures, which is a ground state picture (Figure **6.4**).[182] In Chapters 2 and 5, difference density was discussed, which highlights changing electron density between the ground and excited state. Areas of

yellow density represent an increase in electron density, while sky blue colouration highlights a decrease in electron density (Figure **6.4**). This offers a description of the excited state and highlights a very accurate picture of the pattern linked to MR-TADF, with the positive and negative components sitting on neighbouring atoms. This is a much more appropriate visualization compared to the normally quoted HOMO-LUMO plots and will be used when describing MR-TADF emitters with an alternating pattern of increasing and decreasing density indicative of SRCT and hence MR-TADF (Figure **6.4**).

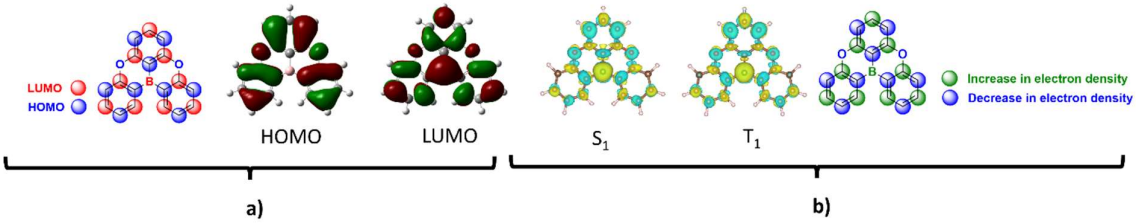

Figure **6.4.** HOMO LUMO plots **a**) and difference density patterns **b**) of **DOBNA**

Two materials, ***in*-DABNA** and ***in*-TABNA** (Figure **6.5**), were first identified and modelled to ascertain if the central boron was essential for MR-TADF design. These two compounds are "inverted" derivatives of **DABNA-1** and **TABNA**. The ΔE_{ST} were calculated to be 0.13 eV and 0.14 eV for ***in*-DABNA** and ***in*-TABNA**, respectively, representing a modest decrease from 0.16 eV and 0.17 eV for **DABNA-1** and **TABNA**. A small red shift was also predicted. The difference density picture is inverted with decreased density located on the centre of the molecule.

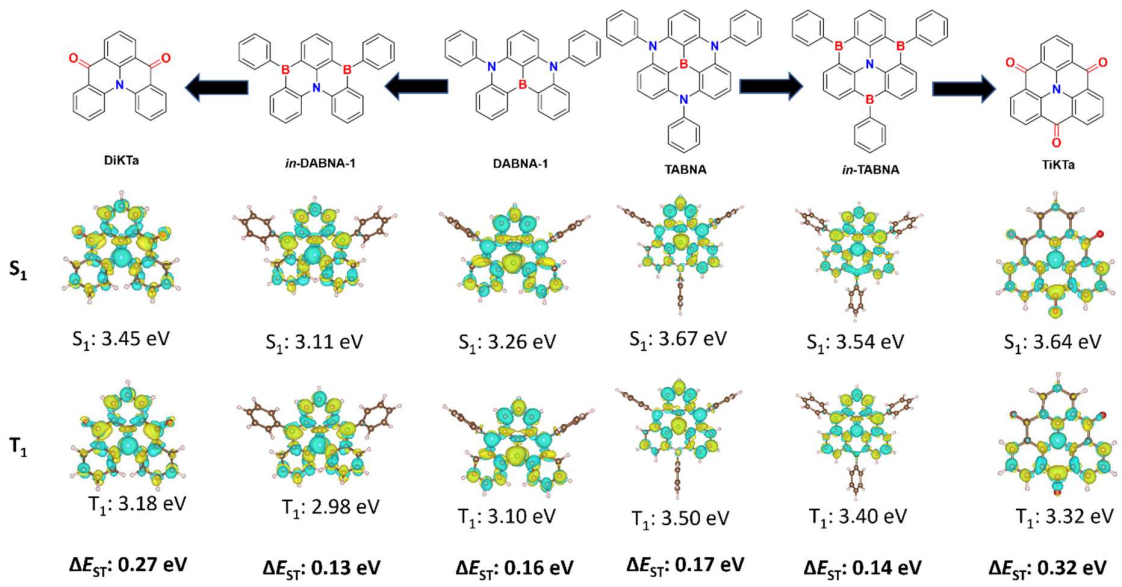

Figure **6.5**. New designs probed from original emitters with excited state energies and difference density patterns.

Derivatives based on the ***in*-DABNA** design have since been published, with sky blue – green emission observed, in line with the predicted S_1 stabilisation.[153, 166, 167, 246] OLEDs based on two of these emitters were fabricated, **ADBNA-Me-Mes** and **ADBNA-Me-Tip**.[166]Compared to **DABNA-1** (λ_{PL} of 460 nm in 1 wt% mCBP) the emission for **ADBNA-Me-Mes** and **ADBNA-Me-Tip** is red-shifted (λ_{PL} of 482 nm and 479 nm, respectively in 1 wt% DOBNA-OAr), a trend in line with calculations. Compared to **DABNA-1**, which has a Φ_{PL} of 88%, τ_d of 88 μs and ΔE_{ST} of 0.16 eV in mCBP, similar Φ_{PL} of 88% and 89%, τ_d of 165 μs and 147 μs and ΔE_{ST} of 0.18 eV and 0.18 eV for **ADBNA-Me-Me** and **ADBNA-Me-Tip** were obtained in 1 wt% DOBNA-OAr. This suggests inversion of the central atom from electron-withdrawing boron to electron-donating nitrogen is a viable strategy for MR-TADF design.

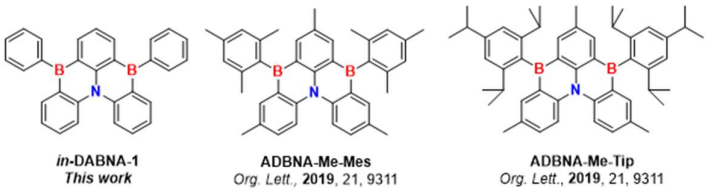

Figure **6.6**. Structure of proposed emitter ***in*-DABNA-1** and subsequently reported emitters.

Target emitter **DiKTa** was next designed, containing a central nitrogen and peripheral ketones (Figure **6.5**). Predicted ΔE_{ST} was 0.27 eV, representing a slight increase compared to the previously modelled boron derivatives; however, this calculated value is still sufficiently small to be considered a TADF emitter. The fully bridged derivative, **TiKTa** was also modelled (Figure **6.5**); however, it displayed a larger ΔE_{ST} of 0.32 eV and was not investigated further. Subsequent work has indicated that **TiKTa** compound undergoes RTP in the solid state.[247] From **DiKTa**, a second derivative was designed, **Mes$_3$DiKTa**, with mesityl groups located *para* to nitrogen (Figure **6.7**). The addition of the mesityl groups was proposed as a strategy to mitigate ACQ, which plagues MR-TADF emitters, and which is why very low doping concentrations are often used in films and devices. SCS-CC2 calculations predicted ΔE_{ST} at 0.26 eV for this material, along with a slight stabilisation of the S_1 energy, from 3.45 eV in **DiKTa** to 3.32 eV in **Mes$_3$DiKTa**. Both materials show similar difference density patterns, with decreased density situated on the nitrogen and increased density on the ketone moieties in an alternating pattern highlighting SRCT. Very little density is situated on the mesityl groups (Figure **6.7**). Predicted oscillator strength for the transition to the S_1 state, *f*, are 0.20 and 0.23 for each **DiKTa** and **Mes$_3$DiKTa**, respectively, which should translate into enhanced Φ_{PL} for the latter compound. Two other materials that were reported coincident with this work, **3-PhQAD** and **7-PhQAD** (Figure **6.2**), were also modelled. Each has a similar ΔE_{ST} to **DiKTa**, of 0.27 eV.

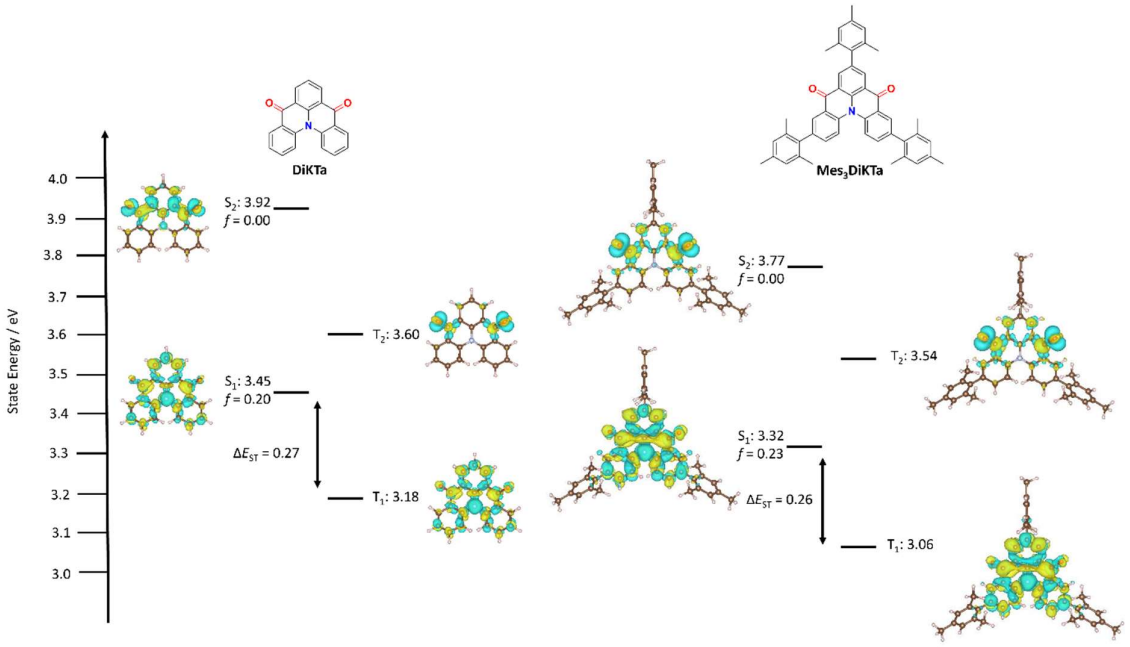

Figure **6.7**. Vertical exctited state energies and difference density pictures of **DiKTa** and **Mes$_3$DiKTa** calculated with SCS-CC2/cc-pVDZ.

6.3.2 Synthesis and crystal structures

DiKTa was synthesized using a similar method to that reported previously (Figure **6.8**).[244] Diester, **12** was obtained in modest yield of 32% via a high temperature Ullmann coupling. The subsequent ring closing reaction produced **DiKTa** in 86% yield. Overall a reduced yield of 26% compared to the original 31% was obtained.[244] **Mes$_3$DiKTa** was obtained in good yield following bromination of intermediate **13**, Friedel-Craft acylation to produce brominated **Br$_3$DiKTa,** and Suzuki-Miyaura coupling with mesityl-2-boronic acid to deliver the target **Mes$_3$DiKTa**.

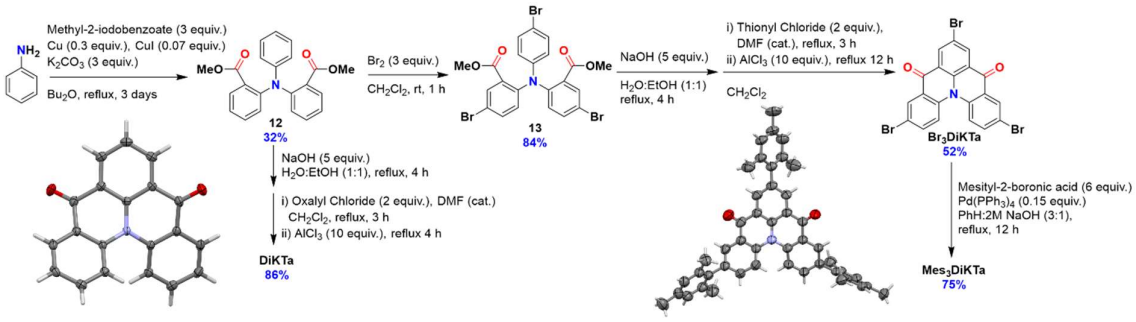

Figure **6.8**. Synthesis of **DiKTa** and **Mes$_3$DiKTa** and single crystals.

Single crystal X-ray diffraction data for both emitters indicated different packing motifs (Figure **6.9**); although neither compound shows strong intermolecular interactions, the presence of the mesityl groups does disrupt π···π interactions in **Mes$_3$DiKTa** [no centroid···centroid distances less than 4.030(3) Å]. The only intermolecular interactions seen in **Mes$_3$DiKTa** are extremely weak C–H···π interactions between a phenyl hydrogen and a mesitylene ring, at distances close to the van der Waals limit (2.85 and 2.06 Å), leading to the formation of weakly interacting molecular stacks along the crystallographic *b*-axis. In **DiKTa** π···π interactions are found [centroid···centroid distance of 3.8793(6) Å] between adjacent emitter molecules, giving rise to interacting stacks running along the *c*-axis (Figure **6.9**). Good thermal stability was observed with 5% weight loss at 323 °C and 437 °C for **DiKTa** and **Mes$_3$DiKTa**, respectively (Figure **6.10**).

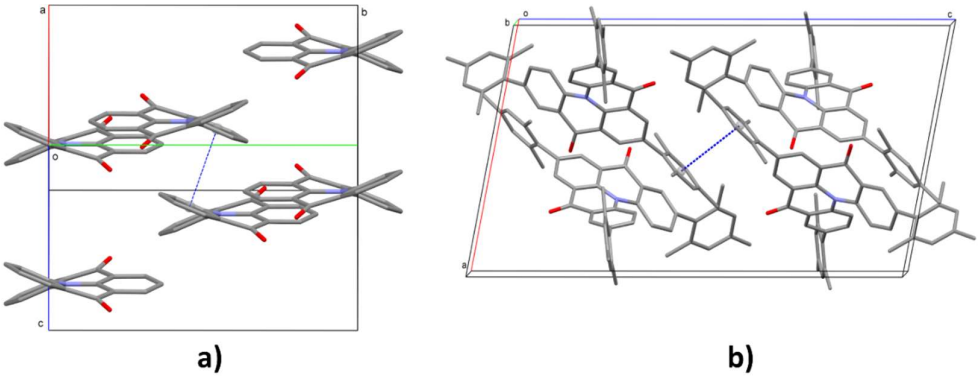

Figure **6.9.** Crystal packing of **a**) **DiKTa** and **b**) **Mes$_3$DiKTa** where Transparent grey spheres represent ring centroids, and dashed blue lines represent shortest centroid···centroid contacts [**DiKTa**: 3.8793(6) Å, **Mes$_3$DiKTa**: 4.030(3)Å].

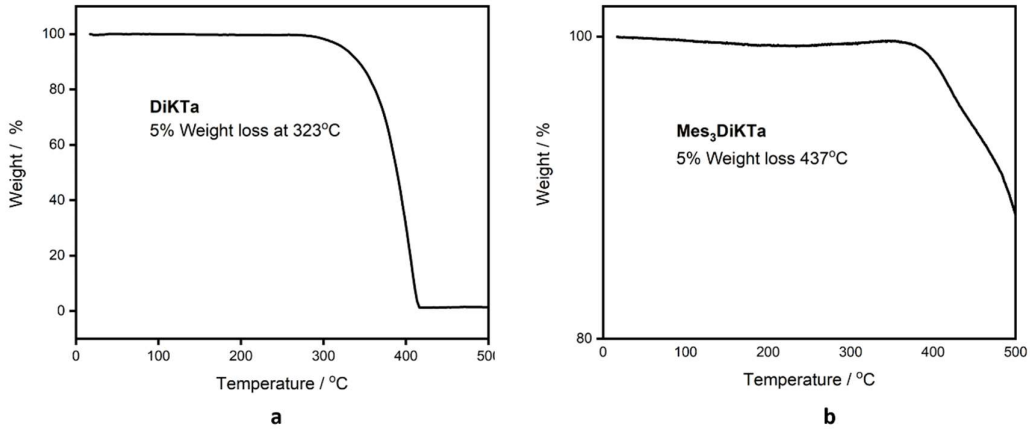

Figure **6.10**. TGA of **a) DiKTa** and **b) Mes$_3$DiKTa** with 5% weight loss temperature.

6.3.3 Electrochemical properties

The electrochemical behaviour of **DiKTa** and **Mes$_3$DiKTa** was studied by CV and DPV in degassed MeCN with [*n*Bu$_4$N]PF$_6$ as the supporting electrolyte (Figure **6.11a**). A slightly destabilized HOMO (-5.86 eV vs -5.96 eV) and stabilized LUMO (-3.26 eV vs -3.11 eV) in **Mes$_3$DiKTa** versus **DiKTa** can be attributed to the mesomeric electron-donating character of the mesityl groups, behaviour that was predicted by DFT (Table **6.1**). The reduced $\Delta E_{H\text{-}L}$ in turn is correlated with the observed red-shifted emission (*vide infra.*) and was captured by DFT. Further, the mesityl groups contribute to the electrochemical stability of the compound with reversible oxidation and reduction waves by inhibiting an electrochemical degradation process located at the *para*-C-H position to the nitrogen.

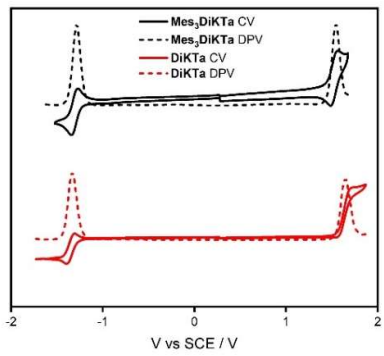

Figure **6.11**. Electrochemical properties of **DiKTa** and **Mes$_3$DiKTa** including CV (solid) and DPV (dotted) obtained in degassed MeCN, scan rate = 0.05 V s^{-1}.

Table **6.1**. Electrochemical data for **DiKTa** and **Mes$_3$DiKTa** at 300 K.

	Electrochemistry [a]					Computational [b]		
Compound	**E^{ox}_{pa} / V**	**E^{red}_{pc} / V**	**HOMO [c] / eV**	**LUMO [c] / eV**	**ΔE_{H-L} [d] / eV**	**HOMO / eV**	**LUMO / eV**	**ΔE_{H-L} / eV**
DiKTa	1.66	-1.33	-5.93	-3.11	2.82	-6.20	-2.23	3.97
Mes$_3$DiKTa	1.54	-1.28	-5.86	-3.26	2.59	-6.00	-2.19	3.81

[a] In degassed MeCN with 0.1 M [*n*Bu$_4$N]PF$_6$ as the supporting electrolyte and Fc/Fc$^+$ as the internal reference (0.38 V vs. SCE) from the DPV maxima.[227] [b.] The HOMO and LUMO energies were determined from PBE0/6-31G(d,p), [c] The HOMO and LUMO energies were determined using the relation $E_{HOMO/LUMO} = -(E^{ox} / E^{red} + 4.8)$ eV, related to Fc/Fc$^+$. [d.] $\Delta E_{H-L} = |E_{HOMO}-E_{LUMO}|$.

6.3.4 Solution-state photophysical properties

UV-Vis absorption spectra in PhMe show a high-energy, low intensity band (λ_{abs} = 321 nm and 330 nm, ε = 2.4 and 6.2 × 10^3 M^{-1} cm^{-1} for **DiKTa** and **Mes$_3$DiKTa**). A second lower energy band with increased intensity was observed at λ_{abs} = 334 nm and 345 nm with ε of 3.5 and 6.7 × 10^3 M^{-1} cm^{-1}, respectively, for **DiKTa** and **Mes$_3$DiKTa**. A low-energy high-intensity band was observed for both with λ_{abs} = 433 nm and 451 nm, ε = 21 and 27 × 10^3 M^{-1} cm^{-1} for **DiKTa** and **Mes$_3$DiKTa**, respectively. The lowest energy band was attributed to a SRCT $S_0 - S_1$ strongly allowed optical transition typical of MR-TADF compounds (Figure **6.12**). This is in good agreement with theory, where a high oscillator strength, *f*, of 0.23 and 0.20 for **Mes$_3$DiKTa** and **DiKTa** is predicted for this transition. The oscillator strength for the transition to the S_2 state is extremely low for both materials (less than 0.0001 for each) and cannot account for the other observed absorption bands. The small oscillator strength can be understood given the nature of this state is n-π*; which is a forbidden transition, as the orbitals show no overlap as they are perpendicular to each other (Figure **6.7**). A very small positive solvatochromism is observed for this band in the ground state (Figure **6.12**). This is again consistent with the SRCT nature of this transition.

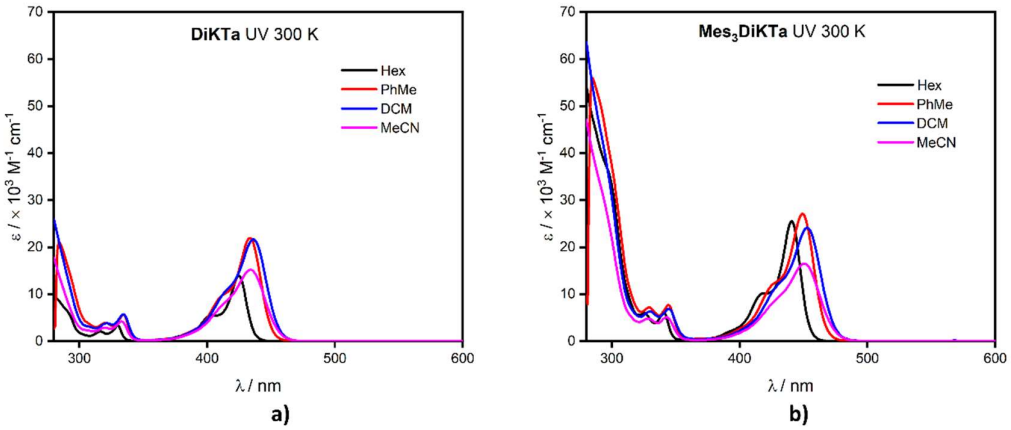

Figure **6.12**. Absorption spectra of **a**) **DiKTa** and **b**) **Mes$_3$DiKTa** in Hex, PhMe, DCM and MeCN. Obtained under aerated conditions at 298 K in dilute solution.

The PL spectrums of **DiKTa** and **Mes$_3$DiKTa** show the expected mirror image profile to the absorption spectrum. There is a small difference between the peaks of the absorption and emission of 29 nm (1020 cm^{-1}) 27 nm (805 cm^{-1}) for **DiKTa** and **Mes$_3$DiKTa** respectively (Figure **6.13**) highlighting the rigid structure of **DiKTa** and **Mes$_3$DiKTa** similarly to **DABNA-1**.[8] The rigid nature and SRCT of the compound is responsible for the narrow emission spectrum at RT. A similar profile but with more pronounced vibronic progression is observed for the phosphorescence spectrum obtained after 70 ms at 77 K in a PhMe glass (Figure **6.13**). The ΔE_{ST} calculated from the onset of phosphorescence and fluorescence is 0.20 eV and 0.19 eV for **DiKTa** and **Mes$_3$DiKTa** and is sufficiently small to enable a RISC process at room temperature. They are in reasonable agreement with the calculated values of 0.27 eV and 0.26 eV, respectively.

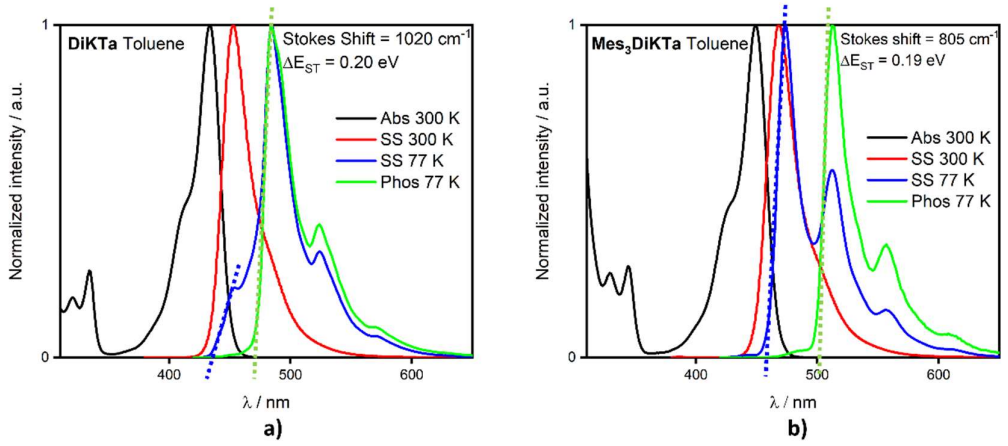

Figure **6.13**. Photophysical data in toluene of **a**) **DiKTa,** and **b**) **Mes$_3$DiKTa,** where SS 77 K is obtained in toluene glass at 77 K and phos is obtained in toluene glass at 77 K after 70 ms for 70 ms, λ_{exc} = 415 nm.

Modest positive solvatochromism (31 nm, or 1522 cm^{-1} for **DiKTa** and 1408 cm^{-1} for **Mes$_3$DiKTa**) was observed in the steady-state PL spectra (Figure **6.14**), in contrast to the larger positive solvatochromism typically observed for conventional D-A TADF emitters (see Chapter 4).[248] This demonstrates that the nature of the excited states of MR-TADF emitters is distinct from conventional D-A TADF emitters. In MR-TADF emitters, both T_1 and S_1 are SRCT excited states (Figure **6.7**), which together with the narrow FWHM of both the fluorescence and the phosphorescence spectra constitute the remarkable characteristics of MR-TADF emitters.

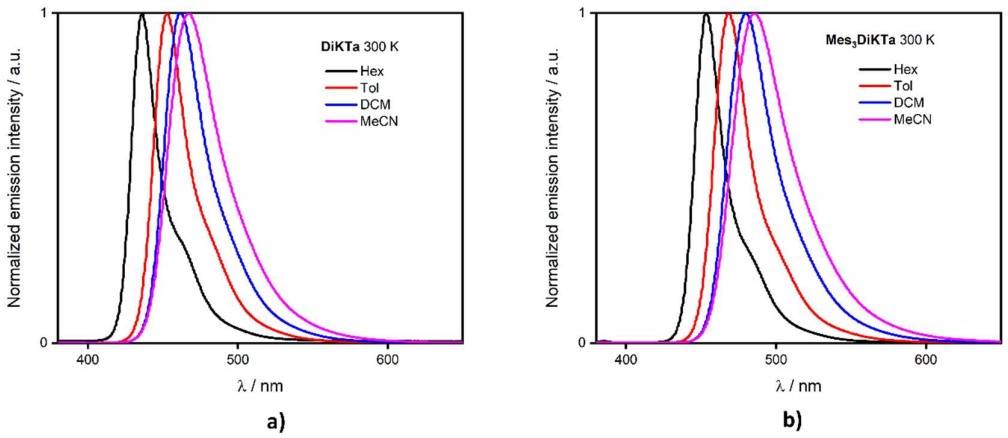

Figure **6.14**. Solvatochromatic PL study of **a) DiKTa** λ_{exc} = 335 nm and **b) Mes$_3$DiKTa**, λ_{exc} = 345 nm.

Time-resolved PL was measured in PhMe. The decays show bi-exponential kinetics with both a prompt, τ_p, ns PL lifetime and a delayed, τ_d, microsecond PL lifetime. Efficient prompt emission is observed with τ_p of 5.1 ns and 6.4 ns, while τ_d was 33 µs and 23 µs, respectively (Figure **6.15**). Φ_{PL} of each emitter was measured, being 26% and 37% for **DiKTa** and **Mes$_3$DiKTa**. There is only a contribution of 1% from the delayed emission in each material. This is consistent with previous studies of MR-TADF emitters that show high radiative decay rates. For example, **DABNA-1** and **DABNA-2** display delayed emission quantum yields, Φ_d, of 4% and 5%, respectively, in 1 wt% mCBP films, while Φ_{PL} is 88% and 90%.[8] The k_{ISC} values are 14.7 and 9.55 × 10^7 s^{-1} for **DiKTa** and **Mes$_3$DiKTa**, respectively. k_{RISC} is slow in both emitters, at 2.3 × 10^3 s^{-1} and 1.3 × 10^3 s^{-1}, values that are much smaller than found in conventional D-A systems[127] but in line with other MR-TADF materials, such as **DABNA-1**, which is 9.9 × 10^3 s^{-1}.[8]

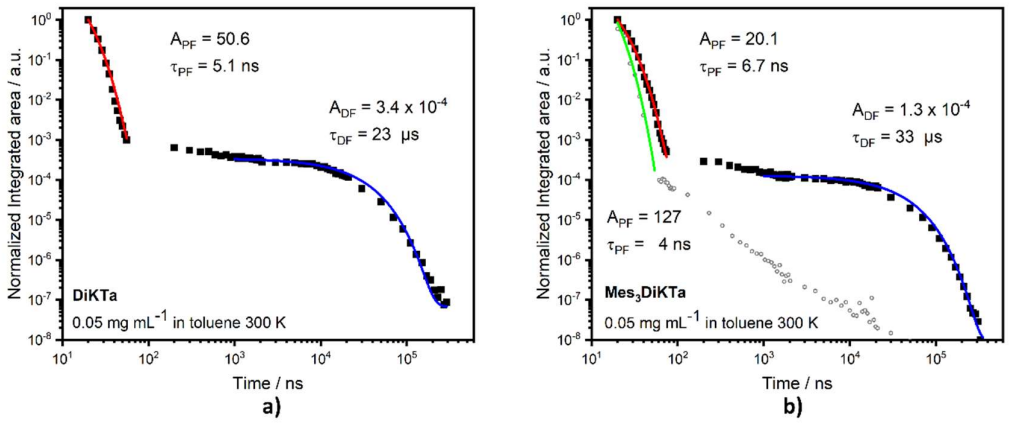

Figure **6.15**. Exponential fitting plots of **a**) **DiKTa** and **b**) **Mes$_3$DiKTa** obtained at 300 K in toluene, λ_{exc} = 355 nm. Prompt and delayed component obtained using the fitting y = A1*exp(-x/t1) + y0. This fit is also used for the fast component of the IRF shown exemplary in **b)** as grey circles.

Table **6.2**. Solution lifetime data, rates and efficiencies for **DiKTa** and **Mes$_3$DiKTa** in dilute PhMe at 300 K.

Compound	λ^a (ε) / nm (/ × 10^3 M^{-1} cm^{-1})	λ_{PL}[b] / nm	FWHM[b] / nm (cm^{-1})	Φ_{PL}[c] (Φ_{DF}[d]) / %	τ_p, τ_d[e] / ns ; µs	k_f[f] / × 10^8 s^{-1}	k_{ISC}[f] / × 10^7 s^{-1}	k_{RISC}[f] / × 10^3 s^{-1}
DiKTa	321 (2.4), 334 (3.5), 412 (9.6), 433 (21)	453[g]	27 (1251)[d]	26 (1)	5.1; 23	1.96	14.7	2.3
Mes$_3$DiKTa	330 (6.2), 345 (6.7), 423 (10), 451 (27)	468[h]	29 (1306)[e]	37 (1)	6.7; 33	1.49	9.55	1.3

[a] Obtained under aerated conditions at 298 K. [b] in degassed toluene,[c] λ_{exc} = 360 nm, [d] Obtained from time-resolved PL decay fitting and Φ_{PL}, [e] λ_{exc} = 355 nm, prompt and delayed fluorescence were fitted as single exponential decays, [f] Obtained using equations from ref,[111] [g] λ_{exc} = 335 nm. [h] λ_{exc} = 345 nm.

6.3.5 Solid-state photophysical properties

The solid-state PL behaviour in thin films was investigated with mCP selected as the host owing to its high triplet energy (2.9 eV) and HOMO-LUMO gap (3.7 eV).[223] A concentration of 3.5 wt% was chosen in order to avoid aggregation of the emitters. Promising Φ_{PL} values of 75% and 80% were observed for vacuum-sublimed 3.5 wt% doped films of **DiKTa** and **Mes$_3$DiKTa**, respectively. To probe whether the higher Φ_{PL} of **Mes$_3$DiKTa** may result from the suppression of interchromophore interactions by the mesityl groups, the Φ_{PL} of both materials in mCP as a function of concentration in spin-coated films was measured (Figure **6.16**), which gives slightly lower Φ_{PL} than the vacuum-sublimed ones. Figure **6.16a** shows how for a neat film of **DiKTa**, a distinct second, broad peak emerges at about 540 nm, likely resulting from excimer formation, while a neat film of **Mes$_3$DiKTa** retains its narrow spectral shape. Increased doping is accompanied by a strong reduction in Φ_{PL} for **DiKTa**, while this tails off far more gently for **Mes$_3$DiKTa** (Figure **6.16b**). Clearly, the introduction of the mesityl groups alleviates close interaction, as was intended by the original chemical design.

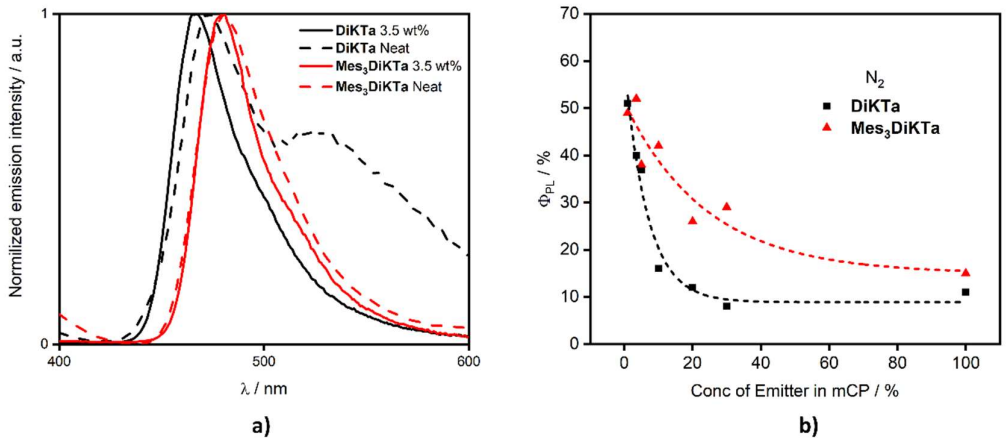

Figure **6.16**. Photophysical properties in mCP films of **DiKTa** (black) and **Mes$_3$DiKTa** (red), where **a**) is the emission spectra in 3.5 wt% mCP (solid) and neat films (dashed) and **b**) is changing Φ_{PL} as a function of emitter concentration, where a dashed exponential fitting has been added to guide the reader.

Figure **6.17** shows the spectral analysis of the prompt fluorescence at 77 K and phosphorescence (time delay 20 ms) at 77 K for **DiKTa** and **Mes$_3$DiKTa** in 3.5 wt% mCP. The ΔE_{ST} was estimated from the onset of these spectra (dotted lines). The slight red-shifted emission observed in **Mes$_3$DiKTa**, for both the S_1 and T_1 states (Table **6.3**) versus **DiKTa** can be correlated to the observed smaller electrochemical gap, and was captured by calculations (Figure **6.7**). Good agreement for ΔE_{ST} between experiment and theory is observed again, with **DiKTa** measured 0.20 eV and calculated of 0.27 eV, while for **Mes$_3$DiKTa** the ΔE_{ST} was found to be 0.21 eV and computed to be 0.26 eV, which is similar to that obtained in toluene.

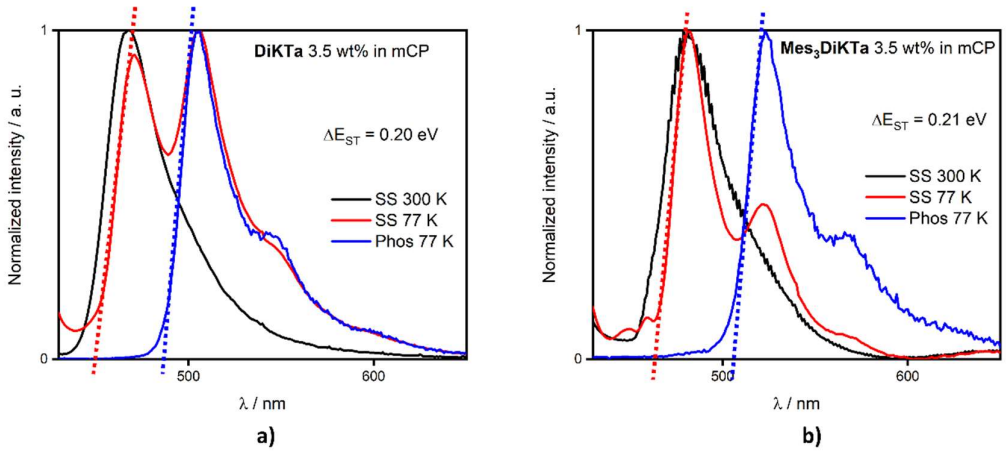

Figure **6.17**. Photophysical data in PhMe of **a**) **DiKTa,** λ_{exc} = 400 nm and **b**) **Mes$_3$DiKTa**, λ_{exc} = 415 nm, where SS 77 K is obtained in toluene glass at 77 K and phos is obtained in PhMe glass at 77 K after 70 ms for 70 ms, where ΔE_{ST} is obtained from the onset of SS 77 K and Phos 77 K (dotted lines).

Figure **6.18** shows the time-resolved PL decay traces at different temperatures for **DiKTa** and **Mes$_3$DiKTa** in 3.5 wt% mCP. At room temperature bi-exponential decay is again observed, with a τ_p of 4.4 ns and 5.9 ns, and a τ_d of 15 µs and 20 µs for **DiKTa** and **Mes$_3$DiKTa**, respectively (Figure **6.18a** and **b**), similar to those obtained in PhMe (Table **6.2**). With changing temperature there is minimal impact on the magnitude of the prompt fluorescence, with identical PL decays (Figure **6.18a** and **b**) and PL spectra (Figure **6.18c** and **d**). There is a temperature dependence of the magnitude of the delayed lifetime, τ_d, which expectedly decreases with decreasing temperature from 300 to 200 K (Figure **6.18a** and **b**), typical of TADF emitters. Prompt fluorescence remains largely unaffected with temperature change, with similar spectral shape for both emitters at varying temperature (Figure **6.18c** and **d**). The delayed emission observed at 300 K and 200 K is fluorescence from the S_1 state with similar spectral shape to prompt fluorescence (Figure **6.18c - f**), while the delayed emission at 100 K and 5 K is phosphorescence from the T_1 state, highlighted by the red shifted emission (Figure **6.18e** and **f**), with RISC completely inhibited at lower temperature (Figure **6.18**). Much like that observed in PhMe, the contribution of the delayed emission to the overall emission in **DiKTa** is more prominent than for **Mes$_3$DiKTa** (Figure **6.19**), indicating higher TADF emission contribution, in line with the increased k_{RISC} observed in toluene.

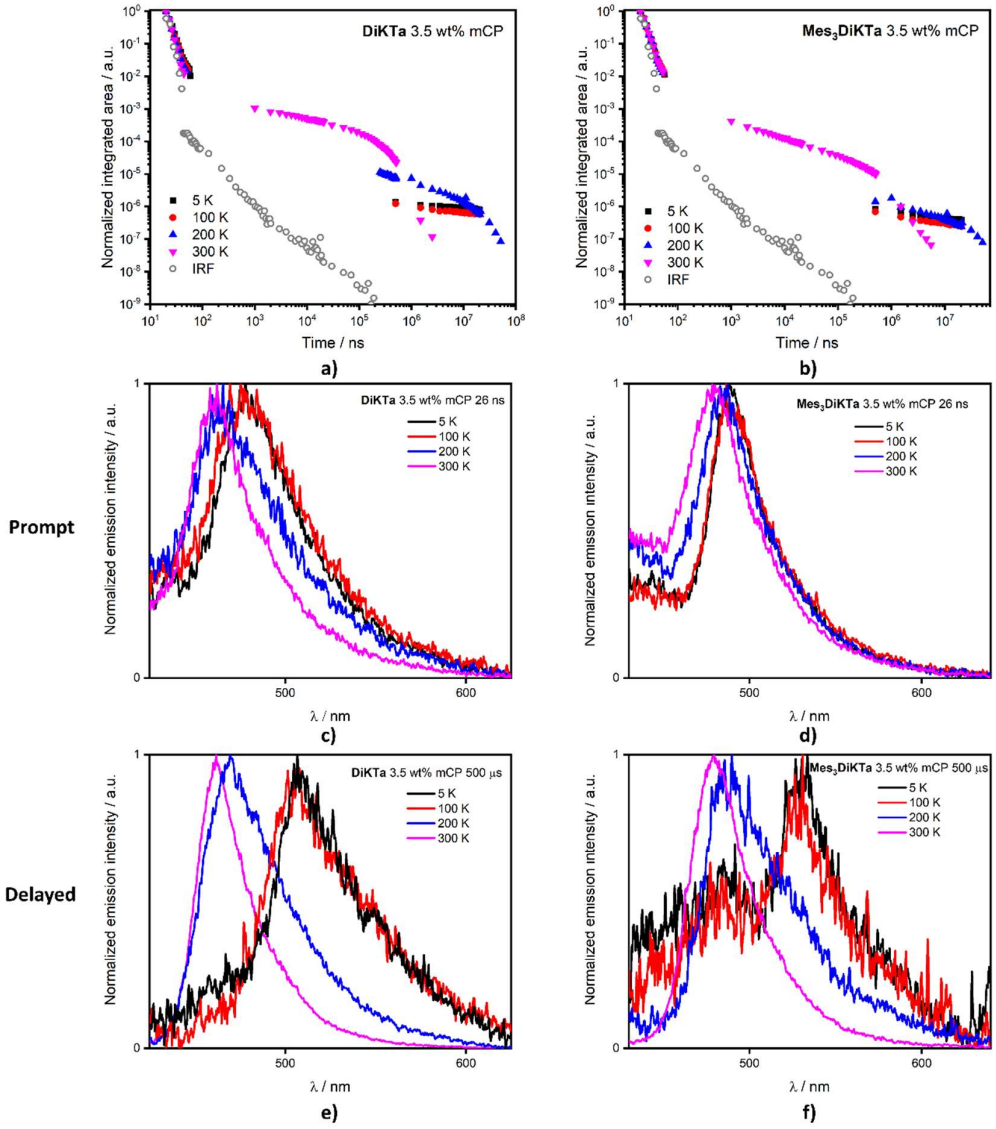

Figure **6.18**. Variable temperature studies in 3.5 wt% mCP films, where **a**) is time-resolved PL spectra of **DiKTa** and **b**) **Mes$_3$DiKTa**, and **c**), **d**), **e**) and **f**) are temperature-dependent photoluminescence spectra at fixed times, where **c**) **DiKTa** at 26 ns, **d**) **Mes$_3$DiKTa** at 26 ns, **e**) **DiKTa** at 500 µs and **f**) **Mes$_3$DiKTa** at 500 µs. λ_{exc} = 355 nm. Where IRF is instrument response function.

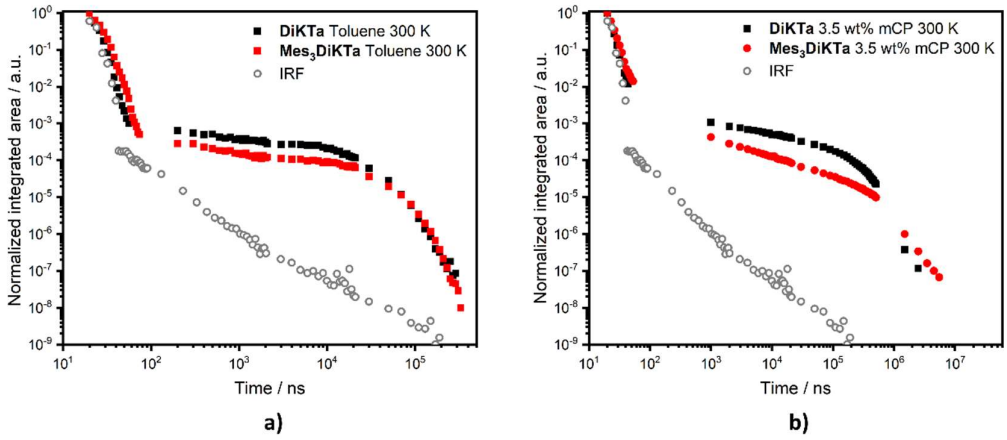

Figure **6.19.** Time-resolved PL decays of **DiKTa** (black) and **Mes$_3$DiKTa** (red) at 300 K in **a**) toluene and **b**) 3.5 wt% mCP films.

Table **6.3**. Thin film photophysical data at 3.5 wt% in mCP.

Compound	**λ_{PL} / nm**	**FWHM / nm (cm^{-1})**	**Φ_{PL} / %**	**$\tau_p;\tau_d$ [a] / ns;µs**	**T_1 [b] / eV**	**S_1 [c] / eV**	**ΔE_{ST} [d] / eV**
DiKTa	463 [e]	37 (1824)	75 [f]	4.4; 15	2.55	2.75	0.20
Mes$_3$DiKTa	477 [e]	37 (1689)	80 [f]	5.9; 20	2.46	2.67	0.21

[a] λ_{exc} = 355 nm at 300 K under vacuum, prompt component obtained using a single exponential, delayed obtained using a stretched exponential [b] Obtained from the onset of the PL spectrum at 77 K after 70 ms, λ_{exc} = 415 nm. [c] Obtained from the onset of the SS spectrum at 77 K, λ_{exc} = 335 nm. [d] $\Delta E_{ST} = E(S_1) - E(T_1)$. [e] Obtained at 300 K, λ_{exc} = 335 nm. [f] Calculated using an integrating sphere, under N_2, λ_{exc} = 335 nm.

6.3.6 Device Properties

To evaluate the potential of **DiKTa** and **Mes$_3$DiKTa** in devices, OLEDs were fabricated. The optimized device structure was: ITO/1,4,5,8,9,11-hexaazatriphenylenehexacarbonitrile [HAT-CN] (10 nm)/TAPC (40 nm)/TCTA (10 nm)/3.5 wt% emitter:mCP (20 nm)/TmPyPb (50 nm)/LiF (1 nm)/Al (100 nm) (Figure **6.20**), where ITO is the anode, HAT-CN acts as the hole injection material, TAPC and TCTA act as HTL, mCP is the host, TmPyPB acts as ETL, and LiF modifies the work function of the aluminium cathode. The doping ratio was optimized at 3.5 wt% for both emitters as a function of Φ_{PL} and to avoid broadening FWHM due to aggregation formation.

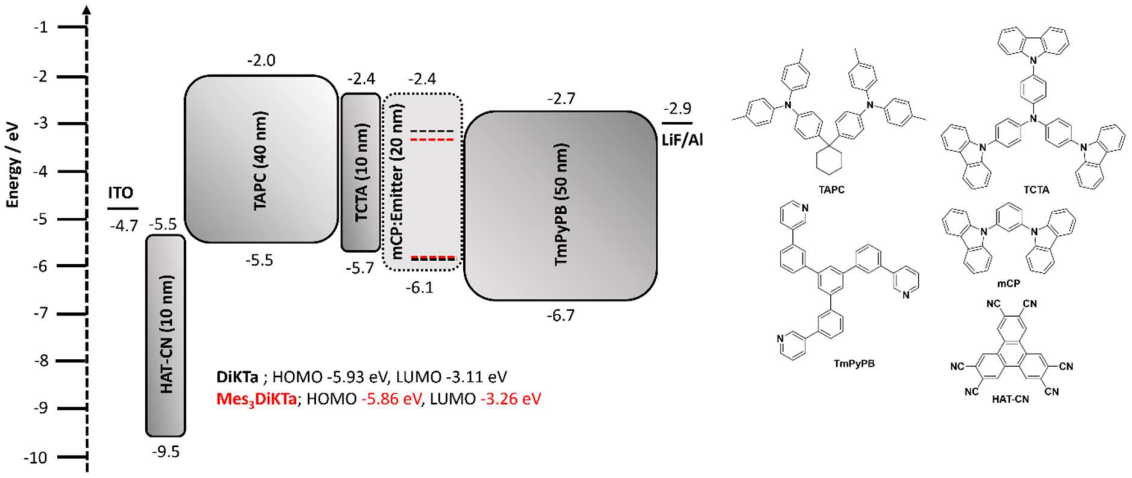

Figure **6.20**. Device architecture and chemical structures of materials used.

Both EL spectra are narrow with FWHM of 39 nm and 36 nm (1848 cm^{-1} and 1572 cm^{-1}), and associated CIE chromaticity coordinates of (0.14, 0.18) and (0.12, 0.32) for **DiKTa** and **Mes$_3$DiKTa**, respectively (Figure **6.21**). These EL spectra are significantly narrower than conventional D-A TADF OLEDs but similar to those EL spectra observed in MR-TADF emitters (Table **6.4**). Figure **6.21** shows EQE versus luminance curves. The **DiKTa** OLED shows an EQE_{max} of 14.7% at 8 cd m^{-2} while the OLED with **Mes$_3$DiKTa** shows an EQE_{max} of 21.1% at 25 cd m^{-2}. Given these EQE_{max} values, the high Φ_{PL} of 80% and 75% in mCP and considering charge balance as 100% and outcoupling efficiency as 25%, the theoretical EQE_{max} for **DiKTa** and **Mes$_3$DiKTa** are ~18% and ~20%, respectively.[249] Inferring that essentially 100% of the triplet excitons are being efficiently harvested and converted to singlet excitons via the TADF mechanism. This is a remarkable and somewhat unexpected result in view of the very low RISC rate in these molecules (see Table **6.2**). It thus appears that, provided the triplets are protected against non-radiative loss mechanisms, a reasonably small ΔE_{ST} value as found in **DiKTa** and **Mes$_3$DiKTa** is enough to quantitatively upconvert all triplet excitations. We thus conclude that the weak coupling between the electronic excitations and the nuclei vibrations associated with the rigid backbone structure not only results in narrow spectral emission but also appears to slow down competitive non-radiative decay channels.

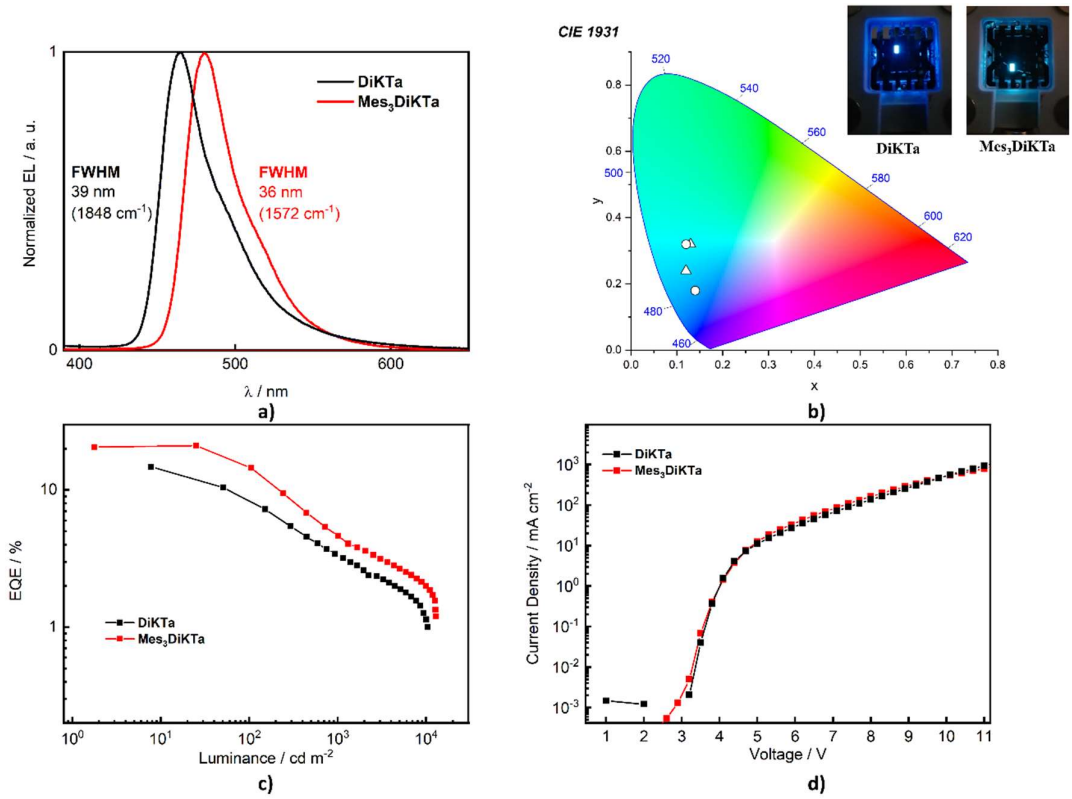

Figure **6.21.** OLED data for **DiKTa** and **Mes$_3$DiKTa**, **a**) electroluminescent spectra, **b**) CIE diagram, where circles are this work, and triangles are previously reported **3Ph-QAD** and **7Ph-QAD** **c**) EQE versus luminance **d**) current density versus voltage curves.

At 100 cd m^{-2} the EQE$_{100}$ value for the OLED with **DiKTa** is 8.3%, decreasing 44% from its maximum value. The EQE$_{100}$ for the device with **Mes$_3$DiKTa** is 14.5%, showing an efficiency roll-off of 31%. At 1000 cd m^{-2} the EQE$_{1000}$ values decrease dramatically to 3.3% and 4.5% for **DiKTa** and **Mes$_3$DiKTa**, which is a decrease of 78% and 79% from their maximum values. This serious efficiency roll-off at high driving voltages was observed in other MR-TADF emitters such as **DABNA-1** and **DABNA-2**,[8] and recently was also observed by Zhang *et al.*,[245] where **3-PhQAD** and **7-PhQAD** EQE values drop more than 85% from their maximum value at 1,000 cd m^{-2}. Thus, we contend that the increased steric bulk afforded by the mesityl groups reduces the efficiency roll-off of the OLEDs when compared to **3-PhQAD** and **7-PhQAD**. Zhang *et al.* have investigated the mechanisms responsible for this strong efficiency roll-off and concluded that both TTA and SPA play significant roles in the efficiency roll-off. Due to the similarity of **3-PhQAD** and **7-PhQAD** with our emitters and the similarity

of the device structures, the cause of our efficiency roll-off is likely to be SPA and TTA as well. Even though the EQE values are poor at high driving voltages, the luminance levels reached by both emitters are excellent (Lum_{max} **DiKTa** = 10,400 cd m^{-2} and Lum_{max} **Mes_3DiKTa** = 13,000 cd m^{-2}), which is not often observed in MR-TADF OLEDs. Both devices operate at similar current densities and show low turn-on voltages of around 3 V (Figure **6.21d**). The previously reported OLEDs with **DiKTa**[250] using a similar device structure to the one used in this study showed EQE_{max} of 19.4% but at luminance lower than 1 cd m^{-2}. At comparable luminance of 10 cd m^{-1}, 100 cd m^{-2} and 1000 cd m^{-2} they obtained similar EQE values of 15%, 9% and 2% to those presented here. As such, **Mes_3DiKTa** demonstrated improved device performance in comparison to previously reported MR-TADF materials, showing the highest EQE value at the relevant luminance of 100 cd m^{-2} among the keto MR-TADF emitters reported at this time (Table **6.4**). In this system, the addition of bulky mesityl substituents clearly has a positive impact within the devices.

Table **6.4.** Device metrics for OLEDs employing **DiKTa** and **Mes_3DiKTa** and those of devices with similar literature emitters.

Emitter	V_{on} / V	EQE_{max} / %	EQE_{100} / %	EQE_{1000} / %	Lum_{max} / cd/m^{-2}	CIE (x,y)	FWHM / nm/	λ_{EL} / nm	Ref
DiKTa	~3	14.7%[a]	8.3	3.3	10,385	0.14, 0.18	39	465	This work
Mes_3DiKTa	~3	21.1 %[b]	14.5	4.5	12,949	0.12, 0.32	36	480	This work
QAD (aka DiKTa)	N/A	19.4[c]	9.4	1.4	1100	0.13, 0.18	39	468	129
3Ph-QAD	N/A	19.1[c]	10.4	3.1	4975	0.13, 0.32	44	480	245
7Ph-QAD	N/A	18.7[c]	5.4	2.1	2944	0.12,0 .24	34	472	245

[a] EQE_{max} calculated at 8 cd m^{-2}, [b] EQE_{max} calculated at 25 cd m^{-2}, [c] EQE_{max} calculated at 0.2 cd m^{-2}

6.4 Conclusions

Based on a new molecular engineering approach to improve the efficiency of MR-TADF emitters in OLEDs, we have designed the molecule **Mes_3DiKTa**. The OLED reached an EQE_{max} of up to 21%. When comparing **Mes_3DiKTa** to the parent **DiKTa** a ~50% improvement in EQE_{max} is observed due to a significant reduction of aggregation-caused quenching by addition of mesityl groups to the

MR-TADF **DiKTa** core. By means of SCS-CC2 quantum-chemical calculations, the ΔE_{ST} was accurately predicted, with calculated values for **DiKTa** and **Mes$_3$DiKTa** being 0.27 eV and 0.26 eV compared to 0.20 eV and 0.21 eV determined experimentally in 3.5 wt% mCP, with SCS-CC2 calculations showcasing a viable strategy to MR-TADF design. The modest ΔE_{ST} value originates from the nature of the involved electronic excitations that involve short-range reorganization in the electronic density offering simultaneously large singlet radiative decay rates and small singlet-triplet exchange interactions. Remarkably, despite a very slow reverse intersystem crossing process, all triplets upconvert into singlets in electroluminescence, a result ascribed to the rigid nature of the emitters mitigating NRD channels. Compared to **DiKTa**, **Mes$_3$DiKTa** shows an improved OLED efficiency with higher EQE_{max} (21.1% vs 14.5%) and reduced efficiency roll-off (EQE at 100 cd m^{-2} 14.5% vs 8.8%). The improvement in device results from the use of mesityl side groups in **Mes$_3$DiKTa** that act to minimize quenching and even improve Φ_{PL}. Their presence only modestly impacts the emission colour, with CIE coordinates red shifted to those measured for the **DiKTa** core.

Chapter 7: The modelling of multi-resonant thermally activated delayed fluorescence emitters – accounting for double excitation is key!

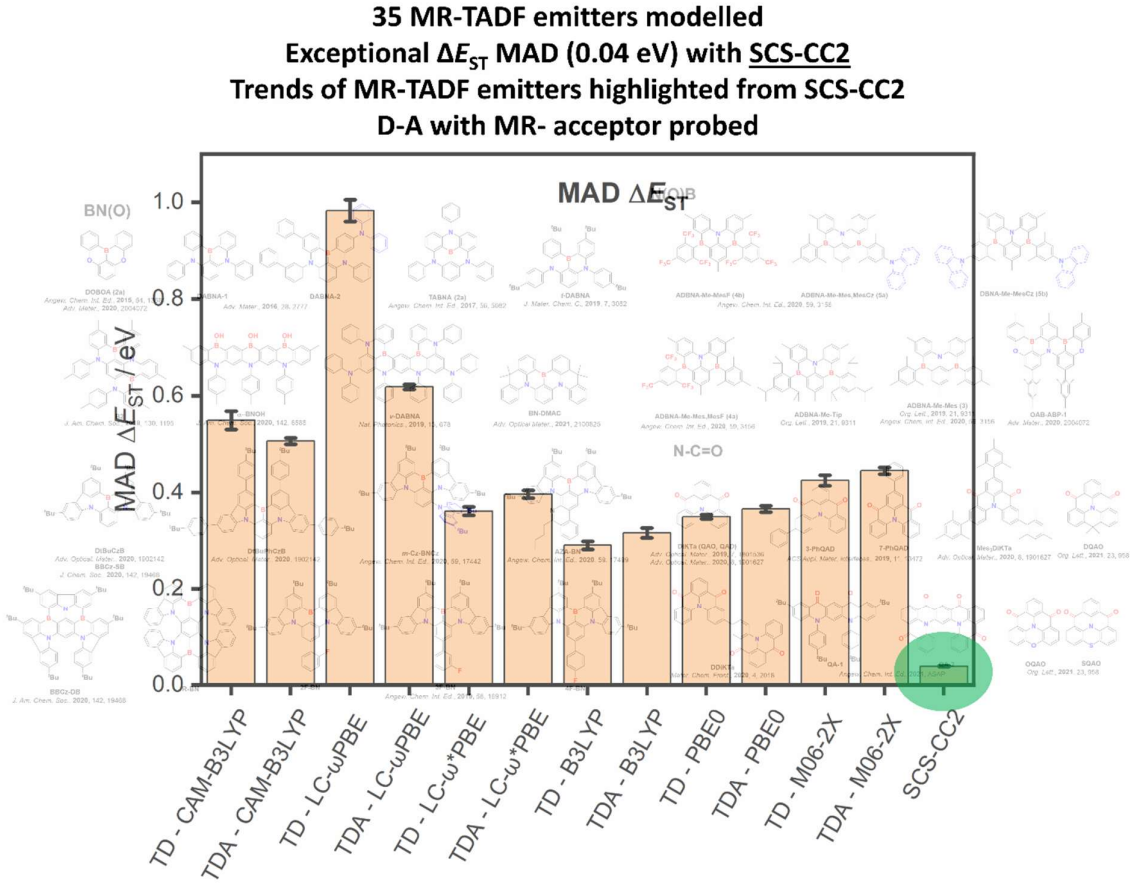

7.1 Introduction

In Chapter 6, two new MR-TADF materials were presented, **DiKTa** and **Mes$_3$DiKTa**. Following the publication of our work the area of MR-TADF emitter development has grown rapidly, with a range of structures reported now covering the full spectral range. The OLEDs using these compounds show in some cases very high EQE_{max} values, albeit efficiency roll-off typically remains large (see Chapter 1 for more detail of structures). Despite the nearly 100 emitters now reported, in each instance the computational analysis provided is limited and erroneous. The focus, in most examples, centres on a DFT ground state picture and an analysis only of the HOMO and LUMO densities, where the identification of a complimentary pattern of the densities in these two orbitals being the primary criterion for MR-TADF.[9] This is problematic as this picture only provides insight into the ground state and doesn't accurately describe the excited state character. The majority of the literature centres on reporting the calculated energy of the S_1 state along with its oscillator strength, while discussion surrounding T_1 is largely neglected and ΔE_{ST} not reported, likely owing to the poor prediction of the latter. Beyond calculations, MR-TADF is often inferred from the small ΔE_{ST}, temperature dependent decay profile, narrow emission spectra and minimal positive solvatochromism. The first two observations are characteristic of any TADF emitters, while narrow emission simply implies a rigid structure and the small solvatochromism showcases a compound with an excited state of weak CT character. Although these characteristics can help to identify MR-TADF compounds they cannot be used exclusively for this purpose. Appropriate calculations are key to MR-TADF assignment, distinguishing clearly SRCT states that are emblematic of MR-TADF from long range CT observed in most D-A TADF emitters (Figure **7.1**).

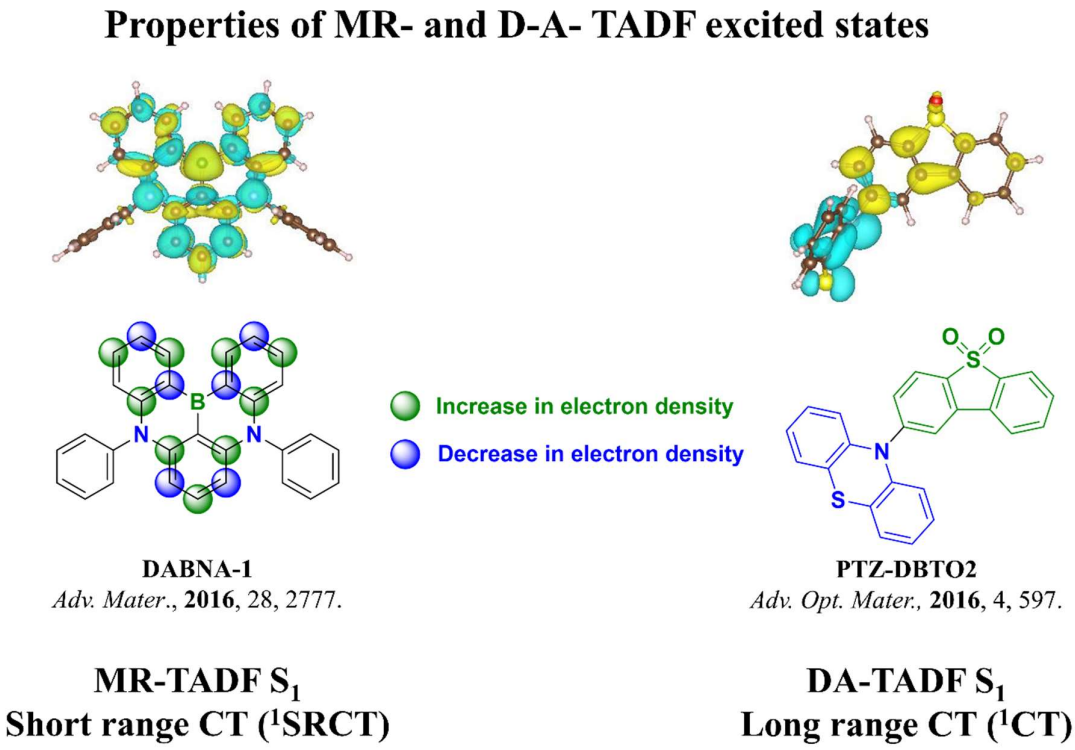

Figure **7.1**. Calculated and simplified difference density plots of the S_1 excited state of prototypical MR-TADF and D-A TADF compounds.

As shown in Chapter 6, the use of SCS-CC2 provides an excellent description of ΔE_{ST}. This is associated with the inclusion of higher-order excitations (double, triple, etc., Figure **7.2**) starting from the Hatree-Fock wavefunction achieved using coupled cluster calculations (see Chapter 2 for more detail). The partial inclusion of double excitations within SCS-CC2, which are neglected in TD(A)-DFT, is the primary reason for the greater accuracy in predicting ΔE_{ST}, where the S_1 state is stabilized thanks to a better description of the Coulomb correlation interaction. However, the increase in accuracy also results in an increase in computational cost. The computational time of coupled-cluster calculations with CCSD scale with N^6, where N is the number of basis sets. These can be reduced somewhat to N^5 for CC2 as double excitations are partially included (see Chapter 2 for more details).[180] The inclusion of higher order excitations would provide greater accuracy but at substantial cost (Figure **7.2**), but previous work (presented in Chapter 6) has highlighted that SCS-CC2 calculations provide sufficiently good agreement between experimental and computed ΔE_{ST}. It should be noted that second-order

algebraic diagrammatic construction, ADC(2)[251] and SCS-ADC(2)[252], that include partial double excitations similar to SCS-CC2 have also been applied to MR-TADF with some success but are not included in this chapter.[153, 251]

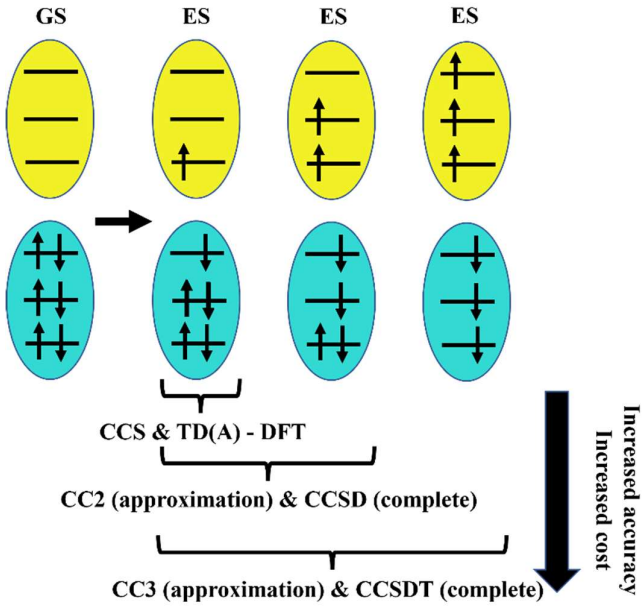

Figure **7.2.** Simplified electronic picture highlighting the excited state contributions to DFT, CCS, CC2, CCSD, CC3 and CCSDT calculations for a singlet excited state, where blue is the ground state and yellow the excited state.

7.2 Motivation and Chapter outline

In Chapter 6, SCS-CC2 was introduced as a computational method to accurately predict ΔE_{ST} of MR-TADF materials. This Chapter aims to document the various modelling approaches of MR-TADF emitters, contrasting these with the robustness of the SCS-CC2 calculations in a benchmarking study. Calculations using well known DFT methods, CAM-B3LYP, LC-ωPBE, LC-ω*PBE, B3LYP, PBE0 and M06-2X considering TD–DFT and TDA–DFT, and SCS-CC2 are compared investigating 35 literature MR-TADF emitters. The ΔE_{ST}, S_1 and T_1 values are compared to experimentally determined values (from the peak maxima of fluorescence and phosphorescence at 77 K, in PhMe where possible). The predictive power is quantified in terms of MAD and σ between calculations and experiments. SCS-

CC2 is clearly the best performing approach with a MAD of 0.04 eV and σ of 0.001 eV. Various trends in MR-TADF emitter design are then discussed across these 35 emitters. These are subsequently used to inform the design of emitters in Chapter 8. The role of higher lying excited states (T_2 and S_2) are discussed in the context of their involvement in RISC. Related Inverted singlet-triplet energy gap (INVEST) materials are also discussed. Beyond MR-TADF emitters, SCS-CC2 is applied to a series of D-A compounds that contain a MR-TADF moiety acting as an acceptor. This chapter reinforces the continued value of using of calculations that include double excitation for MR-TADF design, here championed used SCS-CC2.

7.3 Results and Discussion

7.3.1 Newly modelled emitters

Following the success of SCS-CC2 in Chapter 6, we next studied five other compounds, highlighting their MR-TADF characteristics:[246] **ADBNA-Me-Mes** (originally called **3**), **ADBNA-Me-Mes-MesF** (originally called **4a**) **ADBNA-Me-MesF** (originally called **4b**), **ADBNA-Me-Mes-MesCz** (originally called **5a**) and **ADBNA-Me-MesCz** (originally called **5b**), Figure **7.3**. The experimentally determined ΔE_{ST} values obtained in 1 wt% PMMA were similar, ranging between 0.17 eV and 0.19 eV, values that were well captured in the SCS-CC2/cc-pVDZ calculations (ΔE_{ST} ranging from 0.17 – 0.18 eV). Functionalisation of the mesityl groups had a minimal impact on the emission properties as the S_1 energy in 1 wt% PMMA covered a narrow range between 2.53 eV to 2.56 eV and the emission remained narrow for each compound. SCS-CC2 calculated S_1 levels ranged between 3.02 eV and 3.04 eV. Across the series large Φ_{PL} in 1 wt% PMMA was apparent, 84% - 93%, as is often observed with MR-TADF emitters. Two other derivatives were presented, **ADBNA-Me-Mes-MesNMe2** (originally called **6a**) and **ADBNA-Me-MesNMe2** (originally called **6b**), which possessed noticeably different photophysics, showing broader emission spectra and distinct positive solvatochromsim, along with significantly red shifted emission (S_1 measured in 1 wt% PMMA to be 1.57 eV and 1.28 eV, respectively) and lower Φ_{PL} (26% and 24%, respectively in 1 wt% PMMA). It is clear these two are D-A compounds. One problem here is that the SCS-CC2 calculated S_1 suggested that these states have SRCT character, which is clearly wrong (Figure **7.3**). This topic is revisited, and a solution found in Section 7.3.5.

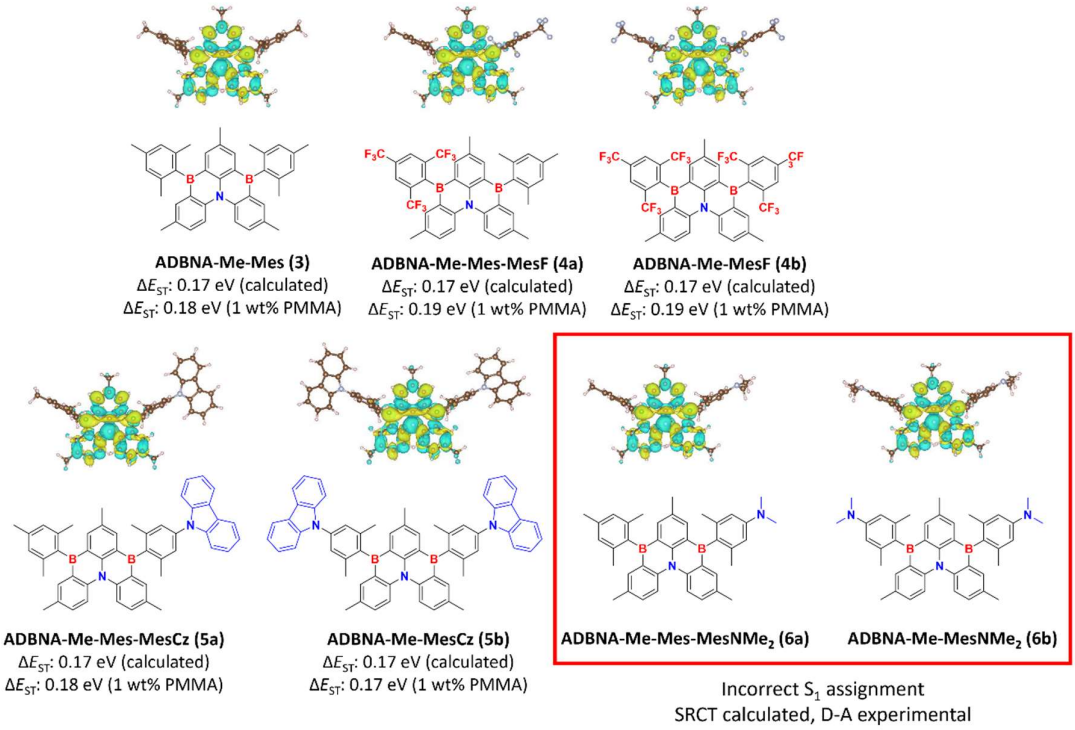

Figure **7.3**. Structures, properties and S_1 difference density patters of modelled **ADBNA-Me-Mes** based emitters.

Computational studies were then undertaken on two linear boron-containing emitters, **α-3BNOH** and **β-3BNOH** (Figure **7.4**).[253] Large differences in the ΔE_{ST} are apparent, being 0.29 eV for **α-3BNOH** and 0.37 eV for **β-3BNOH**, with the specific pattern of B and N atoms directly responsible for these differences. Further, a vastly stabilized S_1 state was predicted for **β-3BNOH** at 2.79 eV, compared to 3.69 eV for **α-3BNOH**. **α-3BNOH** was synthesised and shows a ΔE_{ST} of 0.31 eV in Tetrahydrofuran (THF), in good agreement with calculations. Complex photophysics consisting of both TADF and TTA are observed in solution, with the E_a (0.07 eV) calculated to be much lower than ΔE_{ST}. The role of two intermediate triplet states lying between S_1 and T_1 states are conjectured to be important to mediate RISC in this emitter.

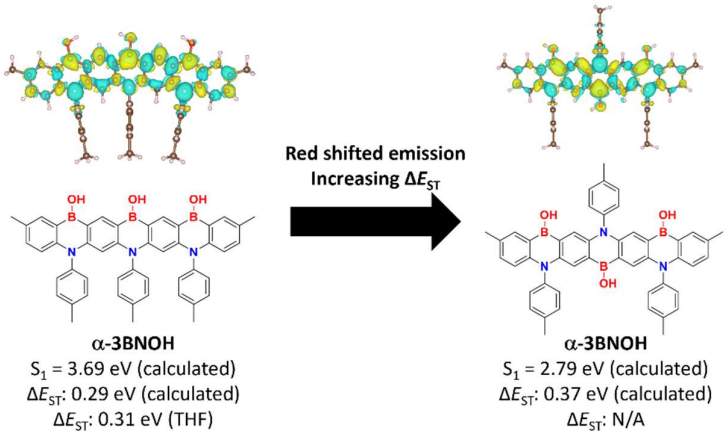

J. Am. Chem. Soc., **2020**, 142, 6588

Figure **7.4**. Structures, properties and S_1 difference density patters of modelled BNOH based emitters.

We next modelled a dimer **DiKTa** derivative, **DDiKTa** (Figure **7.5**).[254] Its ΔE_{ST} was calculated to be identical to that of **DiKTa** at 0.27 eV for both. A modest red shift of S_1 was predicted at 3.39 eV in **DDiKTa** compared with 3.45 eV in **DiKTa**. The experimental ΔE_{ST} in PhMe is 0.21 eV, similar to the calculated value; however, E_a was again much lower at 0.04 eV, again attributed to the presence of intermediate triplet states, which were captured in the calculations. Devices fabricated showed EQE_{max} of 19.0%. The CIE coordinates were (0.18, 0.53) while FWHM of the EL was broader than that for **DiKTa**, (59 nm compared to 39 nm), attributed to the greater conformation freedom between the two **DiKTa** units. Unfortunately, large efficiency roll-off was observed, a continuing problem in MR-TADF emitters.

An extended helically chiral structure, **Hel-DiDiKTa**, was modelled and contrasted with an alternative chiral derivative presented previously (named **Hel-DiKTa-2** here, Figure **7.5**).[255] The ΔE_{ST} in the former was estimated to be 0.24 eV while for the latter it is 0.51 eV. The much larger calculated ΔE_{ST} of the latter, due to the large stabilization of T_1 due to the presence of the naphthalene groups, meant that we excluded its synthesis. Experimentally, TADF was observed in **Hel-DiDIKTa**, with a small ΔE_{ST} of 0.15 eV measured in PhMe, in reasonable agreement with the SCS-CC2 calculations. However, low Φ_{PL} (5% in 3 wt% mCP) and inefficient k_{RISC} (4.1×10^2 s^{-1} in 1 wt% mCP) meant that OLED fabrication was precluded.

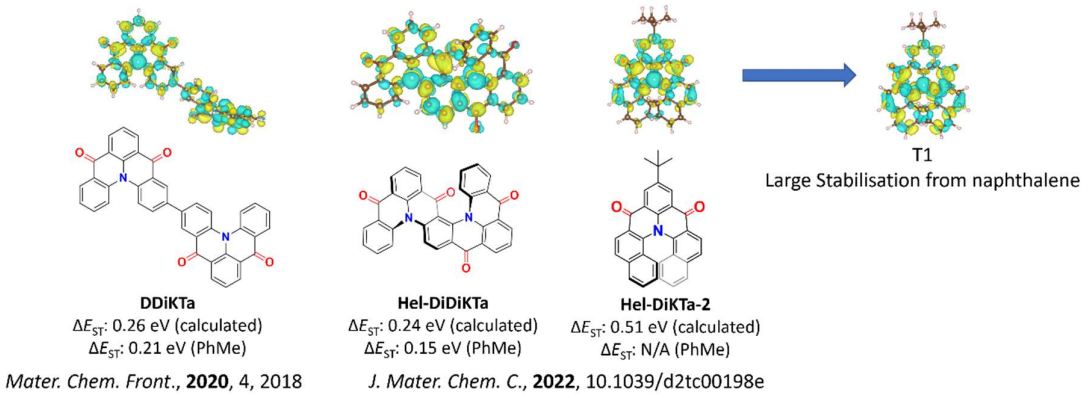

Figure **7.5**. Structures, properties and S_1 difference density patters of modelled ketone-based emitters.

As part of a collaboration,[256] we modelled an unusual series of four-coordinate boron emitters, **BN1, TCz-BN1**, **BN2**, **TCz-BN2** and **BN3** (Figure **7.6**). Unlike most MR-TADF emitters, their emission spectra were broad (82 nm – 151 nm) owing to their larger CT character. SCS-CC2 calculations showcased that these compounds should also be MR-TADF (Figure **7.6**). Similar ΔE_{ST} of 0.03 – 0.08 eV were calculated, with a significant red shift apparent upon changing the coordinating atoms to boron while substitution of the carbazole having only minor effects. S_1 was calculated to be 3.37 eV, 2.80 eV and 2.54 eV for **BN1**, **BN2** and **BN3** respectively. Notably, experimental ΔE_{ST} were somewhat higher than those calculated at 0.16 eV – 0.20 eV. The calculated red-shifted emission was observed experimentally with λ_{PL} in THF of 514 nm, 567 nm and 694 nm for **BN1**, **BN2** and **BN3**, respectively. It is accompanied by decreasing Φ_{PL} of 92%, 64% and 1%, and TADF was observed in all compounds but **BN3**. Improved k_{RISC} was apparent with donor substitution, k_{RISC} of 2.90×10^5 s^{-1} and 2.10×10^5 s^{-1} for with **BN1** and **BN2**, increasing to 4.67×10^5 s^{-1} and 2.44×10^5 s^{-1} for **TCz-BN1** and **TCz-BN2**, respectively. Hyperfluorescence-OLEDs were prepared, and a high EQE_{max} of 25.1% was reported for the **TCz-BN2** device. This work highlights that MR-TADF is possible even with broader emission.

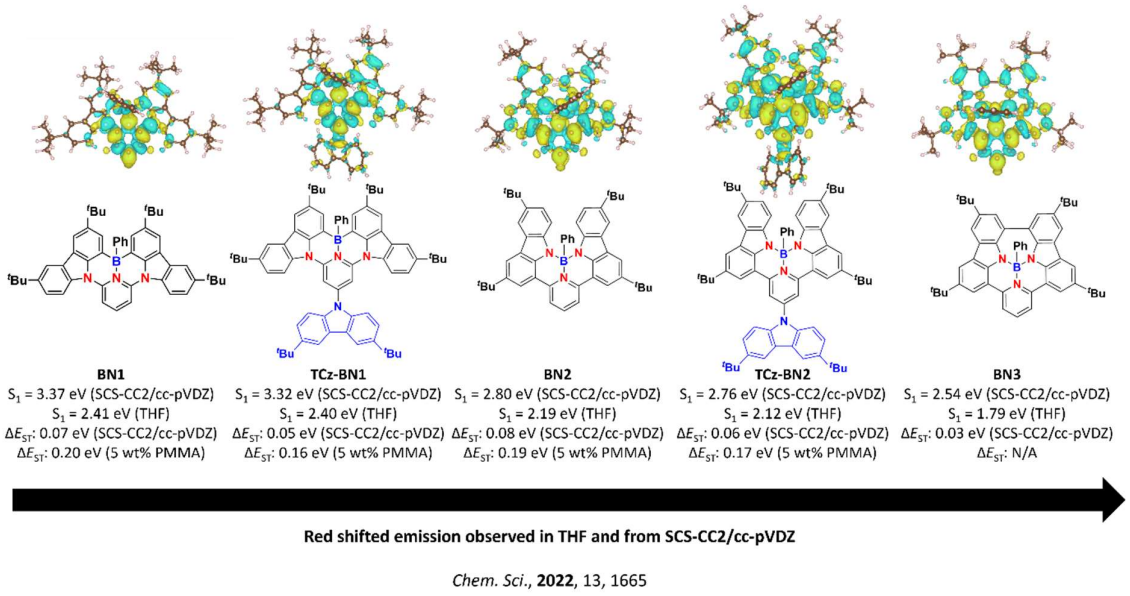

Figure **7.6**. Structures, properties and S_1 difference density patters of modelled 4-coordinate boron-based emitters.

7.3.2 Benchmarking of literature MR-TADF emitters

7.3.2.1 ΔE_{ST} modelling

Beyond this small subset of materials, many compounds from the literature were also modelled using SCS-CC2 and compared to TD(A)-DFT methods employing the functionals CAM-B3LYP, LC-ωPBE, LC-ω*PBE, B3LYP, PBE0 and M06-2X using 6-31G(d,p), that are commonly used by the TADF community. The study aimed to showcase the robustness of SCS-CC2 for MR-TADF emitters, highlighting both some shortcomings using this method but also the problems inherent with DFT calculations. Figure **7.7** shows the chemical structures of the MR-TADF materials selected for this study. The structural diversity of these emitters covers examples across the full spectral range (λ_{PL} ranging from 390 nm to 672 nm, (See Chapter 1 for detailed discussions of each), with examples containing BN(O), N(O)B, and NC=O cores. MAD and σ were presented comparing calculated and experimental values for each computational method.

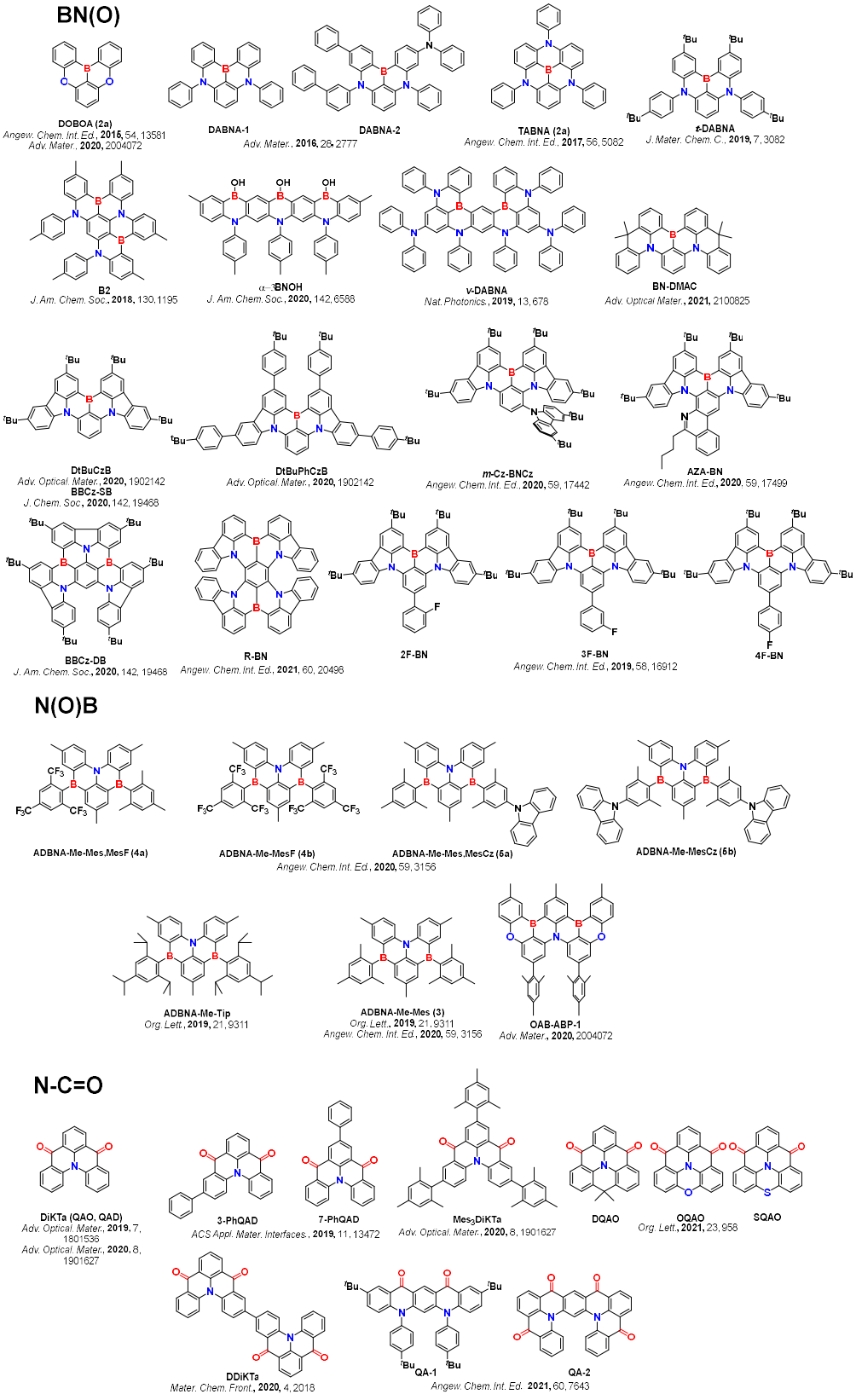

Figure **7.7**. Literature MR-TADF emitters modelled within this study.

TD-DFT or TDA-DFT calculations systematically significantly overestimate ΔE_{ST}. There are, however, two exceptions, **ADBNA-Me-Mes-MesCz** (Figure **7.8a**) and **ADBNA-Me-MesCz** (Figure **7.8b**), where TDA-B3LYP/6-31G(d,p) and TD-B3LYP/6-31G(d,p) both perform well (the use of the PBE0 functional provides similar results). The experimentally determined ΔE_{ST} for **ADBNA-Me-Mes-MesCz** and **ADBNA-Me-MesCz** was 0.18 eV and 0.17 eV in 1 wt% PMMA,[246] while TDA-B3LYP/6-31G(d,p) and TD-B3LYP/6-31G(d,p) estimated ΔE_{ST} to be 0.28 eV and 0.26 eV for **ADBNA-Me-Mes-MesCz**, and 0.18 eV and 0.21 eV for **ADBNA-Me-MesCz**, respectively. ΔE_{ST} was predicted to be 0.17 eV for both compounds using SCS-CC2/cc-pVDZ, which are in excellent agreement with the experimental values.

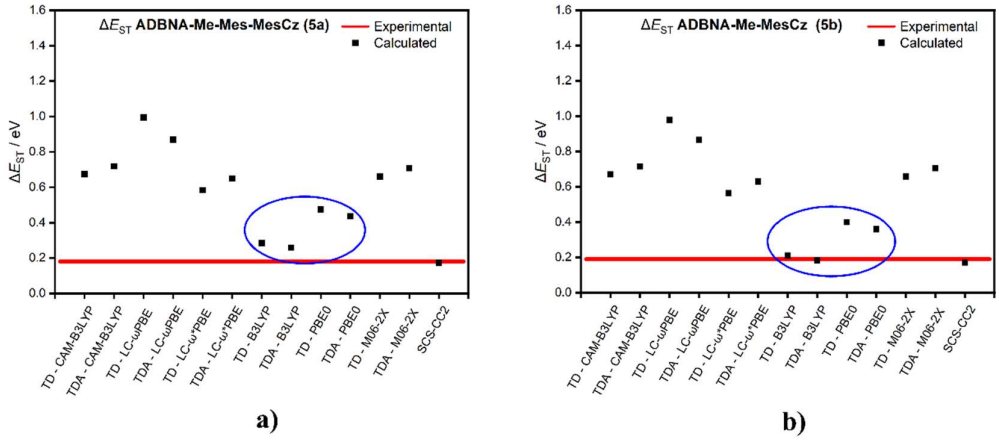

Figure **7.8**. ΔE_{ST} calculated using various methods compared to experimental (red line) for **a**) **ADBNA-Me-Mes-MEsCz** and **b**) **ADBNA-Me-MesCz**, where well predicted ΔE_{ST} from DFT are highlighted (blue circle).

The excited state was assigned experimentally to be SRCT for both **ADBNA-Me-Mes-MesCz** and **ADBNA-Me-MesCz**, which was well reproduced by SCS-CC2/cc-pVDZ (Figure **7.9a** and **c**) as Δρ is localized on adjacent atoms. The SRCT nature was not captured by either TDA-B3LYP/6-31G(d,p) and TD-B3LYP/6-31G(d,p); instead, a ^{1}CT state was predicted where the density transferring from the phenylcarbazole to the MR-TADF core (Figure **7.9b** and **d**). The observation of an

overstabilized CT state has been a well-documented weakness of DFT functionals such as B3LYP and PBE0 and is a consequence of self-interaction due to their low content in HF like exchange.[175]

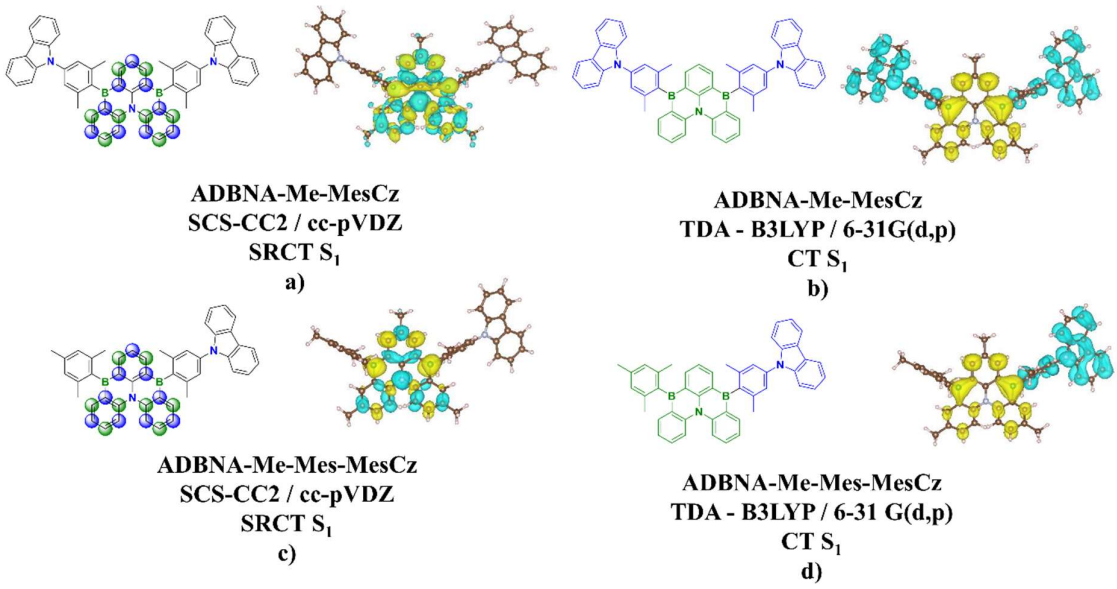

Figure **7.9**. Simplified and calculated difference density plots for first singlet excited states for **a**) **ADBNA-Me-Mes-MesCz** with SCS-CC2/cc-pVDZ, **b**) **ADBNA-Me-Mes-MesCz** with TDA-B3LYP/6-31G(d,p), **c**) **ADBNA-Me-MesCz** with SCS-CC2/cc-pVDZ and **d**) **ADBNA-Me-MesCz** with TDA-B3LYP/6-31G(d,p), where blue balls represent decreased density and green balls increased density with assigned nature included.

Beyond these two emitters, the DFT calculated ΔE_{ST} is consistently too high regardless of the functional employed; the long range corrected functionals CAM-B3LYP and LC-ωPBE were the poorest performing (see Table **7.2** for the MAD values). There is a slight but not significant improvements of the MAD when TDA-DFT calculations are used compared to TD-DFT calculations, this due to an improved T_1 description.[198] When the ω value of LC-ωPBE is tuned for each emitter individually, a dramatic improvement in ΔE_{ST} becomes apparent, with the MAD dropping to 0.36 eV and 0.40 eV for TD-LC-ω*PBE/6-31G(d,p) and TDA-LC-ω*PBE/6-31G(d,p) calculations, respectively, values that are still much higher than those using SCS-CC2/cc-pVDZ (see Table **7.2**). A gradual decrease in the MAD is observed when hybrid functionals are employed with decreasing HF

contribution, moving from 0.42 eV (0.44 eV), 0.35 eV (0.37 eV) to 0.29 eV (0.32 eV) for M06-2X, PBE0 and B3LYP using TD-DFT (TDA-DFT), respectively. This observation was previously reported by us, with the LDA functional (with no HF exchange) performing reasonably well for **DABNA-1** but at the expense of a wrongly predicted nature of the S_1 excited state.[147] When SCS-CC2/cc-pVDZ is applied, a remarkable MAD of 0.04 eV is achieved for these compounds, with low σ of 0.001 eV (Figure **7.10** and Table **7.1**). The vastly superior performance is testament to the (partial) inclusion of double excitations, which is neglected in the TD(A)-DFT calculations.

Table **7.2**. MAD and r^2 of T_1 and S_1 and ΔE_{ST} between computed and experimental data, where r^2 is calculated considering only boron emitters or all emitters.

	CAM-B3LYP		**LC-ωPBE**		**LC-ω*PBE**		**B3LYP**		**PBE0**		**M06-2X**		**SCS-**
	TD	**TDA**	**TD**	**TDA**	**TD**	**TDA**	**TD**	**TDA**	**TD**	**TDA**	**TD**	**TDA**	**CC2**
MAD ΔE_{ST} / eV	0.55	0.51	0.98	0.62	0.36	0.40	0.29	0.32	0.35	0.37	0.42	0.44	0.04
r^2 ΔE_{ST} (B only)	0.56	0.53	0.04	0.66	0.49	0.39	0.13	0.02	0.56	0.24	0.63	0.37	0.72
r^2 ΔE_{ST} (All)	0.53	0.41	0.08	0.37	0.26	0.17	0.16	0.05	0.42	0.21	0.53	0.29	0.53
MAD S_1 / eV	0.90	0.99	1.22	1.33	0.47	0.54	0.35	0.41	0.46	0.52	0.86	0.94	0.55
r^2 S_1 (B only)	0.89	0.94	0.95	0.96	0.88	0.87	0.80	0.73	0.92	0.92	0.90	0.93	0.98
r^2 S_1 (All)	0.80	0.80	0.79	0.80	0.62	0.61	0.71	0.71	0.84	0.82	0.79	0.79	0.69
MAD T_1 / eV	0.36	0.48	0.33	0.72	0.11	0.15	0.07	0.09	0.11	0.16	0.43	0.49	0.56
r^2 T_1 (B only)	0.93	0.94	0.60	0.93	0.92	0.91	0.87	0.85	0.93	0.94	0.92	0.92	0.99
r^2 T_1 (All)	0.81	0.84	0.52	0.81	0.72	0.68	0.79	0.78	0.85	0.86	0.82	0.80	0.71

There is only a modest linear correlation (r^2 of 0.53 for SCS-CC2) between the experimentally determined and calculated ΔE_{ST} (Table **7.2**). The r^2 increases to 0.72 when only the boron-containing emitters (Figure **7.11**) are included in the analysis. The poorer correlation found when the ketone-containing emitters are included can be understood as resulting from the greater degree of positive solvatochromism observed for these molecules compared to the boron-containing compounds (*vide infra*), which is not captured in our gas-phase calculations. Notably, our prediction for **BBCz-DB** (Figure **7.11b** blue circle) deviates considerably from the linear fit; it is not clear at this stage what is

the origin of this deviation. Compared to SCS-CC2, TD(A)-DFT performs worse, with r^2 ranging between 0.02 and 0.66 when only the boron compounds are included in the data set (Table **7.2**).

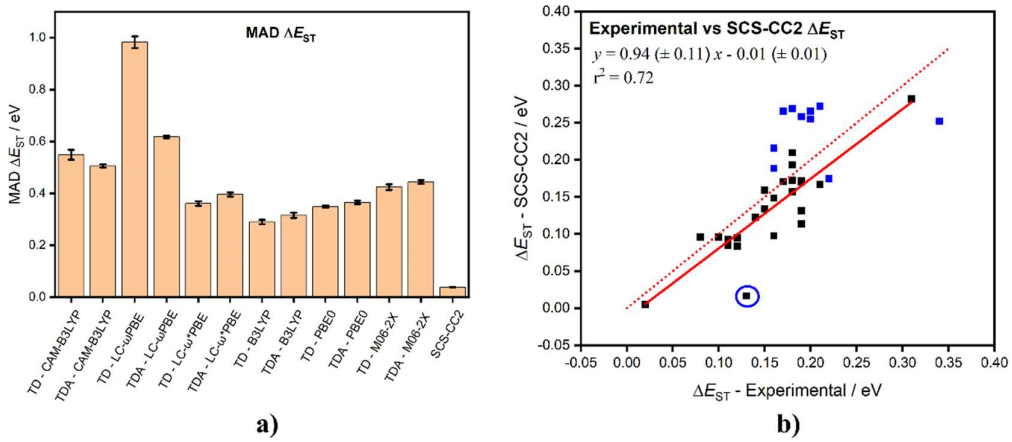

Figure **7.11**. **a)** ΔE_{ST} MAD computed between the different computational methodologies and the experiments and the associated error, **b)** Experimental vs SCS-CC2 calculated vertical ΔE_{ST}, where blue points are N-C=O emitters, the red solid line shows the trend line for the data with the N-C=O emitters excluded, and the dotted red line denotes the theoretical idealized fit. The blue circle corresponds to **BBCz-DB**, a boron-based emitter.

7.3.2.2 Excited state energies

In terms of materials development, it is not only important to accurately predict ΔE_{ST} but it is equally essential that the computational methodology accurately predict the absolute energies of both the S_1 and T_1 states. Owing to the rigid character of MR-TADF compounds, there are small observed Stokes shifts,[8] which supports the use of vertical excitations based on a ground-state optimized geometry as a first approximation to calculating the lowest-lying excited state energies, with the calculated values thus higher in energy than those experimentally determined. Furthermore, the lack of significant observed solvatochromism in solution,[149] and the minimal impact of polarity in the solid state implies that the inclusion of a solvent continuum model is not required for accurate predictions, thus gas phase calculations can be used as reasonable predictors for the optoelectronic properties of this class of emitter. For each DFT functional, a large MAD for the S_1 was energy observed. This ranges

between 0.91 eV and 1.34 eV when the long range corrected functionals CAM-B3LYP and LC-ωPBE are employed, dropping, when ω is tuned, to 0.47 eV and 0.55 eV, for TD-DFT and TDA-DFT respectively. Decreasing the HF like exchange in the functional resulted in smaller MAD, with M06-2X displays the largest MAD and B3LYP exhibiting the smallest MAD among the hybrid functionals evaluated (Table **7.2**). For SCS-CC2 MAD for S_1 is 0.55 eV similar to the low HF content functionals (Table **7.2** and Figure **7.12a**). There is a remarkable linear correlation ($r^2 = 0.98$) between experimental and SCS-CC2 calculated S_1 energies, when only including the boron-containing emitters Figure **7.12b**). When the NC=O compounds are also included within the analysis, the r^2 is only 0.69 as in these emitters the influence from solvents and external polarisation are more pronounced, and are indicated by blue points in Figure **7.12b**. For TD(A)-DFT, an improved correlation (r^2 ranging from 0.73 and 0.96) is apparent only when NC=O emitters are omitted; the r^2 ranges values are between 0.61 and 0.84 when all compounds are included in the study (Table **7.2**).

TD(A)-DFT calculations do a much better job of predicting the energy of the T_1 states where the MAD values are much smaller than those for the S_1 state (Figure **7.12c** and Table **7.2**). The lower MAD observed at TD(A)-DFT for the T_1 in comparison to S_1 highlights the lesser importance of the contributions of double excitations in the description of the triplet state, which also implies that there is a smaller contribution of the Coulomb correlation to the description of the triplet wavefunction. The SCS-CC2 T_1 MAD value is 0.56 eV, which is of the same order as the S_1 MAD (0.55 eV), explaining the remarkably small ΔE_{ST} MAD (Figure **7.11)** and thus predictive power of this methodology. Similarly to the analysis employed for the comparison of the calculated and experimentally determined S_1 energies, when the triplet energy data are fitted a strongly linear correlation is present only when NC=O emitters are excluded from the data set, with r^2 of 0.99 (Figure **7.12d**). Inclusion of the NC=O emitters results in a poorer correlation where the r^2 drops to 0.71; the calculated T_1 states of the NC=O emitters are higher energy than those experimentally determined similar to S_1, again highlighted by blue data points (Figure **7.12d**). DFT functionals perform well in terms of linear fitting, with r^2 values surpassing 0.90 for 9 of the 12 approaches when NC=O are omitted (Table **7.2**). Much like S_1, the r^2 values decrease upon NC=O inclusion, with values ranging from 0.50 – 0.86 (Table **7.2**)

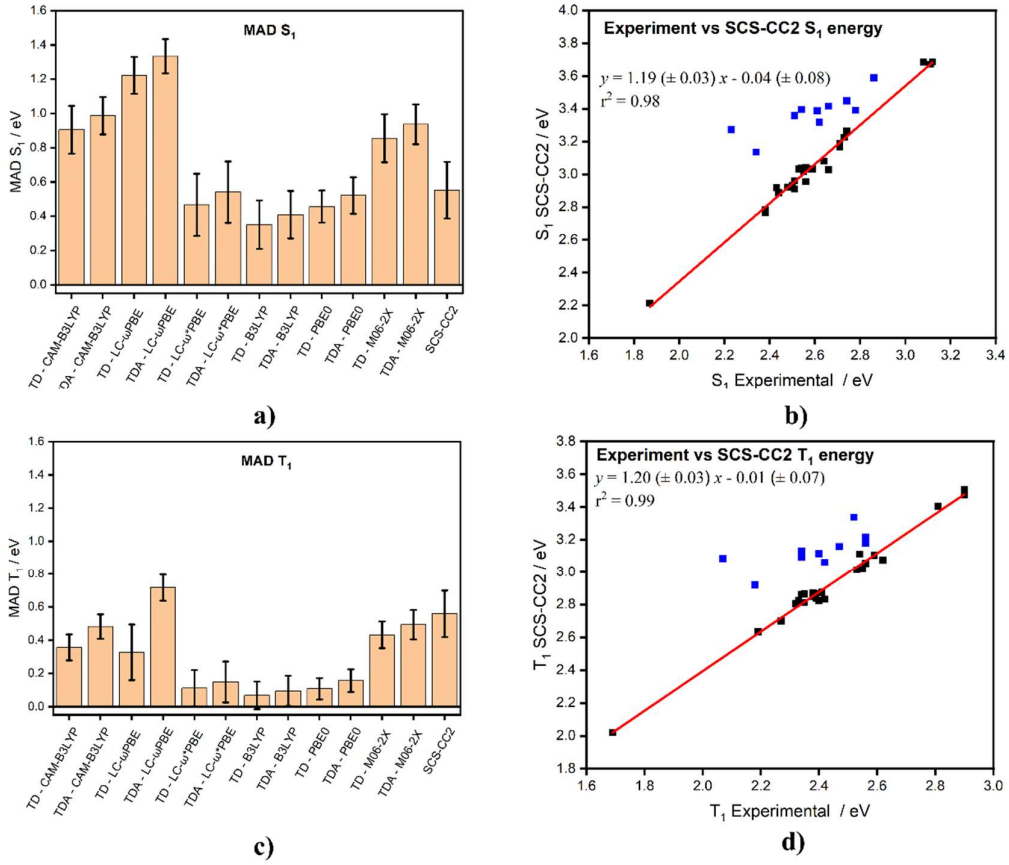

Figure **7.12. a)** S_1 MAD with respect to the experiment, **b)** S_1 experimental vs SCS-CC2 vertical excitation energies for each emitter **c)** T_1 MAD with respect to the experiment and **d)** T_1 experimental vs SCS-CC2 vertical excitation energies for each emitter. The red lines in **b**) and **d**) correspond to a linear fit of the set of data when NC=O are omitted (blue points).

7.3.2.3 Oscillator strength and excited state nature

Taking the SCS-CC2 calculations as the reference method, MAD was reported as the difference between TD(A)-DFT calculated and the SCS-CC2 calculated oscillator strengths. (Figure **7.13**) The MAD values range from 0.04 with TD-CAM-B3LYP/6-31G(d,p) to 0.28 with TD-LC-ω*PBE/6-31 G(d,p) (Table **7.3**). This analysis suggests that TD(A)-DFT calculations predict a similar S_1 nature as the SCS-CC2 calculations as witnessed by the similar (yet not identical) difference density patterns in TD(A)-DFT and SCS-CC2 for most. However, upon closer inspection some significant discrepancies between the difference density patterns predicted between the TD(A)-DFT and SCS-CC2 calculations

are observed. For some molecules, TD(A)-DFT calculations incorrectly assign S_1 has having either CT or n-π* character, when in fact the S_1 state shows SRCT character both experimentally and from SCS-CC2 calculations. For instance, B3LYP and PBE0 both failed to predict the nature of the S_1 state of two emitters, **ADBNA-Me-MesCz** and **ADBNA-Me-Mes-MesCz** (Figure **7.9**). This produced very low oscillator strength for both, calculated at SCS-CC2 to be 0.35 and 0.38 for **ADBNA-Me-Mes-MesCz** and **ADBNA-Me-MesCz** respectively, decreasing to values around 0.01 when B3LYP and PBE0 are employed at TD(A)–DFT, owing to the decoupled ground and excited state densities.

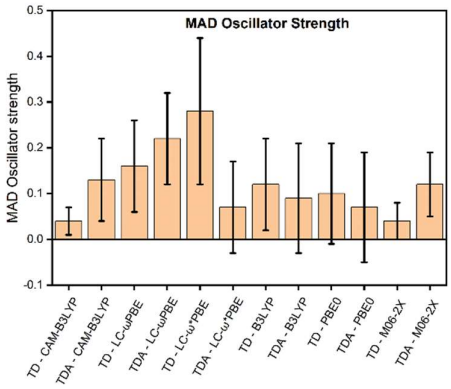

Figure **7.13**. MAD and σ of oscillator strength between TD(A)-DFT and SCS-CC2.

DFT methods such as TD(A)-LC-ωPBE, TD(A)-LC-ω*PBE and TD(A)-M062X do not accurately predict the SRCT nature of the S_1 state of a number of ketone-based MR-TADF compounds **DiKTa**, **DQAO**, **3-PhQAD**, **7-PhQAD**, **DDiKTa**, **QA-2** and **Mes$_3$DiKTa** (Figure **7.14**). Instead, an S_1 state with n-π* character is predicted; notably, SCS-CC2 predicts that the S_2 state for these compounds to have n-π* character and so it appears that DFT methods over stabilize this state at the expense of the SRCT state. The n-π* states predicted have vanishingly small oscillator strength of 0.00 – 0.05, while the oscillator strengths of the SRCT are 0.13 - 0.52. Of the DFT methods assessed, owing to its small MAD of 0.04 and small σ of 0.03, the use of TD-CAM-B3LYP/6-31G(d,p) to capture S_1 excited state character should be sufficient if access to SCS-CC2 or other coupled cluster methods such as (SCS-)ADC2 are not available.

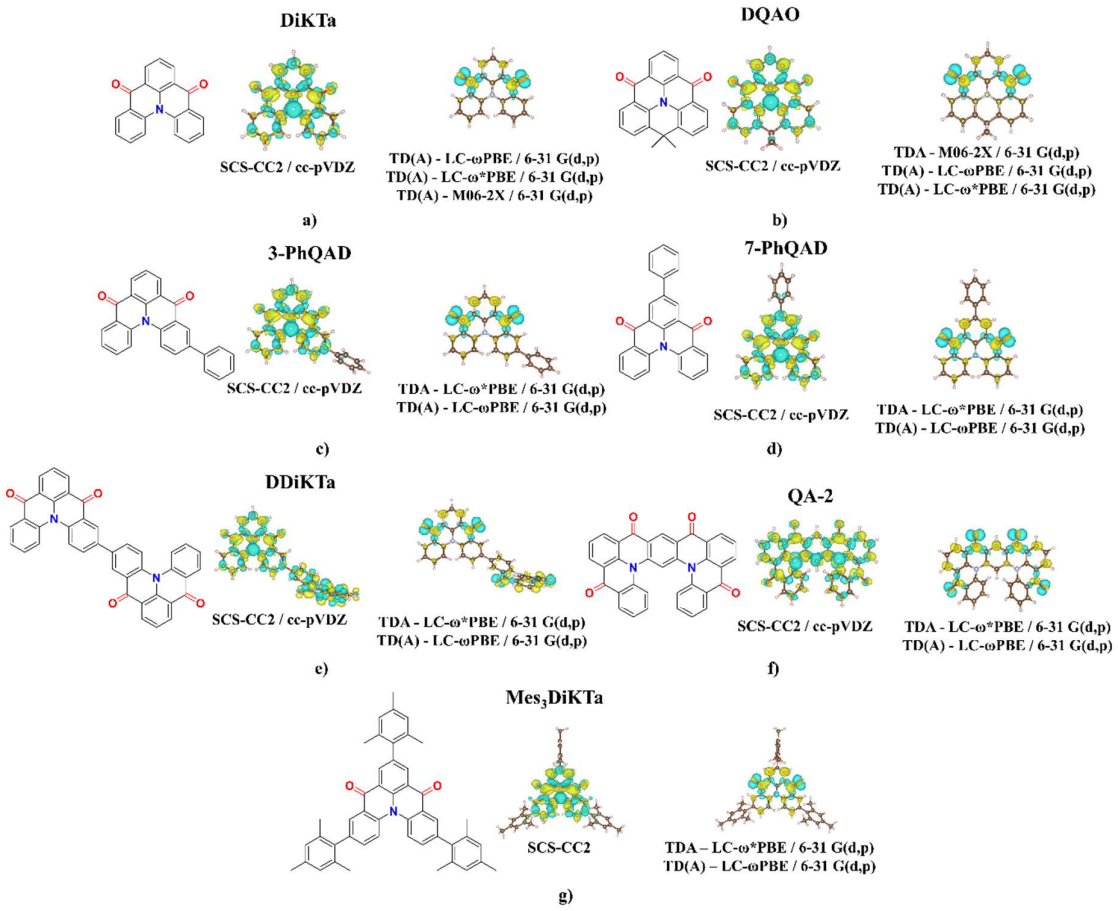

Figure **7.14**. Difference density pictures of S_1 from SCS-CC2 and DFT calculations for **a**) is **DiKTa**, **b**) **DQAO**, c) **3-PhQAD**, **d**) **7-PhQAD**, **e**) **DDiKTa**, **f**) **QA-2** and **g**) **Mes$_3$DiKTa**.

Table **7.3**. Oscillator strength MAD and σ between DFT SCS-CC2 calculations.

	CAM-B3LYP		**LC-ωPBE**		**LC-ω*PBE**		**B3LYP**		**PBE0**		**M06-2X**	
	TD	**TDA**	**TD**	**TDA**	**TD**	**TDA**	**TD**	**TDA**	**TD**	**TDA**	**TD**	**TDA**
MAD	0.04	0.13	0.16	0.22	0.28	0.07	0.12	0.09	0.10	0.07	0.04	0.12
σ	0.03	0.09	0.10	0.10	0.16	0.10	0.10	0.12	0.11	0.12	0.04	0.07

7.3.3 Discussion of RISC mechanism of MR-TADF emitters from an SCS-CC2 perspective

Owing to very accurate predictions of the ΔE_{ST} at the SCS-CC2/cc-pVDZ level, the excited states of these MR-TADF emitters are next discussed. NC=O emitters have a larger predicted ΔE_{ST}

ranging between 0.17 eV and 0.27 eV, while the boron-containing compounds (excluding **α-3BNOH**) have ΔE_{ST} ranging between 0.01 eV and 0.21 eV. Of the C=O emitters, fused **QA-2** has the smallest ΔE_{ST}, likely owing to extended electronic delocalisation afforded by its extended π structure. The largest ΔE_{ST} is observed for **α-3BNOH**, at 0.29 eV, likely due to the smaller electron-withdrawing character of the B-OH compared to other boron emitters. A decreasing ΔE_{ST} is observed across the series of structurally similar **DiKTa**, **DOBNA** and **DABNA-1** (0.27 eV, 0.20 eV and 0.16 eV, respectively). This is in line with an increase in CT character, reflected in the calculated D_{CT}, which rises from 0.81 Å to 0.84 Å and 0.89 Å for S_1 and 0.61 Å to 0.68 Å and 0.75 Å for T_1 for **DiKTa**, **DOBNA** and **DABNA-1**, respectively (Figure **7.15**).

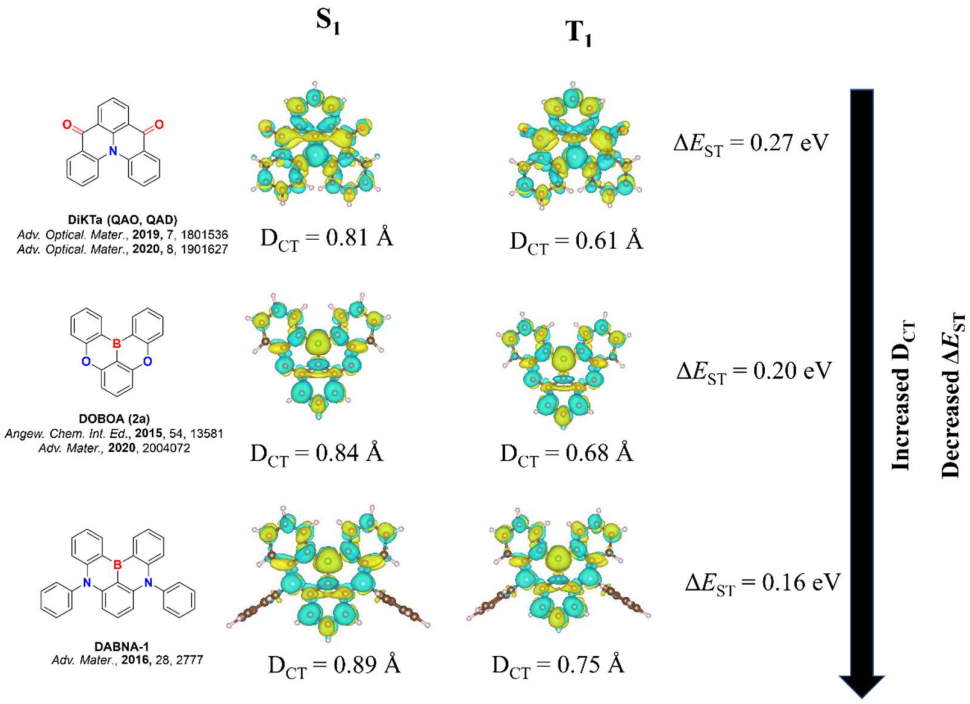

Figure **7.15**. Strategy to decrease ΔE_{ST} with increased D_{CT}, showcased for **DiKTa**, **DOBNA** and **DABNA-1**, with the D_{CT}, ΔE_{ST} and difference density pictures of each included for S_1 and T_1.

Of all the emitters the lowest ΔE_{ST} was achieved for ***ν*-DABNA** (0.01 eV) and **BBCz-DB** (0.02 eV), with the former achieved owing to increased electronic delocalisation and the latter possibly an erroneous calculation, with poor fitting compared to experimental ΔE_{ST} (Figure **7.11**, blue circle). At this stage it is not clear why this boron containing material deviates from the fit. **OAB-ABP-1** had small

ΔE_{ST} of 0.12 eV compared to other nitrogen centred emitters (0.16 eV - 0.17 eV) with extended π-delocalisation afforded by the bridging oxygen atoms key. This π delocalisation explains the modest decrease in ΔE_{ST} when carbazole moieties are incorporated into the molecule in **2F-BN**, **3F-BN**, **4F-BN**, **DtBuCzBN**, **DtBuPhCzBN**, ***m*-CzBNCz** and **AZA-BN** compared to **DABNA-1** and ***t*-DABNA**, (ΔE_{ST} 0.08 eV – 0.13 eV compared to 0.16 eV for both, Figure **7.16**). Similar S_1 and T_1 excited state pictures are apparent for each emitter, visualised according to their difference density patterns, which would suggest small SOC between these two states (see Chapter 1 for more detail).[24]

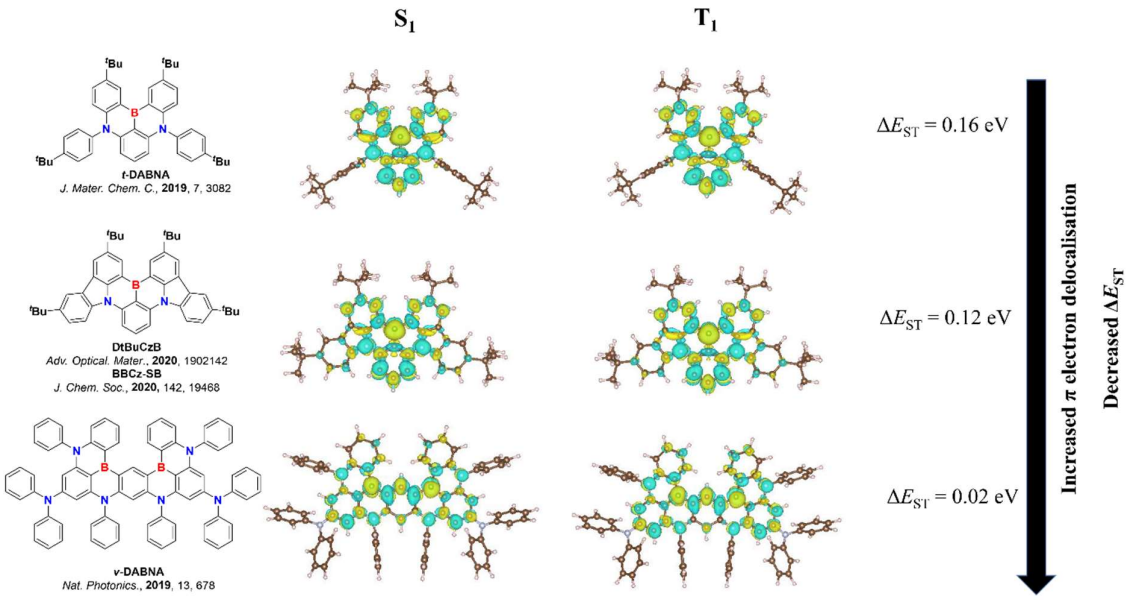

Figure **7.16**. Strategy to reduce ΔE_{ST} with π electron delocalisation, showcased for ***t*-DABNA**, **DtBuCzB** and ***ν*-DABNA** with difference density plots of S_1 and T_1 included for each.

The value of S_1 is an important parameter to accurately predict as it describes the emission colour (Figure **7.17**). Within this series, a few clear trends are apparent, with NC=O emitters generally higher in energy than BN(O) or N(O)B emitters. The higher energy S_1 of NC=O emitters was reported in section 7.3.2.2 and is not observed experimentally owing to greater influence of solvent effects stabilising S_1 (Figure **7.12b**). Replacement of DPA with carbazole in boron emitters results in a stabilisation of S_1 compared to that of **DABNA-1** and its derivatives, as observed for **DtBuCzB**, **2 - 4F-BN**, **DtBuPhCzBN**, **m-Cz-BNCz** and **AZA-BN**. The compounds with the most stabilized S_1 energy

have two boron atoms that are *para* to each other along with two nitrogen atoms *para* to each other (**R-BN**, Figure **7.17b**). Indeed, this red-shifted emission is observed in the literature for this compound and **R-TBN**[257] and **BBCz-R**,[151] both of which were not modelled but follow the same design. Addition of a ^{t}BuCz substituent, ***m*-Cz-BNCz** resulted in red shifted emission. Replacement of the central boron in **DABNA-1** with nitrogen and the peripheral nitrogen atoms with boron as in **ADBNA-Me-Mes** (and derivatives) produced a slight stabilisation in S_1 energy (from 3.26 eV to 3.02 – 30.4 eV across the series), as we initially predicted in Chapter 6 with the proposed emitter ***in*-DABNA**. This trend is observed experimentally.

The roles and positions of higher lying T_2 and S_2 states are discussed, which experimentally are not easily determined (Figure **7.17**). The importance of T_2 has been brought into the centrefold of the TADF mechanism (see Chapter 1).[24, 72, 114, 258] In MR-TADF, RISC can take place either via a super exchange mechanism,[259] or similarly as with D-A TADF materials via a spin-vibronic mechanism involving direct repopulating of these states. For most examples the T_2 is calculated to be much higher in energy than S_1 (Figure **7.17**) which may suggest its contributions to k_{RISC} are minimal. There are, however, six exceptions, namely **α-3BNOH**, **DDiKTa**, **B2**, **QA-1** and **QA-2**. **TABNA** contains a degenerate T_2 state owing to the symmetric HOMO and HOMO-1 orbitals in this system. Notably, **DDiKTa** and **QA-1** all show very efficient RISC rates experimentally,[169, 253, 254] which is consistent with the involvement of T_2 facilitating RISC. Generally smaller ΔE_{S1T2} is observed for the NC=O emitters, which despite their larger calculated ΔE_{ST} values should assist k_{RISC}, beyond this, no clear trends to minimise ΔE_{S1T2} are available at this stage for MR-TADF emitters. The position of higher-lying singlet states has also been conjectured to facilitate RISC in MR-TADF emitters;[260] however, in the majority of the examples S_2 is calculated to be over 0.4 eV destabilized compared to S_1, rendering its influence to the RISC mechanism likely to be minimal. Several exceptions exist namely with **α-3BNOH**, **DDiKTa**, **B2**, **QA-1, TABNA** and **QA-2** which all have low-lying S_2 states. ***v*-DABNA** and **BBCz-DB** also possess smaller S_1-S_2 gaps. The similar S_1 and T_1 nature, the large ΔE_{S1T2} and ΔE_{S2S1} may explain why MR-TADF emitters exhibit much lower k_{RISC} values than the highest performing D-A systems (see Chapter 1). Proposed strategies to improve k_{RISC} in MR-TADF emitters are discussed in Chapter 1.

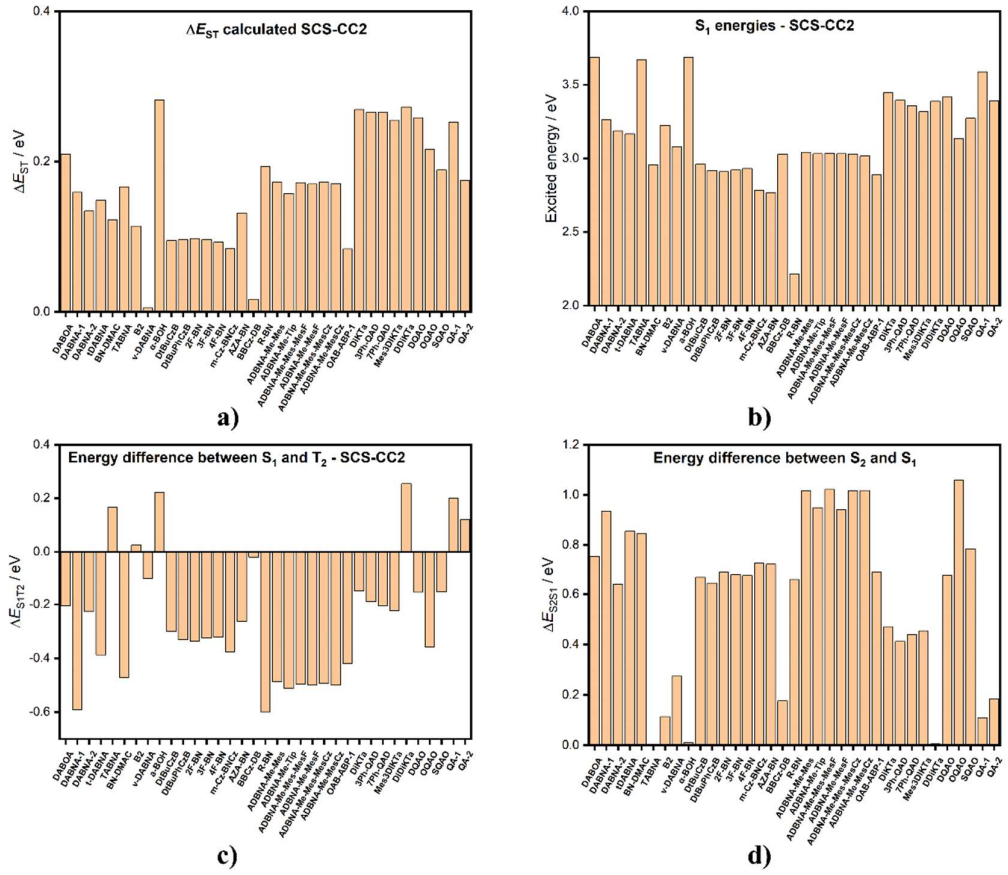

Figure **7.17**. Changing properties of each of the MR-TADF emitters calculated at SCS-CC2/cc-pVDZ, where **a)** is ΔE_{ST}, **b**) is S_1 energy, **c**) is the energy difference between S_1 and T_2 and **d)** is the energy difference between S_2 and S_1.

7.3.4 Outliers and INVEST compounds

Compounds that violate Hund's rule, now coined as INVEST molecules, have been investigated computationally recently where wavefunction calculations predict a negative ΔE_{ST},[252, 261, 262] and more recently some experimental work has evidenced this behaviour in highly symmetric systems.[263] The mechanism is primarily associated to spin polarization,[13] where open shell singlets are stabilized below that of the triplet, which is often associated with a singlet state that bears mono or polyradical character. The spin polarization effect primarily arises from the dominance of the Coulomb correlation energy over the exchange interaction. Wavefunction methods this SCS-CC2 are required as they include double or higher order excitation to correctly evaluate the Coulomb correlation. It has been observed when

considering symmetric systems, primarily based on heptazine[263, 264] or cylazine (Figure **7.18**).[265] Domcke and co-workers,[36] reported their modelling of a family of D_{3h} symmetric heptazine derivatives and one, **TAHz** (Figure **7.18**), investigated photophysically. When wavefunction methods were applied, negative ΔE_{ST} was predicted, while DFT methods predicted a positive value. No triplet state could be observed in transient absorption experiments, and no sensitivity to oxygen or addition influence of the delayed emission by the presence of heavy atoms all suggest that the triplet state is higher in energy than the singlet. A structurally similar heptazine emitter was presented as a TADF emitter in 2014 by Li *et al*, namely **HAP-3MF** (Figure **7.19**).[266] In this, paper no triplet state was observed, with ΔE_{ST} of 0.17 eV inferred from DFT [TD–B3LYP/6-31G(d)]. In this work **HAP-3MF** was modelled with SCS-CC2/cc-pVDZ, with negative ΔE_{ST} of -0.38 eV reported, suggesting INVEST may be occurring here, and may explain the lack of experimental T_1 observed previously.

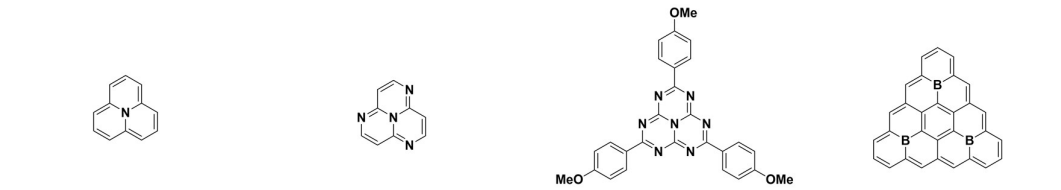

Figure **7.18**. Previous examples of emitters with negative ΔE_{ST} calculated, with the ΔE_{ST} and method used included.

While modelling experimentally identified MR-TADF emitters, two outliers were observed, **B3** and **B4**, which as a result were not included in the data set (Figure **7.19**). Using SCS-CC2/cc-pVDZ, ΔE_{ST} was calculated to be -0.12 eV and -0.06 eV for **B3** and **B4**, respectively, while experimental ΔE_{ST} in 1 wt% PMMA was determined to be 0.15 eV for both.[156] For both outliers and **HAP-3MF** we computed the adiabatic ΔE_{ST}.

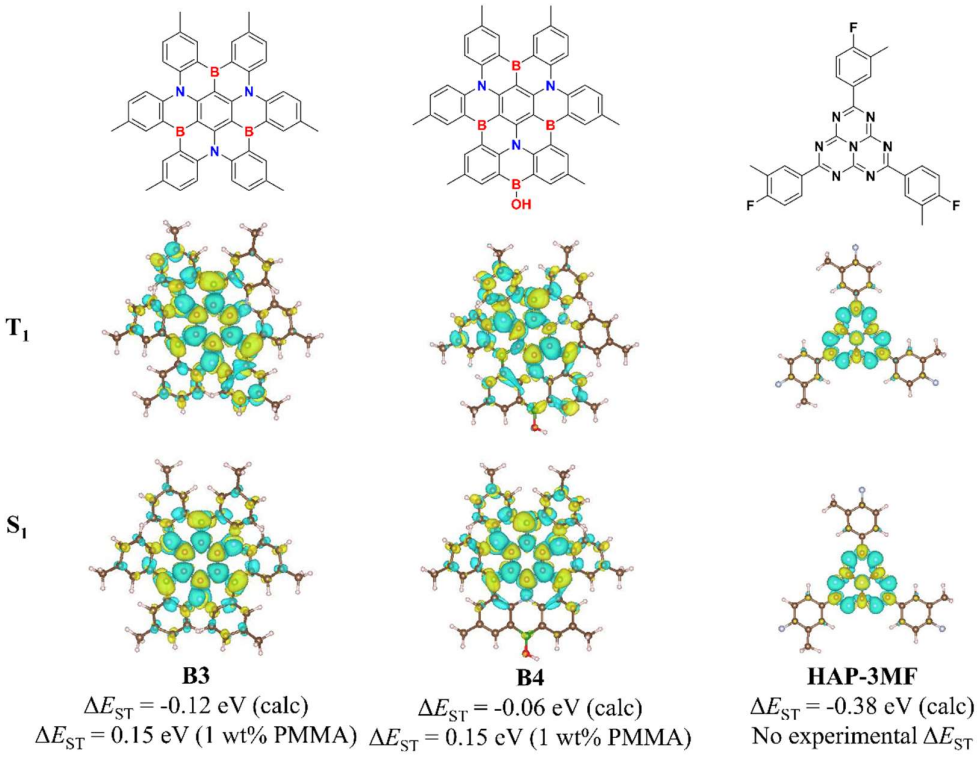

Figure **7.19**. Structures, difference density pictures and calculated and experimental ΔE_{ST} values of **B3**, **B4** and **HAP-3MF**.

The geometries of the excited states were optimized at the DFT (TDA-PBE0/6-31G(d,p)) level and the excited state energies recalculated for **HAP-3MF**, **B3** and **B4**, using SCS-CC2/cc-pVDZ. Negative ΔE_{ST} was still calculated for **HAP-3MF** and **B3** with values of -0.36 eV and -0.14 eV respectively, and there are minimal changes in S_1 and T_1 energies (Table **7.4**). For **B4** a positive ΔE_{ST} of 0.11 eV is now calculated, similar to experimental of 0.15 eV, the result of large changes in T_1 energy. Figure **7.19** shows the difference density patterns of S_1 and T_1 based on ground-state optimized geometries, where **B3** and **HAP-3MF** have nearly identical patterns (Figure **7.19**). On the other hand, **B4** clearly shows different S_1 and T_1 difference density pictures. It is not clear at this stage whether this violation of Hund's rule is an artifact of the coupled cluster calculations, or if it was simply not detected in the experimental observations for **B3** and **HAP-3MF**.

Table **7.4**. Calculated S_1, T_1 and ΔE_{ST} for several emitters appearing to violate Hund's rule, calculated from Ground state calculated and excited state geometry.

Compound	Ground state Geometry [a]			Excited state Geometry [b]			Exp [c]
	S_1 / eV	T_1 / eV	ΔE_{ST} / eV	S_1 / eV	T_1 / eV	ΔE_{ST} / eV	ΔE_{ST} / eV
HAP-3MF	2.78	3.16	-0.38	2.73	3.09	-0.36	N/A
B3	3.13	3.25	-0.12	3.14	3.28	-0.14	0.15
B4	3.11	3.17	-0.06	3.12	3.01	0.11	0.15

[a] Vertical excitation from ground state calculated at SCS-CC2/cc-pVDZ ground state, [b] Vertical excitation from excited state geometry calculated from TDA-PBE0/6-31G(d,p), [c] Determined from the fluorescence and phosphorescence spectra in 1 wt% PMMA doped films.

7.3.5 Modelling of D-A emitters that contain MR-TADF acceptor units

An increasingly popular molecular design is to use MR-TADF core structures as acceptor units in formally D-A TADF systems.[102, 129, 135-138, 246, 267, 268] When a donor is sufficiently strong, the CT state becomes the lowest lying state while the characteristic SRCT state of MR-TADF emitters is relegated to a higher lying excited state. The result of this design is a compound with an emission that is much broader and is more responsive to the polarity of the medium, inferring D-A compared to MR-TADF (Figure **7.1**).

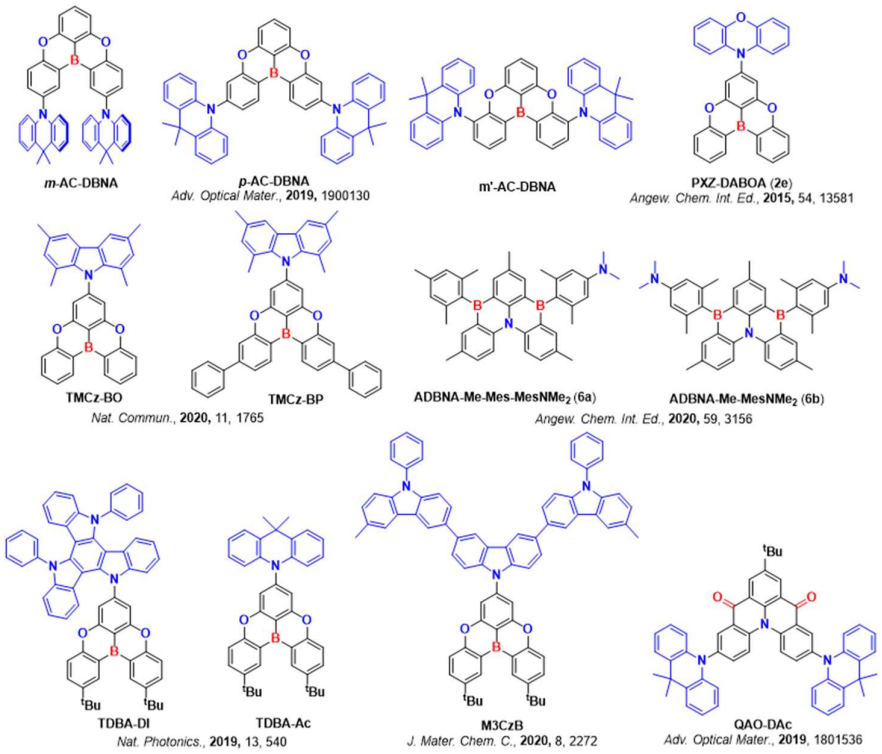

Figure **7.20**. Structures of modelled D-A TADF emitters which have a MR-TADF unit.

Recognizing the importance to accurately model the excited state manifold of this subclass of D-A systems, SCS-CC2 calculations were undertaken focussing on the nature of both the S_1 and S_2 states of 12 emitters, each of which contains a MR-TADF fragment but where experimentally the compound shows a broad emission spectrum and significant positive solvatochromism suggesting D-A nature (Figure **7.20**). Each of these emitters were discussed separately in Chapter 1 in the D-A section (or at the start of this Chapter for **ADBNA-Me-MesNMe2** and **ADBNA-Me-Mes-MesNMe2**). In each case, the extent of CT character was determined using D_{CT}, q_{CT} and S_{+-} metrics, each discussed in Chapter 2. From here the excited state was assigned as either SRCT or CT (Table **7.5** and **7.5**), and was supported according to the difference density plots, with clearly contrasting CT and SRCT pictures apparent. When employing a ground-state optimized geometry, SCS-CC2 incorrectly predicts for most of these compounds a S_1 state with SCRT character. Only for three compounds, **PXZ-DOBNA**, **m-AC-DBNA** and ***p*-AC-DBNA** (Figure **7.20**), do the SCS-CC2 calculations accurately predict the CT character of the S_1 state (Figure **7.21,** Table **7.5**). Each of these three compounds contains the same common MR-TADF acceptor moiety based on **DOBNA**.

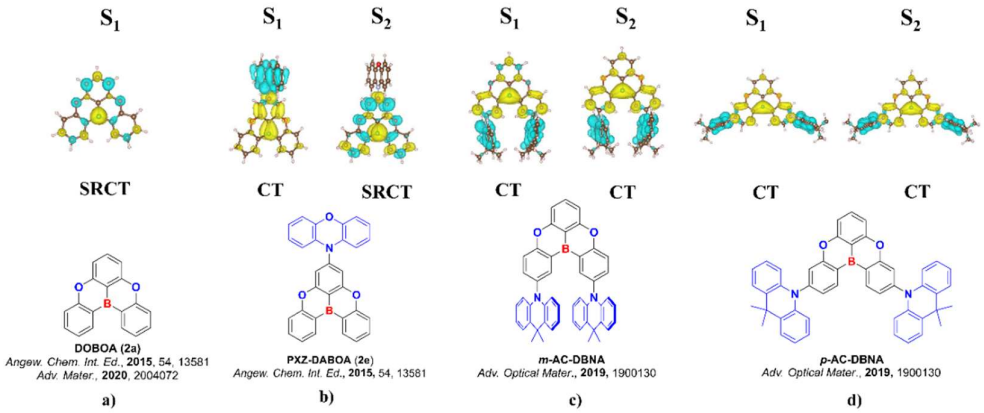

Figure **7.21**. Structures and difference density plots of S_1 and S_2 states of D-A emitters with MR-TADF acceptor with assignment of the nature, where **a**) is the MR-TADF acceptor **DOBNA**, b) is **PXZ-DOBNA**, **c**) is ***m*-AC-DBNA** and **d**) is ***p*-AC-DBNA**.

Table **7.5.** Calculated excited state natures of S_1 and S_2 for breaking MR-TADF emitters where S_1 is D-A-TADF.

	S_1					S_2				
Compound	**Energy / eV**	**D_{CT} / Å**	**q_{CT}**	**S_{+-}**	**Excited state**	**Energy / eV**	**D_{CT} / Å**	**q_{CT}**	**S_{+-}**	**Excited state**
DOBNA	3.68	1.57	0.58	0.92	SRCT	N/A	N/A	N/A	N/A	N/A
PXZ-DOBNA	3.38	5.30	0.95	0.23	CT	3.67	1.31	0.58	0.94	SRCT
***p*-AC-DBNA**	3.51	1.96	0.94	0.51	CT	3.52	1.95	0.94	0.51	CT
***m*-AC-DBNA**	3.47	3.68	0.79	0.62	CT	3.52	4.34	0.91	0.32	CT

For 9 of the emitters (**m'AC-DBNA**, **QAO-Dad**, **TBNA-Ac**, **TBNA-Di**, **ADBNA-Me-MesNMe2**, **ADBNA-Me-Mes-MesNMe2**, **TMCz-BO**, **TMCz-3P** and **M3CzB**) SCS-CC2 calculations predict a SRCT S_1 state, while a close-lying S_2 state displays pronounced CT character (Table **7.6** and Figure **7.22**); the SRCT nature of the S_1 state is based on the similar D_{CT}, q_{CT} and S_{+-} values of these compounds compared to the modelling of the MR-TADF acceptor fragment only. When analysing the nature of the S_2 state of these compounds, we observe a D_{CT} and q_{CT} increasing with

respect to S_1 while S_{+-} drops. Among the different compounds, ***m'*-AC-DBNA** has a smaller D_{CT} (S_1 1.84 Å, S_2 1.76 Å) but this is readily explained by the symmetric nature of this compound which usually biased the estimate of D_{CT}. However based on q_{CT} S_{+-}, we can confirm the long-range CT character of the S_2 state.[176] Each material had a S_2 state difference density pattern reminiscent of long-range CT state, with a decrease in density on donor fragments and an increase in density on the accepting unit. The emitters using **DOBNA** (and derivatives) accepting units are highlighted in Figure **7.21**.

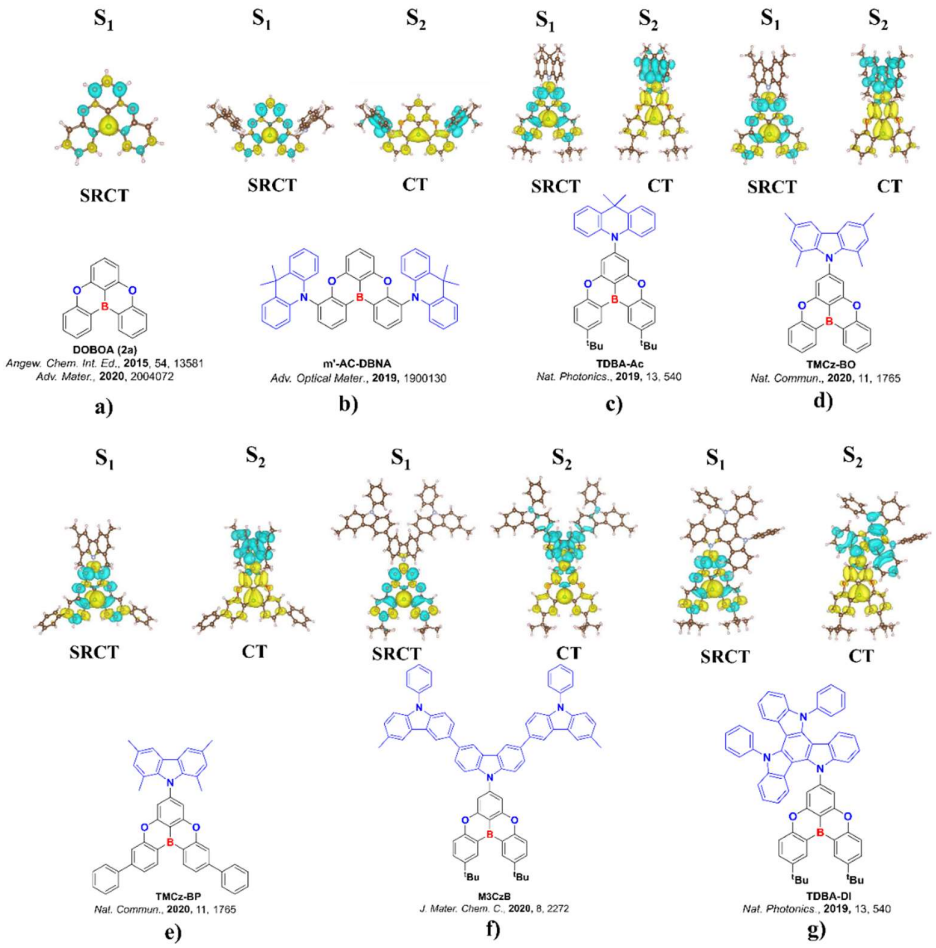

Figure **7.22**. Structures and difference density plots of S_1 and S_2 states of D-A emitters with MR-TADF acceptor with assignment of the nature, where **a**) is the MR-TADF acceptor **DOBNA**, **b**) is **m'AC-DBNA**, **c**) is **TDBA-Ac**, **d**) is **TMCz-BO**, **e**) is **TMCz-BP**, **f**) is **M3CzB** and **g**) is **TBDA-Di**.

ADBNA-Me-MesNMe2 and **ADBNA-Me-Mes-MesNMe2** had the same electron-accepting MR-TADF emitter, **ADBNA-Me-Mes**, which had D_{CT} 1.34 Å, q_{CT} 0.63 and S_{+-} of 0.94 similar to that

we have observed for other MR-TADF emitters. The S_1 state of **ADBNA-Me-MesNMe2** and **ADBNA-Me-Mes-MesNMe2** was once again a SRCT while S_2 is typically a long-range CT (Table **7.6**). Finally considering **QAO-DAc** which had **DiKTa** accepting unit, D_{CT}, q_{CT} and S_{+-} associated to S_1 has a SRCT character (Table **7.6**). S_2 of **QAO-DAc** shows clear long-range CT, with increasing D_{CT}, q_{CT} and decreased S_{+-} (Figure **7.23e**).

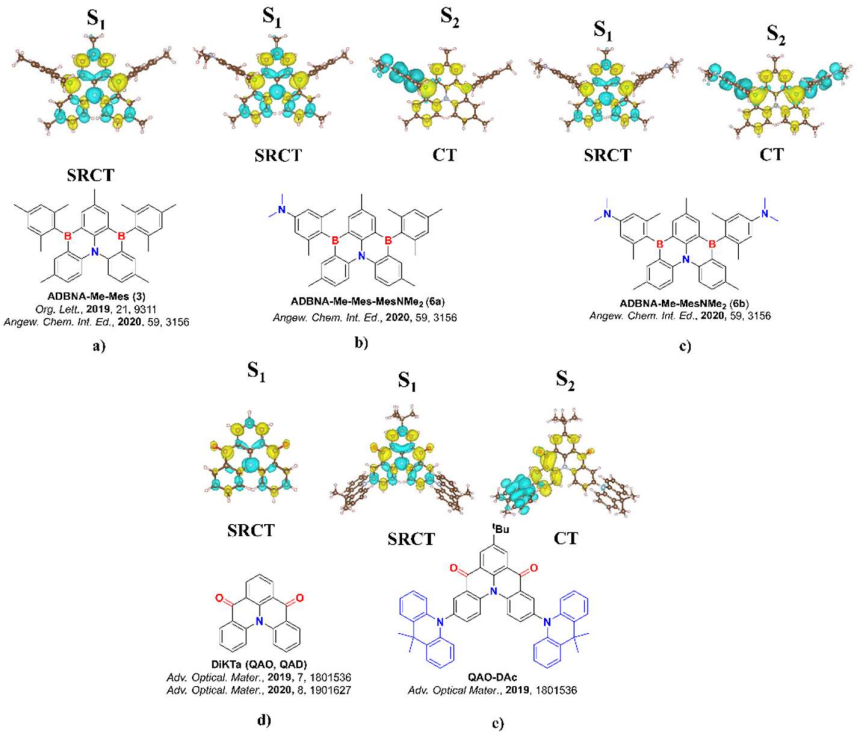

Figure **7.23**. Structures and difference density plots of S_1 and S_2 states of D-A emitters with MR-TADF acceptor with assignment of the nature, where **a**) is the MR-TADF acceptor **ADBNA-Me-Mes**, **b**) is **ADBNA-Me-Mes-MesNMe2**, **c**) is **ADBNA-Me-MesNMe2**, **d**) is the MR-TADF acceptor **DiKTa** and **e**) is **QAO-DAc**.

For each of these excited states S_1 and S_2 are at maximum of 0.52 eV away. The different electron density reorganization implies that the electrical dipole is larger for states with a CT excited state. These will undergo more pronounced stabilization of compared to SRCT states, which is achieved in solvent or solid media, with our calculations performed in the gas phase. In this scenario a predicted CT S_2 will be preferentially stabilized in polar medium compared to S_1 with SRCT, with inversion of

the state apparent (Figure **7.23**). Another element that could drive the S_1-S_2 state inversion is the potential difference in geometry relaxation energy in the excited state that could exist between SRCT and long-range CT states and which is neglected in vertical excitation calculations. Owing to their large S_1-S_2 energy gap (0.52 eV) both **ADBNA-Me-MesNMe$_2$** and **ADBNA-Me-Mes-Mes-NMe$_2$**, display experimentally two clear, distinct bands in the solvatochromic screen[246] as exemplified by the emission spectrum of **ADBNA-Me-Mes-MesNMe$_2$** in CH_2Cl_2 where dual emission is observed with λ_{PL} of 477 nm and 609 nm. The high energy band was assigned to emission from the SRCT state as it is of similar energy to other MR-TADF emitters in the series, and the second, the low energy band to the CT emission. This example illustrates the importance of modelling both the S_1 and S_2 state in this class of compound. Three emitters were modelled in the previous section that contained donors coupled to MR-TADF core, namely ***m*-Cz-BNCz**, **ADBNA-Me-MesCz** and **ADBNA-Me-Mes-MesCz**. In these cases, the emission spectra recorded experimentally from S_1 is typical of MR-TADF emitters with narrow linewidths with the energy gaps between S_1 and S_2 is > 0.70 eV much higher than in the current set of molecules investigated in this section, likely hindering states inversion.

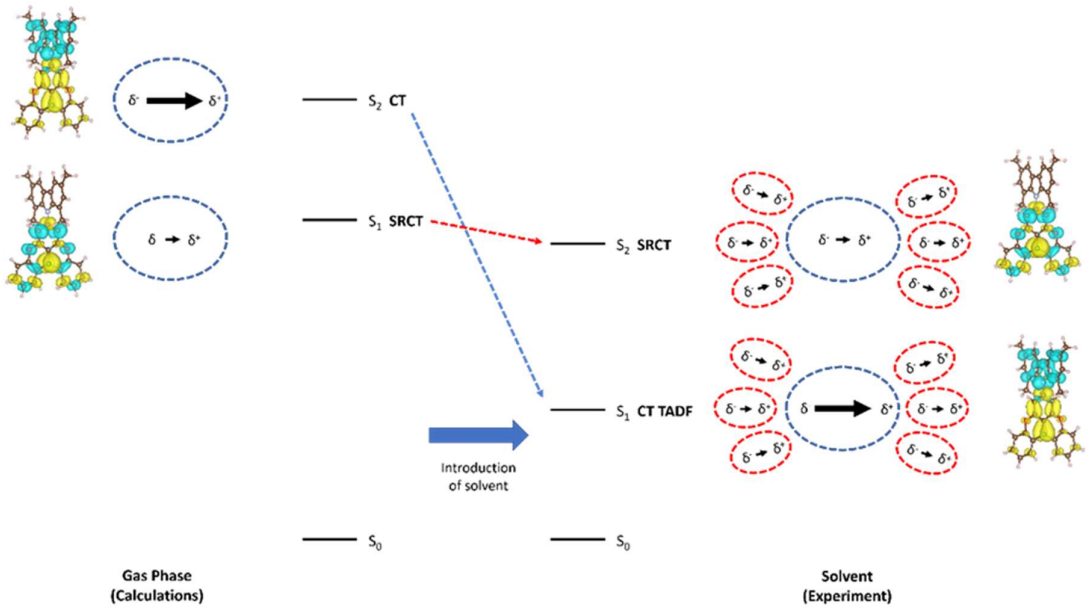

Figure **7.24**. Simplified Jablonski diagram of a MR-TADF singlet state and D-A-TADF singlet state in gas phase (left) and solvent (right) for **TMCz-BO**, where blue circles are the emitter, red is the solvent and solid black arrows present the dipole of the system.

Table **7.6**. Calculated excited state natures of S_1 and S_2 for breaking MR-TADF emitters where S_1 is MR-TADF.

	S_1					S_2				
Compound	**Energy / eV**	**D_{CT} / Å**	**q_{CT}**	**S_{+-}**	**Excited state**	**Energy / eV**	**D_{CT} / Å**	**q_{CT}**	**S_{+-}**	**Excited state**
DOBNA	3.68	1.57	0.58	0.92	SRCT	N/A	N/A	N/A	N/A	N/A
m'-AC-DBNA	3.56	1.84	0.61	0.89	SRCT	3.69	1.76	0.95	0.62	CT
TBNA-Ac	3.57	1.14	0.59	0.95	SRCT	3.61	5.28	0.95	0.24	CT
TBNA-Di	3.56	1.45	0.59	0.93	SRCT	3.69	5.12	0.62	0.62	CT
TMCz-BO	3.65	1.37	0.58	0.95	SRCT	3.81	5.51	0.95	0.34	CT
TMCz-3P	3.58	1.42	0.59	0.94	SRCT	3.74	5.8	0.93	0.24	CT
M3CzB	3.61	1.01	0.58	0.97	SRCT	3.78	5.70	0.74	0.47	CT
ADBNA-Me-Mes	3.04	1.34	0.63	0.94	SRCT	N/A	N/A	N/A	N/A	N/A
ADBNA-Me-MesNMe2 (6b)	3.05	1.29	0.63	0.94	SRCT	3.57	1.73	0.91	0.67	CT
ADBNA-Me-Mes-MesNMe2 (6a)	3.04	1.31	0.63	0.94	SRCT	3.56	4.97	0.92	0.37	CT
DiKTa	3.45	1.45	0.59	0.91	SRCT	N/A	N/A	N/A	N/A	N/A
QAO-DAc	3.37	1.17	0.59	0.93	SRCT	3.45	5.12	0.91	0.33	CT

7.4 Conclusions

MR-TADF emitters and those containing MR-TADF units have been investigated using TD(A)-DFT and SCS-CC2 in an effort to establish an accurate methodology to predict both ΔE_{ST} and the nature of the low-lying excited states of these compounds. Reaffirming previous work, the robustness of the ΔE_{ST} prediction when applying the SCS-CC2 method in comparison to TD(A)-DFT is cemented, as evidenced by the extremely small MAD value of 0.04 eV reported across 35 MR-TADF emitters for SCS-CC2. The overestimation observed at the TD(A)-DFT level is consistent for the set of

functionals investigated and is assigned to the poorly predicted S_1 energy due to the absence of double excitation in TD(A)-DFT impeding an accurate account of Coulomb electron correlation. With SCS-CC2, the method of choice, decreasing ΔE_{ST} is observed when π delocalisation is increased, and when boron is used in place of ketone. The higher-lying S_2 and T_2 excited states were probed, which appear to be in most cases much higher in energy compared to the lower-lying singlet and triplet excited states. Unlike conventional D-A TADF materials, there are only a small fraction of MR-TADF materials that display energetically closely-lying triplet states, whose involvement are believed to facilitate RISC. The slow k_{RISC} measured experimentally for most of the compounds are supported by the very large T_1-T_2, S_1-T_2 and S_1-S_2 energy gaps, suggesting that a spin-vibronic mechanism as observed in D-A TADF is inefficient in MR-TADF compounds. In compounds containing a MR-TADF core that acts as an acceptor in D-A TADF emitters, gas-phase SCS-CC2 calculations predict S_1 and S_2 to be always of SRCT or long-range CT character. Because of the high dependence of the emission properties as a function of the polarity of the solvent in these compounds, it is possible that there is a switch from the narrow SRCT-like to a broad CT-like emission. Both S_1 and S_2 must be modelled in these D-A systems if accounting of solvent effects cannot be included, with energetically close SRCT and CT singlet states likely undergoing inversion experimentally.

Chapter 8: Diindolocarbazole – Achieving Multiresonant Thermally Activated Delayed Fluorescence Without the need for Acceptor Units

8.1 Introduction

Chapters 6 and 7 have showcased a number of MR-TADF materials. The field has grown rapidly in recent years; however, despite more than 100 emitters reported to date, the design is still largely based on compounds containing a central donor or acceptor atom with suitably placed complementary acceptor atoms (or functional groups) or donor atoms, respectively, to ensure a complementary pattern of electron density between the ground and the excited states. From the original boron-centred emitters, improved TADF performance of compounds showing smaller ΔE_{ST} have been reported and these compounds have extended π systems, which increases delocalisation of the electron density. This is evidence in ***ν*-DABNA**, which has a ΔE_{ST} of 0.02 eV;[150] this value was calculated in Chapter 7 to be 0.01 eV. Another family of MR-TADF compounds, introduced by Zhang *et al.* in 2019,[161] relies on boron and nitrogen atoms to direct the electron density pattern, but these compounds incorporate fused donor units, such as in **CzBN**. The fused system results in increased electronic delocalisation, thus stabilizing S_1, which produces a red-shift in the emission and a moderate decrease in ΔE_{ST} (Figure **8.1**). A derivative of this compound **R-BN**,[269] showed deep red emission (Figure **8.1**). The red-shifted emission results from the relative positioning of the donating nitrogen atoms, and thus the withdrawing boron atoms, *para* to each other. This strategy ensures a red-shifted yet narrowband emission. The incorporation of donor and acceptor substituents also red shifts the emission, but at the expense of broader spectra (see Chapter1).

In Chapter 6, SCS-CC2 calculations highlighted that inversion of the donor and acceptor motifs of **DABNA-1** would not adversely affect the SRCT character of the emitter. Indeed, such a compound **ADBNA-Me-Mes** was subsequently reported to be MR-TADF.[166, 246] In Chapter 6, it was showcased that replacing boron with carbonyl acceptors in the form of emitters **DiKTa** and **Mes$_3$DiKTa** conserved the MR-TADF character, albeit at the expense of a relatively larger ΔE_{ST}. Peripheral substitution of the **DiKTa** core with mesityl groups improved the photophysical properties, where this compound showed increased Φ_{PL} but also a red shifted emission.

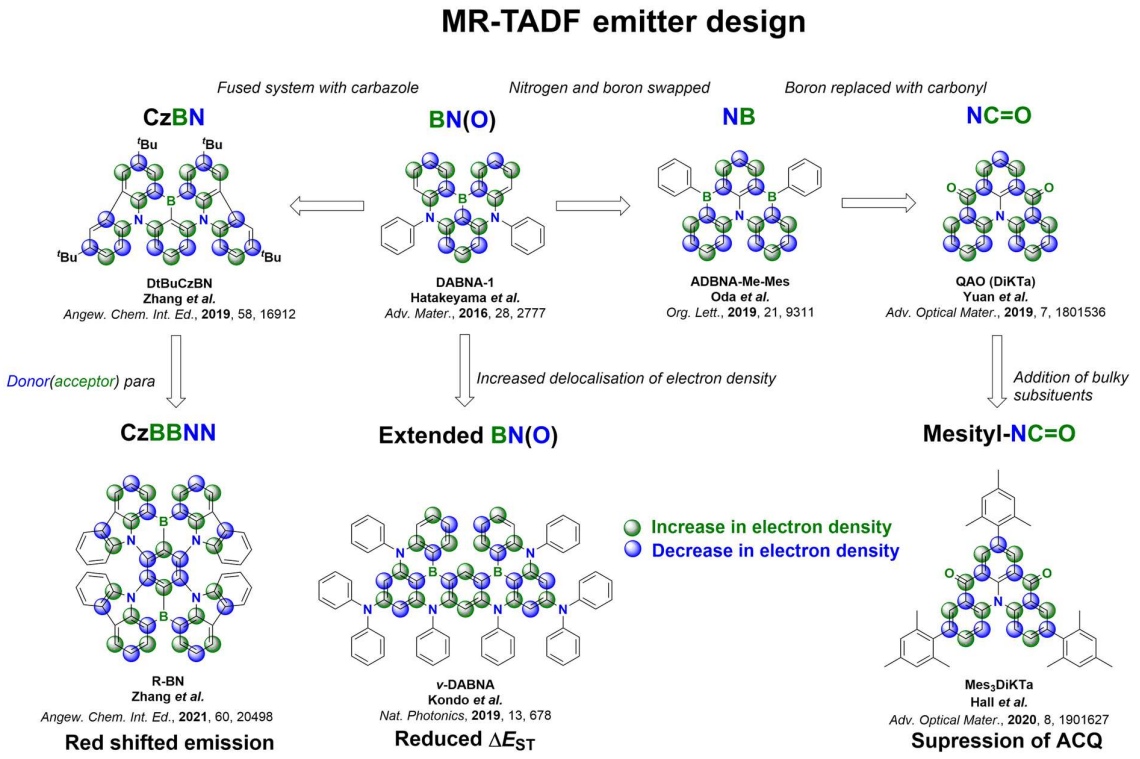

Figure **8.1.** Evolution of MR-TADF emitters including simplified difference density plots for each core.

As showcased in Chapters 1 and Chapter 6, MR-TADF emitters often suffer from inefficient k_{RISC} compared to D-A TADF emitters. An attractive avenue to bypass the problems associated with inefficient k_{RISC} found in MR-TADF emitters, is to incorporate them in Hyperfluorescence-OLEDs (see Chapter 1). Here the MR-TADF compound acts as an emitter only, with RISC occurring on a separate triplet harvester, which can be TADF or phosphorescent. Subsequent energy transfer occurs to the MR-TADF emitter followed by emission. Here, inefficient k_{RISC} of MR-TADF emitters can be bypassed, while maintaining their desirable spectral features. MR-TADF emitter-containing Hyperfluorescence-OLEDs were first reported using ***t*-DABNA** as the emitter and **DMAC-DPS**, acting as the triplet harvester (Figure **8.2**), leading to an improvement in k_{RISC},[155] and EQE_{max} rising from 25.1% to 31.4% in the OLED and Hyperfluorescence-OLED. Further RO_{100} improved from 76% to 13%. Using **DMAC-DPS** shortened the τ_d from 83 μs to 6.1 μs, improving triplet harvesting and reducing roll-off. Switching the assistant dopant to **p4TCPhBN** where k_{RISC} was 2.4×10^6 s^{-1} led to an improved performance of the Hyperfluorescence-OLED (Figure **8.2**).[270] Here EQE_{max} was 32.5%, and RO_{100} was an impressive 5%.

Several examples now exist wherein ***ν*-DABNA** has been used as the terminal emitting species. Chan *et al*. presented hyperfluorescent devices, where ***ν*-DABNA** was used alongside a triplet harvester, **HDT-1** (Figure **8.2**).[271] This had a k_{RISC} of 9.2×10^5 s^{-1}, and good spectral overlap between its emission and the absorption of ***ν*-DABNA** ensuring efficient FRET, corresponding to a high EQE_{max} of 27% at CIE (0.15, 0.20). Although overall EQE_{max} was lower than reported previously (34.4%),[271] efficient energy transfer from **HDT-1** mitigated triplet quenching pathways producing good device stability, with LT_{95} of 11 hours, superior to the emitter only device (< 1 hour). Separate triplet harvesters, **PPCzTrz** and **PCzTrz** were used alongside ***ν*-DABNA** (Figure **8.2**),[272] with EQE_{max} of 33.0% and 33.5%, respectively. In this system a host with a low T_1 state was chosen as this was found to improve device stability. The LT_{50} at 1,000 cd m^{-2} are 151 and 113 hours, respectively. These OLEDs represent an improvement in stability compared to that using ***ν*-DABNA** only, where similar EQE_{max} of 33.2% was reported, but with a LT_{50} of 41 hours.

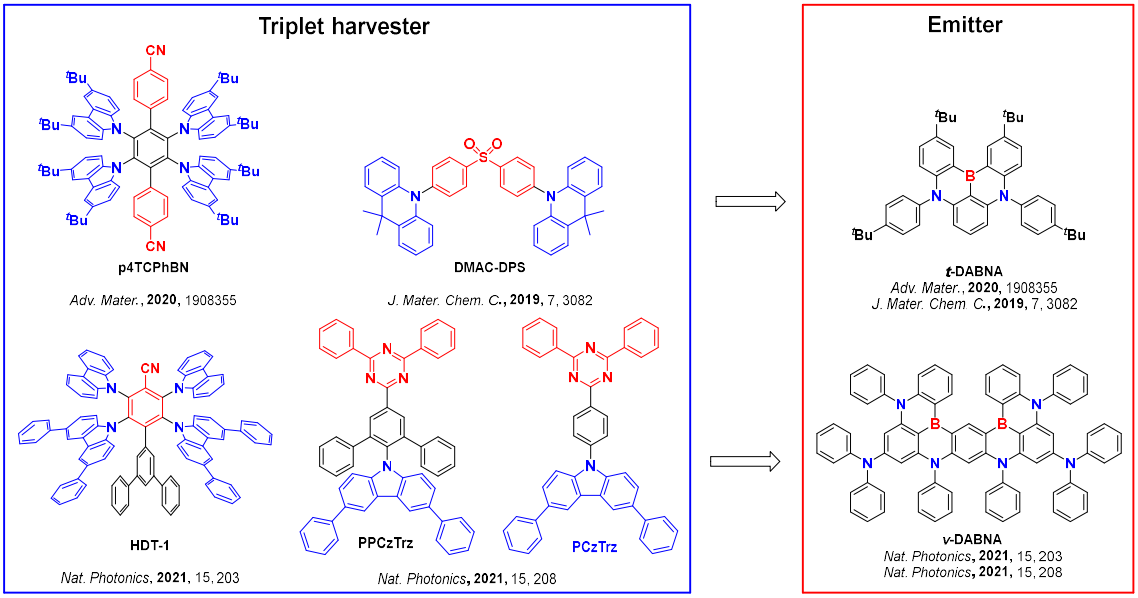

Figure **8.2**. Structures of triplet harvesters (blue box) and emitters (red box) used in Hyperfluorescence-OLEDs containg MR-TADF emitters.

8.2 Motivation and chapter outline

In chapters 6 and 7 SCS-CC2 was introduced as a computational method to accurately predict ΔE_{ST} of MR-TADF materials. The aim of this chapter was to use this same computational approach to design a completely new class of MR-TADF materials, taking into consideration the design principles highlighted in Figure **8.1**. Upon writing this section only a few basic MR-TADF designs existed, they were BN(O), NB(O), and NC=O (Figure **8.1**). In each compound, careful positioning of donor and acceptor atoms (or functional groups) was required to achieve the desired electron density pattern associated with a small ΔE_{ST}. This specific design characteristic has limited the chemical space explored in MR-TADF materials design. It was proposed that MR-TADF should be possible without the use of one of the donor or acceptor components. In this chapter computational approaches are used to model several potential targets centred around indolocarbazole (**ICz**) structures, with **DiICzMes$_4$** selected as the main target. In this compound, *para* nitrogen atoms lead to a desired red shifting of the emission from UV to deep blue, extension of π electron density reducing ΔE_{ST}, while mesityl substitution reduces ACQ in line with previous observations (Figure **8.1**).

In contrast to Chapter 6, we went further than vertical calculations by considering excited state relaxation and show that a ΔE_{ST} in much better agreement with the experiments can be reached. The optoelectronic properties of the parent emitters **ICz** and **ICzMes$_3$** were investigated alongside those of **DiICzMes$_4$** in both solution and films, **DiICzMes$_4$** displays a reduced ΔE_{ST}, an increased Φ_{PL} and red shifted λ_{PL}. Conventional OLEDs with **DiICzMes$_4$** showed low efficiencies owing to its inefficient k_{RISC}. Hyperfluorescence-OLEDs were also fabricated showcasing good EQE_{max} of 16.5% at CIE (0.15, 0.11). While undertaking this work two similar materials, **tBisICz** and **tPBisICz** (Figure **8.3**),[273] were reported and claimed as MR-TADF, while in a separate paper, Hyperfluorescence-OLEDs were also presented with a similar unit, **pICz** (Figure **8.3**), as the terminal emitter. Other ICz-based compounds were also reported around this time;[274] [275] [276] however, MR-TADF was not claimed for these structurally similar derivatives (***m*-FLDID**,[274] **tDiDCz**[275] **ACDID-Ph** and **ACDID-TPDA**[276]). These compounds were instead claimed as emitting by fluorescence or TTA (Figure **8.3**).

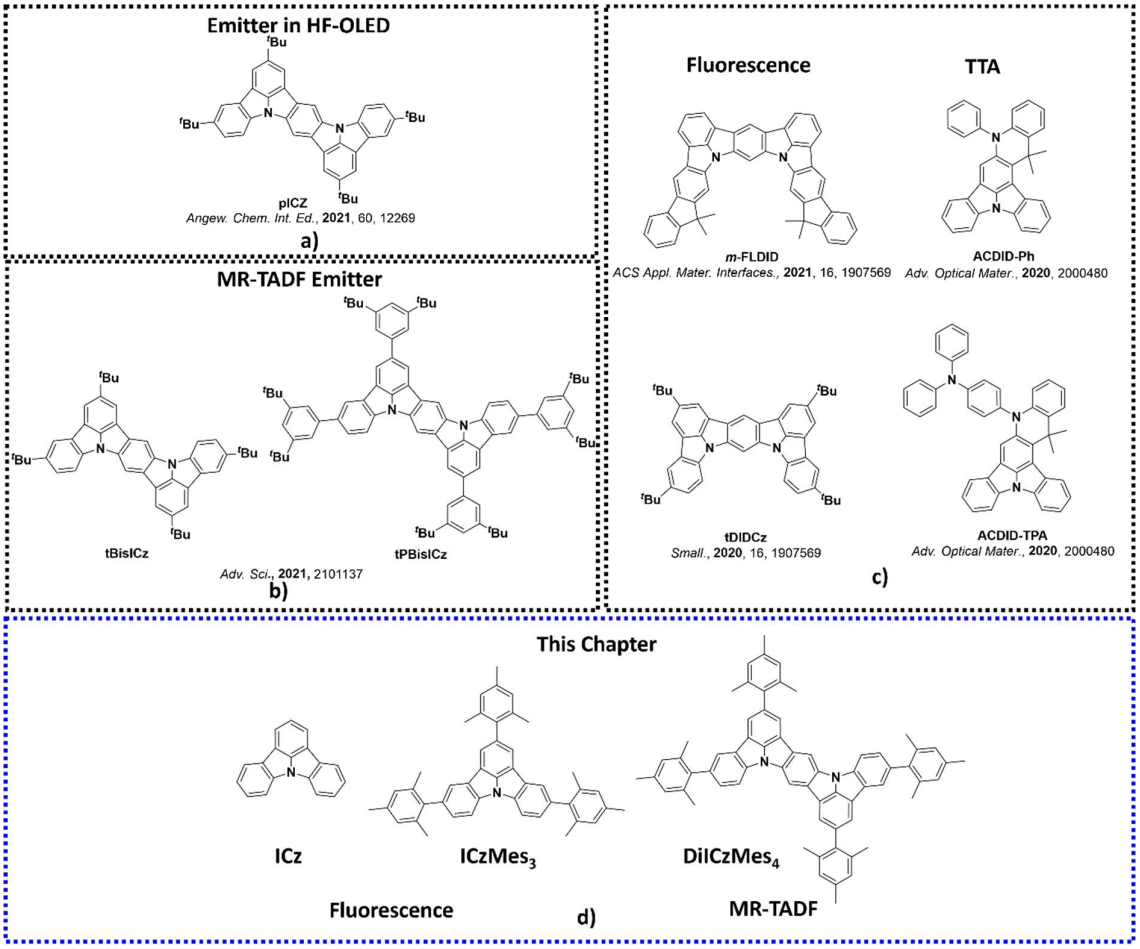

Figure **8.3**. Previously reported diindolocarbazole materials, where **a**) is Hyperfluorescence-OLED emitter, **b**) diindolocarbazole materials undergoing MR-TADF **c**) diindolocarbazole materials undergoing fluorescence and TTA and **d**) the materials studied in this chapter and their decay mechanisms.

8.3 Results and Discussion

8.3.1 Computations

Initial ground state optimisation followed by vertical excitation were performed at the SCS-CC2/cc-pVDZ level of theory. Indolocarbazole (**ICz**) has been frequently used by the TADF community, able to act as both a donor or acceptor[277] depending on to the nature of the substituents. ΔE_{ST} was predicted to be 0.33 eV for **ICz**, which is high for TADF materials but rationalized by the different nature of S_1 and T_1 excited states. Indeed, S_1 displays a typical difference density pattern

characteristic of a SRCT excited state while T_1 exhibits a LE-like pattern, with the latter more stabilized, hence the large ΔE_{ST} (Figure **8.4**). It has been inferred previously that extending the MR-TADF electronic delocalisation could be a viable strategy to decrease ΔE_{ST} at the same time as increasing the oscillator strength.[147] Based on this hypothesis, four derivatives of **ICz** were modelled, with differing patterns of the relative position of the nitrogen atoms: **DiICz-*m*-1**, **DiICz-*m*-2**, **DiICz-*p*-1** and **DiICz-*p*-2** (Figure **8.4**, Table **8.1**). Compared to the parent **ICz**, each of these four emitters had a stabilized S_1 state, decreasing from 3.78 eV for **ICz** to 3.58 eV, 3.57 eV, 3.36 eV and 3.32 eV for **DiICz-*m*-1**, **DiICz-*m*-2**, **DiICz-*p*-1** and **DiICz-*p*-2**, respectively, the result of delocalization of the S_1 wavefunction. As previously reported for other MR-TADF emitters,[269] when the donating nitrogen atoms are located *para* to each other the red-shift is the largest. The *para*-derivatives here also had the smallest predicted ΔE_{ST} of 0.17 eV and 0.15 eV for **DiICz-*p*-1** and **DiICz-*p*-2**, respectively, while ΔE_{ST} is 0.30 eV and 0.32 eV for **DiICz-*m*-1** and **DiICz-*m*-2**.

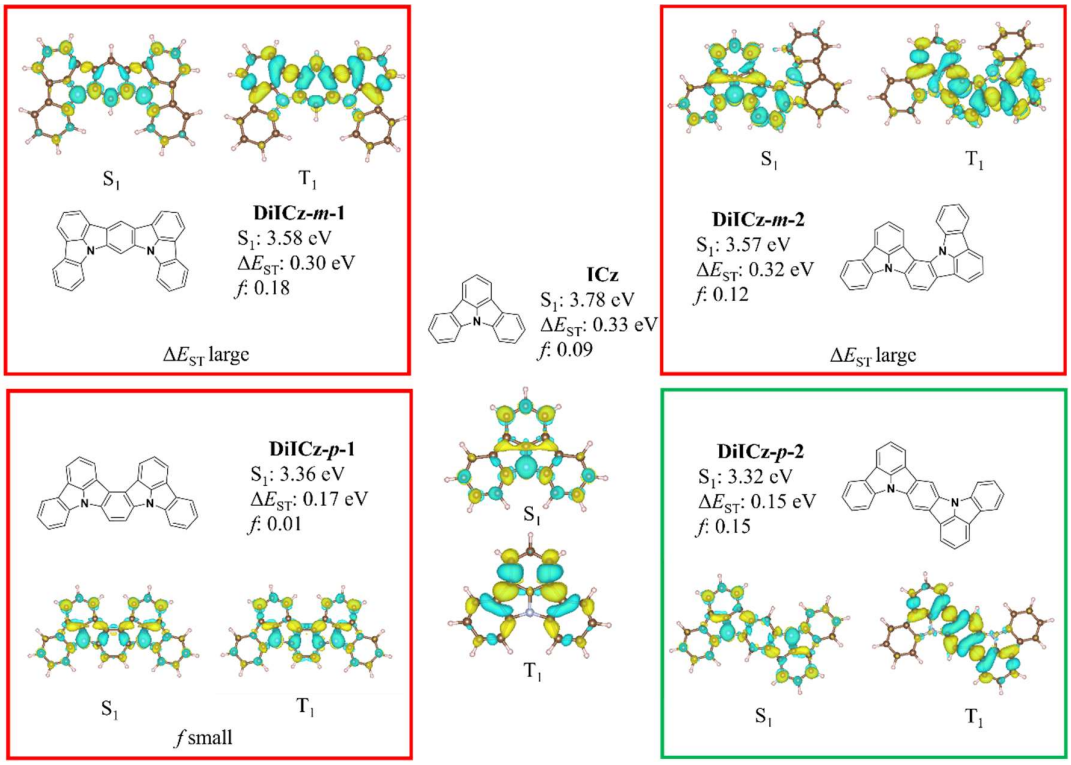

Figure **8.4**. S_1 and T_1 difference density patterns, ΔE_{ST}, S_1 energy and oscillator strength, *f*, for the proposed DiICz units.

Of **DiICz-*p*-1** and **DiICz-*p*-2**, **DiICz-*p*-2** has a considerably larger oscillator strength of 0.15 compared to 0.01 in **DiICz-*p*-1** and thus this motif was assessed as the most promising. As demonstrated in Chapter 6, addition of mesityl groups can mitigate ACQ, which plagues MR-TADF materials.[278] With this in mind, mesityl derivatives of **ICz** and **DiICz-*p*-2** were designed, **ICzMes$_3$** and **DiICzMes$_4$** (Figure **8.5** and Figure **8.6**). Compared to **ICz**, addition of Mesityl groups in **ICzMes$_3$** have the added benefit of reducing ΔE_{ST} (calculated for vertical transitions from the ground state geometry) from 0.33 eV to 0.21 eV. The decrease in ΔE_{ST} is essentially the result of preferential stabilization of S_1, decreasing from 3.78 eV to 3.64 eV for **ICz** and **ICzMes$_3$**, respectively, while the T_1 energy is only minimally affected, being 3.45 eV in **ICz** and 3.42 eV in **ICzMes$_3$** (Figure **8.5**). The small stabilization of T_1 in **ICzMes$_3$** can be explained by the absence of significant orbital contributions from the carbon atoms connecting the mesityl groups in the T_1 difference density pattern (Figure **8.5**).

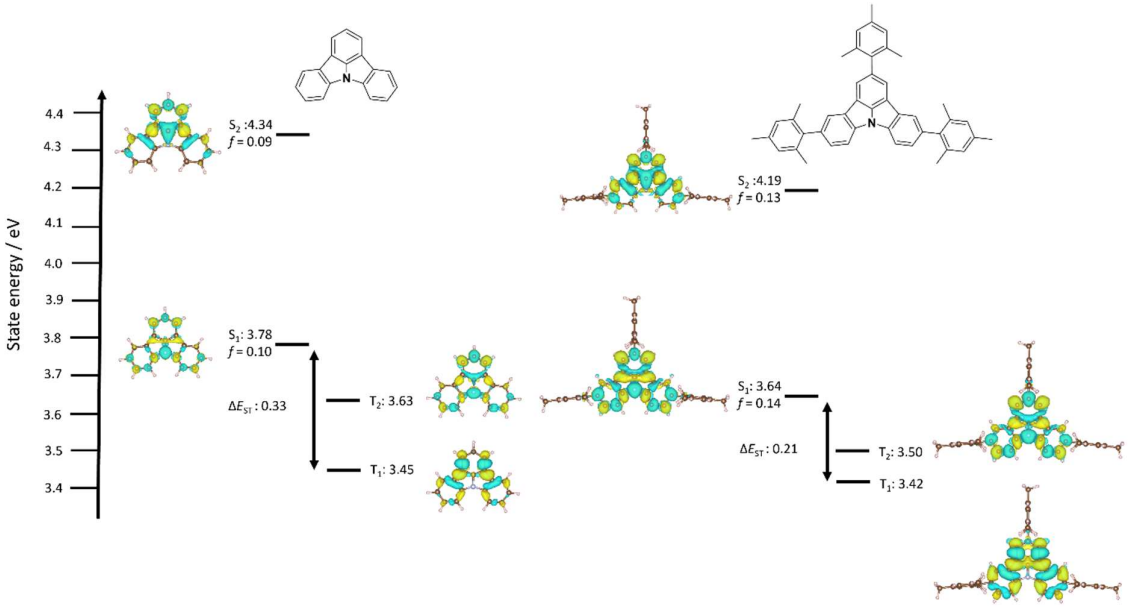

Figure **8.5**. Excited state energies and difference density plots for **ICz** and **ICzMes$_3$** from vertical excitation at SCS-CC2 / cc-pVDZ.

Similar photophysical properties are apparent when comparing **DiICz-*p*-2** with **DiICzMes$_4$**, with the predicted ΔE_{ST} decreasing from 0.15 eV to 0.13 eV (Figure **8.6**). When the ICz core is substituted with mesityl groups, S_1 is stabilized, by 0.11 eV while T_1 is stabilized by 0.09 eV. Due to

the close energy of LE T_1 and the SCRT T_2 states of the **DiICz-*p*-2,** substitution by the four mesityl groups allows inversion between the two. T_1 becomes SCRT in **DiICzMes$_4$** possessing similar, yet slightly different character than S_1.

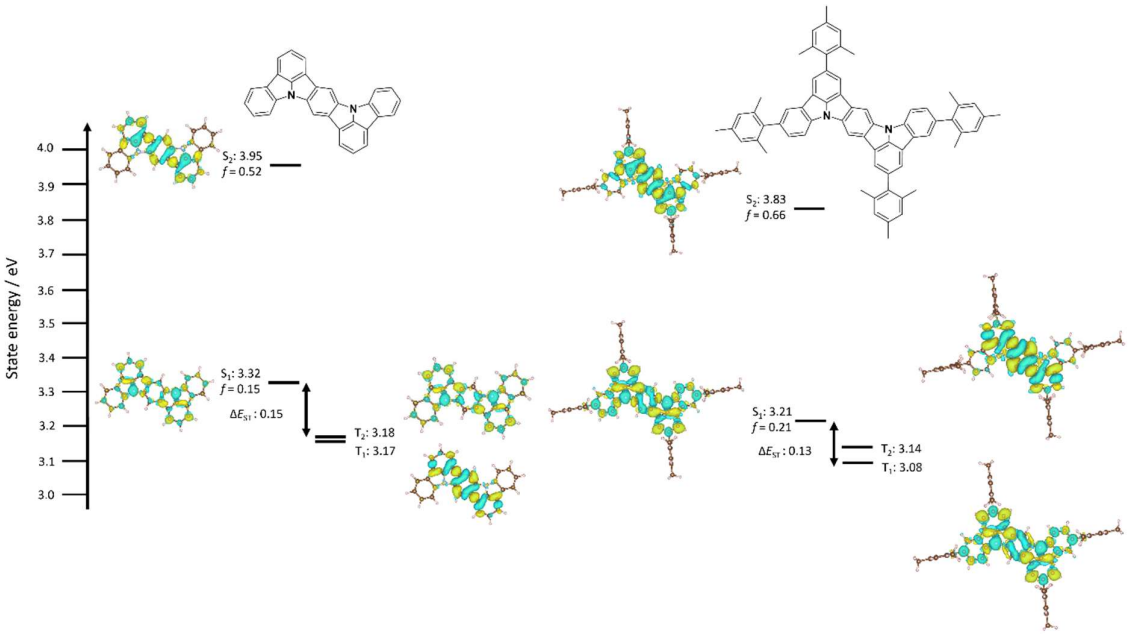

Figure **8.6**. Excited state energies and difference density plots for **DiICz-*p*-2** and **DiICzMes$_4$** from vertical excitation at SCS-CC2/cc-pVDZ.

Table **8.1**. Calculated vertical excited energies of proposed structures from the ground state geometry at SCS-CC2/cc-pVDZ.

Compound	**S_1 (*f*) / eV**	**S_2 (*f*) / eV**	**T_1 / eV**	**T_2 / eV**	**ΔE_{ST} / eV**
ICz	3.78 (0.10)	4.34 (0.09)	3.45	3.63	0.33
DiICz-*m*-1	3.58 (0.18)	3.91 (0.04)	3.29	3.42	0.30
DiICz-*m*-2	3.57 (0.12)	3.86 (0.34)	3.26	3.42	0.32
DiICz-*p*-1	3.36 (0.01)	3.75 (0.65)	3.19	3.22	0.17
DiICz-*p*-2	3.31 (0.15)	3.95 (0.52)	3.17	3.18	0.15
ICzMes$_3$	3.64 (0.14)	4.19 (0.13)	3.42	3.50	0.21
DiICzMes$_4$	3.21 (0.21)	3.83 (0.66)	3.08	3.14	0.13

In contrast to previously investigated MR-TADF emitters, large changes are observed when comparing ΔE_{ST} computed from vertical excitation from the ground state geometry and experiments (*vide infra*.) due to the different nature of T_1 and S_1 states (see difference density plots in Figure **8.5** and **8.3**). In Chapter 7, excellent agreement between calculated and experimental ΔE_{ST} was achieved in over 30 distinct examples based on vertical excitation from the ground-state optimized geometry, while here this methodology poorly predicted ΔE_{ST} (Table **8.2**). To address this issue, an alternative strategy was employed, which was presented in Chapter 7 involving compound **B4,** which resulted in a more accurate prediction of ΔE_{ST}. Initially, ΔE_{ST} was calculated to be negative despite spectroscopic evidence that it is indeed positive. When the geometry of the emitter was reoptimized in the excited state a positive ΔE_{ST} was predicted and the value (0.11 eV) closely aligned to the spectroscopically determined ΔE_{ST} of 0.15 eV. This same methodology was employed here, to try and fix the erroneous ΔE_{ST} prediction. Both the S_1 and T_1 states were optimized within the TDA-DFT using PBE0/6-31G(d,p), and the T_1 and S_1 excited state energies were computed at the SCS-CC2/cc-pVDZ level of theory from the relevant optimized excited state structure for **ICz**, **ICzMes$_3$** and **DiICzMes$_4$** as well as for three literature MR-TADF compounds, **DABNA-1**, **BCzBN** and **DiKTa**. Quantitative agreement with the experiments is reached with ΔE_{ST} increasing for **ICz**, **ICzMes$_3$** and **DiICzMes$_4$**, to 0.59 eV, 0.45 eV and 0.29 eV, (experimentally 0.47 eV, 0.39 eV and 0.26 eV respectively in PhMe), caused by a larger relaxation energy of the T_1 state in line with a greater LE character for this state (Table **8.3**). Interestingly, such an increase in ΔE_{ST} does not manifest for **DABNA-1**, **BCzBN** and **DiKTa**, wherein ΔE_{ST} is only shifted by a maximum of 0.04 eV, owing to the similar SRCT nature of T_1 and S_1, with S_1 and T_1 energies shifting to the same extent (Table **8.2** for ΔE_{ST} and Table **8.3** for S_1 and T_1 energies). The similar orbital character of S_1 and T_1 in many previous emitters, and the ones presented here, implies that RISC between these two states is not symmetry allowed according to El Sayed's rules.[24] Thus, RISC must occur via a spin-vibronic mechanism involving intermediate triplet states lying between S_1 and T_1. Irrespective of the starting geometry, a close lying triplet state of different orbital type is present in this series (Figures **8.5**, **8.6** and **8.7**).[278] Across the series both a smaller ΔE_{ST} and ΔE_{T2T1} were observed, decreasing across the series from **ICz**, **ICzMes$_3$** and **DiICzMes$_4$** (Figure **8.7**). For this class of material

it is essential to optimise the excited states in order to achieve quantitative agreement with experimental ΔE_{ST}, which was not needed for most previously reported examples (Chapter 7).

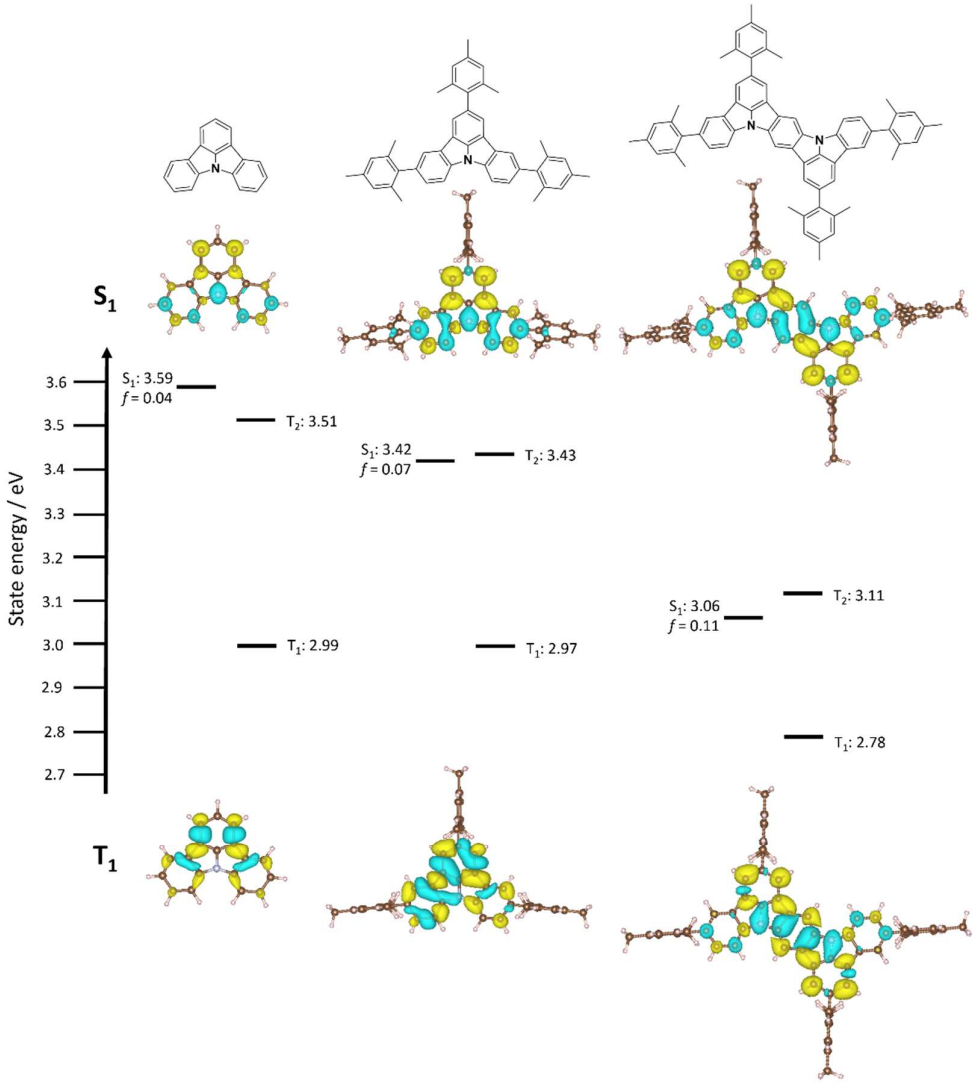

Figure **8.7.** Excited state energies and difference density patterns of **ICz**, **ICzMes$_3$** and **DiICzMes$_4$** from optimized S_1 and T_1 geometries.

Table **8.2**. Calculated and experimental ΔE_{ST} values of the emitters and literature cores.

Compound	ΔE_{ST}-Vert / eV[a]	ΔE_{ST}-Ad / eV[b]	$\Delta\Delta E_{ST}$ / eV[c]	ΔE_{ST}-Exp / eV[d]
ICz	0.33	0.59	0.26	0.47
ICzMes$_3$	0.21	0.45	0.24	0.39
DiICzMes$_4$	0.13	0.29	0.16	0.26
DABNA-1	0.16	0.12	-0.04	0.15[e]
BCzBN	0.09	0.09	0.00	0.12
DiKTa	0.27	0.26	-0.01	0.18

[a] Computed at the SCS-CC2/cc-pVDZ level of theory from vertical excitation of the ground state geometry SCS-CC2, [b] Computed from vertical exaction of the S_1 and T_1 optimized excited state geometries, [c] Difference between ΔE_{ST} computed in b and c, [d] From onset of fluorescence and phosphorescence in dilute toluene at 77 K, [e] Obtained in EtOH.

Table **8.3**. Changes in S_1 and T_1 energies between Ground state and optimized excited geometries.

Compound	S_1 (f) / eV[a]	S_1 (f)/ eV[b]	λ_{S1} / eV[c]	T_1 / eV[d]	T_1 / eV[e]	λ_{T1} / eV[f]
ICz	3.78 (0.10)	3.59 (0.04)	0.19	3.45	2.99	0.46
ICzMes$_3$	3.64 (0.14)	3.42 (0.07)	0.22	3.42	2.97	0.45
DiICzMes$_4$	3.21 (0.21)	3.06 (0.11)	0.15	3.08	2.78	0.30
DABNA-1	3.26 (0.31)	3.14 (0.24)	0.12	3.10	3.02	0.08
BCzBN	2.96 (0.54)	2.90 (0.49)	0.06	2.87	2.81	0.06
DiKTa	3.45 (0.20)	3.31 (0.17)	0.14	3.18	3.04	0.14

[a] From S_1 SCS-CC2/cc-pVDZ optimized geometry, [b] From S_1 (TDA-PBE0/6-31G(d,p) optimized geometry, [c] From a - b, [d] From S_1 SCS-CC2/cc-pVDZ optimized geometry, [e] From T_1 (TDA-PBE0/6-31G(d,p) optimized geometry, [f] From d - e, f is oscillator strength.

8.3.2 Synthesis and crystals structures

The materials were synthesised through a multistep reaction sequence outlined in Figure **8.8**. Carbazole was coupled to 2-bromofluorobenzene under S_{NAr} conditions at elevated temperatures in an excellent yield of 96%. Intramolecular oxidative ring closing of **14** using $Pd(OAc)_2$ afforded **ICz** in a good yield of 85%. Subsequent electrophilic bromination using NBS afforded intermediate **ICzBr$_3$** in 79% yield, which was then decorated with mesityl groups using a Suzuki-Miyaura coupling reaction, producing **ICzMes$_3$** in a good yield of 69%. A similar Suzuki-Miyaura coupling was employed to obtain $CzMes_2$ from dibromocarbazole in 62% following a literature procedure.[279] Intermediate **15** was

obtained in 75% via an S_{NAr} reaction that proceeded at lower temperature (50 °C). Double oxidative cyclization using $Pd(OAc)_2$ generated **DiICzMes$_4$** in 59% yields. Crystals of **ICzMes$_3$** and **DiICzMes$_4$** were grown from slow evaporation of methanol into a saturated solution of toluene over several days. Packing in **ICzMes$_3$** is primarily governed by π–π stacking interactions between mesityl groups on adjacent molecules. For **DiICzMes$_4$** π–π stacking occurs between the mesityl group of one molecule and the DiICz core of an adjacent molecule. The ICz unit in both compounds was not perfectly flat (Figure **8.8b** and **c**).

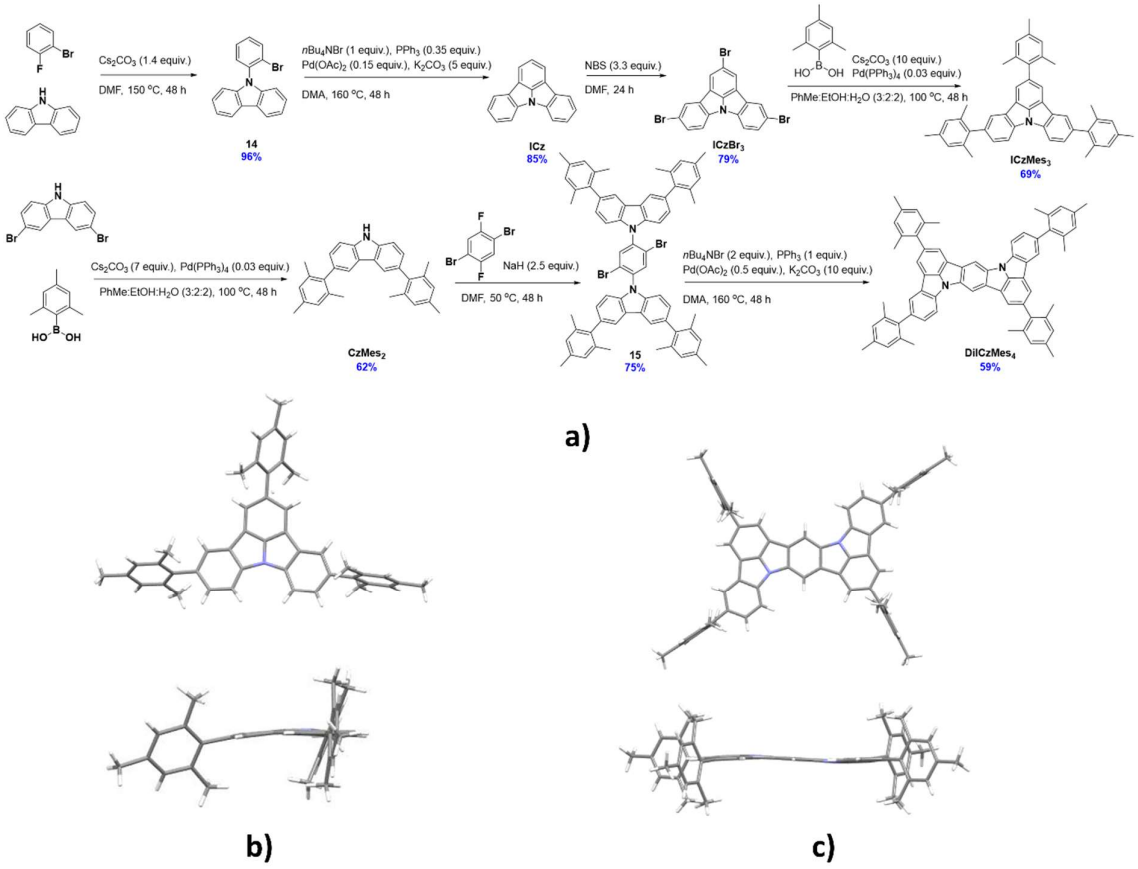

Figure **8.8**. Synthesis of **a**) the emitters and crystal structures of (**b**) **ICzMes$_3$** and (**c**) **DiICzMes$_4$**.

8.3.3 Electrochemical properties

The electrochemical properties were investigated using CV and DPV in DCM for oxidation and dimethylformamide (DMF) for reduction (Figure **8.9**), with the electrochemical potentials reported versus SCE (Table **8.4**). **ICz** showed irreversible oxidation and reduction waves with the former

appearing to undergo polymerisation (Figure **8.9**), which has been previously reported for **ICz**[280] and seen in other carbazole-containing emitters,[217] and reported in Chapter 3. Addition of the mesityl groups in **ICzMes$_3$** renders the oxidation pseudoreversible in a similar manner to what was previously observed for **Mes$_3$DiKTa** in Chapter 6, with E^{ox} at 1.45 V for **ICz** versus 1.43 V for **ICzMes$_3$**. Indeed, McNab *et al*. had demonstrated that the electrochemical instability of **ICz** is associated with dimer formation centred at the *para* positions.[280] There is likewise little change in the irreversible reduction waves with reduction potentials of these two compounds, E^{red}, at -2.21 V and -2.16 V for **ICz** and **ICzMes$_3$**, respectively. By contrast, both oxidation and reduction waves for **DiICzMes$_4$** are largely reversible (Figure **8.9**). The oxidation wave is cathodically shifted to 1.11 V while the reduction wave is anodically shifted to -1.92 V, both a reflection of the larger conjugation length of this molecule compared to **ICz** and **ICzMes$_3$**. This produced a significant reduction in $\Delta E_{H\text{-}L}$. The trends in HOMO and LUMO values are corroborated by the DFT calculations, with a decreased $\Delta E_{H\text{-}L}$ predicted from **ICz**, **ICzMes$_3$** and **DiICzMes$_4$** (Table **8.4**)

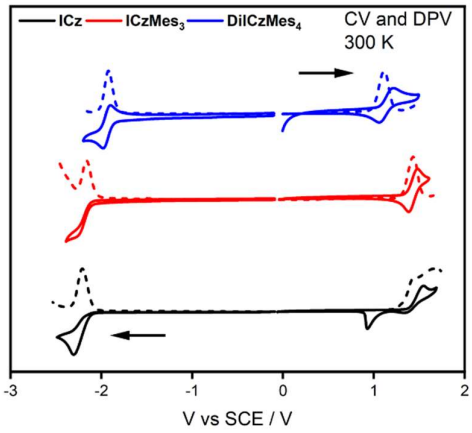

Figure **8.9.** CV (solid) and DPV (dashed) of **ICz**, **ICzMes$_3$** and **DiICzMes$_4$**, where oxidation is in DCM and reduction in DMF at 300 K, at a scan rate of 0.05 V s^{-1}

Table **8.4**. Electrochemical data of each emitter.

	Experimental [a]					Calculated [b]		
Compound	E^{oxac} / V	E^{red} [d] / V	HOMO [e] / eV	LUMO [e] / eV	$\Delta E_{H\text{-}L}$ [f] / eV	HOMO / eV	LUMO / eV	$\Delta E_{H\text{-}L}$ / eV
ICz	1.45	-2.21	-5.79	-2.14	3.61	-5.84	-1.19	4.65
ICzMes$_3$	1.43	-2.16	-5.77	-2.19	3.58	-5.78	-1.28	4.50
DiICzMes$_4$	1.11	-1.92	-5.45	-2.43	3.02	-5.48	-1.62	3.86

[a] Performed in degassed DCM or DMF, [b] Calculated from PBE0/6-31G(d,p), [c] Reported versus SCE in degassed DCM with 0.1 M [*n*Bu$_4$N]PF$_6$ as the supporting electrolyte and Fc/Fc$^+$ as the internal reference (0.46 V vs. SCE) calculated from DPV maxima.[216] [d] Reported versus SCE in degassed DMF with 0.1 M [*n*Bu$_4$N]PF$_6$ as the supporting electrolyte and Fc/Fc$^+$ as the internal reference (0.45 V vs. SCE) calculated from DPV maxima,[216] [e] The HOMO and LUMO energies were determined using the relation $E_{HOMO/LUMO} = -(E^{ox} / E^{red} + 4.8)$ eV,[220] [f] $\Delta E_{H\text{-}L} = |E_{HOMO}\text{-}E_{LUMO}|$.

8.3.4 Solution-state photophysical properties

The photophysical properties of the three emitters in solution were investigated. The UV-Vis absorption data in PhMe, 2-MeTHF (2-methyltetrahydrofuran), EtOAc (ethyl acetate), DCM and DMF can be found in Figure **8.10**. The polarity of the solvent had minimal impact on the absorption spectra, with nearly identical absorption maxima, λ_{abs}, and molar absorptivity values, ε, regardless of solvent, with similar observations reported in Chapter 6. Using the representative data in PhMe (Table **8.5**), there is a high intensity, low energy band at 364 nm (ε of 9×10^4 M^{-1} cm^{-1}), 379 nm (ε of 8×10^4 M^{-1} cm^{-1}) and 431 nm (ε of 11×10^4 M^{-1} cm^{-1}) for **ICz**, **ICzMes$_3$**, and **DiICzMes$_4$**, respectively, assigned by calculations to a SRCT band. There is a second distinguishable band at smaller ε at 350 nm (ε of 6×10^4 M^{-1} cm^{-1}), 363 nm (ε of 6×10^4 M^{-1} cm^{-1}) and 410 nm (ε of 8×10^4 M^{-1} cm^{-1}), respectively, that is likely due to a transition to a different vibronic level of the S_1 state. Both **ICz** and **ICzMes$_3$** possess higher energy bands at 320 nm and 330 nm of similar ε (7 and 8×10^4 M^{-1} cm^{-1} respectively) which were assigned to transitions to the S_2 state. The similar ε values are captured at the SCS-CC2 level where both S_1 and S_2 have similar oscillator strengths, *f*, of 0.10 and 0.09 for **ICz** and 0.14 and 0.13 for **ICzMes$_3$**. A far greater oscillator strength of 0.66 is predicted for the transition to S_2 for **DiICzMes$_4$**

compared to that to S_1 (f = 0.21). Indeed, the band at 365 nm possesses a significantly larger ε of 39 × 10^4 M^{-1} cm^{-1} compared to that at 431 nm (ε = 11 × 10^4 M^{-1} cm^{-1}), suggesting a greater degree of LE character for the transition associated with this band.

Minimal changes in emission energy and band shape were observed upon modulation of the solvent polarity (Figure **8.10b – d**). Such behaviour is characteristic of MR-TADF emitters, which undergo emission from a SRCT excited state and was observed in Chapter 6.[147] Owing to their rigid nature, the emission is narrow and the Stokes shifts are small (10, 8, and 10 nm, respectively, for **ICz, ICzMes$_3$** and **DiICzMes$_4$**) reflecting the very small reorganisation energy between the ground and excited state. The corresponding FWHM for the PL spectra in toluene are 21 nm, 21 nm and 17 nm for **ICz, ICzMes$_3$** and **DiICzMes$_4$**, respectively. There are low energy shoulders apparent in the steady-state PL of all three emitters, assigned to a vibronic level (*vide infra*.).

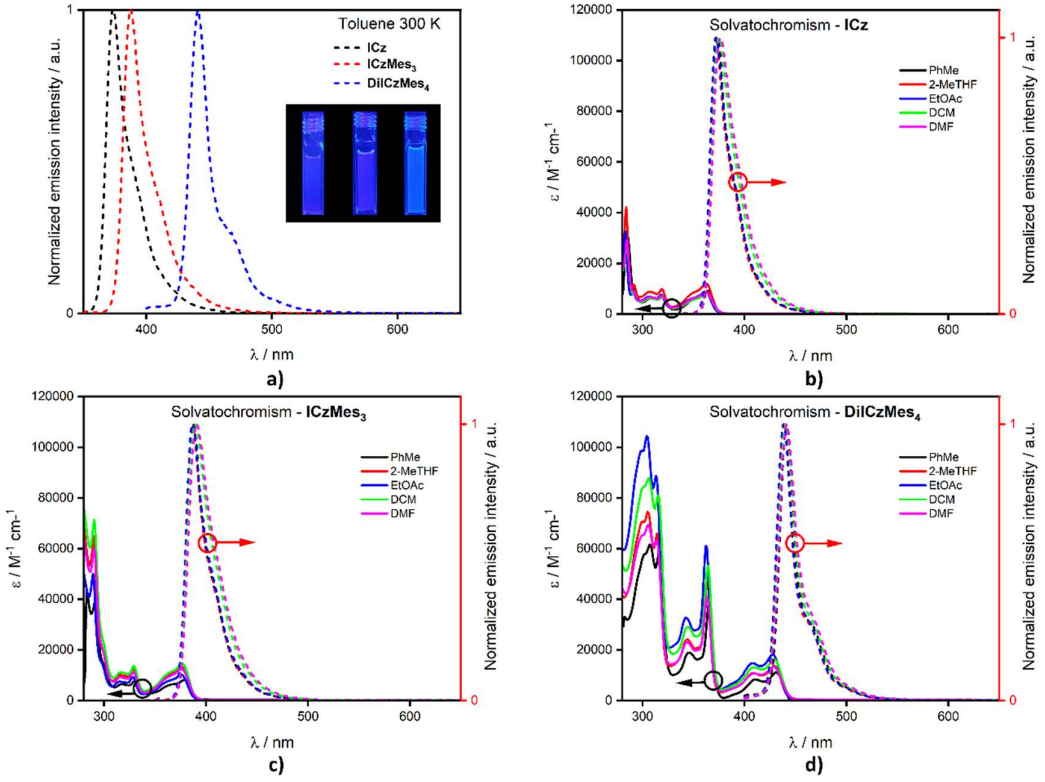

Figure **8.10**. Solution photophysical data, **a**) emission and emitter pictures in PhMe, and solvatochromic screen of **b**) **ICz**, **c**) **ICzMes$_3$** and **DiICzMes$_4$**, λ_{exc} = 320 nm for **ICz** and **ICzMes$_3$** and λ_{exc} = 380 nm for **DiICzMes$_4$**.

The energies of the singlet and triplet states, and hence, ΔE_{ST}, were determined based on the high-energy onset of the prompt fluorescence and phosphorescence spectra obtained at 77 K in PhMe glass (dotted lines in Figure **8.11**). In all cases, the phosphorescence is very well vibrationally structured in strong contrast with respect to the fluorescence (*vide infra*.). There is a progressive decrease in ΔE_{ST} of 0.47 eV, 0.39 eV and 0.26 eV for **ICz**, **ICzMes$_3$** to **DiICzMes$_4$**, respectively, a trend that is well reproduced by SCS-CC2 calculations when considering optimized excited state structures (Table **8.2**). The solution Φ_{PL} increased from 58%, 66% and 70% for **ICz**, **ICzMes$_3$** to **DiICzMes$_4$**, respectively, in line with increasing ε and oscillator strength. Time-resolved PL decays revealed prompt lifetimes of 15.0 ns, 21.6 ns and 40.5 ns for **ICz**, **ICzMes$_3$** and **DiICzMes$_4$**, respectively. A small contribution of delayed emission was observed for **ICz**, which was ascribed to originate from TTA (Figure **8.11b**), while no delayed emission was observed for either **ICzMes$_3$** or **DiICzMes$_4$** (Figure **8.11d** and **f**).

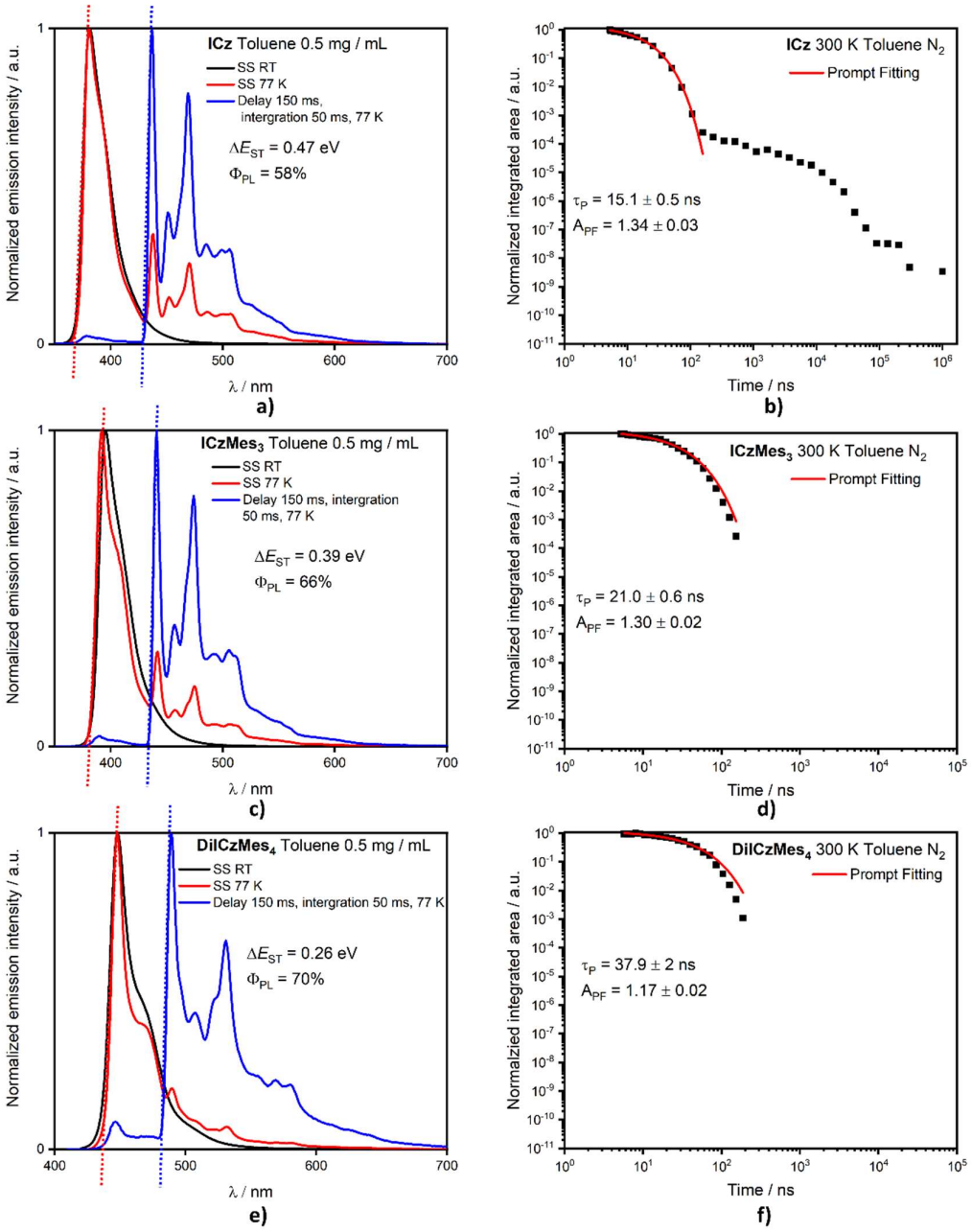

Figure **8.11**. Photophyiscal data in PhMe where **a**), **c**) and **e**) are the RT SS, SS at 77 K and gated emission at 77 K, corresponding to T_1, calculated ΔE_{ST} spectrum for **ICz**, **ICzMes$_3$** and **DiICzMes$_4$**, , λ_{exc} = 330 nm and **b**), **d**), **f**) is the lifetime and mono-exponential fitting of **ICz**, **ICzMes$_3$** and **DiICzMes$_4$**, λ_{exc} = 355 nm.

The vibronically resolved fluorescence and phosphorescence spectra were simulated for **DiCz-*p*-2** (the mesityl groups were omitted from **DiICzMes$_4$** to avoid spurious negative vibration modes) and obtain excellent agreement with the corresponding experimental spectra of **DiICzMes$_4$** (see Figure **8.12**). The lower energy shoulder of the fluorescence spectrum observed experimentally is attributed to a vibronic transition based on the cross-comparison with the simulated one. This shoulder disappears with increasing concentration when aggregate emission begins to contribute significantly to the emission spectrum (Figure **8.14b**). Furthermore, the simulated vibronically-resolved phosphorescence spectrum is also in excellent agreement with the experiment. Interestingly, there is an enhanced vibronic intensity associated with high-frequency (1200-1600 cm^{-1}) vibrations in phosphorescence in comparison to fluorescence. This reflects the more pronounced geometric relaxation taking place in T_1 compared so S_1, producing a larger adiabatic ΔE_{ST} in comparison to the vertical ΔE_{ST} (Table **8.2**) and provides a clear spectroscopic evidence for the different character of the S_1 and T_1 excited states. This behaviour is again in strong contrast with most of the MR-TADF emitters. For example, in Chapter 6, **DiKTa** and **Mes$_3$DiKTa** have fluorescence and phosphorescence with similar shapes, owing to the identical nature of their excited states.

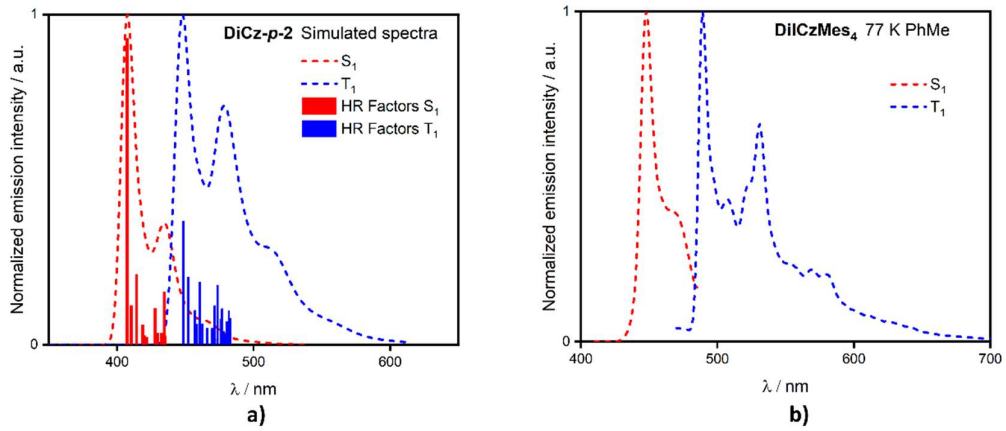

Figure **8.12**. Singlet and triplet emission spectra of **DiICzMes$_4$**, where **a**) is simulated (with Mes omitted) Undistorted displaced harmonic oscillator model. The vertical bars show the Huang-Rhys factors for the most strongly coupled vibrational modes, calculated at TDA-PBE0/6-31G(d,p) and **b**) is experimentally obtained in PhMe at 77 K, λ_{exc} = 330 nm.

Table **8.5**. Optoelectronic data of each emitter in PhMe.

Compound	λ_{abs} (ε) / nm ($\times 10^4$ M^{-1} cm^{-1}) [a]	λ_{PL} (FWHM) / nm[a,b]	Φ_{PL} N_2 / %[c]	S_1 / eV[d]	T_1 / eV[d]	ΔE_{ST} / eV[e]	τ_p / ns[f]
ICz	285 (31), 392 (10), 309 (6), 320 (7), 350 (6), 364 (9)	374 (21)[g]	58	3.35	2.88	0.47	15
ICzMes$_3$	291 (40), 300 (14), 318 (6), 330 (8), 363 (6), 379 (8)	387 (21)[g]	66	3.24	2.85	0.39	22
DiICzMes$_4$	302 (58), 307 (62), 316 (59), 345 (19), 365 (39), 410 (8), 431 (11)	441 (17)[h]	70 [i]	2.83[j]	2.57[j]	0.26	41

[a] at 300 K, [b] Values in parentheses are the FWHM, [c] In degassed PhMe measured an integrating sphere under N_2, λ_{exc} = 330 nm, [d] From the onset of the steady-state emission and phosphorescence in PhMe glass at 77 K, λ_{exc} = 330 nm, [e] Energy difference between the onset of the steady-state and phosphorescence at 77 K, [f] λ_{exc} = 355 nm, [g] λ_{exc} = 320 nm,[h] λ_{exc} = 380 nm, [i] λ_{exc} = 350 nm, [j] λ_{exc} = 350 nm.

8.3.5 Solid-state photophysical properties

The solid-state PL behaviour was investigated in a wide bandgap host, PMMA at 3 wt% doping of emitter. Similar λ_{PL}, ΔE_{ST} and Φ_{PL} were obtained to those in PhMe (Table **8.5**). In 3 wt% PMMA the λ_{PL} are 377 nm, 391 nm and 442 nm for **ICz**, **ICzMes$_3$** and **DiICzMes$_4$**. The ΔE_{ST} values are 0.50 eV, 0.41 eV and 0.29 eV for **ICz**, **ICzMes$_3$** and **DiICzMes$_4$**, respectively, and align with the calculated ΔE_{ST} using optimized excited state structures. The Φ_{PL} are 37%, 58% and 67%, for **ICz**, **ICzMes$_3$** and **DiICzMes$_4$**, respectively. Again, a red-shifted emission, a decreased ΔE_{ST} and an improved Φ_{PL} are observed across the series from **ICz** to **ICzMes$_3$** and to **DiICzMes$_4$** (Figure **8.13**). Owing to their large ΔE_{ST} and S_1 energies, the photophysical properties of **ICz** and **ICzMes$_3$** were not investigated in other hosts.

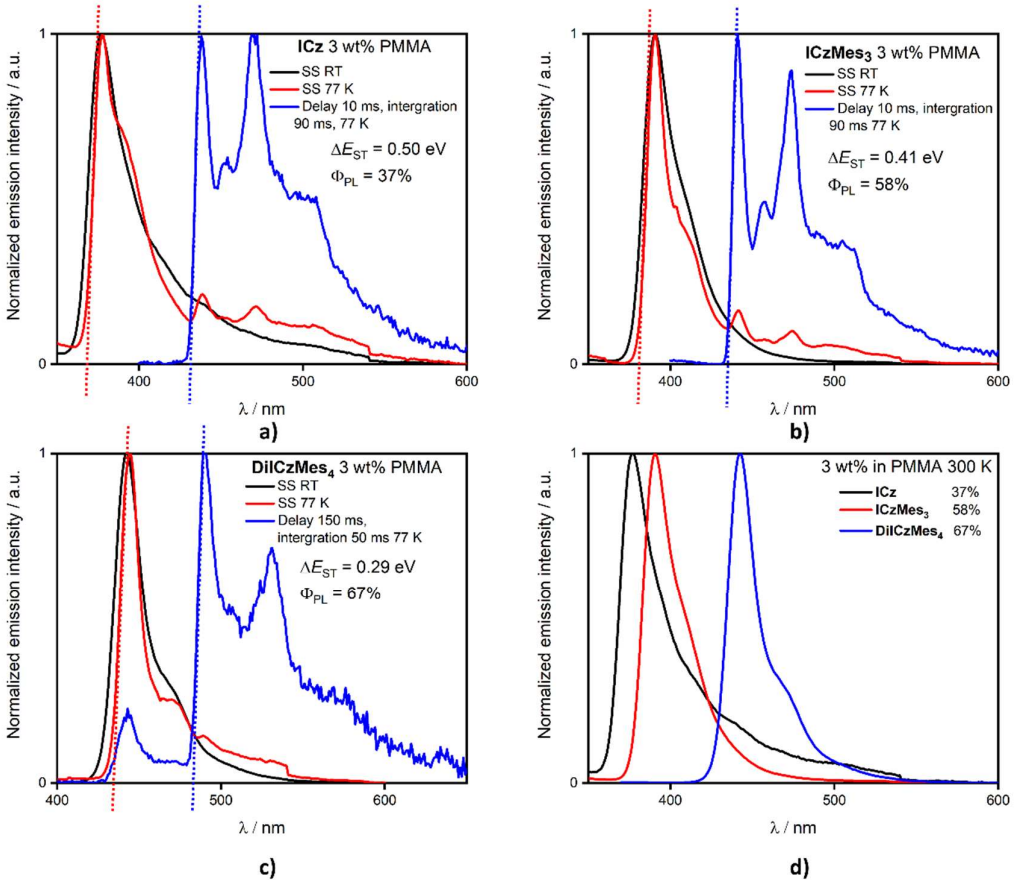

Figure **8.13**. Solid-state photophysical data in 3 wt% PMMA, emission spectra (**a**, **c**, **e**) steady-state at RT, 77 K and gated emission, and **d**) stacked emission spectra. **ICz** (**a**), **ICzMes$_3$** (**b**), **DiICzMes$_4$** (**c**), λ_{exc} = 330 nm.

The photophysical properties of **DiICzMes$_4$** in mCP were investigated as this OLED-compatible host matrix has a suitably large T_1 energy of 2.9 eV.[223] The optimum doping concentration as a function of Φ_{PL} was determined (Figure **8.14a**). No ACQ was observed up to 3 wt%, with Φ_{PL} maintained at 82%; beyond this concentration the Φ_{PL} decreased, with neat films showing a Φ_{PL} of 30% (Figure **8.14a**). The FWHM of a drop-cast 3 wt% doped film in mCP was larger at 40 nm; a low-energy shoulder increased in intensity with increasing doping, which was assigned to an emission from an aggregate (Figure **8.14b**). However, when films were spin-coated, the aggregate formation could be suppressed, with 3 wt% spin-coated films having a FWHM of 21 nm at λ_{PL} 451 nm.

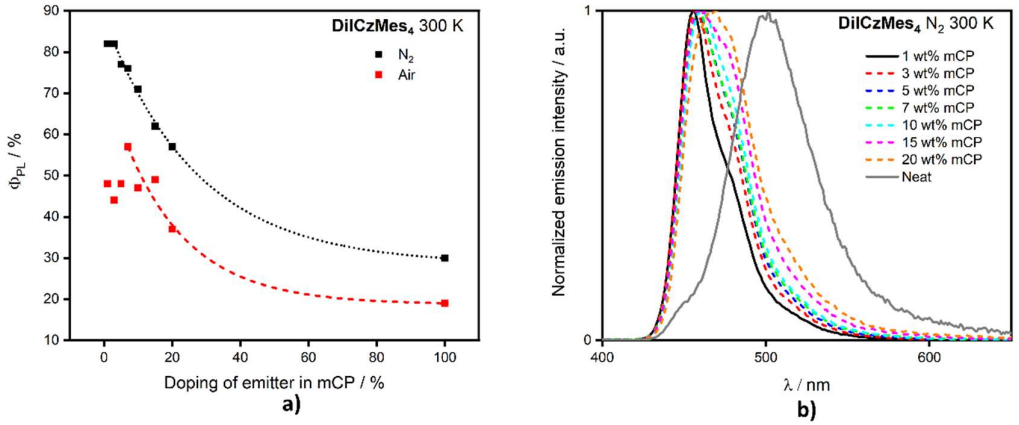

Figure **8.14**. Solid state properties in doped mCP films at various doping concentrations, where **a**) is Φ_{PL} as a function of doping concentration, where an exponential fitting (dotted line) has been added to guide the reader and **b**) is λ_{PL} as a function of changing doping concentration, λ_{exc} = 350 nm.

At 3 wt% doping the ΔE_{ST} was measured to be 0.26 eV (Figure **8.15a**). The lifetime was studied at varying temperature, with prompt emission occurring on the ns regime while a delayed emission on the µs timescale is also observed for temperatures above 240 K, suggestive of TADF behaviour (Figure **8.15b**). At 300 K, a bi-exponential decay profile is observed with fast τ_p of 13.5 ns and a long τ_d of 433 µs (Figure **8.15c**). The delayed emission originates from the same state as the prompt emission based on spectra matching, ruling out any room temperature phosphorescence, which has been observed in other rigid systems[30] (Figure **8.15d**). TTA was ruled out as the emission mechanism owing to the linear power dependence of the emission intensity (Figure **8.15e**).[39] Even at higher doping concentrations (10 wt%) and the use of other hosts (UGH, PPBi, DOBNA, DPEPO, CDBP, CBP and **ICzMes$_3$)** delayed emission remains apparent and its origins assigned to TADF (Figure **8.15f**).

The contribution of the delayed emission to the overall emission is small, Φ_d is 1.2% while overall emission is 82% in 3 wt% mCP films. This has been observed previously in MR-TADF emitters, reflecting the efficient k_r^S (and small Φ_{ISC}) and the slow k_{RISC} (Table **8.6**). For instance, for **DABNA-1** and **DiKTa** the Φ_d is around 4% for 1 wt% **DABNA-1**[8] in mCBP and 1% for **DiKTa** in toluene.[149] For **DiICzMes$_4$**, k_{RISC} is slow, at 1.8 × 10^2 s^{-1} following the methodology of Masui *et al.*[111] This is

substantially slower than most MR-TADF emitters, but similar to **tPBisICz** and **tBisICz**, which were reported at the same time as this work with k_{RISC} of 1.4 and 0.14 × 10^3 s^{-1}, respectively, in 1 wt% mCP:TSPO1 films.[273] In this work, neither **ICz** nor **ICzMes$_3$** show TADF due to their too large ΔE_{ST} of 0.47 eV and 0.39 eV, respectively, measured in PhMe glass; however, **DiICzMes$_4$** shows weak TADF as its ΔE_{ST} of 0.26 eV is much smaller.

Table **8.7**. Solid-state photophysical properties.

Compound [a]	**λ_{PL} (FWHM) / nm**[b]	**Φ_{PL} (Φ_d) / %**[c]	**S_1 / eV**[d]	**T_1 / eV**[d]	**ΔE_{ST} / eV**[e]	**τ_p / ns**[f]	**τ_d / µs**[f]	**k_{ISC} / × 10^7 s^{-1}**	**k_{RISC} / × 10^2 s^{-1}**
ICz	377 (29)	37	3.38	2.88	0.50	N/A	N/A	N/A	N/A
ICzMes$_3$	391 (28)	58	3.26	2.85	0.41	N/A	N/A	N/A	N/A
DiICzMes$_4$	442 (20)[g]	67	2.86[h]	2.57[h]	0.29	N/A	N/A	N/A	N/A
DiICzMes$_4$[i]	451 (22)[g]	82 (1.2)[f]	2.82[h]	2.56[h]	0.26	14	433	1.4	1.8

[a] In 3 wt% doped PMMA films, [b] λ_{exc} = 330 nm, where value in parentheses is FWHM, [c] Determined using an integrating sphere, λ_{exc} = 330 nm, [d] S_1 and T_1 determined from the onset of the steady-state and phosphorescence spectra, respectively, at 77 K, λ_{exc} = 330 nm, [e] Calculated from the energy difference between the energies of the S_1 and T_1 states at 77 K, [f] λ_{exc} = 355 nm, [g] λ_{exc} = 350 nm, [h] λ_{exc} = 350 nm, [i] In 3 wt% doped mCP films.

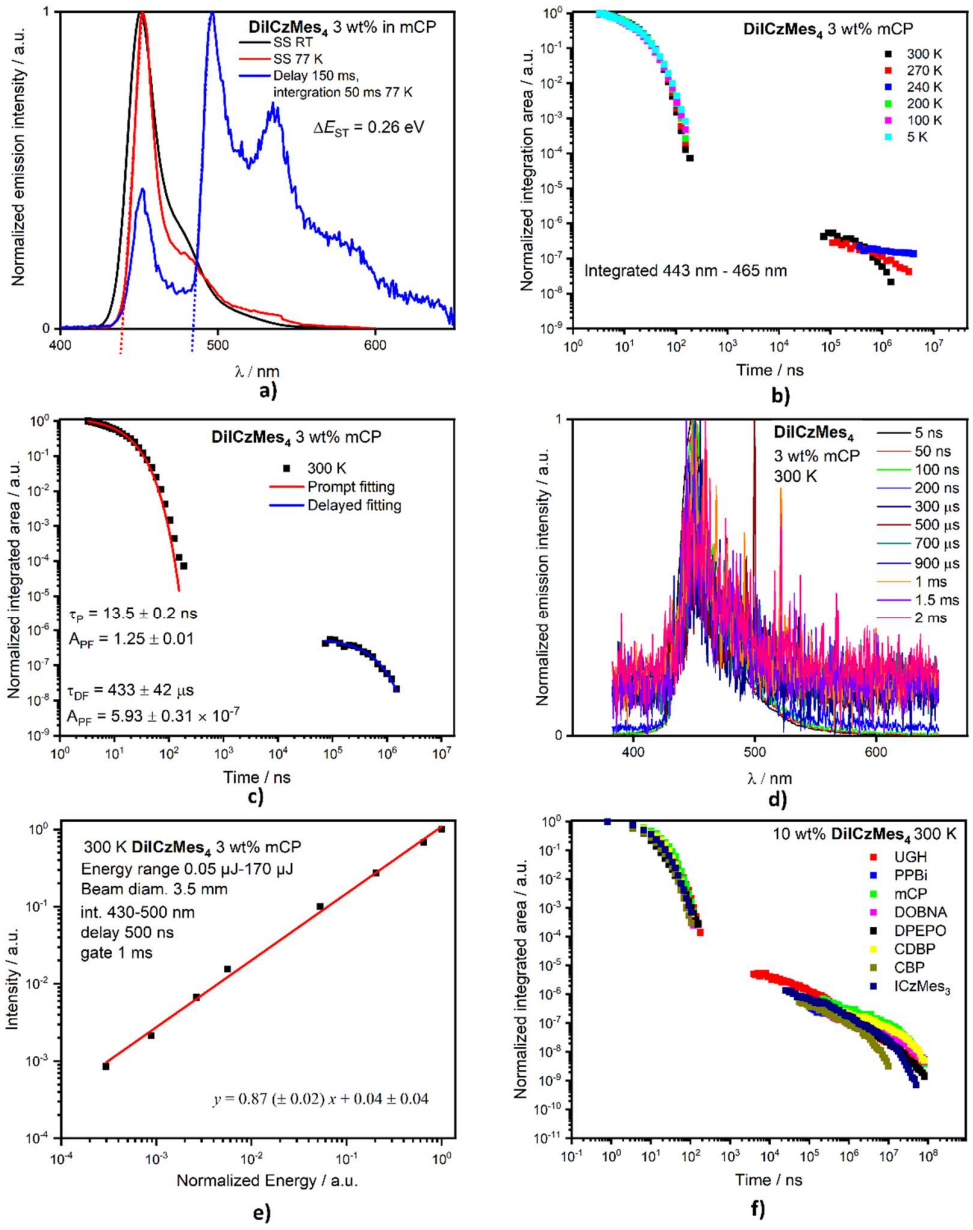

Figure **8.15**. Solid photophysical data of **DilCzMes$_4$** in doped films (3 wt% mCP unless stated), where **a**) is SS emission spectra at RT (λ_{exc} = 330 nm) and 77 K and phosphorescence spectrum at 77 K, (λ_{exc} = 350 nm) determining ΔE_{ST}, **b)** Temperature-dependent time-resolved PL decays, λ_{exc} = 355 nm; **c**) lifetime fitting at 300 K, where prompt (red) and delayed (blue) have been fitted with mono-exponentials , λ_{exc} = 355 nm, **d**) varying λ_{PL} at changing time, λ_{exc} = 355 nm **e)** Intensity dependence as a function of laser power, λ_{exc} = 355 nm and **f**) time-resolved PL decays in 10 wt% films of different hosts at 300 K, λ_{exc} = 355 nm.

8.3.6 Device properties

Having confirmed the weak TADF activity of **DiICzMes$_4$**, its use as an emitter in OLEDs was assessed. Devices using a stack of ITO (HIL/anode)| N,N'-bis(naphthalen-1-yl)- N,N'-bis(phenyl)benzidine [NPB] (HTL, 40 nm) | 4,4'-(Diphenylsilanediyl)-bis(N,N-diphenylaniline) [TSBPA] (EBL, 10 nm) | **DiICzMes$_4$**:DPEPO 10% (EML, 30 nm) | DPEPO (HBL, 10 nm) | TBPi (ETL, 40 nm) | LiF (EIL, 1 nm) | Al (cathode, 100 nm) were fabricated shown in Figure **8.16**. These results show that the low rate of RISC in **DiICzMes$_4$** is insufficient to enable efficient triplet harvesting at the current densities investigated here. The resulting low EQE_{max} values are consistent with the **DiICzMes$_4$** acting akin to a fluorescent dopant, only able to harvest singlet excitons for emission with an upper limit of EQE_{max} < 5%. This result is also in-line with what was observed for previous acceptor-free RIC DF material **TCA_C4**.[281] The OLED shows CIE coordinates of (0.15, 0.11). An analogous system, **tPBisICz** had impressive EQE_{max} of 23.1% at very low brightness, however their efficiency roll-off was severe with the EQE at 100 cd m^{-2} only about 5% while the EQE at 1,000 cd m^{-2} was not reported, in line with our work (Table **8.8**).[273]

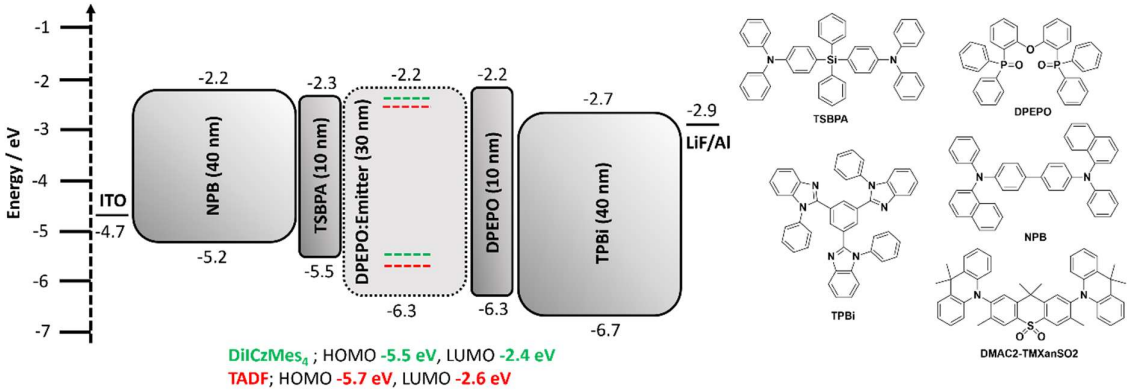

Figure **8.16**. Device architecture and chemical structures of materials employed.

To compensate for the low k_{RISC} of **DiICzMes$_4$** it was also used as a terminal emitter in Hyperfluorescence-OLEDs with a D-A-D TADF co-host. In order to ensure good spectral overlap necessary for energy transfer, dimethylacridine-tetramethylthioxanthene-S,S-dioxide (**DMAC2-TMXanSO2**, Figure **8.16**) was used as the TADF co-host, previously reported to give high EQEs and deep blue emission [CIE of (0.15, 0.19)] in the same OLED stack (Figure **8.17b**, red line).[282] This D-

A-D TADF was co-evaporated at 35% in the EML, alongside 1% **DiICzMes$_4$** and bulk host DPEPO. The resulting OLEDs possessed good efficiency, with an EQE$_{max}$>16% and CIE of (0.15, 0.11) enabled by triplet harvesting of the D-A-D co-host, while outputting narrow blue emission from the **DiICzMes$_4$**. The Hyperfluorescence-OLED showed improved device performance with higher EQE$_{max}$, and improved roll-off, with brightness's surpassing 1,000 cd m^{-2} now observed (Figure **8.17**).

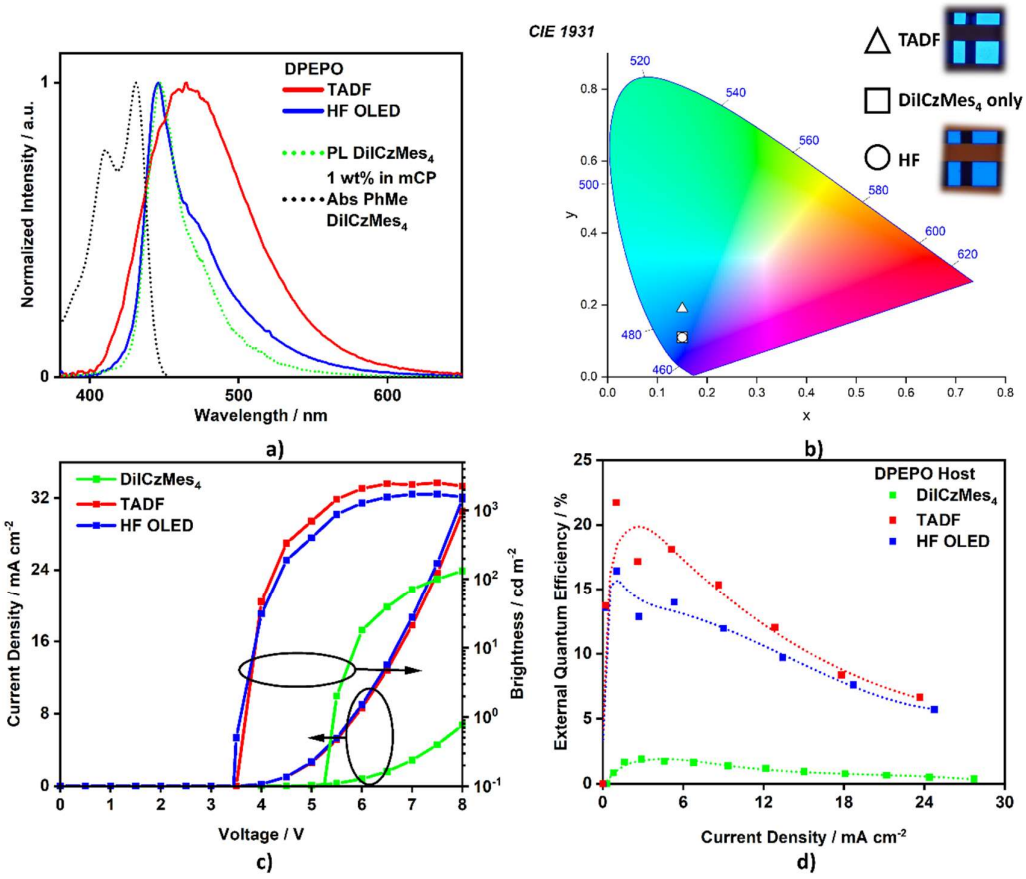

Figure **8.17**. OLED performance for different EMLs. (**a**) EL spectra of TADF D-A-D 35% (red), HF OLEDs 1:35 wt% (blue) in DPEPO host, absorption (black dotted) and PL (green) spectra of **DiICzMes$_4$** 1 wt% in mCP for comparison. (**b**) CIE coordinates, where square (**DiICzMes$_4$** only OLED) and circle (Hyperfluorescence-OLED) overlap, (**c**) JVL curves, and (**d**) EQE vs current density, where fitting has been applied (dotted line) to guide the reader.

As our integrating sphere system is not sensitive to very low luminances, we do not observe the same high maximum EQEs (~32%) previously reported using a similar Hyperfluorescence approach

with **pICz**.[283] However, comparing our device data at equivalent brightness reveals improved performance (Table **8.8**), which we infer is due to the improved efficiency roll-off of our D-A-D co-host. The previously reported **DPAc-DtCzBN**:PPF co-host has a similar intrinsic maximum efficiency as ours, and with slightly blue shifted EL spectrum should also enjoy marginally improved FRET overlap with the MR-TADF emitter in the device. In this work, despite the adequate FRET overlap, a subtle shoulder can still be observed in the EL spectra, indicating residual emission from the D-A-D co-host. As Hyperfluorescence applications of MR-TADF emitters become increasingly popular to circumvent their low RISC rates,[155, 270-272] engineering both their PL spectra (for ideal-blue emission), as well as their absorption spectra (for minimal stokes shift, enabling broad compatibility with D-A-D TADF co-hosts)[284] take on equally important roles for applications. The later of these can significantly alleviate the requirement for D-A-D co-hosts with deep blue EL, which remain challenging to design despite nearly a decade of intense global research in this direction.

In the Hyperfluorescence-OLED reported here and those previously reported, inclusion of the MR-TADF leads to significantly worse efficiencies at reasonable brightnesses compared to the D-A-D co-host alone. While the **DiICzMes$_4$** would be expected to increase device performance due to spontaneously emitter dipole alignment and improved outcoupling[283], other detrimental processes must also be at play to result in an overall detriment to performance. These may include charge trapping or DET due to the slow-RISC MR-TADF dopant, although these processes have proven to be incredibly challenging to even quantify by traditional means.[285] Therefore while the improvement in colour coordinate offered by the MR-TADF Hyperfluorescence-OLED strategy is welcomed, it is clear that a deeper understanding of the relevant *in operando* mechanism and processes is required to unlock their full potential.

Table **8.8.** Device data of emitter only OLEDs and Hyperfluorescence-OLEDs for **DiICzMes$_4$** and similar work.

	Emitter	V_{on} / V	EQE_{max} / %	EQE_{100} / %	EQE_{1000} / %	Lum_{max} / cd/m^{-2}	CIE (x,y)	λ_{EL} / nm	Ref
Emitter only	**DiICzMes$_4$**	5.2	3.0	1.9	N/A	130	0.15, 0.11	446	This work
	BisICz	3.4[a]	6.5	2.5[a]	N/A	130[a]	0.16, 0.04	437	273
	tBisICz	3.2[a]	15.1	3.0[a]	N/A	200[a]	0.16, 0.05	445	273
	tPBisICz	3.2	23.1	4.8[a]	N/A	230[a]	0.15, 0.05	452	273
Hyperfluorescence-OLED	**DiICzMes$_4$**[b]	3.4	16.5	15.5	12.9	1500	0.15, 0.11	446	This work
	pICz[c]	3.5	32.0	6.7	4.0[a]	2400[a]	0.15, 0.10	445	283

[a] Data extracted from graphical fitting software, [b] Obtained alongside triplet harvester **DMAC2-TMXanSO2**, [b] Obtained alongside triplet harvester **DPAc-DtCzBN.**

8.4 Conclusions

A new MR-TADF core has been designed and investigated that does not contain any explicit electron-acceptor units, opening a new design paradigm for MR-TADF emitters. SCS-CC2 calculations guided the design, confirming a strategy to coincidentally decrease ΔE_{ST} and improve oscillator strength with increasing electronic delocalization. Photophysical measurements revealed a reduced ΔE_{ST} and increased Φ_{PL} were observed in both solution and doped films for **DiICzMes$_4$** compared to **ICz** and **ICzMes$_3$**. Although ΔE_{ST} was rather large at 0.26 eV in mCP, TADF was nonetheless observed in this and other solid-state hosts. Activation of TADF occurs through the involvement of higher-lying triplet states of different orbital types to S_1, resulting in non-negligible SOC.[260, 278] Owing to inefficient RISC, simple guest-host OLEDs showed low efficiency, although hyperfluorescent devices achieved good EQE_{max} of 16.5%, at deep-blue colour coordinates (0.15, 0.11) with improved relative efficiency roll-off compared to a similar derivative reported.[283] Discovery of new regions of chemical space suitable for the development of MR-TADF emitters thus opens new paths towards understanding their optical properties and improving their performance, with improved k_{RISC} essential in future development.

Chapter 9: Concluding remarks

This thesis is focused on TADF materials, investigating primarily D-A TADF systems (Chapters 3 – 5) and MR-TADF systems (Chapter 6 – 8). Chapter 3 studied the impact of adopting an extended donor strategy on the performance of D-A TADF emitters, with a series of compounds incorporating extended donors based on the **2CzPN** parent emitter. Upon incorporation of an extended donor there is a decreased ΔE_{ST} accompanied by an increase in k_{RISC}. However, **2CzPN** displayed the largest Φ_{PL} of 93% in films and this property was adversely affected in both ***t*BuDPA-2CzPN** and **PXZ-2CzPN** with values down to 14% and 23%, respectively. Increased flexibility in the donor moieties in ***t*BuDPA-2CzPN** produced large k_{nr}. **PXZ-2CzPN** showed large separation between the hole and the electron densities, resulting in a slow k_r. **Cz-2CzPN** showed a reasonable Φ_{PL} of 78% but k_{nr} increased significantly with increased temperature. It is clear that despite extended donors increasing k_{RISC}, it is detrimental to overall photophysical performance. Chapter 4 introduced a new acceptor to the community, namely pyridyl benzimidazole (BImPy), which was coupled to a PXZ donor. BImPy was N-substituted with methyl, phenyl and *t*Bu groups. Their presence modulated to torsion angle between the pyridine and the benzimidazole, thereby affecting acceptor strength, which was corroborated by a detailed DFT study. TADF was observed in doped films, with delayed fluorescence lifetimes ranging from 260 μs to 770 μs. Substitution of bulky groups contributed to reducing ACQ. Devices were fabricated using **BImPyPXZ**, **BIm(Me)PyPXZ** and **BIm(Ph)PyPXZ** with EQE_{max} of 18.6%, 23.9% and 22.2%, respectively. The higher doping possible in the latter two due to the presence of the N-substituents contributed to the higher maximum luminance values, surpassing 17,000 cd m^{-2} for devices with these two emitters. In Chapter 5, 14 literature TADF emitters were studied using a range of DFT functionals. Cross-comparison of the $\Delta E_{ST,}$ ΔE_{ST2}, ΔE_{T2T1}, and T_1, T_2 and S_1 between SCS-CC2 and TD-DFT and TDA-DFT calculations revealed that TDA-M06-2X and TDA-CAM-B3LYP were found to be the methods that produced the most accurate predictions compared to those from SCS-CC2 calculations. The degree of CT character in the excited states was quantified using the D_{CT}, q_{CT} and S_{+-} metrics. Most DFT functionals perform reasonably to accurately predict the nature of S_1, which was particularly true using M06-2X and CAM-B3LYP. However, the descriptions of T_1 and T_2 are not as

accurately captured, regardless of the functional used still functionals such M06-2X, CAM-B3LYP, LC-ω*PBE and LC-ω*HPBE displayed overall better performances. Chapter 6 introduced ketone-containing MR-TADF emitters. The design originated from in silico modelling using SCS-CC2 calculations, which provide accurate predictions of ΔE_{ST}. Two emitters were introduced, **DiKTa** and **Mes$_3$DiKTa**, with the latter showing improved electrochemical stability and showing reduced ACQ compared to **DiKTa**. TADF was observed in both, although k_{RISC} was low, at ca. 2.3×10^3 s^{-1}. Devices showed EQE_{max} of 14.7% and 21.1% for OLEDs with **DiKTa** and **Mes$_3$DiKTa**, respectively. The latter showed higher EQE at 100 cd m^{-2} of 14.5% compared to 8.3%, for the former but both displayed large efficiency roll-off owing to the slow k_{RISC}. Chapter 7 consists in a computational investigation at the SCS-CC2 and TD(A)-DFT levels of theory of 35 literature MR-TADF emitters. The cross comparison between TD(A)-DFT calculations using a range of DFT functionals and SCS-CC2 revealed that the later method provides by far the best agreement with the experimental ΔE_{ST} with MAD of 0.04 eV, while the MAD for DFT functionals ranged between 0.29 eV and 0.98 eV. SCS-CC2 calculations make clear that ketone-based MR-TADF emitters have higher ΔE_{ST}, assigned to the more localised nature of the S_1 and T_1 excited states. SCS-CC2 calculations were also performed on a series of D-A systems that contain an acceptor that is itself MR-TADF. These calculations show that there is frequently a low-lying CT state that becomes the most stabilized singlet excited state in solution or films and may explain the dual emission observed experimentally in two examples. Chapter 8 summarized how SCS-CC2 calculations were used to design a new class of MR-TADF emitter that did not include acceptor groups. The target material **DiICzMes$_4$** showed a decreased ΔE_{ST} compared to the parent **ICz**, increased Φ_{PL} and red shifted emission. The smaller ΔE_{ST} explained why TADF was observed in doped films. However, k_{RISC} was found to be very slow, 1.8×10^2 s^{-1} likely due to the high energy spacing between T_1 and T_2. The OLEDs showed low EQE_{max} of 3.0%. However, Hyperfluorescence-OLEDs using a TADF assistant dopant, **DMAC2-TMXanSO2** and **DiICzMes$_4$** as the terminal emitter showed an EQE_{max} of 16.5% and CIE of (0.15, 0.11).

Despite the huge interest in TADF emitters, challenges remain, primarily in terms of device stability and efficiency roll-off. In terms of D-A TADF emitter design, it is clear more work is required

to understand the complex RISC mechanism. Although it is widely accepted that close lying higher triplet states are desirable, there is minimal understanding on how to introduce these and control their energies. If this is tackled efficient D-A systems will follow, with improved device stability and lifetime. Clearly based on our own work, conventional DFT approaches still struggle to consistently predict triplet natures compared to higher order methods. With further work and improved methodologies employed this will become a powerful tool to develop efficient D-A TADF emitters. The community must stary away from simple ΔE_{ST} prediction, although useful, is limiting in terms of RISC improvements for materials design.

Although over 100 MR-TADF emitters exist covering the full spectral range their core structures are minimal. Improved ΔE_{ST} using our new established methods will assist this drive to new structures. However, MR-TADF emitters suffer from extremely slow k_{RISC}, much less than their D-A counterparts, and explains their consistent poor roll-off and short device lifetimes. Producing MR-TADF emitters that show high k_{RISC} is a priority, which will require a deeper insight into their RISC mechanism. Unlike D-A systems, the role of intermediate triplet states is poorly understood, with many calculated to have very high ΔE_{T2T1}. It is unclear at this stage if the mechanism for RISC in MR-TADF emitters is identical to that of D-A systems, with further work required. Based on literature emitters the importance of sulfur incorporation and carbazole coupled stuctues appear as a potential avenue to improve k_{RISC} rates. These two design approaches should be investigated further. Other avenues to supress ACQ are also essential, with the low emitter doping problematic at high brightness. One avenue which should be explored is MR-TADF emitter incorporation into dendritic structures which would mitigate ACQ.

Beyond TADF, a deeper understanding into INVEST materials is essential. It is not clear at this stage firstly if they exist or are purely artefacts from calculations, and secondly if they are superior to TADF. Although not an endothermic process like TADF, they will still require some SOC to ensure T_1 to S_1 conversion, with current materials having identical S_1 and T_1 orbital pictures, likely making them El Sayed forbidden. Study of INVEST materials beyond the purely theoretical stand point is required, with minimal photophysical evidence currently available. It would be useful to understand why we

calculate **B3** as INVEST, while experimentally it is not. Currently high symmetry is an essential factor for materials design, which at this stage we cannot understand why, with a more in-depth investigation of the INVEST mechanism required. Radical materials have recently entered the frame of OLED emitters offering very promising efficiencies. This is an extremely new branch of OLED research with only a handful of emitters currently available. Despite the extreme promise of Hyperfluorescence-OLEDs, their emitter layers are complex with a host, triplet harvester and terminal emitter required. This is undesirable industrially, with a maximum of two components often quoted. To bypass this problem, essentially non-doped TADF emitters are required as the triplet harvester bypassing the need of hosts, which are still rare. Further the consistent lower EQE_{max} of the triplet harvester in a Hyperfluorescence stack compared to the equivalent emitter only device needs to addressed.

The use of computational resources to guide improve emitter design is essential for future development pushing TADF beyond the purely academic research interest towards a successful industrial technology. Despite 10 years of intense OLED research in TADF materials the field continues to expand with lots of new structures emerging. TADF research will continue to be the most popular exciton harvesting mechanism investigated academically for the foreseeable future until a new mechanism emerges able to rival it.

Chapter 10: Experimental

10.1 General synthetic procedures

All commercially available chemicals and reagent grade solvents were used as received. Solvents used in the reactions were dry and deaerated using an MBRAUN solvent purification system. Air-sensitive reactions are done under a nitrogen atmosphere using Schlenk techniques. Flash column chromatography was carried out using silica gel (Silia-P from Silicycle, 60 Å, 40-63 μm). Analytical thin-layer-chromatography (TLC) was performed with silica plates with aluminium backings (250 μm with F-254 indicator). TLC visualization was accomplished by use of a 254/365 nm UV lamp. ^{1}H and ^{13}C and Nuclear magnetic resonance (NMR) spectra were recorded on a Bruker Advance spectrometer (500 MHz for ^{1}H and 126 MHz for ^{13}C). The following abbreviations have been used for multiplicity assignments: "s" for singlet, "d" for doublet, "t" for triplet, "dd" for doublet of doublets, "td" for triplet of doublets, "m" for multiplet and "br" for broad. Deuterated chloroform ($CDCl_3$), deuterated dichloromethane (CD_2Cl_2) and deuterated DMSO (DMSO-d_6) were used as the solvents of record. ^{1}H and ^{13}C NMR spectra were referenced to the solvent peak. Melting points were measured using open-ended capillaries on an Electrothermal melting point apparatus and are uncorrected. High-resolution mass spectrometry (HRMS) was performed by the EPSRC National Mass Spectrometry Service Centre at Swansea, the HRMS service in St Andrews and Dr Stuart Warriner at the University of Leeds. Elemental analyses were performed by Mr. Stephen Boyer, London Metropolitan University.

Chapter 3

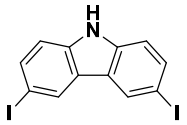

3,6-diiodo-9*H*-carbazole (CzI_2)

The reaction is based on a previously reported synthesis.[286] Carbazole (3 g, 17.9 mmol, 1 equiv.) was dissolved in acetonitrile (120 mL). Several drops of trifluoroacetic acid were added to the solution.

N-Iodosuccinimide (8.1 g, 35.9 mmol, 2.2 equiv.) was added in portions, and the resulting mixture was stirred at room temperature for 24 h. Water (150 mL) was added and the resulting cream-coloured solid was filtered and washed with water and ether. It was used directly without any further purification. Yield**:** 92% (6.9 g). **Mp**: 204 – 209°C (Lit. 204 – 206 °C).[287] **^{1}H NMR (500 MHz, $CDCl_3$) δ (ppm)**: 8.31 (d, *J* = 1.5 Hz, 2H), 7.67 (dd, *J* = 8.5, 1.6 Hz, 2H), 7.20 (d, *J* = 8.5 Hz, 2H). **^{13}C NMR (126 MHz, $CDCl_3$) δ (ppm)**: 138.6, 134.9, 129.5, 124.7, 112.9, 82.5 **HR-MS $[M+H]^+$:** Calculated: 419.8746 ($C_{12}H_7I_2NH$); Found: 419.8750. The characterization matches that previously reported.[288]

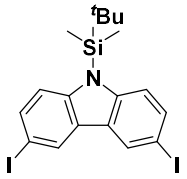

9-(*tert*-butyldimethylsilyl)-3,6-diiodo-9*H*-carbazole (1)

The reaction is based on a previously reported synthesis.[286] **CzI_2** (4 g, 9.5 mmol, 1 equiv.) was dissolved in dry THF (40 mL). To the solution was added NaH (60% in paraffin oil, 0.76 g, 19.1 mmol, 2 equiv.) in portions under a positive flow of N_2. The resulting mixture was stirred at room temperature under a flow of N_2 for 30 min. To the reaction mixture was added *tert*-butylchlorodimethylsilane (1.72 g, 11.4 mmol, 1.2 equiv.) under a positive flow of N_2 and the resulting solution was stirred at room temperature under a flow of N_2 for 1 h. Water was added to quench the reaction and it was extracted with EtOAc, (3 × 100 ml), dried over Na_2SO_4, filtered and concentrated under reduced pressure to afford the crude product as a brown oil. The crude product was purified by silica gel column chromatography (20:80, DCM:hexanes). The corresponding fractions were combined and concentrated under reduced pressure to afford the desired product as a white powder. **Yield**: 69% (3.5 g). **R*f*:** 0.38 (20:80 DCM:hexanes on silica). **Mp**: 179 – 183 °C (Lit. 183 – 184.5 °C).[289] **^{1}HNMR (500 MHz, $CDCl_3$) δ (ppm)**: 8.30 (d, *J* = 1.8 Hz, 2H), 7.62 (dd, *J* = 8.8, 1.8 Hz, 2H), 7.35 (d, *J* = 8.8 Hz, 2H), 1.00 (s, 9H), 0.73 (s, 6H). **^{13}C NMR (126 MHz, $CDCl_3$) δ (ppm)**: 144.4, 134.5, 129.0, 127.7, 116.2, 82.9, 26.6, 20.7, -1.2. **HR-MS $[M]^+$:** Calculated: 532.9532 ($C_{18}H_{21}I_2NSi$); Found: 532.9534. The characterization matches that previously reported.[288]

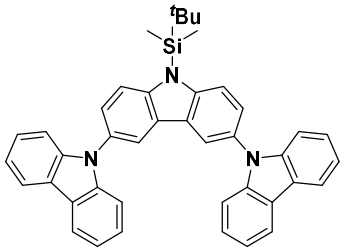

9'-(*tert*-butyldimethylsilyl)-9'*H*-9,3':6',9''-tercarbazole (2)

The reaction is based on a previously reported synthesis.[286] Carbazole (0.84 g, 5.0 mmol, 2.05 equiv.) and tribasic potassium phosphate (3.08 g, 14.5 mmol, 6.05 equiv.) were dried under vacuum for 30 min. The reaction flask was backfilled with N_2 and dry dioxane (21 mL) was added under a positive flow of N_2. The solution was degassed by bubbling N_2 through it for 15 mins. **1** (1.3 g, 2.4 mmol, 1 equiv.) was added under a positive flow of N_2 and the mixture was degassed by bubbling N_2 through the mixture for 15 mins. Copper iodide (0.05 g, 0.2 mmol, 0.1 equiv.) and *trans*-1,2-diaminocyclohexane (0.04 mL, 0.4 mmol, 0.15 equiv.) were added under a positive flow of N_2. The mixture was heated to reflux for 18 hours, cooled and water (40 mL) added. The reaction mixture was extracted with EtOAc (3 × 50 mL), dried over Na_2SO_4, filtered and concentrated under reduced pressure to afford the crude product as a brown solid. The crude product was dry-loaded onto silica and then purified by silica gel column chromatography (20:80, DCM:hexanes). The corresponding fractions were combined and concentrated under reduced pressure to afford the desired product as a white powder. **Yield:** 83% (1.24 g). **R*f*:** 0.53 (20:80, DCM:hexanes on silica gel). **Mp**: 287 – 290 °C. **^{1}HNMR (500 MHz, CD_2Cl_2) δ (ppm)**: 8.22 (d, *J* = 2.1 Hz, 2H), 8.16 (d, *J* = 7.8, Hz, 4H), 7.92 (d, *J* = 8.8 Hz, 2H), 7.59 (dd, *J* = 8.8, 2.2 Hz, 2H), 7.38 – 7.44 (m, 8H), 7.25 – 7.30 (m, 4H), 1.19 (s, 9H), 0.92 (s, 6H). **^{13}C NMR (126 MHz, CD_2Cl_2) δ (ppm)**: 145.3, 142.1, 130.2, 127.4, 126.2, 125.6, 123.4, 120.5, 120.0, 119.2, 115.9, 110.1, 26.8, 21.0, -1.0. **HR-MS $[M+H]^+$:** Calculated: 612.2830 ($C_{42}H_{37}N_3SiH$); Found: 612.2823.

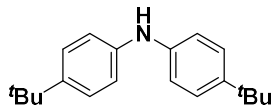

Bis(4-(*tert*-butyl)phenyl)amine (^{t}BuDPA)

Based on a modified literature procedure.[290] Sodium *tert*-butoxide (1.14 g, 11.9 mmol, 2 equiv.) and Pd(dppf)Cl_2 (0.13 g, 0.18 mmol, 0.03 equiv.) were dried under vacuum for 1 h. The reaction flask was backfilled with N_2 and dry toluene (20 mL) was added under a positive flow of N_2 along with 4-(*tert*-butyl)aniline (1.07 mL, 6.70 mmol, 1.13 equiv.). The reaction mixture was degassed by bubbling N_2 through the mixture for 15 min. 1-Bromo-4-(*tert*-butyl)benzene (1.03 mL, 5.93 mmol, 1 equiv.) was added and the reaction mixture was degassed by bubbling N_2 for 15 min. The reaction was heated to reflux for 16 h under a flow of N_2. The mixture was concentrated under reduced pressure. 1 M HCl (20 mL) was added, and the reaction mixture was extracted with DCM (3 × 100 mL). The organic phase was dried over $MgSO_4$, filtered and concentrated under reduced pressure to afford the crude product as a black oil. The crude product was dry-loaded onto silica and then purified by silica gel column chromatography (20:80, DCM:hexanes). The corresponding fractions were collected and concentrated under reduced pressure to afford the desired compound as a light brown solid. Y**ield:** 94% (1.57 g). **R*f*:** 0.40 (20:80, DCM:hexanes on silica gel). **Mp**: 104 – 107 °C (Lit. 106 – 108 °C).[291] **^{1}H NMR (500 MHz, $CDCl_3$) δ (ppm)**: 7.26 (d, *J* = 8.8 Hz, 4 H), 7.02 (d, *J* = 8.8 Hz, 4 H), 5.68 (br-s,, 1 H), 1.31 (s, 18 H).7. **^{13}C NMR (126 MHz, DMSO-d_6) δ (ppm)**:143.8, 141.0, 126.2, 117.6, 34.3, 31.6. **HR-MS [M+H]$^+$:** Calculated: 282.2216 ($C_{20}H_{27}NH$); Found: 282.2213. The characterization matches that previously reported.[291]

General procedure 1: Buchwald-Hartwig coupling to 1.

The corresponding amine (2.05 equiv.) and sodium *tert*-butoxide (3 equiv.) were dried under vacuum for 30 min. The reaction flask was backfilled with N_2 and xylenes (0.05 M) was added under a positive flow of N_2. The reaction was degassed by bubbling N_2 through the reaction mixture for 15 min. **1** (1 equiv.) was added under a positive flow of N_2 and the subsequent mixture was degassed by bubbling N_2 through the mixture for 15 min. $Pd(OAc)_2$ (0.05 equiv.) and [HP(^{t}Bu$_3$)][BF_4] (0.15 equiv.) were

added under a positive flow of N_2. The resulting mixture was heated to reflux for 18 h. The reaction mixture was cooled and brine (50 mL) was added. The reaction was extracted with EtOAc (3 × 50 mL), dried over Na_2SO_4, filtered and concentrated under reduced pressure to afford the crude solid. The crude product was dry-loaded onto silica and then purified by silica gel column chromatography (20:80, DCM:hexanes). The corresponding fractions were combined and concentrated under reduced pressure to afford the desired product.

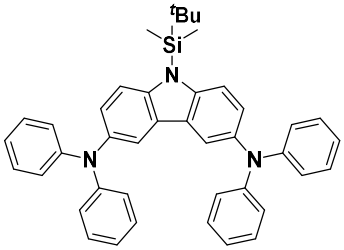

9-(*tert*-butyldimethylsilyl)-N3,N3,N6,N6-tetraphenyl-9*H*-carbazole-3,6-diamine (3)

Reaction was undertaken with diphenylamine using General procedure 1. White solid. Y**ield:** 86% (1.00 g). **R*f*:** 0.39 (20:80, DCM:hexanes on silica gel). **Mp**: 216 – 219 °C. **^{1}HNMR (500 MHz, CD_2Cl_2) δ (ppm)**: 7.64 – 7.67 (m, 2H), 7.55 (d, *J* = 8.9 Hz, 2H), 7.19 (t, *J* = 7.8 Hz, 8H), 7.14 (dd, *J* = 8.9, 2.2 Hz, 2H), 7.03 (d, *J* = 7.8 Hz, 8H), 6.92 (t, *J* = 7.3 Hz, 4H), 1.07 (s, 9H), 0.75 (s, 6H). **^{13}C NMR (126 MHz, CD_2Cl_2) δ (ppm)** 148.9, 143.1, 140.4, 129.3, 127.4, 125.3, 1230.0, 121.9, 118.1, 115.5, 26.7, 20.8, -1.3. **HR-MS $[M+H]^+$:** Calculated: 616.3137 ($C_{42}H_{41}N_3SiH$); Found: 616.3143.

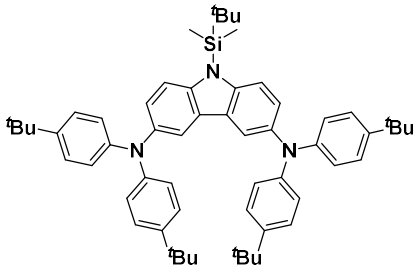

N3,N3,N6,N6-tetrakis(4-(*tert*-butyl)phenyl)-9-(*tert*-butyldimethylsilyl)-9*H*-carbazole-3,6-diamine (4)

Reaction was undertaken with **^{t}BuDPA** using General procedure 1. White solid. Y**ield:** 80% (1.26 g). **R*f*:** 0.64 (20:80, DCM:hexanes on silica gel). **Mp**: 235 – 239 °C. **^{1}HNMR (500 MHz, CD_2Cl_2) δ (ppm)**: 7.63 – 7.66 (m, 2H), 7.52 (d, *J* = 8.9 Hz, 2H), 7.20 (d, *J* = 8.7 Hz, 8H), 7.11 (dd, *J* = 8.9, 2.3

Hz, 2H), 6.94 (d, *J* = 8.7 Hz, 8H), 1.28 (s, 36 H), 1.06 (s, 9H), 0.74 (s, 6H). **^{13}C NMR (126 MHz, CD_2Cl_2) δ (ppm)**: 146.4, 144.6, 142.9, 140.7, 127.4, 126.2, 125.1, 122.4, 117.7, 115.3, 34.4, 31.6, 26.7, 20.9, -1.2. **HR-MS [M+H]$^+$:** Calculated: 840.5647 ($C_{58}H_{73}N_3SiH$); Found: 840.5637.

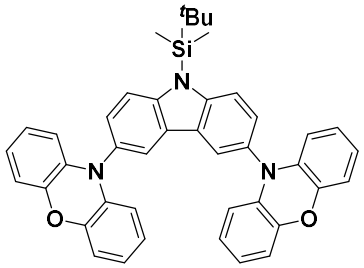

10,10'-(9-(tert-butyldimethylsilyl)-9*H*-carbazole-3,6-diyl)bis(10*H*-phenoxazine) (5)

Reaction was undertaken with phenoxazine using General procedure 1. White solid. Y**ield:** 82% (0.99 g). **R*f*:** 0.45 (20:80, DCM:hexanes on silica gel). **Mp**: 220 °C (decomp.). **^{1}HNMR (500 MHz, CD_2Cl_2) δ (ppm)**: 7.99 (d, *J* = 2.0 Hz, 1H), 7.88 (d, *J* = 8.8 Hz, 2H), 7.34 (d, *J* = 8.8, 2.0 Hz, 2H), 6.66 (d, *J* = 7.8 Hz, 4H), 6.61 (t, *J* = 7.8 Hz, 4H), 6.55 (t, *J* = 7.6 Hz, 4H), 5.95 (d, *J* = 8.0 Hz, 4H), 1.14 (s, 9H), 0.85 (s, 6H). **^{13}C NMR (126 MHz, CD_2Cl_2) δ (ppm)**: 145.6, 144.3, 135.5, 131.3, 128.4, 128.2, 123.6, 122.6, 121.4, 117.3, 115.5, 113.8, 26.7, 20.9, -1.1. **HR-MS [M+H]$^+$:** Calculated: 644.2728 ($C_{42}H_{38}N_3O_2SiH$); Found: 644.2723.

General procedure 2: deprotection of amine

The reaction is based on a previously reported synthesis.[286] The corresponding protected amine (1 equiv.) was dissolved in toluene (0.2 M). TBAF·$3H_2O$ (1.5 equiv.) was added and the resulting solution was stirred at room temperature for 2 h. To the reaction mixture was added saturated ammonium chloride (25 mL) and the reaction was extracted with EtOAc (3 × 50 mL), dried over Na_2SO_4, filtered and concentrated under reduced pressure to afford the crude product. The crude product was dry-loaded onto silica and then purified by silica gel column chromatography (30:70 DCM:hexanes). The corresponding fractions were combined and concentrated under reduced pressure to afford the desired product.

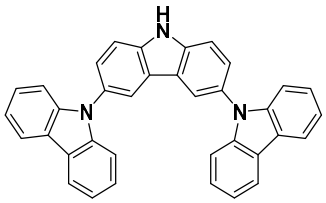

9'*H*-9,3':6',9''-tercarbazole (Cz-Cz)

The reaction was undertaken using general procedure 2 from **2**. White solid. Y**ield:** 94% (0.61 g). **R*f*:** 0.22 (30:70, DCM:hexanes on silica gel). **Mp**: 314 – 317 °C. **^{1}HNMR (500 MHz, DMSO-d$_6$) δ (ppm)**: 11.91 (s, 1H), 8.51 (d, *J* = 2.0 Hz, 2H), 8.24 (d, *J* = 7.7 Hz, 4H), 7.85 (d, *J* = 8.6 Hz, 2H), 7.61 (dd, *J* = 8.6, 2.0 Hz, 2H), 7.41 (td, *J* = 7.7, 7.1, 1.1 Hz, 4H), 7.34, (d, *J* = 8.2 Hz, 4H), 7.24 – 7.28 (m, 4H) . **^{13}C NMR (126 MHz, DMSO-d$_6$) δ (ppm)**: 141.2, 139.7, 128.1, 126.1, 125.4, 123.4, 122.4, 120.4, 120.0, 119.6, 112.6, 109.7. **HR-MS [M+H]$^+$:** Calculated: 498.1965 ($C_{36}H_{23}N_3H$); Found: 498.1959. The characterization matches that previously reported.[292]

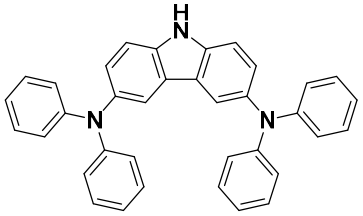

N3,N3,N6,N6-tetraphenyl-9*H*-carbazole-3,6-diamine (DPA-Cz)

The reaction was undertaken using general procedure 2 from **3**. Grey solid. Y**ield:** 89% (0.90 g). **R*f*:** 0.35 (30:70, DCM:hexanes on silica gel). **Mp**: 258 – 261 °C. **^{1}HNMR (500 MHz, DMSO-d$_6$) δ (ppm)**: 11.37 (s, 1H), 7.88 (d, *J* = 2.1 Hz, 2H), 7.50 (d, *J* = 8.6 Hz, 2H), 7.18 – 7.23 (m, 8H), 7.17 (dd, *J* = 8.6, 2.1 Hz, 2H), 6.94 (t, *J* = 7.7 Hz, 8H), 6.90 (t, *J* = 7.3 Hz, 4H). **^{13}C NMR (126 MHz, DMSO-d$_6$) δ (ppm)**: 148.6, 138.8, 138.4, 129.6, 126.5, 123.8, 122.2, 121.8, 119.9, 112.8 **HR-MS [M]$^+$:** Calculated: 502.2278 ($C_{36}H_{27}N_3$); Found: 502.2271.

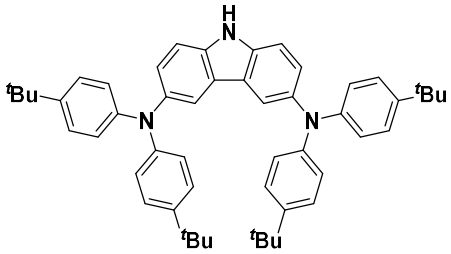

N3,N3,N6,N6-tetrakis(4-(tert-butyl)phenyl)-9*H*-carbazole-3,6-diamine (*t*BuDPA-Cz)

The reaction was undertaken using general procedure 2 with **4**. White solid. Y**ield:** 95% (0.90 g). **R*f*:** 0.46 (30:70, DCM:hexanes on silica gel). **Mp**: 316 – 319 °C. **^{1}HNMR (500 MHz, DMSO-d$_6$) δ (ppm)**: 11.29 (s, 1H), 7.82 (d, *J* = 1.7 Hz, 2H), 7.46 (d, *J* = 8.5 Hz, 2H), 7.21 (d, *J* = 8.5 Hz, 8H), 7.13 (dd, *J* = 8.4, 1.7 Hz, 2H), 6.84 (d, *J* = 8.5 Hz, 8H). ^{13}C NMR could not be reported due to solubility issues. **HR-MS [M]$^+$:** Calculated: 502.2271 ($C_{52}H_{59}N_3H$); Found: 502.2278.

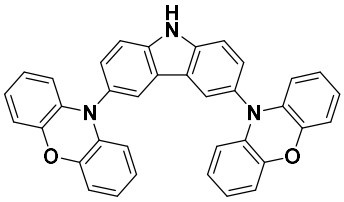

3,6-di(10*H*-phenoxazin-10-yl)-9*H*-carbazole (PXZ-Cz)

The reaction was undertaken using general procedure 2 with **5**. Off-white solid. Y**ield:** 93% (0.46 g). **R*f*:** 0.24 (30:70, DCM:hexanes on silica gel). **Mp**: 350 °C (decomp.). **^{1}HNMR (500 MHz, DMSO-d$_6$) δ (ppm)**: 11.86 (s, 1H), 8.27 (d, *J* = 1.9 Hz, 2H), 7.81 (d, *J* = 8.5 Hz, 2H), 7.39 (dd, *J* = 8.5, 1.9 Hz, 2H), 6.72 (dd, *J* = 7.6, 1.7 Hz, 4H), 6.58 – 6.66 (m, 8H), 5.87 (dd, *J* = 7.6, 1.7 Hz, 4H). **^{13}C NMR (126 MHz, DMSO-d$_6$) δ (ppm)**: 143.1, 139.8, 134.8, 129.4, 127.9, 124.3, 123.7, 122.9, 121.2, 115.1, 114.0, 113.4. **HR-MS [M+H]$^+$:** Calculated: 530.1863 ($C_{36}H_{23}N_3O_2H$); Found: 530.1857.

General procedure 3: nucleophilic aromatic substitution of amine to 4,5-difluorophthalonitrile

The corresponding amine (2 equiv.) was dried under vacuum for 30 min. The reaction flask was backfilled with N_2 and dry THF (0.33 M) was added under a positive flow of N_2. NaH (60% in paraffin oil, 4 equiv.) was added in portions under a positive flow of N_2. The resulting mixture was stirred for 15 min and then 4,5-difluorophthalonitrile (1 equiv.) was added under a positive flow of N_2

and the resulting mixture was stirred at room temperature for 6 hours. Water (20 mL) was added and the reaction mixture was extracted with DCM (5 × 50 mL), dried over $MgSO_4$, filtered and concentrated under reduced pressure to afford the crude product. The crude product was dry-loaded onto silica and then purified by silica gel column chromatography (50 – 100% DCM:hexanes). The corresponding fractions were combined and concentrated under reduced pressure to afford the desired product. The product was then suspended in ethanol and filtered, and subsequently washed with ethanol to afford the desired compound.

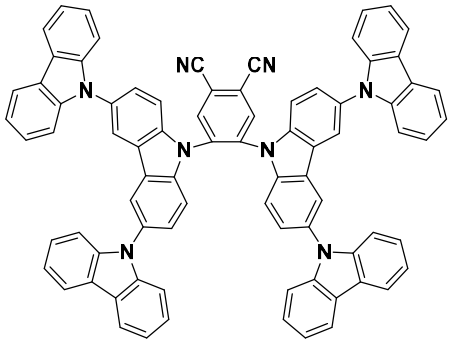

4,5-bis(9'*H*-[9,3':6',9''-tercarbazol]-9'-yl)phthalonitrile (Cz-2CzPN)

The reaction was undertaken using general procedure 3 with **Cz-Cz**. Yellow solid. Y**ield:** 85% (0.48 g). **R*f*:** 0.48 (70:30, DCM:Hexanes on silica gel). **Mp**: 383 – 385 °C. **^{1}HNMR (500 MHz, CD_2Cl_2) δ (ppm)**: 8.71 (s, 2H), 8.11 (d, *J* = 7.9 Hz, 6H), 8.05 (s, 4H), 7.41 (d, *J* = 8.6 Hz, 4H), 7.37 (d, *J* = 8.7 Hz, 4H), 7.17 (br-s, 16H). **^{13}C NMR (126 MHz, CD_2Cl_2) δ (ppm)**: 141.7, 138.3, 138.2, 136.3, 132.5, 126.6, 126.4, 125.4, 123.5, 120.6, 120.3, 119.8, 116.7, 114.9, 111.3, 109.6. **HR-MS $[M+NH_4]^+$:** Calculated: 1136.4184 ($C_{80}H_{46}N_8NH_4$); Found: 1136.4183.

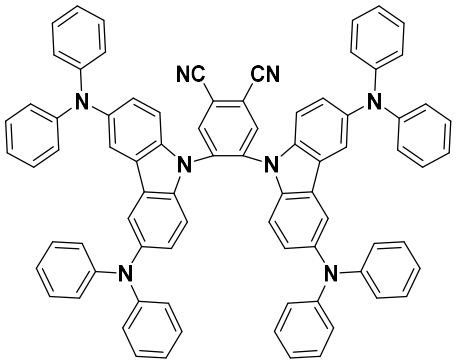

4,5-bis(3,6-bis(diphenylamino)-9*H*-carbazol-9-yl)phthalonitrile (DPA-2CzPN)

The reaction was undertaken using general procedure 3 with **DPA-Cz**, but, owing to poor solubility, purification by column chromatography was not possible, and the product was sonicated in MeOH and subsequently filtered. Orange solid. **Yield:** 73% (0.25 g). **Mp**: 376 – 379 °C. **^{1}H NMR (500 MHz, CD_2Cl_2) δ (ppm)**: 8.37 (s, 2H), 7.45 (d, *J* = 2.1 Hz, 4H), 7.09 (dd, *J* = 8.9, 7.6 Hz, 16H), 6.82 – 6.90 (m, 28H), 6.77 (dd, *J* = 8.7, 2.1 Hz, 4H). Carbon could not be obtained due to poor solubility. **HR-MS $[M+H]^+$:** Calculated: 1127.4550 ($C_{80}H_{54}N_8H$); Found: 1127.4537.

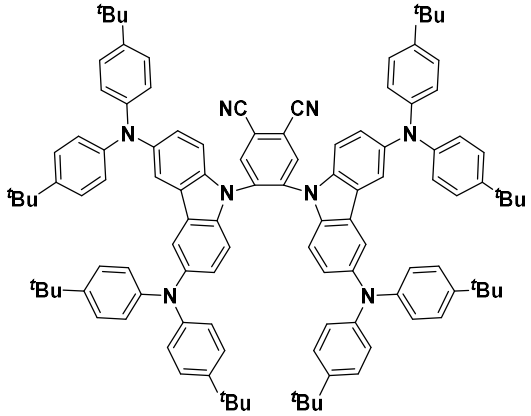

4,5-bis(3,6-bis(di(4-(*tert*-butyl)phenyl)amino)-9H-carbazol-9-yl)phthalonitrile (^{t}BuDPA-2CzPN)

The reaction was undertaken using general procedure 3 with **^{t}BuDPA-Cz**. Red solid. **Yield:** 65% (0.57 g). **R*f*:** 0.69 (70:30, DCM:hexanes on silica gel). **Mp**: 361 – 363 °C. **^{1}H NMR (500 MHz, CD_2Cl_2) δ (ppm)**: 8.38 (s, 2H), 7.48 (d, *J* = 1.8 Hz, 4H), 7.10 (d, *J* = 8.6 Hz, 16H), 6.90 (d, *J* = 8.7 Hz, 4H), 6.80 (dd, *J* = 8.8, 1.8 Hz, 4H), 6.76 (d, *J* = 8.6 Hz, 16H). **^{13}C NMR (126 MHz, CD_2Cl_2) δ (ppm)**:145.9, 144.7, 142.3, 137.9, 135.8, 134.7, 126.2, 125.5, 122.2, 118.8, 115.2, 115.1, 110.6, 34.4, 31.5. **Anal. Found. For $C_{112}H_{118}N_8$**: C, 85.14%; H, 7.50%; N, 6.82%. **Anal. Calcd. For $C_{112}H_{118}N_8$:**

C, 85.34%; H, 7.55%; N, 7.11%. **HR-MALDI [M]$^{+\cdot}$:** Calculated: 1574.9474 ($C_{112}H_{118}N_8$); Found: 1574.9457.

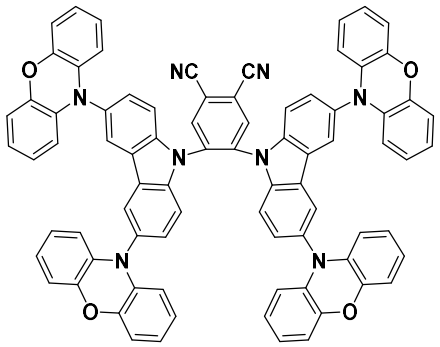

4,5-bis(3,6-di(10*H*-phenoxazin-10-yl)-9*H*-carbazol-9-yl)phthalonitrile (PXZ-2CzPN)

The reaction was undertaken using general procedure 3 with **PXZ-Cz**. Red solid. **Yield:** 83% (0.29 g). **R*f*:** 0.50 (70:30, DCM:hexanes on silica gel). **Mp**: > 400 °C. **^{1}H NMR (500 MHz, CD_2Cl_2) δ (ppm)**: 8.59 (s, 2H), 7.77 (d, *J* = 1.8 Hz, 4H), 7.36 (d, *J* = 8.6 Hz, 4H), 7.09 (dd, *J* = 8.6, 1.8 Hz, 4H), 6.62 (dd, *J* = 7.9, 1.4 Hz, 8H), 6.44 (td, *J* = 7.8, 1.3 Hz, 8H), 6.54 (td, *J* = 7.8, 1.4 Hz, 8H), 5.62 (dd, *J* = 7.9, 1.3 Hz, 8H). **^{13}C NMR (126 MHz, CD_2Cl_2) δ (ppm)**: 144.1, 138.4, 137.9, 136.1, 134.8, 133.8, 129.5, 125.9, 123.6, 123.5, 121.8, 117.0, 115.7, 114.7, 113.4, 112.8. **Anal. Found. For $C_{80}H_{46}N_8O_4$**: C, 81.02%; H, 3.89%; N, 9.47%. **Anal. Calcd. For $C_{80}H_{46}N_8O_4$:** C, 81.20%; H, 3.92%; N, 9.47%. **HR-MS [M+H]$^+$:** Calculated: 1183.3715 ($C_{80}H_{46}N_8O_4H$); Found: 1183.3720.

Chapter 4.

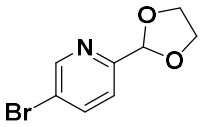

5-bromo-2-(1,3-dioxolan-2-yl)pyridine (6)

The synthesis is based on a modified literature procedure.[293] 5-Bromopyridine-2-carbaldehyde (4.00 g, 22 mmol, 1 equiv.), ethanediol (2.40 mL, 43 mmol, 2 equiv.), *para*-toluenesulfonic acid monohydrate (0.20 g, 1 mmol, 0.05 equiv.) were dissolved in toluene (100 mL) in a round bottomed flask equipped with a Dean-Stark trap. The reaction was heated to reflux for 36 h. The reaction was quenched with saturated sodium bicarbonate solution (100 mL) and extracted with Et_2O (3 × 50 mL),

dried over Na_2SO_4, filtered and concentrated under reduced pressure to afford **6** as a brown solid, which was used directly without further purification. **Yield:** 95% (4.80 g). **Mp**: 48 – 51 °C (Lit 50 – 52 °C).[294] **^{1}HNMR (500 MHz, $CDCl_3$) δ (ppm)**: 8.67 (d, *J* = 2.2 Hz, 1H), 7.86 (dd, *J* = 8.3, 2.2 Hz, 1H), 7.43 (d, *J* = 8.3 Hz, 1H), 5.81 (s, 1H), 4.11 (m, 4H). **^{13}C NMR (126 MHz, $CDCl_3$) δ (ppm)**:155.7, 150.6, 139.6, 122.2, 121.2, 103.1, 65.7. **HR-MS [M+H]$^+$** Calculated: 229.9811 ($C_8H_8BrNO_2$); Found: 229.9805. Spectroscopic data matched those previously reported.[294]

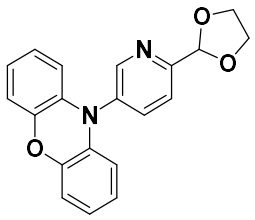

10-(6-(1,3-dioxolan-2-yl)pyridin-3-yl)-10H-phenoxazine (7)

Reaction was undertaken with phenoxazine and **6** based on General procedure 1. The crude product was purified by column chromatography on silica gel (40:60 EtOAc/Hexanes) to afford the desired product as a light brown solid. **Yield:** 83% (4.8 g). **R*f***: 0.51 (40:60, EtOAc:Hexanes on silica gel). **Mp**: 204 – 207 °C. **^{1}HNMR (500 MHz, DMSO-d_6) δ (ppm)**: 8.64 (d, *J* = 2.0 Hz, 1H), 8.04 (dd, *J* = 8.3, 2.4 Hz, 1H), 7.81 (d, *J* = 8.3 Hz, 1H), 6.78 (dd, *J* = 7.7, 1.6 Hz, 2H), 6.72 (td, *J* = 7.6, 1.6 Hz, 2H), 6.68 (td, *J* = 7.6, 1.6 Hz, 2H), 5.86 (d, *J* = 1.5 Hz, 1H), 5.85 (s, 2H), 4.13 – 4.19 (m 2H), 4.01 – 4.10 (m, 2H). **^{13}C NMR (126 MHz, DMSO-d_6) δ (ppm)**: 157.3, 151.3, 143.2, 140.0, 135.5, 133.5, 123.9, 123.0, 122.0, 115.6, 113.3, 102.9, 65.3. **HR-MS [M+H]$^+$** Calculated: ($C_{20}H_{16}N_2O_3H$) 333.1234; Found: 333.1235.

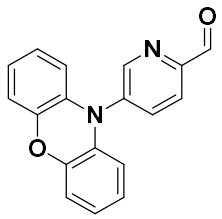

5-(10H-phenoxazin-10-yl)picolinaldehyde (PXZPyCHO)

To **7** (4.35 g, 13.1 mmol, 1 equiv.) in THF (130 mL) was added 10% HCl (43 mL). The resulting solution was heated to reflux for 3 hours, then cooled to 0 ºC using an ice bath. A saturated solution of

Na_2CO_3 was added dropwise to neutralise the solution. The reaction mixture was extracted with EtOAc (3 × 50 mL). The organic phase was dried over Na_2SO_4 and concentrated under reduced pressure. The solid was dispersed in hexane, sonicated and filtered to afford the desired product as a red solid. **Yield**: 98% (3.75 g). **Mp**: 128 – 132 °C. **^{1}HNMR (500 MHz, DMSO-d$_6$) δ (ppm)**: 10.07 (s, 1H), 8.92 (d, *J* = 1.9 Hz, 1H), 8.24 (dd, *J* = 8.2, 1.9 Hz, 1H), 8.18 (d, *J* = 8.2 Hz, 1H), 6.82 (dd, *J* = 7.8, 1.3 Hz, 2H), 6.77 (td, *J* = 7.8, 1.3 Hz, 2H), 6.71 (td, *J* = 7.8, 1.3 Hz, 2H), 5.99 (dd, *J* = 7.9, 1.1 Hz, 2H). **^{13}C NMR (126 MHz, DMSO-d$_6$) δ (ppm)**: 192.7, 152.3, 151.3, 143.4, 140.2, 139.3, 133.0, 123.9, 122.5, 155.8, 113.8. **HR-MS [M+H]$^+$** Calculated: ($C_{18}H_{12}N_2O_2H$) 289.0972; Found: 289.0973.

General Procedure 4: Condensation reaction of PXZPyCHO and relevant diamine

To **PXZPyCHO** (1 equiv.) were added the relevant diaminobenzene (1 equiv.), DMF and H_2O (9:1, 0.1 M). The mixture was heated to 80 °C for 18 hours, cooled to room temperature and concentrated under reduced pressure. Et_2O (20 mL) was added and subsequently removed under reduced pressure to assist the removal of the DMF. The resulting crude sample was purified by column chromatography (0 – 40% EtOAc:Hexanes) to afford the crude product as a powder, which was sonicated in pentane, hexane or Et_2O and filtered to afford the desired product.

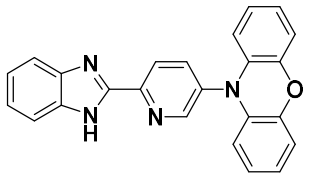

10-(6-(1H-benzo[d]imidazol-2-yl)pyridin-3-yl)-10H-phenoxazine (BImPyPXZ)

The product was synthesised according to General procedure 4, using **PXZPyCHO** and diaminobenzene. Yellow solid. **Yield**: 94% (2.46 g). **R*f***: 0.60 (40:60, EtOAc:Hexanes on silica gel). **Mp**: 262 – 264 °C. **^{1}HNMR (500 MHz, DMSO-d6) δ (ppm)**: 13.29 (s, 1H), 8.82 (d, J = 2.4 Hz, 1H), 8.58 (d, J = 8.9 Hz, 1H), 8.17 (dd, J = 8.4, 2.4 Hz, 1H), 7.75 (d, J = 7.7, 1H), 7.57 (d, J = 7.7 Hz, 1H), 7.22 – 7.31 (m, 2H), 6.81 (dd, J = 7.8, 1.7 Hz), 6.69 – 6.76 (m, 4H), 6.03 (dd, J = 1.7, 7.7 Hz, 2H). **^{13}C**

NMR (126 MHz, DMSO-d_6) δ (ppm): 151.8, 150.0, 148.3, 144.0, 143.3, 140.5, 135.8, 135.1, 133.5, 123.9, 123.5, 123.4, 122.1, 119.5, 115.6, 113.5, 112.2. **HR-MS [M+H]+ Calculated**: ($C_{24}H_{16}N_4OH$) 377.1397; Found: 377.1395. **Anal. Found. For $C_{24}H_{16}N_4O$**: C, 76.49%; H, 4.36%; N, 15.00%. **Anal. Calcd. For $C_{24}H_{16}N_4O$**: C, 76.58%; H, 4.28%; N, 14.88%. Only 17 of 18 ^{13}C NMR resonances are visible.

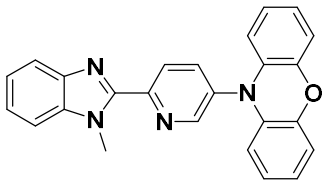

10-(6-(1-methyl-1H-benzo[d]imidazol-2-yl)pyridin-3-yl)-10H-phenoxazine (BIm(Me)PyPXZ

BImPyPXZ (0.40 g, 1.1 mmol, 1 equiv.) and NaO*t*Bu (0.13 g, 1.2 mmol, 1.1 equiv.) were dissolved in THF (8 mL). Methyliodide (0.08 mL, 1.3 mmol, 1.2 equiv.) was added dropwise and the resulting solution was stirred at room temperature for 3 hours. A saturated NaOH solution (3 mL) was added. The reaction mixture was extracted with EtOAc (3 × 20 mL), dried over Na_2SO_4 and concentrated under reduced pressure. The resulting crude solid was purified by column chromatography (20:80. EtOAc:Hexanes) to afford the crude product as an off yellow powder, which was sonicated in MeOH and subsequently filtered and washed with pentane to afford the desired product as a yellow solid. **Yield**: 96% (0.40 g). **R*f***: 0.48 (20:80, EtOAc:Hexanes on silica gel). **Mp**: 225 – 227 °C. **^{1}HNMR (500 MHz, DMSO-d_6) δ (ppm)**: 8.83 (d, *J* = 2.5 Hz, 1H), 8.59 (d, *J* = 8.0 Hz, 1H), 8.16 (dd, *J* = 8.4, 2.5 Hz, 1H), 7.77 (d, *J* = 7.9 Hz, 1H), 7.70 (d, *J* = 8.1 Hz, 1H), 7.37 (td, *J* = 7.6, 1.0 Hz, 1H), 7.31 (td, *J* = 7.7, 1.0 Hz, 1H), 6.81 (dd, *J* = 7.7, 2.7 Hz, 2 H), 6.69 – 6.77 (m, 4H), 6.03 (dd, *J* = 7.7, 1.7 Hz, 2H), 4.30 (s, 3H). **^{13}C NMR (126 MHz, DMSO-d_6) δ (ppm)**: 151.2, 149.9, 149.0, 143.3, 142.1, 140.1, 137.3, 135.4, 133.4, 126.6, 124.0, 123.5, 122.6, 122.2, 119.6, 115.7, 113.5, 111.0, 32.9. **HR-MS [M+H]$^+$** Calculated: ($C_{25}H_{18}N_4OH$) 391.1553; Found: 391.1552. **Anal. Found. For $C_{25}H_{18}N_4O$**: C, 76.79%; H, 4.72%; N, 14.38. **Anal. Calcd. For $C_{25}H_{18}N_4O$:** C, 76.91%; H, 4.65%; N, 14.39%.

General procedure 5: SnAr reaction of 1-fluoro-2-nitrobenzene and the relevant amine

This is a modified protocol based on a previously reported synthesis.[295] 1-Fluoro-2-Nitrobenzene (1 equiv.) and the primary amine (1.5 equiv.) were added to DMF (1.4 M). The resulting mixture was heated to 100 °C for 18 hours. Upon cooling, water (2.0 M) was added and the reaction mixture was extracted with EtOAc (3 × 50 mL). The organic phase was dried over Na_2SO_4 and concentrated under reduced pressure. The resulting crude product was purified by column chromatography (0 - 10% or 0 – 5% EtOAc/ Hexanes) to afford the desired compound.

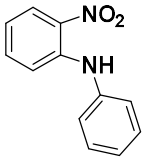

2-nitro-N-phenylaniline (8)

The product was synthesised according to General procedure 5, using aniline. Red solid. **Yield**: 49% (1.49 g). **R*f***: 0.59 (10:90, EtOAc:Hexanes on silica gel). **Mp**: 74 – 77 °C (Lit 73 – 75 °C).[296] **^{1}HNMR (500 MHz, $CDCl_3$) δ (ppm)**: 9.50 (s, 1H), 8.21 (dd, *J* = 8.6, 1.6 Hz, 1H), 7.42 (t, *J* = 8.2 Hz, 2H), 7.37 (ddd, *J* = 8.6, 7.0, 1.6 Hz, 1H), 7.28 (d, *J* = 7.5 Hz, 2H), 7.24 (t, *J* = 8.2 Hz, 2H), 6.77 (ddd, *J* = 8.3, 7.0, 1.2 Hz, 1H). **^{13}C NMR (126 MHz, $CDCl_3$) δ (ppm)**: 143.2, 138.8, 135.8, 133.3, 130.0, 126.8, 125.8, 124.5, 117.6, 116.2. **HR-MS [M+H]+** Calculated: ($C_{12}H_{10}N_2O_2H$) 215.0815; Found: 215.0817. Spectroscopic data matched those previously reported.[296]

***N*-(tert-butyl)-2-nitroaniline (9)**

The product was synthesised according to General procedure 5, using *tert*-butylamine. Orange oil. **Yield**: 54% (0.74 g). **R*f***: 0.21 (5:95, EtOAc:Hexanes on silica gel). **^{1}HNMR (500 MHz, $CDCl_3$) δ (ppm)**: 8.38 (s, 1H), 8.13 (dd, *J* = 8.8, 1.6 Hz, 1H), 7.34 (ddd, *J* = 8.6, 7.0, 1.6 Hz, 1H), 7.07 (dd, *J* = 8.8, 1.0 Hz, 1H), 6.55 (ddd, *J* = 8.3, 6.9, 1.0 Hz, 1H), 1.47 (s, 9H). **^{13}C NMR (126 MHz, $CDCl_3$) δ**

(ppm): 145.0, 135.4, 132.3, 127.3, 115.9, 114.7, 51.6, 29.7. **HR-MS [M+H]$^+$** Calculated: ($C_{10}H_{14}N_2O_2H$) 195.1128; Found: 195.1126. Spectroscopic data matched those previously reported.[297]

General Procedure 6: Reduction of nitro-aniline using Pd/C and $NaBH_4$

The synthesis was adapted from the literature.[296] The relevant nitroaniline (1 equiv.) was dissolved in dry THF (0.3 M). $NaBH_4$ (2.02 equiv.) and Pd/C (0.05 equiv.) were added. Methanol was added dropwise to achieve a concentration of 0.6 M and the reaction mixture was stirred for 30 minutes at room temperature. The reaction mixture was filtered through celite and the filtrate was added to saturated NH_4Cl (0.3 M). The filtrate was extracted with EtOAc (3 × 30 mL), dried over $MgSO_4$ and concentrated under reduced pressure. The resulting crude product was passed through a silica plug (30:70, EtOAc:Hexanes) to afford the desired compound.

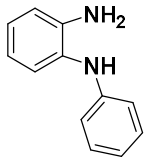

N1-phenylbenzene-1,2-diamine (10)

The product was synthesised according to General procedure 6, from **8**. Brown solid. **Yield**: 90% (1.04 g). **R*f***: 0.52 (30:70, EtOAc:Hexanes on silica gel). **Mp**: 75 – 77 °C (Lit 77 °C – 79 °C).[296] **^{1}HNMR (500 MHz, $CDCl_3$) δ (ppm)**: 7.21 (t, *J* = 7.4 Hz, 2H), 7.14 (dd, *J* = 7.8, 1.4 Hz, 1H), 7.02 (ddd, *J* = 7.8, 7.4, 1.4 Hz, 1H), 6.80 – 6.86 (m, 2H), 6.73 – 6.79 (m, 3H), 5.22 (s, 1H), 3.77 (s, 2H). **^{13}C NMR (126 MHz, $CDCl_3$) δ (ppm)**: 145.4, 141.4, 129.5, 128.9, 125.8, 124.9, 119.7, 119.5, 116.6, 115.5. **HR-MS [M+H]$^+$** Calculated: ($C_{12}H_{12}N_2H$) 185.1073; Found: 185.1072. Spectroscopic data matched those previously reported.[296]

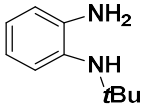

N1-(*tert*-butyl)benzene-1,2-diamine (11)

The product was synthesised according to General procedure 6, from **9**. Black oil. **Yield**: 88% (0.52 g). **^{1}HNMR (500 MHz, $CDCl_3$) δ (ppm)**: 6.92 (dd, *J* = 8.0, 1.5 Hz, 1H), 6.80 (ddd, *J* = 8.0, 7.0, 1.5 Hz, 1H), 6.71 – 6.75 (m, 2H), 3.61 (s, 2H), 2.53 (s, 1H), 1.30 (s, 9H). **^{13}C NMR (126 MHz, $CDCl_3$) δ (ppm):** 140.0, 134.1, 122.0, 121.8, 119.4, 116.7, 52.6, 30.0. **HR-MS [M+H]$^+$** Calculated: ($C_{10}H_{16}N_2H$) 165.1386; Found: 165.1383.

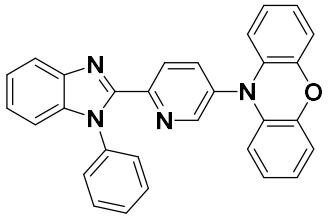

10-(6-(1-phenyl-1H-benzo[d]imidazol-2-yl)pyridin-3-yl)-10H-phenoxazine (BIm(Ph)PyPXZ)

The product was synthesised according to General procedure 4, using **PXZPyCHO** and **10**. It was sonicated in hexane and subsequently filtered to afford the desired product as a pale brown solid. **Yield**: 74% (0.81 g). **R*f***: 0.69 (40:60, EtOAc:Hexanes on silica gel). **Mp**: 157 – 160 °C. **^{1}HNMR (500 MHz, DMSO-d_6) δ (ppm):** 8.44 (d, *J* = 8.4 Hz, 1H), 8.35 (d, *J* = 2.3 Hz, 1H), 8.10 (dd, *J* = 8.4, 2.4 Hz, 1H), 7.87 (dd, *J* = 7.0, 1.3 Hz, 1H), 7.54 (t, *J* = 7.4 Hz, 2H), 7.48 (t, *J* = 7.4 Hz, 1H), 7.42 (d, *J* = 7.5 Hz, 2H), 7.32 – 7.39 (m, 2H), 7.24 (dd, *J* = 7.0, 1.3 Hz, 1H), 6.77 (dd, *J* = 7.6, 1.8 Hz, 2H), 6.72 (td, *J* = 7.6, 1.7 Hz, 2H), 6.69 (td, *J* = 7.4, 1.8 Hz, 2H), 5.87 (*J* = 7.7, 1.7 Hz, 2H). **^{13}C NMR (126 MHz, DMSO-d_6) δ (ppm):** 151.1, 149.7, 148.9, 143.4, 142.4, 140.0, 137.4, 137.3, 135.6, 133.5, 129.6, 128.5, 127.3, 127.1, 124.6, 124.1, 123.5, 122.4, 120.1, 115.8, 113.5, 111.2. **HR-MS [M+H]$^+$** Calculated: ($C_{30}H_{20}N_4OH$) 453.1710; Found: 453.1702. **Anal. Found. For $C_{30}H_{20}N_4O$**: C, 79.47%; H, 4.57%; N, 12.38%. **Anal. Calcd. For $C_{30}H_{20}N_4O$:** C, 79.63%; H, 4.46%; N, 12.38%.

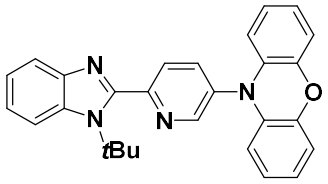

10-(6-(1-(tert-butyl)-1H-benzo[d]imidazol-2-yl)pyridin-3-yl)-10H-phenoxazine (BIm(*t*Bu)PyPXZ)

The product was synthesised according to General procedure 4, using **PXZPyCHO** and **11.** It was sonicated in Et_2O and filtered to afford the desired product as a white solid. **Yield**: 65% (0.29 g). **R*f***: 0.41 (30:70, EtOAc:Hexanes on silica gel). **Mp**: 183 – 186 °C. **^{1}HNMR (500 MHz, DMSO-d_6) δ (ppm):** 8.77 (d, *J* = 2.4 Hz, 1H), 8.17 (dd, *J* = 8.2, 2.5 Hz, 1H), 8.04 (d, *J* = 8.6 Hz, 1H), 7.96 (d, *J* = 7.7 Hz, 1H), 7.69 (dd, *J* = 7.8, 1.0, 1H), 7.25 – 7.34 (m, 2H), 6.80 – 6.84 (m, 2H), 6.71 – 6.78 (m, 4H), 5.92 – 5.96 (m, 2H), 1.64 (s, 9H). **^{13}C NMR (126 MHz, DMSO-d_6) δ (ppm):** 154.1, 151.2, 150.8, 143.3, 142.8, 139.7, 135.1, 134.6, 133.4, 127.7, 123.9, 122.5, 122.2, 121.8, 119.8, 115.7, 115.2, 113.1, 58.9, 30.5. **HR-MS [M+H]$^+$** Calculated: ($C_{28}H_{24}N_4OH$) 433.2023; Found: 433.2021. **Anal. Found. For $C_{28}H_{24}N4O$**: C, 77.63%; H, 5.54%; N, 12.78%. **Anal. Calcd. For $C_{28}H_{24}N_4O$:** C, 77.75%; H, 5.59%; N, 12.95%.

Chapter 6.

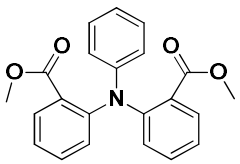

N,N-bis(2-methoxycarbonylphenyl)aniline (12)

A 2-neck flask held under nitrogen was charged with aniline (2.25 mL, 24.65 mmol, 1 equiv.), methyl 2-iodobenzoate (10.87 mL, 74 mmol, 3 equiv.), copper (0.47 g, 7.4 mmol, 0.3 equiv.), copper(I) iodide (0.32 g, 1.73 mmol. 0.07 equiv.), anhydrous potassium carbonate (10.22 g, 74 mmol, 3 equiv.), and 25 mL anhydrous di-*n*-butyl ether. The resulting reaction mixture was heated to reflux and stirred for 3 days. After cooling to room temperature, the reaction mixture was filtered through a pad of celite. The filtrate was then mixed with dichloromethane and washed with water (3 × 50 mL). The organic

layer was then dried using anhydrous sodium sulfate and concentrated under reduced pressure. The resulting dark brown oil was purified by column chromatography on silica gel (EtOAc:hexane, 20:80). The corresponding fractions were collected and evaporated under reduced pressure to afford the desired product as a white crystalline solid, which was then filtered and washed with hexane. **Yield:** 32% (2.9 g). **R_f:** 0.54 (EtOAc:hexane, 20:80 on silica gel). **Mp**:143 - 145 °C**. ^{1}HNMR (400 MHz, $CDCl_3$) δ (ppm)**: 7.65 (dd, *J* = 7.7, 1.6 Hz, 2H), 7.43-7.39 (m, 2 H), 7.20-7.11 (m, 6 H), 6.88-6.84 (m, 1 H), 6.77-6.75 (m, 2 H), 3.39 (s, 6 H). **^{13}C NMR (100 MHz, CDCl3) δ (ppm)**: 168.0, 148.6, 146.6, 132.8, 131.1, 129.1, 128.8, 128.0, 124.1, 121.8, 120.8, 51.9. **HR-MS $[M+H]^+$** Calculated: ($C_{22}H_{19}NO_4$) 362.1387; Found: 362.1387.

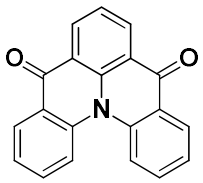

Quinolino[3,2,1-de]acridine-5,9-dione (DiKTa)

Compound **12** (2.5 g, 6.9 mmol, 1 equiv.) was combined with sodium hydroxide (1.4 g, 35 mmol, 5 equiv.) in 30 mL of an ethanol/water (1:1) mixture. The reaction was heated to reflux for 4 h. After cooling to room temperature, the pH was adjusted to 2-3 by adding dilute hydrochloric acid. The diacid precipitated as a light green solid and was collected by vacuum filtration, washed thoroughly with water, dried under vacuum (2.22 g, 95% yield) and used without further purification and characterization. The diacid (2 g, 6 mmol, 1 equiv.) was dispersed in 30 mL dichloromethane under a nitrogen atmosphere. To the reaction mixture were added sequentially oxalyl chloride (1.01 mL, 12 mmol, 2 equiv.) and 4 drops of DMF. After 3 h under reflux, the reaction mixture was cooled to room temperature. Under a positive flow of nitrogen, aluminum chloride (8 g, 60 mmol, 10 equiv.) was added slowly with stirring (exothermic reaction). After refluxing for 4 h, the reaction mixture was cooled to room temperature, and the reaction quenched by slow dropwise of water under vigorous stirring (exothermic reaction). The resulting mixture was combined with more dichloromethane (50 mL), the organic layer separated and washed with water (3 × 50 mL), and then dried with anhydrous sodium sulfate. The solvent was evaporated under reduced pressure, and the solid sonicated in methanol. The

obtained solid was then filtered and washed with hexane. The crude product was further purified by column chromatography on silica gel (50:50, EtOAc:hexanes) to afford the desired product as a yellow crystalline solid. **Yield** from diacid**:** 86%, overall: 82% (1.54 g). $\mathbf{R_f}$: 0.56 (50:50 EtOAc:hexanes on silica gel). **Mp**: 257 - 260 °C. **^{1}HNMR (500 MHz, $CDCl_3$) δ (ppm)**: 8.73 (d, *J* = 7.6 Hz, 2H), 8.48 (dd, *J* = 7.9, 1.6 Hz, 2H), 8.13 (d, *J* = 8.5 Hz, 2H), 7.69 (ddd, *J* = 8.7, 7.1, 1.7 Hz, 2 H), 7.64 (t, *J* = 7.6 Hz, 1 H) and 7.50-7.47 (m, 2 H). **^{13}C NMR (125 MHz, $CDCl_3$) δ (ppm)**: 178.9, 140.1, 139.6, 133.3, 133.1, 128.2, 126.8, 125.5, 123.9, 123.7, 120.6. **Anal. Found. For $C_{20}H_{11}NO_2$**: C, 80.45%; H, 3.58%; N, 4.78%. **Anal. Calcd. For $C_{20}H_{11}NO_2$:** C, 80.80%; H, 3.73%; N, 4.71%. **HRMS $[M+H]^+$** Calculated: ($C_{20}H_{11}NO_2$) 298.0863; Found: 298.0865. 100 % pure on HPLC analysis, retention time 15.1 minutes with 40% MeCN.

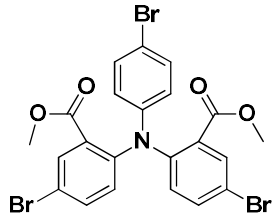

Dimethyl 6,6'-((4-bromophenyl)azanediyl)bis(3-bromobenzoate) (13)

To **12** (4 g, 11.10 mmol, 1 equiv.) in 100 mL dichloromethane, bromine (1.7 mL, 33.3 mmol, 3 equiv.) was added dropwise. After 1 h stirring at room temperature, further bromine (0.1 mL) was added dropwise, and stirring continued for 0.5 h. The reaction was quenched by the addition of a 10% solution of sodium hydroxide (50 mL). The organic layer was separated, washed with water (3 × 50 mL), dried with anhydrous sodium sulfate and concentrated under reduced pressure. The crude product was purified by flash chromatography on silica gel (10:90 EtOAc : hexanes) to afford the desired product as a light yellow solid. **Yield:** 84% (5.6 g). $\mathbf{R_f}$: 0.45 (10:90 EtOAc : hexanes on silica gel). **Mp**: 134 - 136 °C. **^{1}HNMR (500 MHz, $CDCl_3$) δ (ppm)**: 7.81 (d, *J* = 2.4 Hz, 2H), 7.53 (dd, *J* = 8.6, 2.4 Hz, 2H), 7.26-7.22 (m, 2H), 7.05 (dd, *J* = 8.6, 2.4 Hz, 2H), 6.61-6.58 (m, 2H), 3.46 (s, 6 H). **^{13}C NMR (125 MHz, CDCl3) δ (ppm)**: 166.0, 147.1, 144.7, 136.1, 134.1, 132.2, 130.6, 129.4, 122.1, 117.8, 114.8, 52.4. **HRMS $[M+H]^+$** Calculated: ($C_{22}H_{16}Br_3NO_4$); 595.8702 Found: 595.8700.

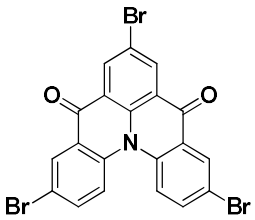

3,7,11-tribromoquinolino[3,2,1-de]acridine-5,9-dione (Br_3DiKTa)

Compound **13** (5 g, 8.4 mmol, 1 equiv.) was combined with sodium hydroxide (1.68 g, 42 mmol, 5 equiv.) in 40 mL of an ethanol/water (1:1) mixture. The reaction was heated to reflux for 12 h. After cooling to room temperature, the pH was adjusted to 2-3 by addition of dilute hydrochloric acid. The diacid precipitated as a light green solid and was collected by vacuum filtration, washed thoroughly with water, dried under vacuum (4.75, 99% yield) and used without further purification and characterization. The diacid (4 g, 7.1 mmol, 1 equiv.) was dispersed in 60 mL dichloromethane under a nitrogen atmosphere. To the reaction mixture were added sequentially thionyl chloride (1.03 mL, 14.2 mmol, 2 equiv.) and 7 drops of DMF. After 3 h under reflux, the reaction mixture was cooled to room temperature. Under a positive flow of nitrogen, aluminum chloride (9.46 g, 71 mmol, 10 equiv.) was added slowly (exothermic reaction). After refluxing for 12 h, the reaction mixture was cooled to room temperature and the reaction quenched by dropwise addition of water with vigorous stirring (exothermic reaction). The resulting mixture was combined with dichloromethane (150 mL), the organic layer was then separated. The remaining aqueous layer was washed with dichloromethane (3 × 50 mL) to completely remove the yellow insoluble product from water. The organic fractions were combined and the solvent volume was concentrated under reduced pressure. The product was filtered, and washed with methanol and hexane to afford the desired product as a yellow solid. **Yield:** 53% (2.0 g). **Mp**: Decomposed at 364 °C. **^{1}HNMR (500 MHz, $CDCl_3$) δ (ppm)**: 8.81 (s, 2H), 8.59 (d, J = 2.2 Hz, 2H), 7.95 (d, J = 8.9 Hz, 2H), 7.81 (dd, J = 8.9, 2.5 Hz, 2H). **^{13}C NMR** was not recorded due to poor solubility of this compound. **HRMS $[M]^+$** Calculated: 530.8100 ($C_{20}H_8Br_3NO_2$); Found: 530.8088.

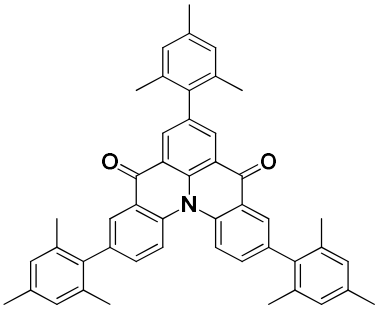

3,7,11-trimesitylquinolino[3,2,1-de]acridine-5,9-dione (Mes_3DiKTa)

To **Br_3DiKTa** (0.6 g, 1.2 mmol, 1 equiv.) under a nitrogen atmosphere were added mesitylene-2-boronic acid (1.18 g, 7.2 mmol, 6 equiv.), benzene (30 mL) and sodium hydroxide solution (2 M, 10 mL). The mixture was bubbled with nitrogen for 15-20 minutes. Under a positive flow of nitrogen, $Pd(PPh_3)_4$ (0.2 g, 0.18 mmol, 0.15 equiv.) was added and the solution was then refluxed for 12 h. The reaction was cooled to room temperature and diluted with ethyl acetate (150 mL). The organic layer was washed with water (3 × 50 mL) and then dried with anhydrous sodium sulfate. The solvents were removed under reduced pressure. The crude product was purified by chromatography on silica gel (10 : 90 EtOAc : hexanes). The corresponding fractions were combined and concentrated under reduced pressure to afford a green oil, which was then sonicated in methanol and filtered to afford the desired product as a bright yellow solid. **Yield:** 75% (0.59 g). **R_f**: 0.48 (10:90, EtOAc:hexanes on silica gel). **Mp**: 249 **°C. ^{1}H NMR (500 MHz, $CDCl_3$) δ (ppm)**: 8.60 (s, 2H), 8.35-8.33 (m, 4H), 7.56 (dd, *J* = 8.7, 2.1 Hz, 2H), 7.00 (d, *J* = 7.3, Hz, 6H), 2.37-2.36 (m, 9 H), 2.09-2.04 (m, 18 H). **^{13}C NMR (125 MHz, $CDCl_3$) δ (ppm)**: 178.8, 138.6, 138.5, 138.3, 137.6, 137.5, 137.04, 137.02, 136.5, 136.1, 136.0, 134.3, 134.1, 128.54, 128.51, 126.6, 123.9, 120.6, 21.23, 21.12, 21.07. **Anal. Found. For $C_{47}H_{41}NO_2$**: C, 86.69%; H, 6.46%; N, 2.19. **Anal. Calcd. For $C_{47}H_{41}NO_2$:** C, 86.60%; H, 6.34%; N, 2.15%. **HR-MS [M]$^+$** Calculated: 652.3215 ($C_{47}H_{41}NO_2$); Found: 652.3224. 98.0 % pure on HPLC analysis, retention time 6.9 minutes in 100% MeCN.

Chapter 8.

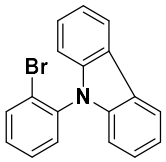

9-(2-bromophenyl)-9H-carbazole (14)

Carbazole (6.69 g, 40.0 mmol, 1.4 equiv.) and oven dried cesium carbonate (13.0 g, 40.0 mmol, 1.4 equiv.) were dried under vacuum for 30 minutes. Dry DMF (80 mL) was added, and the resulting mixture was stirred under N_2 for 30 minutes. 1-bromo-2-fluorobenzene (3.12 mL, 28.6 mmol, 1 equiv.) was added and the resulting mixture was heated to 150 °C for 48 hrs. The reaction was cooled, and water (200 mL) was added. The product was extracted with DCM (3 × 100 mL), dried over Na_2SO_4, filtered and concentrated under reduced pressure to afford the crude product as a off white solid. The crude product was purified by column chromatography on silica gel (5% - 10% DCM:Hexanes). The corresponding fractions were combined and concentrated under reduced pressure to afford a white solid. **Yield:** 96% (8.8 g). **R*f***: 0.37 (10:90, DCM:Hexanes on silica gel). **Mp**: 92 – 95 °C (Lit Mp: 95 – 96 °C).[298] **^{1}HNMR (500 MHz, CDCl3) δ (ppm)**: 8.16 (d, *J* = 7.8 Hz, 2H), 7.87 (dd, *J* = 8.1, 1.3 Hz, 1H), 7.53 (dd, *J* = 7.4, 1.3 Hz, 1H), 7.49 (dd, *J* = 7.8, 1.8 Hz, 1H), 7.38 – 7.45 (m, 3H), 7.28 – 7.32 (m, 2H), 7.07 (d, *J* = 8.2 Hz, 2H). **^{13}C NMR (126 MHz, $CDCl_3$) δ (ppm)**: 141.0, 136.9, 134.4, 131.3, 130.3, 129.0, 126.1, 124.0, 123.4, 120.5, 120.1, 110.2. The characterization matches that previously reported.[299]

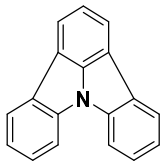

Indolo[3,2,1-jk]-carbazole (ICz)

14 (4.00 g, 12.4 mmol, 1 equiv.), K_2CO_3 (8.58 g, 62.1 mmol, 5 equiv.) and tetrabutylammonium bromide (4.00 g, 12.4 mmol, 1 equiv.) were dissolved in *N,N*-Dimethylacetamide (100 mL), the reaction mixture was degassed by bubbling N_2 through for 15 min. $Pd(OAc)_2$ (0.42 g, 1.9 mmol, 0.15 equiv.) and PPh_3 (1.14 g, 4.3 mmol, 0.35 equiv.) were added and the resulting mixture was heated to 160 °C

for 48 hours. The reaction mixture was cooled, and water (200 mL) was added, and the product was extracted with DCM (3 × 100 mL), dried over Na_2SO_4, filtered and concentrated under reduced pressure to afford the crude product as a grey solid. The product was purified by column chromatography on silica gel (1:9 DCM:Hexanes). The corresponding fractions were combined and concentrated under reduced pressure to afford a white solid, which was washed with cold pentane to produce white needle crystals. **Yield:** 85% (2.55 g). **R*f***: 0.26 (10:90, DCM:Hexanes on silica gel). **Mp**: 129 - 133 °C (lit Mp: 126 – 128 °C).[299] **^{1}HNMR (500 MHz, $CDCl_3$) δ (ppm)**: 8.16 (d, *J* = 8.0 Hz, 2H), 8.06 (d, *J* = 7.5 Hz, 2H), 7.93 (d, *J* = 8.0 Hz, 2H), 7.60 (t, *J* = 7.5 Hz, 1H), 7.57 (td, *J* = 0.9, 7.7 Hz, 2H), 7.37 (td, *J* = 0.9, 7.7 Hz, 2H). **^{13}C NMR (126 MHz, $CDCl_3$) δ (ppm)**: 143.9, 138.9, 130.2, 126.9, 123.3, 123.0, 121.9, 119.6, 118.6, 112.3. 97.6% pure on HPLC analysis, retention time 2.5 minutes in 99% MeOH 1% THF mix. The characterization matches that previously reported.[299]

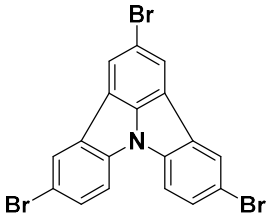

2,5,11-tribromoindolo[3,2,1-jk]carbazole ($ICzBr_3$)

ICz (1.50 g, 6.2 mmol, 1 equiv.) was added to dry DMF (30 mL). *N*-Bromosuccinimide (3.65 g, 20.5 mmol, 3.3 equiv.) was added in portions and the resulting mixture was stirred at room temperature in darkness for 24 hours. Saturated sodium thiosulfate (50 mL) was added, and the resulting reaction mixture was extracted with DCM (5 × 100 mL) and concentrated under reduced pressure. The reaction mixture was sonicated in EtOAc (100 mL), filtered and dried to afford the compound as a white solid. **Yield:** 79% (2.35 g). **Mp**: 297 - 301 °C. **^{1}HNMR (500 MHz, DMSO-d_6) δ (ppm)**: 8.57 (d, *J* = 2.0 Hz, 2H), 8.49 (s, 2H), 8.29 (d, *J* = 8.6 Hz, 2H), 7.81 (dd, *J* = 8.6, 2.0 Hz, 2H). **^{13}C NMR (126 MHz, DMSO-d_6) δ (ppm)**: 141.9, 137.1, 130.5, 130.2, 126.8, 124.1, 118.5, 115.7, 114.9. The characterization matches that previously reported.[300]

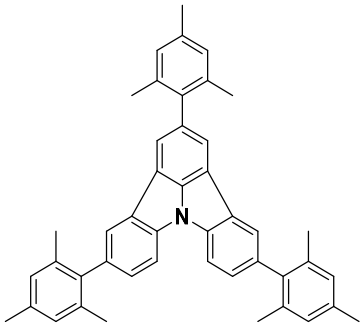

2,5,11-trimesitylindolo[3,2,1-jk]carbazole ($ICzMes_3$)

Cesium carbonate (2.39 g, 7.32 mmol, 7 equiv.), **$ICzBr_3$** (0.50 g, 1.05 mmol, 1 equiv.) and mesitylboronic acid (1.03 g, 6.28 mmol, 6 equiv.) were added to a mixture of toluene (3.75 mL), water (2.50 mL) and ethanol (2.50 mL). The resulting solution was degassed with N_2 bubbling for 30 min. $Pd(PPh_3)_4$ (0.04 g, 0.04 mmol, 0.03 equiv.) was added and the resulting solution was heated to 100 °C for 24 h. The reaction mixture was cooled, and the product was extracted with EtOAc (3 × 50 mL), dried over Na_2SO_4, filtered and concentrated under reduced pressure to afford crude product as a black solid. The product was purified by column chromatography on silica gel (5% DCM:Hexanes). The corresponding fractions were combined and concentrated under reduced pressure to afford a white solid. **Yield:** 69% (0.43 g). **R*f***: 0.23 (5:95, DCM:Hexanes on silica gel). **Mp**: 252 - 255 °C. **^{1}HNMR (500 MHz, $CDCl_3$) δ (ppm)**: 8.01 (d, *J* = 8.2 Hz, 2H), 7.88 (d, *J* = 1.3 Hz, 2H), 7.77 (s, 2H), 7.36 (dd, *J* = 8.2, 1.5 Hz, 2H), 7.01 (s, 6H), 2.37 (s, 9H), 2.10 (s, 12H), 2.06 (s, 6H). **^{13}C NMR (126 MHz, $CDCl_3$) δ (ppm)**: 139.1, 137.8, 136.8, 136.7, 136.5, 134.7, 130.3, 128.1(3), 128.0(7), 128.0(6), 124.0, 120.6, 118.6, 112.1, 21.2, 21.1, 21.0. **HR-MS $[M+H]^+$** Calculated: ($C_{45}H_{41}NH$) 596.3312; Found: 596.3302. 99.7% pure on HPLC analysis, retention time 10.1 minutes in 99% MeOH 1% THF mix.

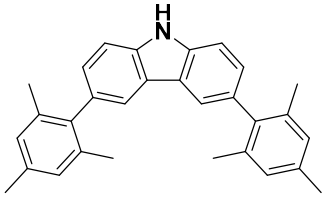

3,6-dimesityl-9H-carbazole (Mes_2Cz)

The reaction is based on a previously reported synthesis.[279] Caesium carbonate (35.1 g, 108 mmol, 7 equiv.), 3,6-dibromo-9H-carbazole (5.00 g, 15.4 mmol, 1 equiv.) and mesitylboronic acid (10.1

g, 61.5 mmol, 4 equiv.) were added to a mixture of toluene (56.3 mL), water (37.5 mL) and ethanol (37.5 mL). The resulting solution was degassed with N_2 bubbling for 30 min. $Pd(PPh_3)_4$, (0.53 g, 0.46 mmol, 0.03 equiv.) was added and the resulting solution was heated to 100 °C for 24 hours. The reaction was cooled and extracted with EtOAc (3 × 100 mL), dried over Na_2SO_4, filtered and concentrated under reduced pressure to give an orange oil. The product was purified by column chromatography on silica gel (30% DCM:Hexanes). The corresponding fractions were combined and concentrated under reduced pressure to afford a white solid. The product was recrystalised by slow evaporation from tetrahydrofuran to afford a white crystalline solid. **Yield:** 62% (3.86 g). **R*f***: 0.35 (30:70, DCM:Hexanes on silica gel). **Mp**: 147 - 151 °C. **^{1}HNMR (500 MHz, CDCl3) δ (ppm)**: 8.14 (s, 1H), 7.78 (d, *J* = 1.3 Hz, 2H), 7.50 (d, *J* = 8.2 Hz, 2H), 7.19 (dd, *J* = 8.22, 1.4 Hz, 2H), 6.98 (s, 4H), 2.36 (s, 6H), 2.06 (s, 12H). **^{13}C NMR (126 MHz, $CDCl_3$) δ (ppm)**: 139.8, 138.7, 136.8, 136.5, 132.4, 128.2, 127.5, 123.6, 120.9, 110.7, 21.2(0), 21.1(7). Spectra in agreement with previously reported.[279]

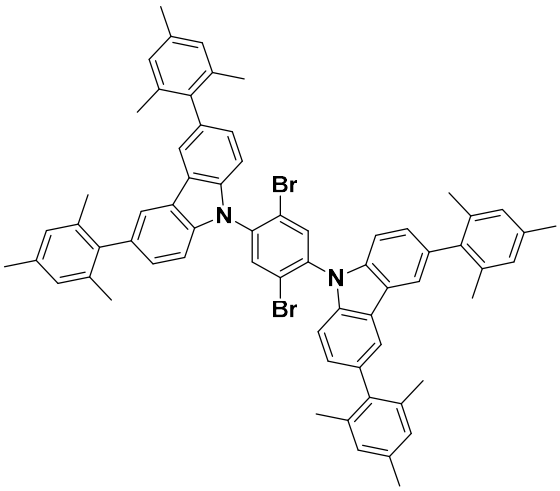

9,9'-(2,5-dibromo-1,4-phenylene)bis(3,6-dimesityl-9H-carbazole) (15)

NaH (60% dispersed in mineral oil, 0.04 g, 1.6 mmol, 2.5 equiv.) was added to dry DMF (12 mL). It was stirred under N_2 and cooled to 0 °C, **Mes_2Cz** (0.65 g, 1.6 mmol, 2.5 equiv.) was added in portions and stirred for 30 min. 1,4-dibromo, 2,5-difluorobenzene (0.18 g, 0.64 mmol, 1 equiv.) was added and the resulting mixture was stirred and heated to 50 °C for 48 h under a N_2 atmosphere. The reaction mixture was cooled and water (30 mL) was added. The product was extracted with DCM (3 × 50 mL), dried over Na_2SO_4, filtered and concentrated under reduced pressure to afford the product as

an off-white solid. The product was purified by column chromatography on silica gel (10% - 20% DCM:Hexanes). The corresponding fractions were combined and concentrated under reduced pressure to afford a white solid. The product was recrystalized in a toluene methanol mix (1:1) to afford a white powder. **Yield:** 75% (0.50 g). **R*f***: 0.32 (15:85, DCM:Hexanes on silica gel). **Mp**: 279 - 283 °C. **^{1}HNMR (500 MHz, $CDCl_3$) δ (ppm)**: 8.15 (s, 2H), 7.88 (d, *J* = 1.1 Hz, 4H), 7.34 (d, *J* = 8.3 Hz, 4 H), 7.28 (d, *J* = 1.1 Hz, 4H), 7.01 (s, 8H), 2.37 (s, 12H), 2.11 (s, 12H), 2.10 (s, 12H). **^{13}C NMR (126 MHz, $CDCl_3$) δ (ppm)**: 139.8, 139.5, 138.6, 136.9, 136.8, 136.1, 133.7, 128.3, 128.0, 123.9, 123.2, 121.2, 110.3, 21.3, 21.2. **HR-MS $[M+H]^+$** Calculated: ($C_{66}H_{58}N_2Br_2H$) 1039.3029; Found: 1039.2990.

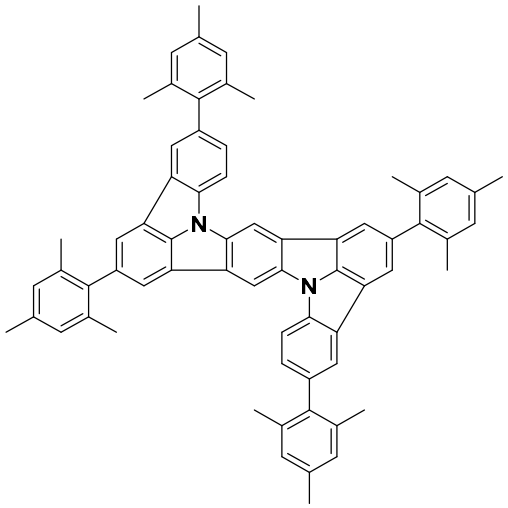

DiICzMes$_4$

15 (0.40 g, 0.4 mmol, 1 equiv.), tetra-*butyl*-ammonium bromide (0.25 g, 0.8 mmol, 2 equiv.), K_2CO_3 (0.53 g, 3.8 mmol, 10 equiv.) were dissolved in *N,N*-Dimethylacetamide (4 mL), the reaction was degassed by bubbling N_2 through the solution for 15 min. $Pd(OAc)_2$ (0.04 g, 0.02 mmol, 0.5 equiv.) and PPh_3 (0.10 g, 0.4 mmol, 1 equiv.) were added and the mixture was heated to 160 °C for 48 h. The reaction was cooled, water (20 mL) was added and the product was extracted with DCM (4 × 50 mL). The organic phase was dried over Na_2SO_4, filtered, and concentrated under reduced pressure to afford the crude product as a black solid. The product was purified by column chromatography on silica gel (5% - 10% DCM:Hexanes). The corresponding fractions were combined and concentrated under reduced pressure to afford a yellow solid. The product was subsequently sonicated in methanol and filtered producing a yellow solid, 0.27 g (80%), which was recrystalized in a toluene methanol mixture

(1:1) and filtered to afford pale yellow crystals. **Yield:** 59% (0.20 g). **R*f***: 0.27 (10:90, DCM:Hexanes on silica gel). **Decomposed**: 392 °C. **^{1}HNMR (500 MHz, $CDCl_3$) δ (ppm)**: 8.67 (s, 2H), 8.15 (d, *J* = 8.2 Hz, 2H), 8.00 (s, 2H), 7.92 (d, *J* = 1.3 Hz, 2H), 7.83 (s, 2H), 7.42 (dd, *J* = 8.2, 1.3 Hz, 2H), 7.06 (s, 4H), 7.02 (s, 4H), 2.42 (s, 6H), 2.38 (s, 6H), 2.12 (s, 24H). **^{13}C NMR (126 MHz, $CDCl_3$) δ (ppm)**: 144.3, 140.4, 139.2, 138.0, 137.0, 136.9, 136.8, 136.7, 136.3, 135.3, 134.7, 130.2, 129.6, 128.3(2), 128.2(8), 128.2(6), 124.1, 120.9, 120.5, 119.0, 118.8, 112.2, 106.8, 21.4, 21.3, 21.2, 21.1. **HR-MS $[M]^+$** Calculated: ($C_{66}H_{56}N_2$) 876.4443; Found: 876.4418. 99.2% pure on HPLC analysis, retention time 9.1 minutes in 85% MeOH 15% THF mix.

10.2 X-ray crystallography

Crystals of **DPA-2CzPN** and **PXZ-2CzPN(B)** were obtained from slow evaporation of toluene. Crystals for **Cz-2CzPN** and **PXZ-2CzPN(A)** were obtained by dissolving the compound in a saturated solution of toluene and layering hexane on top. Crystals for **BIm(Me)PyPXZ** were obtained by dissolving in a saturated solution of chloroform with ethanol layered on top. Crystals for **BIm(Ph)PyPXZ** and **BImPyPXZ** were obtained by slow diffusion of hexane into a saturated toluene solution. Crystals for **BIm(*t*Bu)PyPXZ** were obtained by layering of hexane on top of a saturated dichloromethane solution. Crystals for **PXZPyCHO** were obtained by slow evaporation of a saturated toluene solution at room Crystals for **DiKTa** were obtained following sublimation and subsequent cooling. Crystals for **Mes_3DiKTa** were obtained following slow evaporation of a saturated methanol solution at room temperature over several days. Crystals for **$ICzMes_3$** and **$DiICzMes_4$** were obtained from a saturated solution of PhMe with MeOH layered on top. X-ray diffraction data were collected at 173 or 93 K using a Rigaku MM-007HF High Brilliance RA generator/confocal optics with XtaLAB P100 diffractometer [Cu Kα radiation (λ = 1.54187 Å)] or [Mo Kα radiation (λ = 0.71073 Å)]. Intensity data were collected using both ω and φ steps accumulating area detector images spanning at least a hemisphere of reciprocal space. Data for all compounds analysed were collected and processed (including correction for Lorentz, polarization and absorption) using either CrysAlisPro[301] or CrystalClear.[302] Structures were solved by direct (SIR2011)[303] or dual-space (SHELXT-2018/2)[304] methods and refined by full-matrix least-squares against F^2 (SHELXL-2018/3)[305]. Non-hydrogen atoms

were refined anisotropically, and hydrogen atoms were refined using a riding model. All the toluene solvent molecules in the structures of **Cz-2CzPN**, **PXZ-2CzPN(A)** and **PXZ-2CzPN(B)** were disordered and an initial model was placed and restraints applied using FragmentDB.[306, 307] The structures of **DPA-2CzPN** and **PXZ-2CzPN(A)** showed void space containing electron density for which no chemically satisfactory model could be obtained (1232 and 115 Å3/unit cell, respectively) and the SQUEEZE[308] routine implemented in PLATON[309] was used to remove the contribution to the diffraction pattern of the unordered electron density in the void spaces. . The data from **BImPyPXZ** was found to be a three-component non-merohedric twin, with twin laws of [-0.003 0 -0.997 0 -1 0 -1.003 0 0.003] and [1 0 0.467 0 -1 0 0 0 -1], and refined twin fractions of 0.19 and 0.23, respectively. Further, it could not be distinguished from the data which of the imidazole nitrogens of **BImPyPXZ** was protonated. This was chosen arbitrarily for one, with subsequent independent molecules chosen for systematic hydrogen bonding. All calculations except SQUEEZE were performed using the Olex2 interface.[310] All calculations were performed using the CrystalStructure[175] interface. Selected crystallographic data are presented in the supporting information. CCDC 1935488-1935489, CCDC 2090614-2090617 contains the supplementary crystallographic data for this paper. The data can be obtained free of charge from The Cambridge Crystallographic Data Centre via www.ccdc.cam.ac.uk/structures

10.3 Thermal analysis.

For Chapter 4, TGA was conducted on a Mettler TGA/DSC3 with a heating rate of 10 K/min under nitrogen flow. The samples were heated from 25 °C to 700 °C and the T_d was determined at a 5% weight loss. Differential scanning calorimetry was performed with a Mettler DSC3+ in pierced Al pans at 10 K/min under nitrogen flow. For each sample were carried out 4 cycles. 1st cycle : Heating at 10 K/mins, cooling at 100 K/min; 2nd cycle : Heating at 10 K/min, cooling at 100 K/min; 3rd cycle : Heating at 20 K/min, cooling at 100 K/min; 4th cycle : Heating at 40 K/min, cooling at 10 K/min. The T_g was determined as the midpoint temperature of the step and the T_m was determined as the maximum value of the peak. These calculations were performed by Mettler STARe 15.00a software. For Chapter 6, TGA were measured by the University of St Andrews functional materials characterization service.

10.4 Electrochemistry measurements.

CV and DPV analysis was performed on an Electrochemical Analyzer potentiostat model 620D from CH Instruments. Samples were prepared in MeCN or DCM or DMF solutions, which were degassed by sparging MeCN or DCM or DMF with saturated nitrogen gas for 5 minutes prior to measurements. All measurements were performed using 0.1 M tetra-*n*-butylammonium hexafluorophosphate, [nBu$_4$N]PF$_6$, in MeCN or DCM or DMF. An Ag/Ag$^+$ electrode was used as the reference electrode; a glassy carbon electrode was used as the working electrode; and a platinum electrode was used as the counter electrode. The redox potentials are reported relative to a SCE with a Fc/Fc$^+$ redox couple as the internal standard (0.38 V vs SCE for MeCN,[227] (0.46 V vs SCE for DCM, 0.45 V vs SCE for DMF).[216] The HOMO and LUMO energies were determined using the relation $E_{HOMO/LUMO} = -(E_{ox} / E_{red} + 4.8)$ eV, where E_{ox} and E_{red} are calculated from DPV relative to Fc/Fc$^+$.[220]

10.5 Photophysical measurements.

Optically dilute solutions of concentrations on the order of 10^{-5} or 10^{-6} M were prepared in HPLC grade solvent for absorption and emission analysis. Absorption spectra were recorded at room temperature on a Shimadzu UV-2600 double beam spectrophotometer. Steady-state photoluminescence spectra in solution were recorded at 298 K using Shimadzu RF-6000 Spectro fluorophotometer, Jasco FP-8600 spectrofluorometer and Edinburgh Instruments FLS980 fluorimeter. Relevant excitation is reported alongside data. Photoluminescence quantum yields for solutions in Chapter 4 were determined using the optically dilute method in which four sample solutions with absorbance of ca. 0.100, 0.080, 0.060 and 0.040 at 360 nm were used.[311] Their emission intensities were compared with those of a reference, quinine sulfate, whose Φ_r in 1 M H_2SO_4 was determined to be 54.6% using the absolute method.[239] The quantum yield of the sample, Φ_{PL}, can be determined by the equation $\Phi_{PL} = \Phi_r(A_r/A_s)((I_s/I_r)(n_s/n_r)^2$, where A stands for the absorbance at the excitation wavelength (λ_{exc} = 360 nm), I is the integrated area under the corrected emission curve and n is the refractive index of the solvent with the subscripts "s" and "r" representing sample and reference respectively. A Hamamatsu photonics C9920-02 integrating sphere was employed for quantum yield measurements for thin film samples in

Chapters 3 and 5.[312] A Jasco FP-8600 spectrofluorometer with an integrating sphere was employed for quantum yield measurements for thin film samples in Chapter 8.[312] Evaporated films were prepared to give comparative Φ_{PL} data to devices for Chapters 4 and 6. Doped thin films were prepared by mixing the sample (1, 3, 3.5, 5, 7, 10, 15, 20 or 100 wt%) and mCP in PhMe or $CHCl_3$ followed by spin-casting on a quartz substrate or drop casting in Chapter 8. The Φ_{PL} of the films were then measured in air and by purging the integrating sphere with N_2 gas flow. Time-resolved PL measurements of the thin films were carried out using an iCCD camera with gating times being 10 times shorter compared to the delay times. The samples were excited at 355 nm by a Q-switched Nd:YAG laser (Innolas SpitLight 600). Emission from the samples was focused onto a spectrograph (Oriel MS257) and detected on a gated iCCD camera (iStar A-DH334T-18F-03). The measurements were recorded under vacuum unless otherwise stated. Phosphorescence spectra were obtained using a Jasco FP-8600 spectrofluorometer at 77 K, with a delay time of 2 ms for toluene and mCP with a 10 ms integration time. Fluorescence at 77 K was measured from the SS spectra, or inferred by the subtraction of the phosphorescence spectrum from the steady-state PL spectrum at 77 K.

10.6 Quantum chemical calculations

The calculations were performed with the Gaussian 09[313] revision D.018 and Gaussian 16[314] suite for the density functional theory (DFT) and with the Turbomole/7.4 package[182] for SCS-CC2 calculations, all are in the gas phase. Ground state optimized structures were obtained using B3LYP,[188] PBE0,[189] LC-ωPBE,[192] CAM-B3LYP,[193] M062X,[190] omega tuned[175] LC-ωPBE (LC-ω*PBE) and LC-ω*HPBE[315] (LC-ω*HPBE) functionals each employing the 6-31G(d,p)[316] basis set. Excited state calculations were performed for each functionals at the TD-DFT[317] level as well as TDA-DFT.[318] The attachment/detachment formalism was employed to calculate ϕ_s values for each of the excited states using the NANCY package,[206, 207] with a value of 0.00 – 0.32 representing a pure CT, 0.33 – 0.66 is a mixed state coined CT-LE and 0.67 – 1.00 representing a locally excited state LE state. Molecular orbitals were visualized using GaussView 6.0 software.[319] Bond lengths and torsions were measured using Gaussview 6.0 package. Torsion angle studies were based on previous work with the torsion of interest remained at the fixed angle and optimized based on a similar reported method, with torsions

measured at 5° intervals in Chapter 4.[178] Excited state calculations were then applied using the above-mentioned approach for each angle in the series. A state specific solvation model was applied using cHex and MeCN using Gaussian 16.[314] M06-2X functional was applied employing the 6-31G(d,p) basis set with dispersion effects included for Chapter 5. Ground state optimisation was undertaken for each followed by vertical excitation using TDA. Each specific singlet excited state (S_1-S_4) was probed individually to account for the changing charge distributions of the solvent in relation to each. SCS-CC2 was also used, with optimized ground state using SCS-CC2[320, 321] method considering the cc-pVDZ[200] basis set. Vertical excited states were performed on the ground state optimized structure using SCS-CC2 method. Different density plots and attachment detachments densities were visualized using the VESTA package.[322]

10.7 OLED fabrication and testing

For Chapters 4 and 6, OLED devices were fabricated using pre-cleaned ITO coated glass substrates with ITO thickness of 90 nm. The OLED devices had a pixel size of 2 mm × 1 mm. The small molecules and cathode layers were thermally evaporated using an angstrom deposition chamber at 10^{-7} mbar at 0.3 A/s or 0.6 A/s for organic layers and 3 A/s for cathode. OLED testing was performed using a Keithey 2400 sourcemeter and photodiode, assuming that the OLEDs show Lambertian emission. Eletroluminescence spectra were collected using an Oriel MS125 spectrograph coupled to an Andor DV420-BU CCD camera. For Chapter 8 OLEDs were fabricated on patterned ITO coated glass (VisionTek Systems) with a sheet resistance of 15 Ω/cm^2 using vacuum thermal evaporation. The substrates were sonicated for 15 minutes each in acetone and then IPA. After oxygen-plasma cleaning, the substrates were loaded into a Kurt J. Lesker Super Spectros 200 deposition chamber. All organic and cathode layers were thermally evaporated at a pressure below 10^{-7} mbar, at evaporation rates in the range of 0.1-0.5 A/s and forming pixels of 2×2, 2×4, and 4×4mm. The materials used for the device fabrication were either purchased from the companies pre-sublimed or sublimation purified before use (Creaphys DSU05). Characterization of OLED devices was conducted in a 10-inch integrating sphere (Labsphere) coupled with a calibrated fibre spectrometer (Ocean Optics USB4000) and connected to a Keithley 2400 source measure unit.

References

1. C. W. Tang and S. A. VanSlyke, *Appl. Phys. Lett.,* 1987, **51**, 913.

2. H. Sasabe and J. Kido, *Eur. J. Org. Chem.,* 2013, **2013**, 7653.

3. A. Tsuboyama, K. Kuge, M. Furugori, S. Okada, M. Hoshino and K. Ueno, *Inorg. Chem.,* 2007, **46**, 1992.

4. J. C. Deaton, S. C. Switalski, D. Y. Kondakov, R. H. Young, T. D. Pawlik, D. J. Giesen, S. B. Harkins, A. J. M. Miller, S. F. Mickenberg and J. C. Peters, *J. Am. Chem. Soc.,* 2010, **132**, 9499.

5. A. Endo, M. Ogasawara, A. Takahashi, D. Yokoyama, Y. Kato and C. Adachi, *Adv. Mater.,* 2009, **21**, 4802.

6. A. Endo, K. Sato, K. Yoshimura, T. Kai, A. Kawada, H. Miyazaki and C. Adachi, *Appl. Phys. Lett.,* 2011, **98**, 083302

7. H. Uoyama, K. Goushi, K. Shizu, H. Nomura and C. Adachi, *Nature,* 2012, **492**, 234.

8. T. Hatakeyama, K. Shiren, K. Nakajima, S. Nomura, S. Nakatsuka, K. Kinoshita, J. Ni, Y. Ono and T. Ikuta, *Adv. Mater.,* 2016, **28**, 2777.

9. S. Madayanad Suresh, D. Hall, D. Beljonne, Y. Olivier and E. Zysman-Colman, *Adv. Funct. Mater.,* 2020, **30**, 1908677.

10. P. Atkins and J. d. Paula, *Atkin's Physical Chemistry 9th Edition*. Oxford University Press: 2010.

11. A. Köhler and H. Bässler, *Mater. Sci. Eng., R,* 2009, **66**, 71.

12. W. Sheng, M. Sun and A. Zhou, *Phys. Rev. B,* 2013, **88**.

13. H. Kollmar and V. Staemmler, *Theor. Chem. Acc.,* 1978, **48**, 223.

14. Z. R. Grabowski, K. Rotkiewicz and W. Rettig, *Chemistry Reviews,* 2003, **103**.

15. C. E. Wayne and R. P. Wayne, *Photochemistry*. Oxford University Press: New York, 1996.

16. J. R. Lakowicz, *Principles of Fluorescence Spectroscopy*. Springer US: 2007.

17. A. S. Coolidge, H. M. James and R. D. Present, *J. Chem. Phys.,* 1936, **4**, 193.

18. R. Bonneau, I. Carmichael and G. L. Hug, *Pure Appl. Chem.,* 1991, **63**, 289

19. B. Valeur, *Molecular Fluorescence: Principles and Applications*. Wiley: 2001.

20. A. Steffen and B. Hupp, Design of Efficient Emissive Materials. In *Comprehensive Coordination Chemistry III*, 2021; pp 466-502.

21. M. Kasha, *Discuss. Faraday Soc.,* 1950, **9**, 14.

22. W. McCall, T. M. Christy, D. A. Pipp, B. Jaster, J. White, J. Goodrich, J. Fontana and S. Doxtader, *Environ. Earth Sci.,* 2018, **77**, 373.

23. S. Nigam and S. Rutan, *Appl. Spectrosc.,* 2001, **55**, 362.

24. M. K. Etherington, J. Gibson, H. F. Higginbotham, T. J. Penfold and A. P. Monkman, *Nat. Commun.,* 2016, **7**, 13680.

25. J. Gibson, A. P. Monkman and T. J. Penfold, *ChemPhysChem,* 2016, **17**, 2956.

26. M. A. El-Sayed, *Acc. Chem. Res.,* 1968, **1**, 8.

27. T. J. Penfold, E. Gindensperger, C. Daniel and C. M. Marian, *Chem. Rev.,* 2018, **118**, 6975.

28. D. R. Lee, S. H. Han and J. Y. Lee, *J. Mater. Chem. C.,* 2019, **7**, 11500.

29. R. Huang, J. S. Ward, N. A. Kukhta, J. Avó, J. Gibson, T. Penfold, J. C. Lima, A. S. Batsanov, M. N. Berberan-Santos, M. R. Bryce and F. B. Dias, *J. Mater. Chem. C.,* 2018, **6**, 9238.

30. J. S. Ward, R. S. Nobuyasu, A. S. Batsanov, P. Data, A. P. Monkman, F. B. Dias and M. R. Bryce, *Chem. Commun.,* 2016, **52**, 2612.

31. C. A. Parker and C. G. Hatchard, *Trans. Faraday Soc.,* 1963, **59**, 284.

32. C. A. Parker, *Proc. R. Soc. London, Ser. A,* 1963, **276**, 125.

33. C.-J. Chiang, A. Kimyonok, M. K. Etherington, G. C. Griffiths, V. Jankus, F. Turksoy and A. P. Monkman, *Adv. Funct. Mater.,* 2013, **23**, 739.

34. F. B. Dias, *Philos. Trans. R. Soc. London, Ser. A,* 2015, **373**, 20140447.

35. D. Y. Kondakov, *Philos. Trans. R. Soc. London, Ser. A,* 2015, **373**, 20140321.

36. C. A. Parker and C. G. Hatchard, *Trans. Faraday Soc.,* 1961, **57**, 1894.

37. G. N. Lewis, D. Lipkin and T. T. Magel, *J. Am. Chem. Soc.,* 1941, **63**, 3005

38. F. Perrin, *Ann. Phys.,* 1929, **10**, 169.

39. F. B. Dias, T. J. Penfold and A. P. Monkman, *Methods Appl. Fluoresc.,* 2017, **5**, 012001.

40. C. Baleizao and M. N. Berberan-Santos, *J. Chem. Phys.,* 2007, **126**, 204510.

41. F. A.Salazar, A. Fedorov and M. N.Berberan-Santos, *Chem. Phys. Lett.,* 1997, **271**, 361.

42. M. N. Berberan-Santos and J. M. M. Garcia, *J. Am. Chem. Soc.,* 1996, **118**, 9391.

43. J. W. Arbogast, A. P. Darmanyan, C. S. Foote, Yves Rubin, F. N. Diederich, M. M. Alvarez, S. J. Anz and R. L. Whette, *J. Phys. Chem.,* 1991, **95**, 11.

44. M. W. Wolf, K. D. Legg, R. E. Brown, L. A. Singer and J. H. Parks, *J. Am. Chem. Soc.,* 1975, **97**, 4490.

45. A. Maciejewski, M. Szymanski and R. P. Steer, *J. Phys. Chem.,* 1986, **90**, 6314.

46. C. B. Murphy, Y. Zhang, T. Troxler, V. Ferry, J. J. Martin and J. Wayne E. Jones, *J. Phys. Chem. B,* 2004, **108**, 1537.

47. T. H. Forster, *Discuss. Faraday Soc.,* 1959, **27**, 7.

48. M. A. Bryden and E. Zysman-Colman, *Chem. Soc. Rev.,* 2021, **50**, 7587.

49. D. L. Dexter, *J. Chem. Phys.,* 1953, **21**, 836.

50. R. A. Marcus, *J. Chem. Phys.,* 1956, **24**, 966.

51. E. J. Piechota and G. J. Meyer, *J. Chem. Educ.,* 2019, **96**, 2450.

52. G. Hughes and M. R. Bryce, *J. Mater. Chem.,* 2005, **15**, 94.

53. Y.-J. Pu, G. Nakata, F. Satoh, H. Sasabe, D. Yokoyama and J. Kido, *Adv. Mater.,* 2012, **24**, 1765.

54. G. Lakhwani, A. Rao and R. H. Friend, *Annu. Rev. Phys. Chem.,* 2014, **65**, 557.

55. J. J. M. van der Holst, F. W. A. van Oost, R. Coehoorn and P. A. Bobbert, *Phys. Rev. B,* 2009, **80**, 235202.

56. M. Pope, H. P. Kallmann and P. Magnante, *J. Chem. Phys.,* 1963, **38**, 2042.

57. P. S. Vincett, W. A. Barlow, R. A. Hann and G. G. Roberts, *Thin Solid Films,* 1982, **94**, 171.

58. J. C. Scott, S. Karg and S. A. Carter, *J. Appl. Phys.,* 1997, **82**, 1454.

59. G. Hong, X. Gan, C. Leonhardt, Z. Zhang, J. Seibert, J. M. Busch and S. Brase, *Adv. Mater.,* 2021, **33**, 2005630.

60. A. P. Kulkarni, C. J. Tonzola, A. Babel and S. A. Jenekhe, *Chem. Mater.,* 2004, **16**, 4556.

61. S. R. Forrest, D. D. C. Bradley and M. E. Thompson, *Adv. Mater.,* 2003, **15**, 1043.

62. R. H. Friend, R. W. Gymer, A. B. Holmes, J. H. Burroughes, R. N. Marks, C. Taliani, D. D. C. Bradley, D. A. D. Santos, J. L. Brédas, M. Lögdlund and W. R. Salaneck, *Nature,* 1999, **397**, 121.

63. D. F. O'Brien, M. A. Baldo, M. E. Thompson and S. R. Forrest, *Appl. Phys. Lett.,* 1999, **74**, 442.

64. I. D. W. Samuel, G. Rumbles, C. J. Collison, R. H. Friend, S. C. Moratti and A. B. Holmes, *Synth. Met.,* 1997, **84**, 497.

65. W. Brütting, J. Frischeisen, T. D. Schmidt, B. J. Scholz and C. Mayr, *Phys. Status Solidi A,* 2013, **210**, 44.

66. T. D. Schmidt, T. Lampe, D. Sylvinson M. R, P. I. Djurovich, M. E. Thompson and W. Brütting, *Phys. Rev. Appl.,* 2017, **8**, 037001.

67. C. G. Malte and R. Sebastian, *J. Photonics Energy,* 2015, **5**, 1.

68. B. Geffroy, P. le Roy and C. Prat, *Polym. Int.,* 2006, **55**, 572.

69. C. Murawski, K. Leo and M. C. Gather, *Adv. Mater.,* 2013, **25**, 6801.

70. Z.-J. Yu, W.-Y. Lou, H. Junge, A. Päpcke, H. Chen, L.-M. Xia, B. Xu, M.-M. Wang, X.-J. Wang, Q.-A. Wu, B.-Y. Lou, S. Lochbrunner, M. Beller and S.-P. Luo, *Catal. Commun.,* 2019, **119**, 11.

71. H. Fukagawa, T. Shimizu, Y. Iwasaki and T. Yamamoto, *Sci. Rep.,* 2017, **7**, 1735.

72. L.-S. Cui, A. J. Gillett, S.-F. Zhang, H. Ye, Y. Liu, X.-K. Chen, Z.-S. Lin, E. W. Evans, W. K. Myers, T. K. Ronson, H. Nakanotani, S. Reineke, J.-L. Bredas, C. Adachi and R. H. Friend, *Nat. Photonics,* 2020, **14**, 636.

73. X. Zheng, F. Cao, C. Wang, T. Tsuboi, Y. Zhu, Q. Ai, C. Deng, D. Wang, L. Su, Z. Liu and Q. Zhang, *J. Mater. Chem. C.,* 2020, **8**, 10021.

74. J. Eng and T. J. Penfold, *Chem. Rec.,* 2020, **20**, 831.

75. M. Fröbel, F. Fries, T. Schwab, S. Lenk, K. Leo, M. C. Gather and S. Reineke, *Sci. Rep.,* 2018, **8**, 9684.

76. M. Pedzisz, *SMPTE Motion Imaging J.,* 2014, **123**, 18.

77. S. Reineke, M. Thomschke, B. Lüssem and K. Leo, *Rev. Mod. Phys.,* 2013, **85**, 1245.

78. M. Y. Wong and E. Zysman-Colman, *Adv. Mater.,* 2017, **29**, 1605444.

79. D. Zhang, M. Cai, Z. Bin, Y. Zhang, D. Zhang and L. Duan, *Chem. Sci.,* 2016, **7**, 3355.

80. J. H. Burroughes, D. D. C. Bradley, A. R. Brown, R. N. Marks, K. Mackay, R. H. Friend, P. L. Burns and A. B. Holmes, *Nature,* 1990, **347**, 539.

81. J. Xin, Z. Li, Y. Liu, D. Liu, F. Zhu, Y. Wang and D. Yan, *J. Mater. Chem. C.,* 2020, **8**, 10185.

82. M. A. Baldo, D. F. O'Brien, Y. You, A. Shoustikov, S. Sibley, M. E. Thompson and S. R. Forrest, *Nature,* 1998, **395**, 151.

83. S. K. Lower and M. A. El-Sayed, *Chem. Rev.,* 1966, **66**, 199.

84. C. Adachi, M. A. Baldo, M. E. Thompson and S. R. Forrest, *J. Appl. Phys.,* 2001, **90**, 5048.

85. W. Song, L. Shi, L. Gao, P. Hu, H. Mu, Z. Xia, J. Huang and J. Su, *ACS Appl. Mater. Interfaces,* 2018, **10**, 5714.

86. C. W. Lee and J. Y. Lee, *Adv. Mater.,* 2013, **25**, 5450.

87. S.-Y. Kim, W.-I. Jeong, C. Mayr, Y.-S. Park, K.-H. Kim, J.-H. Lee, C.-K. Moon, W. Brütting and J.-J. Kim, *Adv. Funct. Mater.,* 2013, **23**, 3896.

88. P. Rajamalli, N. Senthilkumar, P. Gandeepan, P.-Y. Huang, M.-J. Huang, C.-Z. Ren-Wu, C.-Y. Yang, M.-J. Chiu, L.-K. Chu, H.-W. Lin and C.-H. Cheng, *J. Am. Chem. Soc.,* 2016, **138**, 628.

89. M. Zhu and C. Yang, *Chem. Soc. Rev.,* 2013, **42**, 4963.

90. M. Godumala, S. Choi, M. J. Cho and D. H. Choi, *J. Mater. Chem. C.,* 2016, **4**, 11355.

91. G. Zhan, Z. Liu, Z. Bian and C. Huang, *Front. Chem.,* 2019, **7**, 305.

92. H. F. Higginbotham, M. Okazaki, P. de Silva, S. Minakata, Y. Takeda and P. Data, *ACS Appl. Mater. Interfaces,* 2021, **13**, 2899.

93. C. A. Parker and E. J. Bowen, *Proc. R. Soc. London, Ser. A,* 1963, **276**, 125.

94. M. A. Baldo, C. Adachi and S. R. Forrest, *Phys. Rev. B,* 2000, **62**, 10967.

95. C. Wang, X. Li, Y. Pan, S. Zhang, L. Yao, Q. Bai, W. Li, P. Lu, B. Yang, S. Su and Y. Ma, *ACS Appl. Mater. Interfaces,* 2016, **8**, 3041.

96. W. Li, Y. Pan, L. Yao, H. Liu, S. Zhang, C. Wang, F. Shen, P. Lu, B. Yang and Y. Ma, *Adv. Opt. Mater.,* 2014, **2**, 892.

97. N. Sharma, M. Y. Wong, D. Hall, E. Spuling, F. Tenopala-Carmona, A. Privitera, G. Copley, D. B. Cordes, A. M. Z. Slawin, C. Murawski, M. C. Gather, D. Beljonne, Y. Olivier, I. D. W. Samuel and E. Zysman-Colman, *J. Mater. Chem. C.,* 2020, **8**, 3773.

98. L. Yao, S. Zhang, R. Wang, W. Li, F. Shen, B. Yang and Y. Ma, *Angew. Chem. Int. Ed.,* 2014, **53**, 2119.

99. Y. Pan, W. Li, S. Zhang, L. Yao, C. Gu, H. Xu, B. Yang and Y. Ma, *Adv. Opt. Mater.,* 2014, **2**, 510.

100. W. Li, Y. Pan, R. Xiao, Q. Peng, S. Zhang, D. Ma, F. Li, F. Shen, Y. Wang, B. Yang and Y. Ma, *Adv. Funct. Mater.,* 2014, **24**, 1609.

101. J. Liu, Z. Li, T. Hu, X. Wei, R. Wang, X. Hu, Y. Liu, Y. Yi, Y. Yamada-Takamura, Y. Wang and P. Wang, *Adv. Opt. Mater.,* 2019, **7**, 1801190.

102. D. H. Ahn, S. W. Kim, H. Lee, I. J. Ko, D. Karthik, J. Y. Lee and J. H. Kwon, *Nat. Photonics,* 2019, **13**, 540.

103. Y. Chen, D. Zhang, Y. Zhang, X. Zeng, T. Huang, Z. Liu, G. Li and L. Duan, *Adv. Mater.,* 2021, **33**, 2103293.

104. M. Inoue, T. SereviĿius, H. Nakanotani, K. Yoshida, T. Matsushima, S. JurškĿnas and C. Adachi, *Chem. Phys. Lett.,* 2016, **644**, 62.

105. N. Notsuka, H. Nakanotani, H. Noda, K. Goushi and C. Adachi, *J. Phys. Chem. Lett.,* 2020, **11**, 562.

106. P. Pander, P. Data and F. B. Dias, *J. Vis. Exp.,* 2018, e56614.

107. A. Niwa, T. Kobayashi, T. Nagase, K. Goushi, C. Adachi and H. Naito, *Appl. Phys. Lett.,* 2014, **104**, 213303.

108. R. Ishimatsu, Y. Kirino, C. Adachi, K. Nakano and T. Imato, *Chem. Lett.,* 2016, **45**, 1183.

109. Y. Tsuchiya, S. Diesing, F. Bencheikh, Y. Wada, P. L. Dos Santos, H. Kaji, E. Zysman-Colman, I. D. W. Samuel and C. Adachi, *J. Phys. Chem. A.,* 2021, **125**, 8074.

110. Y. Tao, K. Yuan, T. Chen, P. Xu, H. Li, R. Chen, C. Zheng, L. Zhang and W. Huang, *Adv. Mater.,* 2014, **26**, 7931.

111. K. Masui, H. Nakanotani and C. Adachi, *Org. Electron.,* 2013, **14**, 2721.

112. Z. Yang, Z. Mao, Z. Xie, Y. Zhang, S. Liu, J. Zhao, J. Xu, Z. Chi and M. P. Aldred, *Chem. Soc. Rev.,* 2017, **46**, 915.

113. T. Hosokai, H. Matsuzaki, H. Nakanotani, K. Tokumaru, T. Tsutsui, A. Furube, K. Nasu, H. Nomura, M. Yahiro and C. Adachi, *Sci. Adv.,* 2017, **3**, 1603282.

114. E. Zysman-Colman, *Nat. Photonics,* 2020, **14**, 593.

115. H. Noda, H. Nakanotani and C. Adachi, *Sci. Adv.,* 2018, **4**, 6910.

116. C. Adachi, H. Matsuzaki, Y. Nakayama, T. Nawata, H. Nakanotani, H. Noda and T. Hosokai, *J. Photonics Energy,* 2018, **8**, 032102.

117. M. Hempe, N. A. Kukhta, A. Danos, M. A. Fox, A. S. Batsanov, A. P. Monkman and M. R. Bryce, *Chem. Mater.,* 2021, **33**, 3066.

118. T.-L. Wu, S.-H. Lo, Y.-C. Chang, M.-J. Huang and C.-H. Cheng, *ACS Appl. Mater. Interfaces,* 2019, **11**, 10768.

119. Y. Liu, C. Li, Z. Ren, S. Yan and M. R. Bryce, *Nat. Rev. Mater.,* 2018, **3**, 18020.

120. M. Y. Wong, S. Krotkus, G. Copley, W. Li, C. Murawski, D. Hall, G. J. Hedley, M. Jaricot, D. B. Cordes, A. M. Z. Slawin, Y. Olivier, D. Beljonne, L. Muccioli, M. Moral, J. C. Sancho-Garcia, M. C. Gather, I. D. W. Samuel and E. Zysman-Colman, *ACS Appl. Mater. Interfaces,* 2018, **10**, 33360.

121. Y. J. Cho, B. D. Chin, S. K. Jeon and J. Y. Lee, *Adv. Funct. Mater.,* 2015, **25**, 6786.

122. H. Wang, L. Xie, Q. Peng, L. Meng, Y. Wang, Y. Yi and P. Wang, *Adv. Mater.,* 2014, **26**, 5198.

123. Q. Zhang, B. Li, S. Huang, H. Nomura, H. Tanaka and C. Adachi, *Nat. Photonics,* 2014, **8**, 326.

124. R. S. Nobuyasu, Z. Ren, G. C. Griffiths, A. S. Batsanov, P. Data, S. Yan, A. P. Monkman, M. R. Bryce and F. B. Dias, *Adv. Opt. Mater.,* 2016, **4**, 597.

125. P. L. dos Santos, J. S. Ward, D. G. Congrave, A. S. Batsanov, J. Eng, J. E. Stacey, T. J. Penfold, A. P. Monkman and M. R. Bryce, *Adv. Sci.,* 2018, **5**, 1700989.

126. C. M. Marian, *J. Phys. Chem. C,* 2016, **120**, 3715.

127. N. Aizawa, A. Matsumoto and T. Yasuda, *Sci. Adv.,* 2021, **7**, eabe5769.

128. S. Y. Lee, T. Yasuda, Y. S. Yang, Q. Zhang and C. Adachi, *Angew. Chem. Int. Ed.,,* 2014, **53**, 6402.

129. Y. Yuan, X. Tang, X. Y. Du, Y. Hu, Y. J. Yu, Z. Q. Jiang, L. S. Liao and S. T. Lee, *Adv. Opt. Mater.,* 2019, **7**, 1801536.

130. H. Kaji, H. Suzuki, T. Fukushima, K. Shizu, K. Suzuki, S. Kubo, T. Komino, H. Oiwa, F. Suzuki, A. Wakamiya, Y. Murata and C. Adachi, *Nat. Commun.,* 2015, **6**, 8476.

131. J. W. Sun, J. Y. Baek, K.-H. Kim, C.-K. Moon, J.-H. Lee, S.-K. Kwon, Y.-H. Kim and J.-J. Kim, *Chem. Mater.,* 2015, **27**, 6675.

132. T. A. Lin, T. Chatterjee, W. L. Tsai, W. K. Lee, M. J. Wu, M. Jiao, K. C. Pan, C. L. Yi, C. L. Chung, K. T. Wong and C. C. Wu, *Adv. Mater.,* 2016, **28**, 6976.

133. T.-L. Wu, M.-J. Huang, C.-C. Lin, P.-Y. Huang, T.-Y. Chou, R.-W. Chen-Cheng, H.-W. Lin, R.-S. Liu and C.-H. Cheng, *Nat. Photonics,* 2018, **12**, 235.

134. F. Tenopala-Carmona, O. S. Lee, E. Crovini, A. M. Neferu, C. Murawski, Y. Olivier, E. Zysman-Colman and M. C. Gather, *Adv. Mater.,* 2021, **33**, 2100677.

135. D. Karthik, D. H. Ahn, J. H. Ryu, H. Lee, J. H. Maeng, J. Y. Lee and J. H. Kwon, *J. Mater. Chem. C.,* 2020, **8**, 2272.

136. G. Meng, X. Chen, X. Wang, N. Wang, T. Peng and S. Wang, *Adv. Opt. Mater.,* 2019, **7**, 1900130.

137. J. U. Kim, I. S. Park, C. Y. Chan, M. Tanaka, Y. Tsuchiya, H. Nakanotani and C. Adachi, *Nat. Commun.,* 2020, **11**, 1765.

138. H. Hirai, K. Nakajima, S. Nakatsuka, K. Shiren, J. Ni, S. Nomura, T. Ikuta and T. Hatakeyama, *Angew. Chem. Int. Ed.,* 2015, **54**, 13581.

139. M. Numata, T. Yasuda and C. Adachi, *Chem. Commun.,* 2015, **51**, 9443.

140. Y. Kitamoto, T. Namikawa, D. Ikemizu, Y. Miyata, T. Suzuki, H. Kita, T. Sato and S. Oi, *J. Mater. Chem. C.,* 2015, **3**, 9122.

141. K. Nasu, T. Nakagawa, H. Nomura, C.-J. Lin, C.-H. Cheng, M.-R. Tseng, T. Yasuda and C. Adachi, *Chem. Commun.,* 2013, **49**, 10385.

142. G. Mehes, H. Nomura, Q. Zhang, T. Nakagawa and C. Adachi, *Angew. Chem. Int. Ed.,* 2012, **51**, 11311.

143. T. Nakagawa, S. Y. Ku, K. T. Wong and C. Adachi, *Chem. Commun.,* 2012, **48**, 9580.

144. H. Ohkuma, T. Nakagawa, K. Shizu, T. Yasuda and C. Adachi, *Chem. Lett.,* 2014, **43**, 1017.

145. N. Sharma, M. Maciejczyk, D. Hall, W. Li, V. Liegeois, D. Beljonne, Y. Olivier, N. Robertson, I. D. W. Samuel and E. Zysman-Colman, *ACS Appl. Mater. Interfaces,* 2021.

146. T. Hatakeyama, K. Shiren, K. Nakajima, S. Nomura, S. Nakatsuka, K. Kinoshita, J. Ni, Y. Ono and T. Ikuta, *Adv. Mater.,* 2016, **28**, 2777.

147. A. Pershin, D. Hall, V. Lemaur, J.-C. Sancho-Garcia, L. Muccioli, E. Zysman-Colman, D. Beljonne and Y. Olivier, *Nat. Commun.,* 2019, **10**, 597.

148. Y. J. Cho, S. K. Jeon, S.-S. Lee, E. Yu and J. Y. Lee, *Chem. Mater.,* 2016, **28**, 5400.

149. D. Hall, S. M. Suresh, P. L. dos Santos, E. Duda, S. Bagnich, A. Pershin, P. Rajamalli, D. B. Cordes, A. M. Z. Slawin, D. Beljonne, A. Köhler, I. D. W. Samuel, Y. Olivier and E. Zysman-Colman, *Adv. Opt. Mater.,* 2020, **8**, 1901627.

150. Y. Kondo, K. Yoshiura, S. Kitera, H. Nishi, S. Oda, H. Gotoh, Y. Sasada, M. Yanai and T. Hatakeyama, *Nat. Photonics,* 2019, **13**, 678.

151. M. Yang, I. S. Park and T. Yasuda, *J. Am. Chem. Soc.,* 2020, **142**, 19468.

152. Y. Xu, C. Li, Z. Li, Q. Wang, X. Cai, J. Wei and Y. Wang, *Angew. Chem. Int. Ed.,* 2020, **59**, 17442.

153. N. Ikeda, S. Oda, R. Matsumoto, M. Yoshioka, D. Fukushima, K. Yoshiura, N. Yasuda and T. Hatakeyama, *Adv. Mater.,* 2020, **32**, 2004072.

154. S. Nakatsuka, H. Gotoh, K. Kinoshita, N. Yasuda and T. Hatakeyama, *Angew. Chem. Int. Ed.,* 2017, **56**, 5087.

155. S. H. Han, J. H. Jeong, J. W. Yoo and J. Y. Lee, *J. Mater. Chem. C.,* 2019, **7**, 3082.

156. K. Matsui, S. Oda, K. Yoshiura, K. Nakajima, N. Yasuda and T. Hatakeyama, *J. Am. Chem. Soc.,* 2018, **140**, 1195.

157. Y. Xu, Z. Cheng, Z. Li, B. Liang, J. Wang, J. Wei, Z. Zhang and Y. Wang, *Adv. Opt. Mater.,* 2020, **8**, 1902142.

158. S. Xu, Q. Yang, Y. Zhang, H. Li, Q. Xue, G. Xie, M. Gu, J. Jin, L. Huang and R. Chen, *Chin. Chem. Lett.,* 2021, **32**, 1372.

159. P. Jiang, L. Zhan, X. Cao, X. Lv, S. Gong, Z. Chen, C. Zhou, Z. Huang, F. Ni, Y. Zou and C. Yang, *Adv. Opt. Mater.,* 2021, **9**, 2100825.

160. T. Hua, L. Zhan, N. Li, Z. Huang, X. Cao, Z. Xiao, S. Gong, C. Zhou, C. Zhong and C. Yang, *Chem. Eng. J.,* 2021, **426**, 131169.

161. Y. Zhang, D. Zhang, J. Wei, Z. Liu, Y. Lu and L. Duan, *Angew. Chem. Int. Ed.,* 2019, **58**, 16912.

162. C. Li, Y. Wang, Y. Xu, Z. Li, J. Wang, J. Xue, Q. Wang and X. Cai, *ChemRxiv. Preprint,* 2021, 10.26434/chemrxiv.14050712.v1

163. Y. Zhang, D. Zhang, J. Wei, X. Hong, Y. Lu, D. Hu, G. Li, Z. Liu, Y. Chen and L. Duan, *Angew. Chem. Int. Ed.,* 2020, **59**, 17499.

164. T. Jella, M. Srikanth, R. Bolligarla, Y. Soujanya, S. P. Singh and L. Giribabu, *Dalton Trans.,* 2015, **44**, 14697.

165. Y. Zhang, D. Zhang, T. Huang, G. Li, C. Zhang, Y. Lu, Z. Liu and L. Duan, *ChemRxiv. Preprint,* 2020, 10.26434/chemrxiv.13202975.v1.

166. S. Oda, B. Kawakami, R. Kawasumi, R. Okita and T. Hatakeyama, *Org. Lett.,* 2019, **21**, 9311.

167. M. Nagata, H. Min, E. Watanabe, H. Fukumoto, Y. Mizuhata, N. Tokitoh, T. Agou and T. Yasuda, *Angew. Chem. Int. Ed.,* 2021, **60**, 20820.

168. S. N. Zou, C. C. Peng, S. Y. Yang, Y. K. Qu, Y. J. Yu, X. Chen, Z. Q. Jiang and L. S. Liao, *Org. Lett.,* 2021, **23**, 958.

169. H. Min, I. S. Park and T. Yasuda, *Angew. Chem. Int. Ed.,* 2021, **60**, 7643.

170. H. Nakanotani, T. Higuchi, T. Furukawa, K. Masui, K. Morimoto, M. Numata, H. Tanaka, Y. Sagara, T. Yasuda and C. Adachi, *Nat. Commun.,* 2014, **5**, 4016.

171. J. Hu, S. Hu, C. Lu, Y. Huang, K. Xu and X. Wang, *J. Lumin.,* 2018, **197**, 187.

172. D. Zhang, L. Duan, C. Li, Y. Li, H. Li, D. Zhang and Y. Qiu, *Adv. Mater.,* 2014, **26**, 5050.

173. S. J. Yoon, J. H. Kim, W. J. Chung and J. Y. Lee, *Chemistry,* 2021, **27**, 3065.

174. A. Dreuw and M. Head-Gordon, *Chem. Rev.,* 2005, **105**, 4009.

175. H. Sun, C. Zhong and J.-L. Brédas, *J. Chem. Theory Comput.,* 2015, **11**, 3851.

176. Y. Olivier, B. Yurash, L. Muccioli, G. D'Avino, O. Mikhnenko, J. C. Sancho-García, C. Adachi, T. Q. Nguyen and D. Beljonne, *Phys. Rev. Mater.,* 2017, **1**, 075602.

177. P. K. Samanta, D. Kim, V. Coropceanu and J. L. Bredas, *J. Am. Chem. Soc.,* 2017, **139**, 4042.

178. Y. Olivier, M. Moral, L. Muccioli and J.-C. Sancho-García, *J. Mater. Chem. C.,* 2017, **5**, 5718.

179. W. Koch and M. C. Holthausen, *A Chemist's Guide to Density Functional Theory*. Wiley: 2001.

180. O. Christiansen, H. Koch and P. J¢rgensen, *Chem. Phys. Lett.,* 1995, **243**, 409

181. J. Sanz-Rodrigo, Y. Olivier and J. C. Sancho-Garcia, *Molecules,* 2020, **25**, 1006.

182. *TURBOMOLE V7.4*, TURBOMOLE GmbH, since 2007; avaliable from http://www.turbomole.com: a development of University of Karlsruhe and Forschungszentrum Karlsruhe GmbH, 2017.

183. S. Grimme, J. Antony, S. Ehrlich and H. Krieg, *J. Chem. Phys.,* 2010, **132**, 154104.

184. C. Hättig and F. Weigend, *J. Chem. Phys.,* 2000, **113**, 5154.

185. S. Grimme, L. Goerigk and R. F. Fink, *Wiley Interdiscip. Rev. Comput. Mol. Sci.,* 2012, **2**, 886.

186. A. Hellweg, *J. Chem. Phys.,* 2011, **134**, 064103.

187. K. Burke, J. P. Perdew and M. Ernzerhof, *Int. J. Quantum Chem.,* 1997, **61**, 287.

188. A. D. Becke, *J. Chem. Phys.,* 1993, **98**, 5648.

189. C. Adamo and V. Barone, *J. Chem. Phys.,* 1999, **110**, 6158.

190. Y. Zhao and D. G. Truhlar, *Theor. Chem. Acc.,* 2008, **120**, 215.

191. E. Bremond, A. J. Perez-Jimenez, J. C. Sancho-Garcia and C. Adamo, *J. Chem. Phys.,* 2019, **150**, 201102.

192. O. A. Vydrov and G. E. Scuseria, *J. Chem. Phys.,* 2006, **125**, 234109.

193. T. Yanai, D. P. Tew and N. C. Handy, *Chem. Phys. Lett.,* 2004, **393**, 51.

194. T. M. Henderson, A. F. Izmaylov, G. Scalmani and G. E. Scuseria, *J. Chem. Phys.,* 2009, **131**, 044108.

195. O. S. Bokareva, G. Grell, S. I. Bokarev and O. Kuhn, *J. Chem. Theory Comput.,* 2015, **11**, 1700.

196. M. A. L. Marques, C. A. Ullrich, F. Nogueira, A. Rubio, K. Burke and E. K. U. Gross, *Time-Dependent Density Functional Theory*. Springer Berlin Heidelberg: 2006.

197. R. Bauernschmitt and R. Ahlrich, *Chem. Phys. Lett.,* 1996, **256**, 454.

198. M. Moral, L. Muccioli, W. J. Son, Y. Olivier and J. C. Sancho-García, *J. Chem. Theory Comput.,* 2015, **11**, 168.

199. D. C. Young, *Computational Chemistry: A Practical Guide for Applying Techniques to Real World Problems*. Wiley: 2001.

200. J. Thorn H. Dunning, *J. Chem. Phys.,* 1989, **90**, 1007.

201. T. H. Dunning, *J. Chem. Phys.,* 1989, **90**, 1007.

202. Y. Olivier, J. C. Sancho-Garcia, L. Muccioli, G. D'Avino and D. Beljonne, *J. Phys. Chem. Lett.,* 2018, **9**, 6149.

203. M. Head-Gordon, A. M. Grana, D. Maurice and C. A. White, *J. Phys. Chem.,* 1995, **99**, 14261.

204. M. Savarese, C. A. Guido, E. Brémond, I. Ciofini and C. Adamo, *J. Phys. Chem. A.,* 2017, **121**, 7543.

205. T. Le Bahers, C. Adamo and I. Ciofini, *J. Chem. Theory Comput.,* 2011, **7**, 2498.

206. T. Etienne, X. Assfeld and A. Monari, *J. Chem. Theory Comput.,* 2014, **10**, 3896.

207. T. Etienne, X. Assfeld and A. Monari, *J. Chem. Theory Comput.,* 2014, **10**, 3906.

208. K. Shizu, H. Tanaka, M. Uejima, T. Sato, K. Tanaka, H. Kaji and C. Adachi, *J. Phys. Chem. C,* 2015, **119**, 1291.

209. K. Suzuki, S. Kubo, K. Shizu, T. Fukushima, A. Wakamiya, Y. Murata, C. Adachi and H. Kaji, *Angew. Chem. Int. Ed.,* 2015, **54**, 15231.

210. W. J. Park, Y. Lee, J. Y. Kim, D. W. Yoon, J. Kim, S. H. Chae, H. Kim, G. Lee, S. Shim, J. H. Yang and S. J. Lee, *Synth. Met.,* 2015, **209**, 99.

211. S. Youn Lee, T. Yasuda, H. Nomura and C. Adachi, *Appl. Phys. Lett.,* 2012, **101**, 093306.

212. T. Jiang, Y. Liu, Z. Ren and S. Yan, *Polym. Chem.,* 2020, **11**, 1555.

213. T. Cardeynaels, S. Paredis, J. Deckers, S. Brebels, D. Vanderzande, W. Maes and B. Champagne, *Phys. Chem. Chem. Phys.,* 2020, **22**, 16387.

214. T. Hosokai, H. Matsuzaki, H. Nakanotani, K. Tokumaru, T. Tsutsui, A. Furube, K. Nasu, H. Nomura, M. Yahiro and C. Adachi, *Sci. Adv.,* 2017, **3**, 1603282.

215. M. K. Etherington, F. Franchello, J. Gibson, T. Northey, J. Santos, J. S. Ward, H. F. Higginbotham, P. Data, A. Kurowska, P. L. Dos Santos, D. R. Graves, A. S. Batsanov, F. B. Dias, M. R. Bryce, T. J. Penfold and A. P. Monkman, *Nat. Commun.,* 2017, **8**, 14987.

216. N. G. Connelly and W. E. Geiger, *Chem. Rev.,* 1996, **96**, 877

217. K. Karon and M. Lapkowski, *J. Solid State Electrochem.,* 2015, **19**, 2601.

218. J. F. Ambrose and R. F. Nelson, *J. Electrochem. Soc.,* 1968, **115**, 1159.

219. K. Karon, M. Lapkowski and G. Juozas, *Electrochim. Acta,* 2014, **123**, 176.

220. C. M. Cardona, W. Li, A. E. Kaifer, D. Stockdale and G. C. Bazan, *Adv. Mater.,* 2011, **23**, 2367.

221. E. Duda, D. Hall, S. Bagnich, C. L. Carpenter-Warren, R. Saxena, M. Y. Wong, D. B. Cordes, A. M. Z. Slawin, D. Beljonne, Y. Olivier, E. Zysman-Colman and A. Köhler, *J. Phys. Chem. B,* 2021, 10.1021/acs.jpcb.1c05749.

222. K. F. Freed and J. Jortner, *J. Chem. Phys.,* 1970, **52**, 6272.

223. S. H. Kim, J. Jang and J. Y. Lee, *Appl. Phys. Lett.,* 2007, **90**, 223505.

224. F. Rodriguez Prieto, M. Mosquera and M. Novo, *J. Phys. Chem.,* 1990, **94**, 8536.

225. Y. Qu, C. Wang, K. Zhao, Y. Wu, G. Huang, X. Han and H. Wu, *J. Coord. Chem.,* 2019, **72**, 3046.

226. A. M. Mansour and K. Radacki, *Dalton Trans.,* 2020, **49**, 4491.

227. V. V. Pavlishchuk and A. W. Addison, *Inorg. Chim. Acta.,* 2000, **298**, 97.

228. K. C. Dash and H. Mohanta, *J. Inoorg. Nuc. Chem.,* 1978, **40**, 499.

229. S. K. Dogra, *J. Photochem. Photobiol. A.,* 2005, **172**, 196.

230. Q. D. Liu, M. S. Mudadu, R. Thummel, Y. Tao and S. Wang, *Adv. Funct. Mater.,* 2005, **15**, 143.

231. P. Rajamalli, N. Senthilkumar, P. Y. Huang, C. C. Ren-Wu, H. W. Lin and C. H. Cheng, *J. Am. Chem. Soc.,* 2017, **139**, 10948.

232. T. Ohsawa, H. Sasabe, T. Watanabe, K. Nakao, R. Komatsu, Y. Hayashi, Y. Hayasaka and J. Kido, *Adv. Opt. Mater.,* 2019, **7**, 1801282.

233. C. Li, D. Li, Y. Shi and Y. Liu, *Org. Electron.,* 2018, **54**, 177.

234. M. Tian, C. Wang, L. Wang, K. Luo, A. Zhao and C. Guo, *Luminescence,* 2014, **29**, 540.

235. F. B. Dias, J. Santos, D. R. Graves, P. Data, R. S. Nobuyasu, M. A. Fox, A. S. Batsanov, T. Palmeira, M. N. Berberan-Santos, M. R. Bryce and A. P. Monkman, *Adv. Sci.,* 2016, **3**, 1600080.

236. R. Dhali, D. K. A. Phan Huu, F. Bertocchi, C. Sissa, F. Terenziani and A. Painelli, *Phys. Chem. Chem. Phys.,* 2021, **23**, 378.

237. Y.-S. Lee, Y.-H. Cho, S. Lee, J.-K. Bin, J. Yang, G. Chae and C.-H. Cheon, *Tetrahedron,* 2015, **71**, 532.

238. H. Tanaka, K. Shizu, H. Miyazaki and C. Adachi, *Chem. Commun.,* 2012, **48**, 11392.

239. W. H. Melhuish, *J. Phys. Chem.,* 1961, **65**, 229.

240. K. Trofymchuk, A. Reisch, I. Shulov, Y. Mély and A. S. Klymchenko, *Nanoscale,* 2014, **6**, 12934.

241. Y. Wada, H. Nakagawa, S. Matsumoto, Y. Wakisaka and H. Kaji, *Nat. Photonics,* 2020, **14**, 643.

242. X. Liang, Z. P. Yan, H. B. Han, Z. G. Wu, Y. X. Zheng, H. Meng, J. L. Zuo and W. Huang, *Angew. Chem. Int. Ed.,* 2018, **57**, 11316.

243. S. Oda, W. Kumano, T. Hama, R. Kawasumi, K. Yoshiura and T. Hatakeyama, *Angew. Chem. Int. Ed.,* 2021, **60**, 2882.

244. J. E. Field and D. Venkataraman, *Chem. Mater.,* 2002, **14**, 962.

245. X. Li, Y. Z. Shi, K. Wang, M. Zhang, C. J. Zheng, D. M. Sun, G. L. Dai, X. C. Fan, D. Q. Wang, W. Liu, Y. Q. Li, J. Yu, X. M. Ou, C. Adachi and X. H. Zhang, *ACS Appl. Mater. Interfaces,* 2019, **11**, 13472.

246. J. A. Knoller, G. Meng, X. Wang, D. Hall, A. Pershin, D. Beljonne, Y. Olivier, S. Laschat, E. Zysman-Colman and S. Wang, *Angew. Chem. Int. Ed.,* 2020, **59**, 3156.

247. E. Hamzehpoor and D. F. Perepichka, *Angew. Chem. Int. Ed.,* 2020, **59**, 9977.

248. P. L. Santos, J. S. Ward, P. Data, A. S. Batsanov, M. R. Bryce, F. B. Dias and A. P. Monkman, *J. Mater. Chem. C.,* 2016, **4**, 3815.

249. M. C. Gather and S. Reineke, *J. Photonics Energy,* 2015, **5**, 057607

250. Y. Yuan, X. Tang, X.-Y. Du, Y. Hu, Y.-J. Yu, Z.-Q. Jiang, L.-S. Liao and S.-T. Lee, *Adv. Optical Mater.,* 2019, 1801536.

251. H. Tanaka, S. Oda, G. Ricci, H. Gotoh, K. Tabata, R. Kawasumi, D. Beljonne, Y. Olivier and T. Hatakeyama, *Angew. Chem. Int. Ed.,* 2021, **60**, 17910.

252. J. Sanz-Rodrigo, G. Ricci, Y. Olivier and J. C. Sancho-Garcia, *J. Phys. Chem. A.,* 2021, **125**, 513.

253. S. M. Suresh, E. Duda, D. Hall, Z. Yao, S. Bagnich, A. M. Z. Slawin, H. Bassler, D. Beljonne, M. Buck, Y. Olivier, A. Kohler and E. Zysman-Colman, *J. Am. Chem. Soc.,* 2020, **142**, 6588.

254. D. Sun, S. M. Suresh, D. Hall, M. Zhang, C. Si, D. B. Cordes, A. M. Z. Slawin, Y. Olivier, X. Zhang and E. Zysman-Colman, *Mater. Chem. Front.,* 2020, **4**, 2018.

255. J. Dos Santos, E. Zysman-Colman, D. Sun, J. Naranjo, M. Fuchter, D. Hall, F. Zinna, S. Ryan, W. Shi, T. Matulaitis, D. B. Cordes, A. Slawin, D. Beljonne, Y. Olivier and S. Warriner, *J. Mater. Chem. C.,* 2022, 10.1039/d2tc00198e.

256. G. Meng, L. Liu, Z. He, D. Hall, X. Wang, T. Peng, X. Yin, P. Chen, D. Beljonne, Y. Olivier, E. Zysman-Colman, N. Wang and S. Wang, *Chem. Sci.,* 2022, **13**, 1665.

257. Y. Zhang, D. Zhang, T. Huang, A. J. Gillett, Y. Liu, D. Hu, L. Cui, Z. Bin, G. Li, J. Wei and L. Duan, *Angew. Chem. Int. Ed.,* 2021, **60**, 20498.

258. H. Noda, X.-K. Chen, H. Nakanotani, T. Hosokai, M. Miyajima, N. Notsuka, Y. Kashima, J.-L. Brédas and C. Adachi, *Nat. Mater.,* 2019, **18**, 1084.

259. I. Kim, K. H. Cho, S. O. Jeon, W.-J. Son, D. Kim, Y. M. Rhee, I. Jang, H. Choi and D. S. Kim, *JACS Au,* 2021, **1**, 987.

260. T. Northey and T. J. Penfold, *Org. Electron.,* 2018, **59**, 45.

261. G. Ricci, E. San-Fabian, Y. Olivier and J. C. Sancho-Garcia, *ChemPhysChem,* 2021, **22**, 553.

262. S. Pios, X. Huang, A. L. Sobolewski and W. Domcke, *Phys. Chem. Chem. Phys.,* 2021, **23**, 12968.

263. J. Ehrmaier, E. J. Rabe, S. R. Pristash, K. L. Corp, C. W. Schlenker, A. L. Sobolewski and W. Domcke, *J. Phys. Chem. A.,* 2019, **123**, 8099.

264. R. Pollice, P. Friederich, C. Lavigne, G. d. P. Gomes and A. Aspuru-Guzik, *Matter,* 2021, **4**, 1654.

265. P. de Silva, *J. Phys. Chem. Lett.,* 2019, **10**, 5674.

266. J. Li, Q. Zhang, H. Nomura, H. Miyazaki and C. Adachi, *Appl. Phys. Lett.,* 2014, **105**, 013301.

267. H. J. Kim, M. Godumala, S. K. Kim, J. Yoon, C. Y. Kim, H. Park, J. H. Kwon, M. J. Cho and D. H. Choi, *Adv. Opt. Mater.,* 2020, **8**, 1902175.

268. D. Song, Y. Yu, L. Yue, D. Zhong, Y. Zhang, X. Yang, Y. Sun, G. Zhou and Z. Wu, *J. Mater. Chem. C.,* 2019, **7**, 11953.

269. Y. Zhang, D. Zhang, T. Huang, A. J. Gillett, Y. Liu, D. Hu, L. Cui, Z. Bin, G. Li, J. Wei and L. Duan, *Angew. Chem. Int. Ed.,* 2021.

270. D. Zhang, X. Song, A. J. Gillett, B. H. Drummond, S. T. E. Jones, G. Li, H. He, M. Cai, D. Credgington and L. Duan, *Adv. Mater.,* 2020, **32**, e1908355.

271. C.-Y. Chan, M. Tanaka, Y.-T. Lee, Y.-W. Wong, H. Nakanotani, T. Hatakeyama and C. Adachi, *Nat. Photonics,* 2021, **15**, 203.

272. S. O. Jeon, K. H. Lee, J. S. Kim, S.-G. Ihn, Y. S. Chung, J. W. Kim, H. Lee, S. Kim, H. Choi and J. Y. Lee, *Nat. Photonics,* 2021, **15**, 208.

273. V. V. Patil, H. L. Lee, I. Kim, K. H. Lee, W. J. Chung, J. Kim, S. Park, H. Choi, W. J. Son, S. O. Jeon and J. Y. Lee, *Adv. Sci.,* 2021, **8**, 2101137.

274. V. V. Patil, J. Lim and J. Y. Lee, *ACS Appl. Mater. Interfaces,* 2021, **13**, 14440.

275. H. L. Lee, W. J. Chung and J. Y. Lee, *Small,* 2020, **16**, 1907569.

276. V. V. Patil, K. H. Lee and J. Y. Lee, *Adv. Opt. Mater.,* 2020, **8**.

277. J. A. Seo, Y. Im, S. H. Han, C. W. Lee and J. Y. Lee, *ACS Appl. Mater. Interfaces,* 2017, **9**, 37864.

278. K. Stavrou, A. Danos, T. Hama, T. Hatakeyama and A. Monkman, *ACS Appl. Mater. Interfaces,* 2021, **13**, 8643.

279. C. Maeda, T. Todaka and T. Ema, *Org. Lett.,* 2015, **17**, 3090.

280. S. I. Wharton, J. B. Henry, H. McNab and A. R. Mount, *Chem. Eur. J.,* 2009, **15**, 5482.

281. P. Pander, R. Motyka, P. Zassowski, M. K. Etherington, D. Varsano, T. J. da Silva, M. J. Caldas, P. Data and A. P. Monkman, *J. Phys. Chem. C,* 2018, **122**, 23934.

282. P. Stachelek, J. S. Ward, P. L. Dos Santos, A. Danos, M. Colella, N. Haase, S. J. Raynes, A. S. Batsanov, M. R. Bryce and A. P. Monkman, *ACS Appl. Mater. Interfaces,* 2019, **11**, 27125.

283. J. Wei, C. Zhang, D. Zhang, Y. Zhang, Z. Liu, Z. Li, G. Yu and L. Duan, *Angew. Chem. Int. Ed.,* 2021, **60**, 12269.

284. A. Monkman, *ACS Appl. Mater. Interfaces,* 2021, doi.org/10.1021/acsami.1c09189.

285. N. Haase, A. Danos, C. Pflumm, P. Stachelek, W. Brütting and A. P. Monkman, *Mater. Horiz.,* 2021, **8**, 1805.

286. *US Pat*., US20210355378, 2019.

287. S. M. Bonesi and R. Erra-Balsells, *Journal of Heterocyclic Chemistry,* 2001, **38**, 77.

288. K. Albrecht, K. Matsuoka, K. Fujita and K. Yamamoto, *Angew. Chem. Int. Ed.,,* 2015, **54**, 5677.

289. L. J. O'Driscoll, X. Wang, M. Jay, A. S. Batsanov, H. Sadeghi, C. J. Lambert, B. J. Robinson and M. R. Bryce, *Angew. Chem. Int. Ed.,* 2020, **59**, 882.

290. J. S. Ward, R. S. Nobuyasu, M. A. Fox, J. A. Aguilar, D. Hall, A. S. Batsanov, Z. Ren, F. B. Dias and M. R. Bryce, *J. Org. Chem.,* 2019, **84**, 3801.

291. M. Xiong, Z. Gao, X. Liang, P. Cai, H. Zhu and Y. Pan, *Chem. Commun.,* 2018, **54**, 9679.

292. S. Hirata, Y. Sakai, K. Masui, H. Tanaka, S. Y. Lee, H. Nomura, N. Nakamura, M. Yasumatsu, H. Nakanotani, Q. Zhang, K. Shizu, H. Miyazaki and C. Adachi, *Nat. Mater.,* 2015, **14**, 330.

293. D. A. Roberts, B. S. Pilgrim, J. D. Cooper, T. K. Ronson, S. Zarra and J. R. Nitschke, *J. Am. Chem. Soc.,* 2015, **137**, 10068.

294. J.-F. Ayme, J. E. Beves, D. A. Leigh, R. T. McBurney, K. Rissanen and D. Schultz, *Nat. Chem.,* 2012, **4**, 15.

295. P. Zhang, E. A. Terefenko, J. Bray, D. Deecher, A. Fensome, J. Harrison, C. Kim, E. Koury, L. Mark, C. C. McComas, C. A. Mugford, E. J. Trybulski, A. T. Vu, G. T. Whiteside and P. E. Mahaney, *J. Med. Chem.,* 2009, **52**, 5703.

296. Q. Sun, R. Wu, S. Cai, Y. Lin, L. Sellers, K. Sakamoto, B. He and B. R. Peterson, *J. Med. Chem.,* 2011, **54**, 1126.

297. H. Liu, N. Fridman, M. Tamm and M. S. Eisen, *Organometallics,* 2017, **36**, 3896.

298. L. Wang, E. Ji, N. Liu and B. Dai, *Synthesis,* 2016, **48**, 737.

299. J. Lv, Q. Liu, J. Tang, F. Perdih and K. Kranjc, *Tetrahedron Lett.,* 2012, **53**, 5248.

300. C. Zhao, T. Schwartz, B. Stoger, F. J. White, J. Chen, D. Ma, J. Frohlich and P. Kautny, *J. Mater. Chem. C.,* 2018, **6**, 9914.

301. Z. Huang, B. Wang, Q. Zhang, S. Xiang, X. Lv, L. Ma, B. Yang, Y. Gao and L. Wang, *Dyes Pigm,* 2017, **140**, 328.

302. Y. Sakai, Y. Sagara, H. Nomura, N. Nakamura, Y. Suzuki, H. Miyazaki and C. Adachi, *Chem. Commun.,* 2015, **51**, 3181.

303. M. C. Burla, R. Caliandro, M. Camalli, B. Carrozzini, G. L. Cascarano, C. Giacovazzo, M. Mallamo, A. Mazzone, G. Polidori and R. Spagna, *J. Appl. Crystallogr.,* 2012, **45**, 357.

304. G. Sheldrick, *Acta Crystallogr., Sect. A,* 2015, **71**, 3.

305. G. Sheldrick, *Acta Crystallogr., Sect. C,* 2015, **71**, 3.

306. D. Kratzert, J. J. Holstein and I. Krossing, *J. Appl. Crystallogr.,* 2015, **48**, 933.

307. D. Kratzert and I. Krossing, *J. Appl. Crystallogr.,* 2018, **51**, 928.

308. A. L. Spek, *Acta Crystallogr., Sect. C, Struct. Chem.,* 2015, **71**, 9.

309. A. L. Spek, *Acta Crystallogr D Biol Crystallogr,* 2009, **65**, 148.

310. O. V. Dolomanov, L. J. Bourhis, R. J. Gildea, J. A. K. Howard and H. Puschmann, *J. Appl. Crystallogr.,* 2009, **42**, 339.

311. G. A. Crosby and J. N. Demas, *J. Phys. Chem.,* 1971, **75**, 991.

312. N. C. Greenham, I. D. W. Samuel, G. R. Hayes, R. T. Phillips, Y. A. R. R. Kessener, S. C. Moratti, A. B. Holmes and R. H. Friend, *Chem. Phys. Lett.,* 1995, **241**, 89.

313. M. J. Frisch, G. W. Trucks, H. B. Schlegel, G. E. Scuseria, M. A. Robb, J. R. Cheeseman, G. Scalmani, V. Barone, B. Mennucci, G. A. Petersson, H. Nakatsuji, M. Caricato, X. Li, H. P. Hratchian, A. F. Izmaylov, J. Bloino, G. Zheng, J. L. Sonnenberg, M. Hada, M. Ehara, K. Toyota, R. Fukuda, J. Hasegawa, M. Ishida, T. Nakajima, Y. Honda, O. Kitao, H. Nakai, T. Vreven, J. A. M. Jr., J. E. Peralta, F. Ogliaro, M. Bearpark, J. J. Heyd, E. Brothers, K. N. Kudin, V. N. Staroverov, R. Kobayashi, J. Normand, K. Raghavachari, A. Rendell, J. C. Burant, S. S. Iyengar, J. Tomasi, M. Cossi, N. Rega, J. M. Millam, M. Klene, J. E. Knox, J. B. Cross, V. Bakken, C. Adamo, J. Jaramillo, R. Gomperts, R. E. Stratmann, O. Yazyev, A. J. Austin, R. Cammi, C. Pomelli, J. W. Ochterski, R. L. Martin, K. Morokuma, V. G. Zakrzewski, G. A. Voth, P. Salvador, J. J. Dannenberg, S. Dapprich, A. D. Daniels,

Ö. Farkas, J. B. Foresman, J. V. Ortiz, J. Cioslowski and D. J. Fox *Gaussian 09*, Gaussian Inc., Wallingford, CT: 2009.

314. M. J. Frisch, G. W. Trucks, H. B. Schlegel, G. E. Scuseria, M. A. Robb, J. R. Cheeseman, G. Scalmani, V. Barone, G. A. Petersson, H. Nakatsuji, X. Li, M. Caricato, A. V. Marenich, J. Bloino, B. G. Janesko, R. Gomperts, B. Mennucci, H. P. Hratchian, J. V. Ortiz, A. F. Izmaylov, J. L. Sonnenberg, Williams, F. Ding, F. Lipparini, F. Egidi, J. Goings, B. Peng, A. Petrone, T. Henderson, D. Ranasinghe, V. G. Zakrzewski, J. Gao, N. Rega, G. Zheng, W. Liang, M. Hada, M. Ehara, K. Toyota, R. Fukuda, J. Hasegawa, M. Ishida, T. Nakajima, Y. Honda, O. Kitao, H. Nakai, T. Vreven, K. Throssell, J. A. Montgomery Jr., J. E. Peralta, F. Ogliaro, M. J. Bearpark, J. J. Heyd, E. N. Brothers, K. N. Kudin, V. N. Staroverov, T. A. Keith, R. Kobayashi, J. Normand, K. Raghavachari, A. P. Rendell, J. C. Burant, S. S. Iyengar, J. Tomasi, M. Cossi, J. M. Millam, M. Klene, C. Adamo, R. Cammi, J. W. Ochterski, R. L. Martin, K. Morokuma, O. Farkas, J. B. Foresman and D. J. Fox *Gaussian 16 Rev. A.01*, Wallingford, CT, 2016.

315. M. A. Rohrdanz, K. M. Martins and J. M. Herbert, *J. Chem. Phys.,* 2009, **130**, 054112.

316. G. A. Petersson and M. A. AI-Laham, *J. Chem. Phys.,* 1991, **94**, 6081.

317. A. K. Dhara and S. K. Ghosh, *Phys. Rev. A,* 1987, **35**, 442.

318. S. Hirata and M. Head-Gordon, *Chem. Phys. Lett.,* 1999, **314**, 291.

319. R Dennington, T. Keith and J. Millam *GaussView, Version 6.1.1*, KS: Semichem Inc.: Shawnee Mission, 2019.

320. A. Hellweg, S. A. Grun and C. Hattig, *Phys. Chem. Chem. Phys.,* 2008, **10**, 4119.

321. C. Hättig, *J. Chem. Phys.,* 2003, **118**, 7751.

322. K. Momma and F. Izumi, *J. Appl. Crystallogr.,* 2011, **44**, 1272.